THE TUMPANGPITU PORPHYRY GOLD-COPPER-MOLYBDENUM AND HIGH-SULFIDATION EPITHERMAL GOLD-SILVER DEPOSIT, TUJUH BUKIT, SOUTHEAST JAVA, INDONESIA

by

Rachel L. Harrison MSci, MEconGeol

A thesis submitted in fulfilment of the degree of Doctor of Philosophy

CODES ARC Centre of Excellence in Ore Deposits

University of Tasmania, Australia

October, 2017

Supervisor: Professor David R. Cooke

Co-Supervisor: Dr Lejun Zhang

CODES

Declaration of Originality

This thesis contains no material which has been accepted for a degree or diploma by the University or any other institution, except by way of background information and duly acknowledged in the thesis. To the best of my knowledge and belief, no material previously published or written by another person, except where due acknowledgement is made in the text of the thesis, nor does the thesis contain any material that infringes copyright.

Rachel L. Harrison

Date: 9/01/2018

Authority of Access

This thesis is not to be made available for loan or copying for two years following the date this statement was signed. Following that time, the thesis may be made available for loan and limited copying and communication in accordance with the Copyright Act 1968.

Rachel L. Harrison
Date: 9/0 /2018

Abstract

The Tumpangpitu porphyry and high- to intermediate-sulfidation epithermal deposit is the largest deposit in the Tujuh Bukit district, southeast Java, Indonesia. The porphyry resource contains 1.9 billion tonnes at 0.45 % Cu and 0.45 g/t Au, for 28.1 Moz Au and 19 billion llbs of Cu. There is an additional 1.9 Moz Au and 60.3 Moz Ag in oxidized high-sulfidation epithermal deposits.

Tumpangpitu is located along a NW-striking structural corridor covering an area of 12 x 5 km that hosts several Cu-Au-Mo mineralized tonalitic porphyries, each with varying degrees of metal enrichment. At least eight discrete intrusions, span the alteration-mineralization sequence at Tumpangpitu. What is unusual, however, is the presence of both a pre-mineralization, relatively dry volcanic breccia pipe (Tanjung Jahe) and a late-mineralization diatreme complex associated with a large magmatic-hydrothermal system (Tumpangpitu) in the same district. Type sections have been constructed for Tumpangpitu based on cross-cutting relationships of intrusions and breccias, supported by radiometric dating. This work has provided the first comprehensive geological model for the deposit.

Magmatism, alteration and mineralization at Tumpangpitu occurred in response to north-directed subduction of the Indo-Australian plate beneath the Asian continental plate margin. The Tujuh Bukit district is floored by Early to Late Miocene sedimentary and andesitic volcanic rocks. Volcanic-hydrothermal activity at Tujuh Bukit began with the formation of the weakly-altered Tanjung Jahe diatreme complex ($U\text{-}Pb_{zircon}$ ages of 8.78 ± 0.22 to 8.52 ± 0.21 Ma). Mineralization at Tumpangpitu was preceded by the intrusion of a large, equigranular, dioritic pluton (5.81 ± 0.20 to 5.18 ± 0.27 Ma). Hydrothermal activity associated with mineralization has been constrained by U-Pb age determinations from syn- to late-mineralization porphyry intrusions that were emplaced in the Early Pliocene from 5.40 ± 0.46 to 3.94 ± 0.69 Ma.

Tumpangpitu is a large, complicated example of telescoped high-sulfidation mineralization and associated advanced argillic alteration (part of a district-scale lithocap) that has overprinted the top of a Cu-Au-Mo porphyry deposit. Mineralization extends from the present-day surface to depths of more than 1,000 m bsl. High-sulfidation mineralization is hosted by five main NW- and N-trending residual quartz ridges known as Zone A, Zone B, Zone B East, Zone C and Zone E, containing Au-Ag oxide ore close to surface with transitional and sulfide Au-Ag-Cu ore at depth. Porphyry mineralization extends from an upper level of 50 m asl to levels of over 1,000 m bsl and the 0.2 % Cu shell extends 1.2 - 1.5 km laterally around the tonalite intrusive complex.

Early magnetite (M), A and B veins and veinlets are associated with hypogene bornite, chalcopyrite, chalcocite and covellite. Native gold occurs as refractory inclusions in these early copper

sulfide minerals and B veins contain most of the molybdenite at Tumpangpitu. Rare C veins contain high-grade chalcopyrite and bornite, but are not extensively developed at Tumpangpitu. Late pyritic D veins with bleached muscovite alteration halos have overprinted all earlier porphyry stage veins.

Late massive pyrite veins that lack quartz typically contain one or more of the following: enargite, luzonite, covellite, bornite, and/or tennantite-tetrahedrite with relict chalcopyrite. These high-sulfidation state epithermal veins are typically associated with high temperature alteration assemblages, including quartz - alunite, quartz - pyrophyllite ± topaz ± diaspore and quartz - dickite ± kaolinite. Late tennantite-tetrahedrite - chalcopyrite veins are associated with pyrophyllite, dickite, kaolinite and illite alteration. The general pattern of metal zoning with respect to the porphyry centres at Tujuh Bukit indicate central Au and Cu associated with deep porphyry mineralization, central and proximal Mo associated with porphyry ore and the occurrence of Mo in the base of the lithocap, highlighting the location of the underlying porphyry deposit. Enargite defines the core of both shallow and deep structurally controlled high-sulfidation mineralization. Enargite has produced a strong As anomaly, grading outwards to Au, Cu, Ag, Sb, Zn associated with tennantite - tetrahedrite. Late stage, distal galena - sphalerite veins with muscovite alteration halos form a Pb-Zn enrichment halo around the zone of advanced argillic alteration.

A zonation both in space, as well as time has been recognized in porphyry-related alteration from central quartz - magnetite - K-feldspar - biotite through rare actinolite to distal epidote - chlorite and chlorite - calcite alteration of country rocks. Early ores and potassic alteration minerals were overprinted by structurally controlled pervasive advanced argillic alteration assemblages. Spectral data has been used to create an alteration model of clay mineral zonations. Quartz - alunite - dickite assemblages are dominant at shallower levels in the epithermal system and pyrophyllite ± diaspore ± topaz at deeper levels. Fluids channelled along structures are interpreted to have formed 750 x 200 m wide vuggy quartz ridges surrounded by >500 m x 1,200 m of advanced argillic envelopes containing dickite - kaolinite with decreasing quartz contents laterally. These late, structurally controlled advanced argillic alteration zones extend for over 12 km along a NW strike through the project area, overprinting all early porphyry-related alteration. The silicic and advanced argillic zones associated with enargite and tennantite are surrounded by illite - smectite and chlorite - calcite ± epidote alteration. A zone of quartz - muscovite ± pyrophyllite alteration separates and has overprinted the deep magnetite-stable potassic alteration and the shallow advanced argillic alteration domains. This muscovite zone is characterized by the alteration of magnetite to hematite.

The areal extent of the late alteration zones are greater than that of the early potassic related alteration, which remains hidden at Tumpangpitu. The advanced argillic alteration provided a large exploration target that was used to vector towards porphyry mineralization at depth. Pervasive chlorite - illite - smectite ± calcite alteration of the diatremes post-dates all other styles of alteration. The highest

grade porphyry mineralization is intersected in magnetic, quartz - magnetite - biotite - K-feldspar altered tonalite. This has allowed airborne magnetics to be used successfully in conjunction with mapping and soil molybdenum geochemistry to facilitate exploration targeting, which ultimately led to the discovery of the deep porphyry deposit.

Fault-controlled high-sulfidation state enargite - luzonite ± covellite ± bornite mineralization and associated advanced argillic alteration (part of a district-scale lithocap) has been overprinted by intermediate-sulfidation state tetrahedrite - tennantite - chalcopyrite mineralization. Sn-sulfides and sulfosalts crosscut bornite, chalcocite and covellite and appear to have formed contemporaneously with tennantite. Both HSE and ISE mineralization have overprinted and significantly upgraded the top of the porphyry orebody. $^{40}Ar/^{39}Ar$ dating of alunite (4.385 ± 0.049 Ma) and Re-Os dating of molybdenite (4.303 ± 0.018 Ma) has defined a short time period between the high-sulfidation epithermal and porphyry mineralization events, respectively. This suggests extremely rapid rates of uplift, exhumation and erosion in the vicinity of the Sunda-Banda magmatic arc.

Volcanic-hydrothermal activity associated with the Tumpangpitu diatreme occurred during epithermal mineralization (breccia matrix zircon age of 2.7 ± 1.0 Ma). Clasts of high-sulfidation state mineralized rocks are a minor, but significant, component of the diatreme, and late-stage epithermal veins cutting the diatreme, demonstrate an inter-mineralization timing with respect to epithermal activity in the district, implying that epithermal mineralization continued intermittently for 1 - 1.5 m.y. after porphyry mineralization ceased at Tumpangpitu.

Acknowledgements

Completion of this thesis has been possible with the support, assistance and encouragement from many individuals. It is also a milestone in pursuing a passion in gold-copper deposit exploration and discovery. Therefore, I would like to express my gratitude firstly to my husband, Adi Maryono for continued support, advice and guidance, including a huge transfer of practical and technical knowledge on porphyry and epithermal systems, particularly those of the Sunda-Banda magmatic arc, which has greatly aided my knowledge on these deposits. My Father, Mother, Stephanie and James and my Javanese family and neighbours provided support and motivation to complete this PhD, in particular during the final stage of writing from home.

Malcolm Norris (Ex-VP Exploration and New Business, Intrepid Mines Ltd) is thanked for facilitating a permanent transfer to the Tujuh Bukit project from the Pilbara, after persistent begging during a period of sixteen months! His technical leadership, along with Dr Bruce Rohrlach (Ex-Consultant Chief Geologist, Intrepid Mines Ltd) facilitated the acquisition of the Tujuh Bukit project in 2007 and subsequent discovery of the Tumpangpitu porphyry deposit in 2008. Malcolm is also thanked for initiating sponsorship from Intrepid Mines and suggesting that I enrol in a Masters of Economic Geology degree at CODES which ultimately lead to this PhD. Damien Lulofs (Ex-Consultant Chief Geochemist, Intrepid Mines Ltd) is thanked for advice on geochemical modelling, data management and adventures in the field during soil auger surveys! Professor David Gray (Consultant Structural Geologist) provided structural and regional geology insights and practical onsite training sessions, as well as brilliant coastal mapping excursions. Chris Moore (Consultant Geophysicist) is thanked for his down-to-earth explanations on the complexities of geophysical methods for exploration. Ray Robinson (Ex-Engineer, Intrepid Mines Ltd) is thanked for providing insights into mining methods and geometallurgical issues to the exploration team. This technical leadership team are thanked for their effective management, mutual respect, provision of training and for giving free-reign to geologists to pursue their individual interests, which created a very positive learning environment at the Tujuh Bukit project in the early days of exploration. This great support inspired the high calibre datasets, models and research which ultimately lead to discovery success. SolGold Ltd and Avalon Minerals Ltd (now Sunstone Metals Ltd; Malcolm and Bruce) are also thanked, along with J Resources Nusantara, AusSpec International Ltd and Almaden Minerals Ltd for consulting contracts, which provided much appreciated living funds during the latter part of this study.

I thank my supervisor Professor Dave Cooke for academic support, advice and endless editing of my long-winded sentences! His huge wealth of knowledge on ore deposits, particularly during the ore deposits of South America MEconGeol fieldtrip, inspired me to pursue this research on Tujuh Bukit. Thanks also to all CODES staff, including my friendly co-supervisor, Lejun Zhang, who always made time

to help in any way, or to chase Dave Cooke! CODES students including Francisco Testa and CSL staff, Karsten Goemann are thanked for advice, help and support. Jay Thompson is thanked for dating zircons and providing help with age determination calculations. Special thanks go to all local geologists who contributed to this study, including Mbak Elfina, Pak Rizfan Hasnur, Pak Paulo Renata, Pak Andrias Kristianto and Pak Hilman Sasmita. Special thanks also to Mbak Nunung, Mbak Susie, Pak Sigit and Pak Ma'ruf for logistical support. Thanks also to the local soil sampling teams and Pulau Merah core shed assistants for efficiently sampling and organising samples for spectral analysis in all weather conditions! Thanks also to Sasha Pontual from AusSpec International for an excellent three day onsite spectral/TSG training course in 2011 and subsequent email contact for support and QA-QC on spectral identification.

Thanks go to Antonio Arribas, Jeff Hedenquist, Steve Sparks, Peter Hollings, Holly Stein and Peter Pollard for constructive reviews that improved both this thesis and a manuscript that is in press. Appreciation goes to the Society of Economic Geologists and Newmont Mining Corporation for a student research grant in 2014. Finally thanks to Intrepid Mines Ltd for initial funding of this study via a prior MEconGeol degree at CODES and for purchasing a TerraSpec in 2010, which consequently led to a spectral revolution at the Tujuh Bukit project, which enhanced understanding of the dimensions of the hydrothermal alteration system and lithocaps in the then newly discovered Tujuh Bukit district.

Table of Contents

List of Figures

Figure

List of Tables

List of Abbreviations

ab	albite
act	actinolite
al	alunite
asl	above sea level
anhy	anhydrite
ASD	analytical spectral device
Au	gold
AusSpec	AusSpec International Limited
bio	biotite
BLEG	bulk leach extractable gold
bn	bornite
BOCO	base of complete oxidation
BOSO	base of semi oxidation
bsl	below sea level
C	centrigrade
cal	calcite

cc	chalcocite
CDT	Canon Diablo Troilite
chl	chlorite
CL	cathodo-luminescence
cm	centimeter(s)
CODES	Centre of Excellence in Ore Deposits
cps	counts per second
cpy	chalcopyrite
CSIRO	Commonwealth Scientific and Industrial Research Organisation
CSL	Central Science Laboratory
Cu	copper
cv	covellite
DH	drillhole
DEM	digital elevation model
diasp	diaspore
E	east
en	enargite
ep	epidote
EMPA	electron microprobe analysis
EDS	energy-dispersive spectrometer
Fm	formation
g	gram(s)
gal	galena
go	goethite
g/t	grams per metric ton
hb	hornblende
hm	hematite
HSE	high-sulfidation epithermal
ICP-MS	inductively-coupled plasma mass spectrometry (or spectrometer)
ID	identification number
ID-TIMS	isotope dilution-thermal ionization mass spectrometry
Ill	illite
JORC	Joint Ore Reserves Committee
Ka	kilo annum (thousands of years before present)
Ka-PX	Poorly crystalline kaolinite
Ka-WX	Well crystalline kaolinite
Kfs	K-feldspar
km	kilometre(s)
KP	Kuasa Pertambangan (Mining Right)
LA-ICP-MS	laser ablation inductively-coupled plasma mass spectrometry (or spectrometer)
LOI	loss on ignition
llb	pound
lz	luzonite
m	meter(s)
Ma	mega annum (millions of years before present)
mal	malachite
Mo	molybdenite
mont	montmorillonite
Moz	million (troy) ounces
mt	magnetite
MSWD	mean squared weighted deviates

N	north
NA	not applicable
NE	northeast
nont	nontronite
NNW	north-northwest
NW	northwest
Pb	lead
ppm	parts per million
ppb	parts per billion
P-T-X	pressure-temperature-composition
py	pyrite
pyroph	pyrophyllite
qtz	quartz
RC	Reverse circulation
RL	Reduced level: refers to the height of a point relative to sea level
rt	rutile
RTP	reduced to pole
S	south
SCC	sericite-clay-chlorite
SE	southeast
SEM	scanning electron microscope
SHRIMP	sensitive-high resolution ion microprobe
smec	smectite
Sn	tin
sphl	sphalerite
SW	southwest
SWIR	short-wavelength infrared spectroscopy
t	metric ton
te	telluride
tet-ten	tetrahedrite-tennantite
TSA	The Spectral Assistant
TSG	The Spectral Geologist
UTM	Universal Transverse Mercator
µm	micrometer(s)
USGS	United States Geological Survey
UST	unidirectional solidification texture
UTM	universal transverse mercator
VHMS	volcanic-hosted massive sulfide
Vis-NIR	visible and near-infrared
W	west
Wt %	weight percent
y	year(s)
WGS	World Geodetic System
zir	zircon
Zn	zinc

Chapter 1: Introduction

1.1 Preamble

Porphyry-type ore deposits are among the world's premier metal resources, supplying most of the copper, molybdenum, and a substantial part of current gold production (Sillitoe, 2010). Porphyry deposits are hosted in continental arcs in the eastern Pacific and island arcs throughout the western Pacific. Indonesia hosts the giant Grasberg porphyry deposit, currently the largest gold-bearing porphyry deposit in the world (91 Moz Au; Leys et al., 2013; Table 1.1). The discovery of the world class porphyry copper-gold deposit at Tumpangpitu in 2008 (Norris, 2011; Fig. 1.1; Table 1.1) stimulated recent exploration in the Sunda-Banda magmatic arc. The eastern Sunda-Banda arc has proven to be an emerging, economically important, porphyry copper-gold belt, with the discoveries of three giant (>300 t Au and >5 Mt Cu; Clark, 1993; Singer, 1995) porphyry deposits at Batu Hijau (Clode et al., 1999), Elang (Maryono et al., 2005) and Tumpangpitu, and two giant epithermal deposits at Pongkor and Kerta (>100 t Au; Basuki et al., 1994; Singer, 1995; Lubis et al., 2012).

Porphyry Au-Cu systems are characterized by multiple magmatic and hydrothermal events that may occur over a period of several million years and consist of numerous short-lived hydrothermal pulses that generally last on the order of 50,000 to 100,000 yr (Arribas et al., 1995; Henry et al., 1997; Muntean and Einaudi, 2001; Ossandón et al., 2001; Padilla Garza et al., 2001; Seedorff et al., 2005). Three radiometric techniques, (zircon), $^{40}Ar/^{39}Ar$ (alunite, biotite, illite) and Re/Os (molybdenite) can be used to determine the duration of magmatic-$^{206}Pb/^{238}U$ hydrothermal systems, from early intrusive emplacement and zircon formation with some zircon formation prior to final magma emplacement, through hydrothermal alteration-mineralization, to late stage cooling, uplift and exhumation (Arribas et al., 1995; Chiaradia et al., 2011, 2014). Integration of geochronological datasets is vital for unravelling the magmatic and hydrothermal history of porphyry and epithermal districts.

Lithocaps are large bodies of hypogene residual quartz (vuggy and massive-textured) replacement with halos of advanced argillic alteration, with variable pyrite contents that are hosted by a permeable lithology and located between the subvolcanic intrusive environment and below the paleosurface (White and Hedenquist, 1990; White, 1991; Sillitoe, 1995a). There is always a structurally controlled feeder zone, and the most intensely developed residual quartz commonly lies directly above or on the shoulder of the causative intrusion (Hedenquist and Taran, 2013). An improved understanding of lithocaps, in part has driven recent discoveries in the Sunda-Banda arc, which has provided an exploration tool for linked porphyry and epithermal deposits. (White, 1991; Sillitoe, 1995; Hedenquist et al., 1998; Chang et al., 2011; Maryono et al., 2017). Spectral data is a vital tool for exploration in the lithocap environment, particularly where mineralized porphyry bodies are concealed beneath lithocaps (Chang et al., 2011; Harrison, 2014).

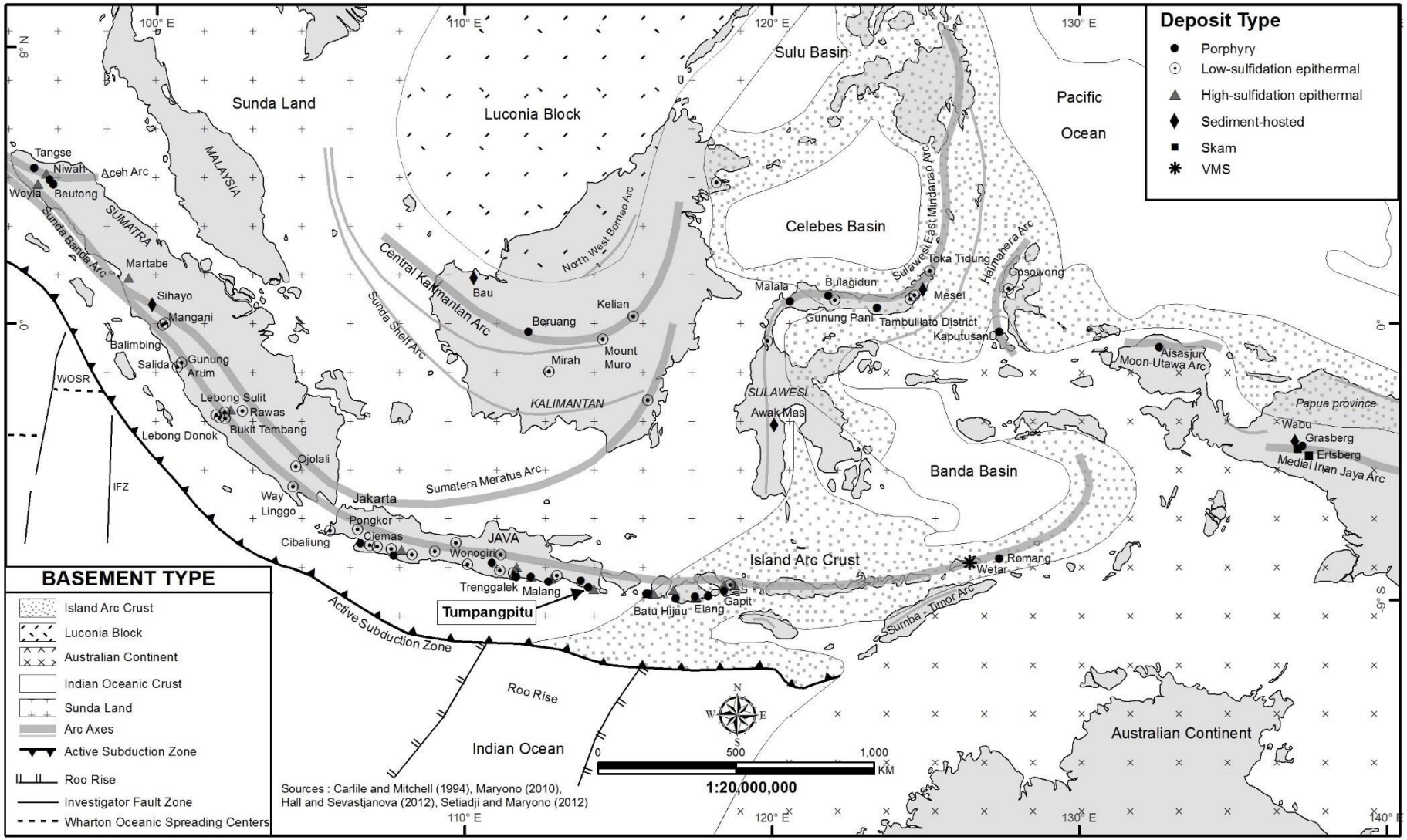

Figure 1.1. Spatial distribution of the major porphyry and epithermal deposits of Indonesia.

TABLE 1.1. Summary of the world's twenty largest known gold-rich porphyry Cu-Au-(Mo) deposits ranked on contained gold.

Name	Province	Age (Ma)	Resource (Mt)	Grades	Contained metal	References
1. Grasberg	Papua	3.3 - 2.5	3583	Au: 0.79 g/t Cu: 0.86 %	Au: 91 Moz Cu: 30.81 Mt	Leys et al. (2013); Freeport (2016)
2. Pebble East and West	Alaska	86 - 89.5	6440	Au: 0.34 g/t Cu: 0.40 % Mo: 0.025 % Ag: 1.66 g/t	Au: 70.38 Moz Cu: 25.75 Mt Mo: 1.54 Mt Ag: 344 Moz	Northern Dynasty Minerals Ltd (2014)
3. Bingham	Utah	38.8	3228	Au: 0.5 g/t Cu: 0.88 %	Au: 51.54 Moz Cu: 28.46 Mt	Cooke et al. (2005)
4. Kal'makyr	Uzbekistan	310 - 294	6080	Au: 0.37 g/t Cu: 0.39 %	Au: 44.18 Moz Cu: 24 Mt	Mutschler et al. (1999); Cooke et al. (2005); USGS (2008)
5. Cadia district	NSW	440	3460	Au: 0.38 g/t Cu: 0.26 % Ag: 0.68 g/t	Au: 43.89 Moz Cu: 8.70 Mt Ag: 69 Moz	Newcrest (2017)
6. Reko Diq	Pakistan	11.22 - 12.0	5900	Au: 0.22 g/t Cu: 0.41 %	Au: 41.73 Moz Cu: 24.19 Mt	Leaman and Staude (2003); Perello, (2008); Tethyan Copper Company Ltd (2011)
7. Kerr-S-M	Canada	195 - 192	2164	Au: 0.55 g/t Ag: 2.74 g/t Cu: 0.21 % Mo: 0.045 %	Au: 38.2 Moz Ag: 191 Moz Cu: 4.49 Mt Mo: 0.097 Mt	Seabridge Gold Inc (2012)
8. Dal'neye	Uzbekistan	310 - 294	545	Au: 0.69 g/t Cu: 0.59 %	Au: 31.51 Moz Cu: 10.08 Mt	USGS (2011)
9. Tumpangpitu	SE Java	3.38 - 5.86	1900	Au: 0.45 g/t Cu: 0.45 % Ag: 26.3 g/t Mo: 0.009 %	Au: 29.9 Moz Cu: 8.6 Mt Ag: 60.3 Moz Mo: 0.18 Mt	Intrepid Mines Ltd (2012); PT Merdeka Copper Gold Tbk (2016); this study
10. Cerro Casale	Chile	13.5	1285	Au: 0.70 g/t Cu: 0.35 %	Au: 28.94 Moz Cu: 4.50 Mt	Kirkham and Dunne (2000); Cooke et al. (2005)
11. Wafi-Golpu	PNG	14	1000	Au: 0.63 g/t Ag: 1.1 g/t Cu: 0.9 %	Au: 28.3 Moz Cu: 9.06 Mt Ag: 50.6 Moz	Newcrest (2012); Menzies (2013)
12. Panguna	Bougainville	3.5	1415	Au: 0.57 g/t Ag: 1.10 g/t Cu: 0.46 %	Au: 25.69 Moz Ag: 50.22 Moz Cu: 6.51 Mt	Kirkham and Dunne (2000)

13. Elang	Sumbawa	2.7	2425	Au: 0.33 g/t Cu: 0.31 %	Au: 25.28 Moz Cu: 7.4 Mt	Garwin (2000); Newmont (2012)
14. Oyu Tolgoi	Mongolia	411	2175	Au: 0.34 g/t Cu: 0.96 % Ag: 2.26 g/t	Au: 23.54 Moz Cu: 20.81 Mt Ag: 157.79 Moz	Turquoise Hill Resources Ltd (2016)
15. FSE/Lepanto	N. Luzon	1.5 - 1.3	892	Au: 0.7 g/t Cu: 0.5 %	Au: 19.8 Moz Cu: 4.5 Mt	Arribas et al. (1995); Hedenquist et al. (1998) Gold Fields (2013)
16. Batu Hijau	Sumbawa	3.7	1640	Au: 0.35 g/t Ag: 0.55 g/t Cu: 0.44 %	Au: 18.45 Moz Ag: 29 Moz Cu: 7.22 Mt	Meldrum et al. (1994); Clode et al. (1999); Garwin (2000)
17. Minas Conga	N. Peru	15.7	641	Au: 0.79 g/t Cu: 0.30 %	Au: 16.28 Moz Cu: 1.92 Mt	Llosa and Veliz (2000); Cooke et al. (2005); USGS (2008)
18. Tampakan	Philippines	4.24 - 4.26	2500	Au: 0.2 g/t Cu: 0.48 %	Au: 16.08 Moz Cu: 12.5 Mt	Rohrlach and Loucks (2005)
19. Ok Tedi	PNG	1.2 - 1.1	911	Au: 0.78 g/t Cu: 0.64 %	Au: 14.34 Moz Cu: 5.5 Mt	Kirkham and Dunne (2000); Cooke et al. (2005); USGS (2008); Ok Tedi Mining Ltd (2014)
20. Bajo de la Alumbrera	Argentina	8 - 7	551	Au: 0.67 g/t Cu: 0.52 %	Au: 11.86 Moz Cu: 2.87 Mt	Kirkham and Dunne (2000); Cooke et al. (2005)

Notes: Figures are quoted for those deposits with available published resource data. Contained metal data contains resource plus production figures.

This PhD study of the Tumpangpitu deposit investigates some of the major questions regarding genetic links between porphyry and epithermal deposits, and their relationships to diatremes and lithocaps. The study also addresses why Tumpangpitu has the largest known metal endowment of porphyry-epithermal deposits along the Sunda-Banda arc, and why porphyry deposits in the western portion of the arc are not as well endowed. Other questions to be addressed include the origin and significance of the elevated molybdenum content at Tumpangpitu, in a region mostly devoid of molybdenum, and what were the factors that contributed to high grade hypogene ore and intense telescoping of epithermal mineralization and alteration on top of porphyry mineralization.

1.2 Background to the current study

The Tumpangpitu porphyry-high-sulfidation deposit is located in the Tujuh Bukit district of southeast Java, Indonesia. Academic research commenced in 2012 as the thesis component towards a Masters of Economic Geology degree at the Australian Research Council (Arc) Centre of Excellence in Ore Deposits, (CODES) University of Tasmania (UTAS). This PhD study was initiated to show appreciation to the high caliber technical work conducted by the exploration team from Intrepid Mines Ltd during 2007 to 2012, and to ensure that the lessons learned during a very successful exploration campaign were recorded.

This PhD study has a practical, as well as an academic purpose. During a period of intense exploration activity involving ten diamond core drill rigs, following the discovery of the Tumpangpitu porphyry in 2008, it became a matter of urgency to identify the key lithologies and intrusive phases, in order to obtain consistency in logging between different geologists. Methodology was established to create a lithology model for the geology team and resource calculations. This model could then be used to define the relative timing of intrusive events by on-going drillcore logging and field mapping (e.g., Einaudi, 1997; Seedorff et al., 2005; Maryono et al., 2012).

Field-based data for this thesis was gathered over three years of full time employment at the Tujuh Bukit project for Intrepid Mines Ltd. up until the company was evicted from the project by their joint venture partners on 19th July 2012. Prior to that date, all work on the geology and alteration models was undertaken onsite at the Tumpangpitu deposit, and regional exploration work was carried out at the Salakan, Katak and Candrian porphyry prospects and the Gunung Manis low-sulfidation epithermal vein prospect. The first consistent surface lithology and structural geology maps were compiled from mapping datasets,

including mapping of the entire coastline around Tumpangpitu by the author in 2009. These were integrated with 15 NE-SW cross-sections constructed by the author through the deposit from 2009 to 2017.

Three years (2014 to 2017) of independent subsequent research included petrographic, SEM, microprobe, SWIR, sulfur isotope and $^{206}Pb/^{238}U$ geochronological analysis, as an external PhD student at CODES, UTAS. The project involved collaborations for geochronologic analysis with the University of Queensland ($^{40}Ar/^{39}Ar$ dating of alunite) and the University of Alberta (Re-Os dating of molybdenite).

1.3 Aims

This PhD, aims to provide a first-hand insight into the geology, alteration and mineralization of this newly discovered, world class mineralized district. This study will focus on five principal objectives:

1) Characterize the geology, alteration and mineralization of the Tumpangpitu ore body
2) Establish the relative and absolute timing relationships between the host rocks, intrusions, alteration and mineralization
3) Evaluate the genetic relationships between porphyry and epithermal mineralization, diatreme volcanism and lithocap formation
4) Place the Tujuh Bukit district in context within the broader geodynamic and metallogenic evolution of the Sunda-Banda arc
5) Illustrate the successful exploration techniques responsible for the discovery of this giant porphyry-epithermal deposit

1.4 Area of Study

1.4.1 Property and location

The Tumpangpitu porphyry Cu-Au-Mo and high-sulfidation epithermal Au-Ag deposit is part of the Tujuh Bukit project. It is located just outside the village of Pulau Merah, Banyuwangi regency, on the south-eastern coast of the island of Java in Indonesia (Fig. 1.3). The property is approximately 205 kilometres southeast of Surabaya, the capital of the province of East Java, and 60 kilometres southwest of the regional centre of Banyuwangi. The Tujuh Bukit project covers 11,621 hectares within adjoining IUPs (Izin Usaha Pertambangan) under Indonesian mining law - an IUP Exploration of 6,623.45 hectares and an IUP Production Operation of 4,998 hectares. The property is bound within UTM co-ordinates 163,000 - 179,000 mE and 9,042,000 - 9,055,000 mN (Figs. 1.3 and 1.4).

1.4.2 Ownership

The IUPs (Izin Usaha Pertambangan) were granted to PT Indo Multi Niaga (PT. IMN) on 25th January 2010 by the Bupati of Banyuwangi (Regional Administrator, Banyuwangi, East Java). Intrepid Mines Ltd and PT. IMN signed a Joint Venture agreement enabling Intrepid Mines Ltd to hold an 80 % economic interest in the Tujuh Bukit project. Operations at the project were terminated on 19th July 2012 by PT. IMN. Intrepid Mines Ltd issued a notice of dispute to PT. IMN and its shareholders in August 2012. The IUP is now owned by PT Merdeka Copper Gold Tbk. Gold extraction from oxide ore via heap leach commenced in March 2017.

1.4.3 Exploration history and discovery of Tumpangpitu

The Tumpangpitu deposit is one of several porphyry deposits and prospects in the Tujuh Bukit district (Fig. 1.4). Exploration was first conducted at the Tujuh Bukit project in 1991 by PT. Hakman Platina Metalindo, with a highly mineralized porphyry stockwork discovered cropping out on Pulau Merah island and its surrounding reef platform (Fig. 1.6B). The island and reef exhibits well developed porphyry stockwork veins overprinted by high-sulfidation epithermal (enargite - covellite-bearing) massive sulfide veins and intermediate-sulfidation epithermal (tetrahedrite - tennantite) veins. The island also exposes a leached cap and copper oxide enrichment zone (Fig. 1.6B). The vein stockwork crops out along the coastline and is accessible at low tide (Fig. 6C). The island was channel sampled in 1999 and returned 47 m at 1.71 g/t Au and 1.29 % Cu (Norris, 2011; Rohrlach, 2011). PT. Hakman signed a series of joint venture agreements with Korean Toosun Holdings in 1994 and Golden Valley Mines of Australia in 1997. Golden Valley Mines identified the Tumpangpitu and Salakan areas (Fig. 1.4) as prospective targets for porphyry copper-gold type mineralization following a regional (1:50,000) drainage stream sediment, BLEG (bulk leach extractable gold) and rock-chip geochemical sampling program conducted during December 1997 to May 1998. Golden Valley Mines also contracted World Geoscience to fly a 400 m line spacing regional magnetic survey over the prospect. Subsequently, a detailed surface geochemical (BLEG, rockchip, float, channel, and soil) sampling program was conducted over Tumpangpitu, resulting in several targets being identified for drilling. An initial drilling program of five diamond drill holes (GT-001 to GT-005) was conducted during March to June 1999 with limited success, mainly due to the limited depth extent of drillholes (maximum 500 m).

In February 2000, Placer Dome Inc. (Placer) entered into a Joint Venture with Golden Valley Mines (GVM) to earn 51% of the project and assumed operational control of the exploration program. In order to better define targets for follow-up drilling on Tumpangpitu, 32.75 km of grid-based geochemical and induced polarization-resistivity (IP) surveys were completed between April and May 2000. Anomalous bedrock geochemistry demonstrated marked consistency with prominent ridges or topographic highs,

trending to the northwest, consisting dominantly of vuggy quartz-altered breccia. The results of the IP survey demonstrated strong correlation between the near-surface resistivity high anomalies and the exposed vuggy quartz zones. Deeper chargeability anomalies (> 200 - 400 m below surface) were recorded in the northern portion of the grid (Norris, 2011). Placer targeted the shallow resistivity high anomalies for high-sulfidation style Au-Ag mineralization with ten diamond drill holes, GT-006 to GT-014. A further 14 holes were designed (2,700 m) on the basis of the results from the second drilling program. However, Placer withdrew from the project, in part due to the influences of the relatively low metal prices at the time, such that the project did not appear to meet corporate thresholds of size and grade. This was combined with an unstable economic and political climate across much of south-east Asia, due to the continuing effect of the 1998 Asian Financial Crisis. There is no report or record of further work being conducted on the project by Placer-GVM and the area became vacant by the time PT. IMN applied for a KP General Survey in 2006 over the project area (Norris, 2011). In June 2006, Hellman and Schofield Pty Ltd, an independent geological consulting group from Australia, assisted in assembling exploration data and designing a drill program aimed at advancing the Tumpangpitu prospect, in order to report resource estimates according to the JORC Code and Guidelines. Hellman and Schofield were able to provide an indication of potential mineralization within the variably oxidized high-sulfidation epithermal gold-silver enriched zone above the deeper copper mineralization by using the limited available drilling data along with soil sample geochemical results. This study suggested that approximately 3 Moz AuEq ("AuEq" was based on based on $650/Oz Au and $10/Oz Ag) was a reasonable target size combining prospects (Zones) A, B and C (Intrepid Mines Ltd, 2010). The technical team from Intrepid Mines Ltd first visited the project in 2006 and considered the project highly prospective due to the following key elements (Norris and Rohrlach, 2006; Norris, 2011):

1. Extensive district-scale alteration footprint (> 40 km^2) with overlapping large magmatic-hydrothermal systems
2. Evidence of at least two porphyry systems cropping out at Pulau Merah island and Salakan
3. Brecciation intensity and extent (including evidence for multiphase brecciation)
4. Encouraging early-stage drill results by GVM and Placer
5. Location in a fertile segment of the Sunda-Banda magmatic arc, with two world class porphyry discoveries; Batu Hijau and Elang. Regional geochemical and magnetic data also indicated the potential for the presence of multiple stocks along the northwest-trending mineralized corridor.

On March 30th, 2007, a Term Sheet was signed between Emperor Mines Ltd (later to become Intrepid Mines Ltd through the merger of Emperor Mines and Intrepid Mines Ltd) and PT Indo Multi Niaga (PT. IMN), which was followed by an Alliance Agreement, in August 2007. Drilling on the project by PT. IMN and Intrepid Mines Ltd commenced in September 2007, with drillhole GTD-07-015.

Two crucial datasets that aided in the targeting of porphyry mineralization were molybdenum, gold and copper anomalism in soil geochemical data and RTP (reduced to pole) magnetic datasets (Norris, 2011; Harrison and Maryono, 2012). Due to the fact that molybdenum generally does not migrate very far from its porphyry source (Sillitoe, 2010), these anomalies were highlighted as potential porphyry targets. Where the molybdenum, gold and copper anomalies coincided with magnetic highs, now known as representative of early hydrothermal magnetite alteration in the potassic zones of the porphyry at depth, this coherent anomalism was allocated a high rank as a porphyry target (Fig. 1.5). In early 2008, Intrepid drilled the main target at Tumpangpitu with diamond hole GTD-08-29, which resulted in the first porphyry intersection of 268 m at 0.47 g/t Au and 0.32% Cu including 100 m at 1.02 g/t Au and 0.55 % Cu. This was followed by drillhole GTD-08-35 which tested a modest IP chargeability response and returned 627 m at 0.45 g/t Au and 0.44% Cu (Intrepid Mines Ltd., 2008). The best porphyry intersection to date was drilled in 2012 from GTD-12-248: 689 m at 1% Cu and 0.85 g/t Au, associated with strong quartz - magnetite - biotite - K-feldspar altered porphyry tonalite that was overprinted by narrow fault-controlled high-sulfidation epithermal mineralization at depth (Intrepid Mines Ltd., 2012; Harrison and Maryono, 2012). GVM hole GTD-001, the first hole drilled on the property (500 m), was terminated less than 100 m above the porphyry orebody, despite the appearance of disseminated chalcocite near the end of the hole (Norris, 2011; Harrison and Maryono, 2012). In 2010, Intrepid drilled hole GTD-10-163 nearby, which intersected 589.5 m at 0.57g/t Au, 0.65% Cu and 122 ppm Mo from 264 m downhole (Intrepid Mines Ltd, 2010; Norris, 2011; Fig. 1.7). Exploration drilling ultimately delineated a world class porphyry resource of 1.9 billion tonnes at 0.45% Cu and 0.45 g/t Au containing 28 Moz Au and 19 billion lbs of Cu (Intrepid Mines Ltd., 2012). The overlying high- to intermediate-sulfidation epithermal gold-silver oxide resource contains 1.9 Moz Au and 60.3 Moz of silver (PT Merdeka Copper Gold Tbk., 2016).

1.4.4 Access and working conditions

Sealed road access to the project is possible from Surabaya (8 - 9 hours) or from Denpasar, Bali (7 - 8 hours) including a 1 hour ferry crossing from Bali to Java (Fig. 1.2). Domestic and international flights operate daily from Banyuwangi Blimbingsari airport to Surabaya and Jakarta. Access via helicopter from Denpasar airport to the project takes 40 minutes (Fig. 1.2). The Tujuh Bukit district is situated at sea level with the peak of Tumpangpitu at 489 m asl. The region surrounding Tumpangpitu is steep, rugged and densely vegetated by teak forests and surrounded by hill country which graduates into alluvial plains near sea level (Fig. 1.6A). The valleys are moderately to steeply dissected with rock exposures mainly along stream courses. Climate is dry from May to November, with the monsoon rains from December to April. Rainfall in the mountain ranges to the north varies from 1,725 mm to 3,500 mm per year, decreasing toward the coast to 1,110 mm to 1,850 mm per year (Intrepid Mines Ltd., 2009). Temperatures range from 25 - 31

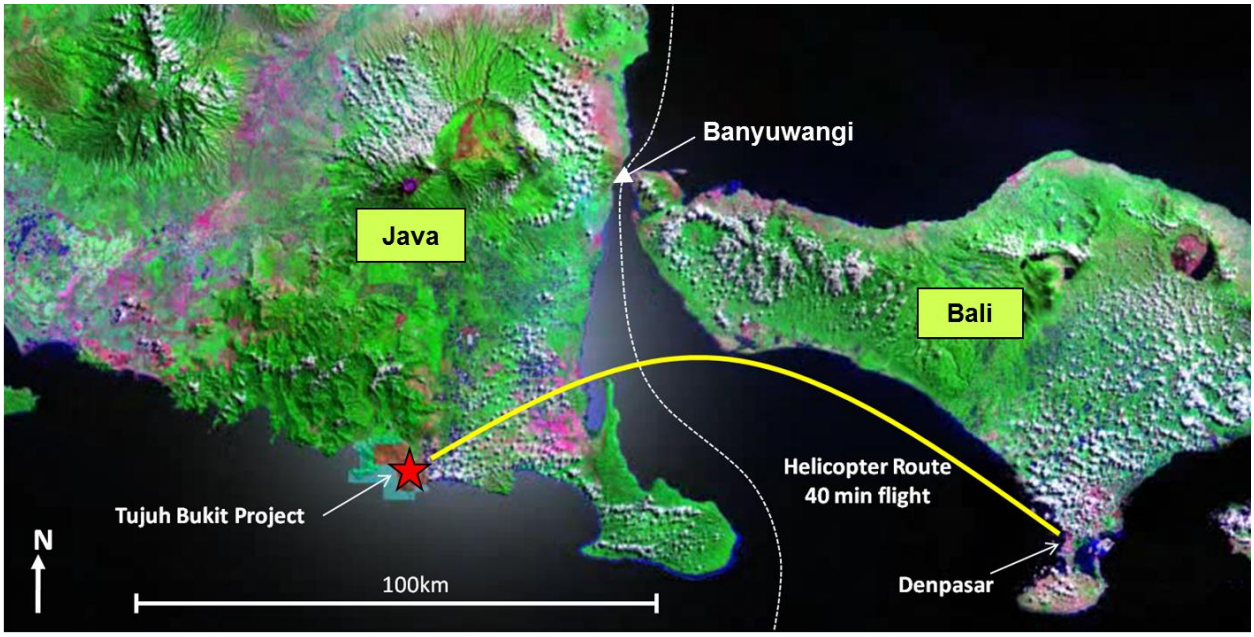

Figure 1.2. Location map and access to the Tujuh Bukit Project (Rohrlach, 2011).

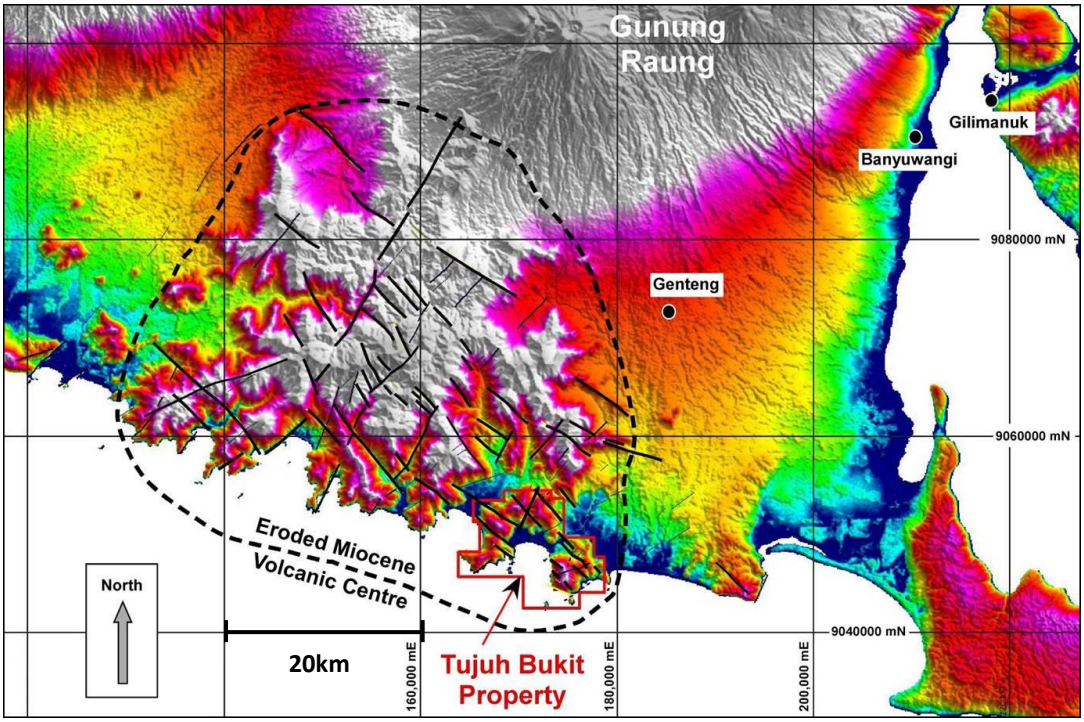

Figure 1.3. Digital elevation model (DEM) of the location of the Tujuh Bukit Project, interpreted by Rohrlach (2011) to be located on the southeast flank of a deeply incised Miocene volcanic centre that is ~50 km in diameter (black dotted outline) south-southwest of the Quaternary volcano Gunung Raung which forms part of a larger composite stratovolcano in east Java (Intrepid Mines Ltd., 2010).

°C during the day down to 22 - 24 °C overnight. Relative humidity is typically high, ranging from 80 - 100 % (Intrepid Mines Ltd, 2009). On the lower slopes, government-owned teak plantations, classified as

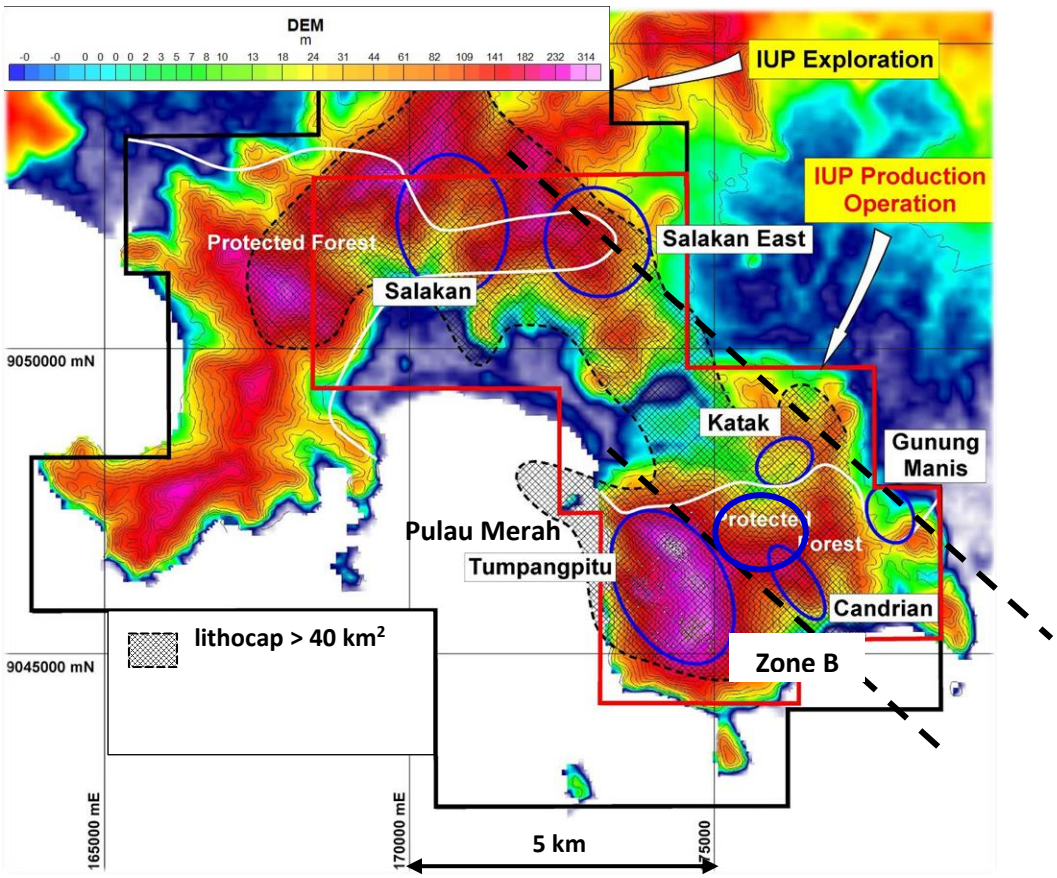

Figure 1.4. Digital elevation image (DEM) showing other Cu-Au-Mo porphyries in the Tujuh Bukit district (modified after Intrepid Mines Ltd., 2010; Rohrlach, 2011).

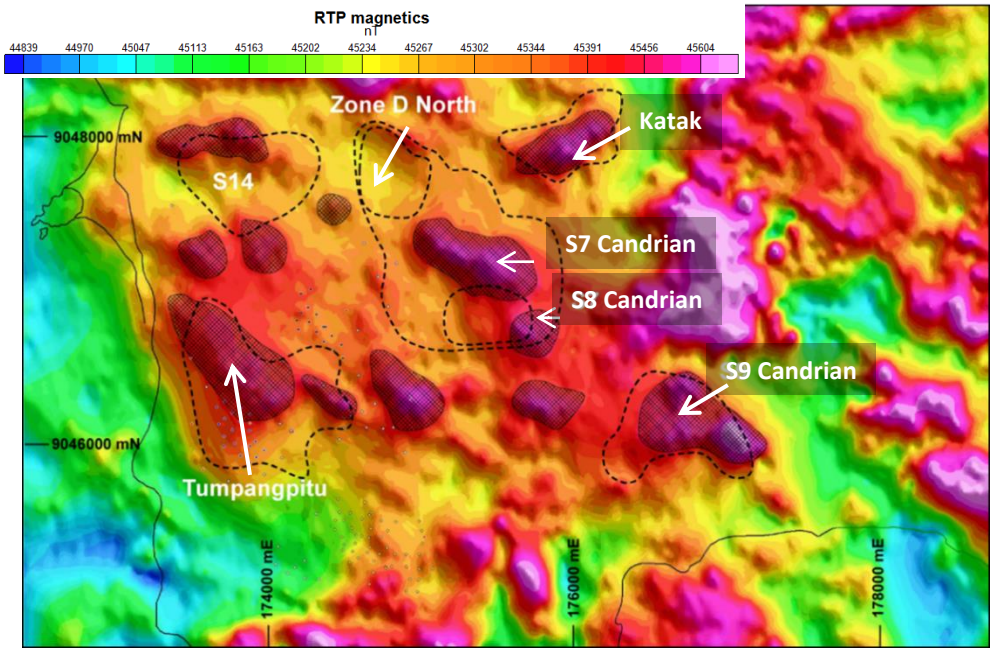

Figure 1.5. Molybdenum anomalies (black hash outlines) clustered around RTP magnetic highs (hash over red-pink high RTP zones) at Tumpangpitu, Katak and Candrian (modified after Intrepid Mines Ltd, 2010).

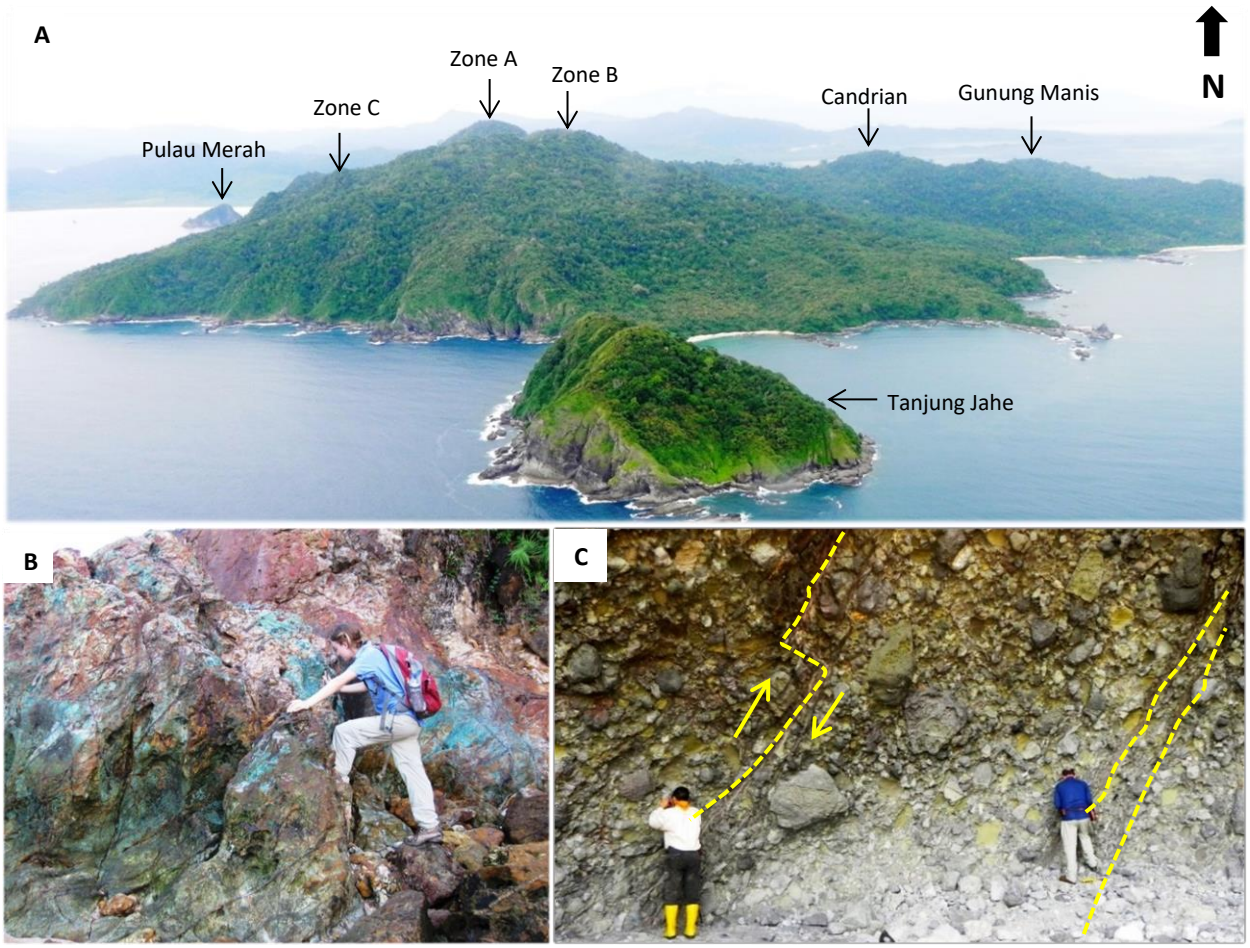

Figure 1.6. A) Photograph looking north of the Tujuh Bukit district. From west to east, the locations of the Pulau Merah island porphyry stock, the resistant silicified high-sulfidation epithermal gold oxide zones A, B and C of Tumpangpitu, Candrian porphyry-high-sulfidation epithermal prospect and Gunung Manis low-sulfidation epithermal prospect. B) Intense porphyry stockwork veins overprinted by epithermal Au-Cu-Ag veins at Pulau Merah island. Note the hematite leached cap (top right) overlying 1 - 2 m of Cu-oxide mineralization. Hypogene copper sulfides are preserved in the wave-cut platform at the base of the Cu-oxide zone. C) Northwest-trending, southwest dipping brittle shear zones cutting the lower facies pre-mineralization diatreme breccia in the cave on the southeast side of Tanjung Jahe peninsula.

Hutan Produksi (Production Forest), are common and are administered by the Perhutani (state forestry company), Banyuwangi. Remnant stands of forest on the upper slopes and top of Gunung Tumpangpitu are classified as Hutan Lindung (Protected Forest). Permits are required, and have been issued, from the Perhutani for undertaking exploration within Protected and Production Forest areas. The project is located 80 km southwest of Ijen, an active andesitic-basaltic volcano with one of the world's largest, acidic volcanic crater lakes (Newhall et al., 1988). The last significant eruption occurred in 1817 for 33 days whereby the lake was ejected and surrounding villages destroyed by the subsequent lahar (Newhall et al., 1988). A large boulder (10 x 30 m) on the foreshore of Pulau Merah was deposited by a 9.4 m tsunami on June 3rd 1994 related to a magnitude 7.6 earthquake. The epicentre was at 10.5°S, 113.0°E (NEIC, USGS), approximately 240 km from the coastline of southeast Java (Tsuji et al., 1995).

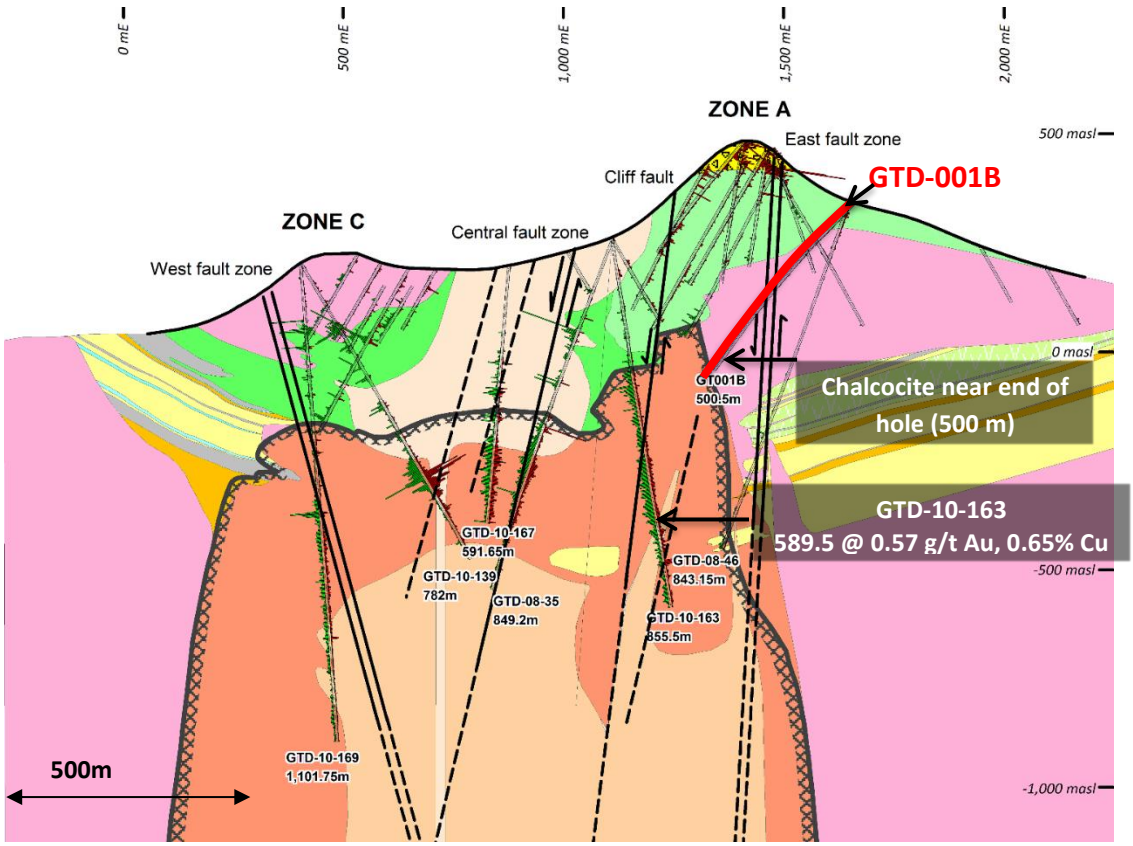

Figure 1.7. Tumpangpitu lithology section 11220 mN showing drillhole GTD-001 (red line) drilled by GVM, which missed the porphyry ore body (dark grey dashed line) by less than 100 m (modified after Norris, 2011). Drillhole GTD-10-163 drilled by Intrepid Mines Ltd in 2010 intersected significant porphyry mineralization.

1.4.5 Resources and reserves

The inferred hypogene sulfide resource estimate for Tumpangpitu Cu-Au-Mo porphyry deposit is 1.9 billion tonnes @ 0.45% Cu, 0.45 g/t Au and 90 ppm Mo, equating to 28.1 Moz Au, 19 Blbs Cu and 400 Mlbs Mo at a 0.2 % Cu cut off (Intrepid Mines Ltd., 2012). The total measured, indicated and inferred resource for the high-sulfidation Au-Ag oxide is 71.4 million tonnes @ 0.80 g/t Au and 26.3 g/t Ag with 1.9 Moz Au and 60.3 Moz Ag at 0.3 g/t Au cut-off grade (PT Merdeka Copper Gold Tbk, 2016). No resource estimate is available for other porphyry or high-sulfidation prospects in the Tujuh Bukit district.

1.4.6 Regional exploration and district potential

Exploration criteria that led to the discovery of four additional tonalite porphyry stocks in the Tujuh Bukit district (Zone B; south of Tumpangpitu, Candrian, Katak and Salakan; Fig. 1.4) included stream sediment, soil, rockchip and BLEG sampling, prospect and regional mapping, airborne magnetic and radiometric surveys, ground IP-resistivity surveys, identification of mineralized porphyry clasts in shallow oxide holes and SWIR analysis (Harrison, 2014). The first drillhole at the Katak porphyry prospect (Fig. 1.4) KTD-10-001 intersected 100 m @ 0.45 g/t Au and 0.3 % Cu. Katak is a porphyry system that is exposed at surface with remnants of a lithocap preserved towards the north that could contain high-sulfidation epithermal mineralization. Drilling at the Salakan porphyry-high-sulfidation prospect to the

north of Tumpangpitu (Fig. 1.4) commenced in 2012. The first drillhole intersected 604 m at 0.22 % Cu, 0.08 g/t Au from surface including 276 m of anomalous molybdenum (135 ppm Mo). Gold-bearing epithermal low-sulfidation quartz veins were discovered by local miners and drilled at Gunung Manis (Fig 1.4) during 2009 to 2010. Diamond drill testing to depths of 300 m returned very narrow (< 0.2 m) intercepts of gold and the epithermal veins were therefore deemed sub-economic.

1.4.7 Previous work

Regional mapping in Java was undertaken by the Geological Survey of Indonesia in 1963, which produced maps at a scale of 1:500,000. In the vicinity of Tujuh Bukit, previous work by the Geological Survey of Indonesia, involved geological mapping (1:250,000 scale) and limited geochemical and fossil sample collection. These maps include generalized chrono-stratigraphic sequences for the major sedimentary and volcanic successions developed from limited field mapping and aerial surveys. Systematic exploration of the region for Au-Cu by PT Hakman started in 1991. Basic lithological and alteration maps were created by exploration geologists. Comprehensive geological, geochemical and geophysical databases along with geological models were developed by Intrepid Mines Ltd from 2007. Academic research at Tujuh Bukit commenced in 2012 as a dissertation by the author on the application of SWIR spectral analysis in exploration for the Candrian porphyry Cu-Au prospect, for the fulfilment of the degree of Master of Economic Geology at CODES, UTAS (Harrison, 2014). A manuscript on the geochronology of Tumpangpitu and evidence for pre- and post-mineralization diatremes is currently in press, as part of a special publication on deposits of the SW Pacific (Harrison et al., 2018).

1.4.8 Field work

Mapping, sampling, diamond drillcore logging and re-logging were completed over three years by the author, whilst employed by Intrepid Mines Ltd from 2009 to 2012. All rock exposures along the coastline were mapped by foot, fishing boat and by helicopter at a scale of 1:500 or 1:1000. Mapping of vein compositions and orientations around Pulau Merah island was conducted at low tide where the coral reef platform and basal sedimentary rocks were exposed and accessible. Mapping was accomplished using a modified version of the method originally developed by Anaconda Geologists at Yerington, Nevada (Einaudi, 1997) and adapted by Newmont Geologists working at Batu Hijau (Maryono et al., 2012). The collection of field data was separated onto three different map sheets, 1) rock type and structure, 2) alteration and 3) sulfide and oxide minerals. Interpretive overlays were created in GIS (MapInfo-Discover) by the author from these fact maps and additional datasets. Structural measurements were collected in the field, plotted as stereonets and uploaded into GIS. Creek mapping was conducted at all regional prospects. The majority of the project area is covered by forests, inhibiting continuous exposure of rock units and structural contacts. Surface maps have been compiled from a number of supporting datasets including; soil

SWIR analyses, using sampling methods from Lulofs (2011) and Harrison (2014), drillhole collar lithology and alteration, extrapolation of geology and alteration to surface from 15 NW-SE deposit-scale sections constructed by the author, coastal and creek mapping data. The orientations of stockwork veins were measured from exposures around Pulau Merah Island, the entire coastline, combined with measurements from orientated drillcore to produce the structural framework for Tumpangpitu. Key contacts and structures have been projected to surface from where they have been intersected by diamond drillholes. Diamond drillholes were logged graphically to record rock type, structure, vein types and paragenesis, cross cutting intrusive and breccia relationships, alteration aided by SWIR spectral data and ore mineral associations. A re-logging method was adapted to record geology and alteration quickly and efficiently to contacts (existing logging system was at 2 m intervals to aid in resource calculations).

All work was conducted on a 4:2 weeks or 20:10 days work:break roster. This work was based out of a core shed at the top of Tumpangpitu mountain and in the Pulau Merah village base camp where a new core shed was constructed in late 2011. Re-logging of diamond drillcore by the author to create the main type porphyry sections involved more than 150 drillholes from both the oxide and porphyry zones totalling over 50,000 m. After the purchase of a TerraSpec spectrometer in 2010, two years of spectral data acquisition and interpretation were conducted.

1.5 Thesis outline and methods employed

This thesis represents the first comprehensive study of the Tujuh Bukit district and provides the first detailed geologic documentation and radiometric age determinations for Tumpangpitu.

1.5.1 Geology and structural framework

The thesis will present the first consistent models and formal documentation for the lithology and structural framework of Tumpangpitu and the Tujuh Bukit district. The sequence of intrusive phases including pre-, syn and post-mineralization intrusions based on crosscutting relationships from logging and re-logging of over 50,000 m of drillcore, field mapping and constructing type sections by the author will be documented. The models are supported by geochemical assays, petrography, SEM, microprobe, sulfur isotope and geochronologic age determinations. The structural evolution of Tumpangpitu is evaluated, based on structural measurements from geologic mapping, core orientation measurements, core logging and SWIR-aided alteration mineral mapping of faults. A particular focus is placed on the documentation of relative and absolute timing of two pre- and late-mineralization diatreme breccia complexes.

1.5.2 Alteration and mineralization framework

SWIR spectral data was obtained, analyzed and interpreted by the author from all drillcore, rockchips and soil samples over two years for this study in order to create spectral-aided alteration surface

maps and models for Tumpangpitu and the Tujuh Bukit district. The alteration models are supported by geochemical assays, petrography, SEM, microprobe, geochronological age determinations and sulfur isotope data. The alteration maps and models are used to provide an accurate estimate of the dimensions of the Tumpangpitu lithocap and the spatial dimensions of the Tumpangpitu mineralized system and other epithermal and porphyry deposits in the Tujuh Bukit district.

Temporal and spatial variations in sulfur isotopic compositions of sulfides and sulfates are used to evaluate potential ore-forming mechanisms. Sulfur isotope data are used to test genetic links between high-sulfidation epithermal and porphyry mineralization. These datasets will be evaluated in order to assess whether they can be used as vectors towards porphyry and/or epithermal mineralization, thereby potentially providing additional exploration tools to aid in the discovery of new porphyry and epithermal deposits in the Tujuh Bukit region. The results of detailed sulfide petrography and mineral paragenesis investigations including gold and copper deportment, are used to constrain the lateral and vertical distribution of Au, Cu, Mo and sulfide species through the mineralized system. Implications for mineral processing will also be discussed.

1.5.3 Radiometric age determinations

Radiometric dating methods are now reliable and sufficiently accurate to provide an insight into the timing and duration of intrusion-related magmatic-hydrothermal systems (Chiradia et al., 2012). Relative timing relationships from logging of geology, alteration and mineralization are coupled with the first radiometric age determinations for pre, syn- and post-mineralization intrusions $^{206}Pb/^{238}U$ (zircon) for Tumpangpitu, in order to constrain the timing and duration of magmatic and phreatomagmatic activity and temporal constraints on the volcanic and sedimentary host rocks, intrusive units and a selection of regional porphyries in the Tujuh Bukit district. High-sulfidation mineralization (alunite $^{40}Ar/^{39}Ar$) and porphyry mineralization (molybdenite Re-Os) will be used to constrain the timing of the magmatic-hydrothermal systems. These age determinations will be used to refine geological relationships obscured by hydrothermal alteration assemblages, and to provide an insight into the rate of exhumation of the porphyry relative to the timing of magma emplacement.

1.5.4 Genetic model of ore formation

This thesis aims to provide a genetic model for Tumpangpitu to illustrate the evolutionary history of the deposit, and the spatial and temporal relationships between porphyry and epithermal ore formation, lithocap development and diatreme volcanism. The genetic model can also be used to recognize new vectors and refine existing exploration criteria to aid in future exploration of additional porphyry and epithermal resources in the Tujuh Bukit district and elsewhere.

Chapter 2: Geology, Geodynamic Setting and Ore Deposits of the Sunda-Banda Arc

2.1 Introduction

Tectonic setting influences the origin, evolution and composition of porphyry and epithermal Au-Cu deposits (Hedenquist and Lowenstern, 1994; Tosdal and Richards, 2001; Cooke et al., 2005; Sillitoe, 2010). An understanding of the tectonic history of the Sunda Banda arc is therefore necessary to understand the evolution of the Tumpangpitu porphyry-epithermal deposit and other porphyry and epithermal deposits along the arc.

This chapter provides a brief overview of the tectonic history of the Sunda-Banda arc from the Paleocene to the present-day. It concludes with a review of the geology, alteration, mineralization and distribution of selected porphyry deposits along the eastern Sunda arc.

2.2 Regional Setting

The Sunda-Banda metallogenic belt is approximately 3,940 km long, extending southeast from the northern tip of Sumatra to west Java, then eastward through east Java, Bali, Lombok, Sumbawa, Flores and Damar islands (Hamilton, 1979; Carlile and Mitchell, 1994; Setijadji et al., 2006; Maryono et al., 2017; Figs. 2.1 - 2.3). These islands share similarities in tectonic setting and regional geology. They are dominated by Neogene and Quaternary volcanic complexes and comagmatic stocks associated with porphyry gold-copper ± molybdenum and low-, intermediate- to high-sulfidation epithermal gold-silver deposits and prospects (Figs. 2.1 - 2.3, Table 2.1).

The Sunda-Banda magmatic arc hosts five major magmatic belts of Late Mesozoic, Paleocene-Eocene, Oligocene-Early Miocene, Late Miocene-Pliocene and Quaternary ages (Hamilton, 1979; Carlile and Mitchell, 1994; Garwin, 2000; Hall, 2002; Setijadji et al., 2006; Maryono et al., 2017). Of these five, the latter three magmatic belts have the greatest spatial distribution (Figs. 2.2 and 2.3). Two distinctive features of the distribution of volcanic belts can be observed in the land surface geomorphology derived from SRTM imagery (Fig. 2.3). The Paleocene-Eocene to Late Miocene-Pliocene and Quaternary belts overlap in the western segment, but a clear separation of the older belts from the Quaternary arc is evident in the eastern segment. The belts form a border to the Sundaland craton, situated along the southern edge of the Eurasian plate and the northern margin of the Australian continental plate. The arc complex lies between Indian oceanic crust to the south and Philippine and Pacific oceanic crust to the north (Fig. 2.1).

The Sunda-Banda magmatic arc is recognized as one of the most prospective Au-Cu magmatic belts in the world, with a total endowment of 92.4 Moz of Au, 279.2 Moz of Ag and 61.92 Blb of Cu (Maryono et al., 2017). Cu-Au-(±Mo) porphyry-style mineralization is the main resource (+ 90 %), with epithermal, VHMS, sediment-hosted and skarn constituting the remaining 10 % of the total metal resources along the arc (Fig. 2.1; Carlile and Mitchell, 1994; Hall and Sevastjanova, 2012; Setiadji and Maryono, 2012; Maryono et al., 2017). Three world class gold-copper porphyry deposits: Batu Hijau (19.9 Moz gold; 19.6 Blb copper; Clode et al., 1999), Elang (25.4 Moz gold; 16.3 Blb copper; Newmont 2012) and Tumpangpitu (29.9 Moz gold and 19 Blb copper; Intrepid Mines Ltd, 2012; Fig. 2.1, 2.2, Table 2.1) constitute the main Cu-Au resources.

The western portion of the arc is dominated by poorly endowed porphyry prospects on the northern tip of Sumatra (Fig. 2.1). The alignment of mineralized centers continues to the southeast via the Martabe high-sulfidation epithermal deposit towards central and eastern Sumatra, which contains several low-sulfidation epithermal deposits. There are minor, poorly endowed porphyry deposits in West Java at Ciemas and central Java at Selogiri, Wonogiri, Trenggalek and Malang. Epithermal deposits and prospects dominate this segment (Figs. 2.1 - 2.3 and Table 2.1). Tumpangpitu lies on the southeast coast of East Java, within the central portion of the Sunda-Banda magmatic arc (Figs. 2.1 - 2.3). It is the first world class occurrence of high grade porphyry copper-gold mineralization discovered in East Java. Continuing eastwards along the arc, the trend of world class porphyry deposits continue with Batu Hijau, Elang and Hu'u in Sumbawa (Figs. 2.1 - 2.3; Carlile and Mitchell, 1994; Garwin, 2002; Maryono, 2012; Maryono et al., 2016, 2017). The far eastern portion of the arc toward Flores and Damar islands hosts epithermal-like VMS deposits at Wetar on Romang island (Fig. 2.1; Seran and Farmer, 2013).

2.2.1 Age variations along the Sunda-Banda arc

The ages of the magmatic arcs span from the Late Mesozoic to Cenozoic (Figs. 2.2 and 2.3; Whitford, 1975; Katili, 1975; Hamilton, 1979; Hutchison, 1989; Maryono et al., 2017). Subduction along the Java trench initiated in the Eocene in western Java, the Oligocene to Pliocene in eastern Java to west Lombok, and in the Miocene to Pliocene for most of Lombok and Sumbawa (Fig. 2.2; Smyth et al., 2005; Setijadji and Maryono, 2012). The Oligocene to Pliocene magmatic belt is widespread in the southern parts of the islands along the Sunda-Banda arc, with some remnant Miocene volcanic centers (Figs. 2.2 and 2.3). Cu-Au-(±Mo) mineralization formed in different stages during arc evolution; however, world class porphyry deposits appear to have formed almost exclusively during the Pliocene (Fig. 2.3).

2.2.2 Tectonic framework of the Sunda-Banda arc

The Sunda-Banda magmatic arc extends from the west with a north-easterly dipping oblique subduction system in Sumatra (the western Sunda arc), through Java, Bali, Lombok and Sumbawa with a north-dipping subduction system (1,800 km; the eastern Sunda arc); the Flores and Banda islands in the east (the Banda arc) have a more complex arc-trench configuration (Fig. 2.1; Hamilton, 1979; Carlile and Mitchell, 1994; Setijadji et al., 2006; Maryono et al., 2017). The recent tectonic regime (subduction vs collision) and reversal in Quaternary arc polarity created major differences between the eastern Sunda and Banda arcs. The eastern Sunda arc is characterized by a Quaternary volcanic chain along the northern parts of the islands and formed from subduction of Indian oceanic crust (Figs. 2.1 - 2.3). The Banda arc comprises a Quaternary volcanic chain in southern parts of the islands due to collision with Australian crust (Fig. 2.1).

The Sunda-Banda arc developed during subduction of the north-moving Indo-Australian plate beneath the Asian continental plate margin (Fig. 2.1; Carlile and Mitchell, 1994; Clements et al., 2009; Hall and Sevastjanova, 2012; Setijadji and Maryono, 2012; Maryono et al., 2017). The Sunda-Banda island arc of Middle Miocene to Pliocene age is thought to have been initiated by subduction reversal following an Oligocene compressive event that was associated with the northward emplacement of ophiolite and island arc assemblages onto the Sunda margin, and associated formation of melanges, ophiolite fragments and deformation zones offshore from western Sumatra (Whitford, 1975; Katili, 1975; Daly et al., 1991; Harbury and Kallagher, 1991). The initiation of northward subduction beneath the Sunda-Banda arc migrated eastward following this collision event. This migration is clearly evident from the east-west alignment of deeply dissected Miocene to Pliocene volcanic centers along the south coast of Java, Lombok and Sumbawa, and by a parallel east-west alignment of juvenile and active Quaternary volcanoes that define the present active arc further north along central Java and northern Bali, Lombok and Sumbawa (Figs. 2.2 and 2.3).

Subduction is highly oblique along the northwest segment of the Sunda-Banda magmatic arc, beneath Sumatra and towards the Andaman Islands and Burma (Moore et al., 1980). The subducting slab beneath the Sunda-Banda arc has a pronounced curve from Sumatra, where it dips ~ 30° to 45° NE, through east Sunda, where it dips ~50° to 70° N, to Banda where it forms a concave spoon-shaped structure with an axis that plunges ~ 40° W (Fig. 2.1; Garwin et al., 2005). The western segment of the eastern Sunda arc (western Java) developed on thick continental crust on the southern margin of Sundaland, where thick sedimentary sequences from the Bengal and Nicobar fans were transported into the subduction zone. By contrast, the eastern segment (eastern Java to Sumbawa) was constructed on thinner oceanic crust bounded by Australian continental crust further east where subduction is near perpendicular to the Sunda- Banda arc, and only a thin cover of sediment has entered the subduction zone. Further to the east, incipient areas of collision are occurring along the arc where fragments of the Australian continental margin are accreting

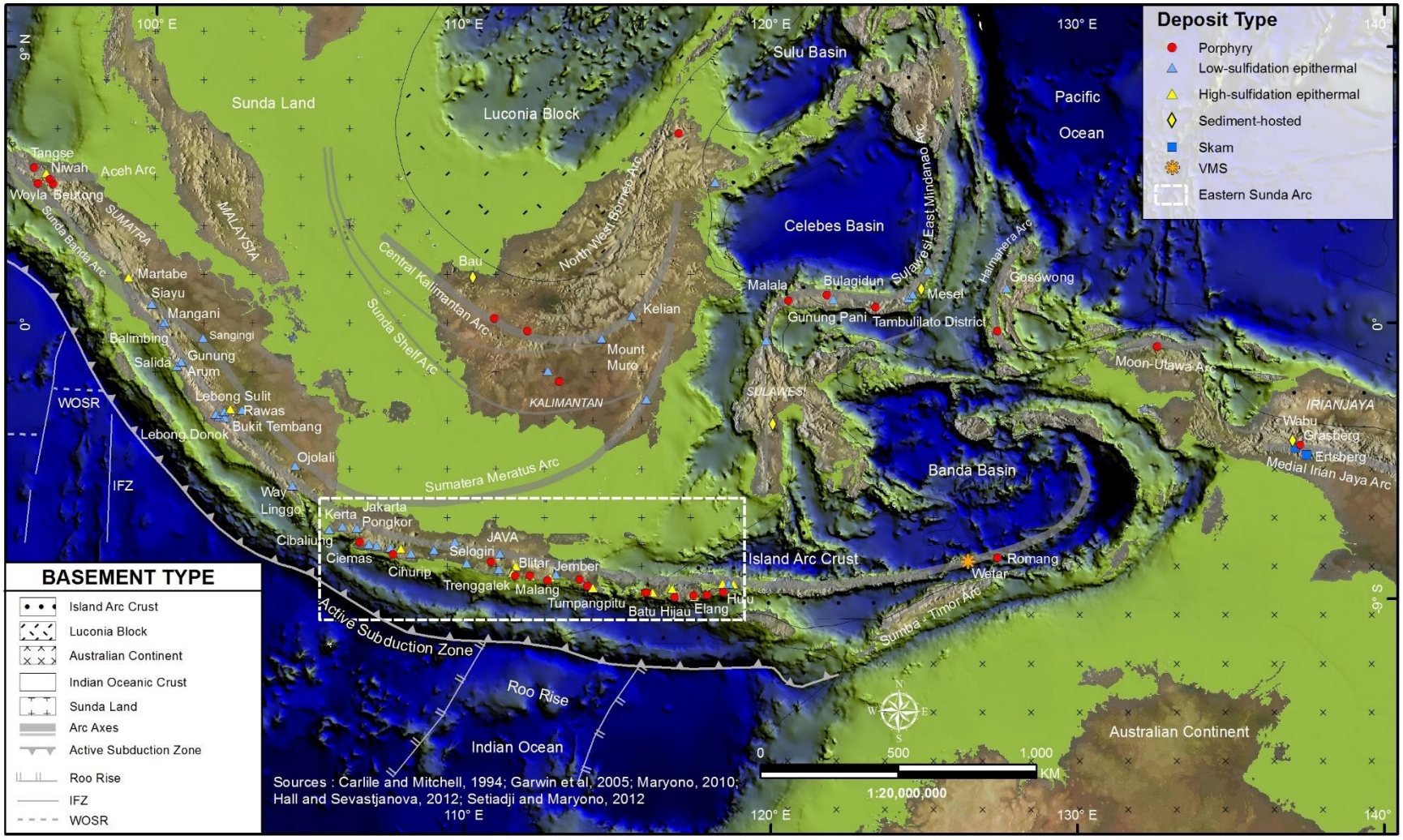

Figure 2.1. Distribution of the major porphyry and epithermal deposits-prospects and tectonic elements of Indonesia, highlighting the eastern Sunda arc (Maryono et al., 2017).

Table 2.1. List of significant epithermal and porphyry deposits with resources along the Sunda-Banda magmatic arc.

Deposit / Prospect	Deposit type	Region/Island	Tonnage (mt)	Grade			Contained metals			References
				Au (g/t)	Ag (g/t)	Cu (%)	Au (t)	Ag (t)	Cu (mt)	
Abong	SHG	North Sumatra	8.49	1.49	10.7	-	12.65	90.81	-	Barisan Gold Cooperation (2012, 2014)
Arinem	ISE	West Java	2.00	5.70	41.5	-	11.40	83.00	-	Yuningsih et al. (2012)
Balimbing	LSE	West Sumatra	NA	-	-	-	0.49	0.30	-	Van Bemmelen (1949)
Batu Hijau	PCG	Sumbawa	1,640.00	0.35	-	0.44	574	-	7.22	Clode et al. (1999)
Beutong	PCG	North Sumatra	505.00	0.13	1.21	0.47	66.19	612.18	2.37	Tigers Realm Group (2014)
Cibaliung	LSE	West Java	1.30	10.42	60.79	-	13.55	79.03	-	Harijoko et. al. (2007)
Cikondang	ISE	West Java	0.70	10.90	-	-	8.00	-	-	Marcoux and Milesi (1994)
Cikidang	LSE	West Java	0.20	14.30	79.90	-	2.86	15.98	-	Rosana and Matsueda (2002)
Cirotan	LSE	West Java	0.97	6.02	148.30	-	5.84	143.89	-	Milési et al. (1994); Wagner et al. (2005)
Dairi	SHX	North Sumatra	11.05	-	7.50	-	-	82.88	-	PT BMR Tbk (2011)
Elang	PCG	Sumbawa	2,267.00	0.46	1.0	0.36	1,042.82	2,267.13	8.16	Huspeni (2012)
Gunung Arum	ISE	West Sumatra	NA	-	-	-	0.90	106.00	-	Van Bemmelen (1949)
Kerta, Cisadang	LSE	West Java	247.69	0.43	-	-	106.51	-	-	Lubis et al. (2012); Sutami (2016)
Lebong Donok	LSE	Bengkulu, Sumatra	2.90	14.30	79	-	41.47	229.10	-	Kavalieris (1988); Henley and Etheridge (1995)
Lebong Simpang	LSE	Bengkulu, Sumatra	NA	-	-	-	0.5	0.30	-	Van Bemmelen (1949)
Lebong Sulit	LSE	Bengkulu, Sumatra	NA	-	-	-	6.81	10.30	-	Van Bemmelen (1949)
Lebong Tandai	ISE	Bengkulu, Sumatra	2.80	15.60	175	-	43.68	490.00	-	Jobson (1994); SCG Plc (2009)
Mangani	LSE	West Sumatra	0.90	6.50	265	-	5.85	238.50	-	Kieft and Oen (1974); Kavalieris et al. (1987)
Martabe	HSE	North Sumatra	190.00	1.20	11.0	-	230.17	2,177.24	-	G-Resources Group Ltd (2015)
Miwah	HSE	North Sumatra	103.90	0.94	2.68	-	97.67	278.45	-	Centurion Minerals Pty Ltd (2011)
Ojolali, Bukit Jambi	LSE	South Sumatra	6.50	0.80	4.80	-	5.44	31.20	-	East Asia Minerals Co (2011) Finders Resources Ltd (2014)
Pangulir	ISE	Sumbawa	21.86	0.66	16.90	-	14.43	369.43	-	SRK (2012) in Dahlius et al. (2012)
Pongkor	LSE	West Java	6.90	17.1	154.30	-	103.22	929.16	-	Basuki et al. (1994)
Pelangan-Mencanggah	HSE / ISE	Lombok	11.78	1.52	4.80	-	17.94	56.64	-	Southern Arc Minerals (2013)
Rawas/Tembang	LSE	South Sumatra	7.20	2.10	27.00	-	14.87	194.61	-	Sumatra Copper Gold Plc (2015)
Salida	LSE	West Sumatra	NA	-	-	-	3.00	97.99	-	Van Bemmelen (1949)
Selodong	PCG	Lombok	66.75	0.43	-	0.27	28.70	-	0.18	Southern Arc Minerals (2013)

Deposit / Prospect	Deposit type	Region/Island	Tonnage (mt)	Grade			Contained metals			References
				Au (g/t)	Ag (g/t)	Cu (%)	Au (t)	Ag (t)	Cu (mt)	
Selogiri	PCG	Central Java	81.56	0.38	-	0.11	31.00	-	0.09	Augur Resources (2016)
Sihayo	SHG	North Sumatra	16.90	2.60	-	-	44.32	-	-	Sihayo Gold Ltd (2013)
Soripesa	ISE	Sumbawa	NA	-	-	-	1.00	-	-	Carlile and Mitchell (1994)
Tambang Sawah	LSE	Bengkulu, Sumatra	NA	-	-	-	2.33	181.00	-	Van Bemmelen (1949)
Tangse	PCG	North Sumatra	600.00	-	-	0.30	-	-	1.80	Van Leeuwen et al. (1987); EAM Corp (2007)
Tengkereng (Upper)	PCG	North Sumatra	276.00	0.63	0.43	-	173.88	118.68	-	Hamid et al. (2014)
Tumpangpitu oxide	HSE	East Java	99.25	0.80	24.80	-	79.40	2,461.40	-	PT Merdeka Copper Gold Tbk (2016)
Tumpangpitu porphyry	PCG	East Java	1,900.00	0.45	-	0.45	855.00	-	8.55	Intrepid Mines Ltd (2012)
Way Linggo	LSE	South Sumatra	1.60	7.89	14.60	-	12.33	108.55	-	Kingrose Mining Ltd (2012)
Woyla	LSE	North Sumatra	NA	-	-	-	62.20	-	-	Tigers Realm Group (2014)

Table modified after Maryono et al. (2017). Abbreviations: LSE = low sulfidation epithermal, ISE = intermediate sulfidation epithermal, HSE = high sulfidation epithermal, PCG = porphyry copper gold, SHG = sediment hosted gold, NA = data not available, mt = million tons, t = tons.

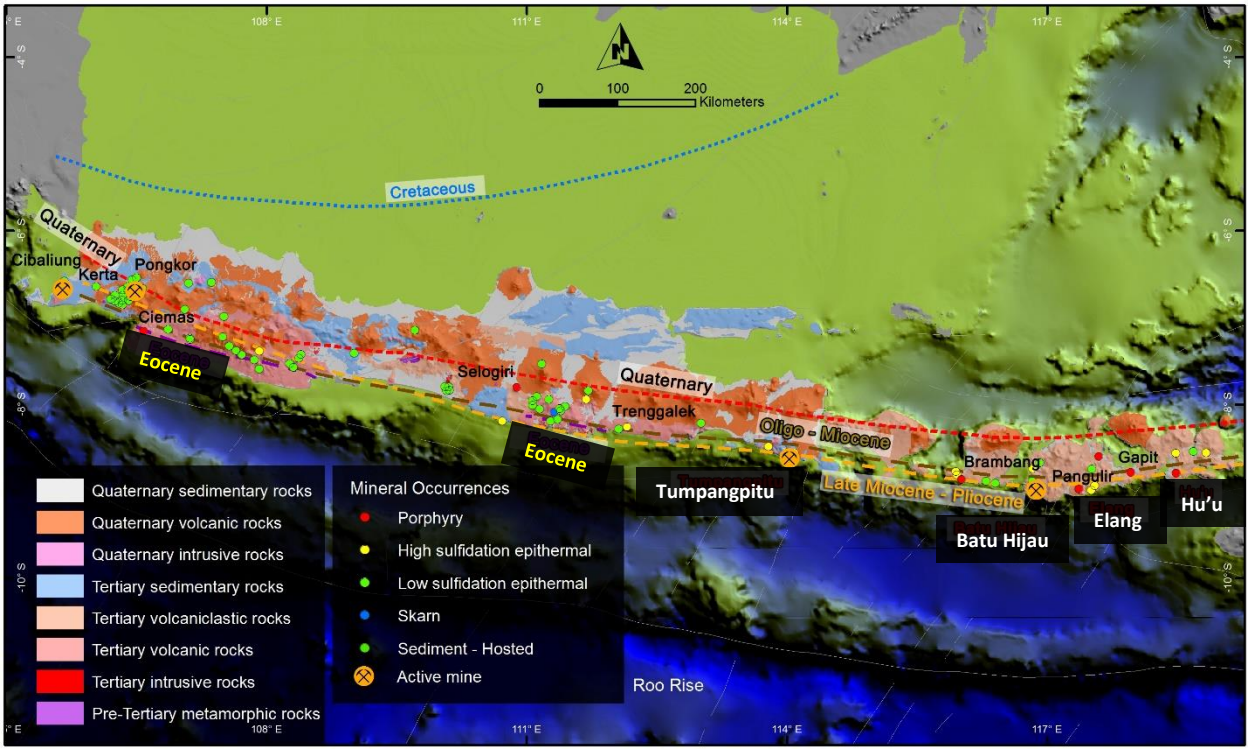

Figure 2.2. Regional geology and gold-copper occurrences of the eastern Sunda Arc (Hamilton, 1979; Carlile and Mitchell, 1994; Suratno, 1995; Metcalfe, 1996; Hall, 2002; Setijadji et al., 2006; Maryono et al., 2017). Five magmatic belts of the Eastern Sunda arc show consistent northward migration from Early Tertiary to Quaternary, the Late Miocene-Pliocene arc reversed southward locally from East Java to Sumbawa.

against the Banda arc (e.g., Sumba and Timor; Fig. 2.1; Hamilton, 1979; Carlile and Mitchell, 1994; Hall, 2002; Setijadji et al., 2006; Hall and Sevastjanova, 2012).

2.2.3 Tectonic framework of the eastern Sunda-Banda arc

The eastern Sunda arc demonstrates several distinctive features that differ from the idealized temporal and spatial schemes of subduction zone magmatism (Foden and Varne, 1980; Soeria-Atmadja et al., 1994; Setijadji et al., 2006; Fiorentini and Garwin, 2010). The eastern Sunda arc underwent migration towards the hinterland during its Cenozoic history, which is different from a typical foreland migration of a subduction zone (Setijadji et al., 2006). Subduction along the eastern Sunda-Banda arc initiated in the Paleocene-Eocene, and the arc underwent a period of extension related to slab rollback around 15 - 12 Ma (Hall, 2002; Smyth et al., 2005; Fiorentini and Garwin, 2009; Spakman and Hall, 2010). This period of extension initiated a polarity shift to southward-directed subduction of oceanic crust of the marginal Banda Sea beneath the arc (Fiorentini and Garwin, 2009). Complexities arose in the Miocene due to the subduction of the Roo Rise, a trapped slab of thickened oceanic crust (Figs. 2.1 - 2.3). Important changes in plate motions and boundaries since 5 Ma (Audley-Charles, 2004) are thought to have caused local reversals in ages from north to south as magmatism migrated closer towards the trench.

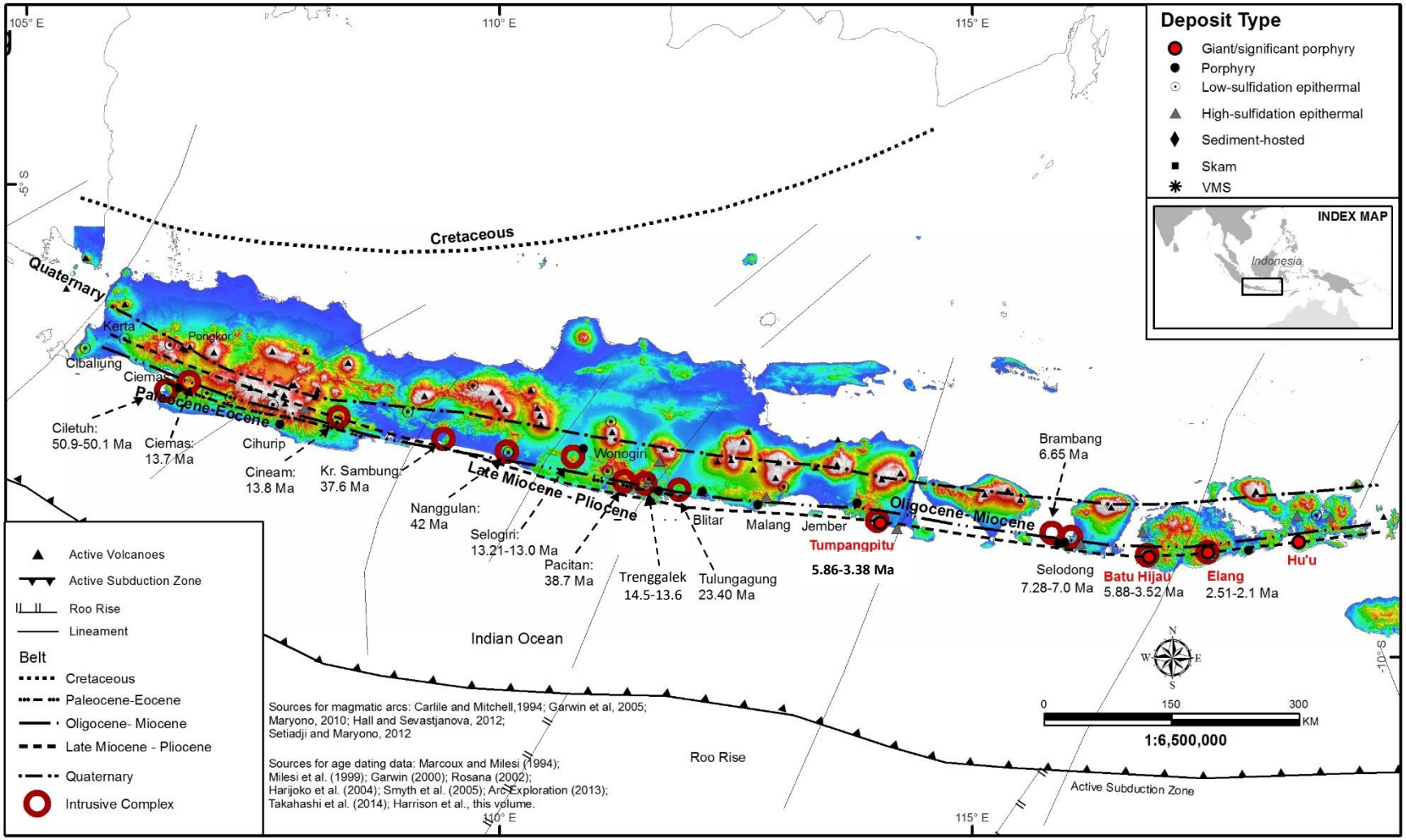

Figure 2.3. Remnant volcanic centers of Paleocene-Eocene age (West Java) and Oligocene to Pliocene age (Java to Sumbawa) along the Southern Mountains, with intrusive centers of Eocene to Pliocene age and SRTM imagery. Age determinations from Soeria-Atmadja et al. (1994); Marcoux and Milesi, (1994); Milesi et al. (1999); Garwin (2000); Rosana (2002); Pertamina-ITB (2002); Harijoko et al. (2004); JICA-JOGMEC (2004); Smyth et al. (2005); Takahashi et al. (2011); Arc Exploration Ltd. (2013); this study and Maryono et al. (2017).

2.2.3.1 Regional geology of the eastern Sunda magmatic arc

Cenozoic volcanic-magmatic rocks dominate the regional geology of the eastern Sunda arc (Fig. 2.2). Basement rocks of Cretaceous age (Hamilton, 1979; Wakita, 2000; Wakita and Munasri, 1994) are thought to be restricted to western Java at Karangsambung and the Jiwo Hills (Fig. 2.2). However, Cretaceous zircons were identified in samples from the Tanjung Jahe diatreme breccia at the Tujuh Bukit project during this study (Chapter 4). Paleocene-Eocene volcanic centers are poorly defined and restricted to the western segment of the arc, whereas Oligocene to Early Miocene magmatic rocks are continuously distributed along the whole eastern Sunda arc (Fig. 2.2). Volcaniclastic-sedimentary rocks of Late Miocene to Pliocene age are more abundant than the older volcanic rocks, and are well exposed throughout the Southern Mountain Range of the islands (Fig. 2.2; Garwin, 2000; Setijadji et al., 2006; Smyth et al., 2008; Setijadji and Maryono, 2012; Maryono et al., 2017). Low-K calc-alkaline to weakly alkaline andesitic volcanic and interbedded volcaniclastic rocks, associated low-K intermediate intrusions and minor shallow water marine sedimentary rocks and limestone, extend from Java to Bali, Lombok and Sumbawa (Meldrum et al., 1994; Suratno, 1995; Maula and Levet, 1996; Sjoekri, 1998; Garwin, 2002; Setijadji et al., 2006).

2.2.3.2 Structure of the eastern Sunda magmatic arc

The eastern Sunda arc is segmented by a series of arc-normal, NE-trending transform faults that are evident in topographic data-sets, including transection of an area of the Roo Rise (Fig. 2.3; Garwin et al., 2005; Hall, 2009). The transform faults are interpreted to have formed due to differences in thickness between the normal and thick oceanic crusts (Garwin et al., 2005; Setijadji et al., 2006; Hall, 2009). Tectonic factors appear to have localized volcanic centers of the Miocene arc at positions near the southwest margins of these transfer structures (Fig. 2.3; Garwin, 2002; Maryono, 2012). Eastern Java shows three of these major sinistral cross faults (Fig. 2.3). Contemporaneous continental to deep-ocean clastic sediments were deposited on the margins of the volcanic centers. Regional scale distribution of porphyry clusters and diorite batholiths reflect proximity to the regions' major arc-parallel NW-trending faults. Later NE-trending cross structures suggest that structural intersections localized zones of magma ascent (Fig. 2.3).

2.3 District geology

2.3.1 Characteristics of porphyry deposits along the Sunda-Banda magmatic arc

The porphyry deposits of the eastern Sunda magmatic arc, (Figs. 2.2 and 2.3; Table 2.2; Selogiri, central Java - Warmada et al., 2007; Imai et al., 2007; Suasta and Sinugroho, 2011; Trenggalek, East Java - Arc Exploration Ltd., 2013; Tumpangpitu, SE Java - Harrison and Maryono, 2012; Harrison et al., 2017; Batu Hijau and Elang, Sumbawa - Garwin, 2000; Maryono et al., 2005; Maryono et al., 2012, 2017; Selodong and Brambang, SW Lombok - Rompo et al., 2012) share a number of characteristic features. These features include their association with remnant Miocene volcanic centers (Figs. 1.3 and 2.3), low- to moderate-K calc-alkaline magmas (Setijadji et al., 2006), pre-mineralization dioritic batholiths, formation in clusters at intersections of major NW-trending arc parallel structures with NNE-trending structures (Figs. 1.3, 1.4 and 2.3) and Neogene magmatism associated with major porphyry Cu-Au style mineralization (Figs. 2.2 and 2.3; nested tonalitic intrusive complexes) and low-, intermediate- and high-sulfidation state epithermal-style mineralization (Figs. 2.2 and 2.3).

2.3.2 Volcano-sedimentary rock succession

Porphyry-epithermal districts of the eastern-Sunda arc are predominantly hosted by andesitic volcano-sedimentary rock units, grouped into lower and upper sequences (Figs. 2.2 and 2.5). The Tujuh Bukit district is hosted by the Batuampar Formation, an andesitic volcaniclastic succession at least 1,200 m thick that contains thin intercalations of limestone, volcanic sandstone, siltstone and mudstone of Early to Late Miocene age (Hamilton, 1979). At Tumpangpitu, this pre-mineralization stratigraphic package is composed of a sequence of well-bedded turbidites and shallow marine sedimentary rocks of Early to Middle Miocene age (20.67 ± 0.47 to 16.68 ± 0.35 Ma; Chapter 4). This volcano-sedimentary package is at least 500 m thick and occurs as continuous beds that can be traced in a concentric fashion, preserved around the fringes of the composite Tumpangpitu porphyry stock (Fig. 2.5; Harrison, 2009; Rohrlach, 2011; Harrison and Maryono, 2012)

Volcano-sedimentary units at Batu Hijau and Elang are relatively well preserved, and exceed 1,000 to 1,500 m in thickness (Garwin, 2002). Both districts display two main coarsening upwards stratigraphic sequences. The lower sequences consist of fine-grained volcanic sandstones and minor mudstone, the upper sequences comprise coarse crystal-rich volcanic lithic breccia, sandstone and conglomerate. Moderately bedded to massive interbeds of limestone (packstone and wackestone) and calcareous siltstones (1 to 25 m thick) are observed within the lower sequences. The limestone interbeds were deposited at paleodepths of 40 to 60 m below sea level from 21 to 15 Ma on the basis of benthonic foraminiferal assemblages (Fig. 2.5; Clode et al., 1999; Garwin, 2000; Maryono et al., 2005).

Table 2.2. Summary of features of porphyry deposits along the eastern Sunda arc.

Deposits / prospects	Causative intrusions	Age (Ma)	Size (km^2)	0.3 % Cu lateral extent (km)	0.3 % Cu vertical extent (km)	Composition	Textures and % phenocrysts	Pre-mineralization intrusions and breccias	Post-mineralization intrusions and breccias	References
Batu Hijau	3 phases: Old, Intermediate and Young Tonalite	5.88 - 3.52	0.16	1.2 x 1.2	1.5	Tonalite	Porphyritic, 45 - 60 % phenocrysts	Equigranular diorite, quartz diorite	Santong diatreme	Meldrum et al. (1994); Clode et. al. (1999); Garwin (2002); Maryono et al. (2017)
Elang	3 Phases: Charlie, Delta and Echo Tonalite	2.51 - 2.10	0.24	1.5 x 0.8	1.2	Tonalite	Porphyritic, 35 - 55 % phenocrysts, 0.5 - 3 mm	Equigranular diorite, microdiorite	Ike diatreme, Dacite dike	Proffett (2005); Maryono et al. (2005); Maryono et al. (2017)
Brambang	3 phases: Early, Intermediate and Late Tonalite	6.65	0.36	0.5 x 0.5	0.8	Tonalite / Quartz diorite	Porphyritic, 25 - 45 % phenocrysts	Fine-grained diorite	Bendung diatreme	Coote (2012); Maryono et al. (2013); Maryono et al. (2017)
Selodong	2 phases: Quartz Diorite 1 and Quartz Diorite 2	7.28 - 7.00	0.20	2 zones (0.35 x 0.4)	0.45	Diorite	Porphyritic, 40 - 60 % phenocrysts	Diorite	Selodong diatreme	Maryono (2007); Schmeider and Clode (2009); Southern Arc Minerals (2012); Maryono et al. (2017)
Tumpangpitu	3 phases: phase 4 (coarse), phase 5 (fine), phase 6 (coarse) tonalite	5.86 - 3.38	0.64	1.5 x 1.2	> 1.2	Tonalite	Porphyritic, 50 - 70 % phenocrysts, 2 - 5 mm	Tanjung Jahe diatreme, Phase 1 quartz diorite, Phase 2 diorite, Phase 3 quartz diorite	Phase 7 and 8 quartz diorites, Tumpangpitu diatreme	Harrison and Maryono (2012); this study
Selogiri	3 phases: hornblende andesite, diorite porphyry and microdiorite	13.21 - 13.00	0.40	NA	NA	Diorite	Porphyritic, 60 % phenocrysts	Microdiorite, equigranular diorite	Diatreme breccia	Warmada et al. (2007); Imai et al. (2007); Suasta and Sinugroho (2011); Maryono et al. (2017)

Abbreviations: NA = data not available.

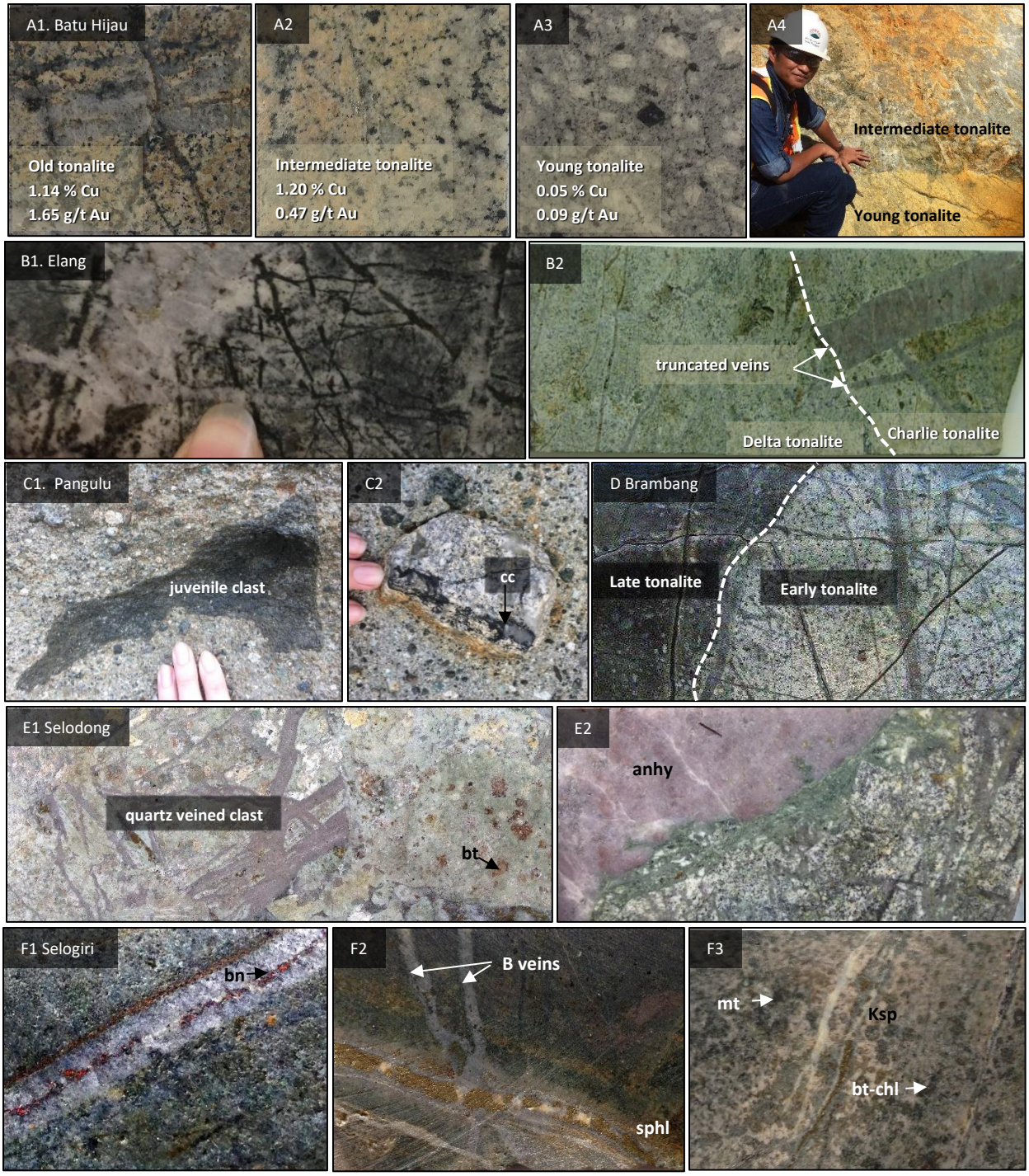

Figure 2.4. Examples of intrusions, diatreme breccias, hostrocks, contact relationships, alteration and mineralization from porphyries of the eastern Sunda arc. A1) Batu Hijau, Sumbawa Old; A2) Intermediate; A3) Young Tonalite; A4) Contact between Intermediate and Young tonalites; B1) Elang, Sumbawa; actinolite vein cut by A vein in Charlie tonalite; B2) Contact between Delta and Charlie tonalites; C1) Pangulu, SW Lombok-juvenile andesitic clast; C2) Quartz - chalcocite porphyry clast in Pangulu diatreme; D) Brambang, SW Lombok, contact between Early and Late tonalites; E1) Selodong, SW Lombok, quartz veined clast in Selodong diatreme; E2) Fine-grained phase 2 quartz diorite; F1) Selogiri, central Java; quartz - bornite B vein in medium-grained diorite; F2) Quartz - chalcopyrite - pyrite - bornite B veins crosscut by pyrite - illite - sphalerite vein in andesite; F3) Quartz - pyrite - chalcopyrite veins with biotite - secondary chlorite - K-feldspar alteration. Harrison, field visits 2012, 2015, 2016; Maryono et al., 2017. Abbreviations: anhy = anhydrite, bn = bornite, cc = chalcocite, Ksp = K-feldspar, mt = magnetite, sphl = sphalerite.

2.3.3 Multiphase intrusive complexes

Multiphase mineralized porphyry intrusions have been distinguished on the basis of crosscutting relationships, textures, grain sizes and compositions, in particular the abundance and size of quartz phenocrysts (Table 2.2; Figs. 2.4 and 2.5; Proffett, 1998; Harrison and Maryono 2012; Maryono et al., 2005; 2017). The scale of the inter-mineralization intrusive complexes of the eastern Sunda arc varies from 0.16 to 0.64 km^2 in area (Table 2.2). The porphyry complexes have been emplaced along the margins or structures crosscutting larger (up to 5 km^2), equigranular, dioritic batholiths (Fig. 2.5). Porphyry clusters of three to six deposits occur in districts of 50 to 100 km^2 at Tujuh Bukit, Batu Hijau, Elang, Hu'u, Selodong and Brambang (Figs. 1.4, 2.3 and 2.5)**.** The volcaniclastic succession at Tumpangpitu has been cut by eight phases of intrusions spanning the Late Miocene to Early Pliocene (Table 2.2). At Batu Hijau, six intrusive phases have been documented, comprising three pre-mineralization and three inter-mineralization (Figs. 2.4A1-A4; 2.5 and Table 2.2; Proffett, 1998; Garwin, 2002; Maryono et al., 2005; 2017). At Elang, seven intrusive phases have been documented, two pre-mineralization, three inter-mineralization and two post-mineralization (Figs. 2.4B1 and B2, 2.5 and Table 2.2; Maryono et al., 2005; 2017).

2.3.4 Pre-mineralization intrusions

Pre-mineralization intrusive phases are typically composed of microdiorite, diorite and quartz diorite, with low K_2O contents (less than 0.8 wt %; Table 2.2; Meldrum et al., 1994; Clode et al., 1999; Maryono et al., 2005, 2017). The dioritic phase has generally formed a large batholith exceeding 10 km^2, e.g., Phase 2 diorite at Tumpangpitu (Fig. 2.5). At Batu Hijau and Elang, large equigranular quartz diorite to diorite stocks and batholiths with surface exposures ranging from 2 to more than 10 km^2 occupy the northern parts of the mineralized intrusive complexes (Table 2.2; Fig. 2.5; Maryono et al., 2005, 2017). Rock textures in the pre-mineralization dioritic batholiths vary from sub-porphyritic to equigranular (2 - 4 mm grain size), consisting dominantly of plagioclase (60 - 70 %) and lesser hornblende. Quartz is less than 5 % by volume and rarely observable as quartz eye phenocrysts, making it distinguishable from later quartz diorite and tonalite intrusions (Table 2.2). Pre-mineralization intrusions have intruded the volcano-sedimentary rock successions, and define the cores of evolved volcanic-plutonic centers. Most of the pre-mineralization intrusions are Miocene in age (Fig. 2.5; Garwin, 2000; Maryono et al., 2017). The Tujuh Bukit district is unique in that it hosts a pre-mineralization diatreme at Tanjung Jahe (Table 2.2, Fig. 2.5).

2.3.5 Inter-mineralization intrusions

The mineralizing intrusive complexes typically consist of two to five intrusive phases (Figs. 2.5 and 2.6; Table 2.2). A series of mineralizing intrusions (early, intermediate and late) have been well documented at Batu Hijau (Clode et al., 1999; Garwin, 2002; Maryono et al., 2017), Elang (Maryono et al.,

2005), Tumpangpitu (Harrison and Maryono, 2012), Selodong (Rompo et al., 2012) and Brambang (Maryono et al., 2013; Figs. 2.4 to 2.6; Table 2.2). The causative intrusions are dominated by plagioclase (>50 vol %) and quartz (~10 to 20 %), and are mostly quartz diorite to tonalite. The inter-mineralization intrusions are elongate, from 200 m to 1,200 m in diameter and >1 km in vertical extent, and formed the cores of Au-Cu±Mo ore zones (Figs. 2.5 and 2.6, Table 2.2). The interpreted depths of emplacement for the porphyry intrusions range from 1 to 5 km below the paleosurface (Garwin, 2000; Idrus et al., 2007).

Batu Hijau has three inter-mineralization tonalite phases, locally termed the Old Tonalite, Intermediate Tonalite and Young Tonalite (Clode et al., 1999; Table 2.2; Figs. 2.4A1-A4, 2.5 and 2.6) emplaced between 3.55 ± 0.13 Ma and 3.52 ± 0.14 Ma (Maryono et al., 2017). $^{206}Pb/^{238}U$ age dating at Elang suggests that three mineralizing intrusions were emplaced from 2.51 ± 0.13 Ma to 2.38 ± 0.18 Ma (Figs. 2.4B1-B2, 2.5 and 2.6; Table 2.2 Maryono et al., 2017). Zircon dating at Selodong of four intrusive phases by Maryono et al., (2017) support crosscutting relationships observed during logging, defining a pre-mineralization old diorite (7.28 ± 0.31 Ma), quartz diorite phase 1 (7.28 ± 0.23 Ma), quartz diorite phase 2 (Fig. 2.4E2 and Table 2.2; 7.22 ± 0.23 Ma), and late quartz diorite (7.04 ± 0.25 Ma). Three samples of inter-mineralization microdiorite intrusions from Selogiri yielded multiple Miocene ages (13.18 ± 0.34 Ma to 13.21 ± 0.22 Ma; Fig. 2.4F1-F3, Table 2.2). An inter-mineralization tonalite intrusion from Brambang has been dated by Maryono et al., (2017) as Late Miocene age (6.65 ± 0.31 Ma; Table 2.2).

2.3.6 Post-mineralization intrusions and breccias

Post-mineralization phreatomagmatic activity resulted in the formation of diatreme breccia bodies that have crosscut porphyry mineralization (Figs. 2.4C1, C2 and E1, 2.5, Table 2.2). Diatreme breccias have been mapped at Elang (Maryono et al., 2005), Rinti (Maryono and Setyandhaka, 2001), Batu Hijau (Priowasono and Maryono, 2000), Selodong and Brambang (Fig. 2.4E1; Maryono et al., 2013), Tumpangpitu (Harrison and Maryono, 2012), Binglis (Rompo et al., 2014), Trenggalek (Arc Exploration Ltd., 2013) and Selogiri (Warmada et al., 2006; Table 2.2). Post-mineralization intrusive activity at Elang is also marked by a dacite intrusion (Fig. 2.5). An excellent exposure of diatreme breccia can also be observed at Pengulu beach, south Lombok with juvenile andesitic clasts and mineralized porphyry fragments (Figs. 2.4 C1 and C2).

The diatreme breccia complexes in the eastern Sunda arc are generally andesitic in composition and have circular bodies with varying sizes, from 0.15 km^2 at Brambang to 6.8 km^2 at Tumpangpitu (Fig. 2.5, Table 2.2). The diatremes have downward tapering, inverted cone-shapes, and their subsurface conduits are sub-vertical. Small-scale pebble dikes that are a few meters wide crosscut the surrounding wallrocks. The diatremes generally post-date all of the intrusions and porphyry mineralization, but locally host late stages of epithermal mineralization.

2.3.7 Alteration and mineralization

Early hydrothermal alteration that characterizes porphyry deposits of the eastern Sunda is centred in and around nested dioritic to tonalitic porphyry complexes (Figs. 2.4 to 2.6). A progression in alteration has been observed from a central domain of quartz - magnetite - biotite - K-feldspar associated with high grade porphyry mineralization (Fig. 2.4F3), laterally outwards through minor actinolite, to epidote and then calcite. These distal assemblages all contain chlorite (Harrison and Maryono, 2012, Maryono et al., 2017). Porphyry mineralization produced stockwork, veins and disseminations of chalcopyrite, bornite, chalcocite and covellite that formed a carapace around mineralized stocks (Figs. 2.4 to 2.6). Highest grade porphyry mineralization shows a strong correlation with magnetite in all porphyry deposits of the eastern Sunda arc (Hoschke, 2012; Harrison and Maryono, 2012).

There is a predominance of secondary biotite alteration at Batu Hijau with only minor to trace K-feldspar (Maryono et al., 2017). Actinolite is part of the early alteration assemblage at both Batu Hijau and Elang, and shreddy chlorite abundant after biotite is a key surface alteration mineral where the potassic alteration is exposed (Maryono, 2000, Garwin, 2002; Maryono et al., 2017). Actinolite in the ore zone at Elang is even more abundant than secondary biotite (Maryono et al., 2017). Au-Cu-(±Mo) porphyry-style mineralization is directly related to sulfide zonation from central bornite + chalcopyrite + gold to chalcopyrite ± bornite, chalcopyrite ± pyrite and outer pyrite-only sulfide zones of porphyry deposits of the eastern Sunda (Maryono et al., 2017). Mineralization is related to porphyry stockwork veins including early phase veins (A and M; Gustafson and Hunt, 1975; EB; Gustafson and Quiroga, 1995) as the major contribution to Au-Cu ore (> 50 %; Maryono et al., 2017). C veins (Dilles and Einaudi, 1992; Gustafson and Quiroga, 1995) are poorly developed in the majority of porphyry deposits of the eastern Sunda (Maryono et al., 2017).

High-sulfidation epithermal mineralization is only well preserved at Tumpangpitu. Low-, intermediate- and base metal sphalerite - galena veins are developed to varying extents at all deposits of the eastern Sunda arc (e.g., Fig. 2.4F2; Maryono et al., 2017). The lateral dimensions of the 0.3 % copper shell of porphyry deposits of the eastern Sunda arc varies from 0.35 x 0.4 km at Selodong to 1.2 x 1.5 km at Tumpangpitu. The vertical extent of 0.3 % Cu varies from 0.45 to 1.5 km (Table 2.2).

2.3.8 Lithocaps of the Sunda-Banda arc

Large lithocaps (> 20 km^2, barren to mineralized) are exposed at surface at all of the porphyry Au-Cu-(±Mo) deposits and epithermal Au-Ag deposits of the eastern Sunda arc (Fig. 2.7; Garwin, 2000; Maryono et al., 2017). Lithocaps follow structural trends and have overprinted early alteration assemblages and underlying porphyry deposits (Fig. 2.7). The lateral extent of lithocaps varies from 0.3 km^2 at Batu Hijau (eroded roots of lithocap, mapped as feldspar-destructive alteration; Clode et al., 1999), 30 km^2 for

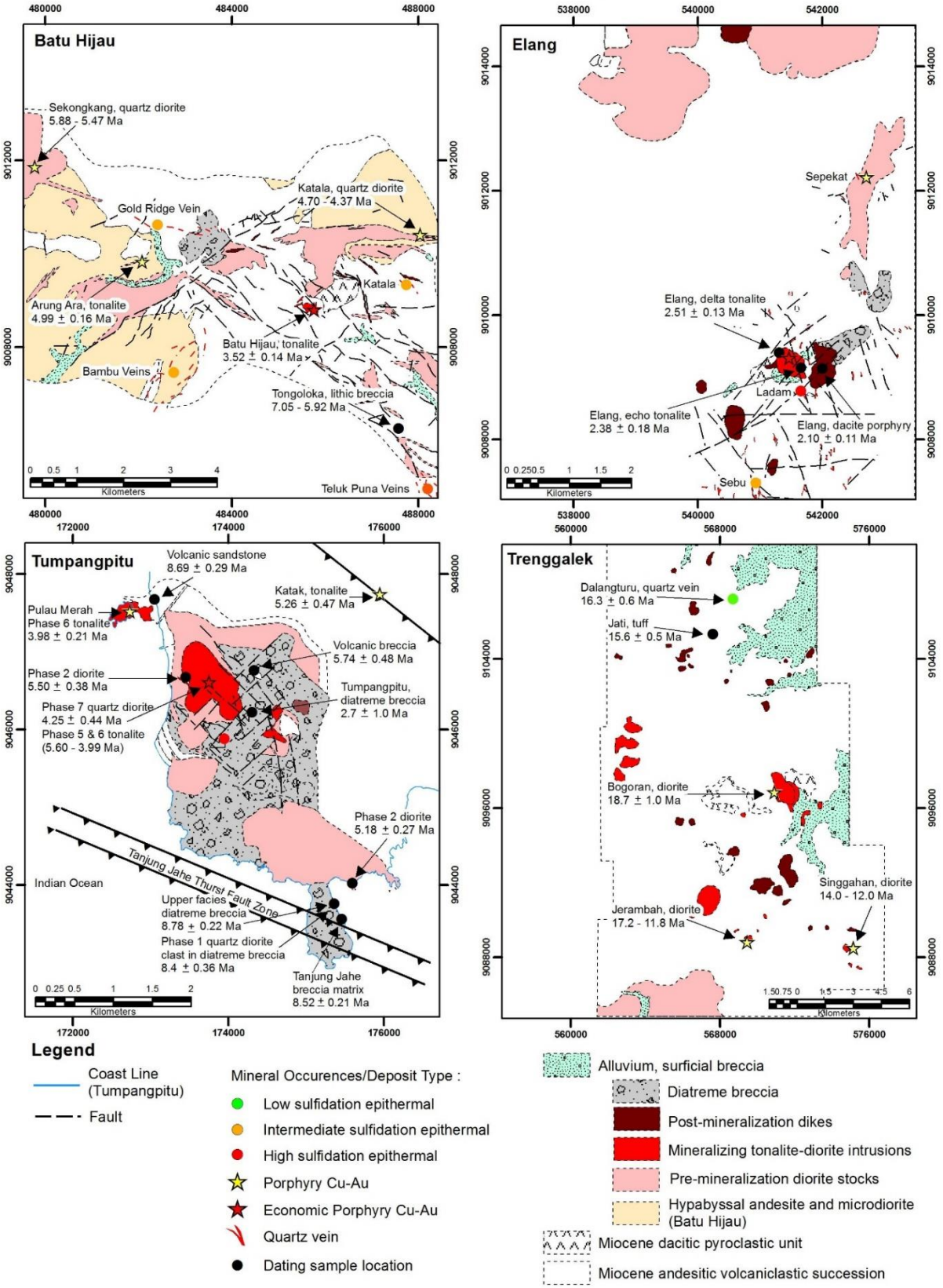

Figure 2.5. District geology of major porphyry systems at Batu Hijau, Elang and Tumpangpitu in comparison with low-grade porphyry systems at Trenggalek. A) Batu Hijau district geology (Garwin, 2000); B) Elang district geology (Maryono et al., 2005); C) Tumpangpitu district geology (this study) and D) Trenggalek district geology (Arc Exploration Ltd., 2013; Maryono et al., 2017).

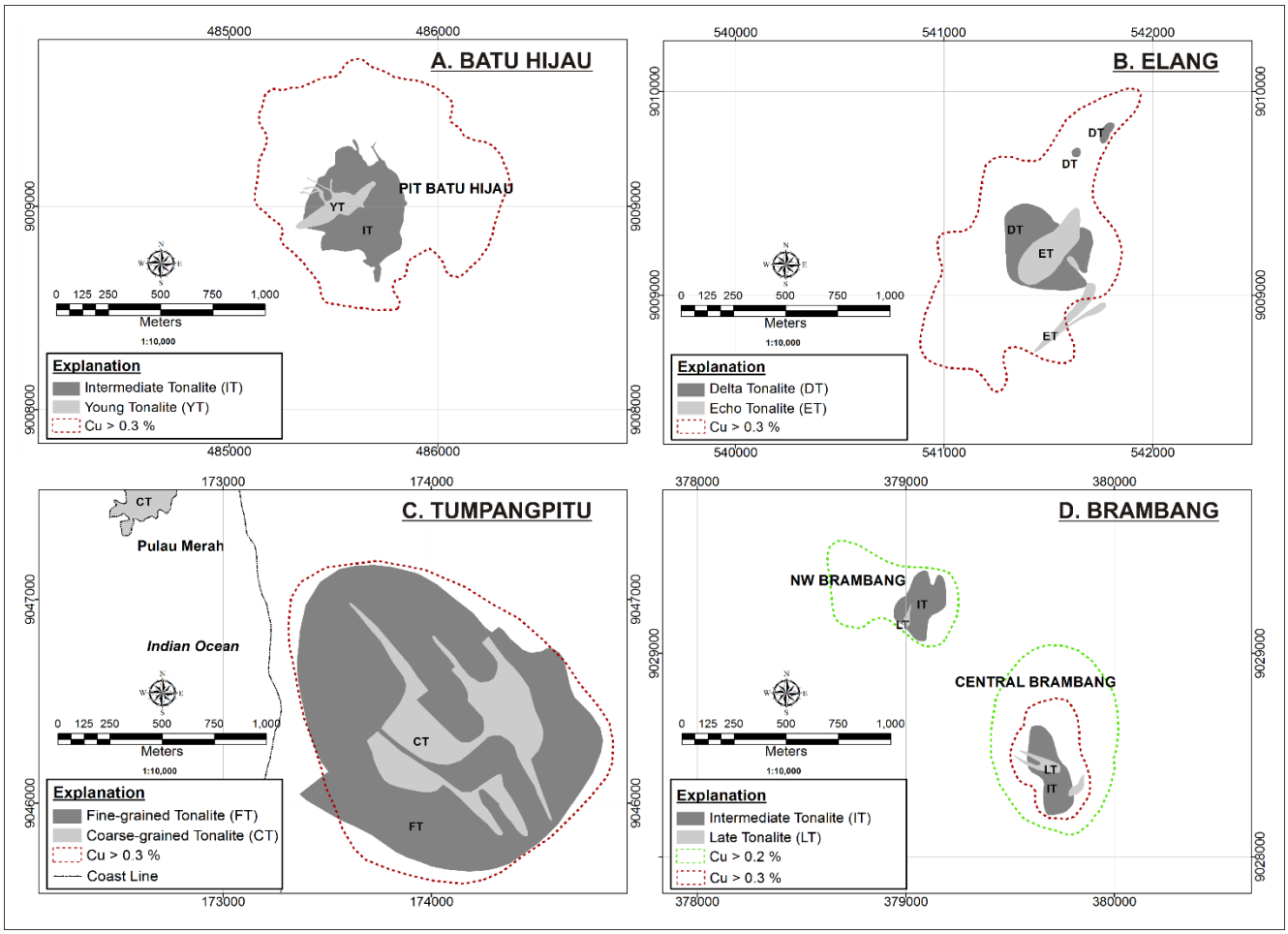

Figure 2.6. Surface projections and footprints of multiphase nested tonalite intrusions and 0.3 % Cu zones; A.) Batu Hijau pit December 2007; B) Elang surface geology and surface projection Cu zone; C) Tumpangpitu 500 m level projection; D) Brambang surface projection geology and Cu zones (this study; Maryono et al., 2017).

Tumpangpitu, 24 km^2 at Elang (Maryono et al., 2005), and Brambang (Maryono et al., 2013) to 48 km^2 at Hu'u (Maryono et al., 2017). At Batu Hijau, the porphyry deposit is exposed at surface, with only deep remnants of the lithocap preserved at East Ridge (Fig. 2.7). At Elang and Selodong, partial preservation of lithocaps is apparent (Fig. 2.7). At Tumpangpitu, Brambang and Hu'u, most of the lithocaps are preserved and the blind porphyry deposits are concealed under 150 m to ≥ 200 m of lithocap (Fig. 2.7). The lithocaps at Tumpangpitu, Elang and Brambang are known to contain high-sulfidation epithermal mineralization, however only Tumpangpitu has a published resource.

2.3.9 Supergene copper enrichment

Supergene copper enrichment is weakly developed under leached caps and lithocaps overlying porphyry deposits of the Sunda-Banda arc. A hematite leached cap overlies 1 - 2 m of Cu-oxide mineralization associated with intense porphyry stockwork veins overprinted by epithermal Au-Cu-Ag

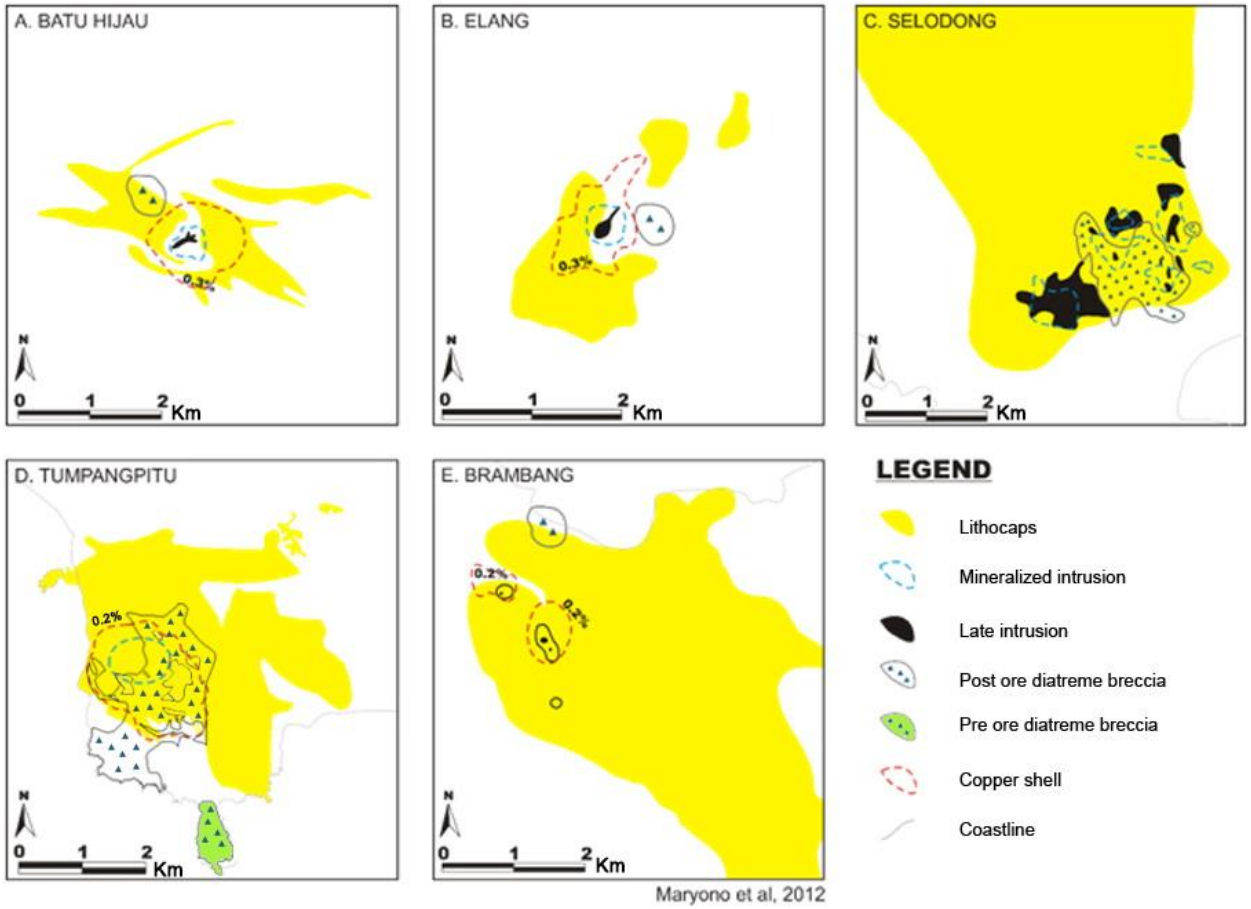

Figure 2.7. Lithocap surface alteration footprints at Batu Hijau, Elang, Selodong, Brambang and Tumpangpitu which show different erosion levels, from deeply eroded at Batu Hijau, partially eroded at Elang and Tumpangpitu and fully preserved at Brambang (modified after Maryono et al., 2012; 2017).

veins at Pulau Merah island. Hypogene copper sulfides are preserved in the wave-cut platform at the base of the Cu-oxide zone. (Fig. 1.6B). Supergene copper is not developed well at Tumpangpitu and is restricted to major fault zones, specifically Cliff fault beneath Zone A Au-Ag oxide deposit (Fig. 5.3). Supergene chalcocite is dominant under geothitic leached caps at Batu Hijau (Maryono, 2002; Maryono et al., 2017). Supergene oxidation and remobilization of copper is mainly restricted to relatively shallow levels (< 150 m) in the eastern Sunda arc, and has typically formed weak supergene enrichment zones. The vertical zonation of supergene features includes leached cap, oxide and supergene-enriched sulfide zones above the hypogene sulfide zones at Batu Hijau and Elang (Clode et al., 1999, Maryono et al., 2005, 2017), with supergene enriched zones having formed only weak chalcocite blankets a few meters to 100 m thick. They underlie goethitic ± hematitic leached caps at Batu Hijau, Elang and Brambang. The copper oxide zone at Batu Hijau consists of chrysocolla, malachite, pseudomalachite, brochantite, cuprite, and goethite. This zone is characterized by acid soluble copper which comprises more than 80 % of the total copper (Maryono

et al., 2017). A small oxide resource of 57 Mt @ 0.37 % Cu has been delineated at Batu Hijau (Clode et al., 1999).

2.4 Discussion

2.4.1 Magmatic-volcanic rocks

The earliest documented volcanism in the eastern Sunda arc is poorly understood, and appears to have been restricted to western Java (Figs. 2.1 - 2.3). It is thought to have developed during the initiation of the Java Trench in the Paleocene-Eocene (Smyth et al., 2005). In the Late Miocene, significant northward migration of volcanic centers occurred in eastern Java (Fig. 2.3). The northward shift of volcanism towards the back arc ended after the Pliocene. In western Java the trench-ward volcanic migration started in the Quaternary. This foreland shift is demonstrated by the partial coverage of late Tertiary volcanic centers by Quaternary volcanoes in western Java (Hall, 2002; Smyth et al., 2005; Fiorentini and Garwin, 2009; Spakman and Hall, 2010). The opposite direction of Quaternary volcanic migration occurred in eastern Java to Sumbawa where Quaternary volcanic activity migrated northward (Setijadji et al., 2006; Maryono et al., 2017). The basement rock units of the eastern Sunda are interpreted as slivers with affinities to arc crust and to ophiolites (Garwin, 2000). Cretaceous zircons from the Tanjung Jahe diatreme (Chapter 4) implies that the Tujuh Bukit district may be close to or on the eastern margin of the Archean fragment of ancient Gondwana that has been interpreted to underlie East Java (Smyth et al. 2007).

2.4.2 Intrusive rocks

Intrusive rock units exhibit similar temporal and spatial distribution patterns to volcanic rock units, younging eastward along the eastern Sunda arc (Fig. 2.3; Maryono et al., 2017). Intrusive rocks in the major mineralized porphyry districts have evolved in terms of their composition, size, and textures during the Pliocene (Garwin, 2000; Proffett, 2004; Maryono et al., 2005; Harrison et al., 2012). The compositions of the Late Miocene to Early Pliocene suite of intrusive rocks become more quartz-rich with time from large volume, pre-mineralization equigranular dioritic phases, e.g., Phase 2 diorite at Tumpangpitu and diorite at Batu Hijau (Fig. 2.5), to small volume, more porphyritic, coarser-grained tonalitic phases (Figs. 2.5 and 2.6; Table 2.2). Coarser-grained porphyry intrusions indicate relatively slower cooling at depth, whereas fine-grained porphyry intrusions imply shallower levels of emplacement (Lang and Titley, 1998; Seedorff et al., 2005).

2.4.3 Geodynamics and structure of the eastern Sunda arc

The eastern Sunda arc is segmented by a series of arc-normal sinistral strike slip structures that trend north-northeast to northeast (Fig. 2.3). Most of the porphyry and epithermal deposits along the eastern

Sunda arc probably developed under stress states imposed by nearly arc-orthogonal compression related to subduction of the Indian plate beneath the Sunda Banda arc, characterized by a north-north-easterly directed maximum compressive stress. In contrast, northwest trending zones of epithermal mineralization are inferred to be related to subsequent relaxation events characterized by a north-north-east-trending minimum compressive stress (Figs. 2.1 - 2.3; Gray, 2011). The Tumpangpitu and Pulau Merah porphyry deposits of the Tujuh Bukit district were emplaced along a northwest striking lineament (Fig. 1.4). Magmatic-hydrothermal systems are attributed to the onset of arc-parallel extension and tensional reactivation of north-easterly trending crustal scale strike slip fault networks in eastern Java. Dilatant movements on these faults were most likely related to the collision of the northern edge of the Roo Rise and the subsequent collision of the Australian craton in the Pliocene (~ 4.0 - 2.5 Ma; Fig. 2.1; Hall and Sevastjanova, 2012). Arc transverse faults most likely localized the rapid ascent of magma and controlled the emplacement of the Miocene intrusive complexes along the eastern Sunda arc and facilitated the efficient release of volatiles and metals at shallow crustal levels. The subduction of the buoyant Roo Rise oceanic plateau, south of Java is inferred to have caused a kink, or tear in the down-going slab (Garwin, 2002; Garwin et al., 2005), which could have enhanced the delivery of mantle-derived melts enriched in copper and gold to the overlying arc, where the episodic reactivation of crustal-scale fault and fractures systems increased crustal permeability (Garwin, 2002, Fiorentini and Garwin, 2010). The Batu Hijau and Elang porphyry copper-gold deposits lie above the northeastern extension of the subducted margin of the Roo Rise and the Tumpangpitu deposit to the north (Fig. 2.1). Major changes in plate motions and boundaries from 5 Ma (Audley-Charles, 2004) most likely favoured the development of these world class porphyry and epithermal deposits along the eastern Sunda arc (Garwin et al., 2005; Maryono et al., 2017).

2.4.4 Gold-copper metallogeny

There are two distinctive patterns of distribution of gold and copper metallogeny across the eastern Sunda Arc (Figs. 2.2 and 2.3). A population of low- to intermediate-sulfidation epithermal gold occurrences defines the western segment. In contrast, the eastern segment is endowed with higher grade porphyry and high-sulfidation epithermal deposits. These distinctive features, to some extent reflect two tectonic-geologic basements and tectonic regimes (Figs. 2.1 - 2.3, Tables 2.1 and 2.2; Hamilton, 1979; Carlile and Mitchell, 1994; Hall, 2002; Setijadji et al., 2006; Setijadji and Maryono, 2012; Maryono et al., 2017).

Maryono et al. (2017) used geochronologic data from selected porphyry deposits of the eastern Sunda magmatic arc to suggest that hydrothermal activity migrated both north and eastwards over a period of 5 m.y and generally became more enriched with time. Initial low-grade copper-gold mineralization events followed the Miocene Eocene northward-dipping subduction of Indian oceanic crust. Zircon age determinations of small porphyry systems at Selodong and Brambang in Lombok and Selogiri, Central Java

indicates Late to Middle Miocene ages (Figs. 2.4 and 2.5; Maryono et al., 2017), older than those from giant porphyry systems (≥ 5 Mt Cu and ≥ 300 t Au; Clark, 1993) at Tumpangpitu, Elang and Batu Hijau (Figs. 2.4 and 2.5). These giant porphyry systems started developing in the eastern segment of the eastern Sunda arc, from 4.89 ± 0.40 to 2.38 ± 0.18 Ma (Chapter 4; Maryono et al., 2017).

2.4.5 Lithocaps and supergene copper enrichment

The lithocaps of the eastern Sunda arc conceal underlying mineralized porphyry systems, but may provide a proxy to the size of the underlying mineralized systems (e.g., Fig. 2.7; White, 1991; Sillitoe, 1995; Hedenquist et al., 1998; Chang et al., 2011). The dimensions of these lithocaps probably relate, in part, to differing erosion levels and exposures of the related porphyry deposits. Age determinations demonstrate that lithocaps are temporally and genetically related to underlying mineralized porphyry intrusions (Fig. 2.7; Maryono et al., 2017). Rapid erosion under high-rainfall conditions (> 2 to 3 m/year; worldbank.org, 2017) have likely limited preservation of enriched copper blankets and oxide copper zones at porphyry deposits of the Sunda-Banda arc.

Chapter 3: Geology and Structure of Tumpangpitu

3.1 Introduction

This chapter documents the geology and structure of Tumpangpitu. It explains the methodologies used to construct the 'type lithology" section, and characterizes the geological setting of Tumpangpitu, based on surface mapping, detailed drillcore logging and observations of hand specimens and thin sections by the author. Key intrusive and breccia phases have been defined and their relative timing has been determined based on cross-cutting relationships. The structural evolution of Tumpangpitu is evaluated, based on structural measurements from geological mapping, core logging, SWIR-aided alteration mineral mapping and type section construction by the author, as well as structural data and models from unpublished consultant reports.

3.2 Construction of the Tumpangpitu type lithology section

3.2.1 Background information

Work on a type section for Tumpangpitu by the author commenced in late 2010 during a period of intense exploration drilling activity, following the announcement of a second indicated porphyry resource based on block model calculations (Intrepid Mines Ltd, 2010). During this time, ten diamond drill rigs were generating huge volumes of drillcore. Concern was arising due to the lack of consistency in logging and correlating lithological units between adjacent drillholes on sections, creating a significant problem for developing a consistent model to geologically constrain the resource calculations. It soon became a matter of urgency to create a logging system whereby each geologist could log the same units between drillholes. This was the platform essential for the creation of a geological model suitable for calculating an inferred porphyry resource for Tumpangpitu. To resolve this problem, a type section was logged by the author so as to identify the typical lithologies and crosscutting relationships. This type section could then be used to define the relative timing of intrusive events by on-going drillcore logging and field mapping (e.g., Einaudi, 1997; Seedorff et al., 2005; Maryono et al., 2012). This section describes the construction of the type section at Tumpangpitu.

3.2.2 Methodology

In order to create the type section, over 25,000 m of diamond drillcore was re-logged over a period of seven months by the author, with guidance from the Tujuh Bukit General Manager, from what was considered the most representative section of the deposit. This section, 11060 mN (Figs. 3.1, 3.2 and 3.3) was selected due to its central location, transecting both Zone A and C high-sulfidation Au-Ag oxide

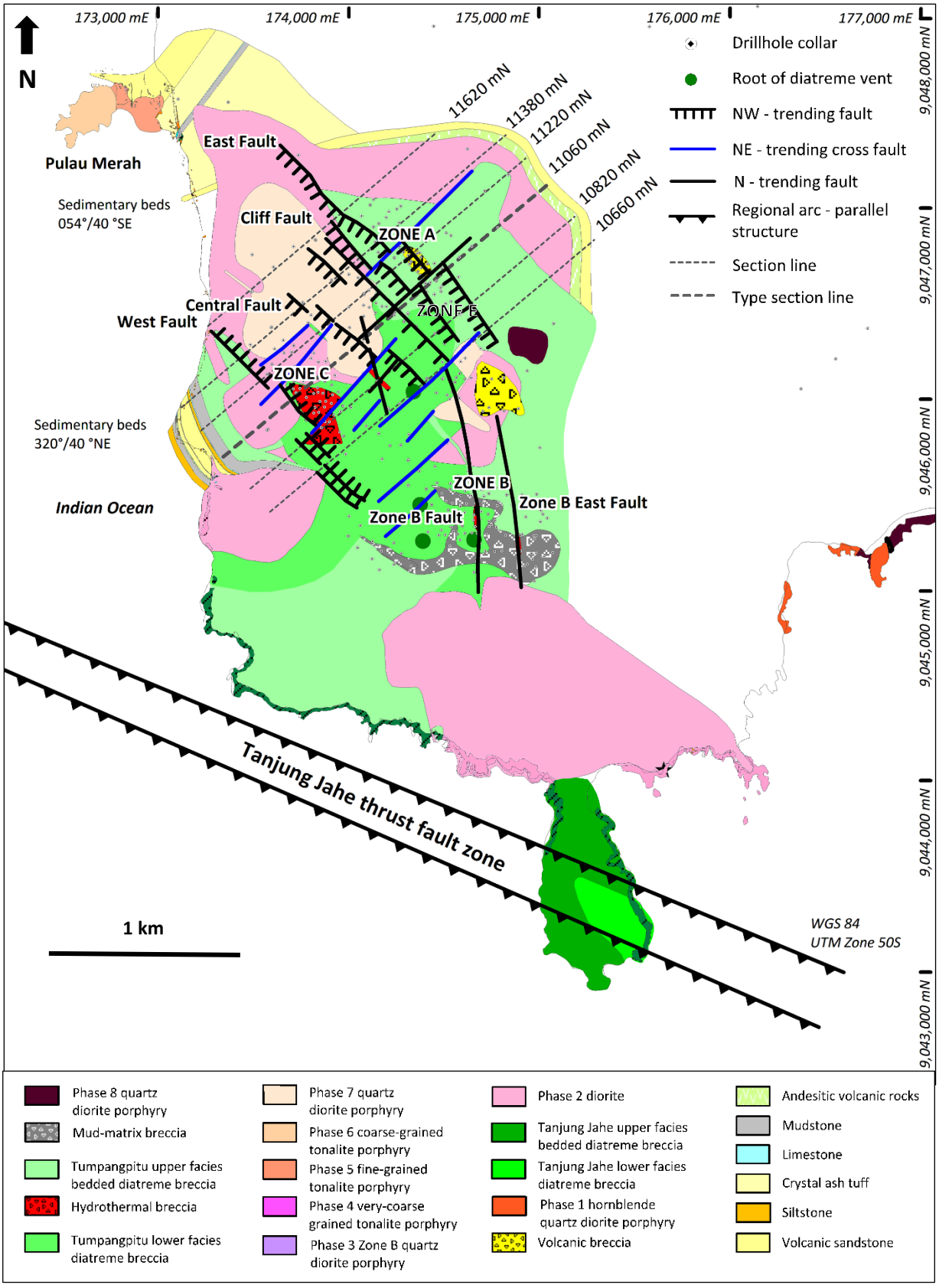

Figure 3.1. Geologic surface plan of Tumpangpitu. Darker shades represent mapped coastal rock exposures.

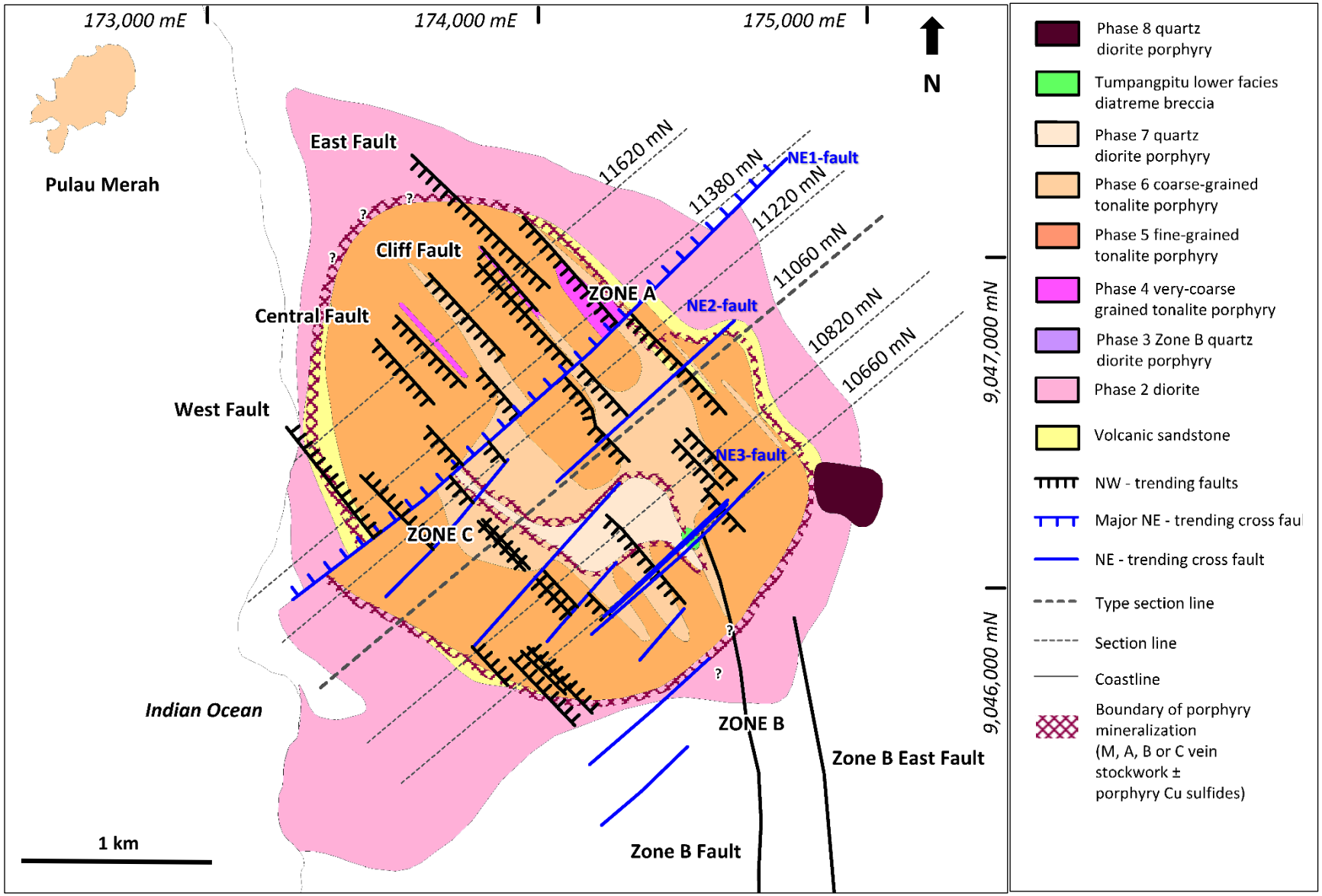

Figure 3.2. Geologic plan at -500 m level of Tumpangpitu.

deposits, the Tumpangpitu porphyry at depth and sedimentary wallrocks fringing the system (Fig. 3.3). It was also chosen due to the greatest abundance and variety of data, including drillhole coverage, complete assay data, SWIR spectral data, petrographic analyses, structural measurements and surface geological mapping data (Harrison, 2009; Coote, 2009; 2011; Gray, 2011; 2012).

A simplified, contact logging format, modified after the Anaconda logging method (e.g., Einaudi, 1997) was adopted to allow drillcore to be scanned rapidly for significant changes in textures and grain size, with a strong focus on identifying key contacts and cross-cutting relationships. During the drillcore re-logging exercise, six intrusive phases were resolved, spanning the entire hydrothermal alteration-mineralization sequence. Two additional pre- and post-mineralization phases were subsequently mapped along the southern coastline (Fig. 3.1). Packages of sedimentary and volcanic facies were also characterized on the margins and above the intrusive complex, respectively. A rock reference library, exhibiting the most representative examples of each unit, was created concurrently with the re-logging exercise. Frequent involvement and communication between all site geologists and consultants was essential for this exercise to be successful, and this process continued throughout the drilling and resource evaluation calculations. Assay data was used as a key supporting dataset to aid in identifying the different porphyry intrusive stages and areas of wallrock, particularly in zones of intense alteration, where primary lithological textures have been obliterated. Every evening, the re-logging results were hand drawn onto an A0 sized section base map with downhole copper, gold, molybdenum and arsenic assays plotted on drillhole traces by the author. The generation of type section 11060 mN facilitated the construction by the author of another fifteen porphyry sections to the northwest and southeast (Fig. 3.1), five of which are shown in Figures 3.4 to 3.8.

3.3 Geology of Tumpangpitu

3.3.1 Introduction

Porphyry Cu-Au-Mo mineralization at Tumpangpitu was localized within and around the Early Pliocene porphyritic nested tonalite complex known as the Tumpangpitu porphyry complex (Fig. 3.1). This composite tonalitic stock intruded a larger hypabyssal diorite pluton and also a sedimentary package interlayered with, and overlain by andesitic volcanic rocks. Massive volcanic breccias occupy the peak of Zone A oxide (Figs. 3.1 and 3.4). The volcanic breccias at Zone A host hydrothermal breccias containing epithermal mineralization. Two diatreme breccia bodies have been identified; the Tanjung Jahe pre-mineralization diatreme that occupies the southern coastline and the Tumpangpitu post-porphyry mineralization diatreme (Fig. 3.1). The Tumpangpitu diatreme has crosscut and removed some porphyry mineralization, but hosts some late stage high-sulfidation epithermal mineralization (Figs. 3.3 - 3.8). The epithermal Au-Cu-Ag mineralization at Tumpangpitu is associated with northwest-trending structural

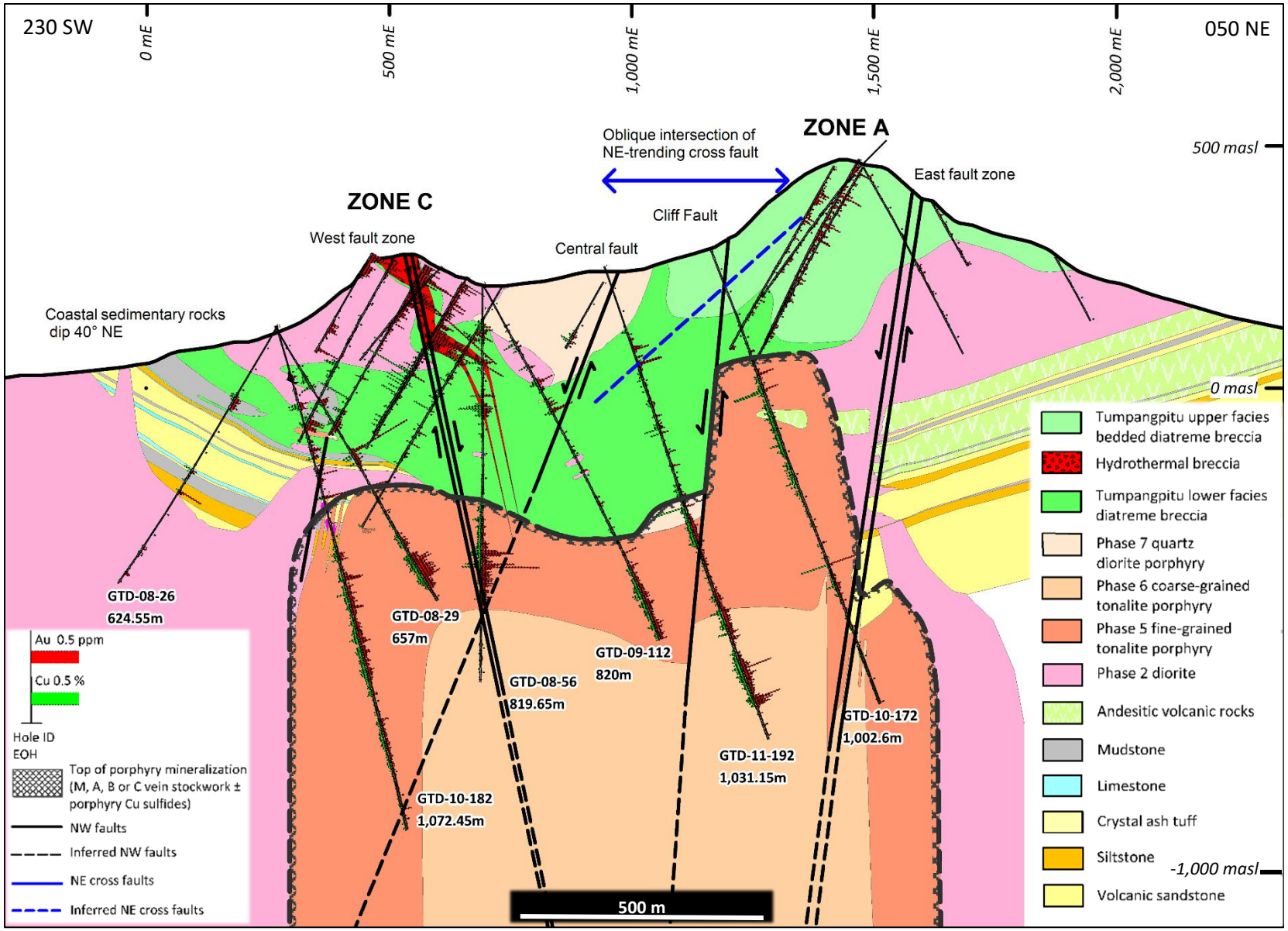

Figure 3.3. Representative type geologic section 11060 mN through Tumpangpitu, showing most of the local rock types. Section line shown in Figure 3.1.

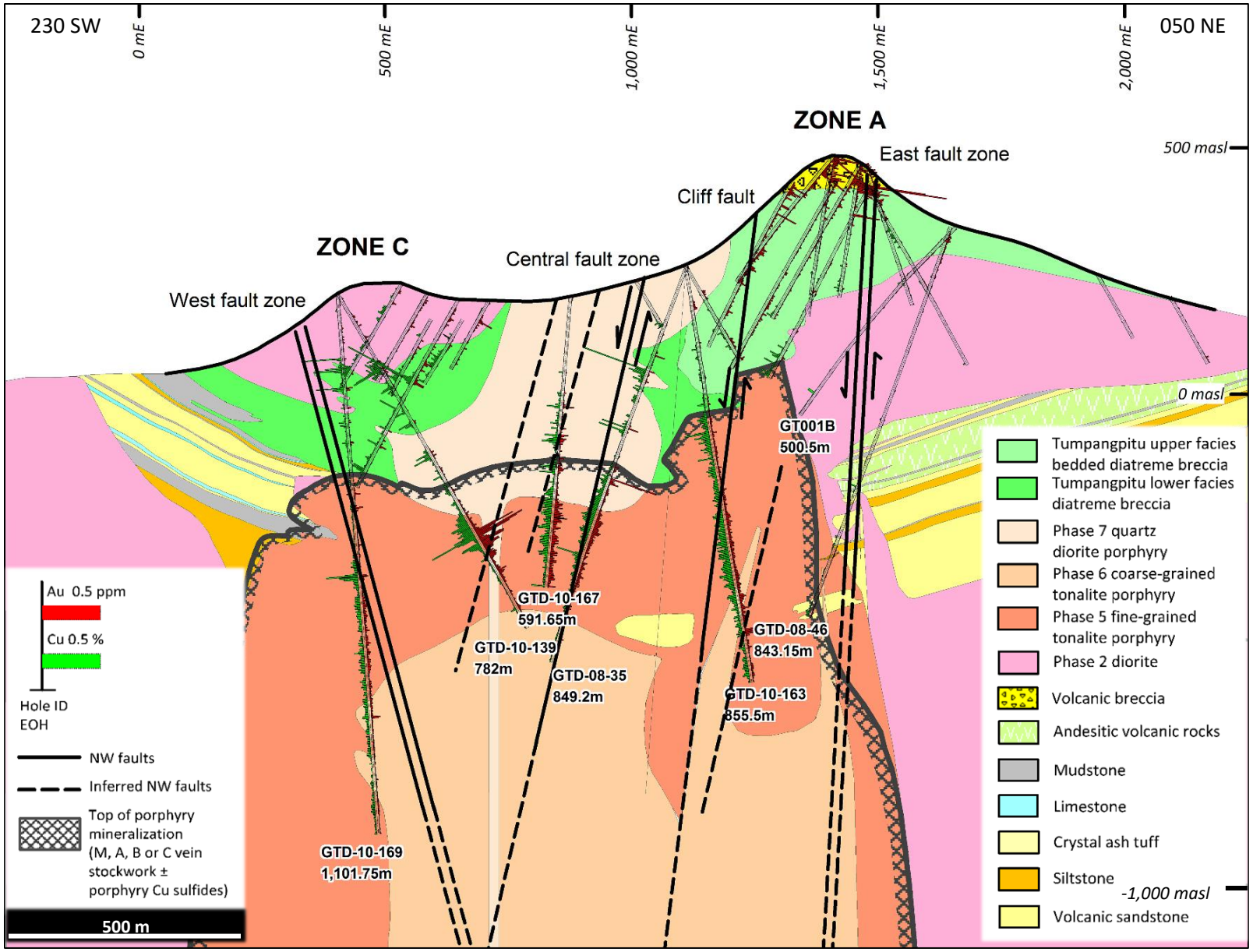

Figure 3.4. Geologic section 11220 mN through Tumpangpitu, showing most of the local rock types. Section line shown in Figure 3.1.

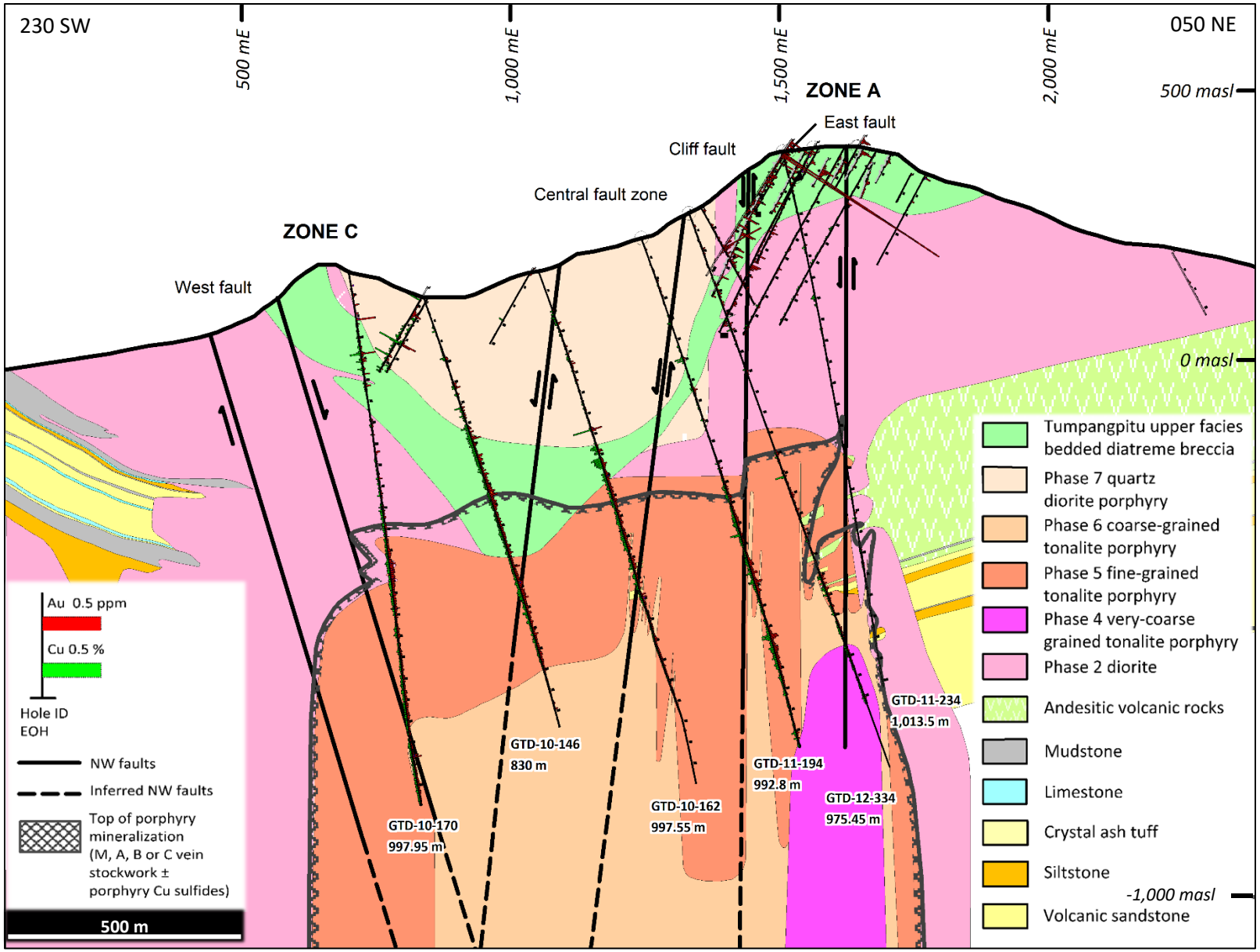

Figure 3.5. Geologic section 11380 mN through Tumpangpitu, showing most of the local rock types. Section line shown in Figure 3.1.

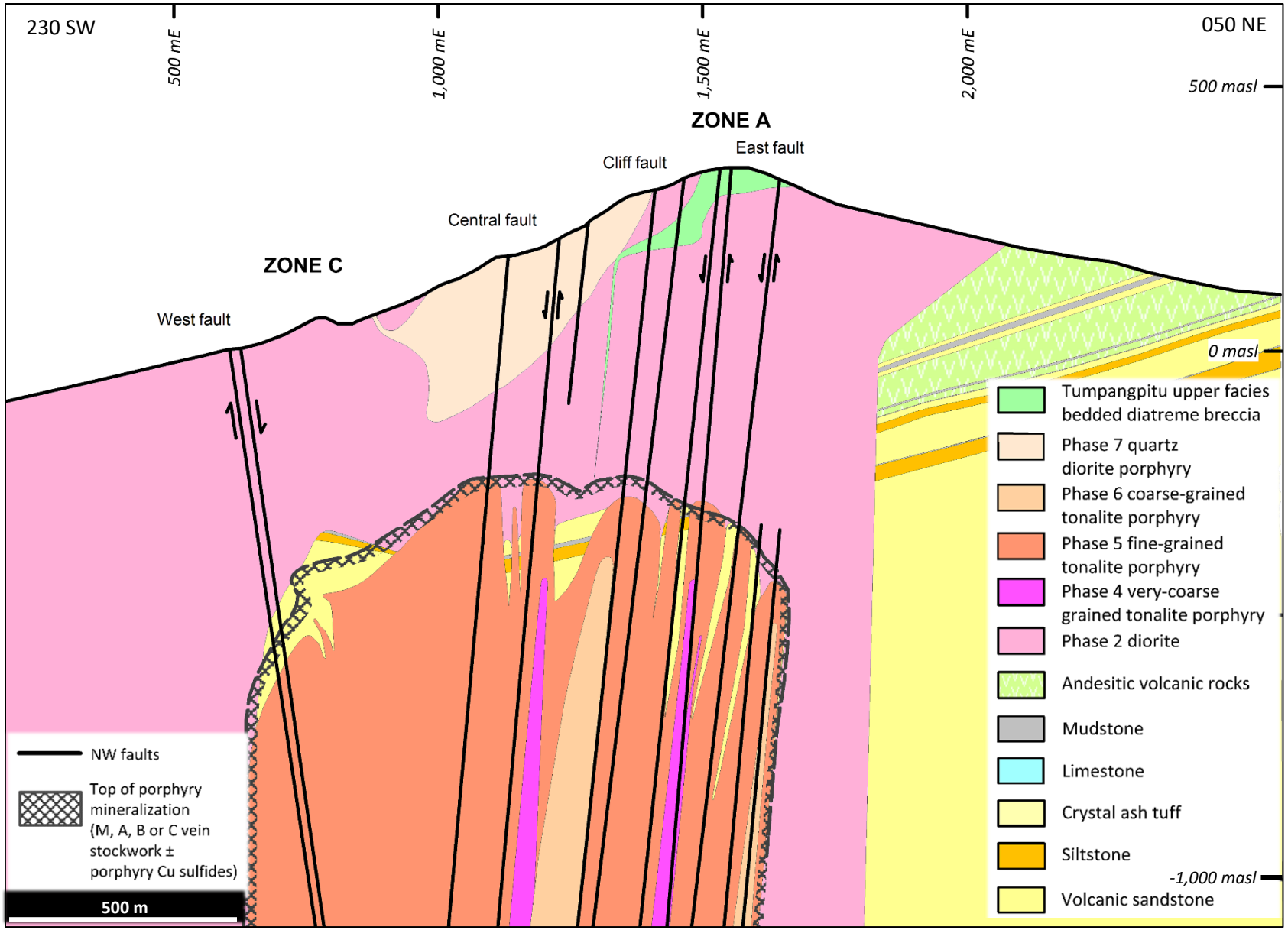

Figure 3.6. Geologic section 11620 mN through Tumpangpitu, showing most of the local rock types. Section line shown in Figure 3.1.

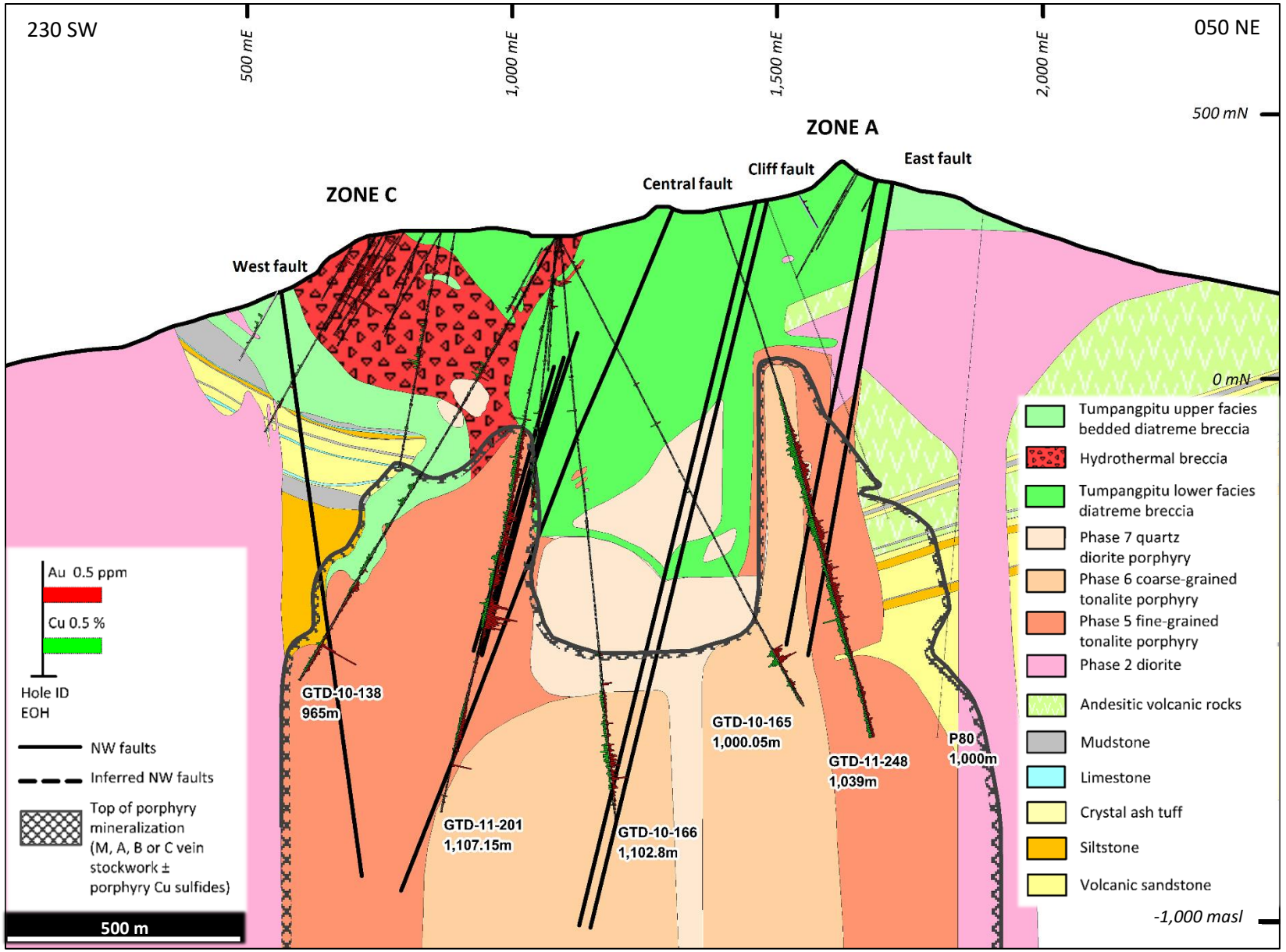

Figure 3.7. Geologic section 10820 mN through Tumpangpitu, showing most of the local rock types. Section line shown in Figure 3.1.

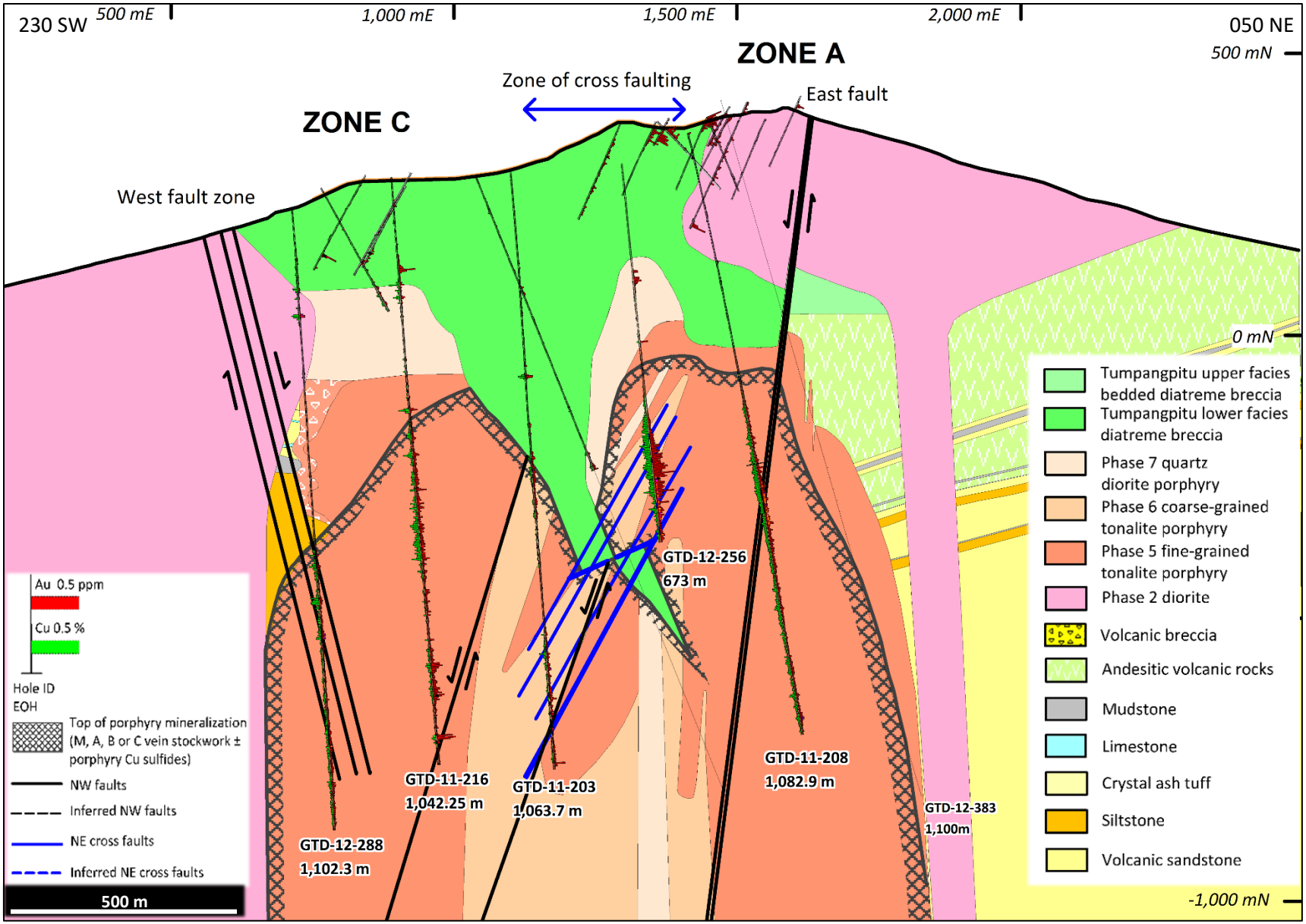

Figure 3.8. Geologic section 10660 mN through Tumpangpitu, showing most of the local rock types. Section line shown in Figure 3.1.

zones, which host massive sulfide veins, in an area that is 4 km long and 1.8 km wide (Fig. 3.1).

The principal rock types at Tumpangpitu are assigned here to six broad units; (1) the pre-mineralization Tanjung Jahe diatreme breccia; (2) sedimentary and andesitic volcanic rocks; (3) volcanic breccia; (4) eight discrete porphyry intrusions, spanning the alteration-mineralization sequence; (5) hydrothermal breccias that host the majority of high-sulfidation epithermal mineralization, and (6) the Tumpangpitu late-mineralization diatreme breccia. All rock types are illustrated in Figures 3.9 to 3.17 and 3.21 to 3.29. The intrusive sequence is summarized in Table 3.1. The non-intrusive host rocks are documented in Figures 3.9 and 3.14.

3.3.2 Sedimentary and andesitic volcanic rocks

The pre-mineralization stratigraphic package at Tumpangpitu is composed of a >500 m thick sequence of well-bedded turbidites and shallow marine sedimentary rocks. These include sedimentary breccias, volcanic sandstones, siltstones, wackes, fine-grained tuff, crystal ash tuff and lesser carbonaceous shales and mudstones, with minor shallow marine limestones. The limestones are restricted to the western, seaward flank of Tumpangpitu (Figs. 3.1 and 3.9). The volcano-sedimentary package is overlain by and intercalated in its upper sections with a package of andesitic volcanic rocks that is restricted to the northeast side of Tumpangpitu (Figs. 3.1 - 3.8). The sedimentary and andesitic volcanic sequence is preserved around the fringes of the composite Tumpangpitu porphyry stock (Figs. 3.1 - 3.8). Above the carapace of the Tumpangpitu stock, the original stratigraphic sequence has been disrupted by the porphyry complex, and partly destroyed by the diatreme and shallow hydrothermal breccias; the former of which contain abundant clasts of the underlying sedimentary and andesitic rock units (Figs. 3.3, 3.4 and 3.23B).

The fine- to coarse-grained sandstones comprise gritty volcaniclastic sands that exhibit graded bedding, load casts and slump structures where in contact with interbedded silty mudstones (Fig. 3.9E). Other sedimentary features include rare compaction dewatering structures (Fig. 3.9F; Rohrlach, 2010). The subordinate mudstones and siltstones tend to be finely bedded (0.5 - 10 cm) and are typically carbonaceous and calcareous. Local lenses of stylolitic limestone and intraformational sedimentary breccia occur within the volcaniclastic sandstones.

Along the shoreline to the east of Pulau Merah island (Figs. 3.1 - 3.4), there are good exposures of chlorite - calcite altered, magnetite-bearing, well bedded volcanic sandstone, siltstones (Fig. 3.9A), fine-grained tuff and silicified mudstones (Fig. 3.9B). These rocks have been intersected by drilling at depths of 350 m below present day surface to the west, and 500 m below present day surface, east of Tumpangpitu (Figs. 3.3 - 3.4).

Table 3.1 Geological characteristics of the Tumpangpitu intrusive complex.

Intrusive unit	Planar dimensions (m)	Texture and composition	Contact relationships	Age (Ma)	Interpretation
Phase 1: hornblende quartz diorite	100 to 600 x 1,700	Medium to very coarse-grained (3 - 15 mm) phenocrysts of subhedral plag, megacrysts of euhedral hbl, minor bt and primary mt; qtz content 5 - 15 %	NNW- trending dikes that crop out along the southern coastline crosscut by phase 8; occur as clasts in Tanjung Jahe diatreme	8.4 ± 0.36	Pre-porphyry and HSE mineralization at Tumpangpitu
Tanjung Jahe: lower facies diatreme breccia	300 x 500	Polymict texture, both clast and matrix-supported entraining clasts locally including sedimentary rock, coral, red thermally oxidized igneous clasts, diorite, quartz diorite, mineralized fragments of qtz - py - cc ± Cu oxides and wispy, ragged fine-grained andesitic clasts in a fine-grained andesitic tuffaceous matrix comprising broken plag, hbl and mt	Crosscut by phase 2 diorite	8.52 ± 0.21	Pre-mineralization at Tumpangpitu, dry volcanic diatreme; wispy andesitic clasts interpreted to be juvenile in origin
Tanjung Jahe: upper facies diatreme breccia	500 x 1,150	Fine-grained, matrix-supported and tuffisite polymict breccias with sub-rounded polymodal fragments of diorite, quartz diorite and sedimentary rocks; interlayered with laminated fine-grained mudstone, sandstone and siltstone	Bedded units generally dip towards the east	8.78 ± 0.22	Pre-mineralization (at Tumpangpitu) breccia apron around diatreme vent
Phase 2: Old diorite	2,500 x 4,600	Equigranular, medium to coarse-grained (2 - 4 mm) subhedral to anhedral phenocrysts of plag, hbl, bt and < 5 % qtz; qtz eye phenocrysts are uncommon	Large batholith extending to the southern coastline, cross-cut by intrusions 3 - 7, overprinted by porphyry and HSE alteration-mineralization; hypabyssal contact with underlying andesitic-sedimentary rocks	4.71 - 5.97	Pre-mineralization batholith country rock
Phase 3: Zone B quartz diorite	100 x 200 (?)	Medium to coarse grained (3 - 8 mm) phenocrysts of subhedral plag, hbl, minor bt and primary mt; qtz content < 5 %	Phase 3 quartz diorite has only been intersected in drillholes underneath Zone B, adjacent to the Zone B fault; the intrusion is in contact with a coarse-grained Cu-Au-Mo tonalite around 790 m downhole depth	4.53 ± 0.48	Bounded by Zone B fault, crosscut by phase 6 tonalite porphyry and HSE mineralization

Table 3.1 *(Cont.)*

Intrusive unit	Planar dimensions (m)	Texture and composition	Contact relationships	Age (Ma)	Interpretation
Phase 4: Coarse-grained tonalite	100 x 250	Porphyritic 3 - 7 mm tabular euhedral to subhedral plag, hbl and bt phenocrysts, 15 - 20 % large granoblastic qtz eye phenocrysts (5 - 10 mm)	Interior of intrusion has minor disseminated and vein-hosted Cu-Au-Mo mineralization; Mo grades increase with depth; overprinted by porphyry stockwork veining and mineralization at its contact with phase 5 tonalite	4.83 ± 0.41	Pre- to inter-mineralization pencil porphyry stock; weakly mineralized
Phase 5: Fine-grained tonalite	1,200 x 1,200	Fine-grained equigranular texture comprising 1 - 2 mm subhedral to anhedral phenocrysts of plag, hbl and minor bt, 15 - 20 % qtz phenocrysts (< 2 mm) observable with hand lens	Forms a 200 - 500 m carapace above phase 6 tonalite	3.60 - 5.29	Inter-mineralization porphyry; hosts most of the porphyry Cu-Au-Mo mineralization at Tumpangpitu; a finer-grained margin to underlying phase 6 tonalite (essentially a textural variant of phase 6)
Phase 6: Coarse-grained tonalite	1,000 x 1,000	Strong porphyritic coarse-grained (2 - 5 mm) texture with crystal-crowded tabular ex-plag phenocrysts, ghosted hbl and 15 - 25 % qtz eye phenocrysts (2 - 5 mm) and qtz-rich crystalline groundmass	Forms a "core" to phase 5, ~ 700 m below surface; no clear/sharp contacts with phase 5 tonalite, only gradational changes in texture	3.36 - 4.74	Main causative inter-mineralization porphyry; second major host of porphyry Cu-Au-Mo mineralization
Phase 7: Quartz diorite	700 x 1,700	Strong porphyritic coarse-grained (2 - 5 mm) texture with crystal-crowded mosaic of tabular plag phenocrysts commonly altered to ill - ka, hbl (ghosted and replaced by chl) and 15 - 25 % qtz eye phenocrysts (2 - 5 mm) in a qtz - rich crystalline groundmass	Ovoid, shallow level porphyry body located directly above the center of Tumpangpitu porphyry Cu-Au-Mo mineralized zone; lower contact with phase 5 tonalite, narrow ~ 3 m feeder intersected on section 11220 mN	3.19 - 4.36	Pre- HSE mineralization, late-inter- mineralization porphyry; devoid of Cu-Au-Mo porphyry mineralization except at contact with underlying phase 5 tonalite
HBX-1 Hydrothermal breccia	500 x < 1	Monomict and polymict, clast supported breccia containing mineralized fragments along with country rock clasts, which range from angular to sub-rounded in form; common textures include crackle, mosaic and jigsaw breccias; in advanced argillic zones, breccias are characterized by qtz - al ± dk ± ka cement locally containing ba	Volumetrically minor breccia bodies towards the NW, increasing in volume SW of the Tumpangpitu intrusive centre; near-vertical geometry, strongly fault controlled; crosscut earlier volcanic breccias but truncated by Tumpangpitu diatreme	_	Brecciation of host rocks; inter-mineralization HSE Cu-Au-Ag and early to inter-mineralization porphyry Cu-Au-Mo

Table 3.1 *(Cont.)*

Intrusive unit	Planar dimensions (m)	Texture and composition	Contact relationships	Age (Ma)	Interpretation
Tumpangpitu DBX-L: Lower facies diatreme breccia	1,700 x 1,800	Polymict texture, both clast and matrix-supported entraining clasts locally from all host rocks at Tumpangpitu, including basal sedimentary rocks, andesitic volcanic rocks, volcanic breccia, intrusive phases 1 - 7 and HBX-1 in a fine-grained tuffaceous matrix of andesitic composition; adjacent to the Tumpangpitu porphyry complex, clasts include mineralized porphyry, HSE fragments with vuggy quartz and ISE fragments containing tet-ten	Large breccia bodies that occupy the throat and main central body of a series of NW-trending diatreme vents; the outer flanks dip inwards concentrically at approximately 25° to 40° then steepens downward truncating the upper 600 m of the Tumpangpitu mineralized system and all associated intrusions and host rocks; near-vertical roots penetrate down at least 900 m below surface to the south of the Tumpangpitu ore body	_	Post-porphyry Cu-Au-Mo mineralization and stage 1 HSE; inter-stage 2 HSE and post stage 3 HSE Cu-Au-Ag mineralization
Tumpangpitu DBX-U: Upper facies bedded diatreme breccia	2,200 x 3,100	Highly comminuted and fragmental, matrix-supported and tuffisite polymict breccias ~ 20:80 clasts : matrix; 1 - 2 mm fragments of host rocks, HSE and porphyry mineralized clasts defining 1 - 2 cm bands; clasts are sub-rounded to sub-angular and exhibit polymodal lithology and alteration types; rare accretionary lapilli and charcoalized wood fragments near to present-day surface	DBX-U fringes DBX-L and the roots of the diatreme bodies; it forms the upward flaring flanks developed distally from DBX-L that appear as shallow level 'floating' breccia bodies on geological sections; the units dip 15 - 30° away from the central root zones; crosscuts intrusions 2 - 7 and all host rocks at Tumpangpitu	2.7 ± 0.5	Post-porphyry Cu-Au-Mo mineralization and stage 1 HSE; inter-stage 2 HSE and post stage 3 HSE Cu-Au-Ag mineralization; near-paleo surface fringes on the flanks of the main diatreme body
MMBX: Upper facies mud-matrix breccias	450 x 1000	Polymict breccia with mudstone matrix; clasts are rounded to sub-angular of wallrocks including mineralized porphyry veined clasts	Irregular crescent shaped body; inner contact with DBX-L and outer contact with DBX-U	_	Post-porphyry mineralization; pre, inter and post HSE
HBX-2 Hydrothermal breccias	500 x 200 to 500 x < 1	Same texture and composition as HBX-1, but with a greater occurrence of polymict and matrix-supported breccias	The breccia bodies cross cut DBX-U, DBX-L and intrusive phases 2-7; occupying proximal as well as distal zones of the Tumpangpitu intrusive centre	_	Inter- stage 2 HSE mineralization, inter to post-porphyry mineralization
Phase 8: quartz diorite	1 to 20 x 1000 (?)	Medium to coarse-grained (3 - 10 mm) phenocrysts of subhedral plag, hbl, minor bt and primary mt; strong alteration of primary mafics to epidote, qtz content 5 - 15 %	North-trending low volume dikes that crop out along the southern coastline, crosscutting phase 1; also a smaller 200 x 200 m body evident in RTP magnetic datasets and intersected by drilling to the SE of Zone A	_	Post-porphyry and HSE Cu-Au mineralization

Abbreviations: Au = gold, ba = barite, bn = bornite, bt = biotite, cc = chalcocite, chl = chlorite, co = colusite, cp = chalcopyrite, Cu - copper, dsp = diaspore, en = enargite, ISE = intermediate sulfidation epithermal, hbl = hornblende, he = hematite, HSE = high-sulfidation epithermal, ill = illite, ka = kaolinite, Kfs = K-feldspar, mag = magnetite, Mo = molybdenum, plag = plagioclase, tet-ten = tetrahedrite-tennantite, qtz = quartz, py = pyrite, - in empty cells = no data. All geochronological data are presented in Chapter 4.

An andesitic unit overlies sedimentary rocks on the eastern flank of Tumpangpitu. It comprises coherent andesite and minor monomictic andesitic breccia (autoclastic breccia). Individual andesitic layers are generally massive but locally can be distinguished by flow banding and alignment of phenocrysts. Individual andesite flows are typically separated by thin sandstone, siltstone or mudstone units.

Minor carbonate units crop out in two main localities along the coastline (Fig. 3.1) and exhibit a characteristic styolitic texture in drillcore (Fig. 3.9C). The units are < 1 m thick and typically interbedded with volcanic sandstone, siltstone and mudstone. They have been altered to chlorite and epidote lateral to the porphyry centre and have been intensely silicified and overprinted by clays at shallow levels above the intrusive complex. Coralline fossils identified include crinoids, coralline algae, coral fragments and echinoids (Harrison, 2009). The paleodepth of deposition was determined using the foraminiferal stratigraphic guides of Murray (1991) and Haig and Perembo (1992), which imply deposition in a mid-neritic environment (paleodepth 40 - 60 m below mean sea level).

Sedimentary breccias are polymodal, clast-supported, medium-grained volcanic wacke or juvenile sandstones. Clasts comprise silicified carbonate fragments, lithic fragments and juvenile siliclastic sands (e.g., Fig. 3.9D). A sedimentary breccia unit overlies the volcanic sandstone and contains clasts of fine-grained chloritic sandstone, most likely derived from the underlying unit.

The sedimentary rocks of Tumpangpitu dip inwards at approximately 40° in a concentric fashion towards the central porphyry intrusive complex (e.g., Fig. 3.3; Harrison, 2009; Rohrlach, 2010). Controls on the orientation and dip of the stratigraphic package are well constrained on the southwest flank of the porphyry system (Fig. 3.3), where coastal mapping has correlated surface exposures of sedimentary rocks with the same sedimentary package intersected by adjacent drillholes (Figs. 3.1 - 3.3). The orientation are contiguous when extrapolated onto sections (Figs. 3.3 and 3.4).

3.3.3 Tanjung Jahe pre-mineralization diatreme

The Tanjung Jahe diatreme forms a distinctive, well exposed headland on the southernmost peninsula of Tumpangpitu (Figs. 3.1 and 3.10). Its dimensions are approximately 1,150 m N-S x 500 m E-W (Fig. 3.1; Table 3.1). It is separated from the younger Tumpangpitu diatreme towards the north by a large exposure of Phase 2 diorite (Fig. 3.1). The headland was mapped both on foot and by helicopter-support by the author in 2009 (Harrison, 2009) and during reconnaissance field trips in 2014, 2015 and 2017. The diatreme can be split into a lower and upper facies described below. Upper facies breccia occurs at the same elevation as lower facies breccia due to a major arc parallel normal fault (Fig. 3.1; Tanjung Jahe normal and thrust faults) separating the two units, seen at the southernmost tip of the headland (Fig. 3.12A). Both facies are altered to chlorite - illite ± smectite (montmorillonite/nontronite) ± epidote ± calcite, consistent with its distal location relative to the Tumpangpitu mineralized center.

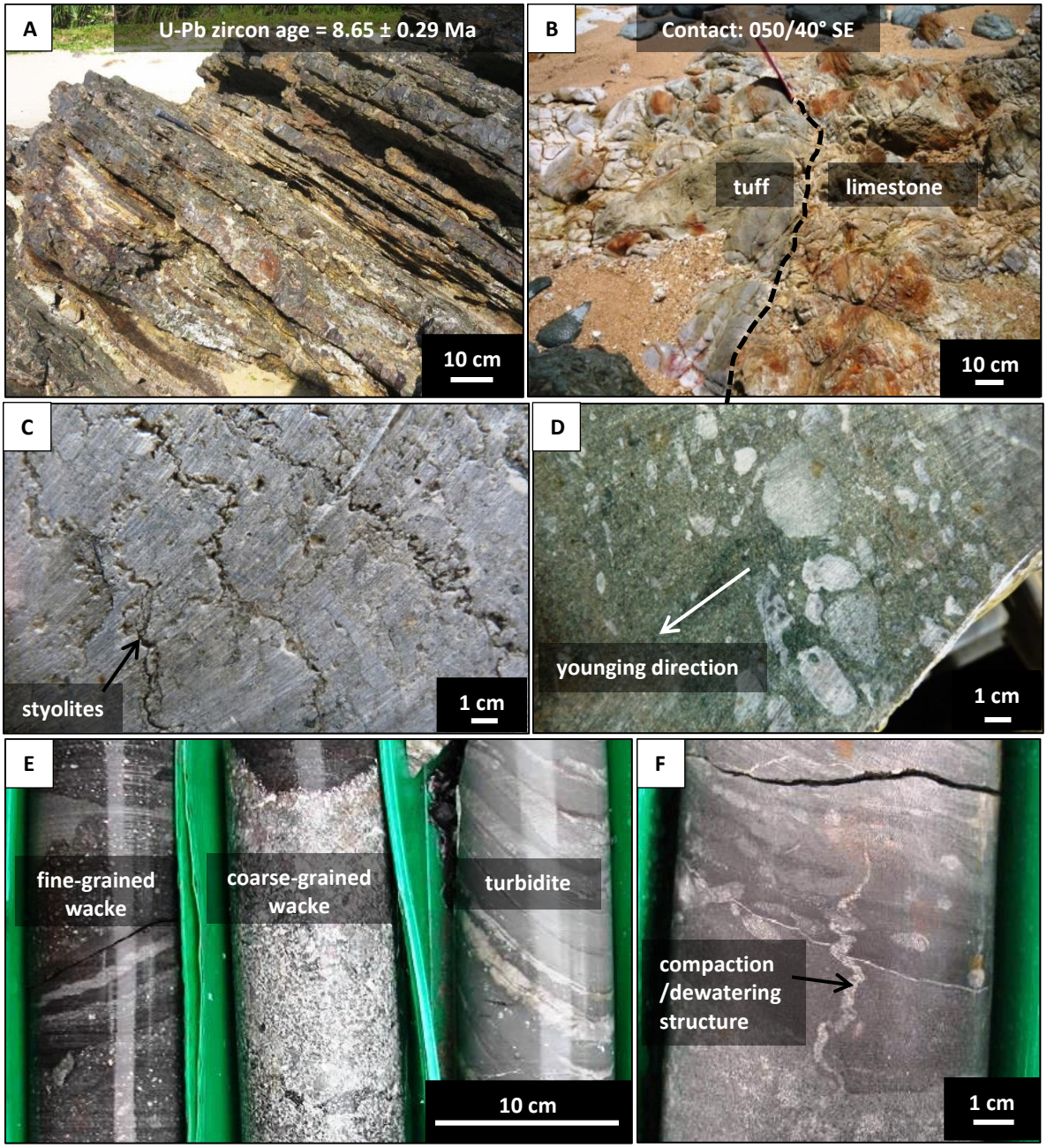

Figure 3.9. Coastal rock exposures and drillcore of sedimentary rocks at Tumpangpitu. Photos E and F from Rohrlach, (2010). All geochronological data presented in Chapter 4.

(A) *9047630 mN 173050 mE, elevation 1 m asl;* Interbedded fine-grained, immature, chlorite - calcite altered volcanic sandstone and recessively weathered siltstone cropping out along the coastal platform adjacent to Pulau Merah island.

(B) *9047410 mN 173110 mE, elevation 1 m asl;* Contact between fine-grained tuff and silicified laminated limestone.

(C) *9045841 mN 173577 mE; drillhole GTD-08-26; 345 m.* Limestone with characteristic stylolitic texture.

(D) *9045841 mN 173577 mE; drillhole GTD-08-26; 348 m.* Sedimentary breccia with chlorite-calcite alteration. Clasts comprise silicified carbonate fragments and chloritic sandstone.

(E) *9045841 mN 173577 mE; drillhole GTD-08-26; 212m.* Left to right. Fine-grained, grain-supported volcanic wacke; coarse-grained volcanic wacke and finely bedded (cm-scale) turbidite debris-flow deposit.

(F) *9045841 mN 173577 mE; drillhole GTD-08-26; 213m.* Alternating 3-5 cm beds of siltstone and sandstone.

Figure 3.10. 9043200 mN 175580 mE, elevation 2m asl. Looking west at the lower facies breccia of Tanjung Jahe headland.

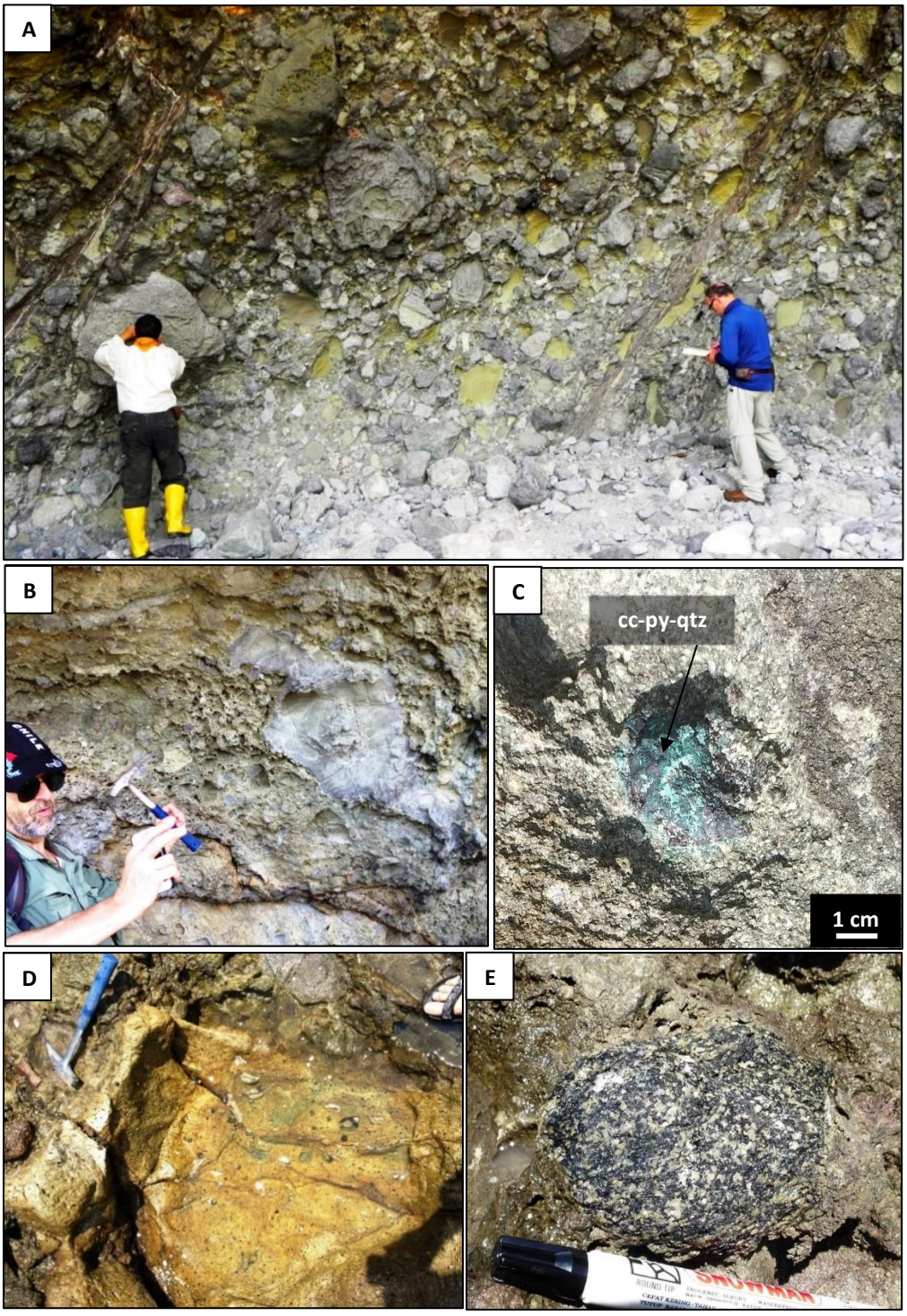

Figure 3.11. Features of lower facies diatreme breccia along coastal exposures at Tanjung Jahe.
A) 9043200 mN 175580 mE, elevation 3 m asl. Clast-supported lower facies diatreme breccia with metre-scale polymict clasts cut by thrust faults.
B) 9043624 mN 175407 mE. elevation 3 m asl. Juvenile andesitic clast with ragged contact in fine-grained tuffaceous andesitic breccia matrix.
C) 9043650 mN 175394 mE. elevation 3 m asl. Mineralized clast of chalcocite - pyrite - Cu oxide and quartz.
D) 9043783 mN 175380 mE. elevation 3 m asl. Large quartz diorite (phase 1) clast charateristic of phase 1 dikes.
E) 9043473 mN 175495 mE. elevation 3 m asl. Clast of unaltered hornblende gabbro in diatreme breccia.

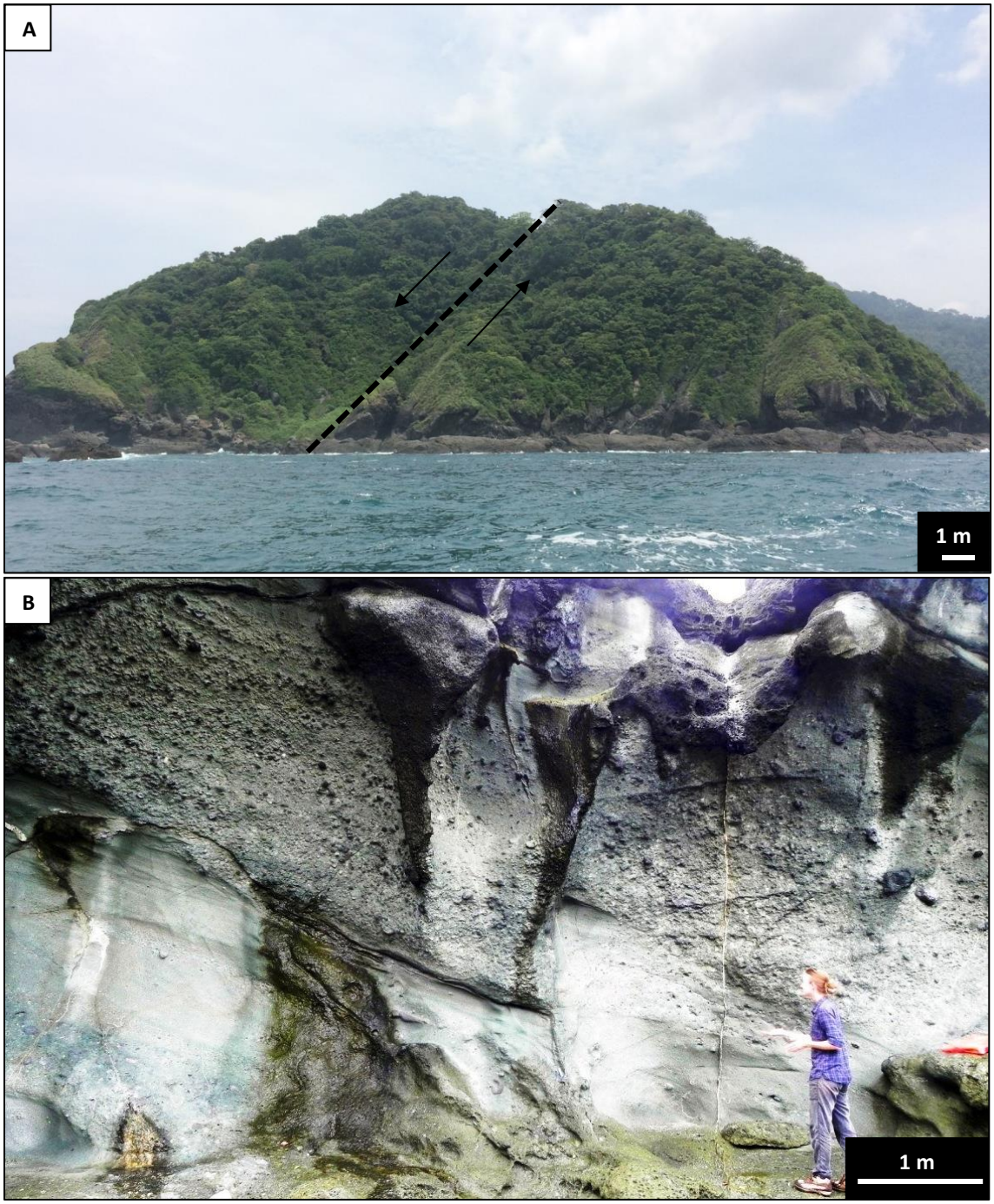

Figure 3.12. Features of upper and lower facies diatreme breccia along coastal exposures at Tanjung Jahe.
A) 9042900 mN 175320 mE, fault contact between upper facies diatreme (left) and lower facies breccia (right)
B) 9043790 mN 175100 mE, elevation 3 m asl. A coastal exposure on the western flank of Tanjung Jahe; upper-facies bedded diatreme breccia with graded bedding and low-angle cross stratification (interpreted as base surge and fallout deposits) offset by a reverse fault.

3.3.3.1 Lower facies breccia at Tanjung Jahe

The south eastern side of the Tanjung Jahe headland is dominated by a polymict, clast supported breccia with clasts up to 1 m in diameter (Figs. 3.1, 3.10 and 3.11A). Polymictic clasts are set in a in a fine-grained

tuffaceous matrix of andesitic composition comprising broken plagioclase, hornblende and magnetite. Clast types recognized are listed below;

- Phase 1 quartz diorite with hornblende megacrysts (Fig. 3.11D)
- Diorite clasts
- Sedimentary rocks; siltstone, sandstone, mudstone and limestone
- Fragments of coral
- Red thermally oxidized igneous clasts (Figs. 3.13A)
- Rare mineralized fragments of quartz - pyrite - chalcocite ± Cu oxides (Fig. 3.11C)
- Rare hornblende gabbro (source exposure unknown; Fig. 3.11E)

Wispy, ragged fine-grained andesitic clasts (Fig. 3.11B) have been recognized in the lower facies breccia. They are interpreted as juvenile magmatic clasts (e.g., Sillitoe, 1985; Davies et al. 2008a) in proximity to a postulated vent or root zone of coherent andesite (Fig. 3.1). Where fresh andesitic rock is present as clasts, up to 1 - 2 mm-sized magnetite and up to 3-mm-long amphibole grains are present. Magnetite also occurs as small (< 1 mm) crystals in the breccia matrix. The large amount of magnetite has produced a positive magnetic anomaly coincident with the Tanjung Jahe breccia headland (Fig. 3.35). The magnetic anomaly has been confirmed by mapping as being due to primary igneous magnetite. The southernmost tip of the headland has been cut by major NNW-trending thrust faults infilled with hematite and calcite (Figs. 3.11A and 3.36).

3.3.3.2 Upper facies breccia at Tanjung Jahe

The western and north-eastern exposures of the headland are characterized by layers of ash with accretionary lapilli and matrix-supported breccia with clear, locally graded bedding and intercalated surficial sedimentary rocks including siltstone, sandstone and mudstone. The beds generally dip gently (15 - 25˚) towards the east (Figs. 3.12 and 3.13). The bedded, comminuted and milled units are interpreted as upper facies diatreme breccia. The upper facies are fault juxtaposed against the lower facies by a NW-trending, SW-dipping fault that has truncated the headland, with a significant but unquantified component of vertical movement (Fig. 3.12A).

3.3.4 Volcanic breccia

Volcaniclastic breccias at Tumpangpitu form a pile approximately 100 - 300 m - thick. They are dominated by lithic and crystal lithic tuffs of andesitic and minor dacitic composition, as defined by a phenocryst assemblage of hornblende, plagioclase and minor quartz (Coote, 2009; Rohrlach, 2010). These pyroclastic rocks are only preserved at the uppermost stratigraphic level, cropping out as

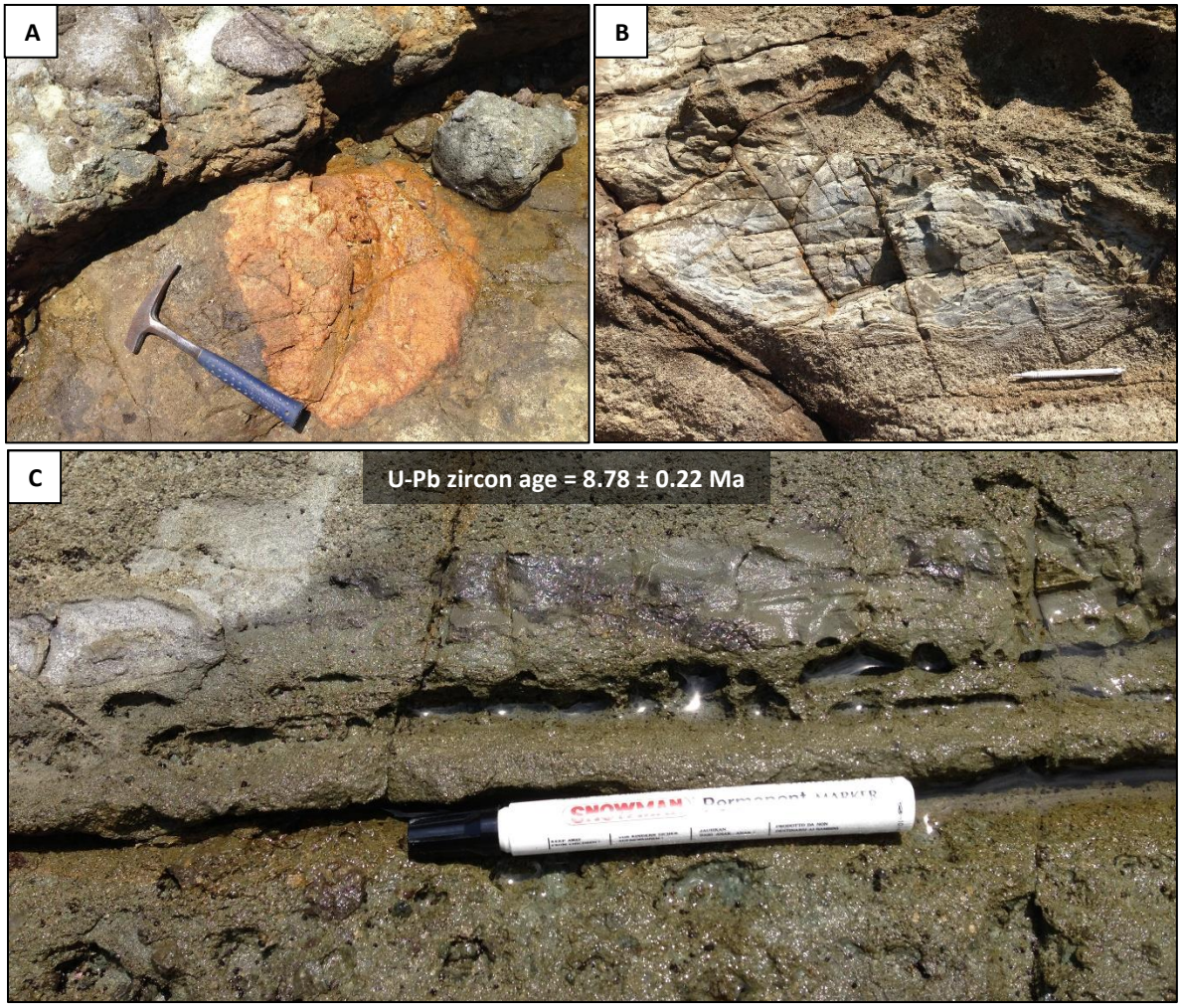

Figure 3.13. Coastal exposures of upper facies bedded diatreme breccias at Tanjung Jahe and clast types. All geochronological data presented in Chapter 4.

A) 9043610 mN 175380 mE, elevation 3 m asl. Thermally oxidized quartz diorite clast.
B) 9043790 mN 175360 mE, elevation 3 m asl. Clast of mudstone in fine-grained andesitic breccia.
C) 9043797 mN 175347 mE, elevation 3 m asl. Fine-grained mudstones and sandstones interlayered with fine grained andesitic milled breccia with 1 - 3 mm hornblende crystals.

prominent hills, overlying a large dioritic unit (phase 2) and coherent andesitic volcanic rocks mainly in the Zone A Au-Ag oxide area (Figs. 3.1 and 3.4). Primary textural features have been strongly distorted by intense alteration and oxidation of sulfides.

The breccia is polymict and composed mainly of rounded to sub-angular clasts in a highly altered fine-grained matrix dominated by andesitic tuff. The clasts are typically 0.5 to 5 cm in size (Fig. 3.14B). The breccias are texturally massive, with very little evidence of bedding or sorting. Some of the clasts have ragged margins, and very locally aligned lenticular flattened pumice clasts or fiamme; these are considered juvenile in origin (e.g., Fig. 3.14A; Bull and McPhie, 2007; Rohrlach, 2010). The dip of the volcanic breccia is unknown, as its basal contact is cut by the Tumpangpitu diatreme (Fig. 3.4).

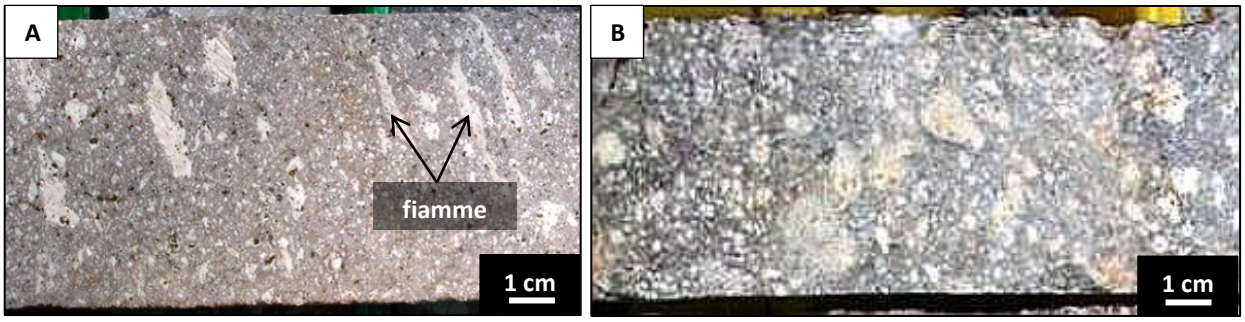

Figure 3.14. Examples from drillcore of volcanic breccia from unoxidized areas of Zone A at Tumpangpitu.

A) *9046766 mN 174361 mE; drillhole GTD-08-34; 15 m.* Matrix-supported quartz-dickite altered lithic-crystal tuff with strong alignment of flattened, fiamme 'pyroclasts.'
B) *9046669 mN 174365 mE; drillhole GTD-08-49; 20 m.* Lithic crystal tuff with quartz-dickite alteration.

3.3.5 Intrusions

The calc-alkaline intrusive complex at Tumpangpitu comprises at least eight individual intrusive phases, ranging in composition from diorite to quartz diorite and tonalite. Textures vary from equigranular to porphyritic. Sizes range from narrow (metre-scale) dikes, to large (2.5 x 4.6 km) intrusive bodies (Table 3.1; Figs. 3.1 - 3.8). The mineralized porphyry complex is a series of nested tonalitic porphyry intrusions that are temporally and spatially associated with Cu-Au-Mo mineralization. A pre-mineralization swarm of very weakly or unaltered NNW-trending quartz diorite dikes (phase 1) crop out along the southern coastline. They constitute the earliest recognized intrusive activity at Tumpangpitu (Fig. 3.1).

The tonalite complex at Tumpangpitu is located at depths of approximately 250 m to 700 m below the present day surface (Figs. 3.3 - 3.8). There are two main inter-mineralization tonalite porphyry intrusions (or alternatively textural variants of one intrusion); a fine-grained tonalite (phase 5) and a coarse-grained tonalite (phase 6), which constitute the well-mineralized part of the composite Tumpangpitu stock. A very coarse-grained, early to inter-mineralization, small volume tonalite pencil porphyry stock (phase 4) is present northwest of Tumpangpitu (Figs. 3.5 and 3.6), but it does not appear to be significantly mineralized at levels intersected so far by drilling. Together, the well-mineralized phases 5 and 6 are approximately 1,200 x 1,200 m wide in plan view (Fig. 3.2), with little appreciable change in width over their currently defined 1,200 m vertical extent (Figs. 3.3 - 3.8). Porphyry mineralization hosted by the tonalite phases remains open at depths below the current drilling capacity of 1,200 m (Figs. 3.3 - 3.8). The highest grade porphyry intersection to date (GTD-12-248: 689 m @ 1% Cu and 0.85 g/t Au; Intrepid Mines Ltd, 2012) is located at a cross-junction of the northwest-trending Cliff Fault with a northeast cross-structure (Fig. 3.2). This suggests that structural controls on the emplacement of the Tumpangpitu composite porphyry stock involved a combination of both northwest and later formed northeast faults (Figs. 3.1 and 3.2).

The mineralized tonalites intruded into, and overprinted a pre-mineralization, large (2.5 x 4.6 km) diorite pluton (phase 2). A late-inter-mineralization quartz diorite intrusion (phase 7), formed an ovoid body that overlies the porphyry centre (Figs. 3.1 - 3.8). The youngest intrusive event was a swarm of N-trending dikes (phase 8), that crop out along the southern coastline (Fig. 3.1). All eight phases are described in detail below.

3.3.5.1 Phase 1 - Pre-mineralization hornblende quartz diorite

Phase 1 is defined by a swarm of NNW- trending, pre-mineralization quartz diorite dikes ranging from approximately 20 to 600 m wide, with strike lengths of up to 1,600 m (Fig. 3.1). The dike swarm has only been encountered south of Tumpangpitu, near the Candrian prospect (Harrison, 2014) and Tanjung Jahe diatreme (Fig. 3.1) where it crops out extensively along the southern coastline. Abundant clasts of phase 1 have been mapped in the Tanjung Jahe diatreme breccia. The phase 1 dikes exhibit columnar jointing, suggesting shallow levels of emplacement (3.15C). They are medium- to very- coarse-grained, with quartz eye phenocrysts up to 5 mm in diameter, hornblende and pyroxene phenocrysts together with plagioclase typically altered to illite. Some hornblende crystals are megacrystic, reaching 4 cm in length (e.g., Fig. 3.15A). Abundant, tabular to prismatic, euhedral to anhedral phenocrysts are contained within a weakly porphyritic to equigranular quartz-rich groundmass (Fig. 3.15A). Equigranular quartz and relict plagioclase, together with minor magnetite, compose the groundmass. The total quartz content is 10 - 20 %. Phase 1 is characteristically unaltered, with only weak, localized replacement of mafic phenocrysts by chlorite. The Phase 1 hornblende quartz diorite has been crosscut by phase 8 dikes along the southern coastline (Fig. 3.15C).

3.3.5.2 Phase 2 - Pre-mineralization old diorite porphyry (OD)

Phase 2 or "old diorite," constitutes a large (2.5 x 4.6 km diameter), pre-mineralization diorite body (Figs. 3.1 and 3.2). It extends to the southern coastline and is cross-cut by phases 3 - 7. It is the earliest recognized large intrusive phase and is located adjacent to the Tumpangpitu tonalite complex, pre-dating both porphyry and epithermal Cu - Au mineralization. Old diorite (e.g., Figs. 3.16A and B) is characterized by an equigranular texture with grainsizes of 2 - 4 mm, consisting dominantly of plagioclase phenocrysts (60 - 70 %). Quartz is less than 5 % volume and rarely observable as quartz eye phenocrysts, making it distinguishable from the later quartz diorite and tonalite intrusions (Fig. 3.17). Subordinate 2 - 4 mm - sized hornblende crystals have been observed in unaltered coastal exposures, and in the chlorite ± epidote - ± calcite altered fringes of the Tumpangpitu deposit, where they have generally been intensely altered to chlorite or replaced by rutile (Figs. 3.16A - B). Occasional mafic xenoliths have been observed in outcrop and drillcore (e.g., Fig. 3.15D). The old diorite unit is the main host to the Zone C Au-Ag oxide deposit in northern sections of the deposit (Figs. 3.3 - 3.4), where high-sulfidation mineralization has been observed

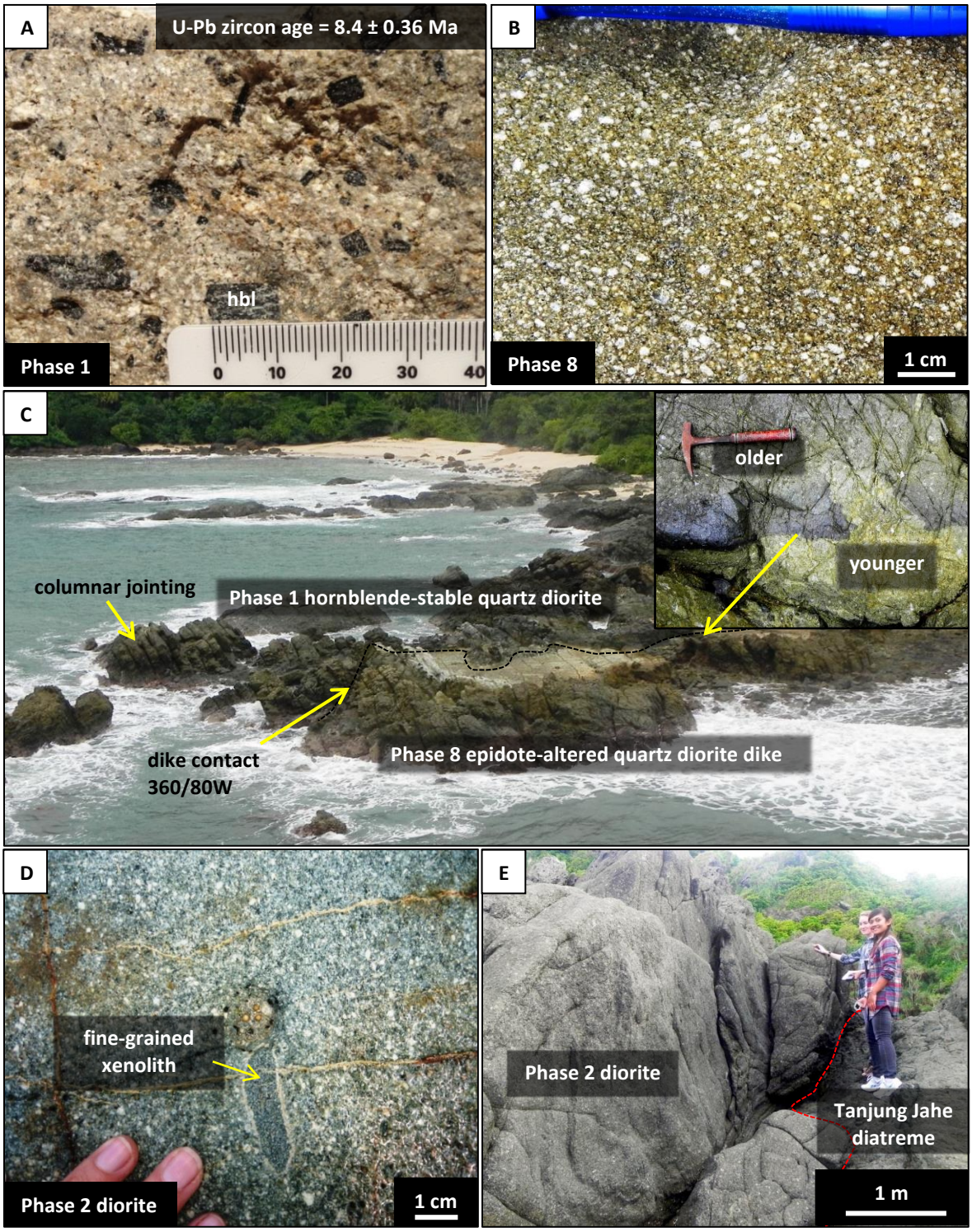

Figure 3.15. Intrusive rocks from coastal exposures at Tumpangpitu. All geochronological data presented in Chapter 4. Abbreviation: hbl = hornblende.

A) 9043783 mN 175380 mE, elevation 3 m asl. Phase 1 quartz diorite dike with hornblende megacrysts.
B) 9045260 mN 176855 mE, elevation 3 m asl. Phase 8 quartz diorite with strong epidote alteration.
C) 9045240 mN 176830 mE, elevation 3 m asl. Contact between phase 8 and phase 1 dikes.
D) 9047515 mN 173092 mE, elevation 3 m asl. Phase 2 diorite with fine-grained mafic xenolith.
E) 9044243 mN 174444 mE, elevation 3 m asl. Contact between phase 2 diorite and Tanjung Jahe diatreme.

along narrow structures. Phase 2 crops out extensively along the coastline (Fig. 3.1) and has been mapped as an intrusive contact with the Tanjung Jahe diatreme towards the south of Tumpangpitu (Fig. 3.15E). The hypabyssal nature of phase 2 diorite is suggested by abundant columnar jointing in coastal exposures and mapped basal contact relationships with the underlying andesitic and sedimentary rocks.

3.3.5.3 Phase 3 - Zone B quartz diorite

Phase 3 has been intersected by drilling at depths below 365 m in the Zone B prospect (Fig. 3.1). It has not yet been recognized at surface. It is interpreted to be a small (100 x 200 m diameter) body of medium- to coarse-grained, sub-porphyritic (3 - 8 mm) quartz diorite with phenocrysts of subhedral plagioclase, hornblende, minor biotite and magnetite (Figs. 3.16D and E). Magmatic biotite has been replaced by chlorite (Fig. 3.16E). The quartz content is less than 15 vol. %. The quartz diorite has been cut by the Zone B Cu-Au-Mo tonalite porphyry at depth, on a major north-trending fault (Fig. 3.1).

3.3.5.4 Phase 4 - Early inter-mineralization very coarse-grained tonalite porphyry (VCT)

A very coarse-grained tonalite phase has been observed in three drillholes on two sections; 11380 mN (Fig. 3.5) and 11620 mN (Fig. 3.6), to the north of the Tumpangpitu porphyry centre (Fig. 3.2). It appears to be a small volume, early pre- to inter-mineralization pencil-shaped stock approximately 250 x 100 m in plan view (Figs. 3.2 and 3.5), with NW-trending associated narrow dikes of 5 - 20 m on section 11620 mN (Fig. 3.6). It has a crystal-crowded porphyritic texture, with large 3 - 7 mm phenocrysts of euhedral rectangular plagioclase crystals (replaced by illite or kaolinite) and large, granoblastic quartz phenocrysts up to 1 cm in diameter (Fig. 3.16C). The VCT has undergone very weak potassic alteration (minor hydrothermal magnetite and replacement of hornblende and minor primary mafic biotite by shreddy biotite, which has in turn been replaced by shreddy chlorite). Observations of crosscutting relationships from drillcore, are interpreted to indicate that the unit has a pre- to inter-mineralization timing, due to the fact that it is overprinted by intense stockwork veining and disseminated copper sulfide porphyry mineralization along its contacts with phase 5 tonalite. The interior of phase 4 porphyry dikes have very low Au-Cu-Mo grades (average 0.1 g/t Au, 0.1 % Cu and 50 ppm Mo). However, molybdenite grades increase to an average of 120 ppm Mo with depth on section 11380 mN (Fig. 3.5), suggesting that phase 4 has the potential to host economic Cu-Au porphyry mineralization at depth, since molybdenite is a pathfinder at Tumpangpitu. Phase 4 tonalite is interpreted as a low grade precursor porphyry to the main Cu-Au-Mo mineralizing tonalite(s) 5 and 6.

3.3.5.5 Phase 5 - Early inter-mineralization fine-grained tonalite porphyry (FT)

Phase 5 fine-grained tonalite porphyry is a large volume stock, approximately 1, 200 x 1, 200 m in diameter when projected from section (e.g., Fig. 3.3) onto the 500 m level plan view (Fig. 3.2). It hosts the

largest volume of porphyry Cu-Au-Mo mineralization intersected to date, down to the limit of drilling (1,200 m below present day surface). It has an early- to inter-mineralization timing. Phase 5 defines a 200 to 500 m thick carapace to the underlying phase 6 coarse-grained tonalite (Figs. 3.2 - 3.8). Its upper contact has been truncated by the Tumpangpitu diatreme, which has entrained large (> 1 m x 1 m) mineralized blocks of this unit (e.g., Fig. 3.3). Phase 5 tonalite appears to have been emplaced along the Cliff fault, one of the major NW-trending structures (Fig. 3.1). This is evident on type section 11060 mN (Fig. 3.3) where Phase 5 was intersected just 250 m from surface below Zone A Au-Ag oxide deposit.

Phase 5 tonalite is unique in that it does not display a classic porphyritic texture. It is distinguishable by a distinctive fine-grained, equigranular texture composed of 1 - 2 mm phenocrysts of plagioclase, commonly altered to illite, kaolinite, dickite, pyrophyllite and/or alunite at shallow levels (3.17A). It has minute (< 2 mm) quartz eyes that are typically only observable during close inspection using a hand lens (3.17B), or under the microscope. The quartz content of the unit is generally ~20 %, with most of it hosted in the crystalline groundmass (Coote, 2010; Figs. 3.17A and B). Phase 5 is the main host rock to high-sulfidation epithermal mineralization, which has overprinted porphyry mineralization (Chapter 5). Phase 5 tonalite is pervasively altered to quartz - pyrophyllite ± alunite ± dickite in central zones, resulting in complete textural destruction due to intense silicification, making phase 5 tonalite difficult to distinguish from other wall rocks (Figs. 3.3 - 3.8 and 3.17A).

3.3.5.6 Phase 6 - Inter-mineralization coarse-grained tonalite porphyry (CT)

Phase 6 inter-mineralization coarse-grained tonalite is the deepest level mineralized Cu-Au-Mo porphyry intersected to date (depths >700 m below surface). Its dimensions are almost 1,000 x 1,000 m at 500 m level plan view (Fig. 3.2) when extrapolated from sections, with NW-trending apophyses (Figs. 3.3 - 3.8). Phase 6 has a characteristic crystal-crowded, strongly porphyritic texture. The 2 - 5 mm diameter phenocrysts include 40 - 50 % feldspar (plagioclase-dominant) and 15 - 25 % distinctive 2 - 5 mm quartz eyes set in a quartz-rich crystalline groundmass (Fig. 3.17C and D). Due to intense hydrothermal alteration, primary ferromagnesian minerals are rarely preserved. Relict outlines of hornblende can be recognized despite strong replacement by shreddy biotite, which have in turn been replaced by chlorite and rutile (e.g., Fig. 3.17C and D). Most of the feldspar phenocrysts have been altered to illite, and subsequently to kaolinite. Plagioclase is the dominant feldspar phenocryst. K-feldspar rarely occurs as a phenocryst phase.

3.3.5.7 Phase 7 - Late inter-mineralization quartz diorite (QD)

The quartz diorite unit (phase 7) defines one of the final major stages of magmatic activity at Tumpangpitu. It is an ovoid body measuring 1,700 x 700 m at surface (Fig. 3.1) and 800 x 300 m in plan view at -500 m RL (Fig. 3.2), where it forms a sigmoidal shape. It sits directly above the tonalite intrusive centre, between the high-sulfidation epithermal Au-Ag oxide Zones A and C (Fig. 3.1). A narrow (20 m)

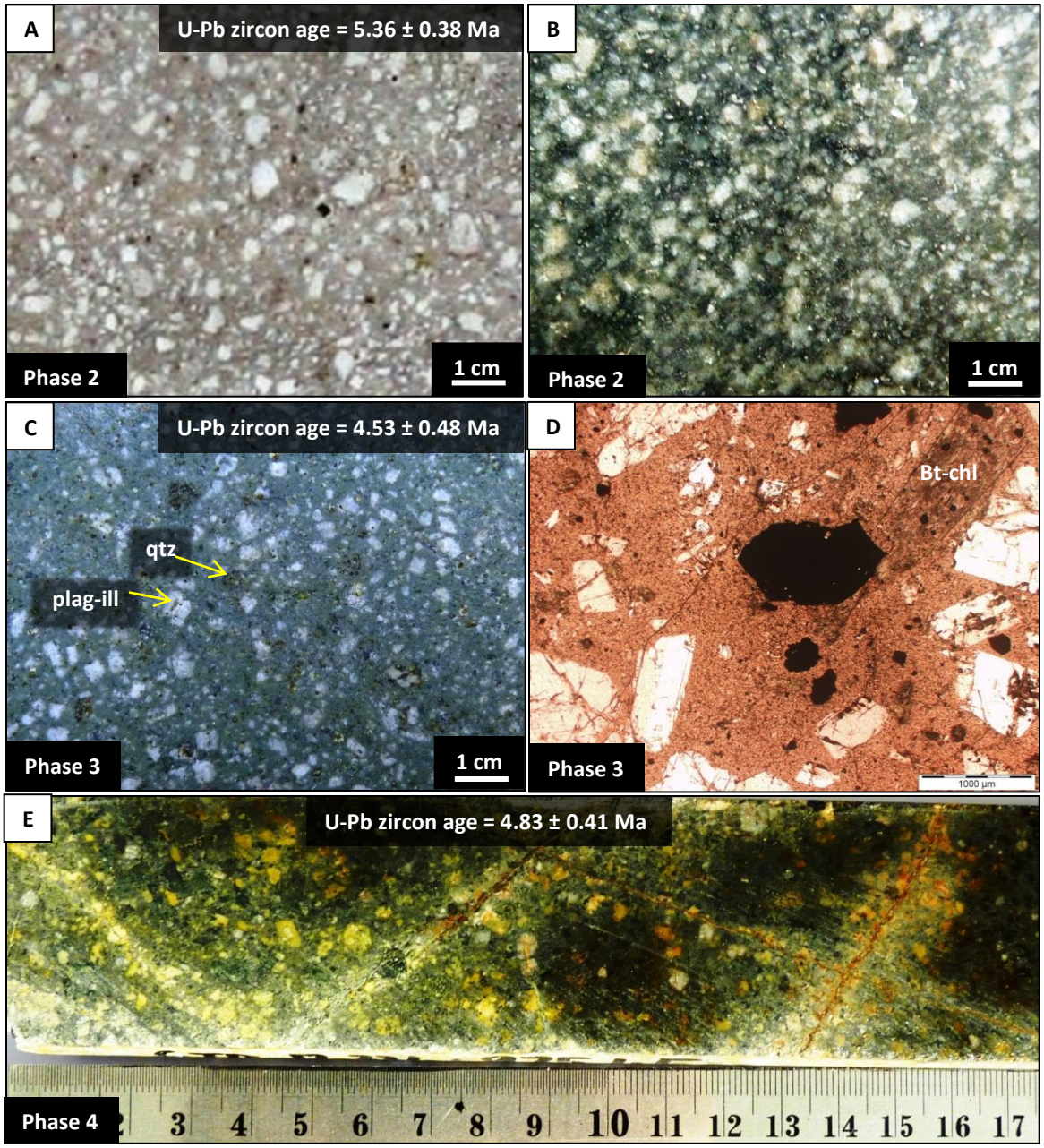

Figure 3.16. Intrusive rocks from Tumpangpitu porphyry center. All geochronological data presented in Chapter 4. Abbreviations: ill = illite, plag = plagioclase, qtz = quartz.

A) *9046564 mN 173495 mE; drillhole GTD-08-42; 241.9 m.* Phase 2 diorite. Feldspar phenocrysts have been pseudomorphed by kaolinite - dickite. < 5% quartz phenocrysts in the fine-grained silicified matrix.
B) *9045841 mN 173577 mE; drillhole GTD-08-26; 49 m.* Phase 2 diorite selectively altered to chlorite - illite.
C) *9045397 mN 175020 mE; drillhole GTD-10-137; 775.7 m.* Phase 3 Zone B quartz diorite, 1- 3 mm. plagioclase phenocrysts, 10 - 15 % quartz, chlorite - illite alteration.
D) *9045397 mN 175020 mE; drillhole GTD-10-137; 775.7 m.* Photomicrograph of phase 3 sample C.
E) *9045841 mN 174001 mE; drillhole GTD-12-334; 975.45 m.* Phase 4 very coarse-grained tonalite; large 3 - 5 mm quartz eye phenocrysts; weak magnetite - chalcopyrite mineralization. Chlorite - biotite - magnetite alteration overprinted by illite - kaolinite.

feeder dike has been identified on section 11020 mN (Fig. 3.4) cross-cutting phase 5 tonalite. Phase 7 is texturally well-preserved in distal zones of the hydrothermal system, exhibiting a crystal-crowded, coarse-grained (2 - 5 mm) texture with large (2 - 5 mm) quartz eye phenocrysts (Fig.3.17E and F). The phase 7 quartz diorite has very similar textural features to the phase 6 tonalite (Fig. 3.17C and D). The differences between the two units includes, a slight reduction in quartz content for phase 7 (< 15 % volume), and a lack of porphyry Cu-Au-Mo mineralization and associated alteration in phase 7 throughout all zones of the Tumpangpitu deposit (Figs. 3.3 - 3.8) except directly adjacent to phase 5 tonalite on section 11220 mN (Fig. 3.4). Phase 7 has been overprinted by narrow intervals of fault-controlled epithermal Cu-Au-Ag mineralization and has xenoliths that contain porphyry stockwork veins and disseminated Cu sulfide mineralization along its basal contacts above the phase 5 mineralized fine-grained tonalite (Fig. 3.4).

3.3.5.8 Phase 8 - Post-mineralization quartz diorite porphyry dikes

Minor occurrences of narrow (1 - 20 m), late stage quartz diorite dikes with mafic xenoliths crop out along the southern coastline of Tumpangpitu (Fig. 3.1 and 3.15C). The dikes have an equigranular, medium-grained texture, composed of hornblende, minor biotite, euhedral plagioclase feldspars and primary magnetite, with quartz contents of 5 - 15 % (Fig. 3.15B). The mafic phenocrysts of phase 8 are characteristically strongly altered to pistachio green epidote, making the unit easily distinguishable from adjacent phase 1 quartz diorite (e.g., Fig. 3.15C). Where the dikes crop out along the southern coastline, they strike due north and dip 80° west (Figs. 3.1 and 3.15C). The dikes have a clear field crosscutting relationship with Phase 1 as shown by the ragged contact between the two phases where material from Phase 8 has intruded Phase 1 (Fig. 3.15C).

3.3.6 Other porphyries in the Tujuh Bukit district

Five additional tonalite porphyries have been recognized in the Tujuh Bukit district (Fig. 3.18). They occur along two major NW- trending mineralized corridors, illustrated in Fig. 3.18, that are known as the Pulau Merah - Tumpangpitu - Zone B corridor and the Salakan - Katak corridor. The Candrian porphyry is located between these two corridors. The Salakan corridor appears to host weaker Au-Cu-Mo porphyry-style mineralization than the Pulau Merah corridor. The five porphyry prospects (Salakan, Katak, Pulau Merah, Candrian and Zone B) are described below and illustrated in Figures 3.19 and 3.20.

3.3.6.1 Pulau Merah tonalite porphyry

On Pulau Merah island (1.7 km northwest of Tumpangpitu; Fig. 3.18) a 370 x 220 m tonalite porphyry stock is well exposed, exhibiting superb coastal exposures of porphyry stockwork mineralization, supergene enrichment and telescoped high-sulfidation epithermal mineralization (Figs. 3.1 and 3.19B). Channel sampling of the porphyry stockwork veins overprinted by high-sulfidation mineralization around

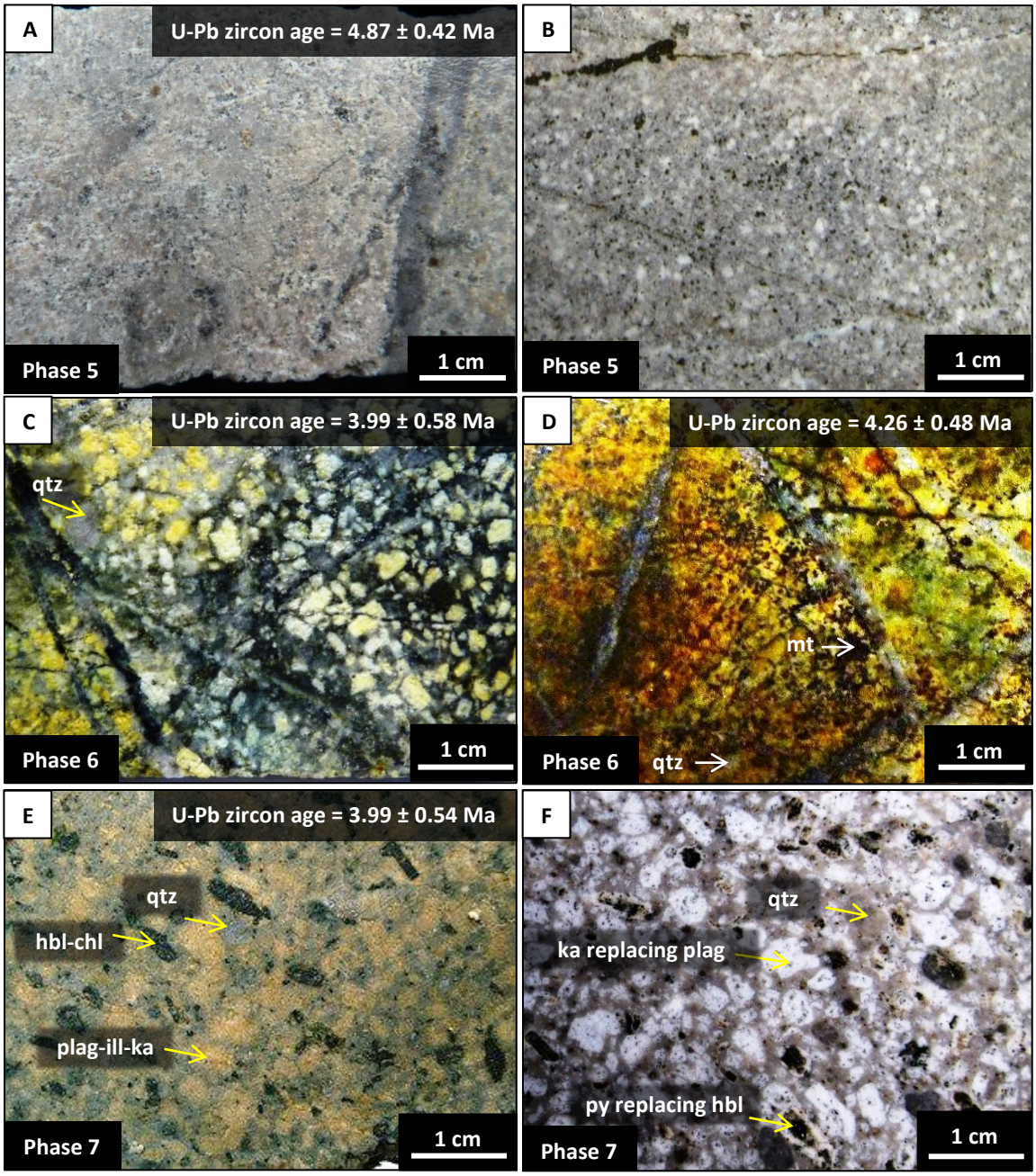

Figure 3.17. Intrusive rocks from Tumpangpitu porphyry center. All geochronological data presented in Chapter 4. Abbreviations: chl = chlorite, hbl = hornblende, ill = illite, ka = kaolinite, mt = magnetite, plag = plagioclase.

A) *9046551 mN 174080 mE; drillhole GTD-08-35; 554.95 m.* Phase 5 fine-grained tonalite. Fine-grained equigranular texture with > 15 % 1 - 2 mm quartz phenocrysts, difficult to see without magnification. Strong quartz - pyrophyllite - alunite alteration has destroyed primary texture; rutile has replaced mafics.

B) *9046508 mN 173760 mE; drillhole GTD-10-162; 412.7 m.* Phase 5 fine-grained tonalite. Quartz - illite alteration, equigranular textural preservation with 1 - 2 mm ex-plagioclase phenocrysts.

C) *9046550 mN 174082 mE; drillhole GTD-12-292; 1012 m.* Phase 6 coarse-grained tonalite. Distinct 1 - 5 mm quartz eye phenocrysts. Chlorite - K-feldspar - magnetite alteration.

D) *9046097 mN 174155 mE; drillhole GTD-11-201; 988 m.* Phase 6 strongly magnetite-biotite (replaced by chlorite) - K-feldspar altered coarse-grained tonalite. 1 - 5 mm quartz eye phenocrysts still visible.

E) *9046136 mN 173503 mE; drillhole GTD-10-139; 355.4 m.* Phase 7 quartz diorite. Large 2 - 5 mm quartz eye phenocrysts. Tabular plagioclase phenocrysts altered to illite. Hornblende altered to chlorite.

F) *9046508 mN 173760 mE; drillhole GTD-10-162; 303.9 m.* Illite-kaolinite altered Phase 7 quartz diorite.

the base of the island, during early stage exploration from 1997 to 2000, returned 47 m @ 1.71 g/t Au and 1.29 % Cu (Rohrlach, 2012). Pulau Merah is the discovery outcrop for porphyry mineralization in the district. The tonalite complex consists of a fine-grained outer tonalite shell exposed along the coral reef platform adjacent to the island, (similar to phase 5 tonalite at Tumpangpitu) and a central coarse-grained quartz eye biotite-hornblende-bearing tonalite forming the main island (similar to phase 6 tonalite at Tumpangpitu; Figs. 3.19A - B). Petrographic samples taken from GTD-03, drilled underneath the island (Fig. 1.6), show that the coarse-grained tonalite phase has at least 25 % quartz (primary phenocrysts and groundmass quartz; Coote, 2010).

3.3.6.2 Katak tonalite porphyry

The Katak tonalite porphyry (2.5 km east of Tumpangpitu; Fig, 3.18) has been intersected around 170 m below surface by exploration drilling (Fig. 3.18). Its lateral dimensions are approximately 800 x 500 m (Fig. 1.6). Average grade from the first drillhole, KTD-10-001 is 100 m @ 0.45 g/t Au and 0.30 % Cu (Intrepid Mines Ltd, 2010). Porphyry-style mineralization is dominated by chalcopyrite, typically intergrown with magnetite (Fig. 3.19C). The tonalite is light green to grey in colour and has a medium-coarse grained texture (2 - 4 mm; Fig. 3.19C). Primary quartz, including phenocrysts and groundmass components, makes up 15 - 25 % of the rock. Other phenocryst phases include hornblende, biotite and plagioclase. Intergrowths of illite and chlorite have partially to totally replaced groundmass plagioclase. Early potassic alteration (secondary biotite, magnetite and minor K-feldspar) has been strongly overprinted by retrograde alteration minerals, including illite and chlorite. Late gypsum veins are common (Fig. 3.19C). A partially eroded lithocap remains to be drill tested for epithermal mineralization to the north of Katak.

3.3.6.3 Candrian tonalite porphyry

The Candrian tonalite porphyry (2.7 km northeast of Tumpangpitu; Fig, 3.18) is mineralized from just 5 m below surface (Harrison, 2014). Its full dimensions require further drilling to test areas of porphyry mineralization that remain open. The prospect contains several porphyritic tonalite pencil stocks over a strike length of 1.6 km NW-SE by 0.5 km NE-SW (Fig. 3.18). Porphyry-style mineralization is dominated by chalcopyrite, typically intergrown with magnetite that is disseminated in a fine to medium grained porphyry tonalite and adjacent wallrock. Primary quartz, including phenocrysts and groundmass components comprises 15 - 25 % of the rock. Other phenocryst phases include hornblende, biotite and plagioclase. Average grades from drillhole CND-11-002 were 138 m 0.8 g/t Au, 0.21 % Cu (Intrepid Mines Ltd, 2011).

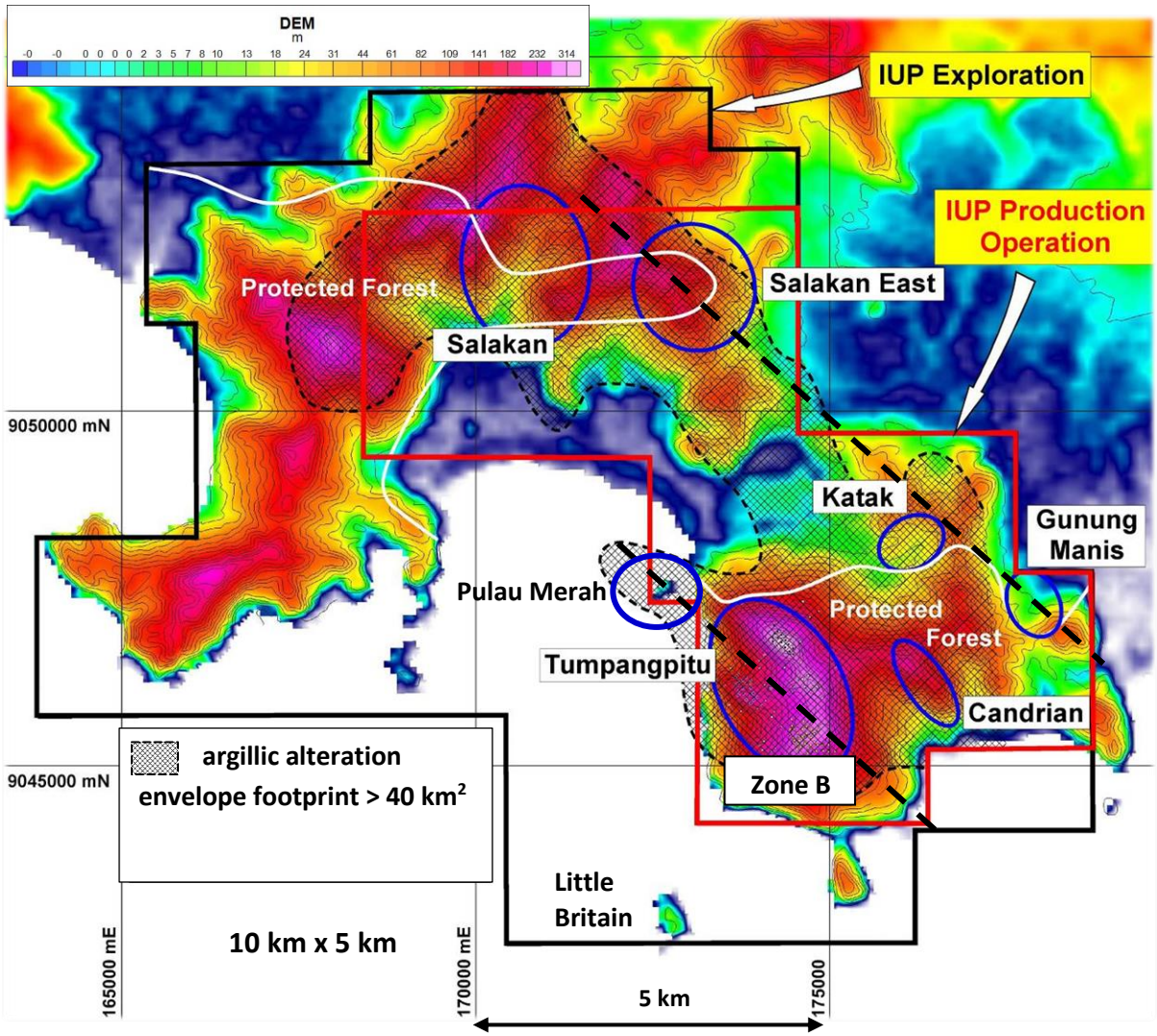

Figure 3.18. Digital elevation image (DEM) showing other Cu-Au-Mo porphyries along NW-trending structural corridors (dashed lines) in the Tujuh Bukit district (modified after Intrepid Mines Ltd. 2010).

3.3.6.4 Salakan tonalite porphyry

The Salakan prospect (7.5 km northwest from Tumpangpitu; Fig. 3.18) contains fine-grained (Fig. 3.20C) as well as coarse-grained (3.20B) inter-mineralization tonalite porphyries, similar to textural observations at Tumpangpitu and Pulau Merah island (Harrison, 2012). Primary quartz comprises 15 - 25 % of both the fine and coarse-grained phases, occurs as phenocryst and groundmass components. Other phenocryst phases include hornblende, biotite and plagioclase. The average grade from drillhole SND-12-001 is 604 m @ 0.008 g/t Au and 0.22 % Cu (Intrepid Mines Ltd, 2012). One main difference compared to the other porphyry prospects in the Tujuh Bukit district is the lower grades of porphyry and HSE mineralization encountered during exploration drilling at Salakan. A dense network of porphyry stockwork veining is present in surface rock exposures and drillcore to depths of over 900 m, although the veins are devoid of copper sulfides (e.g., Fig. 3.20B). However, the B porphyry veins (using the terminology of

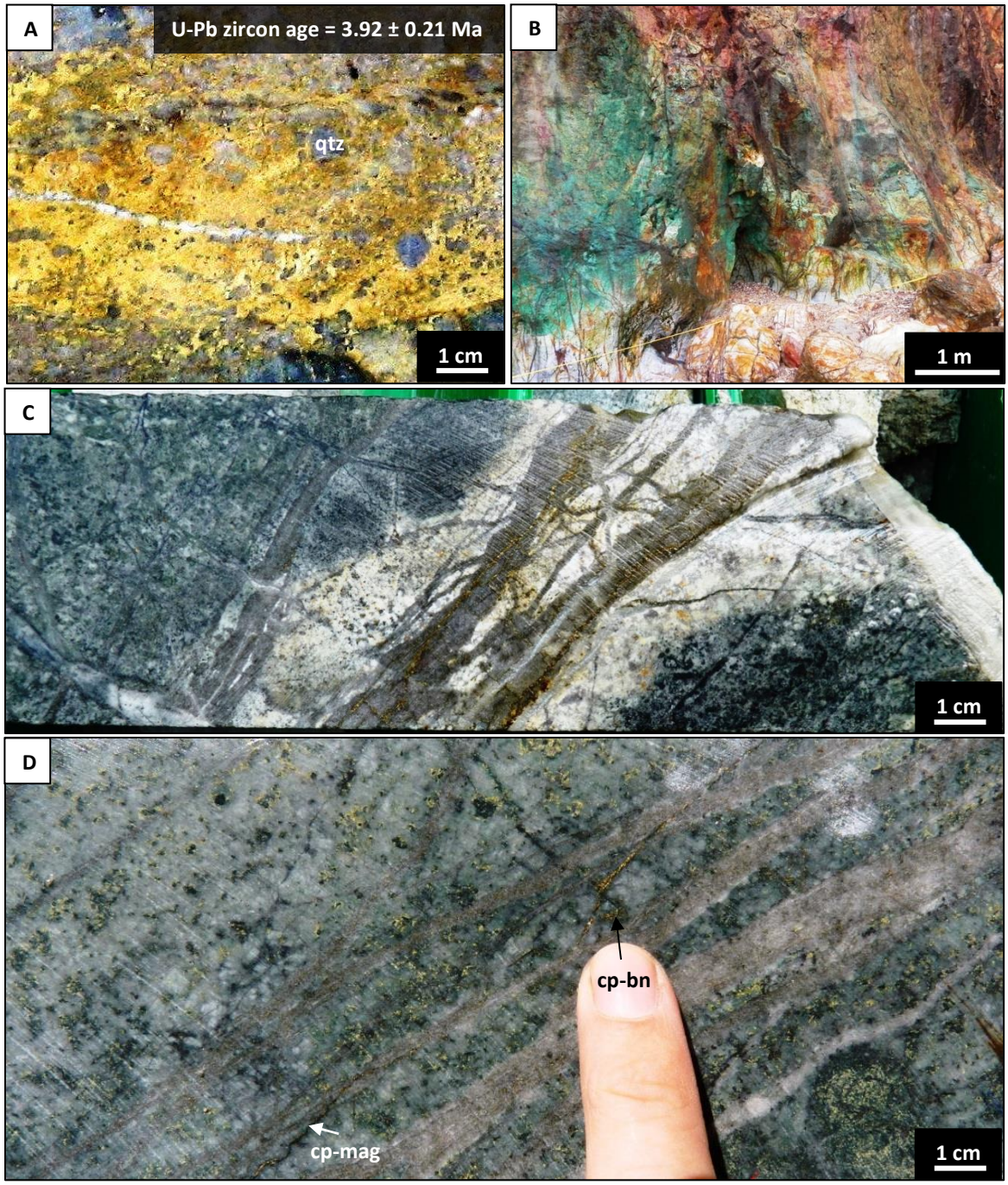

Figure 3.19. Drillcore and rock exposures from porphyries in the Tujuh Bukit district. All geochronological data presented in Chapter 4. Abbreviations: Bn = bornite, cp = chalcopyrite, mt = magnetite, qtz = quartz.

A) *9047573 mN 173106 mE; drillcore GT-003; 489 m.* Pulau Merah coarse-grained tonalite. Distinct 1 - 5 mm quartz eye phenocrysts. Quartz - illite - kaolinite overprint.
B) *9047530 mN 172780 mE;* elevation 1 m asl. Pulau Merah island; coarse-grained tonalite with quartz - dickite - pyrophyllite alteration and HSE veins telescoped on top of strong porphyry stockwork veining.
C) *9047930 mN 176226 mE; drillcore KTD-10-001; 196.6m.* Katak medium-grained magnetite-chlorite (after biotite) - illite altered porphyry tonalite overprinted by late quartz - pyrite vein with illite alteration halo.
D) *9046372 mN 176723 mE; drillcore CND-11-002; 117 m.* Medium-grained porphyritic tonalite from Candrian with quartz - chalcopyrite - bornite stockwork veins. Secondary chlorite - magnetite alteration.

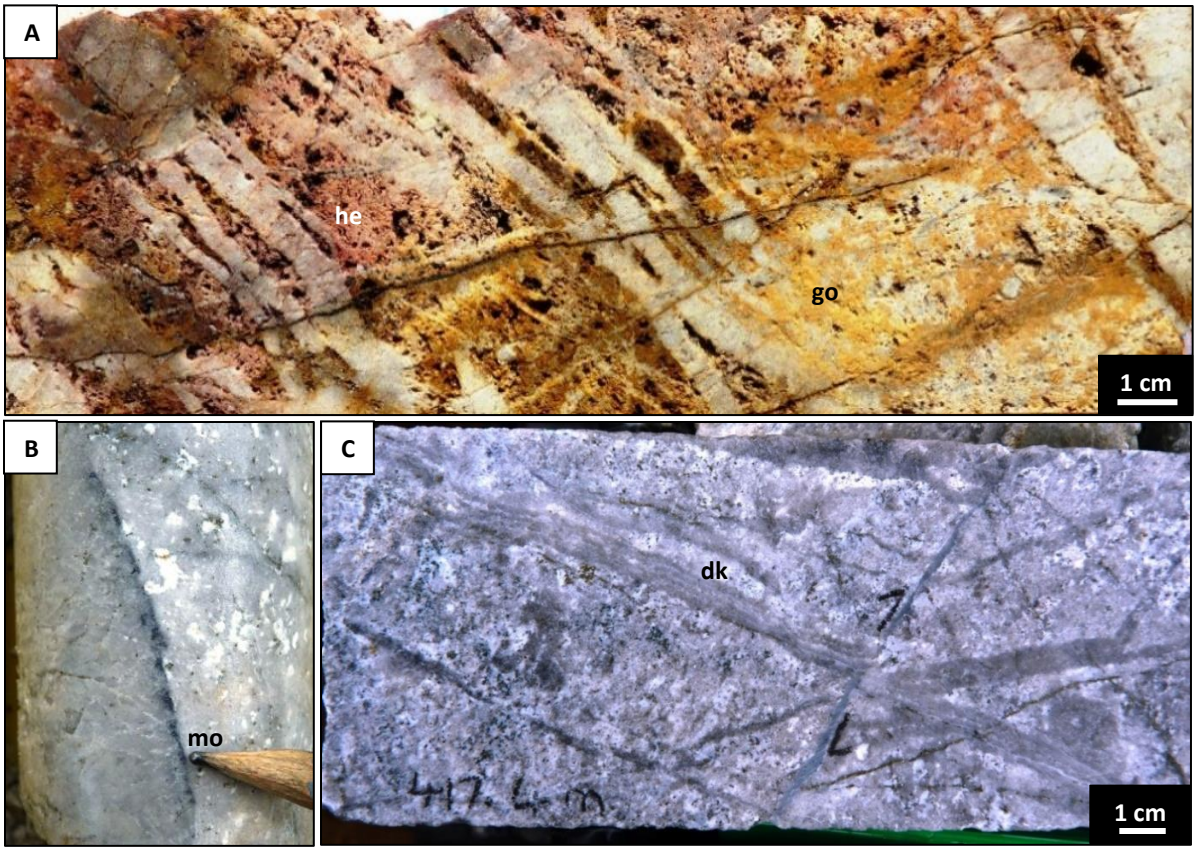

Figure 3.20. Examples of tonalite porphyry from drillhole SND-12-001 (9052317 mN 170001 mE) from the Salakan porphyry prospect. Abbreviations: dk = dickite, go = goethite, he = hematite, mo = molybdenite.

A) *95.8 m.* Coarse - grained, quartz - alunite altered, oxidized tonalite porphyry with characteristic quartz eye phenocrysts. Intense A and B vein stockwork, cut by late iron oxide veins.
B) *602.7 m*. Quartz stockwork vein with molybdenite margin.
C) *417.4 m*. B type porphyry veins cut by dickite vein in quartz - pyrophyllite - kaolinite altered fine-grained tonalite porphyry.

Gustafson and Hunt, 1975) contain abundant molybdenite (Fig. 3.20D).

3.3.7 Hydrothermal breccias

Hydrothermal breccias are defined here as breccias that have formed due to the interaction of hydrothermal fluids with wallrocks and/or magma (e.g., Davies, 2002; Davies et al. 2008b). Diagnostic properties of hydrothermal breccias at Tumpangpitu are hydrothermal cement (e.g., quartz, alunite, barite ± sulfides) and wall-rock clasts that have evidence of pre-existing hydrothermal conditions (altered or mineralized clasts, or clasts containing veins and fragments of veins; Sillitoe, 1985).

Hydrothermal breccias are common towards the center of Tumpangpitu in the shallow epithermal environment, and are the dominant host phase for Au-Cu-Ag high-sulfidation epithermal mineralization. Most of them are volumetrically minor with a narrow (< 1 m) dike-like form and have near-vertical geometries that are restricted to narrow fault zones (e.g., Fig. 3.3). An exception occurs on section 10820 mN (Fig. 3.7), where there is a 300 m - thick zone of hydrothermal breccia, emanating from the apex of a

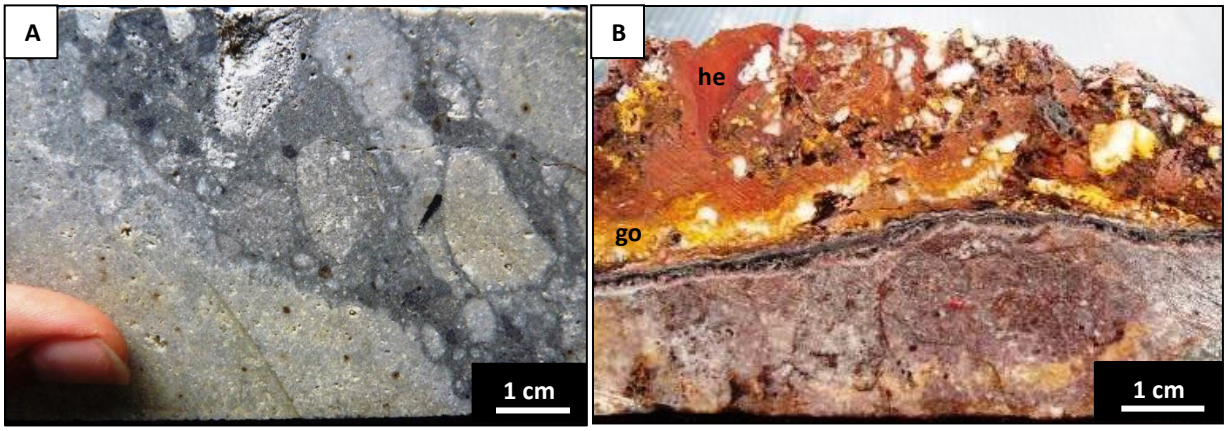

Figure 3.21. Hydrothermal breccias from Tumpangpitu. Abbreviations: go = goethite, he = hematite.

A) 9045837 mN 173574 mE; drillcore GTD-08-29; 92.7 m. Clast-supported hydrothermal breccia with monomict wallrock diorite clasts in a pyrite cement.

B) 9045502 mN 174987 mE; drillcore GTD-09-102; 47 m. Oxidized hydrothermal breccia with sub-angular fragments of quartz and diorite wallrock in a hematite - goethite - alunite cement.

well-mineralized apophyse of phase 5 tonalite porphyry. The breccias are both monomict and polymict and contain a variety of veined and mineralized clasts, which range from angular to sub-rounded in form.

Textures in this unit vary from crackle, mosaic and jigsaw breccia with angular clasts and only minor displacement of material against wall rock to strongly rotated and transported breccia clasts without preferred orientation. Hydrothermal breccias are exposed over a vertical extent of several hundred meters (Figs. 3.3 and 3.7). Common characteristics of all textural variations of hydrothermal breccia are the absence of any layering and a matrix consisting of silt- to sand-sized clastic material cemented by hydrothermal minerals. Contacts with the wall rocks vary from subvertical (Fig. 3.3) to subhorizontal (Fig. 3.7), but generally converge downward to a root zone (Figs. 3.3 and 3.7). The hydrothermal breccias are mainly clast- supported and rarely clast- to matrix- supported, with 70 to 90 volume percent clasts, 10 to 30 volume percent matrix, and local open space partially filled with coarse-grained alunite, barite or sulfides. Generally the fragments are derived from local wall rocks (e.g., Fig. 3.21A). Centimeter-to meter-sized dikes of hydrothermal breccia cut the Tumpangpitu diatreme, phase 2 diorite and sedimentary rock basement (Figs. 3.3 and 3.7). The hydrothermal breccia bodies appear to have followed zones of structural weakness and high permeability formed by the diatreme breccias. Both matrix and clasts are strongly overprinted by feldspar-destructive alteration, including vuggy and massive quartz-alunite, quartz-pyrophyllite, quartz-kaolinite-dickite and quartz-illite. The hydrothermal breccias within the advanced argillic zone are characterized by alunite ± dickite ± kaolinite cement locally containing barite, accompanied by pyrite ± enargite, ± tennantite ± tetrahedrite ± covellite ± bornite. Sphalerite-galena mineralization occurs in the cement of hydrothermal breccias in distal zones of the deposit. Several phases of hydrothermal breccias (HBX-1 and HBX-2; Table 3.1) have been identified at Tumpangpitu, spanning

the entire alteration - mineralization sequence, as intact dikes, and as clasts in the diatreme breccias, therefore both pre- and post-dating the Tumpangpitu diatreme.

3.3.8 Tumpangpitu late-mineralization diatreme

A large (3.1 x 2.2 km diameter) breccia body truncated the upper 550 m of the Tumpangpitu mineralized system (Figs. 3.3 - 3.8). The breccias shares many similarities to diatremes documented from other porphyry and epithermal deposits. The main features of diatremes from selected porphyry and epithermal deposits are summarized in Table 3.2.

The breccia body at Tumpangpitu dips concentrically inwards at approximately 25° to 45° to depths of ~ 200 m bsl (Figs. 3.3 - 3.4 and 3.7 - 3.8). It then steepens, tapering downwards to below 570 m (Fig. 3.8). The breccia body has a champagne flute morphology consistent with a soft-substrate maar-diatreme complex (e.g., Sillitoe and Bonham, 1984; Lorenz, 1986; Lorenz, 2003; Auer et al. 2007). A root of crystalline tonalitic breccia has been intersected on section 10660 mN (Fig. 3.8), penetrating down to 570 m bsl. Three additional root zones have been interpreted from geological sections constructed in the Zone B area (Fig. 3.1). The entire breccia body extends for a distance of at least 2,200 m in a northwest-southeast direction, and 3,100 m in a northeast-southwest dimension, extending to the extensive exposure along the western coastline (Fig. 3.1). The western and southern extent of the diatreme remain undefined, as the breccia continues underneath the ocean (Fig. 3.1). The clasts types identified from coastal mapping and drillcore logging at Tumpangpitu include:

- Mineralized tonalite (phase 5 and 6) porphyries with early disseminated hypogene copper sulfides including bornite, chalcocite and chalcopyrite, as well as porphyry vein fragments of quartz - magnetite ± chlorite ± K-feldspar and quartz - illite - pyrite veins (Fig. 3.22)
- High-sulfidation mineralized clasts with pyrite ± enargite ± bornite ± covellite altered to vuggy quartz, massive quartz - alunite and quartz - dickite ± kaolinite (Figs. 3.23A, C and D)
- Intermediate-sulfidation mineralized clasts with specks of tetrahedrite - tennantite ± chalcopyrite (Fig. 3.23B)
- Phase 2 - 7 porphyry fragments (Fig. 3.26)
- Sedimentary rocks including sandstone, siltstone, limestone and mudstone which increase in size and abundance in proximity to basement sedimentary wallrocks; many of the mudstone fragments are strongly pyrite-altered (Fig. 3.23B)
- Andesitic rock fragments
- Hydrothermal breccia fragments

The clasts include examples of the entire hydrothermal alteration sequence from Tumpangpitu.

TABLE 3.2. Comparison of features from documented diatreme breccia complexes, ranked by size.

Locality	Diameter (km)	Age (Ma)	Type of mineralization	Relationship of ore to diatreme	Number of breccia pipes	Main features	Interpretations	Reference
Cripple Creek, USA	4 x 3.1	27.9 - 29.3	Au telluride veins; sheeted zones and breccia pipes	Post-diatreme, on its margin	1	Upward-flaring body of heterolithic, angular to sub-angular fragments with well sorted matrix of 0.5 - 2 mm rock fragments; carbonized conifer tree trunks and local coal layers to depths reaching 244 m; breccia is massive but locally stratified; interbedded with lacustrine and fluvial sedimentary rocks; phonolite at upper levels, basaltic component at depth; 8 mm diameter accretionary lapilli		Sillitoe and Bonham (1984); Thompson et al. (1985); Thompson (1992); Jensen (2003)
Martabe, Sumatra, Indonesia	4 x 2	< 2	HSE Au-Ag-Cu	Post-diatreme	> 3	Multiphase downward-tapering sub-vertical pipes; eight breccia phases crosscut siltstone and mudstone, angular to sub-rounded 0.5 to 5 cm, locally reaching 50 cm clasts of all wallrock facies; sand-sized fragmental matrix of quartz; mud matrix breccia; varies from clast-supported to matrix-rich, polymict lithic clasts and abundant milled carbonaceous mudstone and sandstone, with dark grey fluidised matrix; internal banding defined by aligned clasts, gauge and/or foliation; accretionary lapilli (2 - 8 mm); charcoal fragments; rare vein fragments and wispy textured juvenile dacitic clasts (mm to 4 cm); sub-horizontal stratified breccia at present day surface with planar to wavy beds cm to m-scale, normally graded, well-sorted, beds of accretionary lapilli, grading upwards to volcanic sandstone beds; 10 cm - 20 m pebble dikes	Accretionary lapilli part of pyroclastic base surges, gravitational collapse breccias; dark gray fluidised matrix from comminuted carbonaceous mudstone host rock; multiphase brecciation evident by clasts of earlier breccia in later breccia	Sutopo (2013)
Tumpangpitu, Java, Indonesia	3.1 x 2.2	2.7 ± 0.5	HSE Au-Ag-Cu and porphyry Au-Cu-Mo	Porphyry mineralization is pre-diatreme and partly destroyed by it; HSE is pre-, syn- and post-diatreme	> 4	See Table 3.1		This study

TABLE 3.2. *(Cont.)*

Locality	Diameter (km)	Age (Ma)	Type of mineralization	Relationship of ore to diatreme	Number of breccia pipes	Main features	Interpretations	Reference
Colquijirca, Peru	2.7 x 2.5	12.12 ± 0.03	HSE Cu-Zn-Pb-Au-Ag	Post-diatreme, on its margin	1	HSE mineralization extends 4 km outward from the diatreme and extends to 1 km below surface		Vidal and Ligarda (2004); Bendezú and Fontboté (2009)
Sari Gunay, Iran	2.7 x 2.5	11.7 - 11.0	LSE Au	Syn- and post-diatreme	2	Steeply dipping, partial ring-shaped, fragmental; subangular - angular 1 - 20 cm polymictic clasts in a matrix of disaggregated igneous crystals; strong flow banding, bedding and peperitic texture recognized; diatreme breccia is crosscut by mineralized hydrothermal breccias with tourmaline cement		Richards et al. (2006)
Cerro de Pasco, Peru	2.6 x 2.5	15.36 ± 0.03	Pb-Zn-Ag-Cu veins and replacements	Post-diatreme, on its margin	1	Diatreme hosts the polymetallic deposit; heterolithic 1 - 100 mm angular to subrounded clasts of phyllite, sandstone, limestone, tuff and minor porphyritic igneous rocks; dacitic accretionary lapilli (0.2 - 0.5 cm) tuff showing crossbedding and ring faults	Crossbedding interpreted as base surge deposits; accretionary lapilli from subaerial tuff ring collapsed into the diatreme	Baumgartner et al. (2009)
Ortiz, New Mexico	2.1 x 1.2	> 30 Oligocene	Au breccia pipe	Post-diatreme, on its margins	1	Polymict wallrock clasts and alkalic lithic tuff that fills a steep-sided elliptical basin; pebbly facies locally containing petrified wood fragments; facies with black rock-flour matrix		Wright (1983); Maynard (1995)

TABLE 3.2. *(Cont.)*

Locality	Diameter (km)	Age (Ma)	Type of mineralization	Relationship of ore to diatreme	Number of pipes	Main features	Interpretations	Reference
Montana Tunnels, USA	2.1 x 0.6	> 50	Au-Ag disseminations and stockworks	Post-diatreme; deposit is located in the central part of the diatreme	3	Near-vertical body of 70 - 90 % matrix-rich heterolithic breccia; sand-sized tuffaceous fragments (< 2 mm) compose the matrix of quartz latitic composition containing sub-angular to well-rounded 3 - 20 cm fragments of volcanic and intrusive wallrocks, sulfide clasts, sulfide vein fragments, mineralized diatreme breccia fragments; carbonized wood 30 x 5 cm; juvenile tuffaceous matrix with sub-angular to sub-rounded crystals and crystal fragments of qtz, bt, plag and K-spar; high matrix to fragment ratio; matrix components are less rounded than lithic clasts; blocks of bedded clastic material that closely resemble the matrix of the diatreme breccia, low angle cross bedding and dune formation	Multiphase brecciation evidenced by fragments of mineralized diatreme breccia; low angle cross bedding and dune formation from subaerially deposited pyroclastic base surge deposits which formed a tuff ring that partially subsided into the diatreme; overlying maar and encircling tuff ring interpreted to have been eroded	Sillitoe et al. (1985)
La Copa, Rio Blanco, Chile	1.8 x 1.8	4.9 - 3.9	Porphyry Cu-Mo and major breccias, minor HSE	Pre-diatreme, northern segment partly destroyed by it	1	Steep walls, tapers slightly at depth; rhyolitic-rhyodacitic breccia and ignimbrite; neck consists of fragmentals and dacitic breccia with aphanitic groundmass of qtz, bt, plag and/or sanidine; flow textures and layering on southern side of neck; fragments include sedimentary rocks, mineralized breccias, andesite and quartz monzonite; dacite porphyry dikes cut through the diatreme but do not cross its perimeter; ENE- trending pebble dikes containing rock flour and sulfides	Pebble dikes interpreted as late stage venting	Sillitoe and Bonham (1984); Warnaars et al. (1985); Piquer et al. (2015)
Grasberg, Papua, Indonesia	1.6 x 1.6	3.33 - 3.19	Porphyry Au-Cu and skarn Cu-Au	Post-diatreme	1	Tapers from 1,600 m diameter at surface to 900 m at depth; most fragments below 3,500 m are dioritic and above are andesitic; banded clay in upper portion; accretionary lapilli in near-surface layered rocks; underlying highly fragmental Dalam fragmental diatreme contains xenoliths of Kucing Liar skarn mineralization	Banded clay in upper portion interpreted as surficial lake sedimentary rocks; remnants of tuff ring; formation of the skarn orebody had already progressed through the retrograde stage prior to maar volcanism	MacDonald and Arnold (1994); Pollard et al. (2005); Leys et al. (2012)

TABLE 3.2. *(Cont.)*

Locality	Diameter (km)	Age (Ma)	Type of mineralization	Relationship of ore to diatreme	Number of pipes	Features	Interpretations	References
Lihir, Papua New Guinea	1.9 x 0.7	< 0.3 - 0.7	Epithermal Au and porphyry Au-(Cu)	Porphyry and epithermal mineralization are pre-diatreme	> 7	Downward tapering, elliptical breccia bodies at Far North, Kapit, Diwai and Saddle; each a complex of breccia pipes and dikes made up of six breccia facies; root zones comprise coherent andesite which grades into jigsaw-fit breccia and upwards into matrix-rich polymictic breccia with juvenile andesitic clasts; upper portions contain charcoal clasts and megablocks with accretionary lapilli; breccias flare strongly near-surface forming a 50 m thick blanket of bedded breccias	Pipes are feeder structures of now-eroded maar-volcanic edifices; megablocks of phreatomagmatic base-surge deposits	Moyle et al. (1990); Blackwell (2010); Lawless et al. (2015)
Balatoc, Baguio, Philippines	1.6 x 0.6	Pleistocene < 5.2 Ma	LSE Au breccias and veins	During and post-diatreme formation, hosts significant breccia related Au on its margins	> 1	Multiphase breccia pipe exceeding 1 km depth, composed of an older clast-supported breccia (the "old plug"; 20 % of diatreme volume), peripheral to a central matrix-supported breccia (the "young plug"; 80 % of diatreme volume); transition from clast- to matrix- supported breccias from margins to the center; charcoal fragments at depths of 650 m below the present-day surface; youngest phase is the dacite plug; epithermal veins transect the old and young plugs but don't crosscut the dacite plug	Breccias occurring around the diatreme perimeter interpreted as collapse breccias; no relict maar or tuff ring (result of significant erosion; > 100 m)	Cooke et al. (1996)
Wau, Papua New Guinea	1.4 x 1.4	< 4 - > 2.4	LSE Au veins and stockworks	Post-maar-diatreme, on its contact and as exotic blocks within it	> 1	Diatreme extends downward for 1 km; angular and rounded fragments of metamorphic rocks and dacite porphyry set in a matrix of finely comminuted rock material; dacitic clasts include pumiceous material and flow-foliated dome material; fragments are mainly < 10 cm but locally > 30 cm; disseminated pyrite is ubiquitous in the rock flour matrix; upper level breccia is coarse, poorly stratified and poorly sorted facies contains interbeds of a fine, silty and well-stratified facies with accretionary lapilli		Sillitoe et al. (1984)
Selodong, Lombok, Indonesia	1.3 x 1	Late Miocene	Epithermal Au-Ag-Cu and porphyry Au-Cu	Porphyry mineralization is pre-diatreme; epithermal Au is post-diatreme	> 1	Angular to sub-rounded clasts of Cu-Au mineralized and altered (biotite - actinolite) porphyry tonalite, quartz diorite, diorite and andesitic-dacitic volcanic rock; matrix is altered to illite ± chlorite ± epidote	Diatreme has destroyed the root of the Selodong porphyry tonalite complex	Rompo et al. (2012)

TABLE 3.2. *(Cont.)*

Locality	Diameter (km)	Age (Ma)	Type of mineralization	Relationship of ore to diatreme	Number of pipes	Main features	Interpretations	References
Braden pipe, El Teniente, Chile	1.2 x 1.2	4.6 - 4.7	Porphyry Cu-Mo deposit	Late- to post-mineralization	1	Inverted cone shape, exceeding 1.6 km depth, 60 - 80˚ inward dipping walls in the center of El Teniente porphyry deposit; lower contact at least 1,400 m below surface; two principal breccia facies; 1 - 60 m thick monomictic, clast-supported (angular wall rock clasts) mineralized marginal breccia with tourmaline-rich cement and barren Braden breccia - poorly sorted, polymictic, rock flour-matrix and both stratified and un-stratified facies; contains abundant sub-rounded to sub-angular sericite-altered wallrock fragments with truncated veins; pebble dikes > 2 m wide occur as incomplete ring dikes around the Braden pipe		Howell and Molloy (1960); Cannell et al. (2005); Klemm et al. (2007)
Santong diatreme (Batu Hijau), Indonesia	1.2 x 0.9	Pliocene	Epithermal Au-Ag-Cu and porphyry Au-Cu	Porphyry mineralization pre-diatreme, epithermal pre-, syn- and post-diatreme	>1	Circular body, cone-shaped, tapers steeply with depth, late stage porphyritic andesite and dacitic dikes cm to several m wide cross cut the breccia (no direct crosscutting relationships with mineralized tonalites); upper poorly-moderately sorted bedded facies with carbonized logs, leaf fragments, sub-rounded to sub-angular polymict, both altered (illite - chlorite - clay ± magnetite), quartz - alunite altered clasts and unaltered fragments of equigranular quartz diorite, andesitic volcanic rock, tonalite, dacite; minor mineralized clasts of quartz diorite containing quartz veinlets with cpy and cc in clay-rich coarse ash to sand-sized matrix lacking organic material; lower massive facies with polymictic and milled angular to sub-rounded rock fragments of lithic-, crystal- and accretionary lapilli-bearing andesitic volcanic sandstone, breccia, quartz diorite, tonalite, comb quartz vein fragments; clast size increases to 50 - 200 cm locally; clasts size decreases northwards with increase in the abundance of fining-upwards, graded sequences of accretionary lapilli-bearing volcanic sandstone; milled and rounded ball-bearing-like clasts 2 - 6 mm common towards the south	Multiphase brecciation interpreted from clasts of breccia in the diatreme	Clode et al. (1999); Maryono and Priowasono (2000)

TABLE 3.2. *(Cont.)*

Locality	Diameter (km)	Age (Ma)	Type of mineralization	Relationship of ore to diatreme	Number of pipes	Main features	Interpretations	References
Caspiche, Chile	1.1 x 1.1 (?)	24.7 ± 0.7	Porphyry Au-Cu and HSE	Porphyry mineralization pre- and syn-diatreme (minor destruction of porphyry); HSE pre (vuggy quartz clasts), syn and post (300 m vuggy quartz ledge crosscuts diatreme); ISE post diatreme	2	Large breccia body dips 30˚ - 40˚ and steepens downwards; highly polymict, matrix supported, contains abundant mineralized clasts (quartz stockwork veins and vuggy quartz fragments) in proximity to contact with Caspiche porphyry, truncates western side of deposit; late, shallowly inclined zone of Au-Zn mineralization abuts the diatreme contact; away from contact zone tuffaceous material comprises matrix to andesite clasts with 50 m blocks of wallrock; local intervals of normally graded, silt- to pebble sized material; deeper parts of vent have a juvenile tuffaceous matrix	Caspiche deposit emplaced within the southern flat-bottomed part of the pre- mineralization diatreme vent; early porphyry development aborted by diatreme formation; Au-peripheral Au-Zn mineralization localized by the enhanced permeability provided by intense fracturing along the underside of the upward-flared diatreme contact; bedded facies interpreted as surge deposits and sunken blocks;	Sillitoe et al. (2013)
Tanjung Jahe, Java, Indonesia	1.15 x 0.5	8.52 ± 0.21	HSE Au-Ag-Cu and porphyry Au-Cu-Mo	Post-diatreme	1	See Table 3.1	See Table 3.1	This study
Rinti, Sumbawa, Indonesia	1 x 1	< 2.5	Epithermal Au-Ag-Cu and porphyry Au-Cu	Porphyry mineralization pre-diatreme, epithermal pre-, syn- and post-diatreme	>1	Apron facies of accretionary lapilli, imbricated structures (alignment of boulders), poorly bedded; vent facies: matrix supported in the middle, clast supported at margins, mineralized porphyry clasts (with stockwork veining and cpy)	Imbricated structures (alignment of boulders) influenced by fluvial processes	Garwin (2000); Maryono and Setyandhaka (2011)
Agua Rica, Argentina	1 x 0.7	Late Miocene	Porphyry Cu-Mo-Au and HSE Cu-Au-Ag-As-Pb-Zn	Pre-diatreme, partly destroyed by it	1	Matrix-supported, 40 - 70 % vol highly polymict clasts; continuous downward transition from bedded breccias to clast-supported breccias with sandy or pumiceous matrix to a solid igneous breccia with a fine-grained porphyritic matrix in the lower core of the conical crater infill breccia body; vertical to sub-vertical 5 - 50 % vol polymict, rounded clasts, matrix-supported sand and pebble dikes, matrix comprises silt and sand-sized clastic grains; dimensions mm - m in width extending several hundreds of metres	Bedded graded, matrix-rich epiclastic sediments subsequently filled the crater formed by surface-venting phreatomagmatic eruption	Landtwing et al. (2002)

TABLE 3.2. *(Cont.)*

Locality	Diameter (km)	Age (Ma)	Type of mineralization	Relationship of ore to diatreme	Number of pipes	Features	Interpretations	References
Yanacocha, Peru	1 x 0.7	Early: 12.4 - 11.9; late: 9.9 - 8.4	HSE Au-Ag-Cu and Au-Cu porphyry	HSE pre-, syn- and post-diatremes, porphyry pre-diatreme	> 5	Multiple, downward tapering low volume breccia pipes with steep morphologies; breccias have a clay-matrix supporting rounded to subangular heterolithic clasts including qtz and clay altered fragments; rare deformed fragments of Yanacocha porphyries; gold ore forms along the margins of the diatreme; chaotic, poorly sorted matrix- and clast-supported breccias; fine-grained granular quartz comprises breccia matrix; multiple steeply and gently dipping pebble dikes and sills with core of coarse well-sorted rounded pebbles (2-6 mm diameter) of massive quartz that grade out to sand-sized (< 1 mm) particles with planar and cross bedded features	Plastic deformation of juvenile clasts of Yanacocha porphyries in diatreme breccias suggest contemporaneous intrusion and brecciation	Turner (1997); Teal and Benevides (2010); Longo et al. (2010)
Boyongan, Philippines	0.9 x 0.9	> 2	Porphyry Cu-Au	Post-diatreme	1	Upwardly flaring polyphase breccia pipe, cylindrical shape, vertical extent at least 1000 m; fine-grained (< 0.5 mm) matrix of silt-sand sized comminuted rock fragments; matrix and clast-supported facies, lacks stratification or internal organization; breccia matrix comprises fine (< 0.5 mm) sand and silt-sized fragments; no vein quartz clasts identified		Braxton (2007); Braxton et al. (2009)
Roșia Montană, Romania	0.9 x 0.4	13.6 - 12.8	ISE epithermal Au-Ag breccia hosted	Post-diatreme; mineralization in open fractures and breccia infills	1	Pipe-like breccia body with downward tapering cone shape (> 550 m below surface); three main diatreme facies: 1) dacite breccia - coarse, monomict, clast supported (70 - 90 %), clasts (cms to 0.5 m) are angular to sub-rounded in a matrix of hydrothermally precipitated quartz, carbonates and sulfides; 2) Grey polymict breccia; matrix supported, matrix 10 - 80 % of sand-sized rock and mineral fragments, rock flour, polymict angular to well- rounded clasts (< 10 cm) of wallrock, crystalline basement rocks and re-brecciated black polymict breccia; carbonized wood fragments; 3) Black polymict breccia comprises angular to moderately rounded wallrock clasts, smaller and less abundant than the grey facies; matrix is black and comprises 60 - 80 % of breccia ; breccia and pebble dikes - matrix supported 30 - 50 cm steep dikes crosscutting black polymict breccia; only 10 - 20 % of well-rounded polymict clasts exceed 0.5 cm	Black facies incorporated pulverised black Cretaceous shale and carbonised organic material; fluidized bed-transport, mixing and milling most intense in central black polymict breccia; diatreme formed by explosive eruption and deposition of parts of volcaniclastic breccia in an open basin structure which at the paleosurface may have developed to a maar environment	Wallier et al. (2006)

TABLE 3.2. *(Cont.)*

Locality	Diameter (km)	Age (Ma)	Type of mineralization	Relationship of ore to diatreme	Number of pipes	Features	Interpretations	References
Tepu, Runcing and Burung, Kelian, Kalimantan, Indonesia	0.75 x 0.75 0.75 x 0.25	Early Miocene	LSE Au-Ag	Epithermal mineralization is post-diatreme	3	Polymict including sandstone clasts in carbonaceous matrix; root zone of juvenile rhyolitic clasts.	Megablocks of base surge deposits dropped down several hundred metres from maar environment into underlying diatreme	Davies et al. (2008a, 2008b)
Wafi-Golpu, Papua New Guinea	0.8 x 0.6	< 2.9	Porphyry Cu-Au, HSE and carbonate base metal Au	Porphyry pre-diatreme, HSE and carbonate base metal post-diatreme	1	Cone - shaped diatreme which tapers at depth to the west of the Golpu porphyry complex, not disrupting the porphyry deposit; rounded (milled) and angular clasts in feldspar and pyrite-rich clastic matrix; dominantly matrix supported; accretionary lapilli in layered bands at surface; bounded by pebble dikes	Intrusion of diatreme due to meteoric incursion on a magmatic source causing phreatomagmatism; inferred to have vented the paleosurface (presence of accretionary lapilli)	Sillitoe (1999); Menzies et al. (2013); Bawasu and Espi (2015)
Elang, Sumbawa, Indonesia	0.7 x 0.5	Late Pliocene	Epithermal Au-Ag-Cu and porphyry Au-Cu	Porphyry and HSE are pre-diatreme; LSE syn- to post-diatreme	3	Three breccia bodies to the east and northeast of Elang; breccias comprise 2 - 20 % rounded to angular 2 - 30 mm fragments of fine-grained andesite, diorite and qtz-py altered clasts in a fine-grained rock flour matrix; accretionary lapilli near to present day surface, narrow LSE qtz and base metal veins within and along the margins of the diatreme		Maryono et al. (2005)
Oyu Tolgoi	0.6 x 0.5	Late Devonian (?)	Porphyry Cu-Au and HSE	Pre-, syn- and post-diatreme (?)	2	Two downward tapering cone shaped breccia pipes at Central and North Oyu; clast- and matrix-supported phases containing sub-angular to sub-rounded pebble-sized clasts; breccia contains 25 - 30 % quartz A type veinlet fragments, lithic clasts of feldspar porphyry and andesitic rocks; vein densities in fragments locally exceed 100/m^2; matrix is clastic, sand- to silt- sized with local tuffaceous material; pebble and breccia dikes cm to decimetre dimensions; matrix supported with rounded to sub-angular, locally spheroidal heterogeneous lithic clasts in the pebble to cobble range and clastic matrices with thinly laminated beds and flow banding structures	Multiphase breccia dikes present-some dikes contain pebbles of earlier formed breccias and massive sulfides; breccias host hypogene and supergene mineralization	Perelló et al. (2001)

TABLE 3.2. *(Cont.)*

Locality	Diameter (km)	Age (Ma)	Type of mineralization	Relationship of ore to diatreme	Number of pipes	Features	Interpretations	References
Toquepala, Peru	0.4 x 0.4	< 57	Porphyry Cu-Mo	Pre-diatreme	1	300 m diameter pipe dominated by angular-subangular clasts is surrounded by a swarm of radial and concentric dipping pebble breccia pipe with and swarm of pebble dikes	Breccia removed a substantial part of the orebody; two outcrops of "slump breccia" at surface	Clark (1990)
Brambang, Lombok, Indonesia	0.3 x 0.2	Late Miocene (?)	Epithermal Au-Ag-Cu and porphyry Au-Cu	Porphyry and HSE are pre- diatreme; LSE syn- to post-diatreme	> 1	2 - 20 % rounded to angular rock fragments set in an illite ± chlorite ± smectite altered dacitic rock flour matrix; fragment size ranges from 2 - 40 mm comprising andesitic volcanic rocks, diorite, quartz diorite, tonalite, mineralized porphyry and vuggy quartz fragments; 2 m wide tuffisite pebble dikes observed in drillcore, narrow Au-bearing LSE quartz veins have developed within and along the margins of the diatreme		Maryono et al. (2013)
Lepanto-Far Southeast, Philippines	?	1.43 ± 0.21	HSE and porphyry Cu-Au	Pre- to syn-diatreme	2	Two large vents centred on quartz diorite porphyry dikes above the FSE porphyry that intruded 300 - 400 m below the vents; the two vents coalesce at elevations between 900 and 1000 m; the vents are; the two breccia bodies crop out at surface; one vent is 1 km NW of the surface projection of the FSE deposit at 1,300 m elevation; breccia contains lithic fragments with bt and mag alteration and bn-cpy mineralization; dacite porphyry and alunite altered rock centrally truncates the deposit; depth extent over 100 m	Barren post-mineralization diatreme vents derived mineralized and altered porphyry clasts from the underlying FSE deposit	Garcia (1991); Hedenquist et al. (1998); Chang et al. (2011)
Resolution, USA	?	66 - 67	Porphyry Cu-Mo	Post-diatreme	?	Dacitic-rhyodacitic tuffaceous breccias with polymictic clasts of schist, quartzite, porphyry, diabase in a tuffaceous matrix composed of broken quartz and feldspar crystals; upper sections are matrix supported, lower sections are more clast-supported units of identical composition with local fine-grained tuffaceous interbeds; breccias locally contain clasts of truncated quartz - molybdenite veins		Hehnke et al. (2012)

Abbreviations: Au = gold, ba = barite, bn = bornite, bt = biotite, cc = chalcocite, chl = chlorite, cp = chalcopyrite, Cu = copper, dsp = diaspore, en = enargite, hbl = hornblende, he = hematite, HSE = high-sulfidation epithermal, ill = illite, ISE = intermediate-sulfidation epithermal, ka = kaolinite, Kfs = K-feldspar, mag = magnetite, mo = molybdenum, plag = plagioclase, qtz = quartz, py = pyrite.

Altered clasts include; chlorite - calcite, illite - chlorite - montmorillonite ± kaolinite, quartz - dickite ± kaolinite, quartz - alunite ± pyrophyllite, massive and vuggy quartz ± alunite assemblages (e.g., Figs. 3.23 - 3.23 and 3.25 - 3.27). Many of the mudstone fragments are strongly pyrite-altered. Andesitic rock fragments, hydrothermal breccia fragments and charcoal fragments are also present.

The breccia body has been split into four distinct facies recognized during surface mapping and drillcore logging; 1) Lower facies - massive breccia; including crystalline tonalitic breccias with mineralized porphyry clasts; 2) Upper facies - an inwardly dipping bedded breccia including polymict matrix-rich breccias; 3) Upper facies - mud matrix breccias; 4) Distal facies - tuffisite sand and pebble dikes and; 5) Apron facies - outward dipping sedimentary rocks in polymictic matrix-rich breccias. Facies 1 is proximal to several vents or feeder breccia pipes such as on section 10660 mN (Fig. 3.8). Facies 2 and 3 occur above the vents, whereas facies 4 and 5 are located distal to the central vents (Fig. 3.1).

3.3.8.1 Tumpangpitu lower facies diatreme breccias

The lower facies breccia occupies the throat and main central body of the diatreme breccia complex (Figs. 3.1 - 3.8). It is polymict, ranging from clast to matrix - supported containing 20 to 70 volume percent sub-angular to sub-rounded clasts generally several millimetres to 2 cm in size. Abundant mineralized clasts of both tonalitic porphyry and high-sulfidation style mineralization occur from present day surface to the lower contact with the Tumpangpitu tonalite complex (around 550 - 900 m; Figs. 3.3 - 3.8). The breccia locally contains large blocks, up to 40 x 40 m, of intrusive phases 2, 5 and 7 (Fig. 3.3). Near the root zone of the vents, the breccias are clast-supported. Polymictic fragments are set in a crystalline tonalitic quartz - feldspar cement, with the abundance of tuffaceous matrix (andesitic composition; Coote, 2011) increasing towards the present-day surface. The tonalitic porphyritic igneous cement consists of fine- to medium-grained phenocrysts of (< 2 mm) illite, kaolinite or pyrophyllite (after magmatic plagioclase) and > 15 % quartz as both phenocrysts and groundmass in a fine-grained pale grey quartz-rich groundmass. The breccias with strongly porphyritic igneous crystalline cement share similarities with breccias described by Landtwing et al. (2002) from the Agua Rica porphyry and high-sulfidation epithermal deposit, Argentina, minus subsequent porphyry stockwork-style quartz veins cutting the breccia cement.

The lower facies breccia is altered to quartz - illite ± pyrophyllite in the root zones. It has been weakly altered to chlorite - illite - smectite ± epidote ± calcite, distal to the root zones where not overprinted by high-sulfidation epithermal mineralization. Drilling here revealed thick intersections (> 600 m), devoid of copper or gold mineralization, particularly towards the southern flank of Tumpangpitu (e.g., Fig. 3.8). The upward flaring flanks of the lower facies diatreme breccia transition gradationally into upper facies bedded diatreme breccia. The breccias appear as shallow, apparently rootless breccia bodies on most of the geological sections (e.g., Figs. 3.3 - 3.5 and 3.7).

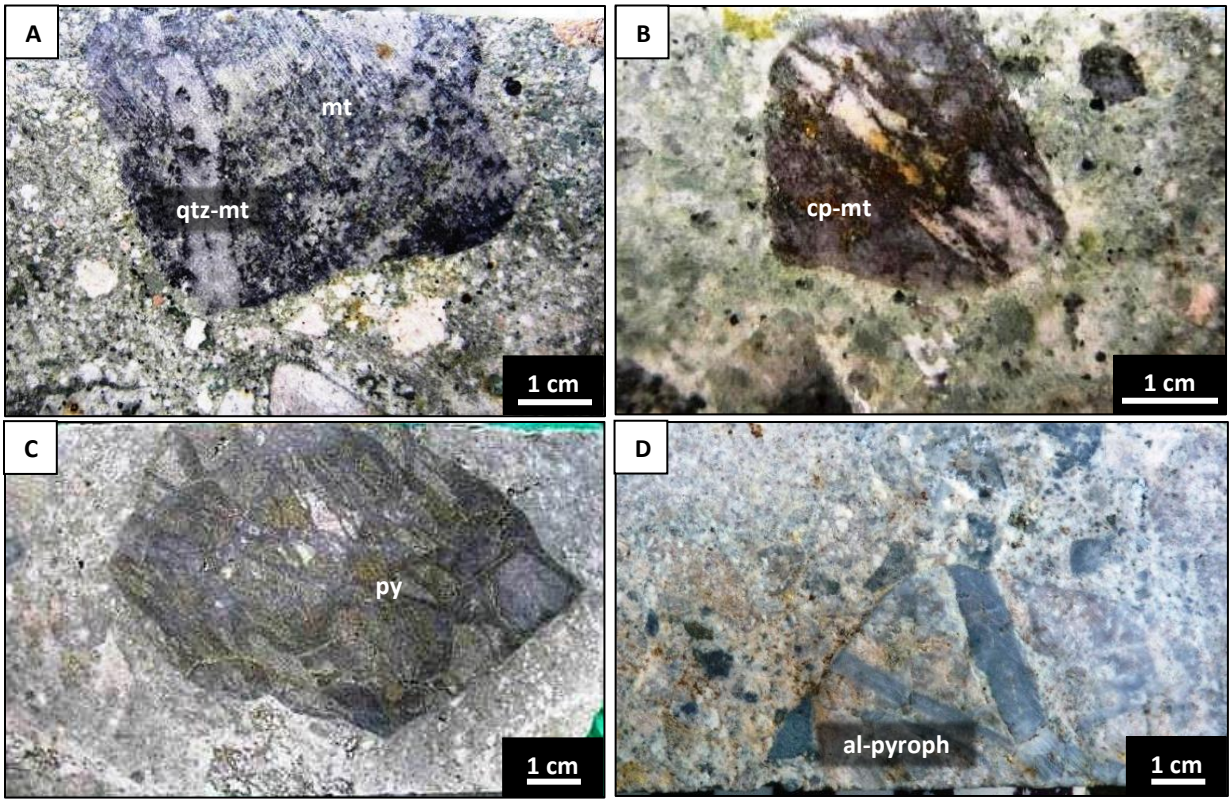

Figure 3.22. Mineralized porphyry clasts in upper and lower facies diatreme breccia from drillcore at Tumpangpitu. Abbreviations: al = alunite, cp = chalcopyrite, mt = magnetite, py = pyrite, pyroph = pyrophyllite.

A) *9045502 mN 174733 mE; drillhole GTD-09-65; 116.75 m, Zone B.* Clast of quartz - magnetite B - type vein stockwork in quartz -magnetite - chlorite altered fine-grained phase 5 tonalite in milled breccia.
B) *9045502 mN 174733 mE; drillhole GTD-09-65; 95.40 m, Zone B.* Porphyry clast containing a network of quartz - chalcopyrite -magnetite veinlets overprinting milky high-temperature and early-stage feldspar veins in milled breccia.
C) *9046152 mN 173815 mE; drillhole GTD-08-22; 120 m, Zone C.* Clast of intense porphyry vein stockwork in a quartz -dickite altered milled breccia.
D) *9046141 mN 173877 mE; drillhole GTD-09-112; 250.6 m.* Clast of B-type porphyry stockwork, both matrix and clasts overprinted by strong quartz - alunite - pyrophyllite alteration in a quartz-rich crystalline cement.

3.3.8.2 Tumpangpitu upper facies - bedded polymictic lithic milled breccias

Bedded breccias dominate the host rocks of the Zone A oxide deposit and the southern flank of Tumpangpitu (Figs. 3.1, 3.3 - 3.8). They form a concentric fringe that is 3.1 km x 2.2 km in diameter. They have an upward-flaring champagne glass morphology around the roots of the lower facies diatreme body, such as the root identified on section 11060 mN (Fig. 3.8) in the central and southern parts of Tumpangpitu (Fig. 3.1). The contacts with wall rocks are steep (75˚- 85˚) at depths below 550 m (Fig. 3.8) but shallower (25˚- 45˚) near the present-day surface (Figs. 3.3- 3.8). Contacts are generally sharp and exhibit laminar textures along the contact in the breccia (e.g., Fig. 3.27D). Orientation measurements from drillcore above the Tumpangpitu porphyry show a gentle dip of 10 - 20˚ toward the center of the circular body and its

interpreted root zones. Orientation measurements from coastal exposures (1.3 - 1.8 km southwest of the root zones) show that units dip gently 15 - 30° westwards away from the central root zone (Fig. 3.1).

The milled breccias at Tumpangpitu have textures characteristic of upper level facies of diatreme breccias (e.g., Sillitoe, 1985; Lorenz, 1986; Landtwing et al., 2002; Sutopo, 2003; Davies et al., 2008a; Lawless et al., 2015). The stratified milled breccias are exposed in outcrop and drill core over a depth interval of at least 550 m (Figs. 3.1 - 3.8). The clast types are highly variable in terms of lithology and alteration types. The breccia components are invariably polymictic. Apart from the abundant porphyry quartz-veined clasts, there are also fragments of vuggy quartz with alunite and rare enargite (Fig. 3.23 C and D) and clasts containing massive covellite - bornite - pyrite mineralization (Fig. 3.23A). High-sulfidation state hydrothermal breccias crosscut this breccia unit (e.g., Figs. 3.3 and 3.8). There are irregular clasts of polymict lithic breccia surrounded by a matrix of finer-grained polymict lithic breccia locally (Fig. 3.26C). Clasts range from sub-angular to well-rounded. Clast sizes within the large milled breccia bodies tend to have a broad size distribution, ranging from large clasts of 10 - 50 cm adjacent to wallrock contacts (e.g., Fig. 3.27A and C), with rare outsized > 10 m blocks, through to intermediate clasts of 1 - 5 cm (3.25A and B), to fine comminuted sandy fragments, 1 - 2 mm in size in a highly milled sand sized matrix (Fig. 3.26). Outsized larger angular to sub-rounded clasts, (> 1 m diameter) occur locally in poorly sorted, poorly stratified zones. These highly comminuted, matrix-supported, polymict breccias commonly have a ratio of 20 % clasts to 80 % matrix (e.g., Figs. 3.25 and 3.26). The matrix of the breccia is composed of clay and mica minerals (montmorillonite/nontronite, illite and chlorite) and subangular to well-rounded clastic sand and silt grains, some of andesitic composition and others with the same compositions as the clasts. The matrix locally contains well-rounded millimetre-sized grains of pyrite. Fine-grained (1 - 2 mm) fragments define 1 - 2 cm thick bands (Fig. 3.26B and D). These bands have been observed within clasts surrounded by a matrix with similar banding. The bedded matrix overlies coarser-grained clast-supported polymict breccias (e.g., Fig. 3.26C). Beds contain intervals of silt- to pebble- sized material, imbricated clasts with both normal and local reverse grading in a single bed (Fig. 3.26B), similar to features described at Kelian by Davies et al. (2008a).

The milled breccia matrix is altered to illite - clay - chlorite ± calcite where not overprinted by HSE mineralization. Clasts exhibit a diversity of alteration types, from chlorite - calcite, illite - chlorite (Fig. 3.26C) and quartz - alunite - dickite (Figs. 3.25A, 3.26) to vuggy quartz - alunite (Fig. 3.23C). Small, 1 - 5 mm diameter fragments, of mineralized porphyry tonalite and stockwork quartz vein fragments are very common adjacent to the contact with the mineralized porphyry carapace. These fragments contain magnetite ± chlorite ± K-feldspar and pyrite, chalcopyrite, bornite, molybdenite and covellite (Figs. 3.25A and B, Fig. 3.26). Close to the present-day surface, predominantly intact, accretionary lapilli (1 mm to 1 cm diameter) occur in sub-horizontal planar bands, such as seen at 14 m in drillhole GTD-10-172 (Fig.

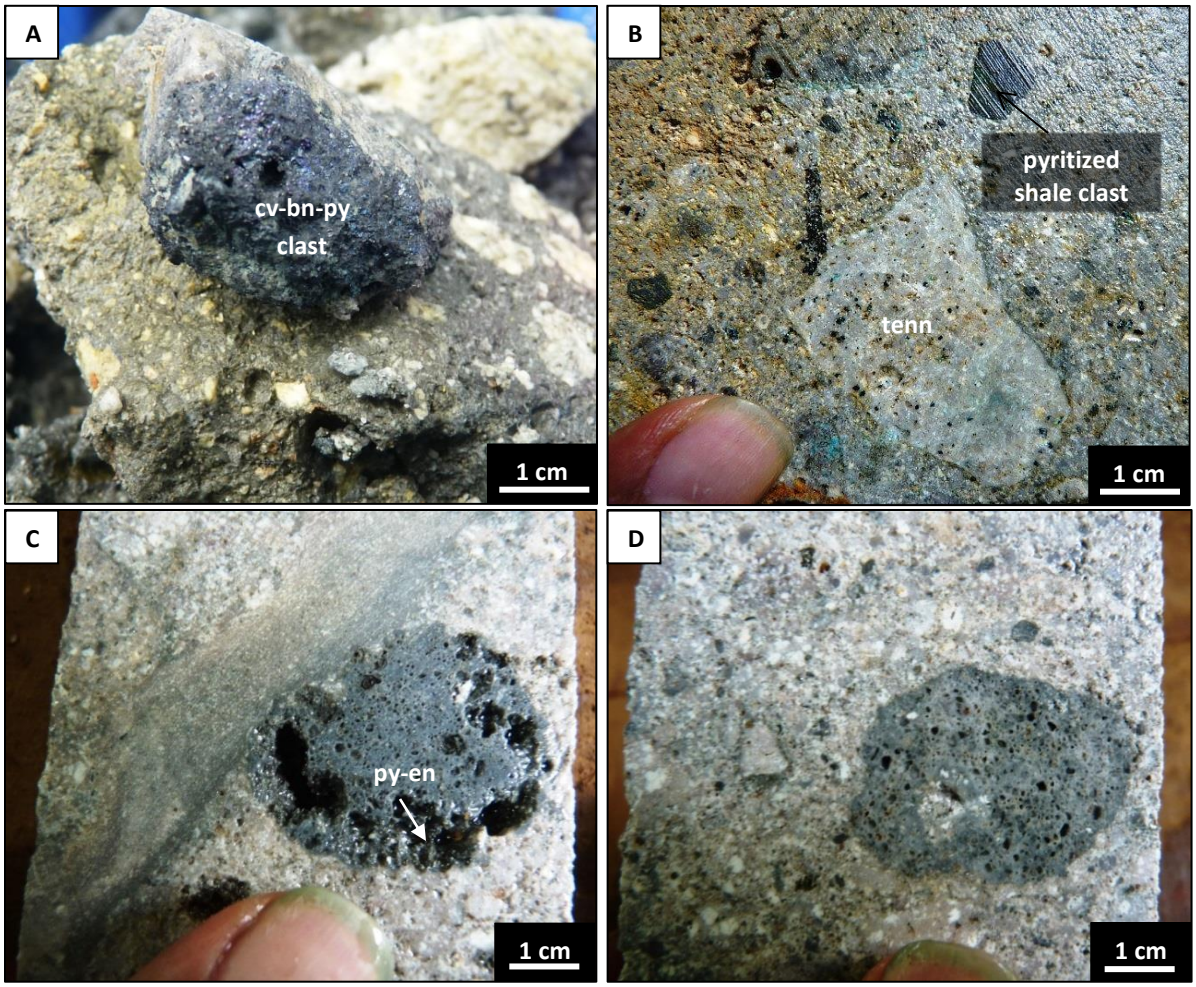

Figure 3.23. Mineralized high-sulfidation epithermal clasts in upper and lower facies diatreme breccias at Tumpangpitu. Abbreviations: bn = bornite, cv = covellite, en = enargite, py = pyrite.

A) *9046440 mN 174240 mE; drillhole GTD-10-172; 9.4m.* Massive covellite - bornite - pyrite clast in polymict chlorite - illite - calcite altered tuffaceous milled breccia matrix.
B) *9046141 mN 173878 mE; drillhole GTD-08-56; 95.10m*. Tenanntite specks in quartz diorite clast in silicified alunite altered matrix. Top of photo: clast of pyritized shale, characteristic of polymict nature of milled breccias.
C) *9046141 mN 173878 mE; drillhole GTD-08-56; 107m*. Rounded clast of vuggy quartz and alunite with pyrite - enargite adjacent to flow - matrix banding in milled polymictic breccia.
D) *9046141 mN 173878 mE; drillhole GTD-08-56; 119m*. Rounded clast of vuggy quartz with enargite in crystalline quartz-ex-feldspar matrix of lower facies diatreme breccia.

3.25C and 3.26C). Fragments of charcoal (1 cm to 20 cm) have been identified in the milled breccias, particularly beneath what is interpreted to be a maar in Zone B to depths of 140 m below present day surface (Fig. 3.25D). Upper facies bedded breccia is characterized by intervals of normally graded silt- to pebble-sized material (Fig. 3.24A - D), imbricated clasts, stratification with normal graded bedding (Fig. 3.26B and D). In the central to southern part of the breccia body, the breccia grades downward to an increasingly clast-supported breccia and finally into igneous cemented breccia.

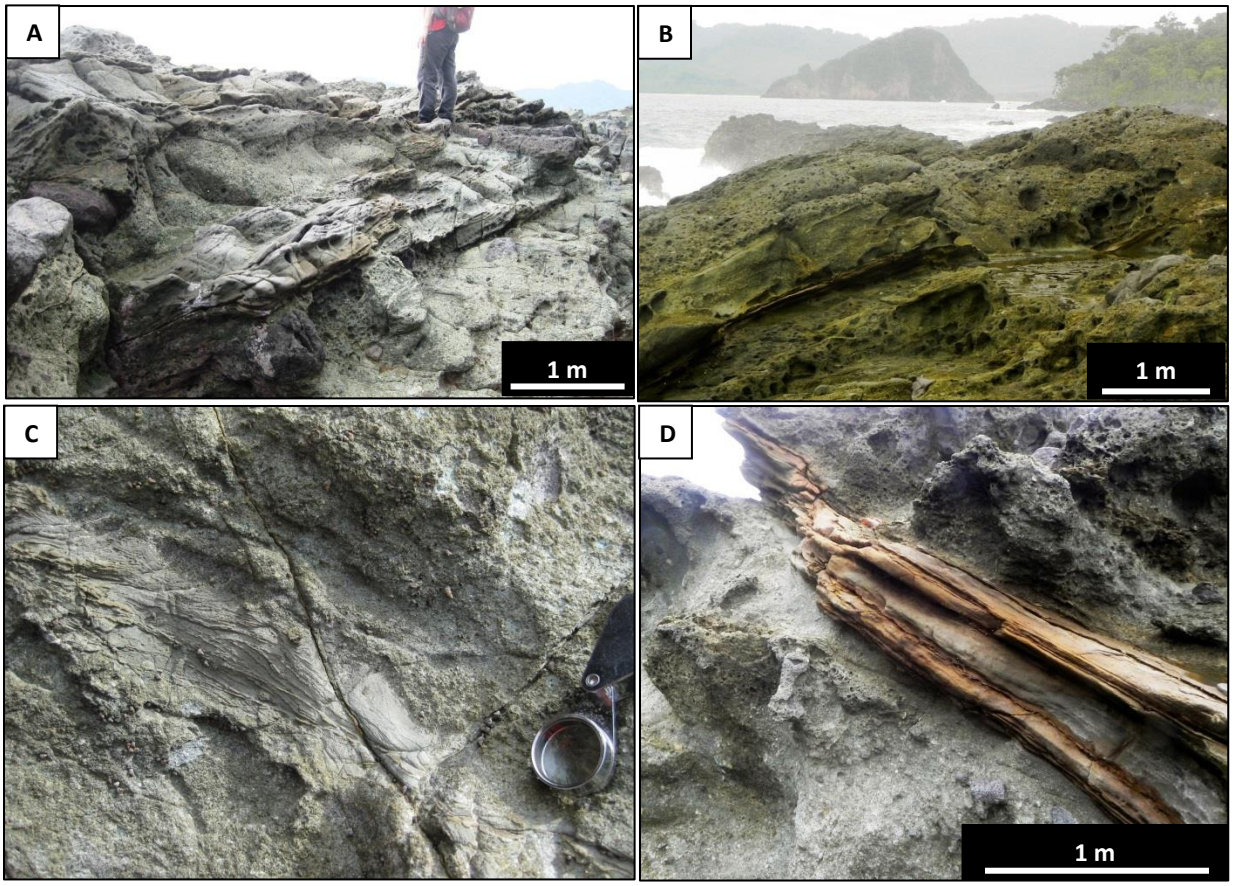

Figure 3.24. Coastal exposures of upper facies bedded apron breccias.

A) *9044840 mN, 173265 mE, elevation 3 m asl*. Mill breccia interbedded with mudstone, sandstone and siltstone altered to chlorite - illite; bed orientation 020/25W.
B) *9044927 mN, 173254 mE, elevation 3 m asl.* Bedded breccias interbedded with sandstone and siltstone and altered to chlorite - epidote; bed orientation 020/25W, orientated with respect to Pulau Merah island in the background.
C) *9044858 mN, 173279 mE, elevation 3 m asl.* Fine-grained mudstone interbed with weak crossbedding in chlorite - illite altered milled breccia.
D) *9044927 mN, 173254 mE, elevation 3 m asl.* Pale orange sandstone interbed in milled breccia, dipping 30° westwards.

3.3.8.3 Tumpangpitu diatreme upper facies - mud-matrix breccias

Mud-matrix-supported breccias are a distinctive breccia facies that occur preferentially within and beneath the Zone B gold oxide area, 1,500 m south of Tumpangpitu (Fig. 3.1). They form an irregular crescent shaped body with north-south dimensions of 450 m and east-west dimensions of 1000 m, tapering with increasing depth. The mud-matrix breccias are located above the upper facies bedded polymict lithic milled breccias, adjacent to three interpreted diatreme root zones (Fig. 3.1). In plan view they form a shell to the southern margin of the lower facies polyphase polymictic massive breccia pipes, and are in turn surrounded by upper facies bedded milled breccias (Fig. 3.1). The mud- matrix breccias are characterized by abundant mudstone matrix, and show soft sediment deformation features (Figs. 3.28A-B).

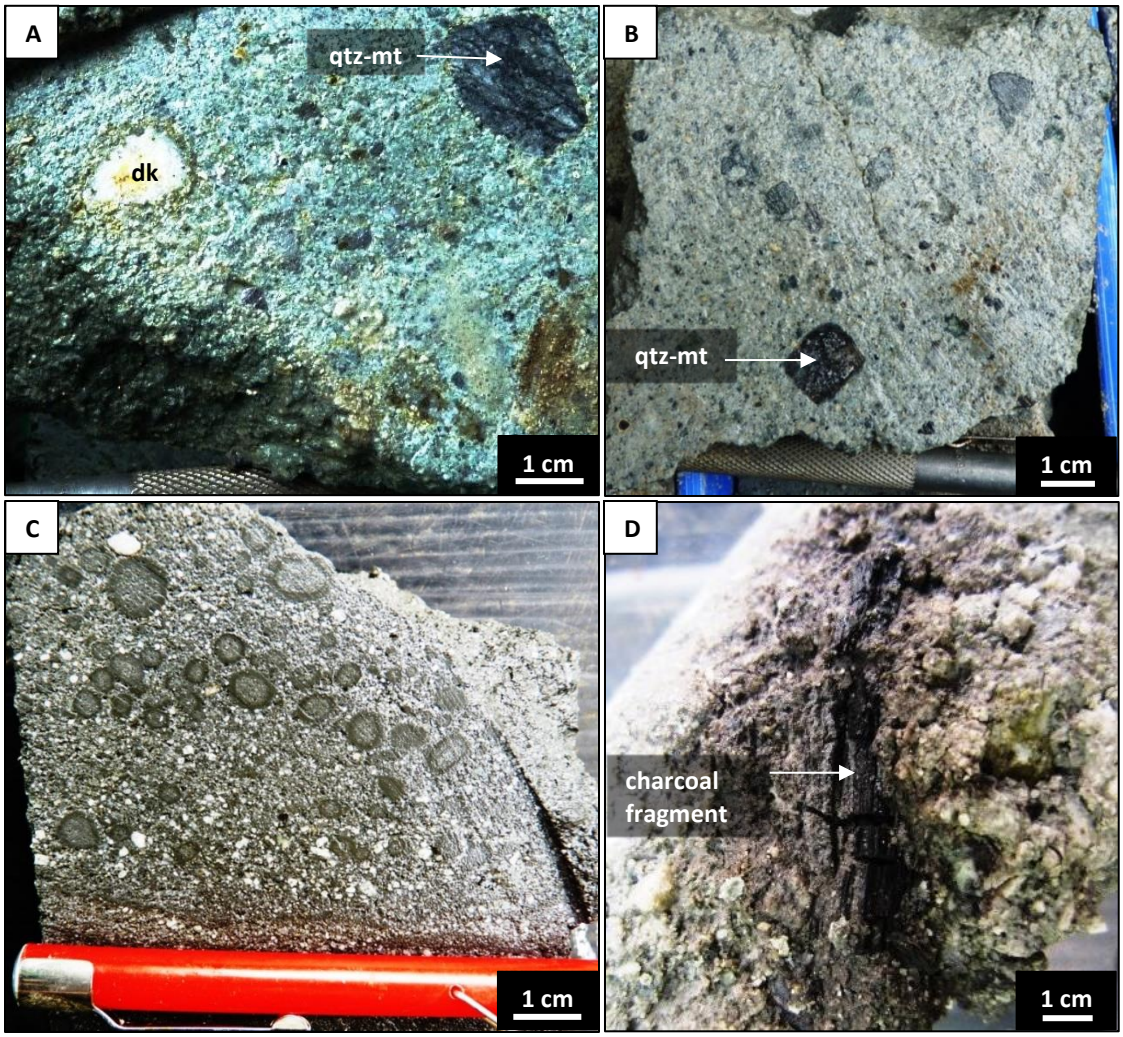

Figure 3.25. Characteristic features of upper facies milled breccias from drillcore at Tumpangpitu. Abbreviations: mt = magnetite, qtz = quartz.

A) *9046193 mN, 174539 mE; drillhole GTD-10-151; 134.2m.* Quartz - magnetite porphyry stockwork vein clast in chlorite - illite- montmorillonite altered milled breccia. Quartz - dickite altered clast (upper left) shows polymodal nature of clast types in the milled breccia.

B) *9046193 mN, 174539 mE; drillhole GTD-10-151; 58m.* Abundant 1 mm - 1 cm quartz - magnetite - K-feldspar altered fragments in chlorite - illite - montmorillonite altered andesitic milled breccia matrix.

C) *9046440 mN 174240 mE; drillhole GTD-10-172; 14m.* Bands of accretionary lapilli in polymictic matrix-supported milled breccia.

D) *9045508 mN, 174492 mE; drillhole GTD-09-88; 120m.* Carbonized wood fragments in chlorite - illite altered polymictic milled breccia.

These breccias contain both angular (e.g., Fig. 3.28A) and sub-angular ragged wallrock clasts (e.g., Fig. 3.28B). They also contain mineralized porphyry clasts, as well as rarer accretionary lapilli and charcoal fragments. The breccia body has been crosscut by Zone B north-trending fault system hosting high-sulfidation epithermal mineralized hydrothermal breccias (Fig. 3.1).

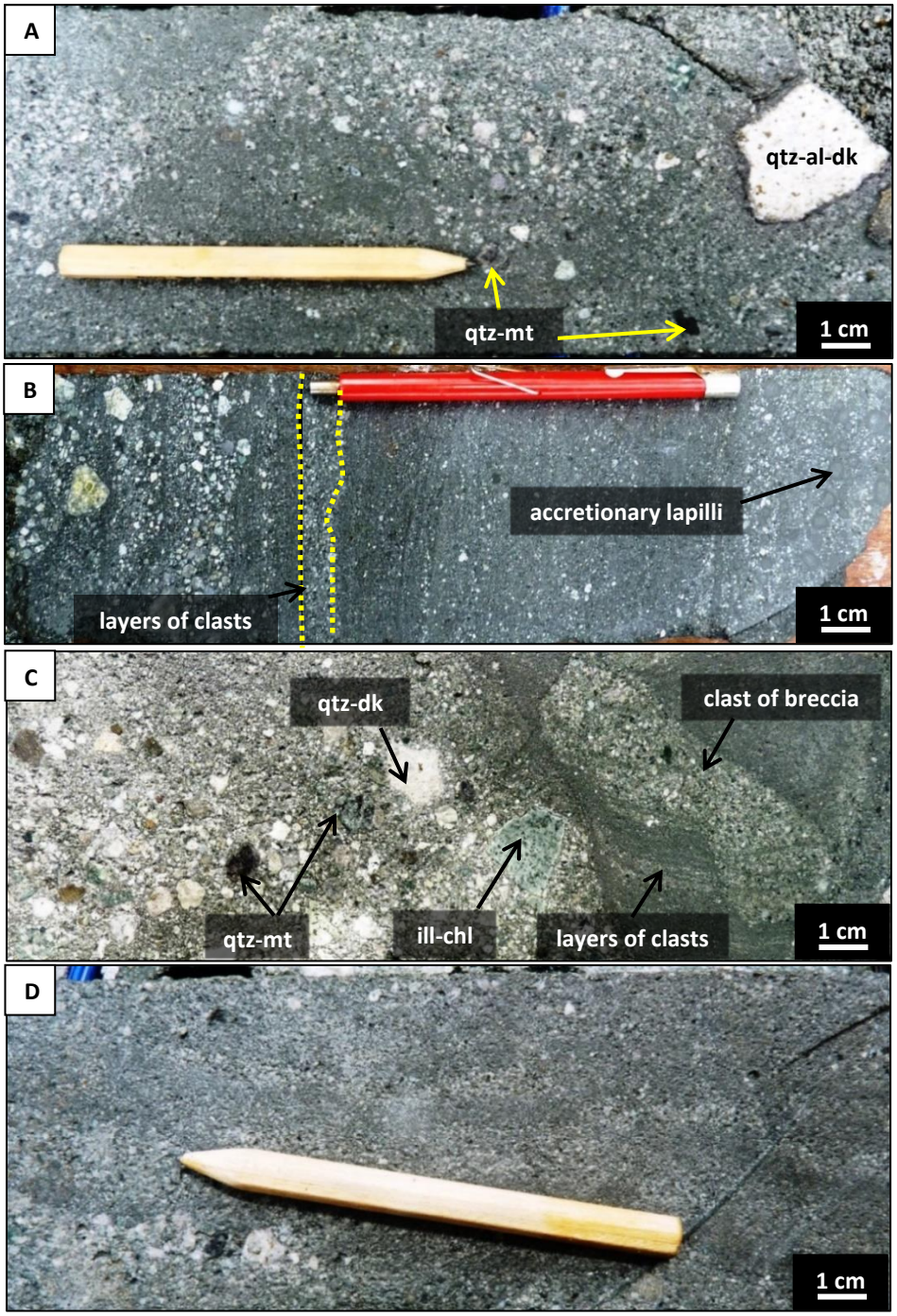

Figure 3.26. Upper facies matrix-rich milled breccias from drillhole GTD-10-172 (*9046440 mN 174240 mE)* at Tumpangpitu. Abbreviations: al = alunite, chl = chlorite, dk = dickite, ill = illite, mt = magnetite, qtz = quartz.

A) *26m.* Zones of 1 - 5 mm sub-rounded quartz - magnetite porphyry tonalite vein fragments, together with diorite and quartz diorite clasts. Larger quartz - alunite - dickite altered quartz diorite clast (upper right). Matrix is altered to chlorite - illite ± calcite.

B) *14m.* Sub-horizontal cm-scale layers of accretionary lapilli (far right), fine (1 - 2 mm) diorite and tonalite clasts (centre) and 1 - 8 mm porphyry clasts (far left).

C) *34.4m*. Example of a polyphase milled breccia. Clast-supported breccia (far left) in contact with very fine-grained matrix-supported milled breccia with 1 mm sized fragments of wallrocks, containing a clast of slightly coarser-grained milled breccia (right).

D) *32.2m.* Fine-grained, comminuted milled breccia with near-vertical flow banding.

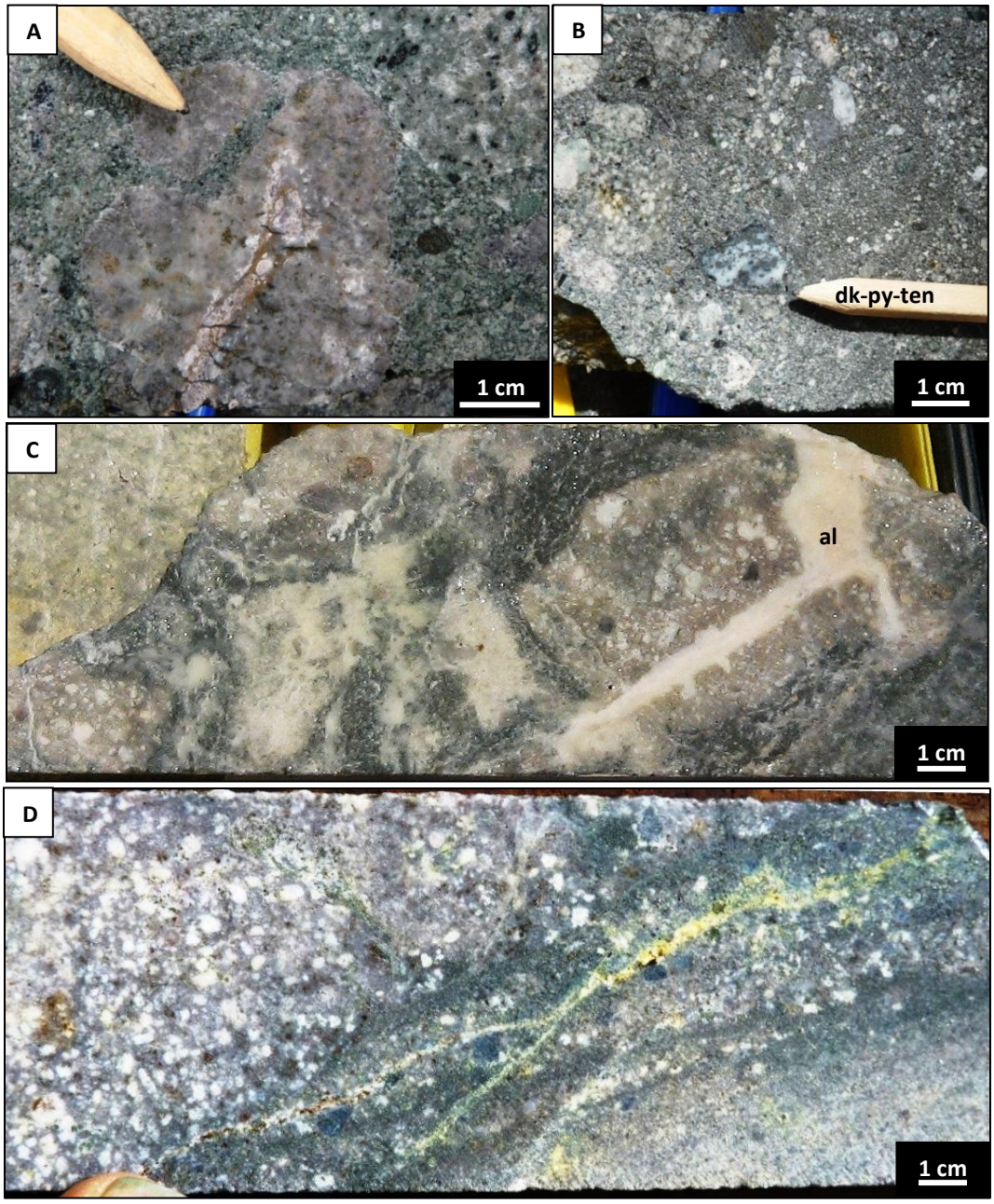

Figure 3.27. Characteristic features of upper and lower facies polymictic milled breccias in drillcore from Tumpangpitu. Abbreviations: al = alunite, dk = dickite, ten = tennantite, py = pyrite.

A) *9046440 mN 174240 mE; drillhole GTD-10-172; 26.3m*. Two tonalite porphyry clasts with rutile - clay vein in sand-sized lithic matrix. Adjacent clasts include phase 7 quartz diorite and small 1 - 3 mm quartz - magnetite - chalcopyrite porphyry fragments.

B) *9046440 mN 174240 mE; drillhole GTD-10-172; 47.7 m*. Angular clast of dickite - pyrite - tennantite in chlorite - illite - calcite altered sand-sized lithic matrix.

C) *9046141 mN 173878 mE; drillhole GTD-08-56; 388m.* Late alunite vein cross-cutting a quartz diorite clast and alunite-altered matrix in lower facies breccia.

D) *9046141 mN 173878 mE; drillhole GTD-08-56; 177.2m.* Flow foliation in in milled breccia along its contact with phase 7 quartz diorite.

3.3.8.4 Tumpangpitu diatreme distal facies - tuffisite sand and pebble dikes

Tuffisite sand and pebble dikes have been documented on the margins of both the upper and lower vent breccia facies at Tumpangpitu, and in other porphyry intrusions in the district (e.g., Salakan; Fig. 3.30C - F). They commonly occur in contact zones between two different lithologies e.g., between phase 5 and 7 porphyries and parallel to bedding between sedimentary rock layers (Figs. 3.3 - 3.6). The dikes are typically several millimetres to several centimeters wide (e.g., Fig. 3.29), locally up to several meters. They are generally irregularly shaped with sub-vertical orientations, some sub-horizontal sills have been observed in bedding planes between sedimentary units below Zone C oxide (Figs. 3.3 - 3.4). The dikes are matrix-supported with a matrix content of 50 to 95 volume percent. They are polymict, incorporating similar clasts types to the upper facies milled breccia, including sedimentary rock, andesitic rock and intrusive phases 2 - 7. Adjacent to and above mineralized zones, the dikes have entrained mineralized clasts, including vuggy quartz, quartz - tennantite and porphyry quartz stockwork vein fragments that contain magnetite ± K-feldspar ± chlorite ± bornite ± chalcocite ± chalcopyrite. The clasts exhibit several alteration types, but the matrix is consistently weakly altered to illite - chlorite ± montmorillonite/nontronite where not overprinted by alteration associated with HSE mineralization. Illitic alteration halos around the tuffisite dikes are uncommon. The dikes exhibit lateral gradation with coarse clasts in the center and laminated rock flour at the margins (Fig. 3.29). The clast size is dependent on the width of the dikes, commonly being smaller than one-tenth of the dike width, similar to observations from other documented sand and pebble dikes (e.g. Landtwing et al., 2002; Davies et al., 2008a). In the sand dikes, clasts are sand- to fine- pebble-sized, whereas in pebble dikes, the clasts range up to cobble-size. The clasts are predominantly rounded, but in places are sub-rounded or angular (Fig. 3.29). The matrix is andesitic in composition and consists of sand- and mud-sized clastic grains (rock flour), micas and clay minerals (montmorillonite, nontronite, illite and chlorite). The dikes predominantly have sharp contacts with the host rock (e.g., Fig. 3.30C), although diffuse contacts are also observed (e.g., Fig. 3.29). Clasts commonly have halos of fine-grained pyrite oxidized to goethite (Fig. 3.29). In mineralized zones, the dikes have incorporated chalcocite in the matrix, and commonly as a layer along contacts with the host rocks (e.g., Fig. 3.30C).

3.3.8.5 Tumpangpitu diatreme distal facies - apron breccias

The western coastline of Tumpangpitu exhibits excellent exposures of milled breccia (Figs. 3.1 and 3.24), interpreted to be an apron of deposits. This facies is characterized by gently dipping (25˚ W) normal and cross-bedded siltstones, sandstones and mudstones that are contininous along a northwest strike for over 1.5 km. The sedimentary rocks are interspersed with upper facies polymict lithic bedded milled breccias. The key identifying feature is that the sedimentary interlayers dip away from the central diatreme vents.

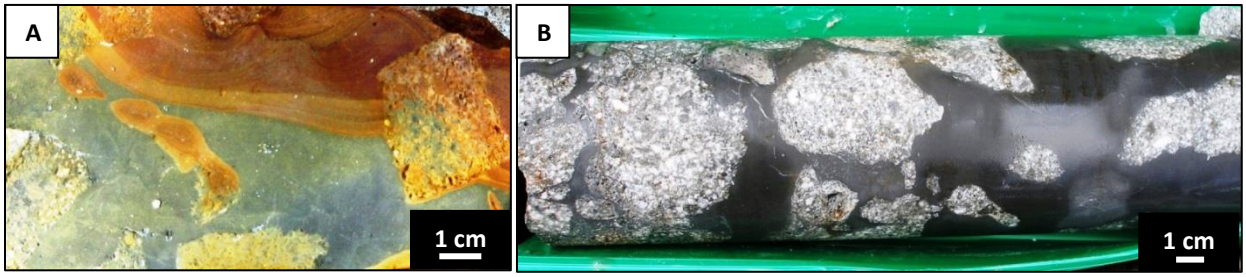

Figure 3.28. Mud-matrix-supported breccias in drillcore from Tumpangpitu (photos from Rohrlach, 2010).

A) *9045682 mN 174316 mE; drillhole GT-007; 119 m.* Partially oxidized mud-matrix breccia with angular quartz diorite clasts.

B) *9045455 mN 174545 mE; drillhole GTD-09-61; 140 m.* Breccia of sub-rounded quartz diorite clasts with mud matrix.

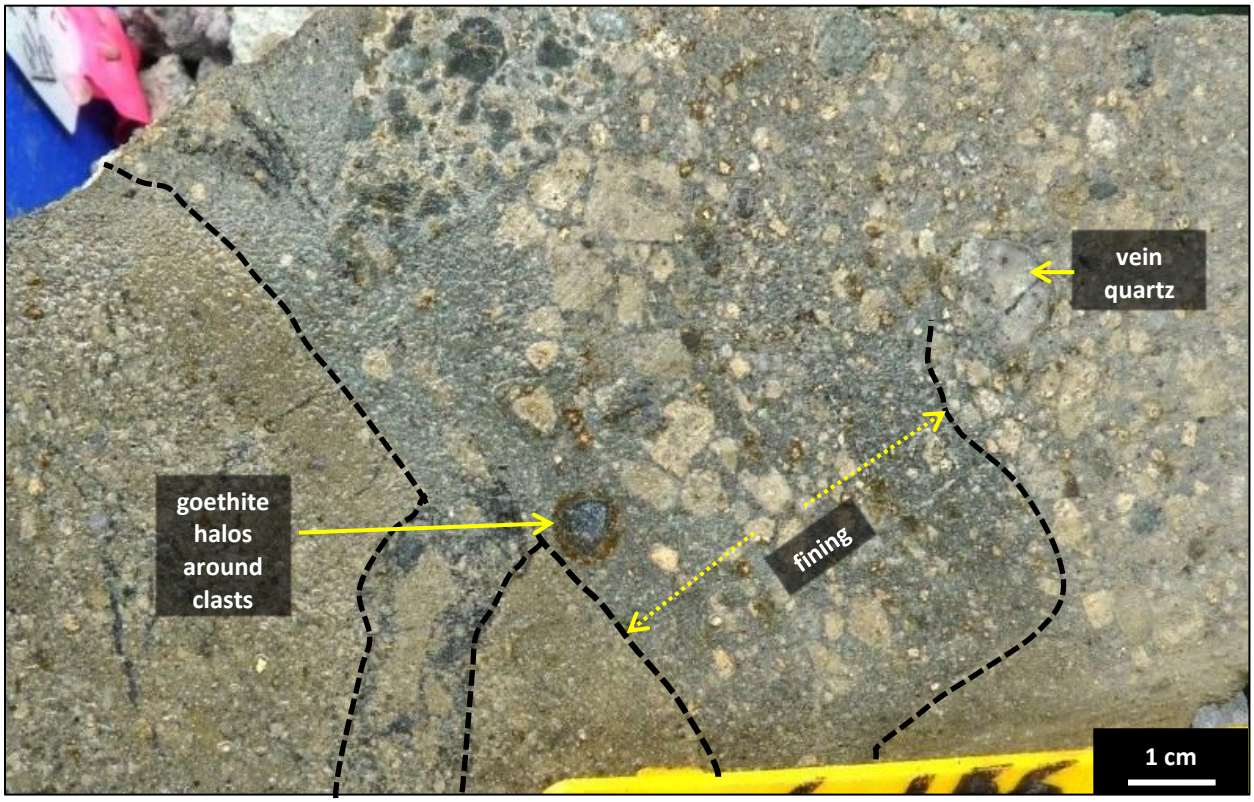

Figure 3.29. *9046285 mN 174385 mE; drillhole GTD-11-248; 68 m.* Tuffisite pebble dike at Tumpangpitu.

3.3.9. Other diatremes in the Tujuh Bukit district

Evidence for multiple diatreme breccia vents has been documented from exploration drilling and mapping at Salakan and Candrian (Fig. 3.18).

3.3.9.1 Salakan diatreme

Tuffisite sand and pebble dikes have been documented from exploration drillcore at the Salakan prospect 7.5 km northwest from Tumpangpitu in narrow 2 cm to 1.3 m intervals from 58 m below present-day surface (Fig. 3.18). The tuffisite dikes have crosscut the tonalite porphyries, resulting in

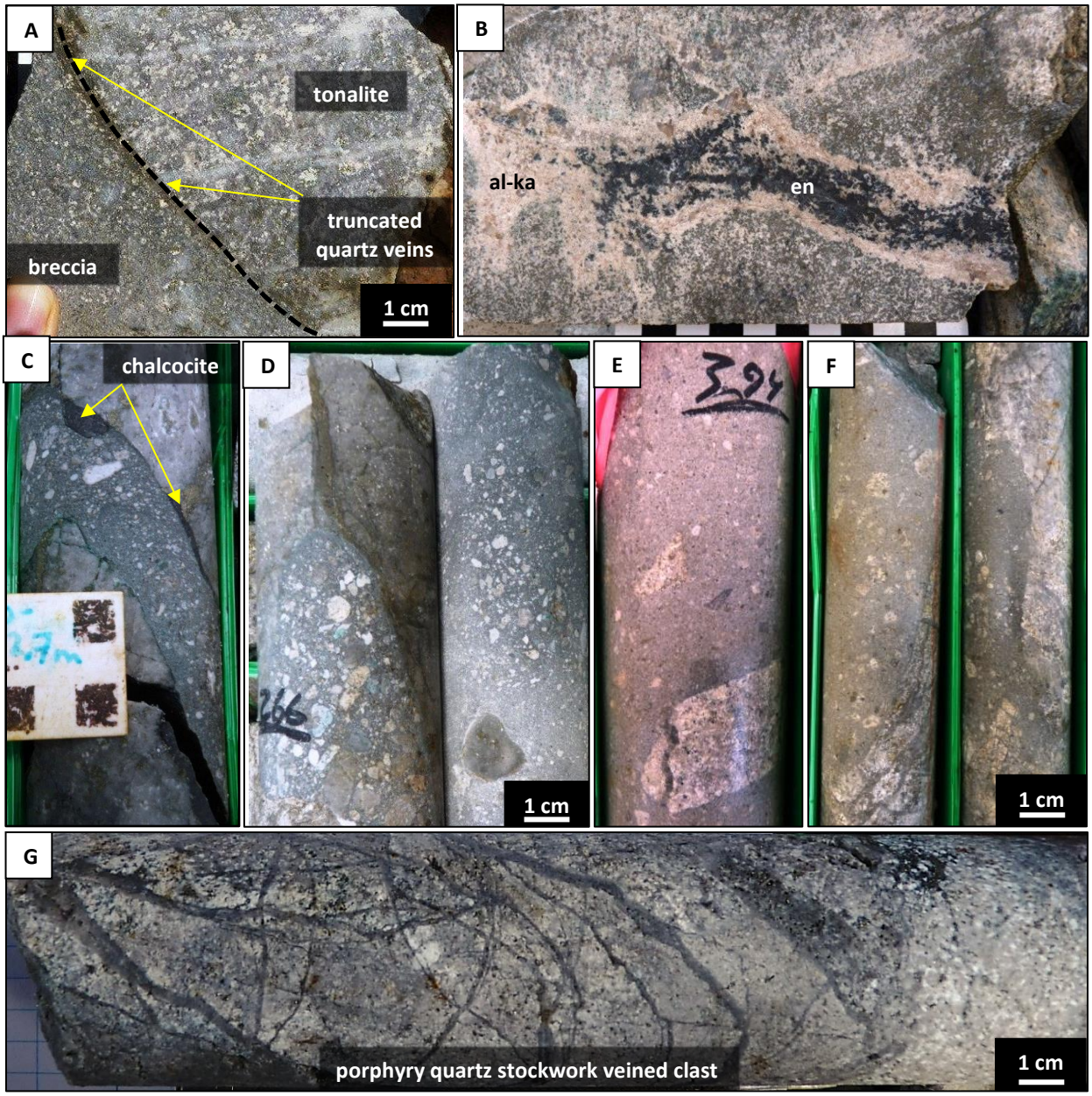

Figure 3.30. Diatreme breccias from Salakan drillhole SND-12-001 (9052317 mN 170000 mE; A-F) and Candrian drillhole CND-11-001 (*9046571 mN 176303 mE*; G) porphyries in the Tujuh Bukit region. Abbreviations: al = alunite, en = enargite, ka = kaolinite.

A) *Drillhole SND-12-001; 143.3 m.* Vein truncation at contact of polymict milled breccia with quartz stockwork veined tonalite.
B) *156.6 m.* Enargite - alunite - kaolinite vein crosscutting polymict breccia.
C) *272.7 m.* Narrow 3 cm tuffisite dike with coarser-grained centre and fine-grained milled matrix margin with chalcocite along sharp contact with tonalite porphyry.
D) *265.2 - 266 m.* Polymict milled breccia tuffisite dike with porphyry vein fragments. Cu-As sulfides oxidized to scorodite; chalcocite oxidized to malachite along fractures.
E) *393.1 - 394.4 m.* Tuffisite dike with stockwork veined tonalite porphyry clasts.
F) *393.1 - 394.4 m.* Tuffisite dike containing mineralized veined clasts. Upper contact with tonalite is 070° towards 80°S (pipe is northeast trending). Lower contact: 035° towards 85° south.
G) *264.2 m.* Porphyry quartz stockwork veined mineralized (chalcocite - bornite - molybdenite) fine-grained tonalite clast in quartz - dickite - pyrophyllite altered diatreme breccia; molybdenite also in breccia matrix.

localized reductions in grade (Fig. 3.30A). High-sulfidation veins, enargite - tennantite - alunite - kaolinite crosscut the breccia dikes (Fig. 3.30B). Contacts of the dikes are generally sharp with the wallrock and entrain fine-grained chalcocite along the margins (Fig. 3.30C).

3.3.9.2 Candrian diatreme

Clasts of fine-grained porphyry tonalite with quartz stockwork veining and chalcocite - bornite - molybdenite mineralization in tonalitic igneous cement, also containing molybdenite have been recorded in drillcore from the Candrian porphyry prospect 2.7 km northeast of Tumpangpitu (Fig, 3.18 and 3.30G; Harrison, 2014). The dimensions of the breccia remain unknown and further drilling is required to fully understand the extent and significance of this breccia complex.

3.4 Structure of Tumpangpitu

3.4.1 Introduction

Many porphyry deposits form in convergent magmatic arcs under compressional to transpressional conditions, commonly after uplift and exhumation (e.g. Cooke et al., 2005; Sillitoe, 2010).

The Tujuh Bukit district is dissected by several large faults (Figs. 3.34 and 3.37). Structural data was obtained both by the author (Harrison, 2009, 2012) and during field mapping mentored by consultant Dr David Gray (Gray, 2011, 2012). These data have been used in the construction of the Tumpangpitu structural model. Data has been collected from mapping coastal exposures by foot, helicopter and small fishing boat, logging drillcore and from surface aeromagnetic images to gain an insight into the structural architecture of the Tumpangpitu deposit and other porphyry deposits in the district (Fig. 3.34).

The Tumpangpitu fault system comprises a series of inter-mineralization northwest-striking steep (70º to 85º), southwest- and northeast-dipping faults that have cut the Tumpangpitu porphyry ore body (Fig. 3.32). These faults have localized the high-grade Au-Ag-(Cu) veins and associated alteration (Fig. 3.38). A second group of faults, striking north-northeast, have crosscut and offset the major northwest-striking faults. These north-east-trending faults have slightly displaced the porphyry ore body, and have both localized and displaced high-grade Au-Ag-(Cu) veins. North-trending thrust faults have been mapped at the Tanjung Jahe peninsula which crosscut the Tanjung Jahe diatreme (Figs. 3.35B and 3.36).

3.4.2 Structure of the eastern Sunda magmatic arc

The eastern Sunda-Banda arc is segmented by a series of arc-normal sinistral strike slip structures that trend northeast and which are evident in topographic data-sets (Fig. 3.31). Tectonic factors appear to have localized volcanic centers of the Miocene arc at positions near the southwest margins of these transfer

structures (Fig. 3.31; Garwin, 2002; Maryono, 2012). Eastern Java shows three of these major sinistral cross faults (Fig. 3.31).

3.4.3 District scale faults

The Tujuh Bukit district sits within a block between two of the major northeast-trending island scale sinistral strike slip faults (Fig. 3.31). Three major arc-parallel northwest-trending (120 °) brittle reverse faults (Fig. 3.34) transect the Tujuh Bukit district:

1) Pasanggaran Fault: 140°/70°SW
2) Lampon-Salakan Fault: 140°/75°SW
3) Tanjung Jahe Fault: 140°/70°SW

These three faults zones are spaced at ~3 km and have widths of 200 - 300 m (Fig. 3.34). Fault kinematic indicators suggest these major fault zones have reverse dip-slip movement (i.e. hanging wall up) formed under approximate northward compression (based on fault-slickenside data at Tanjung Jahe; Fig. 3.36). The Tanjung Jahe fault is a 270 m zone of brittle-ductile reverse faults (Figs. 3.35B, 3.36). The Lampon-Salakan fault, where it cuts the Katak porphyry, has a brittle character, with aeromagnetic images suggesting a 300 m zone of thickness (Fig. 3.34). The Tumpangpitu and Candrian porphyry deposits are situated in the hanging wall of the Lampon-Salakan Fault zone, between the Tanjung Jahe and Lampon-Salakan Fault zones. Both the Katak and Salakan porphyry deposits have been cut by the Lampon-Salakan fault zone (Fig. 3.34).

Interpretation of fracture systems interpreted from the digital elevation model (DEM; Fig. 3.33) across the old Miocene volcanic centre that hosts Tumpangpitu, indicates three main sets of fractures/faults; northwest-trending (145°) northeast-trending (035°), and west-north-west-trending (120°; Fig. 3.33). The Tujuh Bukit district is dominated by the northwest-trending fracture set. These directions match the fault fracture pattern expected from the impingement of the Roo Rise with the Java trench during subduction (Fig. 3.32). Structural measurements from Tanjung Jahe (Figs. 3.35, 3.36), suggest that major structures are zones of southwest dipping thrusts.

3.4.3.1 Lampon-Salakan fault zone

This fault zone extends from Salakan in the west to Lampon in the east and transects the Katak porphyry (Fig. 3.34). The Katak porphyry is cut by two inferred bounding-brittle faults that define this major 120° fault zone. Slickensides measured from drillcore (Gray, 2012), indicate general dip slip movement with fibre steps indicating reverse movement.

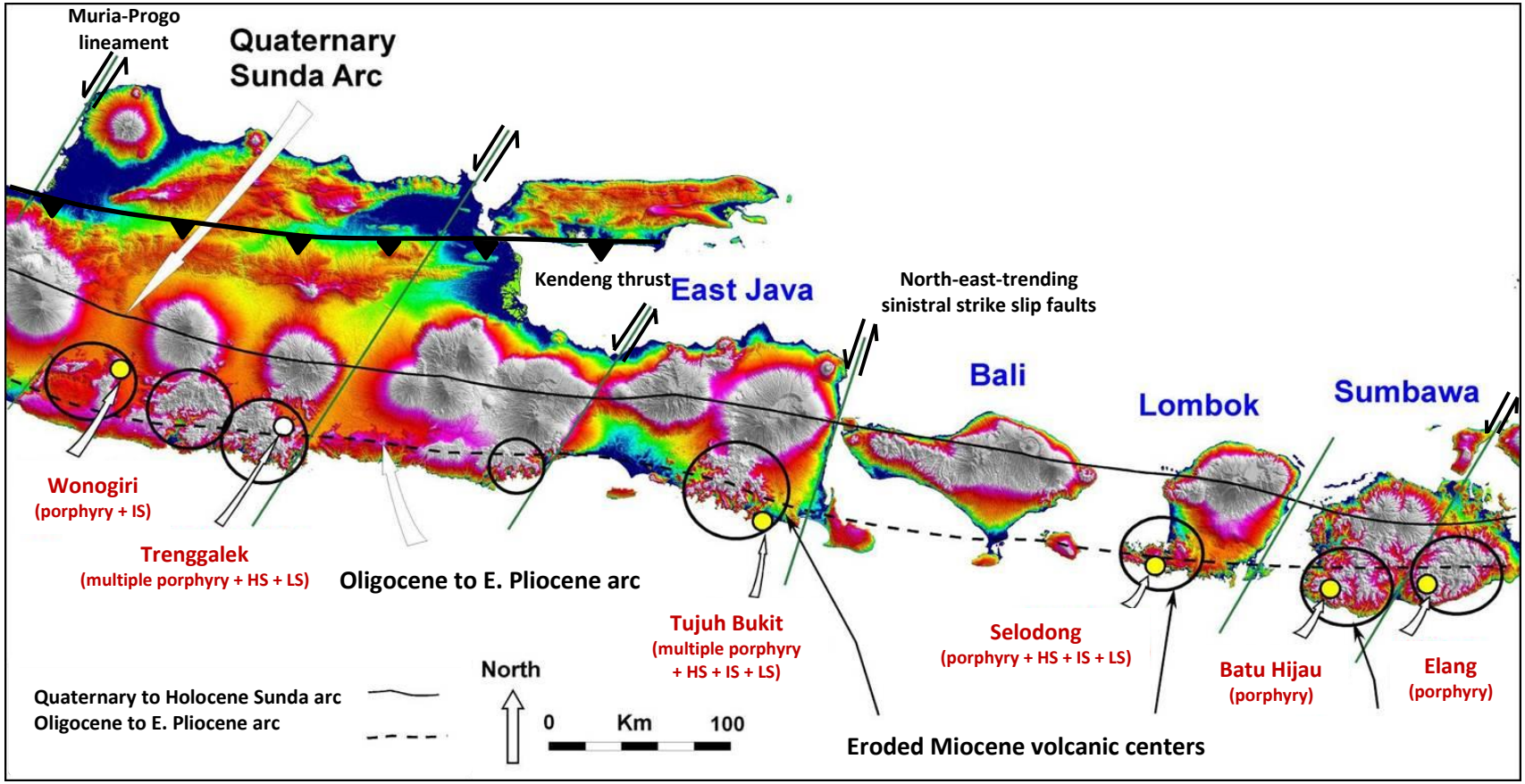

Figure 3.31. Digital elevation model showing the northeast-trending sinistral strike-slip faults (green lines) and the Kendeng thrust (black barbed line) along the Oligocene to E. Pliocene and younger Quaternary to present day eastern Sunda Banda magmatic arc (modified after Rohrlach, 2011). Abbreviations: HS = high-sulfidation epithermal, IS = intermediate-sulfidation epithermal, LS = low-sulfidation epithermal.

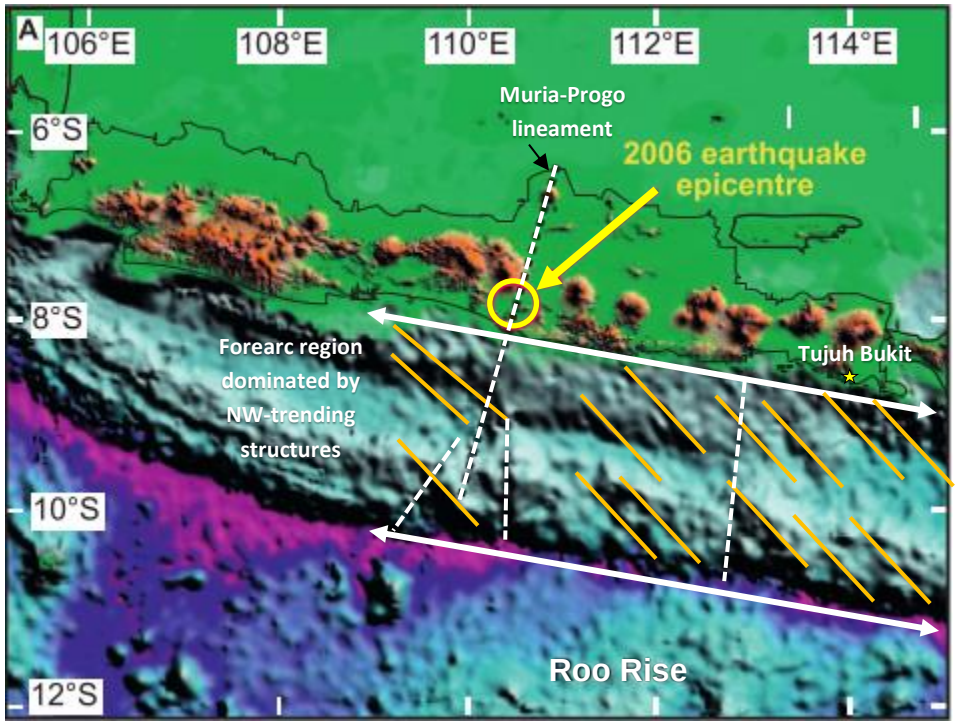

Figure 3.32. Structural grains imposed on the Java forearc due to the subduction of the Roo Rise. The white arrows denote the contact zone of the Roo Rise with the Java trench. Topography from SRTM (shuttle radar topographic mission) and GTOPO30. Yellow star denotes the location of Tujuh Bukit. The orange fracture set in the forearc matches this impingement zone (modified after Clements et al., 2009; Gray, 2012).

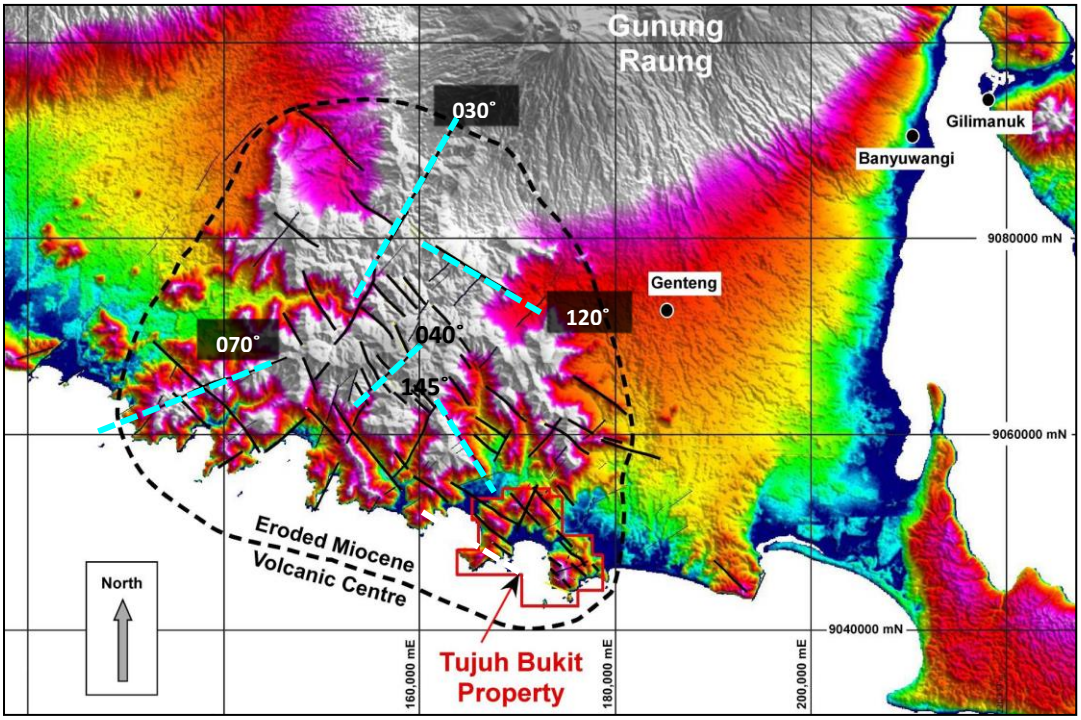

Figure 3.33. Digital elevation model of east Java showing major arc-parallel faults, fracture pattern interpretations (solid black lines) and major structural trends (pale blue hashed lines; modified after Rohrlach, 2011).

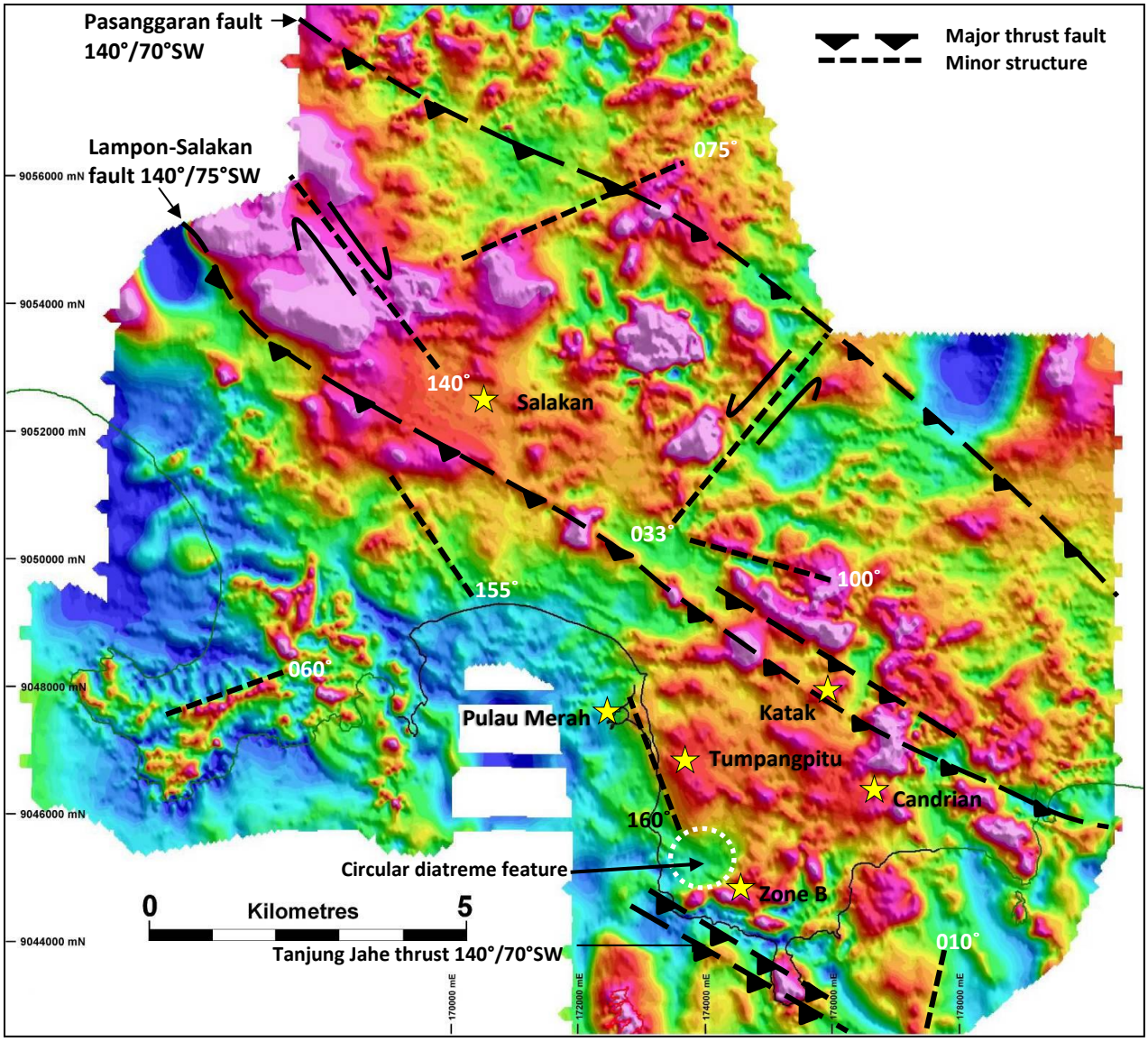

Figure 3.34. Fracture/fault interpretation of TMI (total magnetic intensity) RTP (Reduced to pole) aeromagnetic image of the Tujuh Bukit district showing the three major 120˚- trending arc-parallel faults. Yellow stars denote porphyry deposits/prospects (modified after Gray, 2011).

3.4.3.2 Tanjung Jahe thrust fault

The Tanjung Jahe fault zone is exposed along the south-eastern part of the Tanjung Jahe peninsula (Fig. 3.35A). These faults are WNW- to NW-trending (140°) and dip moderately to steeply (70°) to the southwest (Gray, 2012). The fault zone coincides with a WNW-trending fault/fracture system inferred from the total magnetic intensity (TMI) image (Fig. 3.34). This feature appears continuous over several kilometres. The faults are narrow zones that cut the massive polymict lower facies diatreme breccia (Figs. 3.35B, and 3.36). There are two sets of faults, a flatter set that has truncated and offset a more steeply dipping reverse fault set that tends to dominate the rock exposures (Figs. 3.35B and 3.36). The

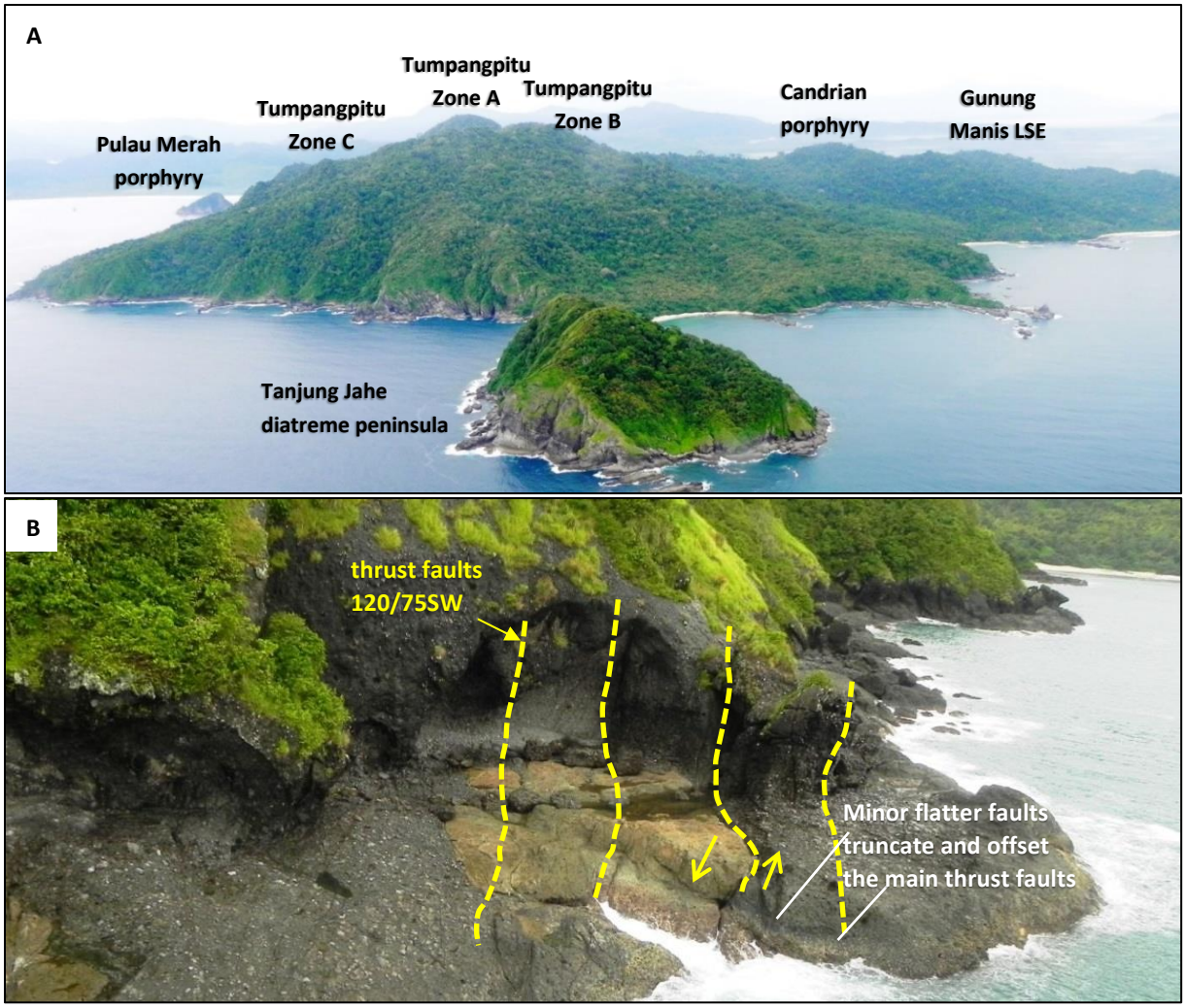

Figure 3.35. Location and thrust fault exposures at Tanjung Jahe peninsula.
A) View looking north of the coastline, deposits and regional prospects.
B) North-west trending, southwest dipping thrust brittle shear zones (yellow dashed lines) offset by secondary faults (blue lines) in lower facies diatreme breccia on the southeast side of Tanjung Jahe peninsular.

south-eastern part of the Tanjung Jahe Peninsula is dominated by NW-trending reverse faults (Fig. 3.35), and appears to define a zone of deformation in the diatreme.

3.4.4 Deposit scale faults

The faults at Tumpangpitu have been divided into four main sets. Criteria used to subdivide them included crosscutting relationships identified from surface mapping (Fig. 3.1), drillcore logging, section construction (Figs. 3.3 - 3.8), aeromagnetic and topographic imagery (Fig. 3.33 - 3.34). These results have been combined with SWIR spectral data to help map clays associated with structurally controlled high-sulfidation epithermal mineralization (Figs. 3.37 - 3.38). The four fault sets are as follows:

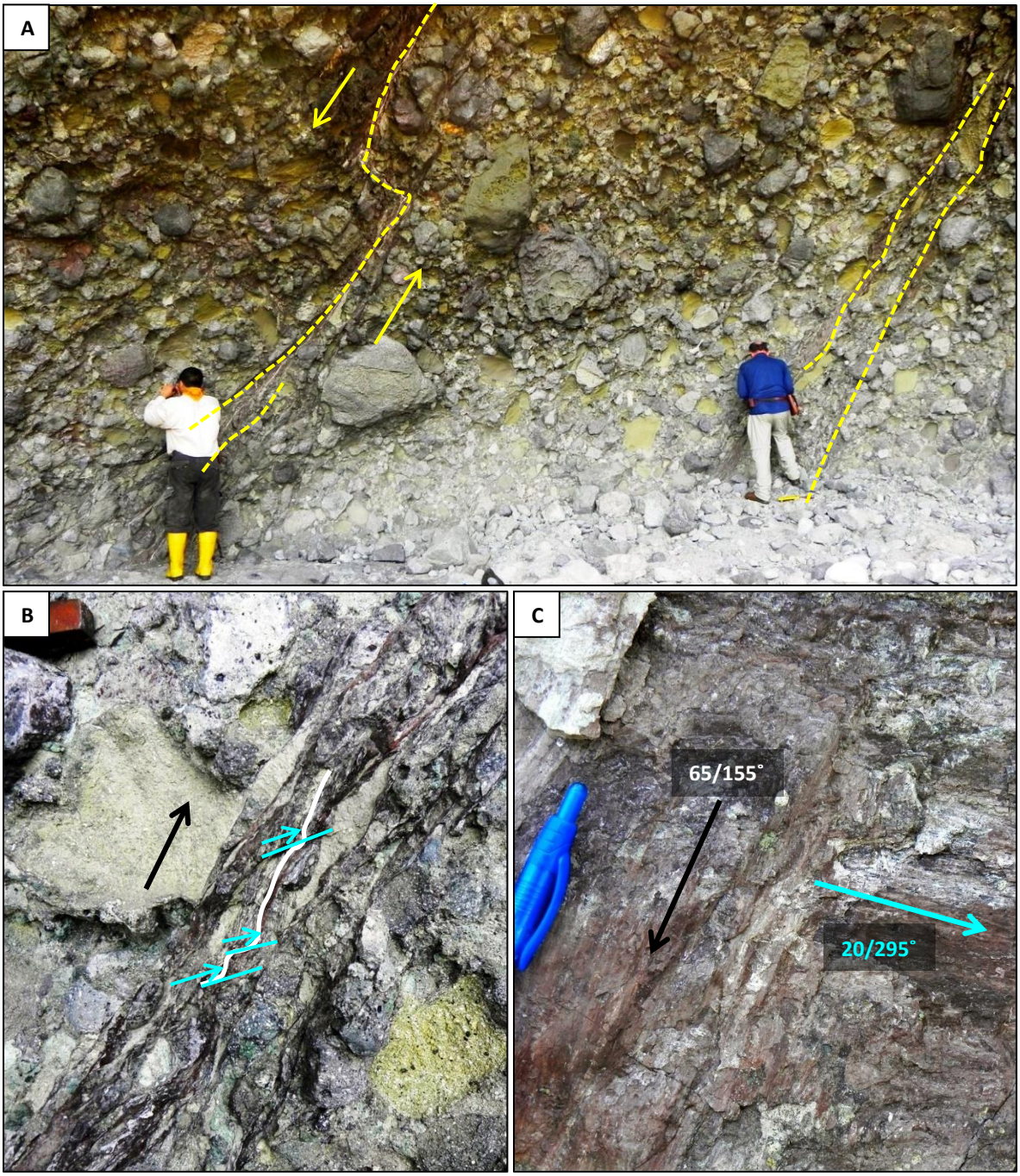

Figure 3.36. Thrust fault features in Tanjung Jahe lower facies diatreme breccia (modified after Gray, 2012).

A) Northwest-trending, southwest dipping normal brittle shear zones cutting the lower facies diatreme breccia in the cave on the southeast side of Tanjung Jahe peninsula. Clast sizes range from pebble to boulder size.
B) Foliated cataclastite nature of brittle-ductile shear zones (up to 4 - 5 cm thickness), with shear bands indicating hanging wall up movement sense (reverse fault movement).
C) Major fault plane (120/75˚ SW) showing two slickenlines indicating at least two stages of movement.

1) Northwest-trending dextral-normal oblique slip faults dipping southwest (140˚/70 - 88º SW); East fault, Cliff fault and Central Fault
2) Northwest-trending dextral-normal oblique slip faults dipping northeast; West fault (140˚/80 - 85º NE)
3) Northeast-trending faults with steep northwest dip (040˚/85º NW); NE1, NE2 and NE3 faults
4) North-north-west- trending faults with steep east dip (345˚/85º E); Zone B fault, Zone B East fault and faults hosting massive sulfide veins adjacent to Pulau Merah island

The first two fault sets include the major northwest-striking faults that extend along strike for over 1.5 km (Fig. 3.37) and are steeply dipping (70º to 88º). The inter-mineralization fault system is interpreted to have been a major control on the formation of the high-sulfidation Au-Ag-(Cu) vein system, based on the NW-orientation of high-sulfidation ore zones at Zones A and C (Fig. 3.1).

The third set of faults are the syn- to post-mineralization sinistral-normal northeast-trending fault system (Fig. 3.37). This set comprises three main northeast-striking faults (NE1, NE2 and NE3; Fig. 3.37), which have offset and displaced the earlier northwest- trending mineralized faults by 50 - 100 m (Fig. 3.37).

The fourth fault set hosts high-sulfidation epithermal mineralization in the Zone B oxide deposit to the south of Tumpangpitu, which is controlled by two north-striking faults; the Zone B and Zone B East faults. They extend along strike for at least 1.2 km and dip steeply towards the east (Fig. 3.37). Similarly, the majority of faults mapped along the southern coastline have orientations around 000˚, but they dip steeply (> 80˚) westwards. The massive sulfide high-sulfidation epithermal Au-Ag-Cu veins that transect the wave cut platform adjacent to Pulau Merah porphyry strike north-northwest and dip steeply (> 80˚) westwards (Harrison, 2009).

3.4.5 Structural model for Tumpangpitu

Each of the major northwest-trending faults at Tumpangpitu (Fig. 3.38; East, Cliff, Central and West) have all been overprinted by advanced argillic alteration associated with high-sulfidation epithermal mineralization. SWIR spectral data, along with structural orientation measurements were crucial for mapping the inter-mineralization faults that host high-sulfidation mineralization associated with alunite, pyrophyllite, topaz, diaspore, dickite and hypogene kaolinite alteration. Due to the section orientation of 050˚, the north-east faults that crosscut the northwest faults cannot be modelled clearly on sections (Fig. 3.38). Both the Central and Cliff faults in the southernmost section (Fig. 3.38) are interpreted to have been truncated by a north-east fault zone and a root zone of one of the diatreme breccia pipes.

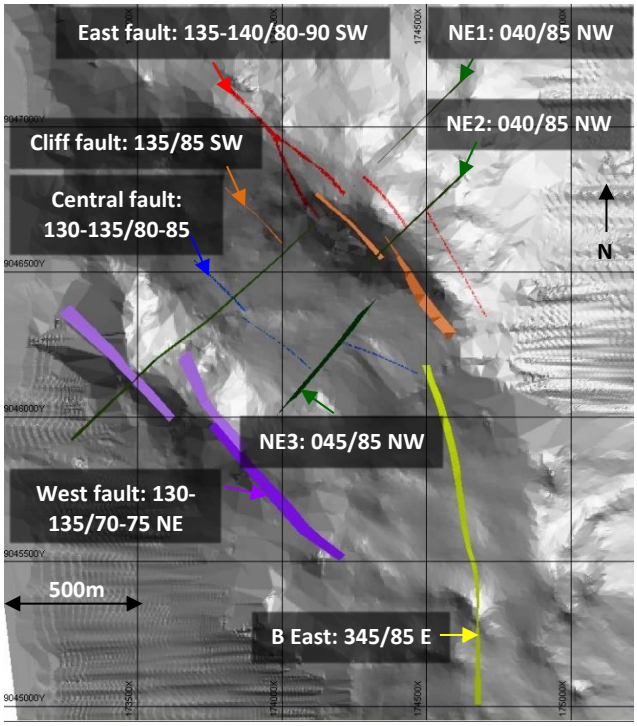

Figure 3.37. Tumpangpitu fault system (modified after Intrepid Mines Ltd., 2012). Fault traces with orientations from drillcore measurements on digital terrain model (DTM).

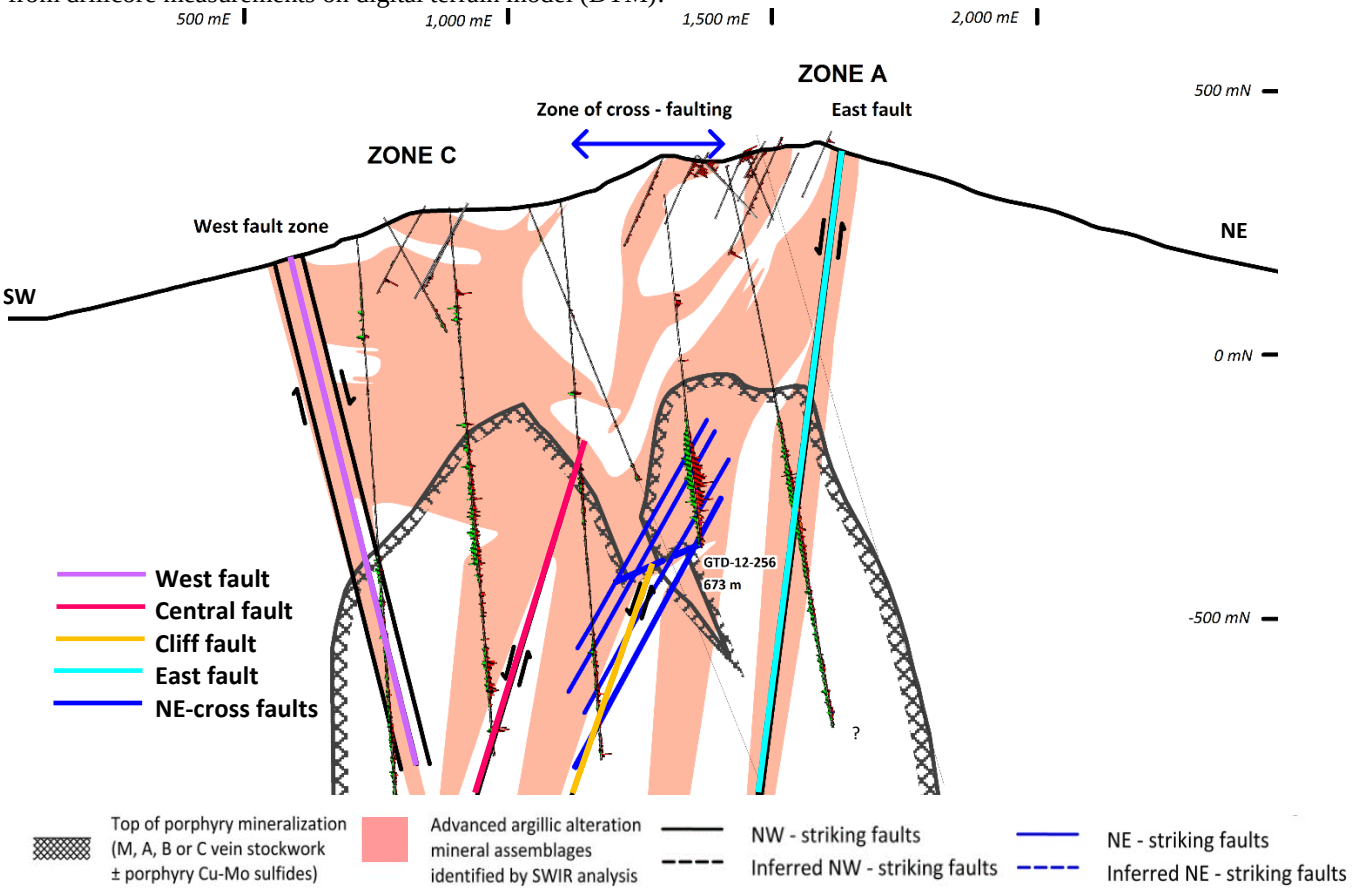

Figure 3.38. Alteration section 10660mN at Tumpangpitu, highlighting major faults and advanced argillic alteration identified by SWIR data (pale pink). Refer to Fig. 3.1 for section location.

3.5 Discussion

3.5.1 Regional structural kinematics

Basement arc parallel structures potentially influenced metal-enriched magma emplacement along the Sunda-Banda magmatic arc (Carlile and Mitchell, 1994; Garwin, 2000; Clements et al., 2009; Hall and Sevastjanova, 2012; Setijadji and Maryono, 2012; Gray, 2012). Regional structural kinematics that can be related to the current plate motion and inferred plate motion since ~8.4 Ma (age of the oldest dated magmatism; Chapter 4) are as follows:

- Phase 1 and 8 quartz diorite dikes along the southern coastline have sub-vertical, north-trending attitudes (Figs. 3.1, 3.15C and 3.32) which suggests E-W extension
- Kinematic analysis of the NW-trending thin ductile-brittle zones of thrust faulting on the southeast peninsula of Tanjung Jahe (Figs. 3.5 - 3.36) display foliated gouge and internal development of shear-bands, reflecting hanging wall up movement under N-directed compression and E-W elongation for development and movement on these fault planes

Structural analysis indicates that the faults that have been measured and documented at Tujuh Bukit (Figs. 3.33 - 3.38) can be explained by activation and reactivation under the same regional plate stress field, where compression is N-S and σ2 vertical with E-W elongation (Gray, 2011, 2012). This is the regional plate compression vector that has most likely been operative since at least 8.4 Ma. The dominant fault set in the forearc sequences suggests that NW-trending faults have been activated and reactivated in East Java since Roo Rise impingement (Fig. 3.32). This deformation may have been superimposed on the existing fracture pattern developed during "normal" subduction-related orthogonal convergence, prior to Roo Rise reaching the Java trench (Fig. 3.32; Clements et al., 2009; Gray, 2012). One implication is that the NW-trending fault set is most likely the dominant active set that has affected the Tujuh Bukit district because these faults have the largest offsets and host epithermal Au mineralization (Fig. 3.7).

3.5.2 Fault re-activation

Multiple slickensides (Fig. 3.36) and younger faults that crosscut and offset older faults (Fig. 3.35B) indicate activation and reactivation of faults under the same, long-lived plate stress regime (since at least 8.4 Ma). This is exemplified by faults at the southeast end of Tanjung Jahe peninsula. A major exposed fault plane shows two slickenlines requiring thrust and oblique slip events under N-S and NE-SW compression respectively (Fig. 3.36). Offsets in the fault plane by younger, steeply dipping conjugate brittle faults also occurred under N-S compression. Flatter thrust faults have truncated and offset steep reverse faults (3.35B; Gray, 2011).

3.5.3 Structure at Tumpangpitu

At Tumpangpitu, pre-existing faults and structural weakness appear to have controlled magma emplacement along northwest- and northeast-striking faults (Figs. 3.1 - 3.2). Some of these later northeast faults have displaced epithermal and porphyry mineralization (e.g. NE1 fault; Fig. 3.2). Based on cross cutting relationships and inter-mineralization faults indicated from mapping clay alteration, as determined by SWIR analysis (Fig. 3.38), some structures acted as major high-sulfidation feeders as well as conduits for mineralized porphyry deposits (e.g., Cliff fault; Figs. 3.37 and 3.38).

3.5.4 Structure associated with diatreme emplacement

The network of fractures and dilated joints in the halo surrounding root zones of diatremes may at any time be used to form arcuate faults during diatreme growth and subsidence (Lorenz and Kurszlaukis, 2007). Such arcuate faults occur as normal faults in cross section and may extend for about 50 - 100 m outward from the crater rim (Lorenz and Kurszlaukis, 2007). Faults played a key role in the localization of the diatreme breccias at Tumpangpitu. Arcuate features have been identified in aeromagnetic datasets, particularly around the Tumpangpitu diatreme root zone (magnetic low on Fig. 3.34), although they are not clearly evident in the field (Harrison, 2009; Gray, 2011, 2012), possible due to lack of rock exposure, or because brecciation destroyed the original fault planes. The structural model for Tumpangpitu (Fig. 3.38) highlights a graben-type structure, whereby the West fault dips towards the northeast and East, Cliff and Central fault dip towards the southwest. This graben most likely formed during diatreme emplacement and subsidence in proximity to root zones, similar to sink hole formation (Fig. 3.39; Lorenz and Kurszlaukis, 2007).

3.5.5 Influence of structure on ore distribution

Truncation and copper ore that occurs in zones (e.g., Fig. 3.39), particularly bounded by the NE-trending cross faults, and the observation that the highest grades occur in the hanging walls of some of the major NW-trending faults (in particular Cliff Fault; Fig. 3.39), suggest a strong structural control on the mineralization at Tumpangpitu (particularly at levels above -500 RL; Fig. 3.39; Gray, 2012).

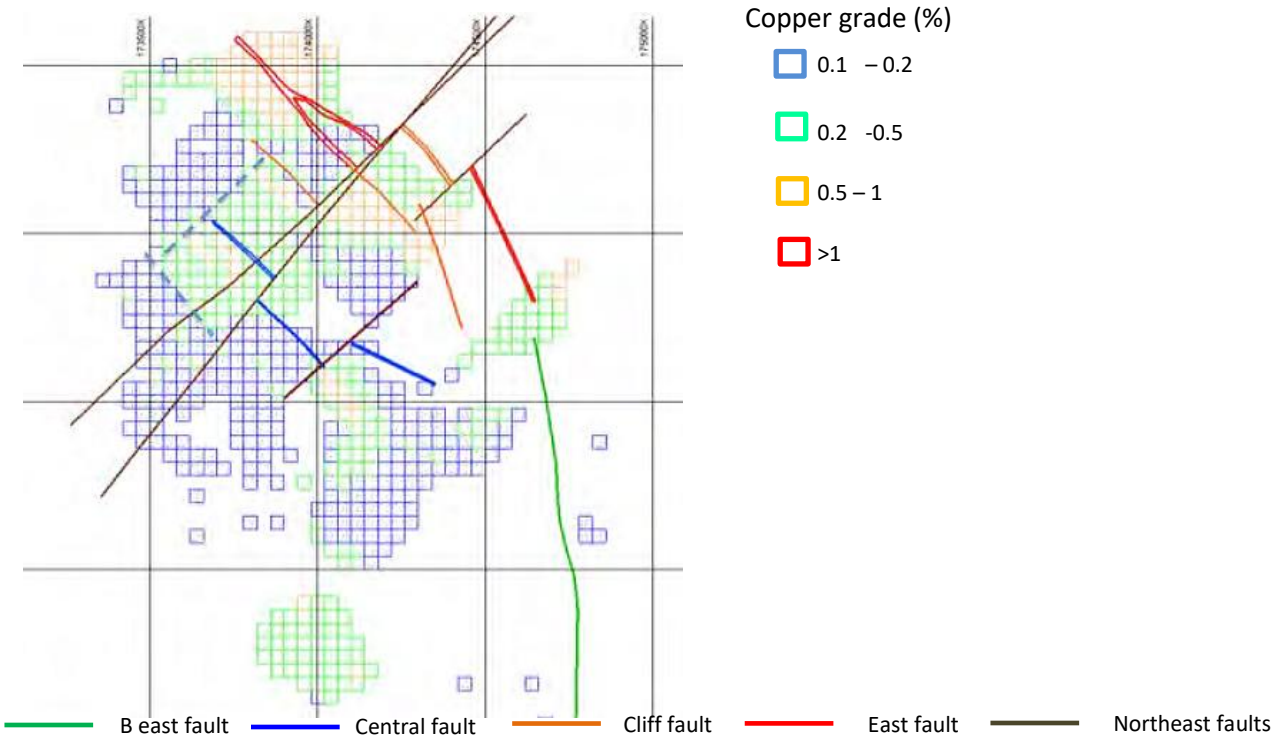

Figure 3.39. 2D slice at -200RL of copper assay data with superimposed fault intersection traces of wire-framed faults from the Tumpangpitu structural model. Dashed lines indicate other possible faults (Gray, 2012).

3.5.6 Sedimentation and volcanism

The limestone at Tumpangpitu occurs as thin (< 1 m) units along the seaward, western flank of Tumpangpitu. Limestone also crops out 4 km to the east at the low-sulfidation Gunung Manis prospect (Fig. 3.18). These exposures are interpreted as an emergent wave-cut limestone platform and fringing coral reef. Coralline fossils identified (crinoids, coralline algae, coral fragments and echinoids) suggest the paleodepth of deposition was in a mid-neritic environment (paleodepth 40 - 60 m below mean sea level; Murray, 1991; Haig and Perembo, 1992). Using timescales of Adams (1984), the fossil assemblage indicates an Early to Middle Miocene age of deposition (20 - 14 Ma; Murray, 1991; Haig and Perembo, 1992) which is consistent with U-Pb radiometric age data obtained for limestone and volcanic sandstone (20.67 ± 0.47 Ma and 16.68 ± 0.35 Ma; Chapter 4). The limestone sequence suggests deposition in a shallow subaqueous to emergent paleoenvironment, similar to the present-day coastal setting at Tujuh Bukit. It is inferred to mark preserved shallow-marine carbonate horizons formed during periods of volcanic quiescence, similar to the environment at Batu Hijau, Sumbawa (e.g., Garwin, 2000).

Mudstones at Tumpangpitu are normally graded, locally with thin beds that grade from silt to clay. The mudstones are interpreted to have been deposited in a subaqueous, quiet depositional environment through suspension settling, originally in sub-horizontal orientations (e.g., Blackwell et al., 2014).

The sedimentary rocks are conformably overlain by, and intercalated with, coherent andesitic volcanic rocks on the eastern flank of Tumpangpitu (Figs. 3.1 - 3.8). The andesitic sequence comprises a series of grey to dark green porphyritic pyroxene-hornblende-andesite flow units. The lack of vesicular textures, breccias or interbedded pyroclastic horizons may indicate that the sequence erupted by quiet effusive lava outpouring rather than explosive volcanism. The massive andesitic to dacitic volcanic breccias at the top of the sequence (oxide Zone A; Figs. 3.1 and 3.4) and crystal ash tuff on the north-western flank adjacent to Pulau Merah island (Fig. 3.1) are concordant with the underlying stratigraphy. The volcanosedimentary stratigraphy is interpreted to be the product of volcanic ash fall, debris flow deposits and pyroclastic deposits. The polymictic nature of clasts in the lithic tuffs is consistent with a near-vent source (Rohrlach, 2010). The volcanic breccias at Tumpangpitu may have formed from a few eruptive cycles, since metre to decimetre scale bedding is typically not observed. These blankets of volcanic ejecta pre-date the Tumpangpitu porphyry and diatreme. The upper contact of the Tumpangpitu diatreme crosscuts the small remnant of volcanic breccia preserved at Zone A (Fig. 3.4).

The sequence of volcanic sandstone and siltstone interbedded with mudstone and minor limestone occurs as continuous beds that can be traced in a concentric fashion, dipping towards the Tumpangpitu intrusive centre (Fig. 3.1). One explanation to this geometry, is that it was a post-depositional feature, with the inward dip of these sedimentary rocks related to the emplacement of the Tumpangpitu porphyry and late-mineralization diatreme complexes (Harrison, 2009; Rohrlach, 2010; Harrison and Maryono, 2012). Magma withdrawal from an underlying magma chamber could have produced concentric features such as ring fractures, promoting subsidence of surrounding wallrocks (e.g., Cannell et al., 2005). In addition, the ejection of country rock clasts from the root zone of the Tumpangpitu diatreme may have resulted in a mass deficiency that caused the overlying material and the adjacent country rocks to subside passively in a sinkhole-like fashion into the root zone (Fig. 3.39; Lorenz and Kurszlaukis, 2007). Geometric similarities are tentatively drawn with the Marcapunta deposit in central Peru, where a diatreme and dome complex is rooted above a porphyry system (Bendezú and Fontboté, 2009).

3.5.7 Tumpangpitu intrusive complex

The sedimentary and volcanic sequence was intruded initially by a large, hypabyssal diorite (phase 2), followed by small volumes of phase 4 very-coarse grained tonalite. The phase 4 tonalite is interpreted as a low grade pre-cursor to the main porphyry Cu-Au-Mo mineralized intrusions; specifically the fine-grained equigranular tonalite (phase 5) and the underlying coarse-grained tonalite (phase 6).

The very fine-grained, equigranular texture exhibited by phase 5 tonalite has led historically to its misinterpretation as a huge variety of different units including; sandstone, andesitic rock and microdiorite (Intrepid Mines Ltd. 2008). There have been a number of previous interpretations as to the evolution of

both phases 5 and 6. One interpretation (Kavalieris and Bat-Erdene, 2012) assumed that phase 5 is a fine-grained andesitic host rock (> 13.5 Ma; Middle Miocene), which has been overprinted by porphyry mineralization from the deeper, coarse-grained porphyry tonalite (phase 6). Another interpretation (Batu Hijau geologists, pers. comm., 2010) suggested that phase 5 formed as a fine-grained outer rim, or a chilled margin, to the underlying coarse-grained tonalite (phase 6). This latter theory seems plausible when viewed on sections (Figs. 3.3 - 3.8), as phase 5 fine-grained tonalite forms a carapace to the underlying phase 6 coarse-grained tonalite. In addition, contacts between the two phases generally exhibit a gradational increase in grain size and porphyritic texture from phase 5 to phase 6. An additional interpretation (Maryono, 2012), suggests that phase 5 is a separate, earlier intrusion than phase 6, with both producing Au-Cu ore, similar to the situation at Batu Hijau and Elang in Sumbawa (Maryono et al. 2012) and Brambang in Lombok (Rompo et al. 2014). A final interpretation (Cooke and White, pers. comm., 2016) suggests that phases 5 and 6 are two different textures of the one tonalite porphyry intrusion and that the fine-grained texture is an alteration or strain feature. After months of careful re-logging, petrographic analysis, type section construction (Fig. 3.3) and new geochronology data gained during this study (Chapter 4); all data supports that phase 5 fine-grained tonalite porphyry is a discrete, Early Pliocene (4.87 ± 0.42 Ma to 4.11 ± 0.51 Ma; Chapter 4) inter-mineralization intrusion that hosts the greatest volume of economic porphyry Cu-Au-Mo ore intersected to date (Figs. 3.3 - 3.8).

The Phase 7 inter-mineralization quartz diorite is interpreted to have cross cut phases 5 and 6 as a dike along a narrow, near-vertical feeder structure (Fig. 3.4). It balloons out to a cryptodome near the present day surface. Based on geochronological results (Chapter 4), phase 7 quartz diorite may be genetically related or contemporaneous with the mineralized phase 6 tonalite, but lacks mineralization at shallow levels. The post-mineralization phase 8 quartz diorite is located towards the south of the project (Fig. 3.1), and fortunately did not disrupt the porphyry ore body at Tumpangpitu.

3.5.8 Textural evidence for paleodepths of emplacement

Coarser-grained porphyry intrusions indicate relative slow cooling at depth, whereas finer-grained porphyry intrusions imply shallower levels of emplacement, although local variations could occur due to catastrophic versus incremental volatile release (Dilles et al., 2004; Seedorff et al., 2005). The main pre-ore intrusion (phase 2) at Tumpangpitu is a large equigranular pluton, more mafic, with lower quartz contents and absence of quartz phenocrysts (Figs. 3.15D, 3.16A - B). Both phase 4 very-coarse grained tonalite (Fig. 3.16E) and phase 6 inter-mineralization coarse-grained tonalite (Fig. 3.17E and D) have distinctive crystal-crowded porphyritic textures with > 15 % quartz content, mainly as 1 - 5 mm quartz eyes phenocrysts. The late- and post-mineralization intrusions return to quartz diorite (< 15% quartz)

compositions. Phase 7 (Fig. 3.17E - F) exhibits similar crystal-crowded porphyritic textures to phase 6, whereas phase 8 (Fig. 3.15B) has an equigranular medium-grained texture.

The question of pressure-depth estimates arises at Tumpangpitu - how much rock was eroded between the potassic alteration and telescoped advanced argillic alteration? In comparison to Batu Hijau where causative Cu-Au porphyry were emplaced at progressively shallower levels through time (Garwin, 2000; Maryono et al., 2012), at Tumpangpitu, the case appears to have been more complex. This will be discussed in detail in Chapter 7, after mineralogical data has been presented.

3.5.9 Magmatic evolution

The intrusive rocks at Tumpangpitu are interpreted to have been sourced from a deep magma chamber that underwent multiple cycles of crystallization and fluid release, and became increasingly fractionated with time, until the peak of porphyry Cu-Au-Mo mineralization. They then evolved to less fractionated compositions during waning and collapse of the magmatic-hydrothermal system, possibly due to an injection into the deep chamber of more primitive magma (e.g., Chiaradia et al., 2014). This inferred evolutionary trend is based on the compositions of the Late Miocene to Early Pliocene suite of intrusive rocks, which become more quartz-rich with time from phase 2 diorite, to phase 4, 5 and 6 tonalites, and return to more intermediate compositions with phase 7 and 8 quartz diorites. The mineralogical evidence for a reversal in fractional crystallization requires testing through whole rock geochemical analyses, which has not been possible in the current study, as sample sizes are too small and access to drillcore has not been possible since 2012.

3.5.10 Hydrothermal breccias

Hydrothermal breccias at Tumpangpitu have been distinguished from other breccia types by the abundance of hydrothermal cement, presence of wall-rock clasts that have evidence of pre-existing hydrothermal conditions (altered or mineralized clast or clasts containing veins and fragments of veins; Sillitoe, 1985), dike-like geometry, near-vertical orientation and a vertical extent of >100 m which suggest that fragmentation occurred due to hydrothermal processes. Hydrothermal breccia facies can record the evolution from the porphyry to the epithermal environment (e.g., Blackwell et al. 2014). The presence of alunite cement in the hydrothermal breccias at Tumpangpitu indicate a pH of ~2 - 4 (Jones and Hemley, 1964) and pyrophyllite in the roots of breccias imply temperatures > 260-270˚C (Reyes et al., 1990; Hedenquist et al., 1998; Cooke and Simmons; 2000; Deyell et al., 2005).

3.5.11 Diatreme breccias

On the basis of the characteristics described in Sections 3.3.7 and 3.3.8 and the evidence presented in Figures 3.22 - 3.30, the breccia complexes at Tumpangpitu and Tanjung Jahe display similarities to ancient and present-day diatreme breccias and maars produced by multiple explosive eruptions that cut deeply into the country rock (e.g., the Costa Giardini diatreme, southern Sicily: Calvari and Tanner, 2010; Lake Taal, Philippines and Rotomahana, New Zealand; White and Ross, 2011) and diatremes associated with a number of porphyry and epithermal systems elsewhere (Table 3.2). What appears to be aytypical, however, is the presence of both a pre-mineralization (Tanjung Jahe) and late-mineralization diatreme complex (Tumpangpitu) in the same district.

3.5.11.1 Diatremes - fundamental processes

Diatremes are the products of phreatomagmatic eruptive activity caused by interaction between subsurface magma and external water (e.g., Sheridan and Wohletz, 1983; Lorenz, 1986). They are downward-tapering, subsurface volcanic conduits, which may lie beneath maars (Lorenz, 1986; Cas and Wright, 1987; Martin et al., 2007). Diatremes are filled by volcaniclastic and epiclastic deposits, commonly stratified and collapsed wall-rock blocks (Lorenz, 1973). Lorenz (1986) and Lorenz and Kurszlaukis, (2007) suggest that the cross-sectional areas of diatremes are similar to those of maars (< 100 - 1,500 m) and their vertical extents may be several kilometres including root zones and feeder dikes. The surface morphology and the amount of slumping of blocks derived from the surface back into the crater can be dictated by the nature of the wall rocks (e.g., “hard-substrate” vs. “soft-substrate” maars; Lorenz, 2003; Auer et al., 2007). Tumpangpitu has been cut by a soft-substrate maar-diatreme complex that has a champagne flute morphology (Figs. 3.3 - 3.8) and large surface dimensions (Fig. 3.1; 3.1 x 2.2 km). These large surface dimensions are suspected to be due to migration and merging of multiple diatreme vents (Fig. 3.1).

Figure 3.40 shows idealized models of diatreme formation after Lorenz and Kurszlaukis, (2007). This model explains many of the features observed in the diatreme facies at Tumpangpitu, including the spatial distributions of un-bedded and bedded facies, the centripedal inward dip of proximal stratified rocks (Figs. 3.3 - 3.8) and outward dip (westwards) of distal stratified rocks (Fig. 3.24), location of mud-matrix breccias (maar; Figs. 3.1 and 3.28), evidence of polyphase brecciation (Fig. 3.26C) and destruction of root zone feeder dikes and juvenile clasts.

3.5.11.2 Relative timing of diatreme breccia events

Tumpangpitu is unique amoung well-documented porphyry and epithermal gold deposits in that the intrusion of the composite tonalite stock and Au-Cu-Mo porphyry and epithermal Au-Cu-Ag mineralization is bracketed by the emplacement of two large-volume diatreme breccia complexes.

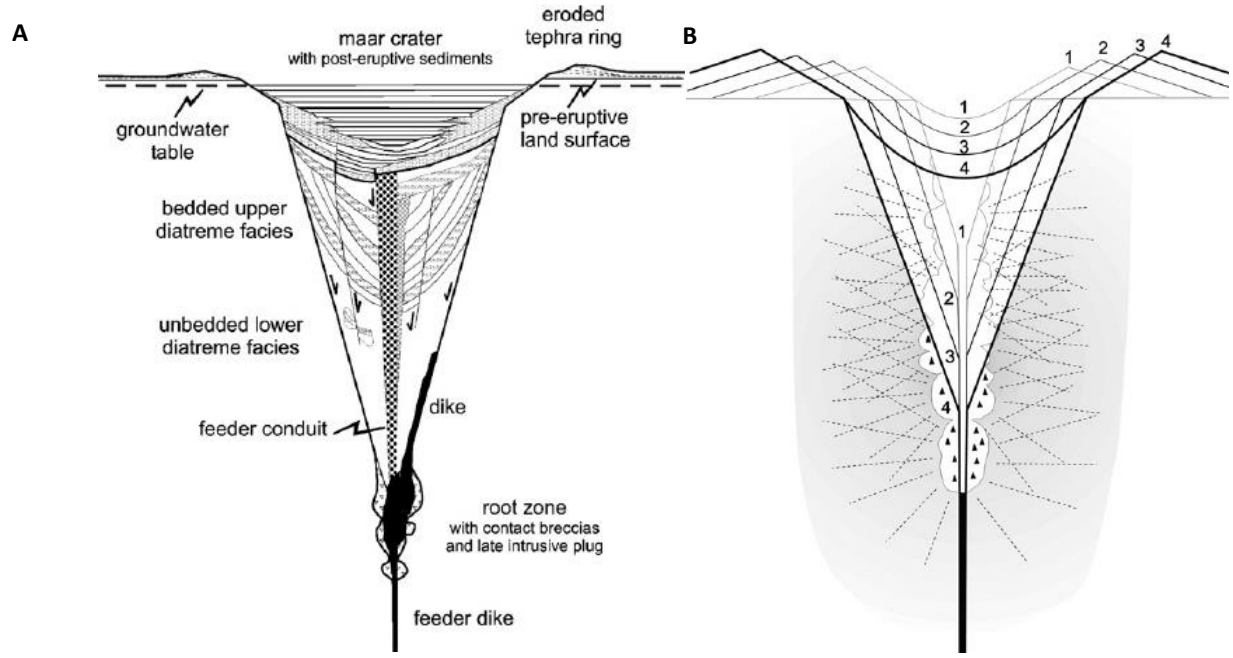

Figure 3.40. A) Schematic diagram of an idealized diatreme breccia pipe. B) Schematic evolution in four stages of a downward penetrating root zone with repeated collapse of the overlying diatreme and surrounding rocks and downward cutting on the feeder dike (Lorenz, 2003; Lorenz and Kurszlaukis, 2007).

Although late-stage diatreme formation is a relatively widespread occurrence in many porphyry and epithermal districts (e.g., Sillitoe and Bonham, 1984; Sillitoe, 1985) recognized pre-mineralization volcanic vents are relatively uncommon in porphyry deposits (e.g., Boyongan, Philippines; Braxton et al., 2009; Grasberg, Indonesia, MacDonald and Arnold, 1994; Table 3.2). The Tanjung Jahe breccia complex is not part of the Tumpangpitu diatreme complex, for reasons discussed in the following sections. The upward-flaring northern contact of the Tumpangpitu diatreme is well defined by drilling (Figs. 3.3 - 3.8). It has truncated both the mineralized porphyry and high-sulfidation deposits. The bulk of the breccia complex, including the throats and roots of multiple vents, lie 3 km to the south of Tumpangpitu (Figs. 3.1, 3.7 - 3.8). The Tumpangpitu diatreme is a late-stage manifestation of the Tumpangpitu hydrothermal system. It post-dates porphyry mineralization, based on the abundant porphyry mineralized clasts derived from the contact with the tonalite complex around 550 m depth to present day surface (Figs. 3.3 - 3.8). The Tumpangpitu diatreme also contains high-sulfidation mineralized clasts of vuggy quartz and enargite (Fig. 3.23C and D), and of massive covellite - bornite - pyrite (Fig. 3.23A) together with intermediate-sulfidation clasts of veins containing tetrahedrite-tennantite (Figs. 3.23B and 3.27B). The diatreme has been cut by vuggy quartz structures, hydrothermal breccia-hosted quartz - alunite - enargite high-sulfidation epithermal mineralization (e.g., gold oxide Zone A; Figs. 3.3 - 3.4), tetrahedrite-tennantite-bearing veins and distal galena - sphalerite veins. These crosscutting relationships demonstrate that diatreme formation postdated

both the porphyry and early-stages of the high- and intermediate-sulfidation epithermal mineralization, but also pre-dated later-formed intermediate-sulfidation, carbonate-base metal veins and high-sulfidation vuggy quartz and cemented breccias. The crosscutting relationships also imply a inter-epithermal timing of diatreme formation and repeated cycles of epithermal mineralization and alteration (e.g., Figs. 3.3 and 3.8). Similar observations have been made at the Salakan prospect, where tuffisite dikes crosscut the tonalite porphyries (Fig. 3.30C - F), resulting in localized reductions in grade. High-sulfidation-state veins of enargite with tennantite and alunite (Fig. 3.30B) crosscut the Salakan diatreme breccia. These observations suggest that the timing of the Salakan diatreme post-dates porphyry mineralization and is synchronous with high-sulfidation epithermal mineralization, as is the case at Tumpangpitu.

3.5.11.3 Tanjung Jahe pre-mineralization diatreme - Interpretation

In contrast to the late-mineralization Tumpangpitu diatreme (Late Pliocene), the pre-mineralization diatreme complex at Tanjung Jahe (Late Miocene) is interpreted to have formed from a relatively dry volcanic event that involved less water input. This interpretation is supported by a lack of abundant mineralized and strongly altered clasts. There is only weak alteration (chlorite - montmorillonite/nontronite ± illite) of the breccia matrix, and there are abundant unaltered clasts at Tanjung Jahe (e.g., Fig. 5A). The pre-mineralization timing of the Tanjung Jahe diatreme complex with respect to Early Pliocene mineralization at Tumpangpitu, has been interpreted from crosscutting relationships during mapping (Fig. 5E) and confirmed by absolute age determinations from U-Pb dating of zircons from the breccia matrix (Table 1, Fig. 10K). The presence of minor mineralized clasts of chalcocite - pyrite and copper oxides in the Tanjung Jahe diatreme lower facies breccia suggests that mineralization also occurred prior to 8.78 ± 0.22 Ma in the Tujuh Bukit district. The diatreme at Tanjung Jahe has not been drilled, and so its full morphology, including vertical extent, remains unknown.

3.5.11.4 Lower facies breccias at Tanjung Jahe - Interpretation

Wispy clasts with ragged edges (e.g., Fig. 5B), have been identified in the lower facies breccia at Tanjung Jahe. These are interpreted to be juvenile clasts, comparable to those recognized at Kelian (Davies et al., 2002), Wau (Sillitoe et al., 1984), Yanacocha (Turner, 1997) and Agua Rica (Landtwing et al., 2002). The transition between the coherent magma in the feeder dike and the juvenile clasts inside the pipe, occurs at the site where fragmentation of the magma and of the surrounding country rocks takes place (Lorenz and Kurszlaukis, 2007). The magma chamber from which the juvenile component was derived is inferred to be of andesitic composition. The juvenile clast-bearing breccias are matrix-supported, with a high (> 5 %) primary magmatic magnetite component, and have chaotic textures, indicating that disaggregation of the andesitic magma was more advanced in the lower facies breccias. Juvenile clasts are most likely to be best

preserved in the root zones of a diatreme, and are a key feature to recognize as they can provide evidence of a direct magmatic contribution to breccia formation and help to infer fragmentation processes (Davies, 2002, 2008a). The only intrusion phases that have been recognized as clasts are Phase 1 quartz diorite and rare hornblende gabbro, supporting the paragenetically early timing of the Tanjung Jahe breccia complex.

3.5.11.5 Upper facies bedded breccias at Tanjung Jahe - Interpretation

Normally graded breccias with minor low-angle cross-stratifications interbedded with fine ash layers that contain accretionary lapilli, are well exposed on the western face of the Tanjung Jahe breccia headland (Fig. 3.12). The presence of accretionary lapilli and low-angle cross stratification, in combination with features such as slumping along faults, channelling of beds and lack of sag structures beneath large fragments, suggests that low-temperature, wet pyroclastic base surge deposits overlie fall out and co-surge ash-fall deposits (e.g., Lorenz and Kurszlaukis, 2007; Calvari and Tanner, 2010; Sutopo, 2013). Base surge deposits are ubiquitous products of maar-forming phreatomagmatic or phreatic eruptions (Moore, 1967; Fisher and Waters, 1970; Lorenz, 1973; Walter, 1984). Deposits from slumping suggest that the early explosive activity produced deposits located closer to the initial eruptive vent than the preserved material exposed in outcrops at Tanjung Jahe. The accretionary lapilli may have formed in eruption columns of tephra ejected as Surtseyan jets and then fallen as a component of ash or, more probably, grew in the base surges themselves (Lorenz, 1974; Self and Sparks, 1978; Calvari and Tanner, 2010). Davies et al. (2008a) demonstrated that some accretionary lapilli formed subsurface, in the vents.

3.5.11.6 Lower facies breccias at Tumpangpitu - Interpretation

The lower facies diatreme breccia at Tumpangpitu features differ markedly from the upper breccia facies. The lower facies contain clasts set in a quartz-rich crystalline igneous cement and is devoid of stratification (e.g., Figs. 3.22D and 3.23D). The upper facies has a tuffaceous, fine-grained matrix (e.g., Fig. 3.23A). Whilst this siliceous groundmass of the lower breccia facies locally has a component of secondary quartz due to hydrothermal alteration, petrographic analysis has identified the quartz as being mostly of magmatic origin (Coote, 2010; Rohrlach, 2010).

The availability of magma at the time of diatreme emplacement is demonstrated by the presence of juvenile clasts in the breccia matrix (e.g., Sheridan and Wohletz, 1983; Davies et al. 2008a; Blackwell at al. 2014). Wispy clasts with ragged edges (e.g., Fig. 3.11B), have been identified as rare occurrences in the lower facies breccia at Tumpangpitu. These are interpreted to be juvenile clasts, as seen at Kelian (Davies et al., 2008) and many similar geologic settings (e.g., Wau, Sillitoe et al., 1984; Yanacocha, Turner, 1997; Agua Rica, Landtwing et al., 2002). The transition between the coherent magma in the dike and the juvenile clasts inside the pipe, must occur at the site where the fragmentation of the magma and of the surrounding

country rocks takes place (Lorenz and Kurszlaukis, 2007). The magma chamber from which the juvenile component was erupted is inferred to be of andesitic composition. These juvenile clast breccias are matrix-supported, with a high (> 5 %) primary magmatic magnetite component, and lack the jigsaw-fit textures adjacent to wallrock, indicating that disaggregation of the andesitic magma was more advanced in the lower facies breccias. Juvenile clasts can occur in the root zones of a diatreme and are a key feature to recognize as they can provide evidence of a direct magmatic contribution to breccia formation and help to infer fragmentation processes (Davies, 2002, 2008a; Sutopo, 2003). Juvenille clasts are rare in breccia facies at Tumpangpitu. This could be a result of their irregular shapes being easily modified during transport, abrasion and overprinting by silicification and clay alteration, so they have a low preservation potential (e.g., Davies et al., 2008).

The carbonaceous sedimentary rocks (mudstone), siltstone, sandstone and limestone clasts that occur in the lower breccia facies above the Tumpangpitu tonalite complex are interpreted to have been derived from the basal sedimentary package (e.g., Fig. 3.3). The clasts have similar compositions to these wallrocks, are pyritized (particularly the carbonaceous mudstone) and the clast gradations are from in-situ sedimentary units into monomict and then polymict breccias with increasing distance from the sedimentary wallrocks. It is interpreted that the carbonaceous sedimentary rocks surrounding the pipe were disrupted during emplacement and may have been brecciated due to boiling of ground water. At Kelian the Cretaceous silts were mobilized to form the muddy matrix of much of the phreatomagmatic fragmental material (e.g., Davies 2002, 2008a).

In contrast to the well-bedded facies in the upper levels of the Tumpangpitu diatreme, the breccia in the lower part of the diatreme lacks distinct bedding, and is well-mixed, massive and poorly sorted, similar to diatreme breccias elsewhere (e.g., Landtwing et al. 2002; Cannell et al. 2005; Lorenz and Kurszlaukis, 2007; Davies et al., 2008a; Calvari and Tanner, 2010; White and Ross, 2011). Vapour-solid fluidization during emplacement (Sparks et al., 2006), has been proposed to explain the homogenous "well-mixed" aspect of lower facies diatreme breccias. White and Ross (2011) describe "debris jets" formed by multiple eruptions in the root zone which can generate enough vapour through depressurization to mobilize newly fragmented magma and existing debris upwards. Debris jets will also contribute to homogenizing the vent fill and destroying any bedding features in the lower diatreme. Breccia in the lower levels of the diatreme could represent breccia from the eruptive/tephra ring collapsing early in the formation of the maar-diatreme and forming thick debris flow deposits on the small crater floor (Lorenz and Kurszlaukis, 2007). Due to the downward reduction in cross-sectional area of the diatreme, the subsiding beds, which still largely preserve their original volume, must either increase in thickness, or deform and disrupt the bedding during subsidence. At depth, the tephra is closer to the explosion sites and affected by numerous shock waves emitted from eruptions related to fuel-coolant interactions (Lorenz and Kurszlaukis, 2007; Wilson

and Head, 2007). These processes, along with primary texture-destructive silicification from hydrothermal alteration at Tumpangpitu, most likely contributed to relict juvenile clasts and root-zone feeder dikes being obscured or destroyed, as these features are not obvious in the current exposures and drillhole intersections of the Tumpangpitu diatreme. Features documented during the eruption of Volcano Island in Lake Taal, Philippines in 1965 by Moore et al. (1966), including the migration of explosion sites back and forth along a line parallel to the crater elongation, show similarities to the multiple NW-trending root zones at Tumpangpitu interpreted from cross sections and maps (e.g., Fig. 3.1).

3.5.11.7 Upper facies bedded breccias at Tumpangpitu - Interpretation

This breccia facies is characterized by well-developed stratification, including planar, dune bed and minor low angle cross beds. These features are consistent with deposition from turbulent, gas-rich flows at the transition from low to high-energy flow regimes (Walker, 1984; Valentine and Fisher, 2000).

The crater above the diatreme vents at Tumpangpitu is interpreted to have formed by phreatomagmatic to phreatic eruptions and subsequent sedimentary infill. This intra-maar sequence shares many similarities with the "crater infill breccia" at Wau, PNG, by Sillitoe et al. (1984); at Agua Rica, Argentina by Landtwing et al. (2012) and diatremes not related to porphyry-epithermal districts (Calvari and Tanner, 2010; White and Ross, 2011), including kimberlites (Sparks, 2013). The upper facies breccia at Tumpangpitu dips centripetally at 10 - 20˚ (influenced locally by underlying hostrock; phase 2 diorite; Figs. 3.3 - 3.8). Inward dips most likely resulted from subsidence and slumping of unconsolidated, partly water-saturated beds during accumulation of material within the maar (Lorenz and Kurszlaukis, 2007; Davies et al. 2008a; Sillitoe, 2013). The intra-maar sequence at Tumpangpitu is most likely both pyroclastic and epiclastic in origin and exceeds 550 m in thickness (Fig. 3.3 - 3.8). The epiclastic part of the intra-maar sequence is interbedded with and overlies the pyroclastic component. Clast size decreases, and the amount of ash matrix increases, away from the vent, becoming intercalated with the epiclastic component of the intra-maar sequence.

The stratified breccia facies shows increasing evidence of mixing and milling, transitioning upward to polymict lithic bedded breccias. Clasts of the upper-breccia facies range from sub-rounded to sub-angular with a wide spectrum of clast sizes, including clasts of breccia within breccia (polyphase brecciation; Fig. 7D). Evidence for polyphase brecciation implies propogation of the root zone downwards toward sites of eruption generation, causing repeated collapse and broadening of the volcanic crater. Growth of the diatreme engulfed the earlier-formed higher level parts of the breccia complex, incorporating them into deeper, younger parts of the diatreme (Lorenz and Kurszlaukis, 2007). The recycling of the lower facies diatreme breccia occurred by fragmentation of previously deposited breccia that was already partially consolidated (Calvari and Tanner, 2010). The upper facies breccia is most clearly characterized by its fine-

grained matrix, which is inferred to have formed during eruptions under high water/magma ratios and/or as a result of highly efficient fuel-coolant mixing (Lorenz and Kurszlaukis, 2007). The high proportion of wall rock fragments in the breccias of the upper facies breccias dictates that eruptions were fragmenting mostly country rock, not magma, reflecting the relative proportion of magma and country rock (Calvari and Tanner, 2010). The upper facies bedded milled breccias do not contain obvious juvenile clasts. This is most likely due to the increased distance away from the root zones, so that the wispy and blocky shapes were eroded, reworked and modified by hydrothermal alteration to the point where they cannot be identified on a textural basis (e.g., Davies et al., 2002, 2008a).

Upper facies bedded breccias at Tumpangpitu are characterized by narrow bands (1 mm to 2 cm) consisting of well- rounded (1 - 2 mm diameter) mineralized porphyry clast and wallrock fragments (Fig. 3.26). Most of the fragments that form the banding are mineralized tonalite porphyry. Larger (> 1 cm) sub-angular clasts contain high and intermediate-sulfidation mineralized and altered material (e.g., 3.25A, 3.26B and 3.27B). This difference in grain size is interpreted to reflect the greater distance travelled by the porphyry clasts towards the present-day surface (>500 m; Figs. 3.3 - 3.8), resulting in a greater degree of comminution compared to the epithermal clasts sourced from near the paleo surface. The banding is orientated both at right angles to core axis (near-horizontal; Fig. 3.26B) from surface to 30 m downhole, and near-parallel to the drillcore axis (near-vertical; Fig. 3.26D) > 30 m downhole depth. The vertical orientation is interpreted to be produced by flow of a particle slurry along near-vertical structures (e.g., Cliff fault; Fig. 3.3; Rohrlach, 2011). The near-surface sub-horizontal orientation are interpreted to be representative of the gently dipping paleosurface of the underlying wallrocks and gently inclined champagne flute morphology of upper levels of the soft substrate maar-diatreme at Tumpangpitu.

The upper facies breccia at Tumpangpitu is characterized by imbricated clasts, graded bedding (Fig. 3.26), sedimentary structures and 1mm to 1 cm diameter accretionary lapilli (Fig. 3.25C and 3.26B). Accretionary lapilli at Tumpangpitu that occur in sub-horizontal beds are interpreted to have formed by air fall (e.g., Davies et al. 2008a; Calvari and Tanner, 2010; Blackwell et al. 2014). The accretionary lapilli suggest a subaerial origin for the well-stratified upper breccia facies at Tumpangpitu (as opposed to gas-segregation pipes in the subvolcanic environment e.g., Self, 1983; Carman, 1994) and were probably also formed by progressive accretion of numerous layers of wet volcanic particles (Sillitoe, 1984).

Similar to observations made elsewhere (e.g., Landtwing et al., 2002; Lorenz and Kurszlaukis, 2007; Davies et al., 2008a), both lower and upper facies breccia show a similar sequence of breccia textures at the contact of the vent with the immediately surrounding country rocks. The organization ranges from monomictic or “contact breccia” (Clement, 1982) and jigsaw fit on the margins to polymictic, well mixed and chaotic in the voluminous center of the diatreme. This sequence of breccia textures are interpreted to have formed during the phreatomagmatic eruption that generated the breccias by fragmentation of wall

rocks by mechanical abrasion; and/or hydraulic fracturing or phreatomagmatic brecciation in response to pressure gradients between the wall rocks and evacuated conduits (Lorenz and Kurszlaukis, 2007).

Eruptive activity that gives rise to the ascent of a column of brecciated material in diatremes including kimberlite pipes was periodically followed by subsidence (e.g., Lorenz and Kurszlaukis, 2007; White and Ross, 2010; Sillitoe, 2013; Sparks, 2013). Evidence for ascent of material in the diatreme at Tumpangpitu is provided by the tuffaceous matrix to the breccia (Figs. 3.22 - 3.27); the presence of sedimentary and andesitic rock clasts, given that these rock types do not abut the diatreme at or near the surface (Fig. 3.2); tonalite clasts hosting porphyry-type mineralization (Figs. 3.22, 3.25 and 3.26) and epithermal mineralized clasts (Figs. 3.25A, 3.26B and 3.27B). Significant subsidence of material in the Tumpangpitu diatreme is shown to have taken place by (1) the occurrence of both large (> 2 m) and small subsided blocks of phase 2 diorite and phase 7 quartz diorite (Fig. 3.3) in the diatreme, although most of these subsided blocks match the adjacent wall rocks, and (2) the occurrence of fragments of charcoal (carbonized wood) overprinted with pyrite, as inclusions in the breccia (Fig. 3.25D). The presence of charcoal fragments indicates incorporation of material derived from the paleo-surface, with slumping of vegetated surficial blocks to depths of over 100 m below surface.

3.5.11.8 Mud-matrix breccias at Tumpangpitu - Interpretation

Mud-matrix-supported breccias are prevelant in the Zone B gold oxide area, interspersed with polymictic lithic breccias (Figs. 3.1 and 3.28). The mud-matrix breccias have been crosscut by the Zone B north-trending fault system, which contains high-sulfidation state hydrothermal breccias (Fig. 3.1). A late phase of high-sulfidation epithermal activity therefore post-dated diatreme formation in Zone B.

The facies is interpreted to be associated with sedimentation in a maar paleoenvironment, representing an upper facies within the larger, multiphase diatreme breccia complex at Tumpangpitu. The process of maar lake formation after the end of diatreme eruptions is commonly a result of the groundwater table restoring itself to the original levels after the eruption ends (Lorenz, 1986). The 1 x 0.5 km crescent zone of mud-matrix breccia defines the extent of the maar (Fig. 3.1). The mud-matrix breccias at Zone B contain blocky angular quartz diorite clasts (Fig. 3.28A), as well as clasts with wispy curviplanar margins (Fig. 3.28B). Subsurface interaction of magma with ground water or hydrothermal fluid may have produced these distinctive ragged-shaped ("wispy") juvenile magmatic clasts derived by fragmentation of a parental magma (Sheridan and Wohletz, 1983). The wispy clasts at Zone B are interpreted to be a variety of intrusive peperite produced by mingling of magma with unconsolidated, wet mud. The peperite-like magma-country-rock clast mixtures get ejected during subsequent eruptions as xenolith-bearing juvenile pyroclasts (e.g., Lorenz and Kurszlaukis, 2007). It is interpreted that the disaggregation of the late quartz diorite intrusion into wispy and blocky clasts generally resulted in complete fragmentation of the intruding magma

batch within the unconsolidated sediment. It is likey that partly consolidated maar-lake sediments were periodically incorporated into the underlying breccia pipe at Zone B. In many areas, the mudstone appears to have been injected or flowed downwards into fractures and cracks within the clasts (Fig. 3.28B). They could have also been injected into breccias as a result of eruption and over-pressuring of soft maar- lake sediments by fallout within the vent of the maar (Rohrlach, 2010). It is likely that the mudstone matrix is a combination of pulverisation of the mudstone-siltstone-sandstone basement rock surrounding Tumpangpitu (Fig. 3.1), combined with shallow-level mud generated in situ during diatreme eruptions. It is unlikely that all the mud generated in the maar could be streaming up from underlying mudstone basement. It most likely formed during multiple phreatomagmatic eruptions as fine-grained beds deposited by suspension settling in lacustrine settings that were then disrupted by later explosions, similar to observations at Wau, PNG (Sillitoe et al., 1984) and recent maar volcanism at the Taupo volcanic zone in New Zealand (e.g., Simmons, 1995; Lorenz, 2003). Mud was then deformed and squeezed in between the clasts (Fig. 3.28B).

In post-eruptive times, the maar crater was probably filled by coarse sediments on its margins and finer grained lacustrine sedimentary rocks in its center (e.g., Lorenz and Kurszlaukis, 2007). The diatremes at Tujuh Bukit appear to have lost a proportion of their tuff ring ejecta deposits (Fig. 3.1), similar to many other Tertiary and older maar-diatreme volcanoes (Table 3.2; Lorenz and Kurszlaukis, 2007).

3.5.11.9 Tuffisite sand and pebble dikes at Tumpangpitu - Interpretation

The terminology of ‘tuffisite dikes’, originally coined by Cloos (1941), has been used to classify rocks that are texturally tuff-like, but demonstrably intrusive, relating to contemporaneous magma injection and degassing (Allan et al., 2011). The tuffisite sand and pebble dikes that surround the main vent facies at Tumpangpitu and other diatremes in the Tujuh Bukit district (Fig. 3.30) are interpreted to form from fluidization of rock fragments in upward escaping fluid channels similar to those described at Kelian, Indonesia, by Davies et al. (2008a) and compositionally heterogeneous late dikes that radiate from the core of the Southern porphyry at Mount Leyshon, Queensland, Australia documented by Allan et al. (2011).

Observations of crosscutting relationships and occurrence of sand and pebble dike material as breccia clasts (e.g., Fig. 3.29) indicate multiple styles of dike formation. Dikes are most common in contact zones between two different lithologies e.g., between phase 5 and 7 porphyries, or parallel to bedding in sedimentary rocks beneath Zone C (Figs. 3.3 - 3.6). The rounded clasts in milled breccias and pebble dikes are generally attributed to shearing, rotation, and attrition of originally angular rock fragments during transport in a particle-charged gaseous stream (e.g., Boothroyd, 1971). Extensive downward or upward movement of clasts in breccia pipes has been well documented in several mining districts (e.g. Clark, 1990). Sand and pebble dikes most likely formed throughout the post-porphyry and pre-inter and post-epithermal

history at Tumpangpitu genetically related to the phreatomagmatic diatreme activity and venting. Due to their permeable matrix, they locally contain considerable chalcocite (Fig. 3.30C).

3.5.11.10 Distal facies bedded apron breccias at Tumpangpitu - Interpretation

Excellent exposures of fine-grained polymictic lithic milled breccia intercalated with laterally continuous (> 1.5 km) well bedded siltstones, sandstones and mudstones (Figs. 3.1 and 3.24) crop out along the western coastline of Tumpangpitu. They dip between 25˚ and 30 ˚ westwards away from the diatreme vents. This facies is interpreted to represent the distal fringe of the uppper portions of the diatreme body. Bedding is interpreted to have formed insitu due to its continuity along the coastline, whereas other bedded intervals in drillcore (e.g., Fig. 3.26) that are proximal and dip towards the vents are interpreted to be both insitu and disrupted surficially-derived blocks. The outwardly dipping facies is interpreted to define an apron around the flanks of the crater-maar and underlying vents that was subsequently re-worked and affected by fluvial processes (deposition of sedimentary interbeds; Fig. 3.24). The features and location of this breccia facies with respect to the inferred diatreme vents (Fig. 3.1) are consistent with the eroded tephra ring (Fig. 3.31A) described by Lorenz and Kurszlaukis, (2007). Since this bedded breccia is present largely beyond the maar at Zone B (1.4 km to the east), it was most likely originally of substantially greater extent. Similar remnants of the northern and eastern portions of the maar encircling tuff ring apron are likely to exist, but concealed underneath thick soil profiles and teak forest.

3.5.11.11 Relationship of diatreme activity to epithermal mineralization

Groundwater ingress to late-mineralization porphyry stocks (e.g., phase 7 quartz diorite) could have been the trigger for late stages of phreatomagmatic activity at Tumpangpitu (e.g., Sheridan and Wohletz, 1983; Davies et al., 2008; Sillitoe et al., 2013). With the infiltration of groundwater into diatreme tephra, hydrothermal systems are established above and around later intrusions, evidenced at Tumpangpitu by later hydrothermal breccias crosscutting the diatreme breccias (e.g., Fig. 3.3). Such meteoric fluids were presumably also responsible for forming diatremes, in both shallow-level epithermal settings (e.g., Wau, Papua New Guinea: Sillitoe et al., 1984; Cerro de Pasco, Peru: Baumgartner et al., 2009; Pueblo Viejo, Dominican Republic: Russell and Kesler, 1991) and the late stages of porphyry deposit development, as a result of their interaction with hot magmas.

3.6 Conclusions

The regional scale fault-fracture directions are repeated in the Tujuh Bukit district (Fig. 3.32), reflecting the fractal or scale-invariant nature of such fault-fracture systems (Fig. 3.32; Clements et al. 2009; Gray, 2011). Across the Tujuh Bukit district, there is a strong relationship between faulting and

hydrothermal activity, particularly high-sulfidation epithermal mineralization. The mapping of inter-mineralization and post-mineralization faults, aided by SWIR mapping of alteration minerals (Fig. 3.38) was crucial to provide a structural constraint for the construction of the type section and subsequent geological, alteration and resource models for Tumpangpitu.

At Tumpangpitu, detailed drill core logging, type section construction and mapping as part of this study has led to a better understanding of the wallrocks, and also the intrusive phases that span the entire hydrothermal alteration-mineralization sequence. The documentation of different types of breccias into volcanic, hydrothermal and phreatomagmatic breccia phases, along with the recognition of eight discrete porphyry intrusions and each of their associations with mineralization, was crucial for developing the geological model used to calculate the indicated porphyry and epithermal resources for Tumpangpitu.

Diatreme breccias were not initially recognized at Tujuh Bukit during early exploration and drilling. The features from the diatreme complex at Tumpangpitu highlighted in Figures 3.22 to 3.27, including evidence of clasts of porphyry and epithermal style mineralization, fluidization, mixing, rounding and comminution of clasts, the presence of accretionary lapilli and charcoal fragments at depths greater than 100 m below present-day surface, are consistent with a large diatreme breccia complex that formed by multiple eruptions from vents during catastrophic phreatomagmatic activity. The Tumpangpitu diatreme preserves a transition downwards from bedded breccias to clast-supported breccias with sandy matrix to a crystalline breccia with a fine-grained porphyritic tonalite cement in the centre to lower core of the crater. Graded, matrix-rich epiclastic sedimentary rocks subsequently filled the crater.

Good evidence exists at Tanjung Jahe of a lower facies breccia with juvenille magmatic clasts, rare mineralized clasts and an upper stratified facies incorporating material from phreatomagmatic airfall deposits around the fringes of the diatreme root zone, locally slumping and forming surge deposits (e.g., Fig. 3.12). The Tujuh Bukit district has evidence for both a pre-mineralization diatreme complex at Tanjung Jahe and a late mineralization diatreme at Tumpangpitu, the latter was associated with higher water contents and a significant, mineralized magmatic-hydrothermal system.

The presence of rare mineralized clasts in the Tanjung Jahe diatreme suggests that mineralization also occurred prior to the Late Miocene (8.78 ± 0.22 Ma) in the Tujuh Bukit district. Late Miocene phreatomagmatic activity in the Tujuh Bukit district may be related to diatreme breccias that formed post-Middle Miocene porphyry-style mineralization, as recognized in other parts of east and central Java (e.g., Singgahan, Trenggalek and Selogiri; Maryono et al., 2017), and therefore provides additional exploration targets. The excellent exposures of maar-diatreme facies in outcrop and drillcore from the Tujuh Bukit district can be used as an aid to increase recognition, documentation and understanding of maar-diatremes, to drive accurate generation of deposit and resource models, as well as advance understanding of other diatreme systems not related to porphyry-epithermal mineralization.

Chapter 4: U-Pb Geochronology

4.1 Introduction

This chapter presents the first geochronological data for the Tumpangpitu deposit, providing temporal constraints on the volcanic and sedimentary host rocks, seven of the intrusive units, including the main mineralized intrusions, and two diatremes. Copper-gold-molybdenum mineralization at Tumpangpitu occurred in response to multiple phases of intrusive activity. One of the main aims of this PhD project has been to determine the timing and duration of magmatic activity by obtaining absolute age dates by U-Pb laser ablation-inductively coupled plasma mass spectrometry (LA-ICPMS) on zircon samples from all geological units at Tumpangpitu, and a selection of porphyries from other prospects in the Tujuh Bukit district. To gain a perspective of age variations of economic and sub-economic porphyries in the eastern Sunda Banda arc, a review of published geochronological data has been conducted and two additional samples were analyzed from a porphyry at Singgahan, Trenggalek project, approximately 120 km west of Tumpangpitu (Fig. 4.4) to help constrain metallogeny in this fertile magmatic arc. Chapter 5 presents Re-Os and ^{40}Ar-^{39}Ar geochronological results that constrain ages of alteration and mineralization.

4.2 Methodology

Zircon is a highly refractory mineral and is known to be capable of surviving numerous sedimentary cycles, hydrothermal alteration, magmatic episodes and diagenesis (e.g., Mange and Maurer, 1992; Kosler and Sylvester, 2003). Zircon U-Pb geochronology was undertaken at the Centre of Excellence in Ore Deposits (CODES), University of Tasmania, using the LA-ICPMS method. Thirty-nine samples of intrusions, diatreme breccias, volcanic and sedimentary host rocks from Tumpangpitu and other porphyry prospects from the Tujuh Bukit region and eastern Sunda Banda arc (Figs. 4.1 - 4.4) were selected for zircon dating, based on the units defined from field relationships (Fig. 4.1) and section construction (Fig. 4.2).

In order to constrain the absolute timing and duration of magmatism, samples were collected from each mapped intrusive phase, spanning the entire alteration-mineralization sequence. The initial sampling targeted 1 - 2 kg samples of drillcore and rockchips from coastal exposures from the least altered, unweathered and coherent zones, where textural preservation allowed the units to be identified with confidence. A minor portion of samples were also taken from zones of intense alteration, where primary lithological textures have been obliterated, in order to resolve younger intrusive rocks from their wall rocks. Due to limited access to the project after 2012, later sampling had to utilise samples from petrographic offcuts; of which only a few samples contained enough zircons for U-Pb analysis. In total, twenty-six drillcore samples were taken from intrusive rocks, four from andesitic and sedimentary basement rocks,

one from a volcanic breccia and one from the Tumpangpitu diatreme. Drillcore samples from a selection of Tujuh Bukit porphyries (Fig. 4.12), including Katak, Zone B and Pulau Merah island and two samples from Trenggalek were also included to constrain the temporal evolution of magmatism in the district and wider eastern Sunda-Banda arc. Four surface rock chip samples were collected for analysis from coastal exposures: two samples of matrix and intercalated sedimentary rocks from the Tanjung Jahe diatreme breccia, a sandstone from the north-western sedimentary package and a sample of diorite from the Pulau Merah coastline (Fig. 4.1).

A second round of U-Pb analyses was conducted after multiple age populations - indicative of inherited zircon cores, were identified in data from three samples (Table 4.3; Figs. 4.7 - 4.8). Cathodo-luminescence (CL) imaging of these zircon grains (Fig. 4.7) was conducted to highlight characteristics of their growth history, to allow more precise targeting with the laser probe during rim-core analyses.

4.2.1 Zircon separation and preparation

Zircon separations were performed at the Centre of Excellence in Ore Deposits (CODES), University of Tasmania. Approximately 100 to 400 g of rocks were was repeatedly sieved and crushed in a Cr-steel ring mill to a grain size less than 400 microns. Heavy minerals were separated using a gold pan and magnetic minerals were separated using a Fe-B-Nd magnet. The zircons were hand-picked from the heavy mineral concentrate whilst viewed under a microscope in cross-polarised transmitted light. Each sample contained between 7 and 30 euhedral to subhedral, doubly-terminated zircon crystals, with a variety of sizes (30 µm and 100 µm) and morphologies (Fig. 4.7). The selected crystals were placed on double sided sticky tape and epoxy glue was then poured into a 2.5 cm diameter mould on top of the zircons. The mount was dried for 12 hours and polished using silica carbide sandpaper and a 0.3 micron alumina polishing lap. The samples were then washed in distilled water in an ultrasonic bath.

4.2.2 Laser ablation ICP-MS method

The LA-ICPMS method is commonly used for U-Pb dating of zircons (e.g., Fryer et al., 1993; Compston, 1999; Black et al., 2003; Kosler and Sylvester, 2003; Black et al., 2004; Jackson et al., 2004; Chang et al., 2006; Harley and Kelly, 2007). Laser microprobes operate with spot diameters of 20 - 40 microns, comparable to ion microprobes, but the laser beam is used to vaporize a volume of zircon by drilling several microns deep into the zircon grain, and then collecting and analysing the ablated material. Microbeam techniques allow in-situ analysis of very small volumes and thus high-spatial resolution (Kosler and Sylvester, 2003). In addition the analyses can be done relatively rapidly (many tens of analyses per day for LA-ICPMS). In-situ microbeam techniques, coupled with CL imaging are essential for characterizing complex, zoned zircons exhibiting evidence for inheritance (i.e., older cores with younger overgrowths)

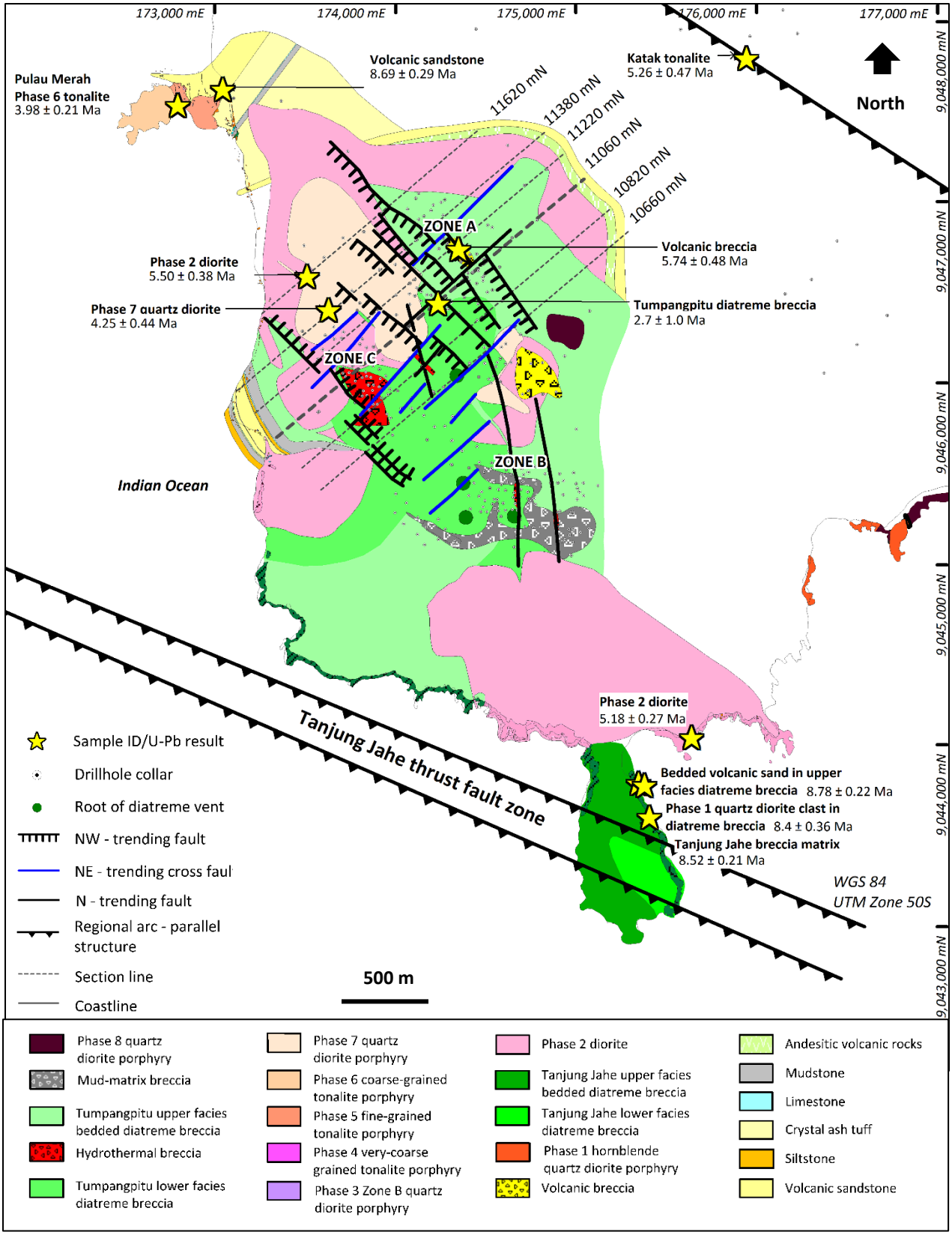

Figure 4.1. Geologic surface plan of Tumpangpitu showing surface and shallow drillhole sampling locations with results of U-Pb zircon analyses. All analytical results are listed in Table 4.1.

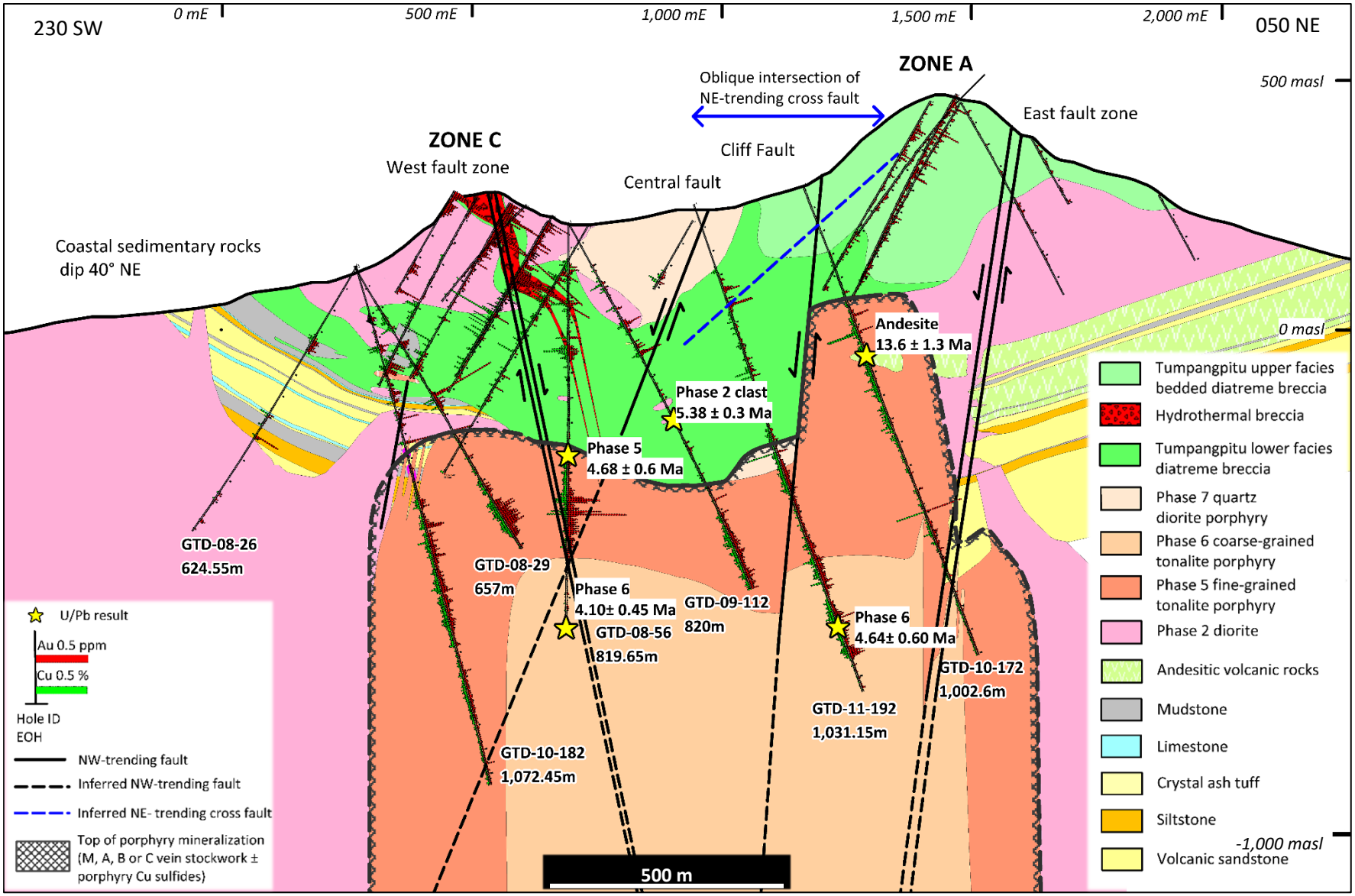

Figure 4.2. Sampling locations and results of U-Pb zircon analyses on type section 11060 mN at Tumpangpitu. Section line location shown on Fig. 4.1. All analytical results are listed in Table 4.1.

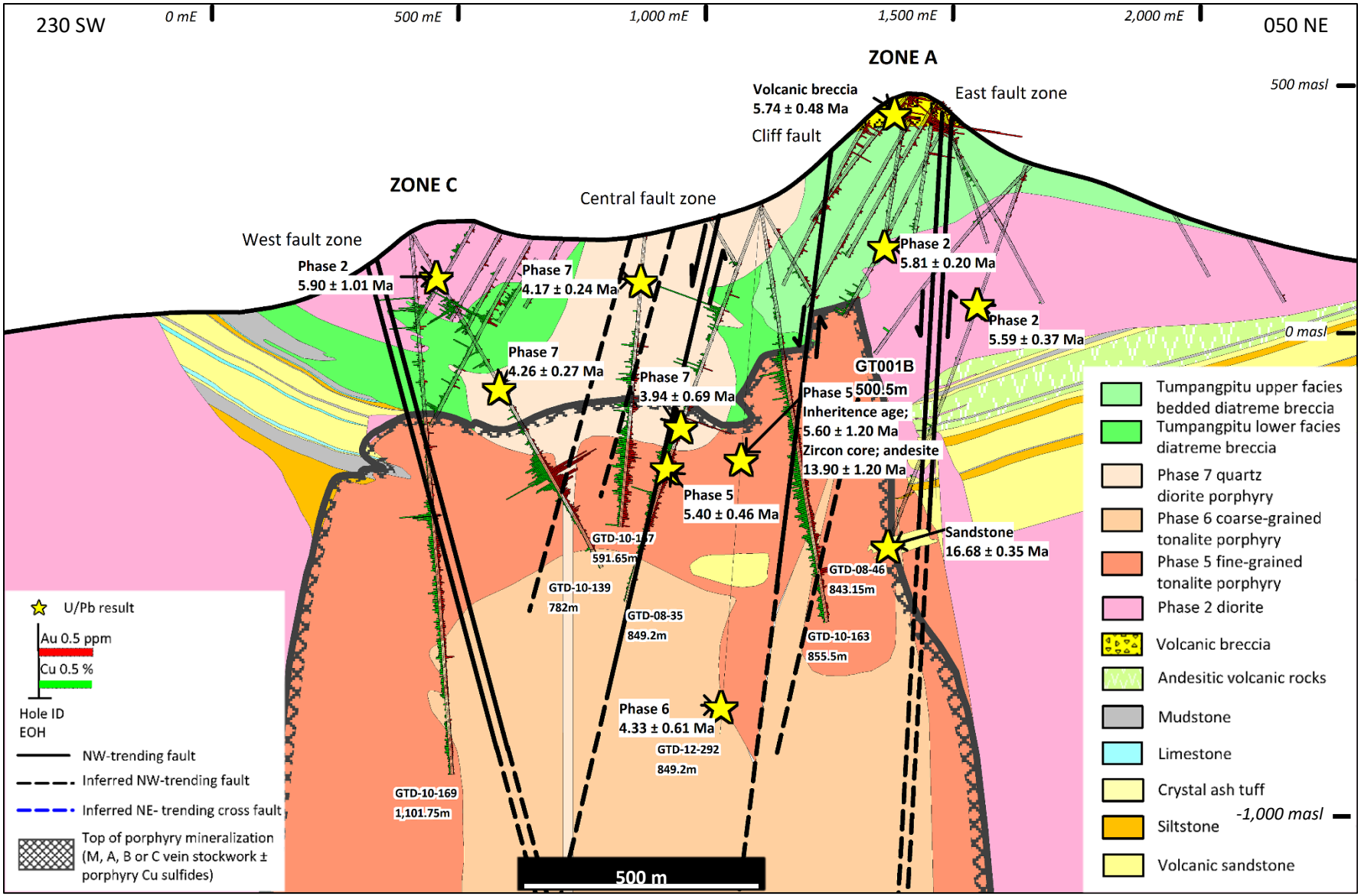

Figure 4.3. Sampling locations and results of U-Pb zircon analyses on section 11220 mN at Tumpangpitu. Section line location shown on Fig. 4.1. All analytical results are listed in Table 4.1.

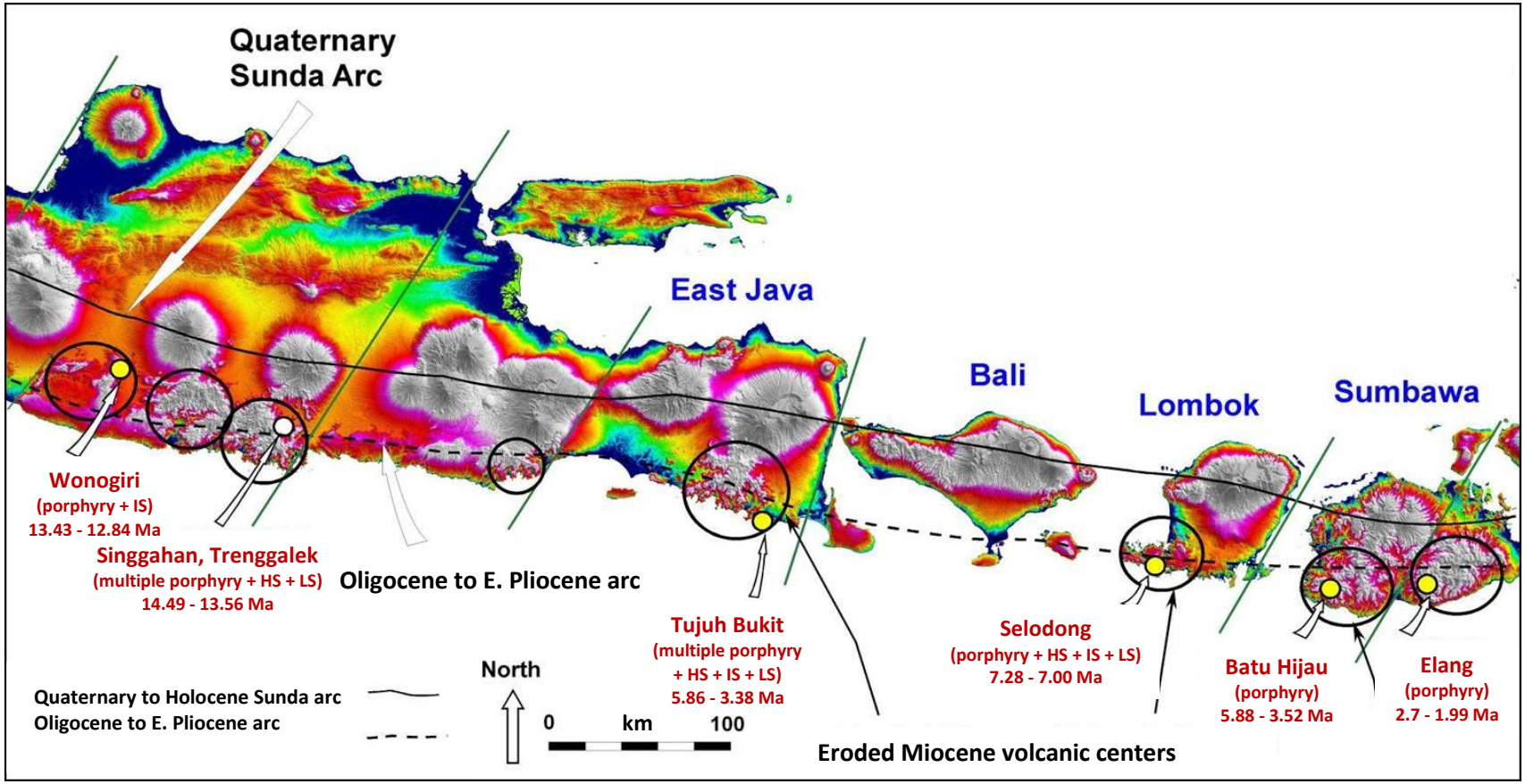

Figure 4.4. Digital elevation model (coloured image) and Au-Cu deposits and prospects along the Oligocene to E. Pliocene eastern Sunda-Banda magmatic arc and location of active volcanism (modified after Rohrlach, 2011). Sources of zircon age data from Garwin (2000), Maryono et al. (2017) and this study. Abbreviations: HS = high-sulfidation epithermal, IS = intermediate-sulfidation epithermal and LS = low-sulfidation epithermal-style mineralization.

from volcanic rocks. They are also required for characterizing detrital populations in sedimentary rocks, which can provide robust estimates of the minimum age of a sequence.

4.2.3 Instrument operating parameters

The U-Th-Pb isotopic compositions of zircons were analyzed on both an Agilent 7500cs and Agilent 7900 quadrupole ICPMS with a 193 nm Coherent Ar-F gas laser and the Resolution S155 ablation system at CODES. Isotopic masses collected were ^{49}Ti, ^{56}Fe, ^{90}Zr, ^{178}Hf, ^{202}Hg, ^{204}Pb, ^{206}Pb, ^{207}Pb, ^{208}Pb, ^{232}Th and ^{238}U, with each element being measured every 0.18 seconds. Longer counting times were used for the Pb isotopes (0.025 seconds) and for U, Th, Hg and Ti (0.01 seconds), than for the other elements (0.002 seconds). Between 7 and 22 spot analyses were collected per sample (not including reference zircons). Spot analyses generally focused on the younger zircon rims of larger crystals (> 40 µm), and only on cores of crystals smaller than the 32 µm beam diameter (e.g., Fig. 11). Each analysis on the zircons began with a 30 second blank gas measurement followed by a further 30 seconds of analysis time when the laser was switched on. Zircons were analyzed with a ~30 µm beam using the laser at 5 Hz and a density of approximately 2 J/cm^2. A flow of helium carrier gas at a rate of 0.35 litres/minute carried particles ablated by the laser out of the chamber to be mixed with argon gas and carried to the ICP-MS.

4.2.4 Data collection and reduction

The downhole fractionation, instrument drift and mass bias correction factors for Pb/U ratios on zircons were calculated using the 91500 zircon of Wiedenbeck et al. (1995) and updated values from Horstwood et al. (2016). The NIST610 was used to calibrate the ^{207}Pb/2^{06}Pb ratio and trace element concentrations using the method of Kosler (2001) with ^{90}Zr as the internal standard element and assuming stoichiometric proportions. Validation of the calibration was done with a range of secondary zircon reference materials of know age: AusZ-5 (Kennedy et al., 2014), GJ-1 (Jackson et al., 2004), using updated values from Horstwood et al. (2016), Penglai (Li et al., 2010), Plesovice (Slama et al., 2008), and Temora (Black et al., 2004). For the zircons with relatively low concentrations of Pb (< 100 ppb) the 'ratio of the mean' method for the isotope ratios was used to avoid bias in the detector at low counts from either low sample concentration or short dwell times (Horstwood et al., 2016 and Fisher et al., 2010) .

4.2.5 Zircon rim-core analyses

A second round of U-Pb analyses was conducted after multiple, heterogeneous age populations - indicative of inherited zircon cores, were identified in data from three samples (GTD-12-292; 513 m, GTD-10-166; 1082.7 m and GTD-08-35; 472.1 m; Table 4.1; Appendix Table 1A). Cathode-luminescence (CL) imaging of these zircon grains (Fig. 4.8) was conducted at the University of Tasmania to highlight

characteristics of their growth history, to allow more precise targeting with the laser probe during rim-core analyses. Analytical precision of LA-ICPMS zircon analyses is primarily a function of count rate, which is controlled by spot diameter, abundance of U and Th, and age of the grain (Meffre et al., 2008). Areas of zircon overgrowths on the three samples were then identified and manually re-targeted by reducing the laser beam to 17 microns, to increase the resolution of dating of the overgrowth. However, the smaller spot size had a negative effect on the counting statistics of ^{206}Pb. Another issue with reducing the laser beam diameter on young zircons is the high relative abundance of common Pb, making it hard to measure any radiogenic Pb, as there is not enough time for the decay of U to produce sufficient ^{206}Pb for precise dating which was a minor issue in samples from this study (Li et al., 2008).

4.3 U-Pb age data

Tables 4.1 and 4.2 summarize analytical results for each laser spot analysis. Dates for the 516 individual analyses ranged between 22.7 and 2.1 Ma, with 32 exceptions shaded grey in Appendix 1. In this age range, these results represent approximately 0.047 - 0.50 % of the ^{238}U/^{206}Pb half-life of 4.5 Ga. The radiogenic ^{206}Pb component is small in young zircons such as these. Common ^{206}Pb comprises a large proportion of the total ^{206}Pb in certain samples, a problem compounded by low U-zircons; because they have not in-grown as much radiogenic Pb (Li et al., 2008). Some of the zircons analyzed contained only common Pb, with no radiogenic Pb detected (Appendix 1). Calculation of ^{238}U/^{206}Pb ages has therefore excluded two spot analyses with a high proportion (> 70 %) of common ^{206}Pb, because these samples inflated the uncertainty in the common-Pb-corrected age determinations. Three additional spot samples from inherited zircons were excluded from age calculations, as they were deemed mixtures of rim and cores (Table 4.3). Concordia intercept ages were calculated from the lower intercept of the zircon analyses on the Tera-Wasserburg plots, anchoring to a common Pb composition of 0.836 ± 0.01 for the ^{207}Pb/^{206}Pb ratio.

The Isoplot software (Ludwig, 2001) was used for plotting and calculating sample ages and 2σ errors of each of the zircon fractions. Systematic errors are then added to these 2σ standard errors and are reported in Table 4.1 for the intercept age of each sample. The full dataset is presented in the electronic appendix. Errors in text do not include systematic errors as they are relatively small compared to the counting statistic errors.

Figures 4.5 to 4.7 present the error-weighted age spectra (^{207}Pb corrected ^{206}Pb/^{238}U ages) and Concordia plots. Three samples listed in Table 4.1 (GTD-12-292; 513 m, GTD-10-166; 1082.7 m and GTD-08-35; 472.1 m) yielded dual age dates, taken as evidence of zircon inheritance. Figure 4.8 presents the CL-images of reanalyzed zircons from the three samples. All U-Pb age data is summarized in Figure 4.10. Appendix Table A1 tabulates all details of each U-Pb zircon analyses completed in this study.

4.3.1 Zircon rim-core analyses

Zircon is a refractory mineral that can have a complicated magmatic growth history, forming xenocrysts and inherited older cores within newly crystallized zircons (Chiradia et al., 2013). Xenocrysts are zircon crystals incorporated into magma from the country rocks that lack any new magmatic zircon overgrowths. In contrast, inherited zircons form cores to new zircon rims that crystallized from the host magma. Inherited zircons are distinctly older than the crystallization age of the rock (Miller et al., 2007). All zircons analyzed display oscillatory and sector zoning that is typically igneous (Hoskin and Schaltegger, 2003). All zircons contain magmatic sector zoning which in many examples shows replacement by structureless high-luminescent zones. Three samples listed in Table 4.3 (GTD-12-292; 513 m, GTD-10-166; 1082.7 m and GTD-08-35; 472.1 m) yielded dual age dates, taken as evidence of zircon inheritance. The three samples were then imaged using cathode-luminescence (CL) at the University of Tasmania in order to evaluate whether the individual zircon crystals had rims overgrowing older zircon cores (Fig. 4.8). The images in Figure 4.8 show that the 32 micron pits from initial laser analysis had analyzed material from both rim and core, therefore producing an apparent age of 6 Ma ± 1.3 Ma that was intermediate to the known ages of basement rocks and inter-mineralization porphyries. Areas of zircon overgrowths on the three samples were then identified and manually re-targeted by reducing the laser beam to 17 microns, to increase the resolution of dating of the overgrowth (Fig. 4.8; Table 4.3). Sample GTD-12-292; 513 m (Table 4.3, Fig. 4.8C, D and E) yielded a core age of 13.9 Ma ± 1.42 Ma (2 σ error; 10 analyses) and an overgrowth age of 5.6 Ma ± 1.2 Ma (2 σ error; 8 analyses). This sample is interpreted to comprise zircon cores derived from the older andesitic basement that was intruded by the phase 5 early inter-mineralization fine-grained tonalite, contributing younger, overgrowth rims to the inherited zircon grains (Fig. 4.8C, D and E). Three data points in between the two ages have not been included in the new age calculation, as they are interpreted to be mixtures of rim and core material (Table 4.3, Figs. 4.8C, D and E).

Table 4.1. Summary of new $^{206}Pb/^{238}U$ age determinations from intrusive and host rocks at Tumpangpitu.

Sample ID/depth (m)	Coordinates /RL (m)	Mine unit	Alteration	Mineralization	Veins/paragenesis	Age (Ma) ± 2σ	Number of analyses	Rock description
Sedimentary and andesitic volcanic rocks								
GTD-10-138/964	E174148 N9046090/266	SED	Quartz - illite	-	-	20.67 ± 0.47/ 0.50	14	Fine-grained basement sedimentary rock
GTD-08-46/825.5	E174512 N9046872/338	SED	Quartz - illite	-	-	16.68 ± 0.35/ 0.37	15	Fine-grained sandstone basement with 1 - 2 cm laminations
GTD-12-292/513	E174082 N9046550/257	AND	Quartz - kaolinite - pyrophyllite - barite	Pyrite - chalcopyrite - bornite - chalcocite - enargite	1) Pyrite - chalcopyrite - bornite - chalcocite; 2) Enargite; 3) Colusite	*13.90 ± 1.20/ 1.2*	10	Fine-grained, equigranular andesitic rock crosscut by phase 5 fine-grained tonalite
GTD-10-172/363	E174240 N9046440/290	AND	Quartz - alunite-pyrophyllite - diaspore - dickite	-	-	13.6 ± 1.30/ 1.31	8	Strongly altered equigranular fine-grained andesitic rock
ARM-TB-56	E173050 N9047657/1	SED	1) Chlorite - calcite; 2) Quartz - dickite - kaolinite	-	-	8.69 ± 0.29/ 0.30	16	Bedded volcanic sandstone exposure along Pulau Merah coastline
Phase 1; hornblende quartz diorite								
ARM-TB-43	E173050 N9047657/3	-	-	-	-	8.46 ± 0.36/ 0.37	14	20 by 15 cm clast of phase 1 coarse-grained hornblende quartz diorite in upper facies Tanjung Jahe diatreme breccia
Tanjung Jahe diatreme								
ARM-TB-44	E175347 N9043797/3	-	Chlorite - illite	-	-	8.78 ± 0.22 / 0.24	18	Intercalated sedimentary rock (sand and mudstone) in upper facies diatreme breccia
ARM-TB-40	E175408 N9043609/3	-	Epidote - chlorite - calcite	-	-	8.52 ± 0.21/ 0.23	19	Fine-grained matrix of diatreme breccia, andesitic composition with small hornblende-bearing (mm to cm) clasts
Volcanic breccia								
GTD-08-49/19.7	E174365 N9046669/485	VBX	Quartz - kaolinite	-	-	5.74 ± 0.48/ 0.49	12	Welded crystal tuff
Phase 2; Old diorite								
GTD-09-129/102	E173503 N9046136/203	OD	Quartz - kaolinite - dickite	-	-	5.90 ± 1.0/ 1.01	7	Phase 2 medium-grained diorite; plagioclase replaced by kaolinite - dickite; no quartz eye phenocrysts

Table 4.1. *(Cont.)*

Sample ID/depth (m)	Coordinates /RL	Mine unit	Alteration	Mineralization	Veins/paragenesis	Age (Ma) ± 2σ	Number of analyses	Rock description
GT010/319.6	E174315 N9046735/482	OD	Quartz - illite - kaolinite	-	-	5.81 ± 0.20/ 0.21	15	Phase 2 medium-grained diorite, illite has replaced feldspar (plagioclase)
GTD-08-46/300	E174512 N9046872/338	OD	Chlorite - calcite	-	-	5.59 ± 0.37/ 0.38	10	Phase 2 medium-coarse grained diorite; subhedral plagioclase phenocrysts; primary magnetite; < 5 % quartz as phenocrysts and matrix
GTD-08-42/54.4	E173495 N9046564/69	OD	Quartz - pyrophyllite - kaolinite	Pyrite - chalcopyrite - covellite	-	5.50 ± 0.38/ 0.39	15	Phase 2 medium-grained strongly altered diorite; covellite intergrown with kaolinite replaced early chalcopyrite
GTD-09-112/446	E173877 N9046141/214	OD	Quartz - illite - kaolinite - pyrophyllite	Pyrite - chalcopyrite	-	5.38 ± 0.30/ 0.31	13	Phase 2 medium-grained diorite clast with ghosted hornblende and biotite phenocrysts; anhedral ex-feldspar phenocrysts altered to illite - kaolinite - pyrophyllite in Tumpangpitu diatreme
GTD-09-104/357.2	E174185 N9046808/405	OD	Quartz - alunite - pyrophyllite - diaspore	Tetrahedrite - tennantite	-	5.28 ± 0.55/ 0.56	4	Phase 2 strongly silicified fine-grained diorite, lack of quartz phenocrysts
ARM-TB-48	E175652 N9044061/3	OD	Chlorite - calcite	-	-	5.18 ± 0.27/ 0.28	14	Phase 2 chlorite altered medium-grained diorite
Katak tonalite porphyry								
KTD-10-001/185.8	E176226 N9047930/45	-	1) K-feldspar - biotite - magnetite; 2) Illite - chlorite - calcite	1) Chalcopyrite - bornite; 2) Pyrite - chalcopyrite	1) Quartz - magnetite - chalcopyrite - bornite - pyrite; 2) Chlorite - illite	5.26 ± 0.47/ 0.48	14	K-feldspar altered coarse-grained hornblende tonalite porphyry with 20 % primary quartz
Phase 3; Zone B quartz diorite porphyry								
GTD-10-137/775.7	E175020 N9045397/364	-	1) Biotite - K-feldspar - magnetite; 2) Quartz - illite - chlorite	Pyrite - chalcopyrite	-	4.71 ± 0.47/ 0.49	14	Phase 3 quartz diorite porphyry; quartz comprises 15 % of porphyry; chlorite has replaced secondary biotite and illite has replaced groundmass plagioclase

Table 4.1. *(Cont.)*

Sample ID/depth (m)	Coordinates /RL (m)	Mine unit	Alteration	Mineralization	Veins/paragenesis	Age (Ma) ± 2σ	Number of analyses	Rock description
Phase 4; Very coarse-grained tonalite								
GTD-12-334/911.1	E174001 N9046654/275	VCT	1) Chlorite - magnetite; 2) Illite	1) Chalcopyrite 2) Pyrite - chalcopyrite	-	4.89 ± 0.40/ 0.41	12	Phase 4 weakly mineralized coarse-grained tonalite with crowded subhedral plagioclase and large granoblastic quartz eye phenocrysts; magnetite - chalcopyrite association
Phase 5; Fine-grained tonalite								
GTD-12-292/513	E174082 N9046550/257	FT	1) Quartz - kaolinite - pyrophyllite; 2) Barite	1) Pyrite - chalcopyrite - bornite - chalcocite; 2) Pyrite - enargite; 3) Colusite	1) Pyrite - chalcopyrite - bornite - chalcocite; 2) Enargite; 3) Colusite	*5.60 ± 1.2/ 1.2*	8	Phase 5 fine-grained, strongly quartz-altered equigranular tonalite that intruded into andesite basement rocks; evidence of zircon inheritance
GTD-08-35/555	E174080 N9046551/257	FT	1) Biotite 2) Illite 3) Kaolinite	Pyrite - chalcopyrite - chalcocite	1) Quartz - magnetite - chalcopyrite/A; 2) Quartz - illite - pyrite/D	5.4 ± 0.46/ 0.47	14	Phase 5 biotite overprinted by illite alteration in fine-grained tonalite, crowded tabular to prismatic ghosted hydrothermal biotite and feldspar phenocrysts; contained in a fine-grained equigranular groundmass
GTD-08-56/463	E173878 N9046141/214	FT	Magnetite - chlorite	Chalcopyrite	-	4.68 ± 0.60/ 0.61	16	Phase 5 magnetite altered fine-grained equigranular tonalite; 1 - 2 mm quartz eye crystals and quartz groundmass compose 20 % of rock
GTD-11-201/600	E174155 N9046097/267	FT	Quartz - pyrophyllite - alunite	Covellite - bornite - chalcocite - tetrahedrite - tennantite - enargite	1) Quartz - chalcopyrite - bornite/A; 2) Pyrite-bornite - chalcocite - covellite - tetrahedrite-tennantite enargite/HSE	4.27 ± 0.54/ 0.55	11	Phase 5 strongly mineralized fine-grained equigranular tonalite

Table 4.1. *(Cont.)*

Sample ID/depth (m)	Coordinates /RL (m)	Mine unit	Alteration	Mineralization	Veins/paragenesis	Age (Ma) ± 2σ	Number of analyses	Rock description
Phase 6; Coarse-grained tonalite								
GTD-11-192/891	E174074 N9046298/251	CT	Quartz - illite ± kaolinite - dickite	1) Chalcopyrite - bornite - chalcocite - covellite; 2) Molybdenite; 3) Enargite	1) Quartz - chalcopyrite - bornite/A/B; 2) Quartz - illite - pyrite/D	4.64 ± 0.60/ 0.61	16	Phase 6 coarse-grained tonalite; porphyritic, crystal-crowded texture; euhedral to subhedral ex-plagioclase phenocrysts altered to illite and kaolinite
GTD-11-201/988	E174155 N9046097/267	CT	Biotite - chlorite	Chalcopyrite	Quartz - magnetite - chalcopyrite - pyrite/A	4.34 ± 0.48/ 0.49	15	Phase 6 coarse-grained tonalite; potassic alteration; chlorite replaced secondary biotite that replaced magmatic hornblende
GTD-12-292/1012	E174082 N9046550/257	CT	1) Biotite - magnetite; 2) Chlorite 3) Illite	Chalcopyrite	Quartz - magnetite/A	4.33 ± 0.61/ 0.62	13	Phase 6 potassic altered well-mineralized coarse-grained tonalite with crowded ex-plagioclase anhedral feldspars altered to illite; strong quartz - magnetite veining and magnetite - chalcopyrite association
GTD-10-166/1082.7	E174156 N9046095/267	CT	1) Biotite - magnetite - K-feldspar; 2. Chlorite	Chalcopyrite	1) Quartz - chalcopyrite - magnetite; 2) Magnetite - chalcopyrite ± quartz	4.32 ± 0.87/ 0.88	7	Phase 6 biotite coarse-grained tonalite; large quartz phenocrysts up to 0.5 cm; chlorite has replaced biotite; magnetite is closely associated with chalcopyrite
GTD-11-201/1097	E174155 N9046097/267	CT	1) Magnetite - biotite - K-feldspar - chlorite; 2) Quartz - illite - kaolinite	Chalcopyrite	1) Biotite/EB; 2) Quartz - pyrite - magnetite - chalcopyrite/A	4.26 ± 0.45/ 0.46	14	Phase 6 medium-grained crowded plagioclase-phyric tonalite; 15 - 20 % quartz eye phenocrysts and relict mafics in fine-grained illite-altered groundmass; quartz - illite overprint on K-feldspar alteration
GTD-08-56/807	E173878 N9046141/214	CT	1) Biotite - magnetite; 2) Chlorite - magnetite - hematite	Chalcopyrite	1) Quartz/A; 2) Quartz/B 3) Quartz - illite - pyrite/D	4.10 ± 0.45/ 0.46	11	Phase 6 potassic altered coarse-grained tonalite with granoblastic quartz eyes (up to 1cm); hydrothermal chlorite has replaced secondary biotite; absence of copper sulfide in the early porphyry veins
GTD-11-248/409	E174385 N9046285/322	CT	1) Biotite - magnetite; 2) Chlorite; 3) Illite	Chalcopyrite	Magnetite/M	4.03 ± 0.65/ 0.66	14	Phase 6 potassic altered well-mineralized coarse-grained tonalite; strong M vein network and magnetite - chalcopyrite association

Table 4.1. *(Cont.)*

Sample ID/depth (m)	Coordinates /RL (m)	Mine unit	Alteration	Mineralization	Veins/paragenesis	Age (Ma) ± 2σ	Number of analyses	Rock description
Phase 7; Quartz diorite								
GTD-10-139/355	E173503 N9046136/203	QD	Chlorite - illite	-	-	4.26 ± 0.57/ 0.58	14	Phase 7 barren very coarse-grained quartz diorite; crowded tabular euhedral plagioclase phenocrysts have been replaced by illite; large (up to 1 cm) stable hornblende phenocrysts
GTD-10-146/156	E173595 N9046376/107	QD	Quartz - kaolinite	-	-	4.25 ± 0.44/ 0.45	15	Phase 7 barren crystal-crowded coarse-grained quartz diorite
GTD-10-167/91.7	E173890 N9046413/194	QD	Chlorite - calcite	-	-	4.17 ± 0.24/ 0.25	15	Phase 7 barren very coarse-grained quartz diorite with large 1 cm quartz eyes; anhedral plagioclase phenocrysts, hornblende and biotite in a fine crystalline chloritic groundmass
GTD-10-166/651	E174156 N9046095/267	QD	1) Chlorite; 2) Quartz - illite - kaolinite	-	Quartz - illite - pyrite/D	4.09 ± 0.42/ 0.43	14	Phase 7 medium-grained quartz diorite/tonalite; hornblende phenocrysts replaced by chlorite, anhedral plagioclase phenocrysts replaced by illite - kaolinite in finer-grained crystalline quartz-rich groundmass; weak to no mineralization
GTD-08-35/472.1	E174080 N9046550/257	QD	Quartz - kaolinite - dickite	-	-	3.94 ± 0.69/ 0.70	22	Phase 7 barren coarse-grained quartz diorite with crowded ex-plagioclase phenocrysts altered to kaolinite - dickite
Pulau Merah tonalite porphyry								
GT003/489.2	E173106 N9047573/10	-	1) Quartz - K-feldspar - biotite - magnetite; 2) Illite - chlorite, Fe-carbonate, hematite	Chalcopyrite - pyrite	Quartz - magnetite - chalcopyrite - pyrite/A	3.98 ± 0.21/ 0.22	15	Potassic altered Pulau Merah coarse-grained biotite - hornblende tonalite; primary phenocryst and groundmass quartz comprises 25 % of the porphyry; chalcopyrite - magnetite association
Tumpangpitu diatreme								
GTD-10-172/12	E174240 N9046440/290	UF-DBX	Chlorite - illite - montmorillonite	-	-	2.7 ± 0.50 / 1.0	1 of 22	Diatreme breccia with 1 mm - 2 cm mineralized clasts of phases 1 - 7 in fine-grained matrix of andesitic composition

193 nm laser @ 5 Hz, 60 % power, 2J/cm^2, 32 µm spot size, 17 µm spot size in italics. Abbreviations: EB = Early biotite, M = magnetite veins, A, B and D type veins after Gustafson and Hunt, (1945) HSE = high-sulfidation epithermal veins, RL = reduced elevation. All coordinates/RL are recorded for drill hole collar locations. Text in italics signifies samples with two ages from zircon inheritance.

Table 4.2. Summary of new $^{206}Pb/^{238}U$ age determinations from intrusive rocks at Singgahan, Trenggalek project, East Java.

Sample ID/depth (m)	Coordinates/RL (m)	Alteration	Mineralization	Veins/ paragenesis	Age (Ma) ± 2σ	Number of analyses	Rock description
ARMTRDD-055-1/174	E574956 N9088554/351	1) Chlorite - magnetite; 2) Illite; 3) Calcite	Pyrite - chalcopyrite	1) Quartz - magnetite - pyrite/A; 2) Magnetite - chalcopyrite	14.00 ± 0.44	20	Medium-grained tonalite; late coarse-grained calcite veining; chlorite-magnetite alteration with illite overprint. Weak quartz stockwork veining; quartz - magnetite - pyrite, minor magnetite - chalcopyrite
ARMTRDD-057-1/156	E574958 N9088554/351	1) Chlorite - magnetite; 2) Illite	Pyrite - chalcopyrite	Quartz - magnetite - pyrite - chalcopyrite/A	14.04 ± 0.45	20	Fine-grained tonalite; chlorite-magnetite alteration with illite overprint; quartz-magnetite - pyrite - chalcopyrite stockwork veining

213 nm laser @ 5 Hz, 60 % power, 2J/cm^2, 32 µm spot size, 17 µm spot size in italics. Abbreviations: A type veins after Gustafson and Hunt, (1945). All coordinates/RL are recorded for drill hole collar locations.

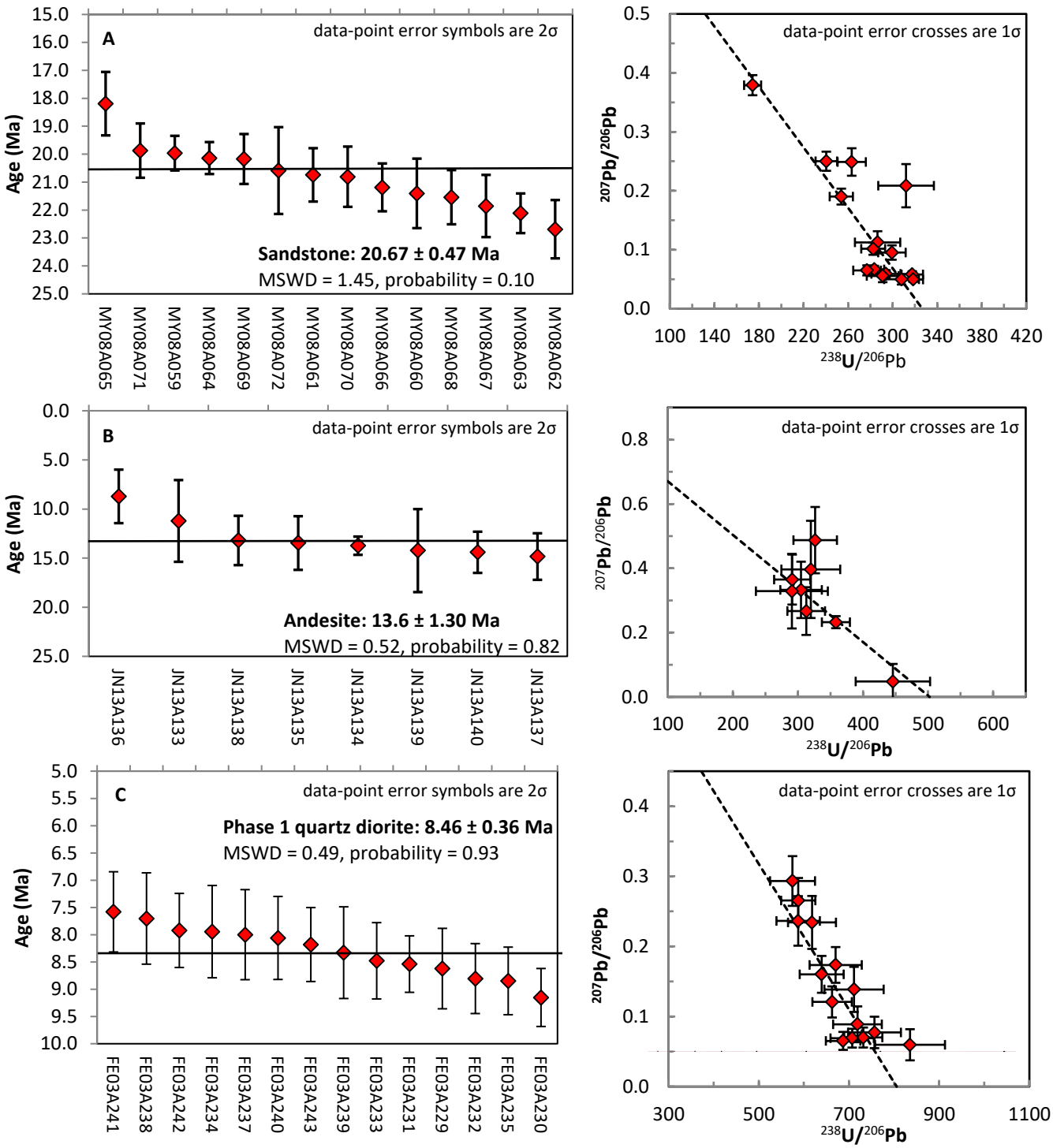

Figure 4.5. Representative U-Pb age determinations for drillcore and rockchip samples from the host rocks at Tumpangpitu. Ages are calculated based on the weighted mean ^{207}Pb-corrected ^{206}Pb/^{238}U histograms. Concordia diagrams shown for each sample demonstrate the presence of common Pb, Pb loss and inheritance in some of the analyzed zircons. Analyses excluded from the age calculation shown in grey. All data listed in Table 4.1 and Appendix 1. All sample locations shown on Figures 4.1 - 4.3.

A) *GTD-10-138; 964 m; drillcore sample.* Well-bedded volcanic sandstone.
B) *GTD10-172; 363 m; drillcore sample.* Andesitic volcanic rock.
C) *ARM-TB-43; rockchip sample.* Phase 1 hornblende quartz diorite.

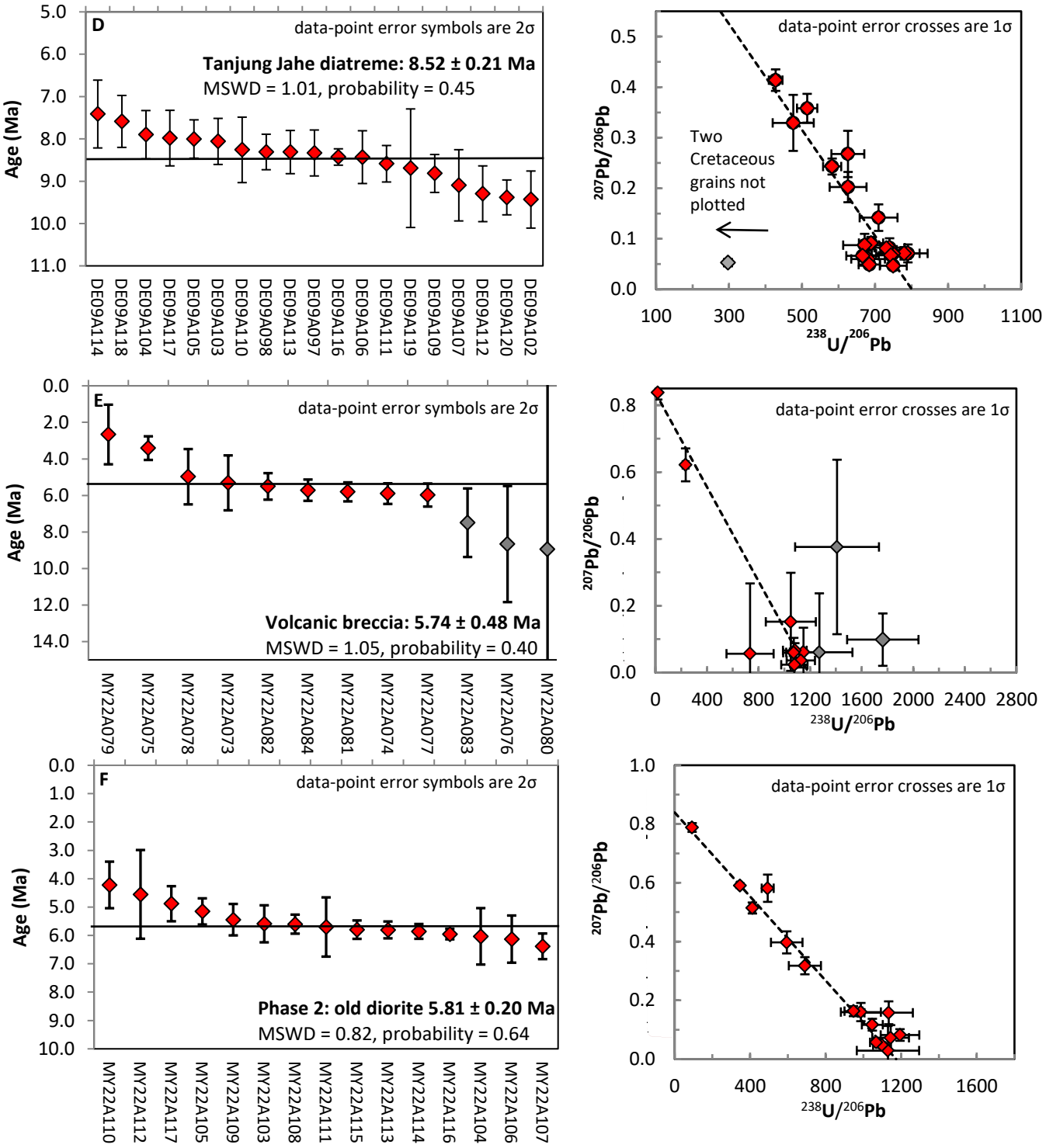

Figure 4.5. *(Cont.)*

D) *ARM-TB-40; rockchip sample*. Intercalated sedimentary rock in upper facies Tanjung Jahe diatreme breccia.
E) *GTD-08-49; 19.7 m; drillcore sample.* Volcanic breccia (welded crystal tuff).
F) *GTD-010; 319.6 m; drillcore sample.* Phase 2 diorite.

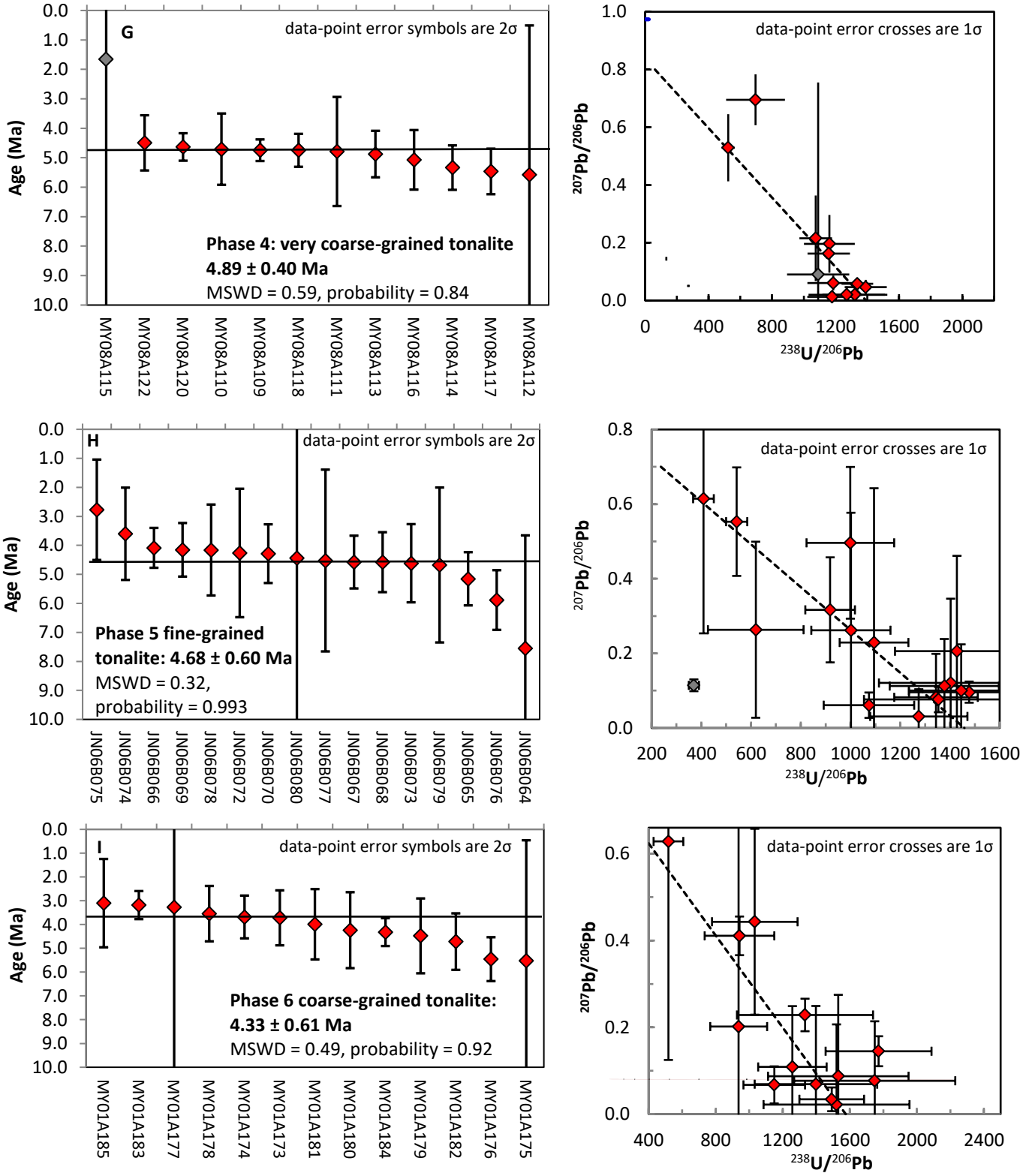

Figure 4.5. *(Cont.)*

G) GTD-12-334; 911.12 m; drillcore sample. Phase 4 very coarse-grained tonalite.
H) GTD-08-56; 463 m; *drillcore sample.* Phase 5 fine-grained tonalite.
I) GTD-12-292; 1012 m; drillcore sample. Phase 6 coarse-grained tonalite.

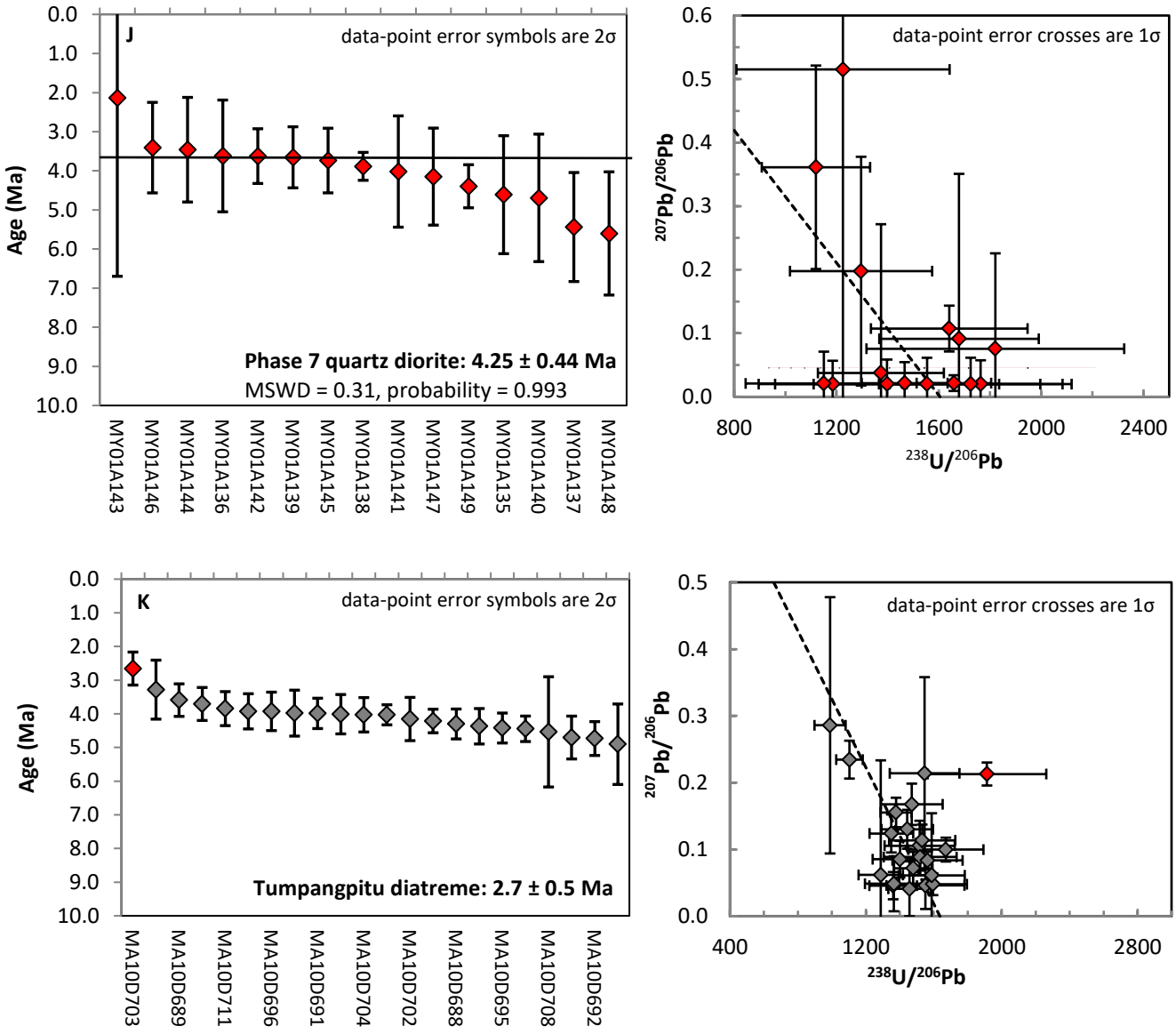

Figure 4.5. *(Cont.)*

J) GTD-10-146; 156 m; drillcore sample. Phase 7 quartz diorite.
K) GTD-10-172: 12 m; drillcore sample. Tumpangpitu diatreme breccia.

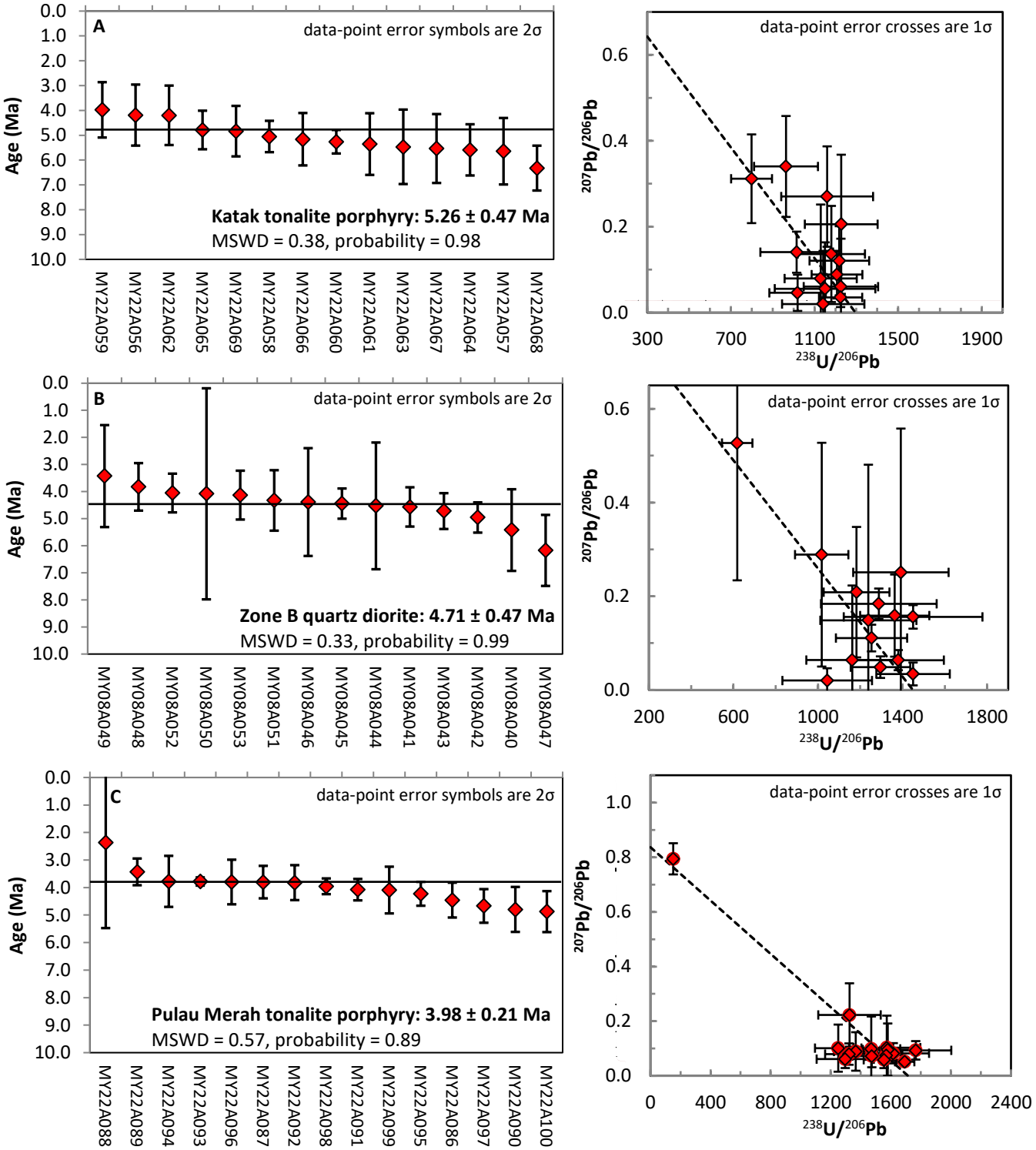

Figure 4.6. Representative U-Pb ages for samples from regional porphyries. Ages are calculated based on the weighted mean ^{207}Pb-corrected ^{206}Pb/^{238}U histograms. Concordia diagrams shown for each sample demonstrate the presence of common Pb, Pb loss and inheritance in some of the analyzed zircons. All data listed in Table 4.1 and Appendix 1. All sample locations are shown on Figures 4.1 - 4.3.

A) KTD-10-001; 185.8 m; drillcore sample. Katak tonalite porphyry.
B) GTD-10-137; 775.7 m; drillcore sample. Zone B quartz diorite.
C) *GT003; 489.2 m; drillcore sample.* Pulau Merah coarse-grained tonalite porphyry.

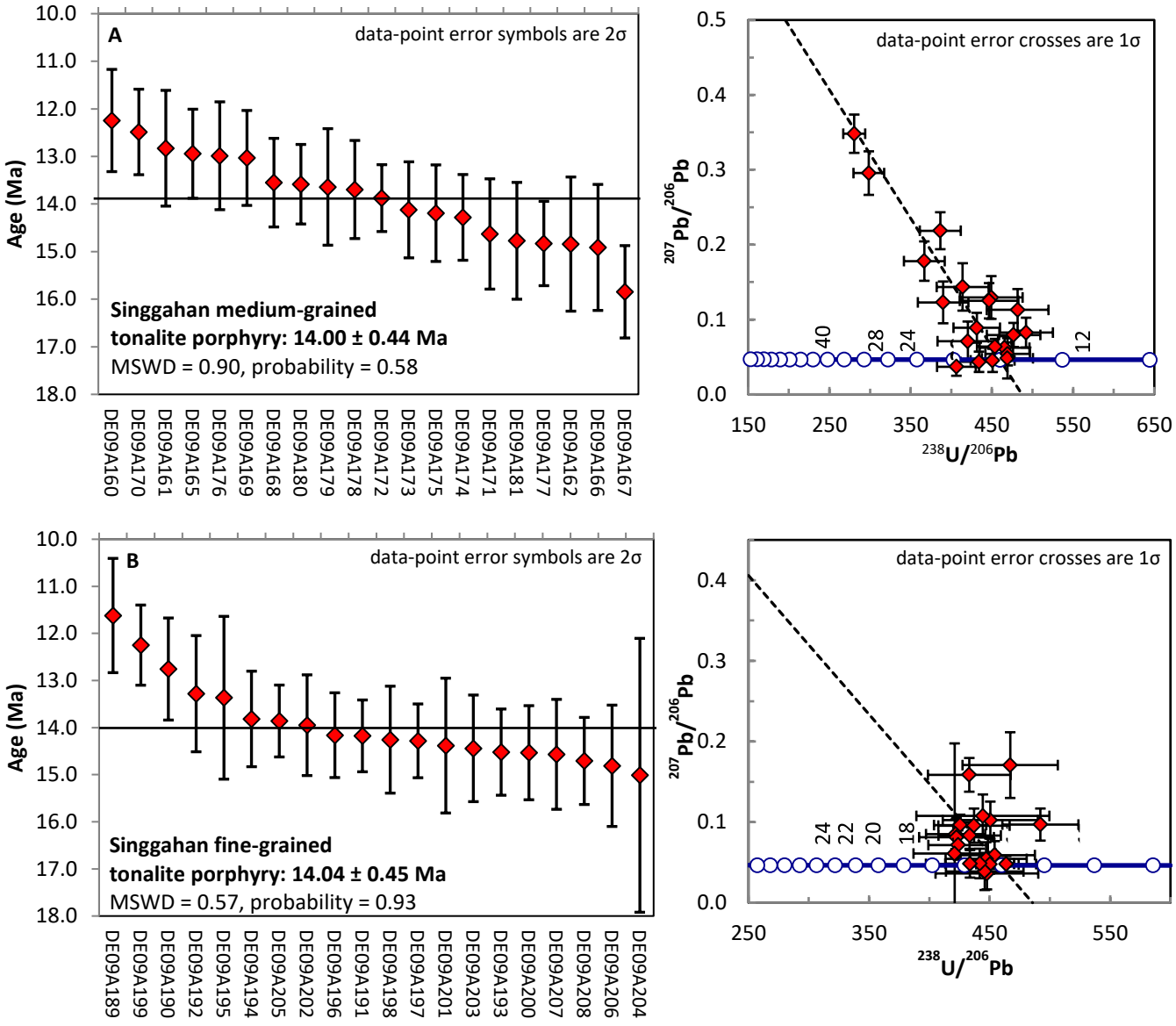

Figure 4.7. Representative U-Pb age determinations for samples from Singgahan porphyry, Trenggalek project, east Java. Ages are calculated based on the weighted mean ^{207}Pb-corrected ^{206}Pb/^{238}U histograms. Concordia diagrams shown for each sample demonstrate the presence of common Pb, Pb loss and inheritance in some of the analyzed zircons. All data listed in Table 4.2 and Appendix 1. Prospect location shown on Figure 4.4.

A) *ARM_TRDD055_1 174 m; drillcore sample.* Medium-grained tonalite porphyry.
B) ARM_TRDD057_1 156 m; drillcore sample. Fine-grained tonalite porphyry.

Table 4.3 U-Pb data from analyses of rim and core of zircon grains suspected of inheritance from Tumpangpitu.

Sample	^{204}Pb (ppm)	^{206}Pb (ppm)	^{207}Pb (ppm)	^{208}Pb (ppm)	^{232}Th (ppm)	^{238}U (ppm)	^{208}Pb/^{232}Th	± 1σ	^{207}Pb/^{206}Pb	± 1σ	^{238}U/^{206}Pb	± 1σ	^{206}Pb/^{238}U	± 1σ	^{206}Pb/^{238}U age (Ma)
Phase 5; Fine-grained tonalite overprinting andesitic volcanic rock															
Drillhole GTD-12-292; 513 m															
Rim-core re-analyses															
AU21B011	0.00	0.46	0.17	0.43	288	416	0.0013	8.48	0.3593	43.85	997.19	101.31	0.0010	10.16	**3.9 ± 1.3**
AU21B010	0.00	0.85	0.38	0.78	275	455	0.0021	10.47	0.4497	66.54	697.05	95.32	0.0014	13.67	**4.5 ± 3.6**
AU21B006	0.00	0.07	0.03	0.03	26	43	0.0009	43.08	0.3983	78.85	646.16	240.17	0.0015	37.17	**5.5 ± 4.5**
AU21B007	0.00	0.11	0.04	0.08	18	40	0.0040	23.06	0.3250	95.40	400.46	106.47	0.0025	26.59	**10.4 ± 6.9**
AU21B009	0.00	0.10	0.04	0.14	11	25	0.0096	16.19	0.3688	58.63	298.68	76.86	0.0033	25.73	**12.8 ± 6.7**
AU21B008	0.00	0.21	0.03	0.11	53	72	0.0017	17.68	0.1187	143.17	386.62	61.55	0.0026	15.92	**15.1 ± 4.3**
Zircon rims; Phase 5 tonalite; Analyses < 7 Ma: Mean = 5.6 ± 1.2 Ma [20 %] 95 % confidence MSWD = 0.37, probability = 0.92									**Zircon cores; Andesite; Analyses > 10 Ma: Mean = 13.9 ± 1.2 Ma [9.6 %] 95 % confidence MSWD = 1.07, probability = 0.39**						
Previous analyses															
MY08A105	0.03	0.61	0.47	1.09	79	92	0.0148	6.34	0.7653	9.73	140.25	12.45	0.0071	8.87	**4.2 ± 4.4**
MY08A106	0.00	0.33	0.19	0.48	66	122	0.0072	5.64	0.5930	13.50	383.17	44.38	0.0026	11.58	**5.2 ± 1.8**
MY08A093	0.02	0.33	0.19	0.52	24	42	0.0251	5.10	0.7486	7.11	133.12	10.19	0.0075	7.65	**5.5 ± 3.3**
MY08A096	0.03	0.59	0.36	0.91	133	185	0.0072	4.21	0.6148	5.10	297.77	16.43	0.0034	5.52	**6.1 ± 0.9**
MY08A094	0.02	0.46	0.29	0.72	81	127	0.0089	4.26	0.6179	5.65	273.83	15.89	0.0037	5.80	**6.5 ± 1.1**
MY08A102	0.00	0.18	0.05	0.19	72	90	0.0026	7.09	0.2921	11.09	483.27	34.42	0.0021	7.12	9.2 ± 0.9
MY08A101	0.03	0.50	0.38	0.90	19	37	0.0528	6.40	0.7665	10.34	66.41	6.45	0.0151	9.71	9.2 ± 9.8
MY08A097	0.02	0.40	0.16	0.45	178	136	0.0025	6.49	0.3929	11.20	356.06	23.60	0.0028	6.63	10.2 ± 1.2
MY08A100	0.01	0.10	0.00	0.02	25	44	0.0010	18.09	0.0431	84.45	450.09	39.99	0.0022	8.88	**14.3 ± 1.4**
MY08A095	0.01	0.09	0.01	0.01	20	39	0.0006	22.98	0.0691	38.62	426.38	41.10	0.0023	9.64	**14.7 ± 1.5**
MY08A098	0.00	0.22	0.11	0.23	32	37	0.0065	12.37	0.5078	27.33	180.61	28.81	0.0055	15.95	**14.9 ± 6.7**
MY08A103	0.00	0.34	0.06	0.13	54	115	0.0023	8.66	0.1968	10.81	349.16	23.23	0.0029	6.65	**14.9 ± 1.1**
MY08A104	0.00	0.15	0.04	0.12	34	46	0.0036	8.16	0.2642	57.42	308.42	25.99	0.0032	8.43	**15.1 ± 4.2**
MY08A099	0.11	2.20	1.77	4.42	76	55	0.0577	4.27	0.8039	2.17	25.14	0.85	0.0398	3.40	**15.4 ± 6.3**

213 nm laser @ 5 Hz, 60 % power, 2J/cm^2, 17 µm spot size (previous analyses 32 µm spot size). Absolute element concentration assumed stoichiometric zirconium in the zircons. The standard NIST 610 was used to calculate mass bias and drift. Analyses on zircon rims (phase 5 tonalite) shown in bold in red text, analyses on zircon cores (andesite) shown in bold in blue text. Analyses excluded from the age calculation shown in grey. Ages in bold coloured text are concordia intercept ages.

Table 4.3 *(Cont.)*

Sample	^{204}Pb (ppm)	^{206}Pb (ppm)	^{207}Pb (ppm)	^{208}Pb (ppm)	^{232}Th (ppm)	^{238}U (ppm)	^{208}Pb/^{232}Th	± 1σ	^{207}Pb/^{206}Pb	± 1σ	^{238}U/^{206}Pb	± 1σ	^{206}Pb/^{238}U	± 1σ	^{206}Pb/^{238}U age (Ma)
Phase 7; Quartz diorite															
Drillhole GTD-08-35; 472.1 m															
Rim-core re-analyses															
AU21B023	0.00	0.11	0.08	0.13	45	91	0.0027	16.81	0.7192	64.17	855.02	276.22	0.0012	32.31	**1.1 ± 4.4**
AU21B017	0.00	0.16	0.11	0.15	51	77	0.0024	13.41	0.6851	40.37	550.81	93.07	0.0018	16.90	**2.2 ± 4.1**
AU21B018	0.02	0.65	0.51	1.38	50	98	0.0237	6.54	0.7837	20.96	158.66	17.18	0.0063	10.83	**2.8 ± 8.4**
AU21B025	0.03	0.05	0.01	0.03	47	107	0.0006	38.10	0.1078	264.17	2057.63	826.11	0.0005	40.15	**2.9 ± 1.6**
AU21B022	0.02	0.04	0.00	0.01	29	54	0.0002	124.26	0.0306	118.29	1622.76	566.39	0.0006	34.90	**4.0 ± 1.4**
AU21B024	0.02	0.11	0.04	0.10	43	99	0.0020	19.68	0.3221	68.87	962.89	232.94	0.0010	24.19	**4.4 ± 2.2**
AU21B016	0.00	0.15	0.08	0.15	18	65	0.0066	13.62	0.5198	74.07	514.66	87.27	0.0019	16.96	**5.0 ± 6.2**
AU21B020	0.00	1.31	1.04	2.44	32	79	0.0683	6.43	0.7953	10.30	60.94	5.91	0.0164	9.70	**6.3 ± 11.0**
Previous analyses															
Ap24B042	0.04	0.96	0.80	2.16	20	42	0.1123	9.93	0.8297	6.08	41.27	4.65	0.0242	11.26	**3.1 ± 10.0**
Ap24B041	0.00	0.41	0.32	0.77	27	59	0.0269	5.22	0.7790	8.36	152.17	13.21	0.0066	8.68	**3.2 ± 3.5**
Ap24B040	0.02	0.19	0.11	0.23	78	117	0.0031	11.00	0.6064	22.60	581.95	99.60	0.0017	17.12	**3.2 ± 2.0**
Ap24B029	0.00	0.04	0.01	0.02	29	47	0.0007	31.58	0.3301	48.03	1214.21	269.73	0.0008	22.21	**3.4 ± 1.3**
Ap24B031	0.01	0.04	0.01	0.03	23	55	0.0013	22.10	0.1486	81.37	1524.04	347.58	0.0007	22.81	**3.7 ± 1.1**
Ap24B034	0.00	0.09	0.05	0.11	29	64	0.0039	12.85	0.5070	68.47	704.86	101.45	0.0014	14.39	**3.8 ± 4.1**
Ap24B037	0.01	0.08	0.03	0.10	29	72	0.0033	19.63	0.3852	43.80	963.09	150.53	0.0010	15.63	**3.8 ± 1.5**
Ap24B035	0.00	0.15	0.02	0.10	202	224	0.0005	13.12	0.1425	39.82	1477.35	214.86	0.0007	14.54	**3.8 ± 0.6**
Ap24B039	0.00	0.06	0.01	0.01	29	86	0.0005	39.18	0.0952	170.69	1471.32	247.66	0.0007	16.83	**4.1 ± 1.1**
Ap24B030	0.01	0.07	0.01	0.01	37	92	0.0004	48.45	0.1384	114.62	1343.30	223.86	0.0007	16.67	**4.2 ± 1.2**
Ap24B032	0.00	0.06	0.01	0.02	38	70	0.0006	29.99	0.1722	103.34	1205.95	228.30	0.0008	18.93	**4.5 ± 1.5**
Ap24B036	0.04	0.05	0.01	0.03	27	61	0.0011	23.00	0.1732	138.06	1154.84	200.50	0.0009	17.36	**4.7 ± 1.9**
Ap24B033	0.01	0.10	0.05	0.16	20	46	0.0078	9.33	0.5223	33.11	449.49	64.34	0.0022	14.31	**5.7 ± 3.2**
Ap24B038	0.00	0.08	0.03	0.06	23	42	0.0027	17.11	0.3493	98.16	516.64	132.84	0.0019	25.71	**7.7 ± 5.8**

213 nm laser @ 5 Hz, 60 % power, 2J/cm^2, 17 µm spot size (previous analyses 32 µm spot size.) Absolute element concentration assumed stoichiometric zirconium in the zircons. The standard NIST 610 was used to calculate mass bias and drift. Ages in bold text are concordia intercept ages.

Table 4.3 *(Cont.)*

Sample	^{204}Pb (ppm)	^{206}Pb (ppm)	^{207}Pb (ppm)	^{208}Pb (ppm)	^{232}Th (ppm)	^{238}U (ppm)	^{208}Pb/^{232}Th	± 1σ	^{207}Pb/^{206}Pb	± 1σ	^{238}U/^{206}Pb	± 1σ	^{206}Pb/^{238}U	± 1σ	^{206}Pb/^{238}U age (Ma)
Phase 6; Coarse-grained tonalite															
Drillhole GTD-10-166; 1082.7 m															
Rim-core re-analyses															
AU21B030	0.00	0.26	0.10	0.22	347	307	0.0005	21.46	0.3793	152.43	1284.40	295.65	0.0008	23.02	**2.9 ± 3.7**
AU21B027	0.00	0.16	0.06	0.23	184	191	0.0011	21.56	0.3609	39.92	1147.51	331.55	0.0009	28.89	**3.4 ± 1.4**
AU21B028	0.00	0.07	0.02	0.04	72	77	0.0005	39.80	0.2349	17.12	1182.20	436.58	0.0008	36.93	**4.1 ± 1.6**
AU21B029	0.02	0.57	0.08	0.64	1932	627	0.0003	8.14	0.1446	46.30	1101.57	131.68	0.0009	11.95	**5.1 ± 0.8**
Previous analyses															
MY01A153	0.00	0.06	0.00	0.00	60	99	0.0001	416.7	0.0200	169.44	1815.48	337.50	0.0006	18.59	**3.5 ± 0.7**
MY01A155	0.00	0.05	0.01	0.01	41	67	0.0003	55.48	0.2296	61.83	1336.01	311.38	0.0007	23.31	**3.7 ± 1.2**
MY01A154	0.00	0.26	0.10	0.29	170	239	0.0017	8.36	0.3920	36.91	863.39	102.27	0.0012	11.85	**4.2 ± 1.5**

193 nm laser @ 5 Hz, 60 % power, 2J/cm^2, 17 µm spot size (previous analyses 32 µm spot size). Absolute element concentration assumed stoichiometric zirconium in the zircons. The standard NIST 610 was used to calculate mass bias and drift. Ages in bold text are concordia intercept ages.

Table 4.4 Summary of secondary zircon reference materials analyzed in study, measured with unknowns.

Zircon	^{206}Pb/^{238}U age (Ma)	± 2σ	Accepted age (Ma)	± 2σ	Reference
AusZ-5	38.22	0.68 / 0.76	38.9022	0.0035	Kennedy et al. (2014)
GJ-1	603.8	2.7 / 5.3	601.86	0.437	Horstwood et al. (2016)
Penglai	3.92	0.21 / 0.22	4.36	0.1	Li et al. (2010)
Plesovice	337.3	1.3 / 2.85	337.13	0.37	Slama et al. (2008)
Temora	417.4	1.3 / 3.42	416.8	1.1	Black et al. (2004)

Data reported at the two sigma confidence level. Errors are reported as random error sources/random + systematic errors.

Table 4.5 Uplift rate calculations for Tumpangpitu

Unit	Age	Max Age (Ma)	Max age error (Ma) ± 2σ	Absolute max age (Ma) ± 2σ	Min Age (Ma) ± 2σ	Min age error (Ma) ± 2σ	Absolute min age (Ma) ± 2σ	Assumed depth 1 (m)	Assumed depth 2 (m)	Current depth below diatreme (m)	Diatreme thickness (m)	Amount of uplift 1 (m)	Amount of uplift 2 (m)	Max time period (Ma)	Min time period (Ma)
Phase 5 tonalite	5.40 ± 0.46 Ma to 4.27 ± 0.54	5.4	0.46	5.86	4.27	0.54	3.73	3000	2000	430	280	2290	1290	4.16	0.03
Tumpangpitu diatreme	2.7 ± 1.0 Ma	2.7	1	3.7	2.7	1	1.7								

Starting depth 3 km, difference in timing of 4.16 Myr = uplift rate of 0.55 km per Myr
Starting depth 3 km, difference in timing of 0.03 Myr = uplift rate of 76.3 km per Myr (unrealistic)
Starting depth 2 km, difference in timing of 4.16 Myr = uplift rate of 0.31 km per Myr
Starting depth 2 km, difference in timing of 0.03 Myr = uplift rate of 43.0 km per Myr (unrealistic)

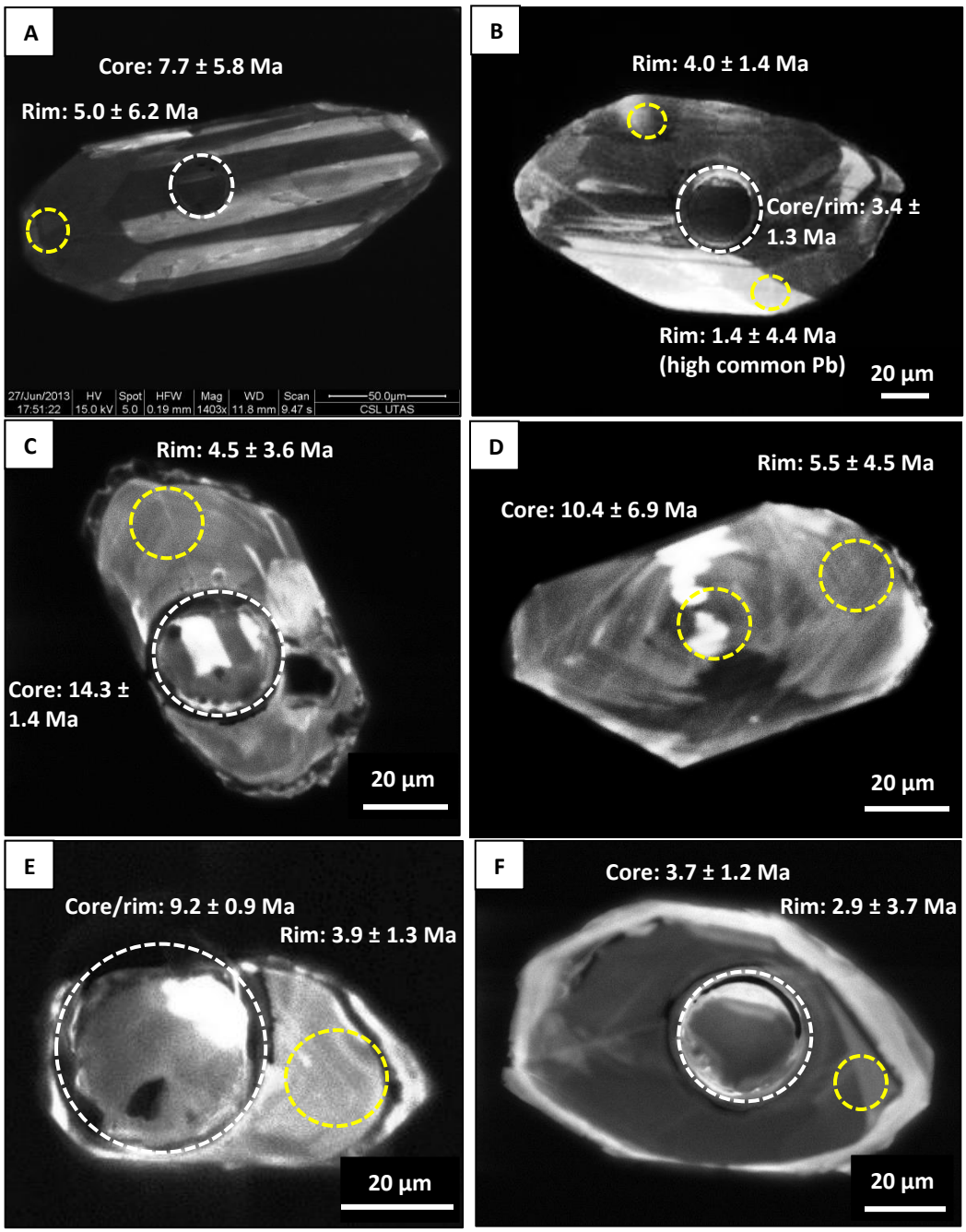

Figure 4.8. CL images of analyzed zircon grains from Tumpangpitu drillcore samples. Locations of ion-probe re-analyses for dated grains are shown as 17 µm diameter hashed yellow circles. Original ablated spots are 32 µm diameter shown as white hashed circles.

A) *GTD-08-35; 472.1m.* Phase 7 late inter-mineralization quartz diorite.
B) *GTD-08-35; 472.1m.* Phase 7 late inter-mineralization quartz diorite.
C) *GTD-12-292; 513m.* Andesite basement intruded by phase 5 fine-grained tonalite.
D) *GTD-12-292; 513m.* Andesite basement intruded by phase 5 fine-grained tonalite. Zircon grain unablated during initial analysis.
E) *GTD-12-292; 513m.* Andesite basement intruded by phase 5 fine-grained tonalite. Initial analysis (6 Ma ± 1.3 Ma) mixes rim and core data.
F) *GTD-10-166; 1082.7m.* Phase 6 inter-mineralization coarse-grained tonalite.

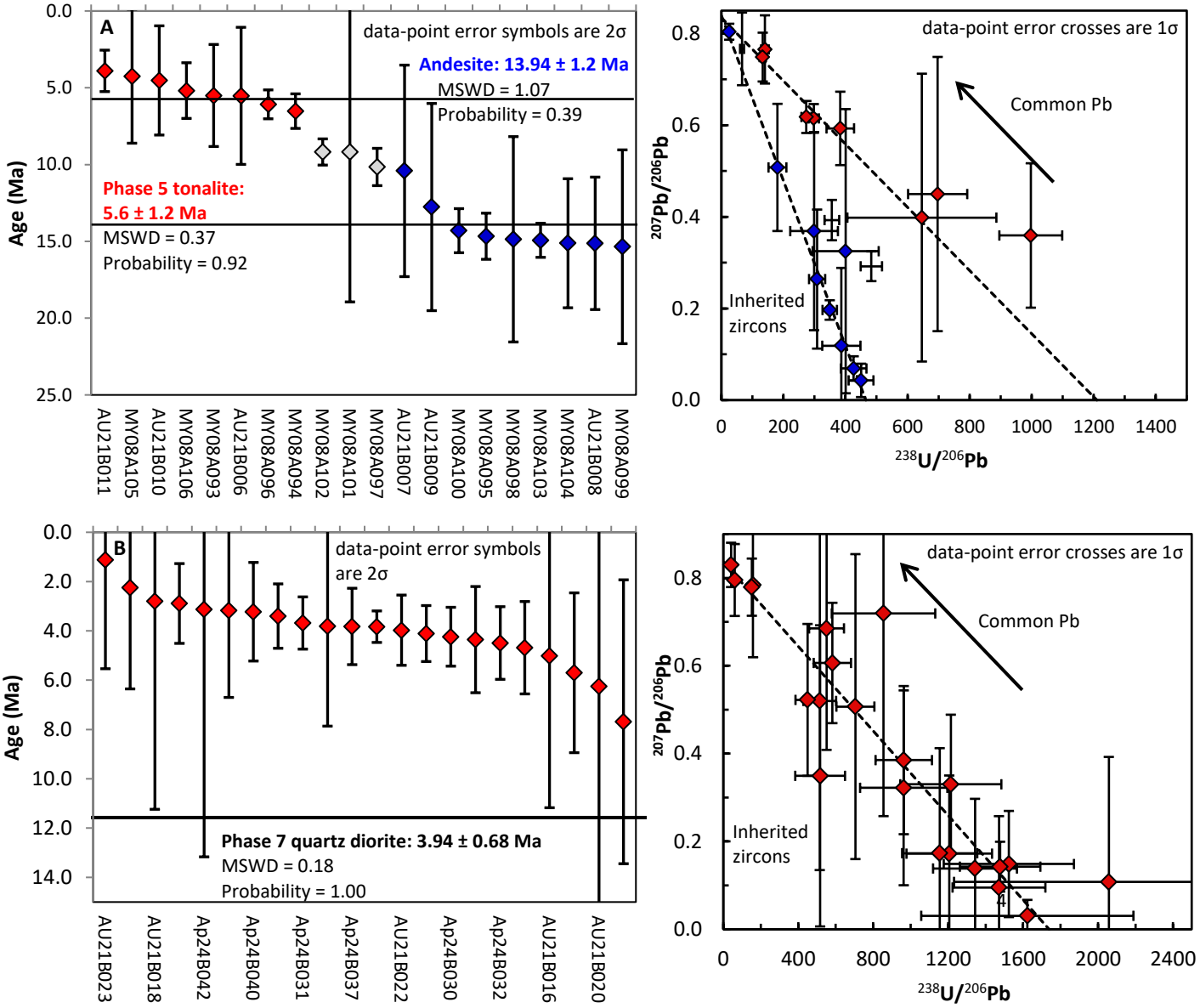

Figure 4.9. U-Pb ages from rim-core re-analyses of zircons that are suspected of inheritance from Tumpangpitu drillcore samples. Ages are calculated based on the weighted mean ^{207}Pb-corrected $^{206}Pb/^{238}U$ histograms. Concordia diagrams demonstrate the presence of common Pb, Pb loss and inheritance in the analyzed zircons. Analyses excluded from the age calculation shown in grey.

A) *GTD-12-292; 513 m.* Two distinct ages are apparent; older zircon cores (shown in red) of the andesite host rock and younger zircon rims (shown in blue) of phase 5 tonalite porphyry.
B) *GTD-08-35; 472.1 m.* Phase 7 quartz diorite showing minor zircon inheritance.

4.4 Discussion

4.4.1 Age of the host rocks at Tumpangpitu

Figure 4.10 summarizes all of the U-Pb zircon ages obtained during this study and places them in the context of relative age for the intrusions, as determined by field relationships. Zircons from two drillcore samples of the basal sedimentary rocks to the southwest of Tumpangpitu form single age populations, plotting close to concordia (Table 4.1; Fig. 4.5A) for the Early Miocene period, having Concordia intercept ages of 20.67 ± 0.47 Ma and 16.68 ± 0.35 Ma. Zircons from one sample of well-bedded volcanic sandstone exposed along the Pulau Merah coastline to the northwest of Tumpangpitu, form a single age population for the Late Miocene period, having a Concordia intercept age of 8.69 ± 0.29 Ma (2σ error; Table 4.1). Zircons from two samples of andesitic volcanic rocks yielded Middle Miocene ages of 13.9 ± 1.42 Ma and 13.6 ± 1.30 Ma (Fig. 4.5B). Zircons from two samples of diatreme breccia at Tanjung Jahe form single age populations, plotting close to Concordia (Fig. 4.5A) for the Late Miocene period, having Concordia intercept ages of 8.52 ± 0.21 Ma (breccia matrix) and 8.78 ± 0.22 Ma (bedded volcanic sandstone from upper facies breccia). It is interesting to note that two Cretaceous zircon grains were found in one sample of bedded intercalated sandstone from the upper facies of the Tanjung Jahe diatreme (98.5 ± 2.0 Ma and 98.5 ± 1.6 Ma; Appendix 1) suggesting that the breccia sampled Cretaceous basement. In contrast, the volcanic breccia has a Concordia intercept age of 5.74 Ma ± 0.48 Ma from one sample with a single age population for the Late Miocene period from low U zircons (Fig. 4.5C).

U-Pb dating results from the various intrusive phases at Tumpangpitu are consistent with the relative age relationships derived from observed field relationships as shown in Figures 4.1 to 4.3. Figure 4.10 highlights the U-Pb zircon ages obtained for seven of the eight intrusive phases (no zircons were present in a sample of phase 8), together with three of the porphyry intrusions from elsewhere in the district. Zircons from one sample of the earliest intrusive phase recognized at Tujuh Bukit; phase 1 hornblende quartz diorite (hosted as a clast in the Tanjung Jahe diatreme breccia) provided a Late Miocene age of 8.46 ± 0.36 Ma (Table 4.1; Fig. 4.5C).

Zircons from seven samples of the pre-mineralization, early diorite porphyry (phase 2) provided an accurate, consistent age range within the Late Miocene period spanning 5.90 ± 1.00 Ma to 5.18 ± 0.27 Ma (Tables 4.1 and 4.2; Fig. 4.5D). Zircons from one sample of Phase 3 Zone B quartz diorite porphyry provided an Early Pliocene intercept age of 4.71 ± 0.47 Ma. Zircons from one sample of phase 4 coarse-grained tonalite porphyry provided an Early Pliocene intercept age of 4.89 ± 0.40 Ma (Table 4.1, 4.3 and Fig. 4.5E). Zircons from four samples of well-mineralized phase 5 fine-grained equigranular tonalite porphyry have an age range spanning the Late Miocene to Early Pliocene (Table 4.1, 4.2 and Fig. 4.5F). One sample with a late Miocene age of 5.6 ± 1.2 Ma exhibited evidence of zircon inheritance (Table 4.3; Fig. 4.9A) identified by CL-imaging (Figs. 4.8C, D and E). Zircons from this sample were re-analyzed,

targeting the rim with a reduced laser spot size. However, some of the older zircon core material may still have been ablated and incorporated into the signal, particularly from the smaller (< 30 μm) zircon grains (Figs. 4.8C, D, and E), thereby skewing the data towards an older age. The three remaining samples displayed single age populations within the early Pliocene period from 5.40 ± 0.46 Ma to 4.27 ± 0.54 Ma, which are deemed representative of this unit (Table 4.3). Zircons from seven samples of the main ore-bearing, phase 6 coarse-grained Cu-Au-Mo tonalite porphyry displayed Early Pliocene single age populations, from 4.34 ± 0.48 Ma to 4.03 ± 0.65 Ma (Tables 4.1, 4.2 and Fig. 4.5G). Zircons from five samples of phase 7 quartz diorite have single age populations and rare low-U zircons, all spanning the Early Pliocene from 4.17 ± 0.24 Ma to 3.94 ± 0.69 Ma (Tables 4.1, 4.2 and Fig. 4.5H).

Despite the distinct textural differences between the two main ore-bearing porphyry tonalites, phase 5 (very fine-grained equigranular texture), and phase 6 (coarse-grained strong crystal-crowded porphyritic texture), uncertainty still remains as to the exact timing of these two phases. It remains unclear as to whether phase 5 is simply a textural variant of phase 6. Type section construction (Fig. 4.2), identifies the spatial distribution of phase 5 as a clear, upper carapace to the deeper phase 6 tonalite. However, contacts between the two phases are generally gradational, with an increase in grain size and porphyritic texture from phase 5 to phase 6 with increasing depth. There have been no clear contacts between the units observed to date, or evidence of xenoliths that would suggest clear relative timing relationships between the two phases. The geochronological results do not resolve the question, because the ages for both phases overlap within uncertainty (Fig. 4.10). It remains unproven as to whether phase 5 is a chilled margin, or a carapace with distorted fine-grained equigranular texture to the deeper phase 6 tonalite, or a discrete intrusive phase. More precise age dating using isotope dilution-thermal ionization mass spectrometry (ID-TIMS) and CL imaging of quartz in phase 5 tonalite is required to resolve this problem. This geochronological study does however, put an end to the speculation discussed in section 3.4.1, that the phase 5 fine-grained tonalite porphyry could be pre-mineralization andesitic wallrock that was overprinted by phase 6 coarse-grained tonalite porphyry (e.g., Kavalieris and Bat-Erdene, 2012). The U-Pb data clearly shows an Early Miocene (4.87 ± 0.42 Ma to 4.11 ± 0.51 Ma) age for phase 5 tonalite and Middle Miocene (14.7 Ma ± 1.40 Ma and 13.5 Ma± 1.40 Ma) for andesite wallrock; a total age difference of over 8 m.y. (Fig. 4.10).

The age of the Tumpangpitu diatreme is interpreted here based on the youngest zircon age from the breccia matrix (2.7 ± 1.0 Ma.) which is considered to be the crystallization age (e.g., Baumgartner et al., 2009; Von Quadt et al., 2011). A total of 22 zircons were analyzed from the sample of upper facies diatreme breccia containing clasts of phases 2 - 7. Calculating the mean age (4.17 ± 0.21 Ma) is therefore meaningless as it represents a mixture of both clast and matrix ages. The presence of clasts of phase 7 quartz diorite in the breccia provide evidence that the age of the breccia must be younger than the phase 7

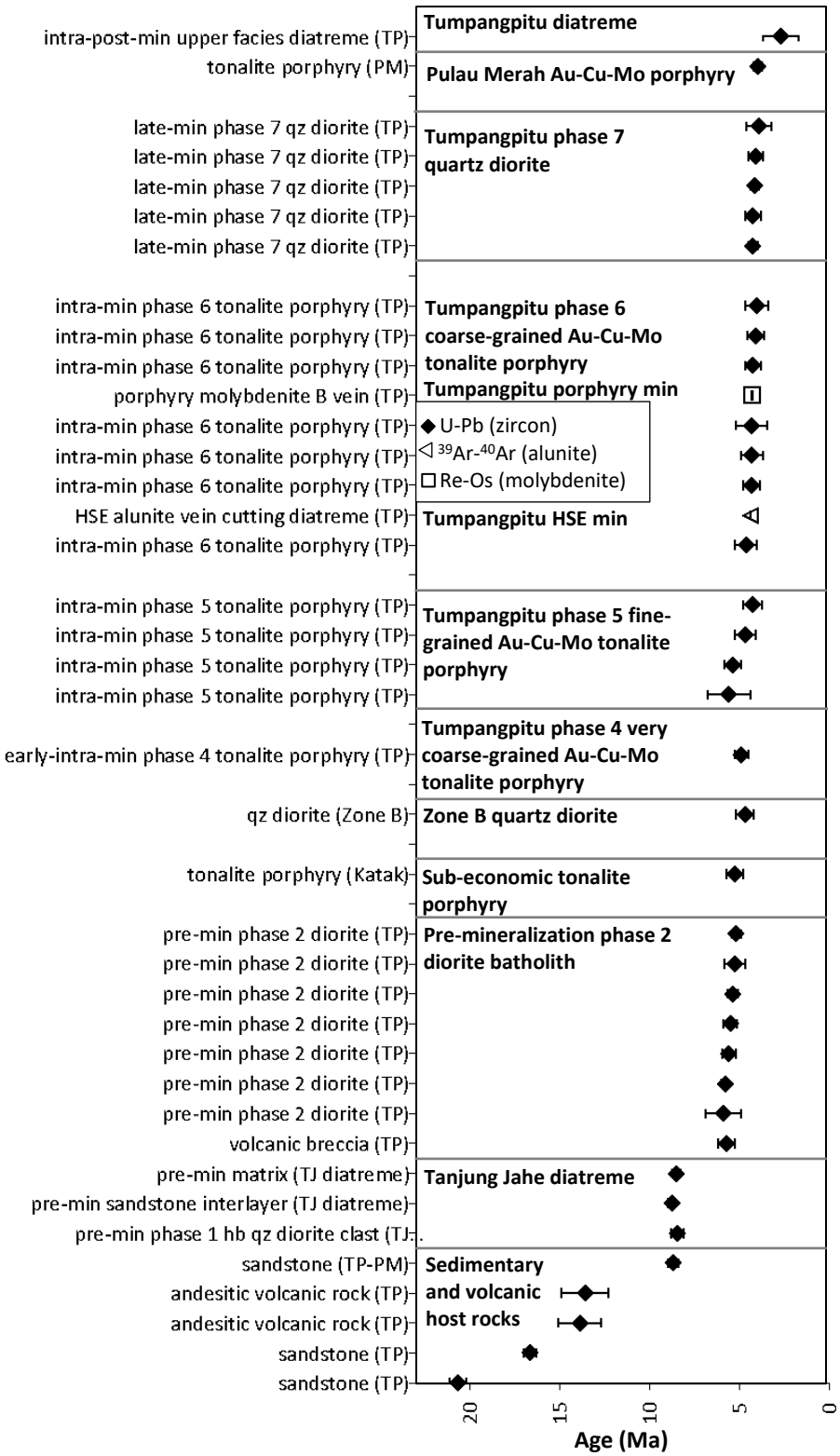

Figure 4.10. Summary of geochronology from host rocks and multiple porphyry intrusions at Tumpangpitu and other porphyries in the Tujuh Bukit district. Data-point error symbols are 2σ. Abbreviations: min = mineralization, PM = Pulau Merah island, qz = quartz, TJ = Tanjung Jahe diatreme, TP = Tumpangpitu. Data point error symbols are 2σ. All data are listed in Tables 4.1, 4.2, Chapter 5 and Appendix Table A1.

age range of 4.17 ± 0.24 Ma to 3.94 ± 0.69 Ma. All zircon dates older than this range are interpreted to be derived from wallrock clasts.

4.4.2 Timing and duration of magmatism in the Tumpangpitu intrusive complex

The U-Pb ages from Tumpangpitu reveal two main episodes of magmatism; a Late Miocene event that predates mineralization, followed by a Late Miocene to Early Pliocene event associated with mineralization. Late Miocene phreatomagmatic activity at Tanjung Jahe (8.78 ± 0.22 Ma) was associated with early intrusive activity (phase 1 hornblende quartz diorite 8.46 ± 0.36 Ma) and sedimentation near Pulau Merah (8.69 ± 0.29 Ma). Late Miocene magmatic activity was associated with the emplacement of the pre-mineralization phase 2 diorite batholith from 5.81 ± 0.2 Ma to 5.18 ± 0.27 Ma. A short-lived period of Late Miocene to Early Pliocene magmatism resulted in the formation of the Tumpangpitu mineralized intrusive complex, from 4.89 ± 0.40 Ma (phase 4 tonalite) to 4.03 ± 0.65 Ma (phase 6 tonalite). Cu-Au-Mo mineralization associated with the intrusive complex was terminated by the Tumpangpitu diatreme event; with the youngest breccia matrix zircon dated as 2.7 ± 1.0 Ma. The maximum age of the mineralized intrusive complex as defined by the U-Pb zircon dating in this study is 5.29 Ma (phase 4 tonalite), and the minimum age is 3.38 Ma (phase 6 tonalite), implying a duration of up to 1.91 m.y Ma for the porphyry complex. The minimum age as defined by late-stage phreatomagmatic activity is 1.7 Ma, implying a duration of up to 3.59 m.y for epithermal mineralization. The emplacement of the post-mineralization dikes (phase 8), and the formation of the Tumpangpitu diatreme signalled the end of magmatism, and ultimately the termination of magmatic-hydrothermal activity.

4.4.3 Rate of uplift and exhumation

By the time of diatreme formation, the top of phase 5 tonalite was 710 m below the paleosurface (Figs. 3.3 - 3.8; 4.2 - 4.3). The maximum time difference between phase 5 tonalite and the Tumpangpitu diatreme is 4.16 m.y and minimum is 0.3 m.y (Table 4.1). Assuming the upper surface of phase 5 tonalite was at a depth of 2 km when it was emplaced, an uplift rate of between 0.31 and 43 km/m.y can be estimated. If at 3 km depth, the uplift rate is between 0.55 and 76.3 km/m.y (Table 4.5). The large errors on the ages for both the phase 5 tonalite and Tumpangpitu diatreme has led to a huge range in the estimated uplift rates. It is not possible to better constrain the uplift rates and depth of porphyry mineralization without fluid inclusion studies and more precise dating (e.g., ID TIMS).

4.4.4 Timing of magmatism - a district context

Samples from porphyry prospects in the Tujuh Bukit district (Table 4.1, Figs. 1.4, 4.1 and 4.6) provide insights into the magmatic evolution of the district and have implications for the tectonic plate

configuration beneath the Tujuh Bukit region. Zircons from the Katak porphyry, 2.7 km northeast of Tumpangpitu (Fig. 4.6A and 4.14), form a single age population plotting close to concordia for the Late Miocene period with a mean $^{206}Pb/^{238}U$ age of 5.26 ± 0.47 Ma. Zircons from a quartz diorite porphyry at Zone B, 1.5 km south of Tumpangpitu (Fig. 1.4) form a single age population plotting close to concordia for the Early Pliocene period, with a mean $^{206}Pb/^{238}U$ age of 4.53 ± 0.48 Ma (Fig. 4.6B). Zircons from the Pulau Merah tonalite porphyry have provided the youngest inter-mineralization porphyry age to date, with a single mean $^{206}Pb/^{238}U$ age population for the Early Pliocene period at 3.92 ± 0.21 Ma (Fig. 4.6C).

In general, the porphyry intrusions in the Tujuh Bukit dataset have been emplaced along two major NW-trending mineralized corridors; the Pulau Merah - Tumpangpitu - Zone B corridor and the Salakan - Katak - Gunung Manis corridor, 2 - 2.7 km to the northeast (Fig. 4.12). Results of exploration drilling suggest that the latter corridor is host to weaker, lower grade Au-Cu-Mo mineralization, when compared to the former corridor. The U-Pb geochronology results (5.26 ± 0.47 Ma for the Katak porphyry; Fig. 4.6A) tentatively implies that the Salakan - Katak - Gunung Manis corridor formed approximately 1 m.y prior to the emplacement of the mineralizing intrusions along the more strongly mineralized southern corridor that hosts the high grade Tumpangpitu deposit and Pulau Merah island porphyry (Fig. 4.12). However, additional geochronological dating of porphyry prospects including Salakan, Candrian and the low-sulfidation epithermal veins at Gunung Manis, are required to substantiate this hypothesis.

Age determinations for Batu Hijau, Sumbawa island by Garwin (2000) returned SHRIMP $^{206}Pb/^{238}U$ zircon ages for four major felsic intrusive episodes, each separated by 0.6 to 0.9 m.y. These results defined ages in the district that range from 5.9 to 3.7 Ma (Table 4.6, Fig. 4.11 and Fig. 4.13; Garwin, 2000). The duration of the Batu Hijau hydrothermal system was estimated to be 80 ± 80 k.y. (2σ), as determined from the $^{40}Ar/^{39}Ar$ closure of early biotite and late sericite (3.73 ± 0.08 Ma and 3.65 ± 0.02 Ma respectively; Garwin, 2000). An age date for the inter-mineralization Delta tonalite from the Elang porphyry deposit to the east of Batu Hijau (Fig. 1.4), returned a SHRIMP $^{206}Pb/^{238}U$ age of 2.71 Ma ± 0.14 Ma (Table 4.6; Fig. 4.13; Garwin, 2000; Lubis et al., 2005). The poorly endowed porphyry, Katala is located 2 km northeast of Batu Hijau (Fig. 4.12), with the range of pre- to inter-mineralization porphyries and early hydrothermal alteration bracketing the Early Pliocene (U-Pb zircon ages; 4.86 - 4.29 Ma and ^{40}Ar-^{39}Ar age of secondary biotite; 4.4 Ma; Table 4.6; Garwin, 2000). Similar to age dates at Tujuh Bukit, this implies that the sub-economic Katala porphyry formed approximately 1 m.y prior to the emplacement of the well mineralized Batu Hijau porphyry complex (Figs. 4.12 and 4.13). The geochronological results from both the Tujuh Bukit and Batu Hijau districts suggest a local reversal in the overall south to north younging direction at the district scale, and therefore complexity in the underlying tectonic slab configuration, with respect to large-scale magmatism along the Sunda-Banda arc. There has been a north-eastwards migration of volcanic centres since the Eocene resulting in the present-day position of active volcanoes (Fig. 4.4).

Table 4.6. Summary of geochronological age determinations from selected porphyries, host rocks and alteration minerals ranked by age from west to east along the Sunda-Banda magmatic arc.

Deposit/prospect	Sample ID/depth (m)	Coordinates/ RL (m)	Sample type	U-Pb zircon	Re/Os molybdenite	K-Ar alunite	K-Ar adularia	Relationship to alteration and mineralization	Reference
Northwest Sumatra									
Barisan	NA	NA	Molybdenite vein	-	2.14 ± 0.01	-	-	Syn Cu-Au porphyry mineralization	Barisan Gold Corp. (2013)
Purnama, Martabe	APSD073_59.75	NA	Alunite	-	-	2.14 ± 0.10	-	Syn-HSE mineralization (supergene alunite replacing feldspar)	Sutopo (2013)
Baskara, Martabe	APSD249_137	NA	Hornblende-phyric andesite	2.8 ± 0.3	-	-	-	Pre-HSE mineralization;	Sutopo (2013)
Purnama, Martabe	APSD150_18	NA	Hornblende-phyric andesite	3.1 ± 0.4	-	-	-	Pre-HSE mineralization;	Sutopo (2013)
Purnama, Martabe	APSD156_115.3	NA	Alunite vein	-	-	3.3 ± 0.11	-	Syn-HSE mineralization (hypogene age)	Sutopo (2013)
Purnama, Martabe	APSD071_63	NA	Quartz-phyric dacite	3.8 ± 0.5	-	-	-	Pre to syn-HSE mineralization; host rock to HSE	Sutopo (2013)
West Java									
Ciawitali	-	NA	Au-Ag LSE veins	-	-	-	1.5 ± 0.1	Syn-LSE mineralization	Marcoux and Milesi (1994)
Cirotan	-	NA	Au-Ag ISE veins	-	-	-	1.7 ± 0.1	Syn-ISE mineralization	Marcoux and Milesi (1994)
Gunung Pongkor	-	NA	Au-Ag LSE veins	-	-	-	2.05 ± 0.05	^{40}Ar-^{39}Ar age; syn-LSE mineralization	Milesi et al. (1999)
Cipangleseran	-	NA	Au-Ag LSE veins	-	-	-	2.1 ± 0.6	Syn-LSE mineralization	Marcoux and Milesi (1994)
Cikidang	-	NA	Au-Ag LSE veins	-	-	-	2.4 ± 0.1	Syn-LSE mineralization	Rosana (2002)
Cibaliung	-	NA	Au-Ag LSE veins	-	-	-	11.14 ± 0.06 - 11.1 ± 0.09	Syn-LSE mineralization	Harijoko et al. (2004)

Table 4.6. *(Cont.)*

Sample ID/depth (m)	Sample ID/depth (m)	Coordinates/ RL (m)	Sample type	U-Pb zircon	^{40}Ar-^{39}Ar hornblende	^{40}Ar-^{39}Ar adularia	^{40}Ar-^{39}Ar sericite	Relationship to alteration and mineralization	Reference
East Java									
Jerambah, Trenggalek	TRDD054/136.2	E569933 N9088734 / 640	Andesite porphyry	11.8 ± 1.2	-	-	-	Post-porphyry mineralization	Arc Exploration (2013)
Jerambah, Trenggalek	TRDD054/188.5	E569933 N9088734 / 640	Quartz diorite/tonalite	12.6 ± 0.8	-	-	-	Syn-porphyry mineralization	Arc Exploration (2013)
Jerambah, Trenggalek	TRDD054/501	E569933 N9088734 / 640	Tonalite	13.8 ± 1.0	-	-	-	Syn-porphyry mineralization	Arc Exploration (2013)
Jati, Trenggalek	090329-01/0	E567486 N9105658 / 415	Hornblende from crystal tuff	-	15.6 ± 0.5	-	-	Pre-mineralization; crystal tuff/sandstone interbedded with limestone capping the epithermal system	Takahashi et al. (2014)
Jerambah, Trenggalek	TRDD054 /576.6	E569933 N9088734 / 640	Fine-grained diorite	17.2 ± 0.7	-	-	-	Pre-mineralization	Arc Exploration (2013)
Bogoran, Trenggalek	ARXBOG-03/0	E571264 N9096636 / 313	Diorite	18.7 ± 1.0	-	-	-	Pre-mineralization	Arc Exploration (2013)
Singgahan, Trenggalek	ARMTRDD-055-1/174	E574956 N9088554 / 351	Medium-grained tonalite	14.00 ± 0.44	-	-	-	Syn-porphyry mineralization; weak quartz stockwork veining, quartz - magnetite - pyrite, minor magnetite - chalcopyrite; late calcite veining	This study
Singgahan, Trenggalek	ARMTRDD-057-1/156	E574956 N9088554 / 351	Fine-grained tonalite	14.04 ± 0.45	-	-	-	Syn-porphyry mineralization; quartz - magnetite – pyrite - chalcopyrite stockwork veining	This study
Dalangturu, Trenggalek	YS080519-11/0	E568906 N9107365 / 305	Quartz-adularia Au-Ag LSE veins	-	-	16.29 ± 0.56	-	Syn-LSE mineralization; gold-bearing banded chalcedony - adularia - sulfide	Takahashi et al. (2014)
Tulungagung	ARX-TA-01/0	E609486 N9093540 / 289	Quartz feldspar porphyry	23.40 ± 1.0	-	-	-	Syn-HSE mineralization	Arc Exploration (2013)

Table 4.6. *(Cont.)*

Deposit/prospect	Sample ID/depth (m)	Coordinates/ RL (m)	Sample type	U-Pb zircon	^{40}Ar-^{39}Ar biotite	^{40}Ar-^{39}Ar sericite	Relationship to alteration and mineralization	Reference
Southwest Sumbawa								
Batu Hijau	SBD15/36	NA	Quartz - sericite - pyrite D vein in porphyritic dacite	-	-	3.65 ± 0.02	Syn-porphyry mineralization; 1 cm wide D vein cutting porphyritic dacite	Garwin (2000)
Batu Hijau	SBD91/416	NA	Old tonalite	3.67 ± 0.12	-	-	Early-porphyry mineralization; cut by A and B veins	Garwin (2000)
Batu Hijau	SBD41/414	NA	Young tonalite	3.74 ± 0.14	-	-	Late-porphyry mineralization; cut by B and D veins	Garwin (2000)
Batu Hijau	SBD04/157	NA	Intermediate tonalite	3.76 ± 0.10	3.73 ± 0.08	-	Syn-porphyry mineralization; quartz rinds; cut by A and B veins	Garwin (2000)
Batu Hijau	SBD91/444	NA	Hornblende-phyric andesite	-	3.74 ± 0.12	-	Pre-porphyry mineralization	Garwin (2000)
Batu Hijau	SBD10/279	NA	Equigranular hornblende quartz diorite	-	3.72 ± 0.06	-	Pre-porphyry mineralization	Garwin (2000)
Batu Hijau	SBD12/329	NA	Porphritic dacite	3.89 ± 0.08	-	-	Pre-porphyry mineralization; cut by A and B veins	Garwin (2000)
Katala, Batu Hijau	97101030	NA	Equigranular hornblende-biotite quartz diorite	4.43 ± 0.14	-	-	Early-to syn-porphyry mineralization; cut by aplite veins and local A and B veins	Garwin (2000)
Katala, Batu Hijau	97100808A	NA	Equigranular biotite granodiorite dike	4.49 ± 0.12	-	-	Syn-to late porphyry mineralization; cut by D veins	Garwin (2000)

Table 4.6. *(Cont.)*

Deposit/prospect	Sample ID/depth (m)	Coordinates/ RL (m)	Sample type	U-Pb zircon	^{40}Ar-^{39}Ar biotite	^{40}Ar-^{39}Ar sericite	Relationship to alteration and mineralization	Reference
Katala, Batu Hijau	SKD01/276	NA	Porphyritic hornblende tonalite	4.70 ± 0.16	4.48 ± 0.08	-	Pre-porphyry mineralization; cut by A veinlets	Garwin (2000)
Katala, Batu Hijau	SKD01/468	NA	Porphyritic hornblende tonalite	-	4.37 ± 0.08	-	Pre-porphyry mineralization; cut by A veinlets	Garwin (2000)
Arung Ara	SRD02/305	NA	Porphyritic hornblende tonalite	4.99 ± 0.16	-	-	Syn-porphyry mineralization; cuts A veinlets and is cut by B and D veins	Garwin (2000)
Sekongkang	97091713A	NA	Equigranular biotite granodiorite dike	5.88 ± 0.14	5.47 ± 0.08	-	Syn-porphyry mineralization: contains quartz rinds; magmatic biotite forms clusters with pyrite; biotite alteration of wallrock	Garwin (2000)
Sekongkang	SAD05/296	NA	Sub-porphyritic biotite tonalite	-	5.47 ± 0.06	-	Syn-porphyry mineralization: shreddy hydrothermal biotite with pyrite - ilmenite -chalcopyrite	Garwin (2000)
Tongoloka	98100401	NA	Fault-volcanic lithic breccia	-	-	5.92 ± 0.06	Syn-base metal mineralization 3 m wide sericite zone from 0.1 - 0.5 m quartz - sphalerite - galena - chalcopyrite - pyrite vein	Garwin (2000)
Teluk Puna	98112302	NA	Dacitic volcaniclastic breccia	6.84 ± 0.16	-	-	Pre-mineralization; cut by Teluk Puna quartz veins	Garwin (2000)
Tongoloka	98111802	NA	Fault-volcanic lithic breccia	-	-	7.05 ± 0.11	Pre-mineralization; 50 cm wide fault gauge breccia zone internal to quartz diorite	Garwin (2000)
Elang	SGDLD08/423	NA	Delta tonalite	2.71 ± 0.14	-	-	Syn-porphyry mineralization	Garwin (2000)

All ages are quoted in Ma ± 2σ. Abbreviations: Au = gold, Ag = silver, HSE = high-sulfidation epithermal, LSE = low-sulfidation epithermal, A, B and D type veins after Gustafson and Hunt (1945). NA = data not available.

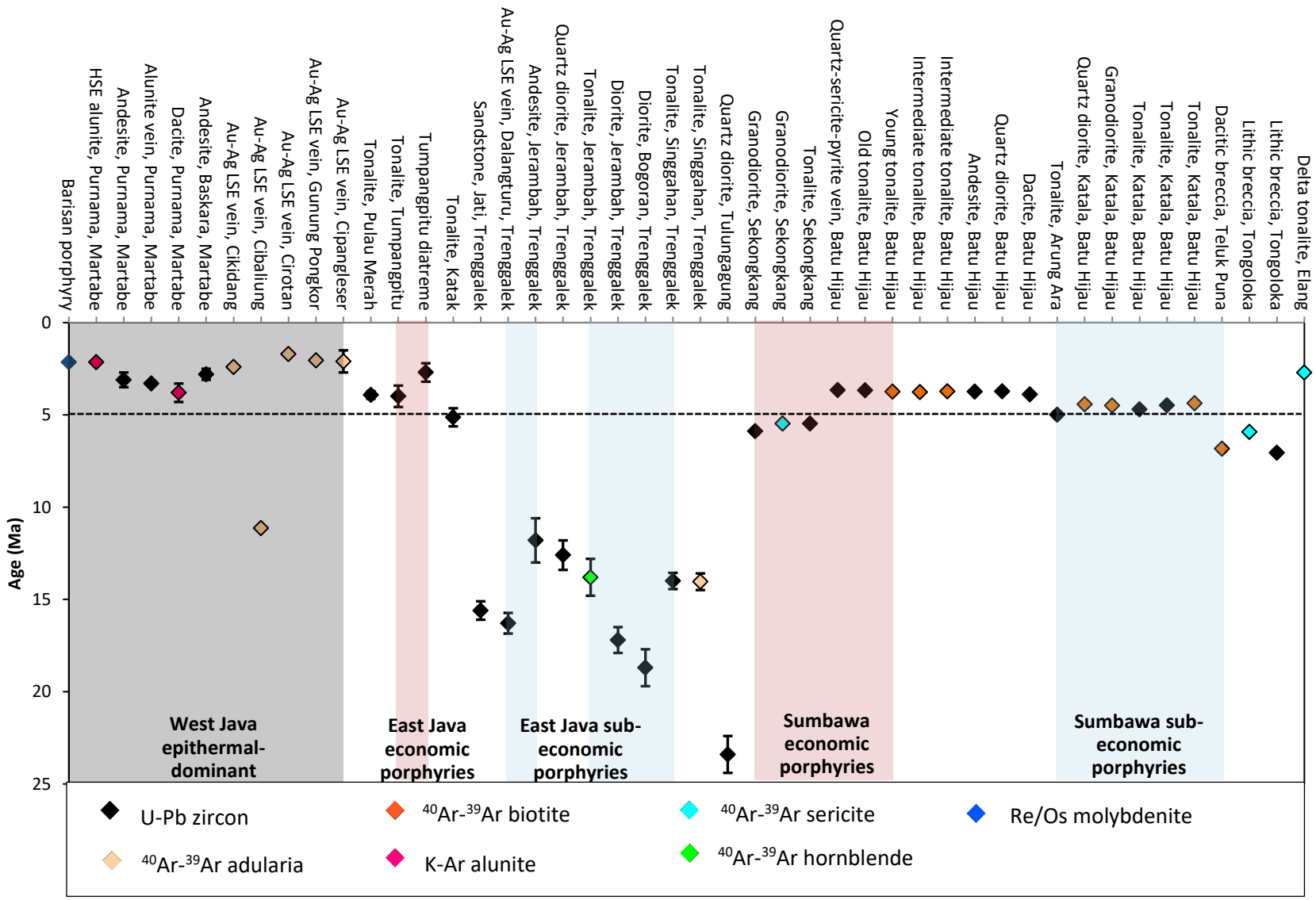

Figure 4.11. Summary of geochronological age determinations from selected porphyry deposits, host rocks and alteration minerals along the Sunda-Banda magmatic arc listed from west to east. Data-point error symbols are 2σ. All data and references listed in Tables 4.1, 4.2 and 4.6. Grey shading represents epithermal-style mineralization, pink shading = well-endowed porphyry deposits and blue shading = poorly-endowed porphyry deposits.

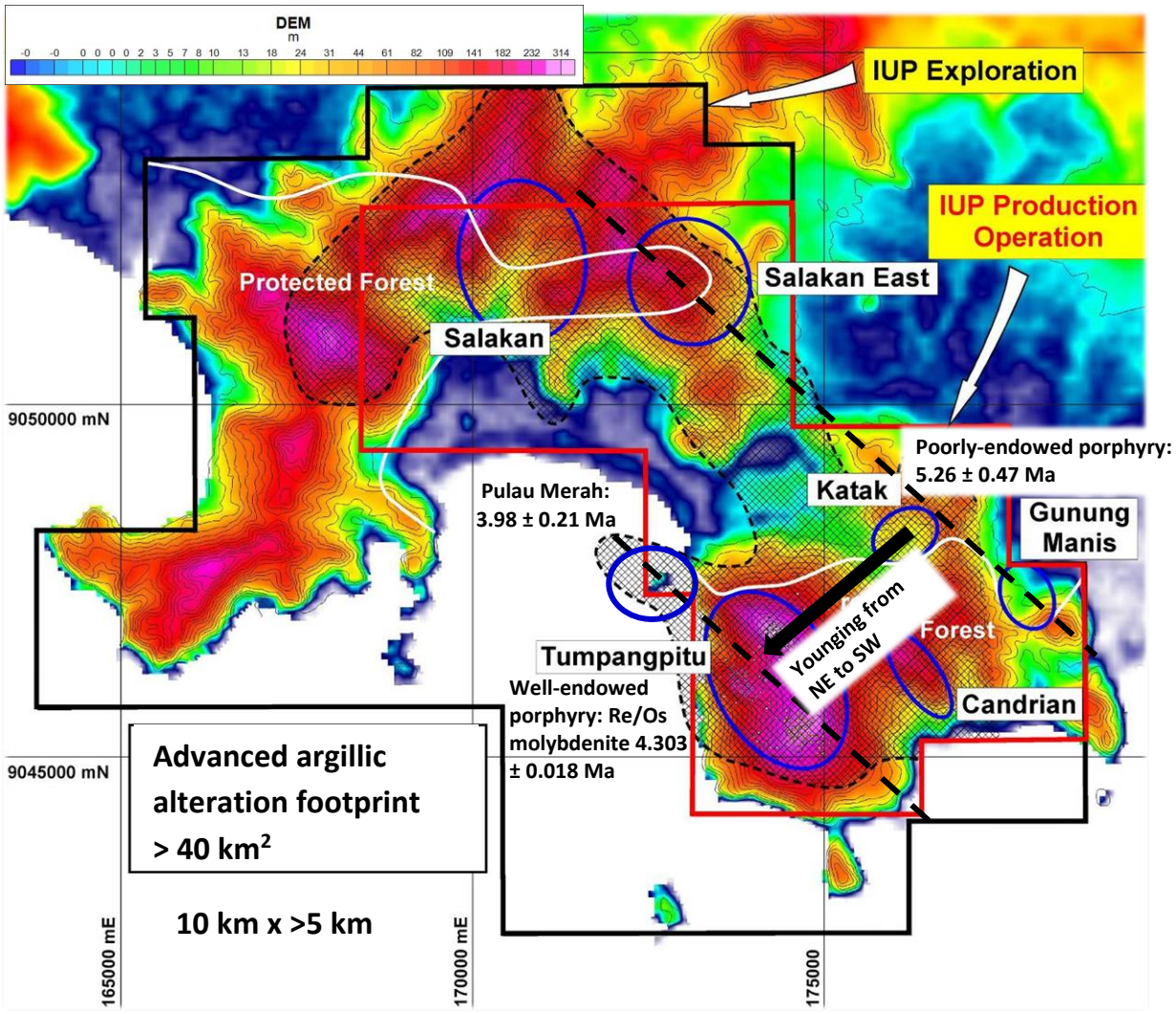

Figure 4.12. U-Pb zircon age determinations for Pulau Merah, Tumpangpitu and Katak tonalite Cu-Au-Mo porphyries. All data listed in Table 4.1 and Chapter 5.

At Tujuh Bukit and Batu Hijau, the intrusions in both districts are progressively younger and more fertile from north to south (Figs. 4.12 - 4.13).

4.4.5 Timing and duration of magmatism along the Sunda-Banda magmatic arc

The absolute age data presented in this study confirms a consistent younging age from Trenggalek (~ 15 Ma) eastwards along the Sunda-Banda arc to the well-endowed porphyry deposits of the Tujuh Bukit district (~ 4 Ma) to Batu Hijau (~ 3.7 Ma) to Elang (~ 2.7 Ma) in Sumbawa (Figs. 4.4, 4.13 and Table 4.6). The economic Au ± Ag ± Cu epithermal and Au - Cu ± Mo porphyry deposits in the Tujuh Bukit district including Tumpangpitu and Pulau Merah formed during the Pliocene. The 5 Ma line on Figure 4.11 represents an approximate cut off between well-endowed porphyry and epithermal deposits (e.g., West Java LSE and ISE, Barisan porphyry, Martabe HSE, Tumpangpitu, Pulau Merah, Batu Hijau and Elang

porphyries) and poorly-endowed deposits (e.g., Singgahan and Jerambah porphyries, Trenggalek project, East Java).

The eroded remnants of the Southern mountains arc are exposed along the southern coast of Java. They were thought previously to be of Oligo-Miocene age, based on their position along the eroded segment of the Sunda Banda magmatic arc (Fig. 4.4, 4.15A; Bemelen, 1949; Rohrlach, 2011). Smyth et al. (2007) postulated that the Sunda-Banda arc was active from the middle Eocene until the Early Miocene. The current study has provided the youngest geochronologic ages ever recorded for East Java, allowing the age bracket of the Southern mountains to be redefined as middle Eocene to Early Pliocene (Tables 4.1 - 4.3; Fig. 4.4).

Table 4.6 and Fig. 4.11 present a summary of the geochronological age determinations from Au epithermal and porphyry deposits and prospects along the Sunda-Banda magmatic arc. The data shows that epithermal and porphyry deposits in NW Sumatra formed during the Pliocene. These ages are similar to those from low-sulfidation epithermal deposits in West Java which formed between 2.5 and 1.6 Ma (Late Pliocene to Early Pleistocene), not including the older Cibaliung deposit (Table 4.6).

U-Pb zircon and ^{40}Ar-^{39}Ar hornblende dates from porphyries and host rocks at Trenggalek, East Java, along with a ^{40}Ar-^{39}Ar age of low- and intermediate- sulfidation epithermal mineralization from adularia, point to an Early to Middle Miocene age of mineralization in this segment of the Sunda-Banda arc (Table 4.6). The wide range of ages from the mineralized porphyry at Jerambah (Fig. 4.11, Table 4.6; 13.8 ± 1.0 Ma to 12.6 ± 0.8 Ma), Singgahan (14.04 ± 0.45 Ma to 14 ± 0.44 Ma; Arc Exploration, 2013) and low-sulfidation epithermal mineralization at Dalangturu (16.29 ± 0.56 Ma; Takahashi et al., 2011) is indicative of multiple Middle Miocene porphyry and epithermal systems in the Trenggalek district.

4.4.6 Geodynamic evolution

The Sunda-Banda arc initiated in the middle Miocene, and underwent a period of extension related to slab rollback around 15 - 12 Ma (Fortuin et al. 1997; Hall, 2002; Fiorentini and Garwin, 2005; Spakman and Hall, 2010). This initiated a polarity shift to southward-directed subduction of oceanic crust of the marginal Banda Sea beneath the arc (Fig. 2.1; Fiorentini and Garwin, 2009).

Local reversals in ages noted between well-endowed and poorly-endowed porphyries in the Tujuh Bukit and Batu Hijau porphyry districts may be associated with complexities relating to subduction of the Roo Rise - a trapped slab of thick oceanic crust (Fig. 1.1). A series of northwest-trending major transform faults have been indirectly mapped by the alignment of earthquake epicentres transecting an area of the Roo Rise (Fig. 1.4; Hall, 2009). These northwest-trending faults are part of the same fault system that has intersected and displaced Java, Lombok and Sumbawa (Fig. 1.4). The transform faults are interpreted to have formed due to differences in thickness between the oceanic crust (Setijadi, 2006; Hall, 2009).

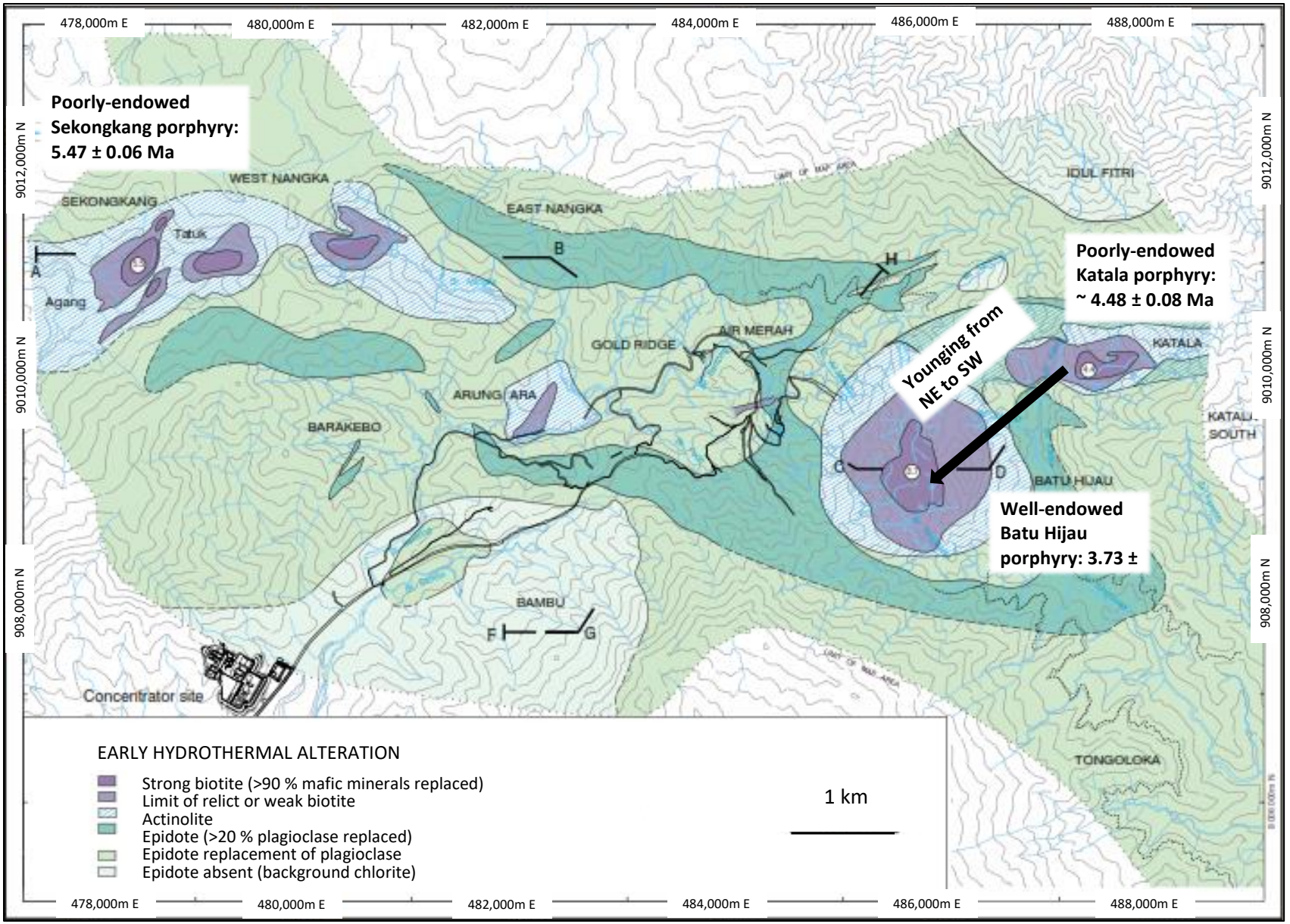

Figure 4.13. ^{40}Ar-^{39}Ar ages of secondary biotite from porphyries in the Batu Hijau district (Garwin, 2000).

The fact that the Roo Rise is thick and cool, compared to ridges elsewhere that are anomalously hot, may influence the tonalite versus diorite compositions that characterize the Sunda-Banda arc. When oceanic crust was being subducted underneath the continental crust of Sundaland (part of Java and Sumatra), it may have torn (Setijadi, 2006; Fiorentini and Garwin, 2009; Maryono, 2012). A low angle of subduction thickens the crust due to thrust fault stacking. A high subduction angle promotes extension and thins the crust. The resultant thin segment had a high subduction angle, being anomalously hot and buoyant, whereas the thick segment was subducted at a lower angle. The impact to magmatism is migration closer towards the trench, i.e., from northeast to southwest, as identified at Tujuh Bukit and Batu Hijau (Garwin, 2000; Garwin, 2005; Setijadi, 2006; Fiorentini and Garwin, 2009; Maryono, 2012; Maryono et al., 2017; Figs. 4.12 - 4.13).

4.4.7 Basement architecture of the Sunda Banda arc - comparison of U-Pb zircon dates

Smyth et al. (2007) found that inherited zircons in Cenozoic sedimentary and igneous rocks of East Java range in age from Archean to Cenozoic (Fig. 4.14). The age distribution was interpreted to reflect two different basement types at depth. The igneous rocks of the early Cenozoic arc found along the southeast coast of East Java in their study area (Fig. 4.14) contained only Archean to Cambrian zircons (Fig. 4.14). Clastic rocks of north and west of East Java contain Cretaceous zircons, which are not found in the arc rocks in the study area to the south (Fig. 4.14; Smyth et al., 2007). Occurrences of Cretaceous zircon grains support interpretations that much of eastern Java is underlain by arc and ophiolitic rocks accreted to the Southeast Asian margin during Cretaceous subduction, consistent with the findings of Hamilton (1979). The age populations of Archean to Cambrian zircons found in eastern Java by Smyth et al. (2007) are interpreted to signify the source rocks as Gondwanan crust. They interpreted the eastern Java Early Cenozoic arc to be underlain by a continental fragment of Gondwanan origin, and not Cretaceous material as previously suggested by Hamilton (1979). Melts that rose through or pooled in the continental crust, fed the Early Cenozoic arc, and picked up the ancient zircons through assimilation or partial melting. The presence of continental crust beneath eastern Java is supported by the evolved character of the products of the Southern Mountains Arc and the rocks that intruded them, as well as the evolved geochemical signature, including elevated molybdenum and tin (Chapter 5). Smyth et al. (2007) and Hall and Sevastjanova (2012) suggested a Western Australian origin for the continental fragment, based on similarities of the Cambrian-Archean data set from East Java with sedimentary rocks of the Pilbara and Yilgarn Cratons of Western Australia. East Java and the Malino Complex of NW Sulawesi (van Leeuwen et al., 2007) are the only parts of Indonesia so far where Archaean zircons with ages greater than 3 Ga have been found (Hall, 2012). The Western Australian fragment is interpreted to have rifted from Australia during the Mesozoic (Jurassic; Fig. 4.16; Hall and Sevastjanova, 2012) and collided with Southeast Asia, resulting in the termination of

Cretaceous subduction. Continental crust was therefore present at depth beneath the arc in south Java when Cenozoic subduction began in the Eocene (Smyth et al., 2005; 2007).

The absence of Archean zircon grains from the 516 analyses in the Tujuh Bukit dataset could be due to the following reasons:

1) There is no Archean basement below Tujuh Bukit
2) The igneous rocks sampled are not the type that normally inherit significant crustal material
3) If there was assimilation, the level at which assimilation took place was shallow, and not in the Archean basement
4) Laser ablation analysis preferentially targeted zircon rims to gain the magmatic age and therefore avoided inheritance of Archean zircons

Two Cretaceous zircon grains (98.5 ± 1.0 Ma and 98.5 ± 0.8 Ma; Fig. 4.5D; Appendix Table A1) were found in the Late Miocene Tanjung Jahe diatreme breccia (9.00 - 8.31 Ma) during this study. Smyth et al. (2007) documented a clear geographical pattern of the presence of Archean zircons and a clear absence of Cretaceous grains east of Rembang in East Java, including a sample from Jember less than 50 km west of Tujuh Bukit (Fig. 4.14B). The occurrence of Cretaceous grains towards the far eastern coastline of Java at Tujuh Bukit, may imply that the Tanjung Jahe diatreme tapped andesitic material outside of the eastern boundary of the interpreted suture zone of the fragment of Archean Gondwanan crust (Figs. 4.14 - 4.16; Smyth et al., 2007; Hall, 2012).

The zircon grains identified in the sedimentary rocks at Tujuh Bukit (Fig. 4.5A; 4.10 and Table 4.1) could have been incorporated through erosion and transport of sediment from exposed source areas, such as the local sedimentary basement or from volcanic sources by airfall and subsequent reworking. As well as being resistant to weathering, zircon is known to survive episodes of melting (Hanchar and Hoskin, 2003). Material of Cretaceous origin found in the Tanjung Jahe diatreme may have been introduced to magma driving phreatomagmatic activity along the Southern Mountains Arc.

Hall and Sevastjanova (2012) speculated that a large fragment of Gondwana could extend beneath Sulawesi (Fig. 4.15B and 4.16) and Hall et al. (2009) and Hall (2012) interpreted the East Java-West Sulawesi basement as the Argo block. Continental fragments of the Argo block were added to SE Asia around 90 Ma (Hall, 2012). The absence of any Archean age zircons in this study's 516 zircon analyses from the Tujuh Bukit district, could signify that the basement underneath Tumpangpitu is only as old as the Cretaceous, or it may be that Archean material is present, but has not yet been analyzed. The Tujuh Bukit district is located on or near the eastern suture zone of the Archean Argo block (Fig. 4.15).

4.5 Conclusions

This U-Pb zircon study has provided absolute ages for basal sedimentary and andesitic host rocks, volcanic breccia, and most of the porphyry intrusions at Tumpangpitu and other porphyry prospects in the district. It has also constrained the ages of both a pre-mineralization, relatively dry volcanic breccia pipe event (Tanjung Jahe) and a late-mineralization diatreme complex associated with a significant, large magmatic-hydrothermal system (Tumpangpitu) in the same district. The absolute age determinations support cross-cutting relationships determined from drillcore re-logging, type section construction (Fig. 4.2) and coastal mapping (Harrison, 2009). The new zircon dates have helped to refine the geological model and resolved uncertainty in a number of areas at Tumpangpitu. Some of the samples were taken from zones of intense hydrothermal alteration and quartz flooding, where primary lithological textures had been obliterated. In these zones, it can be very difficult to distinguish altered wall rocks from the porphyry intrusions, particularly the finer grained porphyries, such as phase 5 fine-grained tonalite (e.g., Fig. 4.5H). The age determinations have provided confidence for assigning strongly altered material to wall rocks (Middle to Early Miocene), early diorite (Late Miocene) or inter-mineralization porphyries (Early Pliocene).

Assuming the phase 5 tonalite was emplaced at a depth of 2 km and uplifted to ~700 m below present day surface by the time of diatreme formation, a conservative uplift rate of 0.3 km/yr has been estimated if 4 m.y separates the two events, and faster rates if the time period was less. This suggests extreme rates of uplift (> 0.3 km/m.y; Seedorff et al. 2005) and erosion in the vicinity of the Sunda-Banda magmatic arc.

The new U-Pb data has shown that the Tanjung Jahe pre-mineralization (Late Miocene) diatreme is significantly older than the Tumpangpitu late-mineralization diatreme (Late Pliocene), suggesting that a phase of phreatomagmatic activity on the southeast end of the Tumpangpitu diatreme pre-dated mineralization at Tumpangpitu by > 4 m.y. This magmatism then migrated northwest (Fig. 4.1), following the structural trend of the district (Fig. 4.4). Based on the age of the Katak porphyry at Tujuh Bukit (5.26 ± 0.47 Ma; Fig. 4.12), the Salakan - Katak - Gunung Manis corridor formed approximately 1 m.y prior to the emplacement of the mineralizing intrusions along the more strongly mineralized southern corridor determined by Tumpangpitu and Pulau Merah (Fig. 4.12).

Overall, zircon age determinations in the Tujuh Bukit and Batu Hijau districts indicates that district scale magmatism younged from northeast to southwest in both districts, opposite to the trend of present day volcanism along the Sunda-Banda arc (Fig. 4.4; Maryono et al., 2012, 2017). This study has also provided the youngest geochronological age determinations recorded for igneous rocks in East Java, allowing the age bracket of the Southern mountains of Java to be redefined as middle Eocene to Early Pliocene (Tables 4.1 - 4.3; Fig. 4.4). The presence of Cretaceous zircons, coupled with the absence of Archean zircons in

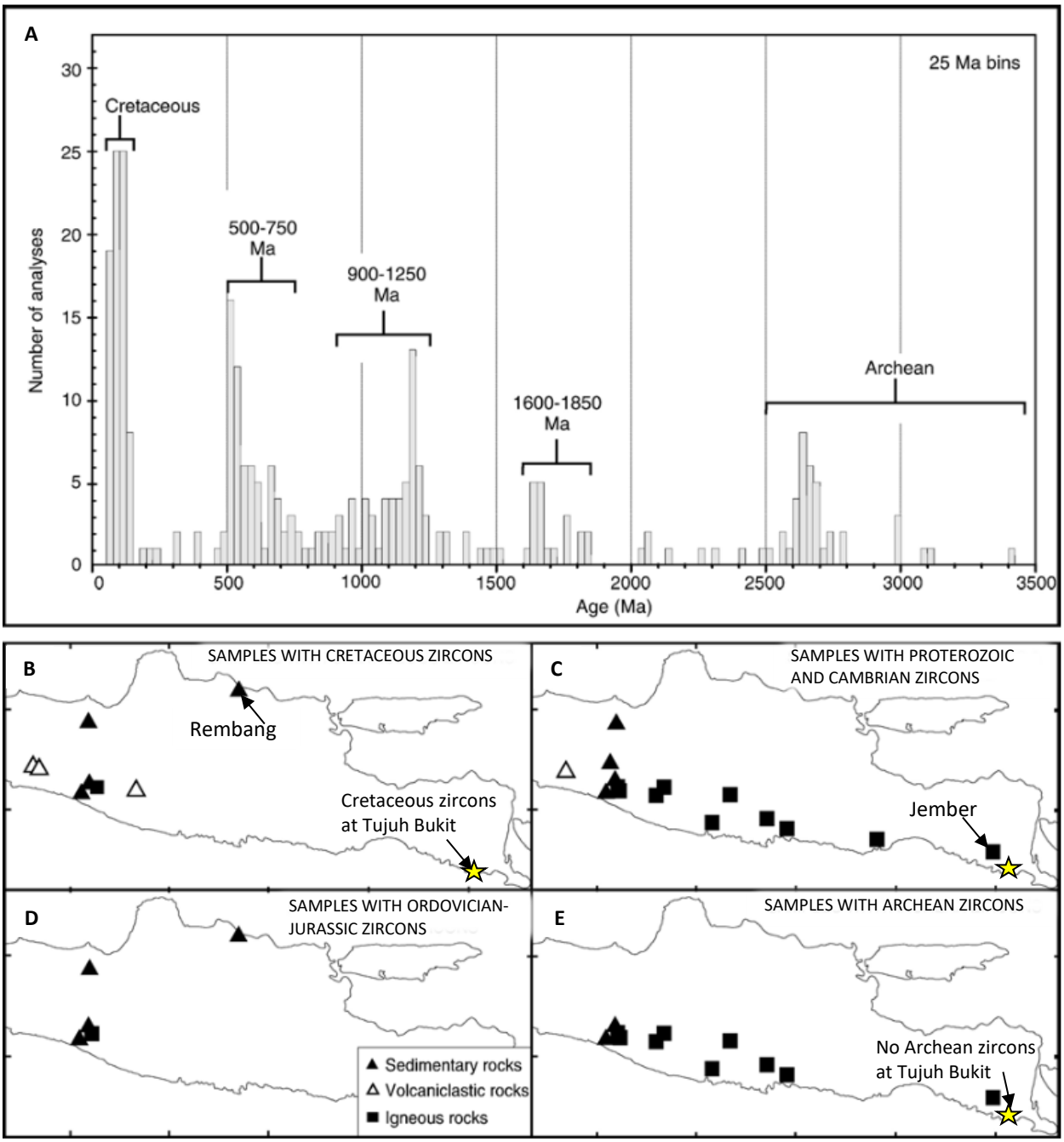

Figure 4.14. Location of Tujuh Bukit (yellow star) with respect to age ranges of zircons (bins on the histogram represent 25 Ma and the values are plotted with 2σ errors) B. Samples with Cretaceous zircons. C. Samples with Ordovician to Jurassic zircons. D. Samples with Proterozoic to Cambrian zircons. E. Samples with Archean zircons. Modified after Smyth et al. (2007)

the 516 analyses from the Tujuh Bukit region, has provided important insights into the potential source(s) of the underlying continental basement of the eastern Sunda magmatic arc. The ages of zircons from Tujuh Bukit implies that the district may be close to or on the eastern margin of the Archean fragment of ancient

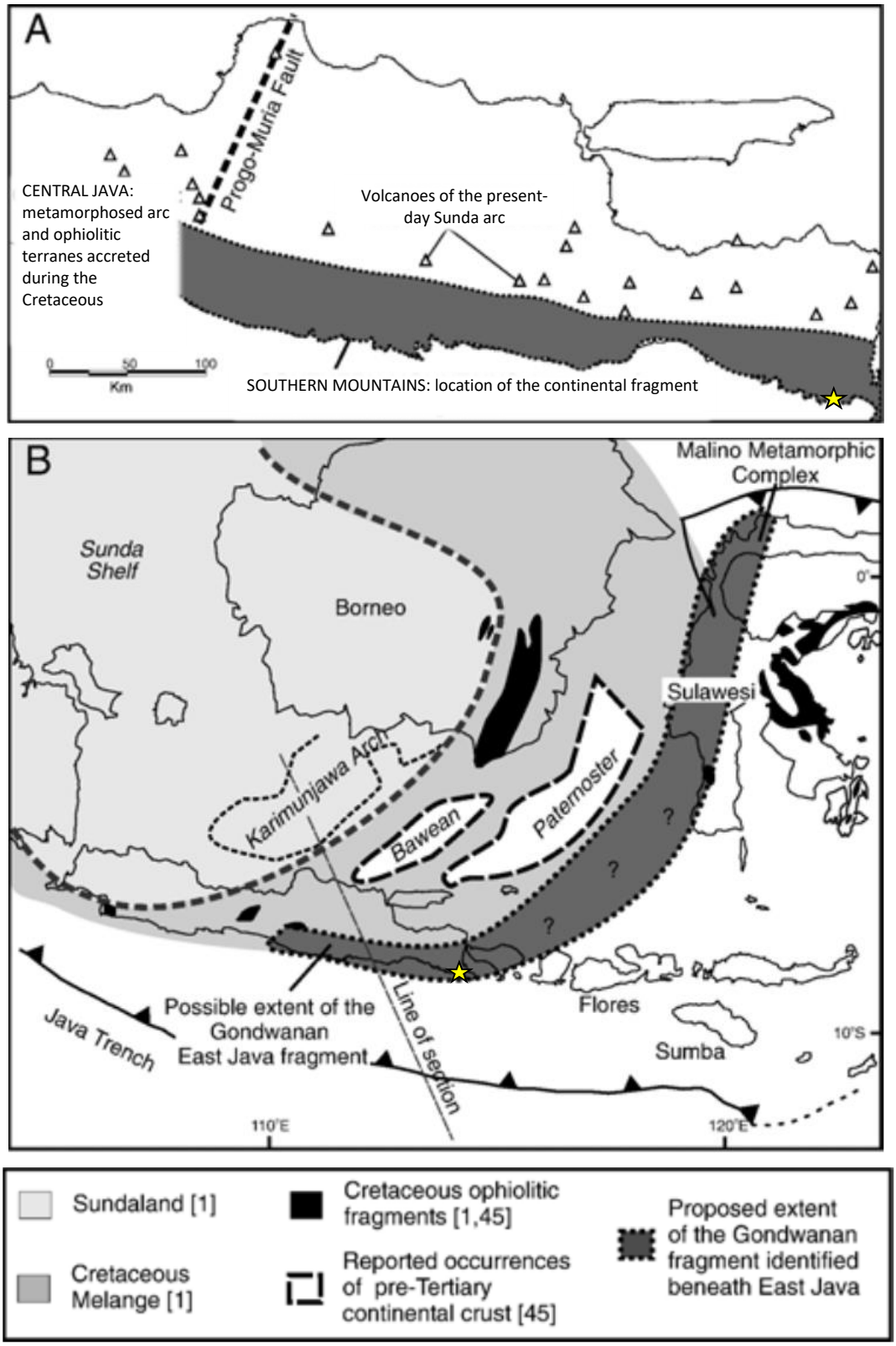

Figure 4.15. Character of the crust on the south-eastern margin of Sundaland. Tujuh Bukit (yellow star) located on the boundary of the proposed Gondwanan fragment A. Extent of the continental fragment onshore East Java. B. Map showing the proposed extent of the East Java fragment beneath Sulawesi. Modified after Smyth et al. (2007).

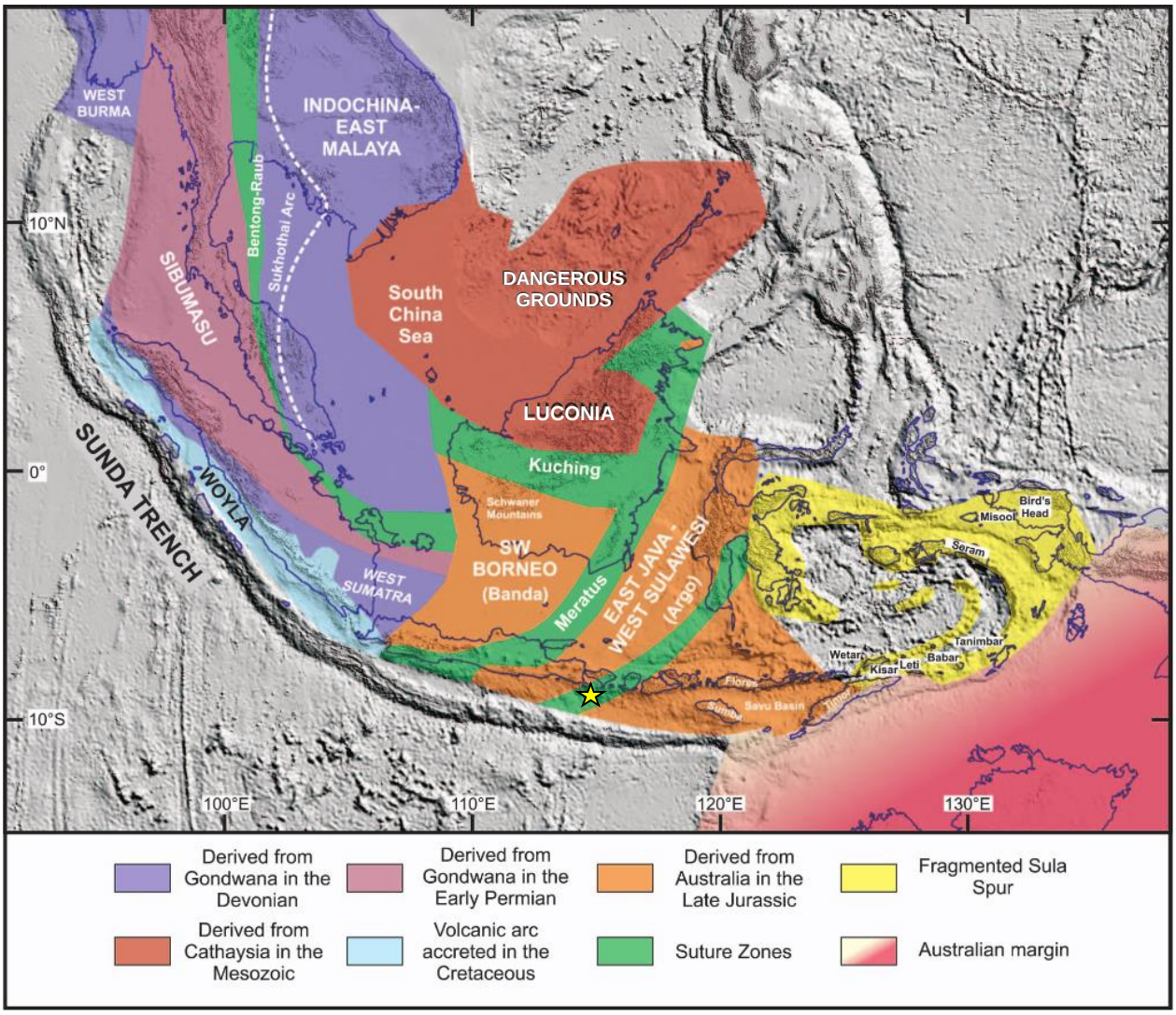

Figure 4.16. The principal blocks of SE Asia with the location of Tujuh Bukit (yellow star) on the boundary of the suture zone of the East Java - West Sulawesi Argo block (modified after Hall and Sevastjanova, 2012).

Gondwana that has been interpreted to underlie East Java (Smyth et al. 2007; Fig. 4.15).

Chapter 5: Alteration and Mineralization

5.1 Introduction

This chapter describes the paragenesis and mineralogy of porphyry-style hydrothermal alteration mineral assemblages and cross-cutting enargite - tennantite-bearing epithermal-style veins and alteration assemblages at Tumpangpitu. It explains the methodologies used to construct the type alteration section, and characterizes the types of alteration minerals associated with a district-scale mineralized lithocap that has overprinted the Tumpangpitu porphyry deposit. Re-Os and ^{40}Ar-^{39}Ar geochronological data from molybdenite and alunite respectively are used to constrain ages of alteration and mineralization to determine the timing and duration of magmatic activity. The evolution of Tumpangpitu is evaluated, with a strong focus placed on SWIR-aided alteration mineral mapping in the lithocap and porphyry environment, in conjunction with field mapping, detailed drillcore logging, cross-section construction, observations of hand specimens and petrographic, SEM and electron microprobe analysis on thin sections by the author.

5.2 Background

5.2.1 Lithocaps

Porphyry deposits are associated with large volumes of hydrothermal fluids that can produce alteration halos zoned concentrically around intrusive complexes. Early-formed alteration assemblages are associated with shallower lithocaps of hypogene advanced argillic and residual quartz (vuggy and massive-textured) alteration with pyrite (White and Hedenquist, 1990; White, 1991; Hedenquist and Lowenstern, 1994; Sillitoe, 1995a; Chang et al., 2011). Partially eroded lithocaps can be topographically prominent due to resistant vuggy or massive residual quartz alteration that forms horizons with deeper feeder zones. Some lithocaps host high-sulfidation epithermal deposits, particularly within their fracture-controlled roots, e.g., Chuquicamata, northern Chile (Sillitoe, 2010), Lepanto-Far Southeast, Philippines, (Arribas et al., 1995; Hedenquist et al., 1998; Chang et al., 2011) and Tampakan, Philippines, (Rohrlach, 2002; Sillitoe, 2010).

The advanced argillic alteration assemblage typically forms at shallow crustal levels (0.2 - 1 km below the paleowater table; (Arribas, 1995; Cooke and Simmons, 2000), in contrast to the zone of potassic alteration (ca. 1 - 3 km; Sillitoe, 2000). Lithocaps are temporally and genetically related to intrusions that may be associated with deeper porphyry-style mineralization (Sillitoe, 1995a, 1999, 2011; Hedenquist et al., 1998; Chang et al., 2011). Many of the porphyry deposits along the Sunda Banda magmatic arc of Indonesia, including Elang and Hu'U on Sumbawa island (Maryono et al., 2011), and in other countries, e.g., Chuquicamata (Sillitoe, 2000), Rosario (Masterman, 2003) and Caspiche in Chile (Sillitoe, 2013) are

characterized by zones of advanced argillic alteration associated with high-sulfidation mineralization superimposed or telescoped directly onto potassic altered rocks associated with older porphyry mineralization.

5.2.2 Porphyry and epithermal mineralization at Tumpangpitu

The characterization of vein types with respect to mineralogy, morphology, orientation and texture has proven important in determining the spatial location of ore within the Tumpangpitu ore body.

Tumpangpitu is a large system with Au-Ag (oxide) and Au-Ag-Cu (sulfide) high-sulfidation mineralization and associated advanced argillic alteration (part of a district-scale lithocap) has overprinted and significantly upgraded the top of a Cu-Au-Mo porphyry. High and intermediate-sulfidation epithermal mineralization at Tumpangpitu extends from present day surface (486 m asl) to depths of more than one km bsl, overprinting > 800 m of porphyry Au-Cu-Mo mineralization (Figs. 5.3 and 5.4), making Tumpangpitu one of the best examples in the world of a giant, telescoped epithermal-porphyry deposit (Norris, 2011; Rohrlach, 2011).

The alteration features at surface are part of the large Tujuh Bukit lithocap which extends for more than 6 x 3 km along a NW- trending corridor proximal to Tumpangpitu and over 12 km regionally towards the Salakan porphyry-high-sulfidation epithermal prospect (Figs. 3.18 and 5.2).

Early hydrothermal alteration at Tumpangpitu is centred in and around a nested tonalite porphyry complex. A progression in alteration has been observed from a central domain of quartz - magnetite - biotite - K-feldspar associated with high-grade porphyry mineralization, laterally outwards through minor actinolite, to epidote and then calcite. These distal assemblages all contain chlorite. Porphyry mineralization produced stockwork, veins and disseminations of chalcopyrite, bornite, chalcocite and covellite that formed a carapace around mineralized tonalite stocks. Highest grade porphyry mineralization shows a strong correlation with magnetite.

High-sulfidation mineralization is hosted by three main NW-trending quartz ridges known as Zone A, Zone B and Zone C (Fig. 5.2). They contain Au-Ag oxide mineralization close to surface and transitional and sulfide mineralization at depth. Porphyry mineralization is not exposed at surface, but extends from an upper level of 200 m below present day surface at Zone A, 500 m below present day surface at Zone C, to depths greater than 1,200 m below surface (Figs. 5.3 and 5.4). The 0.2 % Cu shell extends 1.2 - 1.5 km laterally around the tonalite intrusive complex. Quartz - alunite - dickite assemblages are dominant at higher levels in the epithermal system and quartz - pyrophyllite ± diaspore ± topaz occur at deeper levels. The district comprises vuggy quartz - alunite ridges 750 x 200 m in size, surrounded by > 500 m x 1200 m halos of quartz - dickite - kaolinite alteration extending outwards to illite - montmorillonite/nontronite ±

kaolinite ± chlorite and chlorite - calcite ± epidote alteration, with decreasing quartz content away from the central vuggy quartz - alunite zones.

Fault-controlled high-sulfidation state enargite ± covellite ± bornite with pyrite mineralization is overprinted by intermediate-sulfidation state tetrahedrite - tennantite - chalcopyrite mineralization. These epithermal features overprinted porphyry mineralization at deeper levels of the system (below 280 m bsl to more than 1,200 m bsl), with complex sulfide overprinting relationships and hypogene upgrading at the interface between the porphyry and epithermal domains. The areal extent of the late alteration zones is greater than that of the early potassic-related alteration, which does not crop out at Tumpangpitu. Pervasive chlorite - illite - montmorillonite/nontronite ± calcite alteration associated with the syn- to post-mineralization Tumpangpitu diatreme post-dates all other earlier styles of alteration. Base metal veins containing sphalerite and galena comprise the final event of mineralization and form a concentric halo within and around epithermal and porphyry mineralization at Tumpangpitu.

5.2.3 Terminology

5.2.3.1 Alteration mineral assemblage vs association

A hydrothermal mineral assemblage is a group of minerals that are interpreted to occur in chemical equilibrium and to have formed contemporaneously, based on textural relationships observed at the mesoscopic and microscopic scales. Such assemblages are geochemically significant because they can be used to estimate restricted physio-chemical conditions of formation assuming local equilibrium thermodynamics (e.g., Seedorff et al., 2005). A hydrothermal mineral association is a group of minerals that occurs together regardless of whether the minerals formed at the same time or at different times. These associations are the result of time-integration of a number of events (Seedorff et al., 2005). Only assemblages of alteration minerals have been documented in all alteration models at Tumpangpitu.

5.2.3.2 Vein terminology

Different vein types and vein densities reflect copper grades in many porphyry systems e.g., El Salvador, Chile, (Gustafson and Hunt, 1975) and Batu Hijau, Sumbawa, (Maryono et al., 2012). Vein generations provide vectors to ore and careful field mapping of vein styles is a key tool in exploring for porphyry deposits (e.g., Seedorff et al., 2005). Porphyry stockwork veins have a spatial and temporal relationship with alteration and mineralization at Tumpangpitu (Figs. 5.3 and 5.4). At Tumpangpitu, vein assemblages have been grouped into early, transitional, late and very late stages (Table 5.1). All alteration zones at Tumpangpitu have been documented from observations of alteration minerals aided by SWIR data, as opposed to grouping mineral assemblages under generic alteration zones (e.g., Fig. 5.1). The ± symbol indicates alteration minerals that may not always be present in the documented alteration zone.

Table 5.1. Summary of porphyry vein nomenclature, listed in sequence from oldest to youngest.

Stage	Vein type	Vein textures	Vein infill						Wallrock alteration halo			Reference
			Major		Minor							
			Gangue	Opaque	Gangue	Opaque	Thickness (cm)	Structure	Major	Minor	Thickness (cm)	
EARLY	**M (Magnetite)**	Sheeted and stockwork of narrow stringers to massive, thick monomineralic veins of fine-grained magnetite; diffuse ptygmatic veins; locally dense stockworks of planar veins with tracks of magnetite along vein margins or centreline	qtz	mt	qtz - act - anhy	cp - bn - cc - cv	0.1 - 5	Diffuse walls; lack internal structure				Arancibia and Clark (1996)
	EB (Early biotite)	Chains of shreddy biotite, wavy, discontinuous	bt		qtz - chl	cp	0.1 - 0.2	Irregular walls				Brimhall (1977); Gustafson and Quiroga (1995);
	A	Discontinuous, dismembered, wispy textures, granular (sugary) qtz	qtz	py - cp - bn - cc - cv	Ksp - bt - anhy - hm - rt	mt	0.3 - 1.5	Irregular diffuse walls; no internal structure; rare alteration halos		bt - ksp - ab	< 0.2	Gustafson and Hunt (1975)
TRANSI-TIONAL	**B**	Syntaxial subhedral - euhedral coarse-grained drusy or comb qtz crystals, sulfide centreline, molybdenite along vein margins	qtz - musc - ill	py - cp - bn - mo	rt	py - cp - bn - cc - cv -mo	0.3 - 2.0	Continuous, planar fractures with parallel walls that form sharp contacts with country rock	qtz - musc - ill	Ksp - ab - and - cor - chl - ap - anhy	< 0.5	Gustafson and Hunt (1975)
	C	Sulfide-rich, minor qtz		cp - bn	qtz	py - cc - cv	< 0.5	Regular, continuous, sharp walls	musc - ill - chl	rt - Kspar - ab - musc	< 0.5	Dilles and Einaudi (1992)
LATE	**D**	Semi-massive sulfide, euhedral quartz		py	qtz - musc - ill - rt - hm	cp - ten	0.1 - 3.0	Regular, continuous, planar walls, sheeted orientations parallel to faults	musc - ill - qtz	chl - rt	0.2 - 5	Gustafson and Hunt (1975)

Abbreviations: ab = albite, and = andalusite, anhy = anhydrite, ap = apatite, bn = bornite, bt = biotite, cc = chalcocite, chl = chlorite, cor = corrundum, cp = chalcopyrite, hm = hematite, ill = illite ksp = K-feldspar, musc = muscovite, mt = magnetite, mont = montmorillonite, py = pyrite, qtz = quartz, ten = tennantite. Porphyry vein terminology after Gustafson and Hunt (1975); Dilles and Einaudi (1992).

Veins at Tumpangpitu have been classified entirely on descriptive criteria. The terminology used by Gustafson and Hunt (1975), Brimhall (1977), Gustafson and Quiroga (1993), and further developed by Arancibia and Clark (1996), Skewes and Atkinson (1985) and Dilles and Einaudi (1992) for describing vein sequences from the El Salvador porphyry copper orebody, Chile, and other deposits, has been adopted and modified for ease of documenting crosscutting relationships and modelling purposes. This terminology and sequence of hydrothermal events will be used as a framework to compare events in the Tumpangpitu porphyry ore body with the addition of C veins, first described by Dilles and Einaudi (1992; Table 5.1). Nine major vein stages were recognized during field mapping, drillcore logging and petrographic work (Table 5.2). Seven of these vein stages (M1, M2, EB, A, B, C and D veins) are interpreted to be related to porphyry-style mineralization and alteration, based on their mineralogy, of which there are three distinct alteration assemblages. These are the 1) quartz - magnetite ± biotite ± K-feldspar ± actinolite; 2) quartz - illite and 3) chlorite - calcite ± epidote mineral assemblages. The late enargite-tennantite bearing massive sulfide veins are classified as high-sulfidation epithermal (HSE-1) where enargite is dominant, HSE-2 where both enargite and tennantite exist in the same vein and intermediate-sulfidation epithermal (ISE) where enargite is absent and tetrahedrite-tennantite and other Ag sulfosalts dominate the late sulfide assemblages at Tumpangpitu. Four distinct alteration assemblages have been interpreted to be related to epithermal mineralization. In order from early to late, and based on dominant alteration minerals (not listing accessory minerals that may or may not be present), these are: 1) vuggy residual quartz - alunite; 2) massive residual quartz - alunite; 3) topaz; 4) quartz - pyrophyllite; 5) quartz - dickite; and 6) illite - smectite. The paragenesis of veins and alteration from observed crosscutting relationships is summarized in Table 5.2.

The majority of the porphyry copper-gold mineralization at Tumpangpitu is related to early stage veins, including M, A, B and C veins, although the latter are poorly developed. The spatial and temporal distribution of veins and associated alteration based on vein cross cutting relationships and detailed petrography to determine sulfide and alteration mineral overprinting relationships is illustrated in Figures 5.7 - 5.31 and summarized in Table 5.2.

5.3 Alteration mineral mapping

5.3.1 SWIR Spectroscopy - Introduction

Although ASDs (analytical spectral devices) have been used successfully in aiding exploration in a number of projects worldwide, there is relatively little published information about the applications of spectral analysis in defining these alteration systems. Some examples of applications of SWIR data to aid in exploration for ore deposits, and towards alteration studies in existing deposits, have been documented from porphyry (e.g., Pebble Cu-Au-Mo porphyry deposit, Alaska; Harraden et al., 2013), high-sulfidation epithermal (e.g., Quimsacocha; Ecuador, IAMGOLD, 2007; Candrian, Indonesia, Harrison, 2014) and

volcanogenic massive sulfide deposits (e.g., Rosebery, Tasmania; Herrmann et al., 2001). The SWIR method is useful for field work during exploration, because it is non-destructive, simple to use and can quickly provide large quantities of relevant mineral data.

Spectral data are crucial for exploration in the lithocap environment, because mineralized porphyry bodies can be concealed beneath lithocaps, and there can be complex mixtures of fine-grained alteration minerals which are difficult to identify by visual observation alone (e.g., Chang et al., 2011). Hydrous alteration minerals can easily be detected by shortwave infrared (SWIR) spectral analysis using portable ASDs such as the TerraSpec spectrometer. The TerraSpec produces rapid (2 - 5 second) data acquisition of spectra in the visible-near infrared-short wavelength infrared (vis-NIR SWIR) region. Reflectance spectra in the Vis-NIR range (350 - 1300 nm) was used to determine Fe oxide species (hematite, goethite, jarosite) and chlorite Fe-features. Normalised hull quotient spectra from the SWIR range (1300 - 2500 nm) were used to identify alteration minerals in samples from Tumpangpitu.

5.3.2 SWIR Spectroscopy - Methodology

SWIR spectroscopy was conducted on a total of 44,376 samples from a variety of media from Tumpangpitu and other epithermal and porphyry prospects in the Tujuh Bukit district. The data were used to document the distribution of alteration assemblages, in particular the advanced argillic alteration assemblages associated with high-sulfidation state epithermal mineralization. SWIR spectral data were essential for the generation of the alteration model for Tumpangpitu (Figs. 5.2 - 5.7).

Spectral analysis was conducted on 30,885 diamond drillcore, 847 surface rockchip, 9000 soil and 3644 coarse reject samples. Absorption spectra were obtained with a TerraSpec model A100810 (350 - 2500 nm) near-infrared and SWIR spectrometer. The TerraSpec was calibrated with a white Spectralon disk as a standard to recalibrate the TerraSpec after every 20 samples. The field of view for analysis was 2 cm. Portions of the samples that contained higher than average concentrations of quartz, sulfides, feldspars or magnetite were avoided to minimize reductions in the spectral response by these opaque minerals. 1 - 2 cm sized chips from diamond drillcore were sampled at 2 m intervals downhole (to match assay sample intervals) from all 450 drillholes at Tumpangpitu. Soil samples for spectral analysis were preferentially sampled from the base of the C soil horizon or B-C transition using auger sampling methods detailed by Lulofs (2011) and Harrison et al. (2014, 2015). All samples were air dried in the sun to avoid contamination by external water.

Prior to the purchase of a TerraSpec spectrometer, 21,715 samples of drillcore, 3644 coarse rejects and 2747 soil samples were shipped to Australia and analyzed by AusSpec International Pty. Ltd. After the purchase of a TerraSpec by Intrepid Mines Ltd, spectra from 12,814 drillcore, 6,252 soil and all 847 rockchip samples were analyzed using the contact probe of the TerraSpec by trained geotechnical assistants,

under the supervision and guidance of the author to allow rapid, unbiased data acquisition of thousands of drillcore samples. Specific alteration minerals in vein selvedges and along fractures were analyzed independently by the author. Spectra were acquired using RS3 software linked to the TerraSpec. Data processing and spectral analysis was undertaken manually by the author using The Spectral Geologist (TSG Pro version 7.1.0.044) processing software developed by CSIRO for AusSpec International Pty Ltd. Mineral identification was conducted by comparing each spectrum to reference spectra from GMEX spectral interpretation manuals (Pontual and Merry, 2008), multiple reference spectral databases and customised vertical reference lines using TSG. This aided the identification of individual minerals in samples containing up to six different minerals. TSA (The spectral assistant) from the TSG software was avoided due to its high degree of inaccuracy when dealing with mixtures of minerals, as these exhibit mixed spectra that do not match spectra from individual mineral reference spectra. Batches of the spectra were also sent for interpretation by Dr Sasha Pontual of AusSpec International for quality control purposes.

A library of absorption features or "v-lines" were created in TSG by the author for all alteration minerals including clay, sulfate, hydroxylated silicate, carbonate and iron oxide species identified at the project. Up to six minerals and relevant mineral parameters were calculated for all samples. Alteration minerals were recorded in order of spectral abundance. Mineral 1 dominates the spectrum, followed by Mineral 2, Mineral 3, with Minerals 4 - 6 existing only as a minor feature. This does not necessarily reflect the actual concentration of alteration minerals in the sample. For example, minerals such as pyrophyllite and topaz have strong spectral signatures, even when they exist in small quantities in mineral mixtures (Pontual et al., 2008).

Spectral mineral identification was verified by detailed petrographic, SEM and electron microprobe analyses at CODES, whereby fine-scale compositional variations of individual minerals could be resolved.

5.3.3 SWIR Spectral parameters - Alunite absorption feature

In SWIR spectra, K-Na alunite has a strong absorption feature between 1,480 - 1490 nm wavelength (Fig. 5.22; Pontual et al., 2008; Chang et al., 2011). The alunite absorption peak at ~1,480 - 1490 nm generally shifts to higher wavelengths where the sample is closer to the intrusive center, due to higher Na and lower K content in the alunite (Chang et al., 2011). The exact position of this feature is related to the chemical composition of alunite (Thompson et al., 1999). SWIR data was used to plot the wavelength of alunite at Tumpangpitu from drillcore on sections 11060 mN (Fig. 5.5) and 10820 mN (Fig. 5.6).

5.3.4 Electron probe microanalysis - Methodology

Compositional mineral analyses were acquired on sulfides, sulfosalts and alteration minerals from 207 probe sites from nine polished slab and thin section samples. Data were acquired on an electron

microprobe (Cameca SX100 (TCP/IP Socket) equipped with five tunable wavelength dispersive spectrometers at the Central Science Laboratory, University of Tasmania. Operating conditions were 40 degrees take-off angle, and a beam energy of 20 keV. The beam current was 15 nA, and the beam diameter was between focused beam and 10 microns, depending on the size of the respective mineral grain. All data are listed in Appendix Table A-2. The standards, counting time, analytical error and detection limits are listed in Appendix tables A2-2 and A2-3.

5.4 Construction of the Tumpangpitu type alteration section

5.4.1 Background information

Work on a type alteration section for Tumpangpitu by the author commenced after the acquisition of a TerraSpec by Intrepid Mines Ltd in 2010 and in conjunction with the construction of the type lithology section described in Chapter 3.

Prior to the generation of the SWIR-aided type alteration section, a lack of consistency in logging was apparent due to the misleading use of generic alteration assemblage nomenclature such as, advanced argillic, intermediate argillic, phyllic and potassic, and confusion about terminology arising where epithermal alteration mineral assemblages overprint porphyry alteration mineral assemblages. Generic logging codes (Fig. 5.1A) and general uncertainty associated with the identification of fine-grained alteration minerals without the aid of SWIR data, led to difficulties in correlating alteration zones between adjacent drillholes on sections, creating a significant problem for developing consistent alteration and mineralization models. To resolve this problem, a type alteration section was logged by the author (Fig. 5.3), aided by SWIR analysis, so as to identify the typical alteration mineral assemblages and crosscutting relationships at Tumpangpitu. This type section could then be used to define the alteration mineral assemblages by on-going drillcore logging and field mapping (e.g., Einaudi, 1997; Seedorff et al., 2005; Maryono et al., 2012).

SWIR-aided type section construction was not only crucial to construct the first consistent alteration model of the Tumpangpitu porphyry and epithermal system, it was also essential for the inferred resource calculations for both the high-sulfidation epithermal and porphyry deposits. The SWIR-aided alteration model was used to define and isolate zones of alteration that accompany ore associated with enargite, tennantite and other As-bearing sulfosalts associated with processing penalties. The model was also successfully used in exploration targeting towards zones of mineralization that remained untested. SWIR-assisted targeting of drillholes helped to more than triple the Tumpangpitu porphyry resource from 500 Mt @ 0.4% Cu and 0.5g/t Au containing 8 Moz Au and 4.6 billion lbs of Cu in 2010 to 1.9 Gt @ 0.45% Cu and 0.45 g/t Au containing 28 Moz Au and 19 billion lbs of Cu in 2012 (Intrepid Mines Ltd., 2010, 2012; Harrison, 2014).

5.4.2. Methodology

In order to create the type alteration section, over 25,000 m of diamond drillcore was re-logged with SWIR data over a period of seven months by the author, from type section 11060 mN (Figs. 5.2 and 5.3). The type lithology section (Chapter 3) was used as a base layer when generating the type alteration section in order to identify zones of alteration that are influenced by lithological permeability or contacts between host rocks. It was crucial to combine the spectral data with visual observations of anhydrous or opaque alteration minerals that cannot be detected by SWIR analysis, e.g., feldspars, magnetite, anhydrite, quartz and minerals that are dark coloured and therefore poorly detected, such as chlorite, biotite, epidote and actinolite. It was also crucial to estimate the abundance of quartz and document key textures; either vuggy or massive-textured residual quartz in the high-sulfidation epithermal zones or massive quartz flooding adjacent to porphyry stockwork mineralization. Small batches (< 10 spectra) of complicated mixed mineral spectra were submitted regularly to Dr Sasha Pontual of AusSpec International for verification of the author's interpretations.

SWIR spectral analysis was combined with visual observations of alteration minerals from drillcore, and also with petrography and structural data to create the first detailed alteration model for Tumpangpitu (Fig. 5.3). Zones of topaz were isolated for geometallurgical modelling purposes. The model revealed that overprinting of early equilibrium assemblages by late assemblages resulted in composite alteration zones. For example, the quartz - magnetite **±** K-feldspar ± biotite equilibrium assemblage has been overprinted by chlorite and illite, designated here with the ± symbol. The alteration assemblages used in all alteration models (Figs. 5.1 - 5.3) are summarized below, SWIR identifiable minerals labelled in bold text, vis-NIR identifiable minerals in italics and SWIR and vis-NIR - unidentifiable minerals in normal text, (± indicates mineral is not always present).

- Quartz - magnetite **±** K-feldspar **± biotite ± chlorite** ± *hematite* **± actinolite ±** albite **± illite**
- **Chlorite - calcite ± epidote**
- Quartz **- illite ±** *hematite*/magnetite **± chlorite ± biotite ±** K-feldspar
- Vuggy quartz ± **alunite**
- Massive quartz **- alunite** ± **dickite** ± **kaolinite** ± **pyrophyllite**
- Quartz **- pyrophyllite** ± **alunite** ± **kaolinite** ± **dickite** ± **diaspore ± zunyite**
- **Topaz**
- Quartz **- dickite ± kaolinite ± alunite**
- **Illite - montmorillonite/nontronite ± kaolinite ± chlorite ± calcite**

A simplified, contact logging format was adopted to allow drillcore to be scanned rapidly for significant changes in alteration mineral assemblages, with a strong focus on identifying key contacts and cross-cutting relationships (Fig. 5.1C). During the drillcore re-logging exercise, nine alteration mineral assemblages were resolved (Fig. 5.1B), spanning the entire hydrothermal alteration-mineralization sequence. Assay data and petrographic analyses were used as key supporting datasets to aid in identifying the alteration mineral, sulfide and sulfosalt species associated with porphyry, base metal and epithermal style- alteration and mineralization. Every evening, the re-logging results were hand drawn onto an A0 sized section base map with downhole copper, gold, molybdenum and arsenic assays plotted on drillhole traces. The generation of the alteration type section 11060 mN (Fig. 5.3) facilitated the construction of another fifteen alteration sections to the northwest and southeast by the author (Fig. 5.1), six of which are shown in Figure 5.4 and the remaining included in Appendix 1. Mineral parameter calculations including alunite composition have been plotted on selected sections at Tumpangpitu (Figs. 5.5 and 5.6).

5.5 SWIR-aided surface alteration maps

Spectral-aided surface alteration interpretive maps for Tumpangpitu and other epithermal and porphyry deposits in the Tujuh Bukit district have been created in GIS (MapInfo) using GIS Coordinate System: UTM Zone 17, Northern Hemisphere (WGS 84; Fig. 5.2). Surface maps were generated using a combination of datasets from coastal mapping (Harrison, 2009), spectral data from soil, rockchip and drillhole collar and extrapolation of alteration zones to surface from all cross sections at Tumpangpitu (Figs. 5.3 and 5.4).

Primary alteration minerals identified during the analysis of soil and rock chip samples included; alunite (Na to K compositions), pyrophyllite, diaspore, topaz, dickite, hypogene kaolinite, paragonite, muscovite, Fe-chlorite, Fe-Mg-chlorite (intermediate), Mg-chlorite, epidote and calcite. Almost all soil samples contained secondary weathering minerals whereby poorly crystalline kaolinite was dominant. Gibbsite (Al-hydroxide) was also identifiable in spectra and smectites including montmorillonite and nontronite. Iron oxides identified from vis-NIR spectra included goethite, hematite and minor jarosite.

5.6 Porphyry veins and related alteration assemblages

5.6.1 Magnetite veins and veinlets

Magnetite (M) veins are the earliest recognized vein stage at Tumpangpitu. They occur within and around the high grade mineralized core of the porphyry ore body, extending approximately 100 m outwards into sedimentary and intrusive wallrocks. M veins can be classified into two types based on paragenesis and composition. They are in order from early to late; M1 veins (magnetite > quartz) and M2 veins (quartz

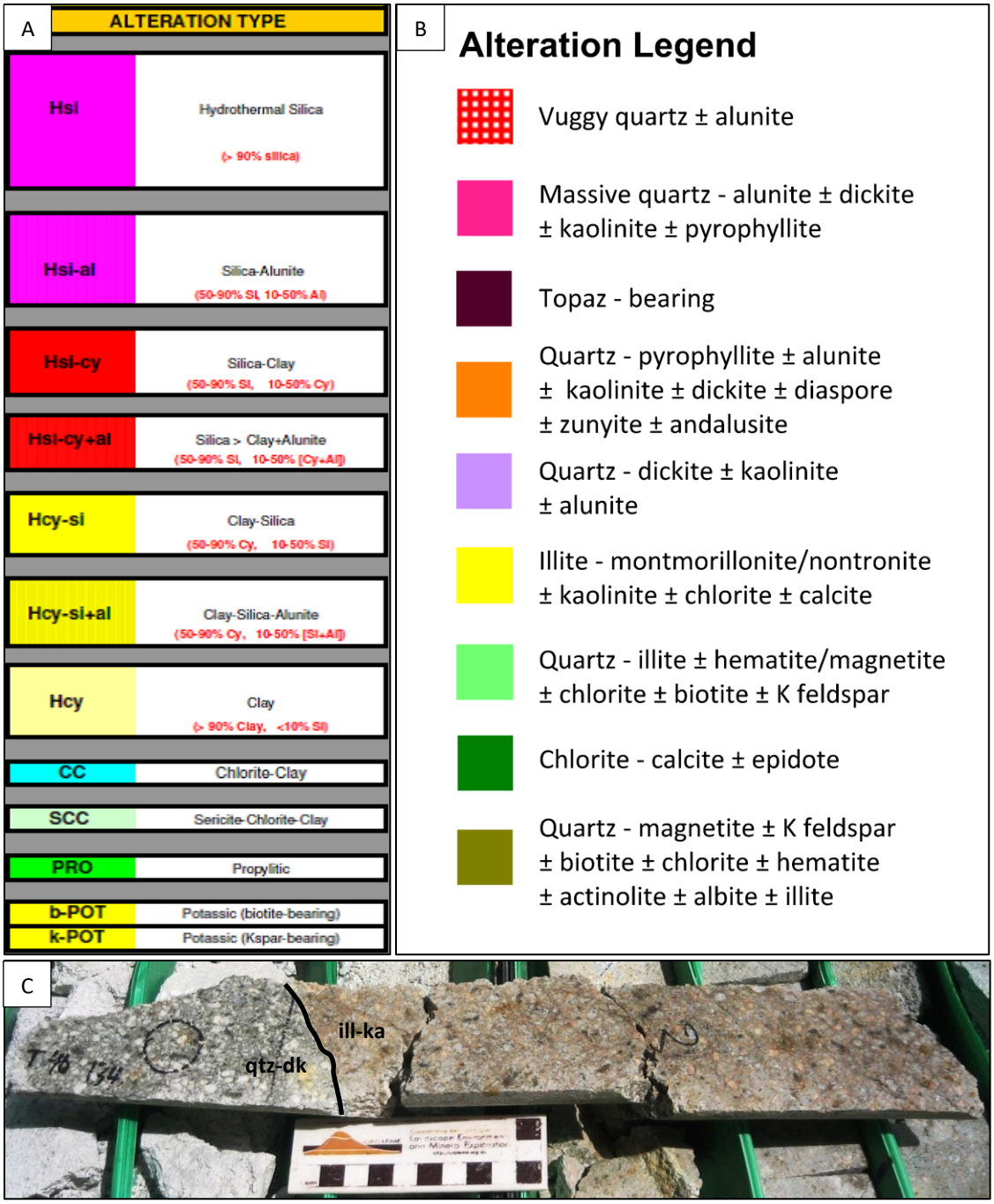

Figure 5.1. Alteration logging at Tumpangpitu. Abbreviations: al = alunite, dk = dickite, Hsi/si/silica = quartz, Hcy/cy = clay, ill = illite, ka = kaolinite, Kspar = K-feldspar, qtz = quartz. Black hashed circle represents TerraSpec contact probe site.
A) Alteration logging system pre-SWIR-aided logging.
B) Alteration mineral assemblage classification post-SWIR-aided logging.
C) *Drillhole GTD-08-35; 134.52 m, 174080 mE, 9046550 mN.* Example of an alteration contact aided by SWIR-analysis between quartz - dickite and illite - kaolinite altered phase 7 quartz diorite.

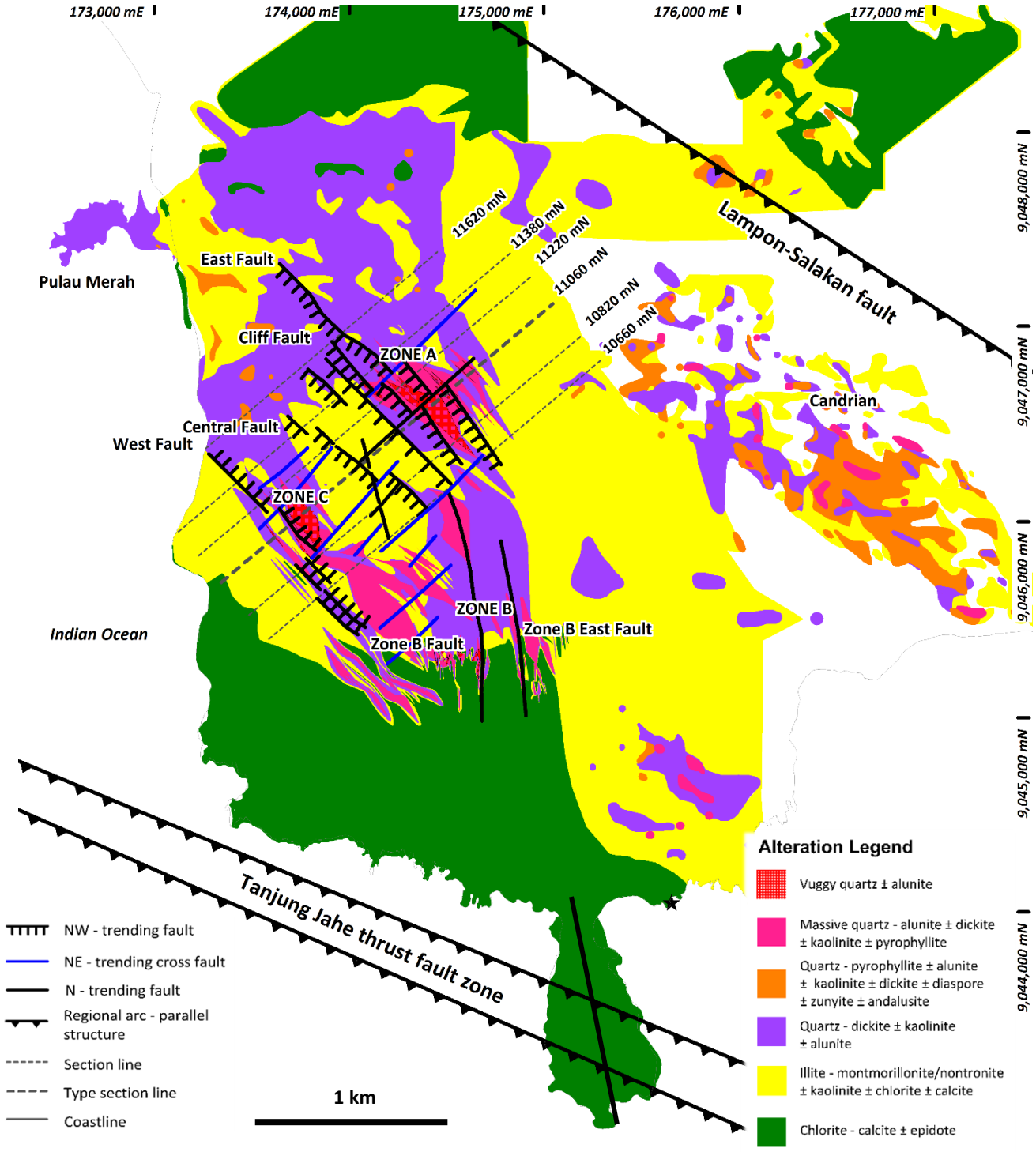

Figure 5.2. Alteration surface plan map for Tumpangpitu based on SWIR soil, rock chip and drillcore collar data, extrapolation from cross sections and field observations.

.

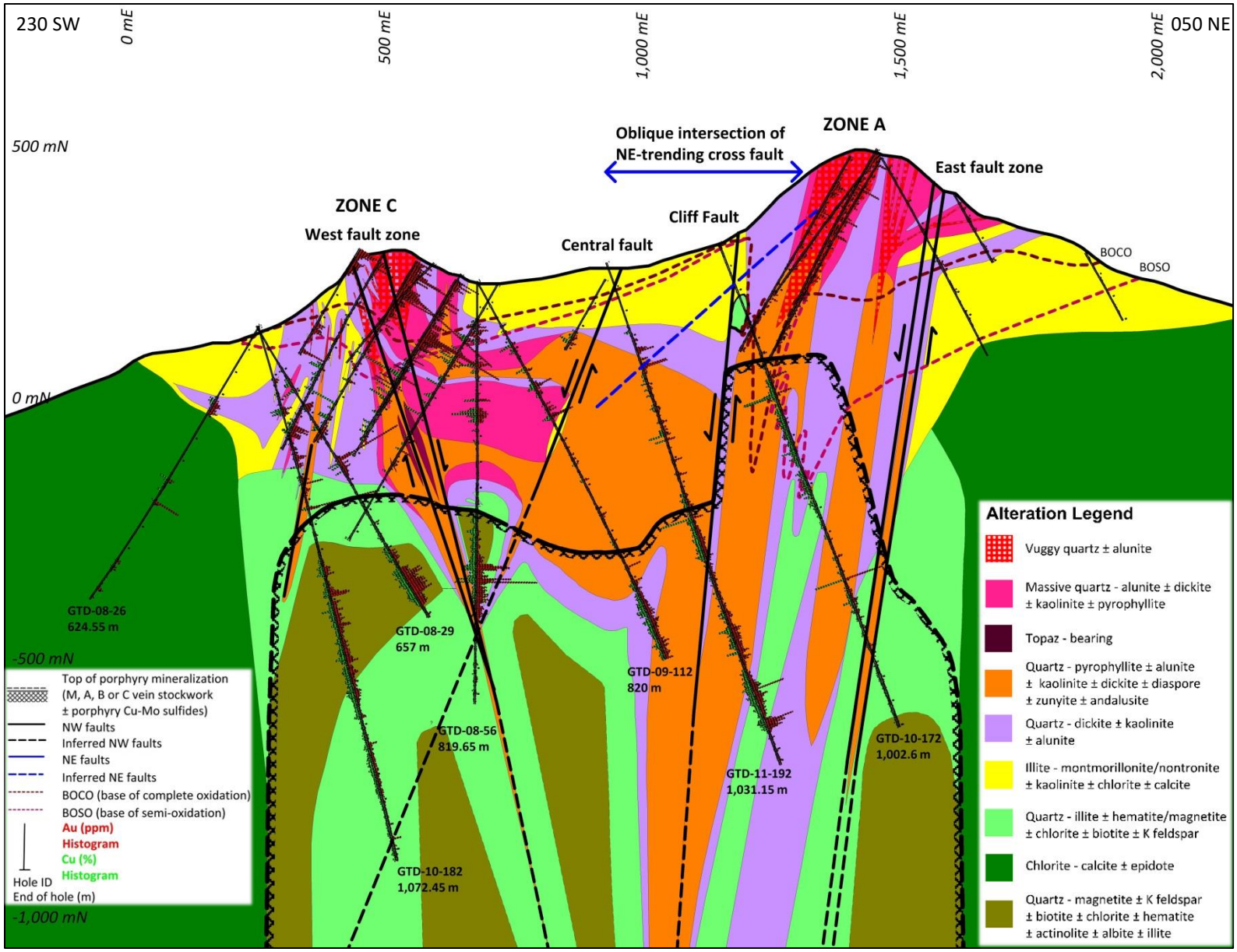

Figure 5.3 Interpreted alteration section 11060 mN for Tumpangpitu based on SWIR data and drillcore logging.

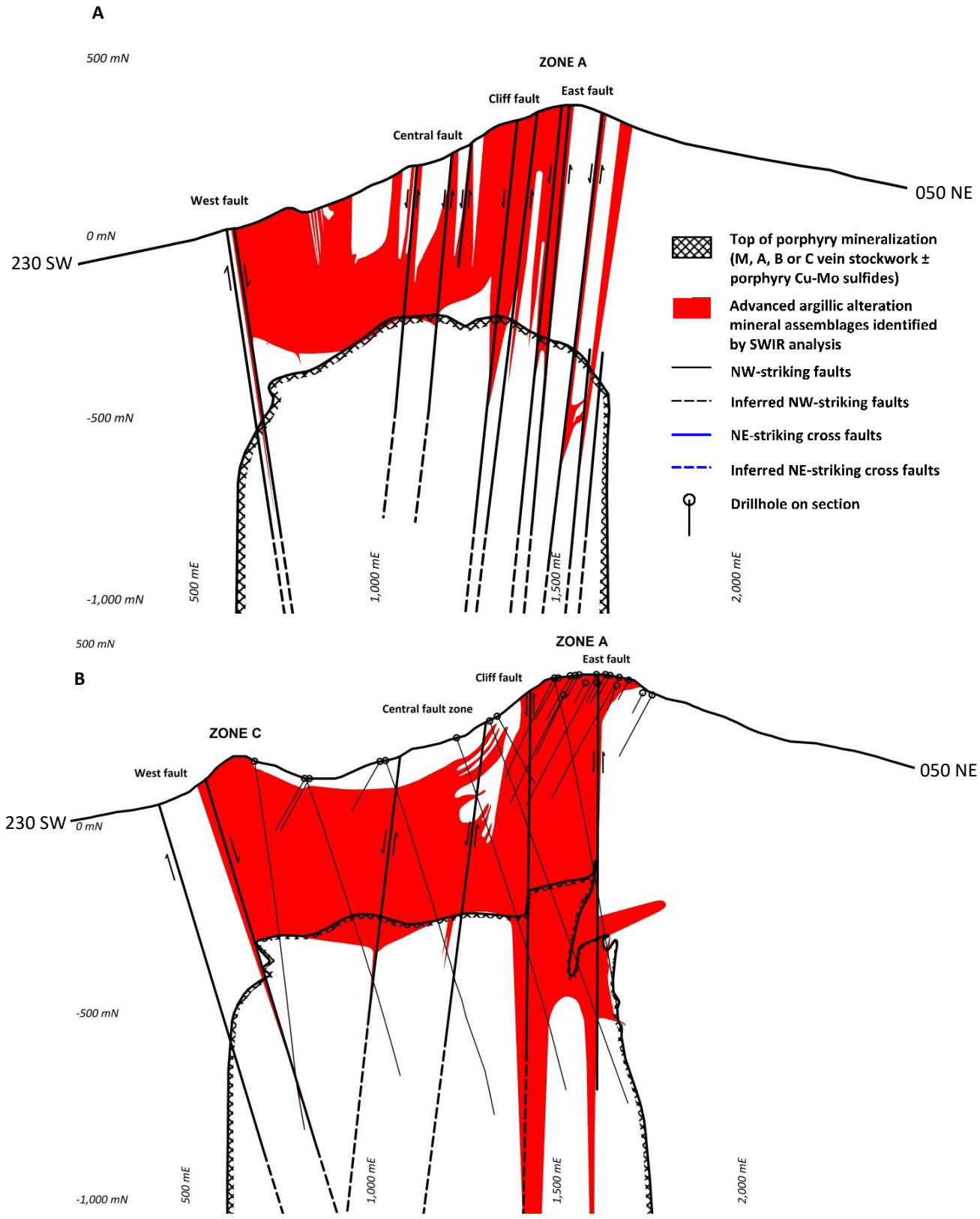

Figure 5.4. Alteration sections through Tumpangpitu, showing advanced argillic alteration assemblages identified by SWIR data (red; alunite, pyrophyllite, dickite, kaolinite, topaz, diaspore and zunyite). Section lines shown in Figure 5.2. A) 11620 mN B) 11380 mN.

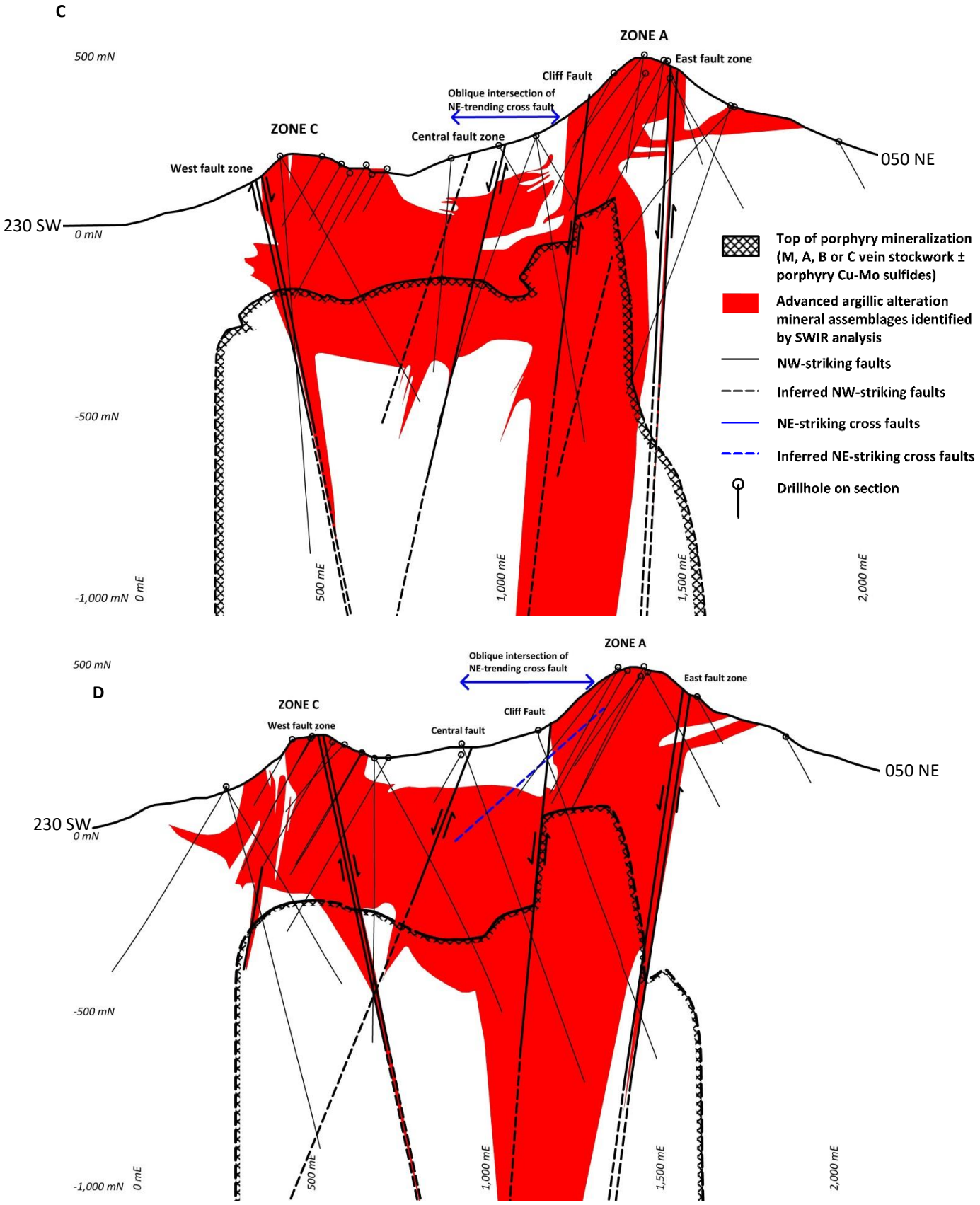

Figure 5.4 (*Contd.)* C) 11220 mN D) 11060 mN.

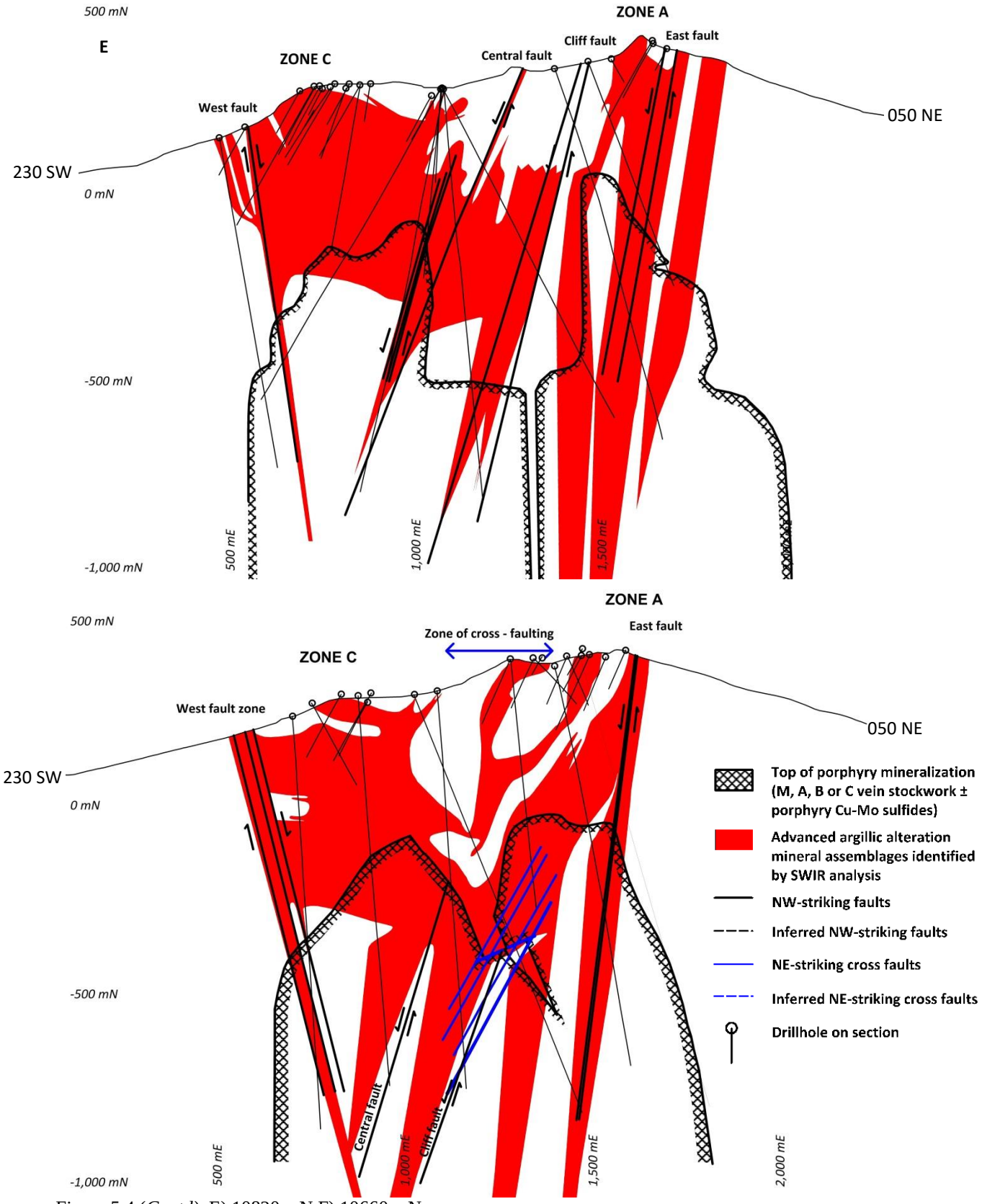

Figure 5.4 (*Contd)*. E) 10820 mN F) 10660 mN.

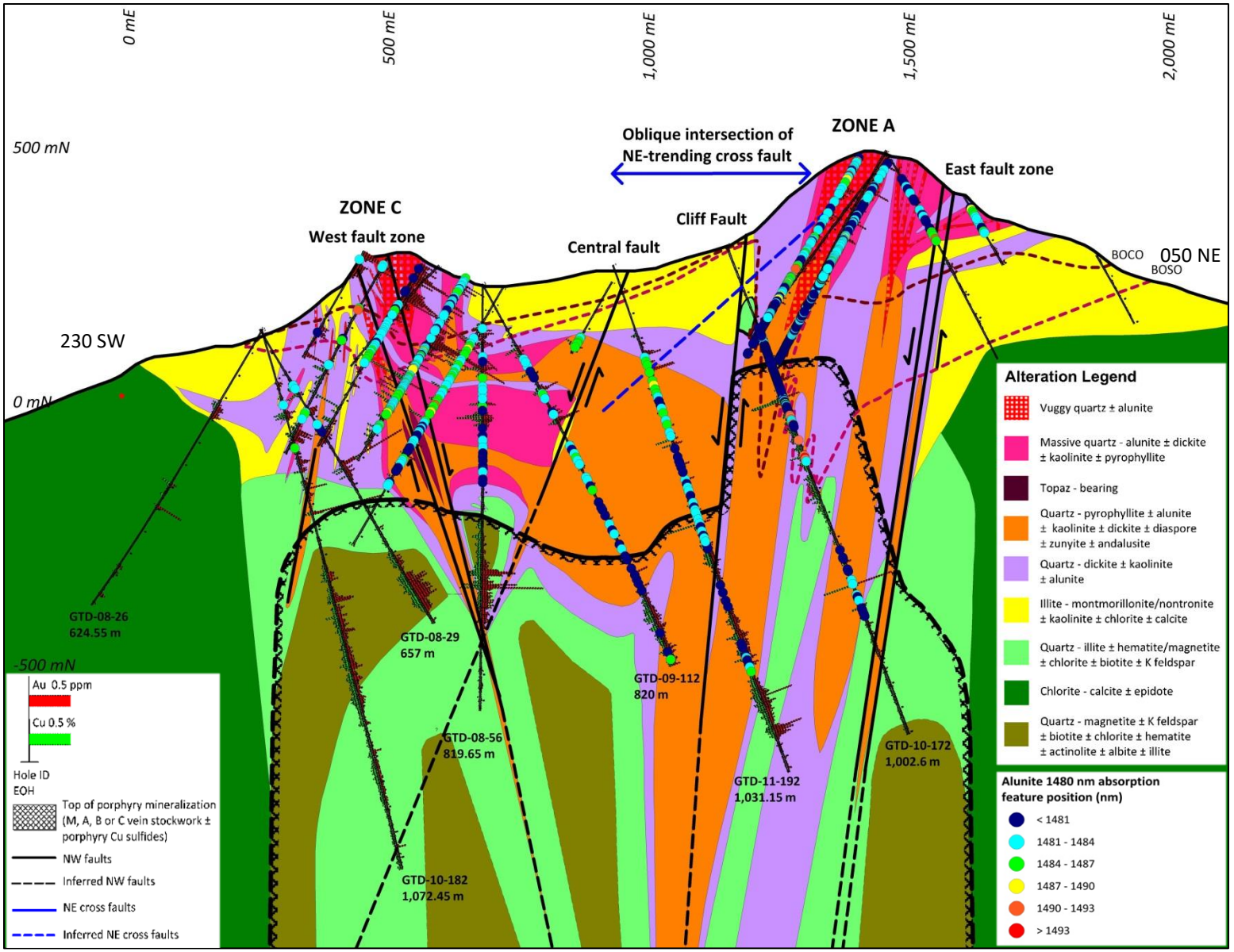

Figure 5.5. Alunite absorption feature between 1480 - 1490 nm for type alteration section 11060 mN.

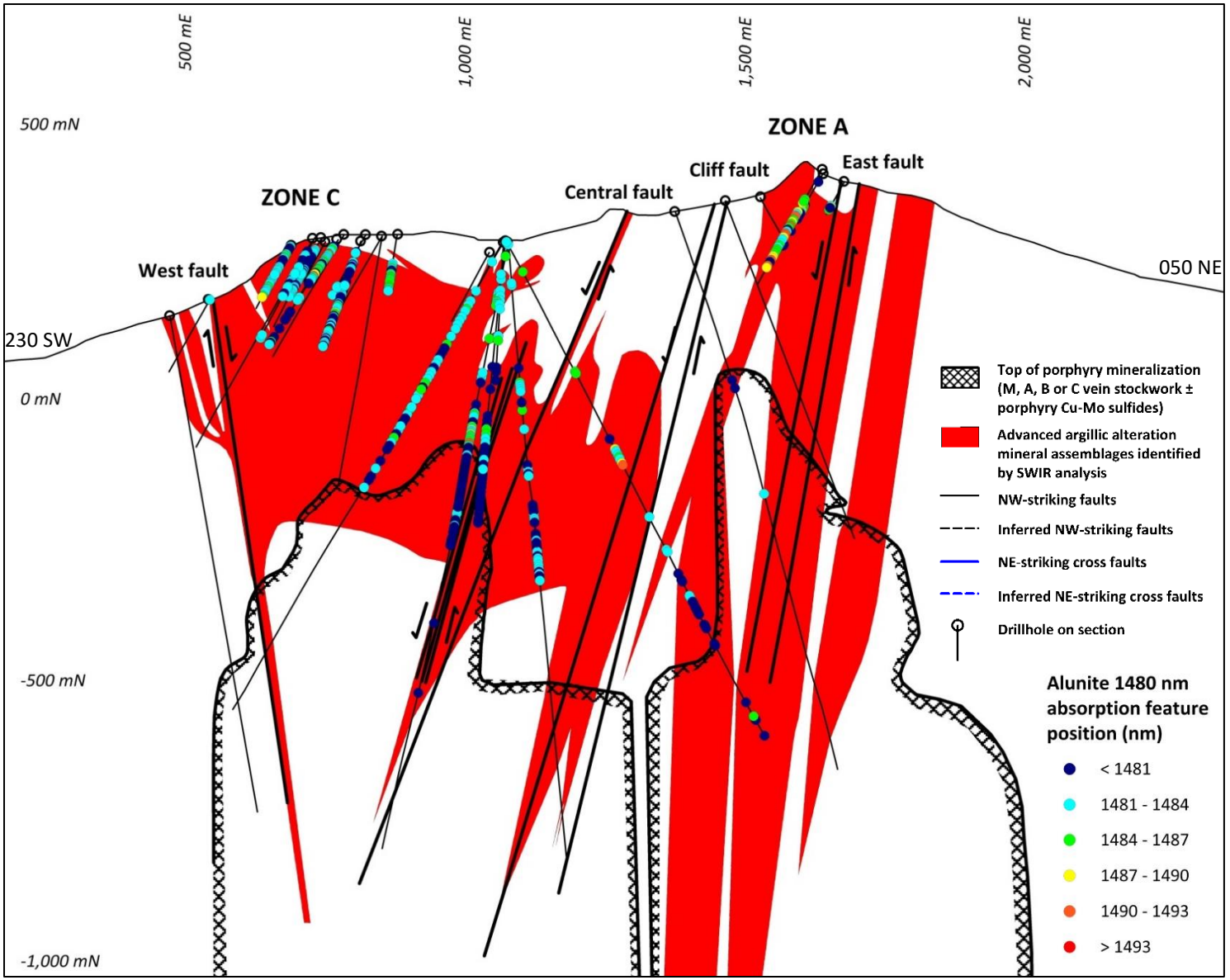

Figure 5.6. Alunite absorption feature between 1480 - 1490 nm for section 10820 mN showing advanced argillic alteration assemblages identified by SWIR data (red; alunite, pyrophyllite, dickite, kaolinite, topaz, diaspore and zunyite). Section lines shown in Figure 5.2.

> magnetite). In zones where late stage alteration assemblages have overprinted M veins, particularly in proximity to Cliff fault (Figs. 5.3 and 5.4), magnetite has been replaced by hematite (illite alteration zones; Fig 5.13A and 5.15A and C) or to pyrite (alunite, pyrophyllite and dickite alteration zones; Fig. 5.25C).

5.6.1.1 M1: Magnetite - quartz veins and veinlets

M1 veins and veinlets are dominated by massive fine-grained magnetite with absent or minor quartz ± chalcopyrite ± bornite ± chalcocite ± covellite (Figs. 5.7D, 5.8A and D, 5.9A and B). These magnetite-dominant, quartz-poor veinlets typically formed as sheeted narrow stringers generally < 0.1 cm wide. There are also thicker, monomineralic magnetite veins up to 5 cm wide (Fig. 5.8A and D). The magnetite stringers have formed chains or beads, lack vein walls, alteration halos and have no internal structure. M1 veins are generally the earliest vein type observed at Tumpangpitu, but locally they crosscut M2-stage quartz - magnetite veins (Fig. 5.8D); implying more than one M1 vein-forming event.

5.6.1.2 M2: Quartz - magnetite veins and veinlets

M2 veins and veinlets are composed of quartz - magnetite ± chalcopyrite ± bornite ± chalcocite ± covellite (Figs. 5.8D, E and 5.9A, B and D). M2 veins form locally irregular and discontinuous blebs close to the core of the Tumpangpitu porphyry ore body (Fig. 5.8D), but also exhibit extensive, dense stockworks of planar veins (Fig. 5.9D). Tracks of magnetite have also been deposited adjacent to vein walls (Fig. 5.9D). There are rare magnetite-bearing USTs (unidirectional solidification textures; Shannon et al., 1982) that are assigned here as M2 features due to the dominance of quartz over magnetite in the USTs.

5.6.2 EB: Early biotite veinlets

Early biotite (EB) veins have been documented in drillcore from Pulau Merah tonalite porphyry (Fig. 5.7B). They are rarely observed visually in drillcore from Tumpangpitu and were mainly identified during petrographic analysis (Fig. 5.7E). They occur as narrow (0.1 - 0.5 cm) wavy strings of shreddy biotite with minor quartz and chalcopyrite. Veinlet walls are irregular and they lack internal structure. Biotite is commonly partially or totally replaced by chlorite, particularly in zones of quartz - illite alteration.

5.6.3 A: Quartz veins

A-type quartz veins occur within and around the high grade mineralized core of the Tumpangpitu ore body, extending approximately 150 m outwards through the sedimentary and intrusive wallrocks. A veins are characteristically discontinuous, ptygmatic with a sugary, granular texture (Fig. 5.8B, E and F, 5.9B and C and 5.12C). They are composed dominantly of quartz with or without disseminated pyrite, chalcopyrite, bornite, chalcocite and covellite. Minor gangue and opaque minerals include magnetite, hematite and rutile. They range from < 0.3 mm to 1.5 cm in width and have irregular walls, either with no

alteration selvedge or a biotite, K-feldspar or albite (after primary magmatic plagioclase) selvedge. A veins have generally crosscut M stage veins (Fig. 5.7D), but locally the A veins have been crosscut by M veins.

5.6.4 Quartz - magnetite - biotite - K-feldspar alteration assemblage

This alteration zone is defined by the stability of hydrothermal magnetite with K-feldspar and quartz and is associated with M1, M2, EB and A-type veins and veinlets. Secondary or shreddy, hydrothermal biotite has replaced primary hornblende or biotite. Replacement features, (Figs. 5.7E and 5.10D) where magnetite and shreddy biotite (partially altered to chlorite) have formed along 120/60° cleavage planes after primary amphibole. Accessory alteration minerals that are locally present in this alteration zone include albite, anhydrite and actinolite adjacent to quartz - illite alteration zones. K-feldspar is pale pink salmon coloured, fine-grained and pervasive throughout phases 5 and 6 porphyry tonalites, or associated with selvedges around early M1, M2 or A veins with shreddy biotite replaced by secondary chlorite (Figs. 5.9A and 5.10C). This magnetite-stable zone defines the potassic alteration zone and is associated with the highest porphyry Au-Cu-Mo grades in the Tumpangpitu porphyry complex, in particular elevated gold (Fig. 5.3). Hydrothermal magnetite is disseminated throughout phase 5 and 6 porphyry tonalites and has extended > 200 m laterally into the sedimentary and volcanic wall rocks. Disseminated hydrothermal magnetite has a strong association with chalcopyrite at Tumpangpitu, with intergrowths of magnetite - chalcopyrite very common (Fig. 5.9A). Bornite, chalcocite and covellite also occur disseminated throughout the magnetite-stable zone. Bornite has formed an inner core to porphyry mineralization. The bornite core is surrounded by chalcopyrite and distal pyrite.

A late stage overprint of quartz - alunite and quartz - pyrophyllite alteration on top of the Tumpangpitu porphyry tonalites, in particular adjacent to major faults, has caused a large portion of the original quartz - magnetite - biotite - K-feldspar alteration to be mostly destroyed, so that it is only preserved in windows away from late stage fault zones (Fig. 5.3). The intersection of deep zones of magnetite-stable alteration and mineralization has been limited due to the deep overprint of late stage alteration. The best examples of preserved quartz - magnetite - biotite - K-feldspar alteration are in drillhole GTD-03, drilled in 2003 by Placer Dome Ltd., underneath Pulau Merah island (Fig. 5.7B). This drillhole contains pervasive secondary shreddy biotite that has not been completely replaced by shreddy chlorite.

5.6.5 B veins

B veins occur within and around the high grade mineralized core of the Tumpangpitu ore body and extend approximately 200 m laterally into the wallrocks. B veins have distinctive textural features that make them easily distinguishable from A veins. B veins show syntaxial subhedral-euhedral quartz crystal growth with pyrite ± chalcopyrite ± bornite ± chalcocite ± molybdenite precipitated down the centreline of the vein (Figs. 5.11A, 5.12A, B, 5.13C). They range from < 0.3 mm to 2 cm in width. B veins are

Table 5.2. Summary of vein types and associated mineral assemblages, listed in sequence from oldest to youngest.

Stage	Vein type	Distribution	Vein textures	Vein infill						Wallrock alteration halo		
				Major		Minor						
				Gangue	Opaque	Gangue	Opaque	Thickness (cm)	Structure	Major	Minor	Thickness (cm)
EARLY	*M-veins/veinlets*											
	M1: mt - qtz	Within phase 4, 5 and 6 tonalite porphyries; extend 100 m laterally into country rock	Sheeted and stockwork of narrow stringers to massive, thick monomineralic veins of fine-grained magnetite		mt	qtz - act	cp - bn - cc - cv	0.1 - 5	Diffuse walls; lack internal structure	-	-	-
	M2: qtz - mt		Sheeted and stockworks of diffuse ptygmatic veins; locally dense stockworks of planar veins with tracks of magnetite along vein margins or centreline	qtz	mt	act - anhy	cp - bn - cc - cv	0.1 - 3	Diffuse walls	-	-	-
	Inner propylitic veins/veinlets											
	act - mt	Within magnetite zone of phase 5 and 6 tonalite porphyries; extend 100 m laterally into country rock	Irregular stockwork veins and veinlets; overlap with M1 and M2 veins	act	mt - qtz	chl	cp	0.1 - 1	Diffuse walls	-	-	-
	Early biotite veinlets											
	EB: bt - qtz	Within Pulau Merah tonalite porphyry, phase 5 and 6 tonalites at Tumpangpitu; extend 100 m laterally into country rock	Chains of shreddy biotite, wavy, discontinuous	bt	-	qtz - Ksp - chl	cp	0.1 - 0.2	Irregular walls	-	-	-
	A veins/veinlets											
	qtz - py - cp	Within phase 5 and 6 tonalite porphyries; extend 150 m laterally into country rock	Wavy, ptygmatic, anhedral granular (sugary) qtz; sulfide along vein fractures; irregular discontinuous blebs and local USTs	qtz	py - cp - bn - cc - cv	Ksp - bt - anhy - hm - rt	mt	0.3 - 1.5	Irregular diffuse walls; no internal structure; rare alteration halos	-	-	-

Table 5.2. *(Contd.)*

Stage	Vein type	Distribution	Vein textures	Vein infill						Wallrock alteration halo		
				Major		Minor						
				Gangue	Opaque	Gangue	Opaque	Thickness (cm)	Structure	Major	Minor	Thickness (cm)
TRANSIT-IONAL	*B-veins*											
	qtz - mo	Within phase 5 and 6 tonalite porphyries; extend 200 m laterally into country rock	"train-track" molybdenite along vein margins	qtz - musc - ill	mo	rt	py - cp - bn - cc - cv	0.3 - 2.0	Continuous, planar fractures; parallel walls; sharp contacts with country rock	qtz - musc - ill	chl	< 0.5
	qtz - py - cp - bn - cc		Syntaxial subhedral - euhedral quartz, sulfide centreline	qtz - musc - ill	py - cp - bn	rt	mo - cc - cv	0.3 - 2.0	Continuous walls; sharp contacts with country rock	qtz - musc - ill-	chl	< 0.5
	C veins/veinlets											
	cp - bn	Poorly developed in outer zone of qtz - mt - bt - Ksp and throughout the qtz - musc - ill alteration zones; extend up to 200 m laterally into wallrock	Sulfide-rich, very minor or no qtz	-	cp - bn	qtz	py - cc - cv	< 0.5	Regular, continuous walls	musc - ill - chl-	rt	< 0.5
LATE	*D veins*											
	qtz - musc - ill - py	Strongly developed adjacent to major fault zones, overprint phases 5 and 6 tonalite porphyries and 250 m of hostrock	Semi-massive sulfide, euhedral quartz	-	py	qtz - musc - ill - rt - hm	cp	0.1 - 3	Regular, continuous, planar walls	musc - ill - qtz	chl - rt	0.2 - 5
	Outer propylitic veins/veinlets											
	ep - chl	Between act - mt and chl - ca zone; overprints 1.5 km of wallrock; associated with Tumpangpitu and Tanjung Jahe diatremes	Irregular to planar veins	ep - chl	-	ill - ca	mt	0.1 - 0.3	Diffuse to continuous walls	-	-	-
	ca - chl	Adjacent to ep zone; overprints up to 2.5 km of wallrock; associated with Tumpangpitu and Tanjung Jahe diatremes	Planar, laminated veins with qtz - ch margins; syntaxial cavity-fill crystal growth of calcite in vein centrelines	ca - chl	-	qtz - ep	-	0.1 - 2.0	Regular, continuous walls	-	-	-

Table 5.2. *(Contd.)*

Stage	Vein type	Distribution	Vein textures	Vein infill						Wallrock alteration halo			
				Major		Minor							
				Gangue	Opaque	Gangue	Opaque	Thickness (cm)	Structure	Major	Minor	Thickness (cm)	
	Epithermal veins												
	HSE-1: en/lz - py	Associated with Tumpangpitu fault system; dominate upper 250 m of lithocap; Zones A, B and C Au-Ag oxide deposits	Semi-massive to massive sulfide, associated with vuggy qtz	al	en/lz - py	pyroph - dk - ka - qtz - ba - S - dsp - tpz - zny - and - APS	cv - bn - cc	0.1 - 50	Regular, continuous walls	al	pyroph - dk - qtz - ba - dsp - tpz - zun - APS - rt	1.0 - 50	
	HSE-2: en/lz - ten/tet - py	Associated with Tumpangpitu fault system; dominate 250 bsl in lithocap; Zones A, B and C Au-Ag oxide deposits	Semi-massive to massive sulfide, associated with minor massive qtz	al	en/lz - py - ten - tet	pyroph - dk - qtz - ba - ka - ill - dsp - tpz - zny - and - APS	cp - cv - bn - st - col - nek - maw - stann - vin	0.1 - 50	Regular, continuous walls	al	pyroph - dk - qtz - ba - ka - ill - dsp - tpz - zun - APS - rt	1.0 - 50	
FINAL	ISE: ten/tet - py - cp	Associated with Tumpangpitu fault system; within and surrounding lithocap; overprint HSE-1 and HSE-2 veins	Semi-massive to massive sulfide, associated with minor euhedral qtz	ka - musc - ill	tet - ten - cp	ka - ill - qtz - dk - ba	cc - st - col - nek - maw - stann - vin	0.1 - 10	Regular, continuous walls	ka - musc - ill	dk - rt - mont	1.0 - 10	
	Base metal veins												
	sph - gal - py	Concentric halo around Tumpangpitu porphyry and lithocap; associated with fault zones	Semi-massive to massive sulfide; minor euhedral qtz	ka - musc - ill	sphl - gal - py	mont - ba - qtz	cc - tet/ten - cp	0.1 - 10	Regular, continuous, planar walls	ill - musc - mont - ep - chl	ka	0.1 - 10	
	Gypsum veins/veinlets												
	gyp	Upper 270 m paleowater table; crosscut Tumpangpitu and Tanjung Jahe diatremes	Regular veins	gyp	-	cal - chl	py	0.1 3	Sharp walls; no alteration halo	-	-	-	

Abbreviations: and = andalusite, APS = aluminium phosphate sulfate, ba = barite, bn = bornite, bt = biotite, cc = chalcocite, chl = chlorite, col = colusite, cp = chalcopyrite, dsp = disapore, gyp = gypsum, hm = hematite, ill = illite ksp = K-feldspar, lz = luzonite, maw = mawsonite, musc = muscovite, mt = magnetite, mont = montmorillonite, nek = nekrasovite, py = pyrite, qtz = quartz, S = native sulfur, st = stannite, tet = tetrahedrite, ten = tennantite, tpz = topaz, USTs = unidirectional solidification textures, vin = vinciennite, zun = zunyite.

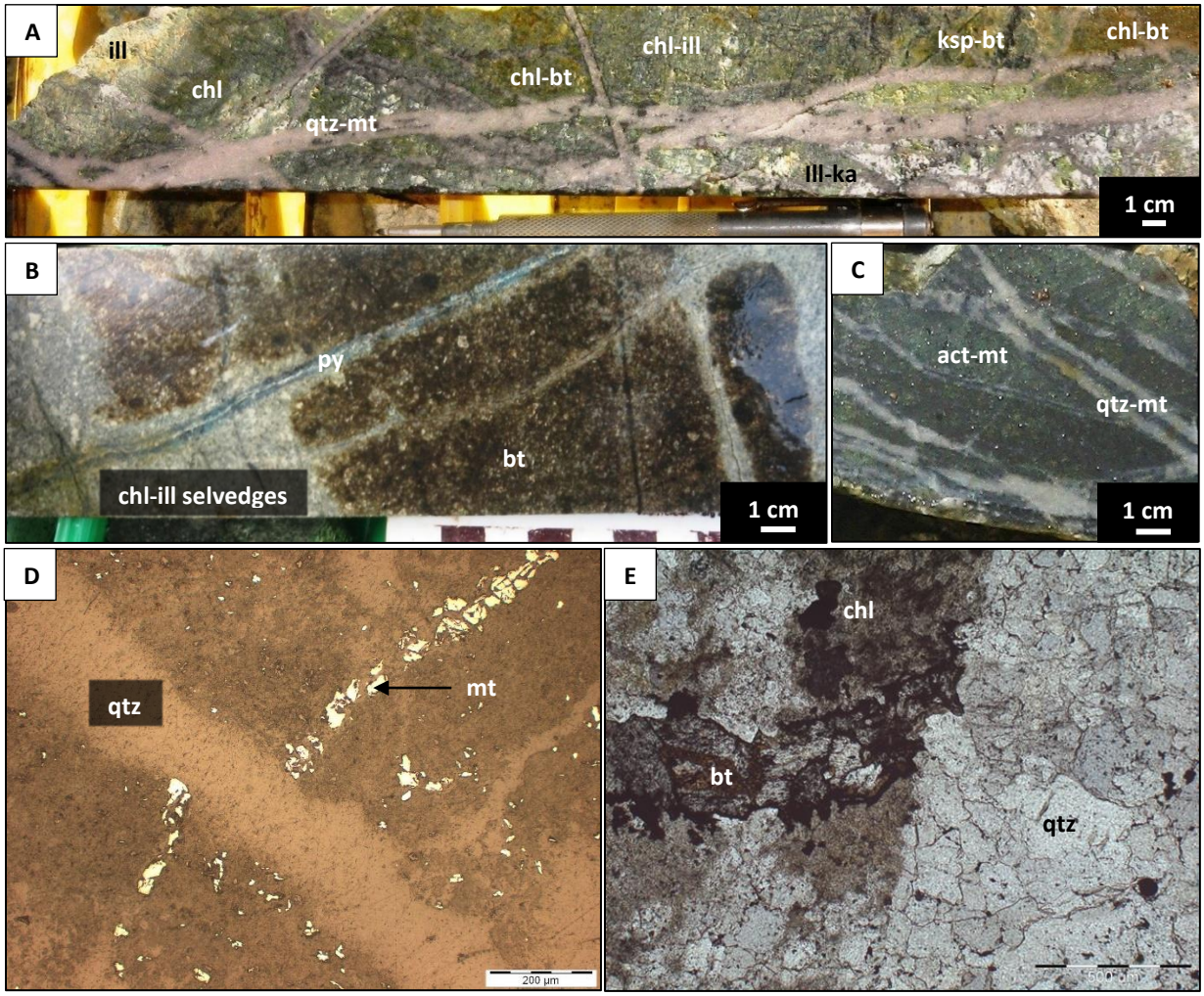

Figure 5.7. Quartz - magnetite alteration and associated veins in drillcore and petrographic samples from Tumpangpitu. Abbreviations: act = actinolite, bt = biotite, chl = chlorite, ill = illite, ksp = K-feldspar, ka = kaolinite, mt = magnetite, py = pyrite, qtz = quartz.

A) *Drillhole GTD-10-146; 756.2 m, 173595 mE, 9046376 mN.* K-feldspar - shreddy biotite, shreddy biotite replaced by chlorite, chlorite - illite and bleached white illite - kaolinite alteration of phase 6 tonalite with M2 quartz - magnetite vein stockwork.

B) *Drillhole GT003; 230.4 m, 173106 mE, 9047573 mN.* Pervasive secondary biotite alteration partially destroyed by chlorite - illite alteration selvedges around narrow pyrite veins in Pulau Merah fine-grained tonalite.

C) *Drillhole GTD-08-42; 568.8 m, 173495 mE, 9046564 mN.* Actinolite - magnetite alteration of phase 5 tonalite with M2 quartz - magnetite and M1 magnetite vein stockwork.

D) *Drillhole GTD-08-56 780m, 173878 mE, 9046141 mN.* Sugary quartz (A) vein that has crosscut and offset M1 magnetite stringer.

E) *Drillhole GTD-11-201 1097m, 174155 mE, 9046097 mN.* Granular quartz (A) vein crosscutting early biotite vein. Shreddy biotite partially replaced by chlorite; late stage illite has replaced feldspars.

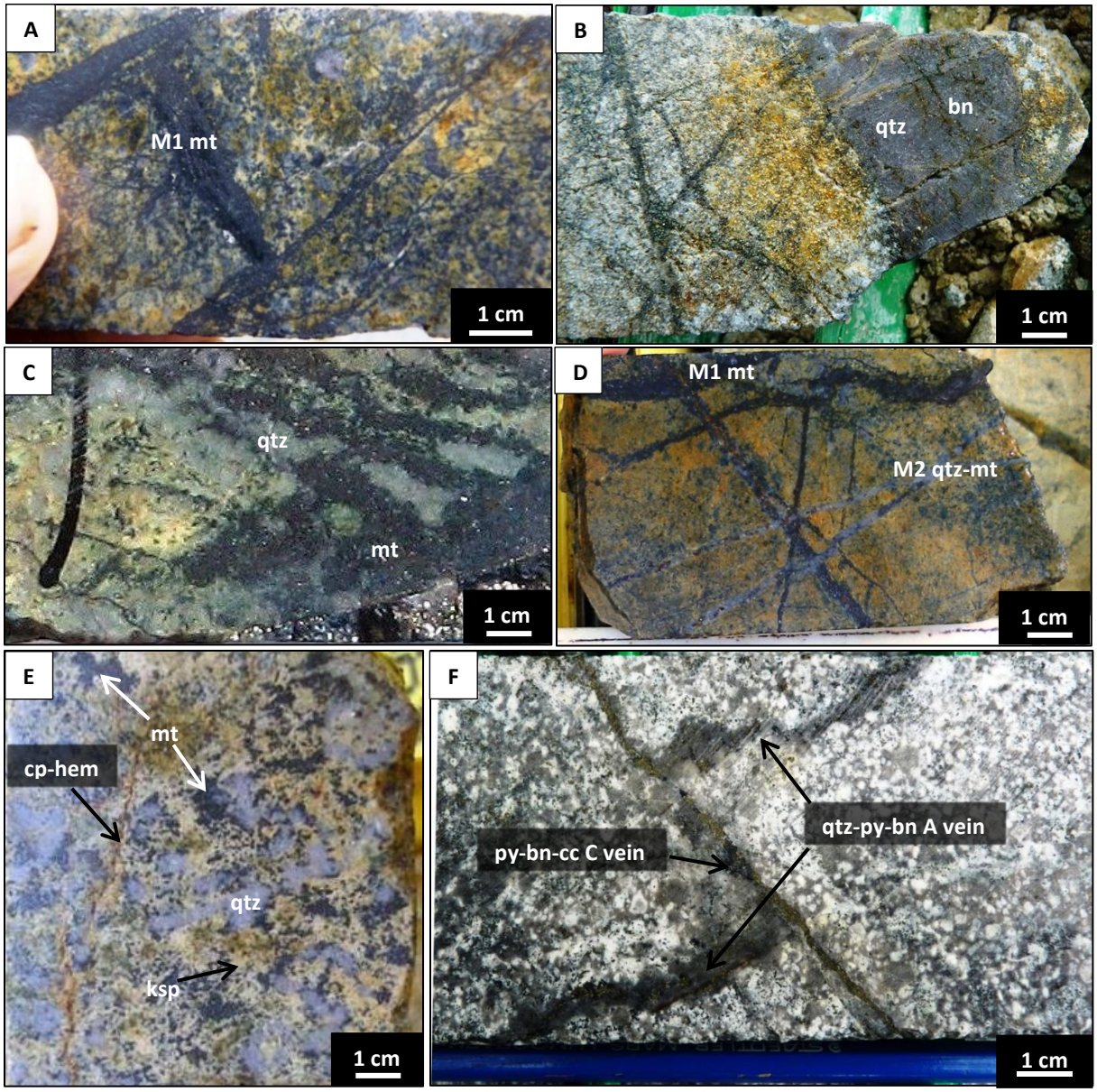

Figure 5.8. Examples of M and A-type veins and veinlets in drillcore from Tumpangpitu. Abbreviations: bn = bornite, cc = chalcocite, cp = chalcopyrite, hem = hematite, ksp = K-feldspar, mt = magnetite, py = pyrite, qtz = quartz.

A) Drillhole GTD-08-29; 620 m, 173574mE, 9045837mN. M1 magnetite-dominant veins in quartz - magnetite - biotite - K-feldspar ± illite ± chlorite-altered phase 6 coarse-grained tonalite.

B) Drillhole GTD-12-248; 479 m, 174385 mE, 9046285 mN. Quartz - chalcopyrite-bornite A vein in quartz - illite-altered phase 5 fine-grained tonalite.

C) Drillhole GTD-08-42; 580 m, 173495 mE, 9046564 mN. Discontinuous, irregular magnetite and quartz M2 veins, possibly with USTs in quartz - illite - chlorite-altered siltstone.

D) Drillhole GTD-08-29; 575 m, 174385 mE, 9046285 mN. M1 magnetite - chalcopyrite veins crosscutting and cut by M2 quartz - magnetite - chalcopyrite veinlets in quartz - magnetite - biotite - K-feldspar-altered phase 5 tonalite that has been overprinted by quartz - illite - kaolinite alteration.

E) Drillhole GTD-08-29; 532m, 174385 mE, 9046285 mN. Discontinuous, ptygmoidal blebs of quartz A veins and magnetite M2 veins in magnetite - biotite/chlorite - K-feldspar-altered phase 5 tonalite.

F) Drillhole GTD-10-167; 404 m, 173890 mE, 9046413 mN. Wavy quartz - pyrite - bornite (A) vein crosscut and offset by pyrite - bornite - chalcocite (C) vein that has overprinted phase 7 quartz diorite.

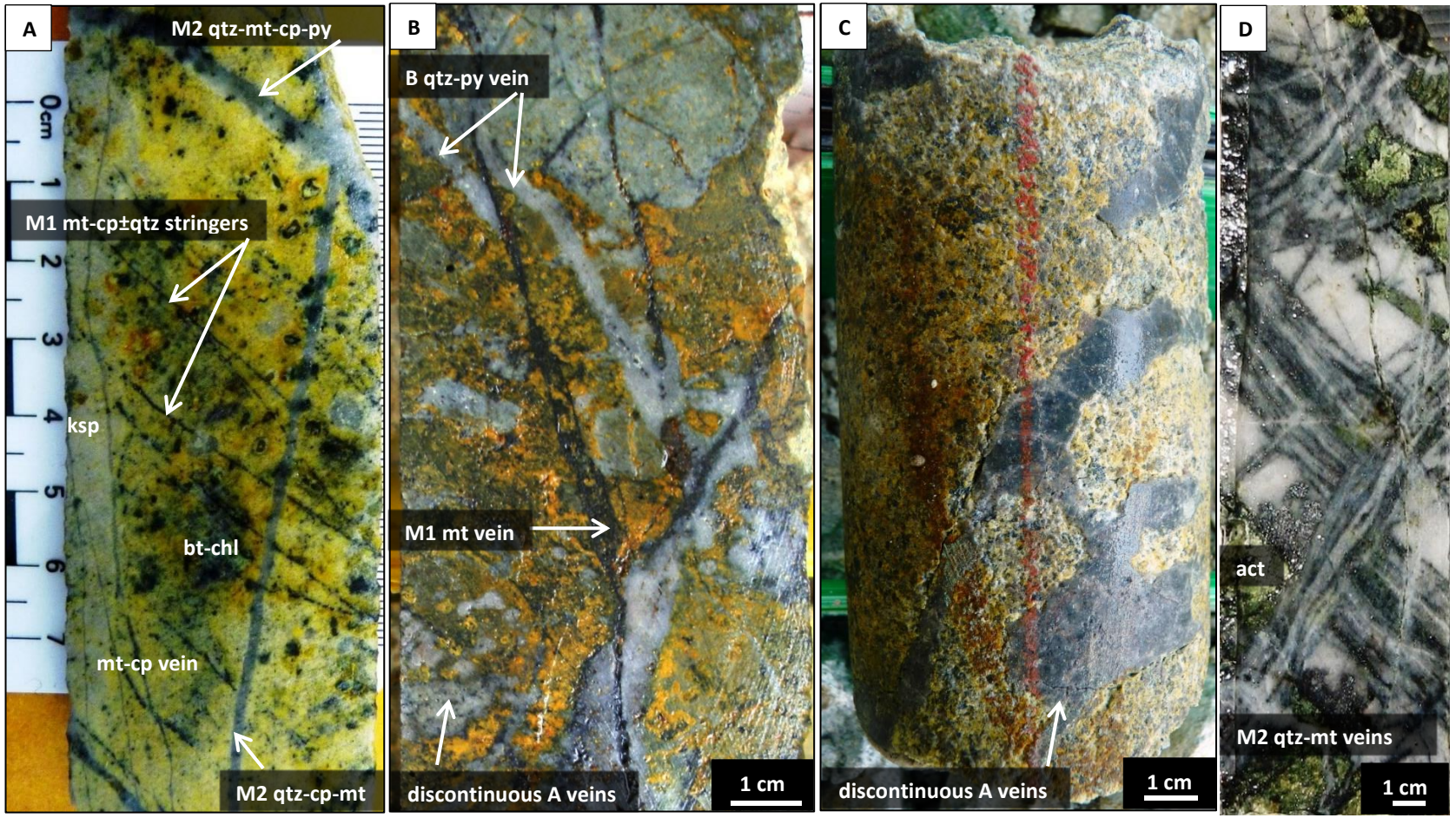

Figure 5.9. Examples of quartz - magnetite alteration and associated M and A-type veins in drillcore from Tumpangpitu. Abbreviations: act = actinolite, bn = bornite, bt = biotite, cc = chalcocite, chl = chlorite, cp = chalcopyrite ksp = K-feldspar, mt = magnetite, py = pyrite, qtz = quartz.

A) Drillhole GTD-10-166: 1082.7 m, 174156 mE, 9046095 mN. Quartz - magnetite - biotite - K-feldspar altered coarse-grained phase 6 tonalite. Narrow 1 1 - 2 mm M1 magnetite ± chalcopyrite veinlets cross cut M2 quartz - magnetite ± chalcopyrite vein stockwork. Biotite is replaced by chlorite.

B) Drillhole GTD-08-29; 814m, 173574 mE, 9045837 mN. Clear vein reversal relationship of a M1 magnetite vein cross-cutting and offsetting a quartz B vein with pyrite centreline through chlorite - illite - kaolinite altered sedimentary breccia.

C) Drillhole GTD-11-248; 479 m, 174385 mE, 9046285 mN. Discontinuous quartz - magnetite - chalcopyrite - bornite A veins in phase 5 tonalite.

D) Drillhole GTD-08-42; 578.6 m, 173495 mE, 9046564 mN. M2 Quartz - magnetite vein stockwork crosscut by chalcopyrite veinlets in sandstone.

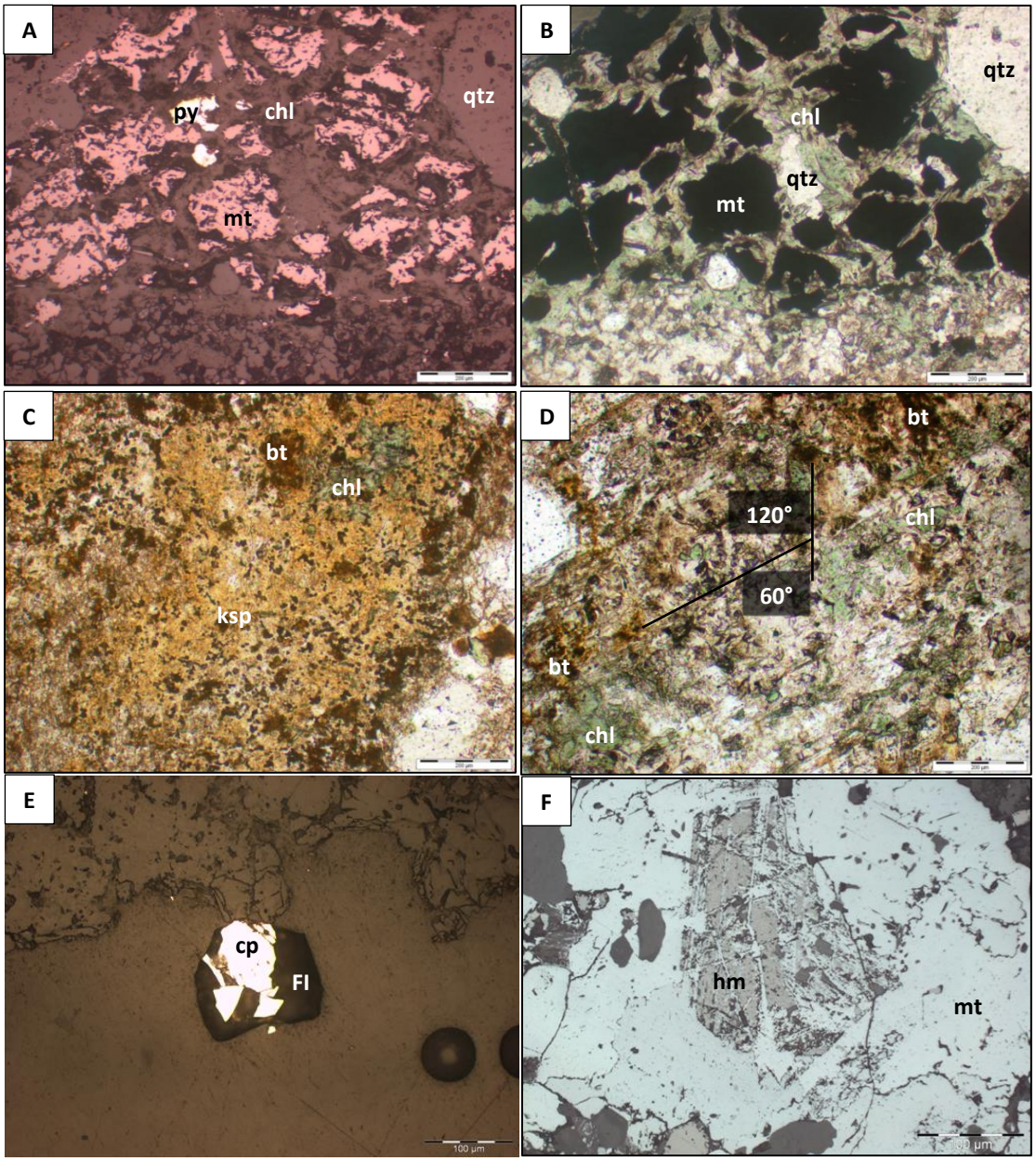

Figure 5.10. Photomicrographs under 10 x magnification of quartz - magnetite - K-feldspar - biotite (replaced by chlorite) alteration assemblage. Abbreviations: bt = biotite, chl = chlorite, cp = chalcopyrite, FI = fluid inclusion, hm = hematite, ksp = K-feldspar, mt = magnetite, qtz = quartz.

A) *Drillhole GTD-10-166: 1082.7 m, 174156 mE, 9046095 mN*. Reflected light image of magnetite, shreddy biotite partially replaced by chlorite, all replacing primary magmatic hornblende phenocryst. Clear 120/60° amphibole cleavage can be observed in phase 6 tonalite.
B) Photomicrograph A under crossed polars.
C) *Drillhole GTD-10-166: 1082.7 m, 174156 mE, 9046095 mN*. K-feldspar - biotite - chlorite alteration of phase 6 tonalite.
D) *Drillhole GTD-10-166: 1082.7 m, 174156 mE, 9046095 mN*. Replacement of primary magmatic hornblende with 120/60° amphibole cleavage by secondary biotite and chlorite in phase 6 tonalite.
E) *Drillhole GTD-11-192 891 m, 174074 mE, 9046298 mN*. Chalcopyrite in fluid inclusion.
F) *Drillhole GTD-11-201 988 m, 174155 mE, 9046097 mN*. Magnetite with hematite core after hornblende with relict 120/60° cleavage in phase 6 tonalite.

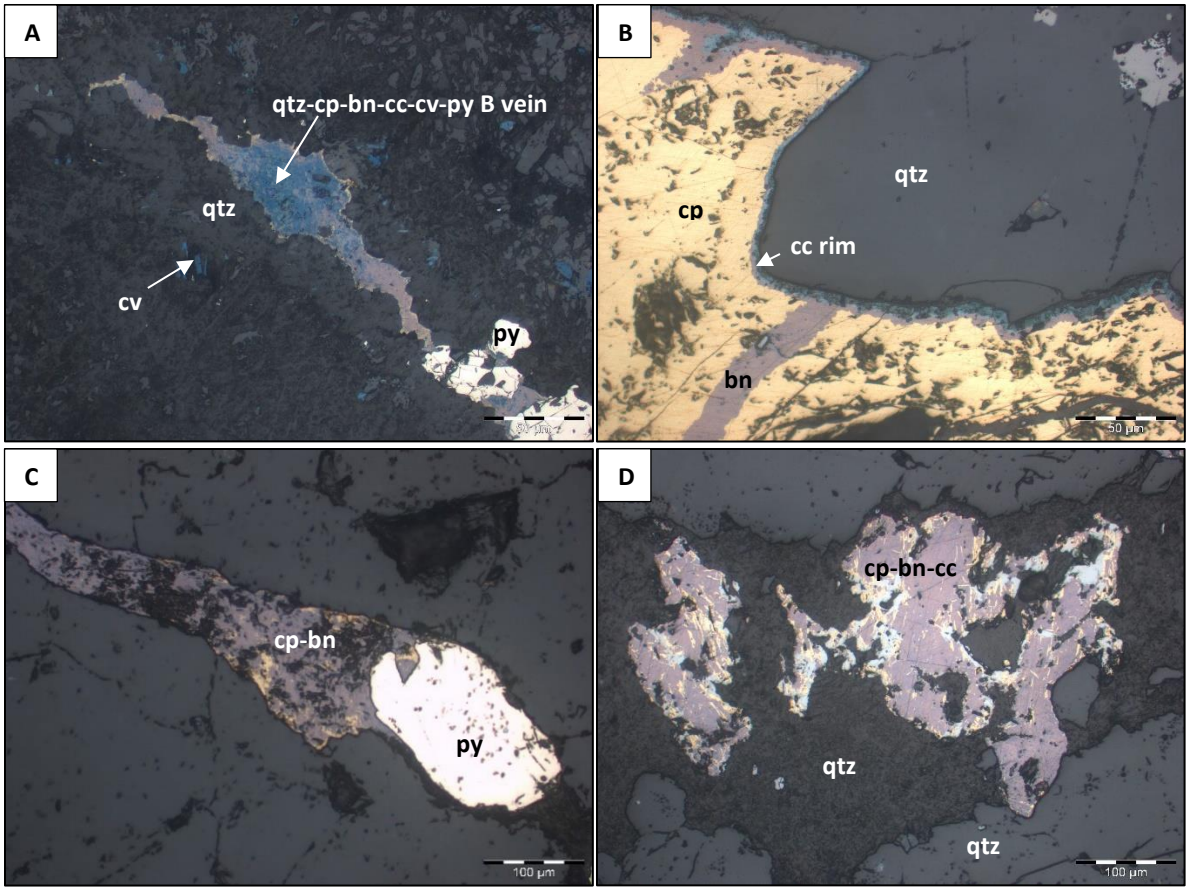

Figure 5.11. Photomicrographs under 10 x magnification of porphyry vein hosted copper sulfides. Abbreviations: bn = bornite, cc = chalcocite, cp = chalcopyrite, cv = covellite, py = pyrite, qtz = quartz.

A) *Drillhole GTD-09-112; 808 m, 173877 mE, 9046141 mN*. B vein with sulfide centreline of chalcopyrite - bornite - chalcocite - covellite with disseminated covellite in matrix and alunite - tennantite Grade 0.64 ppm Au, 5440 ppm Cu, 1620 ppm As, 2 ppm Ag, 0.5 ppm Sb (assay interval 52 - 54 m).

B) *Drillhole GTD-10-138; 886.75 m, 174149 mE, 9046090 mN*. Chalcopyrite C vein replaced along vein margins by bornite then chalcocite in sandstone (drillcore photo Fig. 5.12C).

C) *Drillhole GTD-10-137; 812m, 175020 mE, 9045397 mN*. Chalcopyrite - bornite C veinlet cutting into pyrite grain.

D) *Drillhole GTD-10-137; 812m, 175020 mE, 9045397 mN*. Chalcopyrite - bornite - chalcocite with exsolution lamellae in A vein.

continuous, planar fractures with parallel walls that form sharp contacts with the country rock. They contain most of the molybdenite at Tumpangpitu. Molybdenite typically defines "train-tracks" or parallel bands of molybdenite intergrown with quartz along the outer margins of the B veins (Fig. 5.12A). B veins have weak (fine-grained muscovite) or no alteration selvedges (<5 mm in width).

5.6.6 C veins and veinlets

C veins are narrow < 5 mm copper sulfide-rich veinlets that locally contain pyrite. They have little or no quartz (Fig. 5.8F, 5.11B, C, 5.12C, D). Copper sulfide species include chalcopyrite, bornite, chalcocite and covellite. C veins have regular, continuous walls and are paragenetically later than A, B and

M veins, cross cutting each of these vein sets. C veins are poorly developed at Tumpangpitu. Where present, they occur in the outer zone of the quartz - magnetite - biotite - K-feldspar alteration zone, and throughout the quartz - illite alteration zones. They extend laterally up to 200 m into the wallrocks. Where quartz - alunite, quartz - pyrophyllite or quartz - illite alteration have overprinted C veins, chalcopyrite has been replaced by bornite, and by reaction rims of chalcocite, that were in turn replaced by covellite and pyrite (Fig. 5.11B and C). C veins locally exhibit muscovite or illite alteration envelopes which grade out to chlorite (<5 mm in width; Fig. 5.12D).

5.6.7 D veins

D veins are very common throughout the Tumpangpitu ore body and overprint all earlier porphyry vein sets (M1, M2, A, B and C veins). They have overprinted the high grade mineralized core of the Tumpangpitu ore body and extend approximately 250 m laterally into the wallrocks. D veins range from < 0.1 cm to 5 cm in width and have a characteristic fine-grained muscovite alteration halo, up to 5 cm in width, which bleaches the wallrock white (Fig. 5.13B). The muscovite halo is typically surrounded by a chlorite halo where D veins have overprinted the quartz - magnetite - biotite - K-feldspar alteration assemblage. D veins are continuous, planar and composed predominantly of quartz - muscovite - pyrite with trace chalcopyrite, features typical of the assigned D vein classification by Gustafson and Hunt (1975; Figs. 5.12B, 5.13B and C). Their orientation is generally parallel to deposit-scale faults.

5.6.8 Quartz - muscovite alteration assemblage

The quartz - muscovite alteration zone at Tumpangpitu is defined by the dominance of white micas, predominantly of muscovitic composition and commonly replacing magmatic plagioclase. Magnetite has been altered to hematite where quartz - muscovite alteration has overprinted quartz - magnetite - biotite - K-feldspar alteration (Figs. 5.12B and 5.13). Accessory minerals include remnants of secondary chlorite after hydrothermal biotite. This quartz - muscovite alteration zone forms a carapace around preserved windows of quartz - magnetite alteration, commonly at the contact with the overprint of quartz - alunite and quartz - pyrophyllite alteration associated with high-sulfidation epithermal mineralization adjacent to deeply penetrating structures (Fig. 5.3). The quartz - muscovite alteration zone is dominated by D veins, but also hosts relict B and minor A veins.

5.6.9 Quartz flooding

Two massive zones of quartz, with quartz contents greater than 95 %, occur at depths of over 220 m bsl at Tumpangpitu (Fig. 5.2). Quartz alteration has commonly obliterated the texture of the primary lithology. The morphology of the quartz zones appear to mimic the carapace of the porphyry stockwork.

Quartz alteration is mainly associated with zones of quartz - muscovite alteration, or where preserved, quartz - magnetite-stable alteration assemblages. Locally, quartz-rich zones have been overprinted by quartz - alunite or quartz - pyrophyllite alteration adjacent to inter-mineralization faults. Where quartz has overprinted breccia units, quartz has flooded the breccia matrix and spared the clasts (Fig. 5.14C). There is no clear correlation of mineralization with zones of quartz alteration; some quartz zones are unmineralized (e.g., Figs.5.14A and C); others host high grade Au-Cu intervals (e.g., Fig. 5.14B and D). Massive and fracture-fill bornite, chalcocite and covellite, as well as C type veins have overprinted zones of quartz alteration locally (Figs. 5.14B and D).

5.6.10 Unmineralized porphyry stockwork zone

There is a dense (> 90 %) sheeted and banded quartz vein stockwork in the centre of Tumpangpitu, hosted by phase 6 tonalite, that is devoid of Cu, Au and Mo mineralization (Fig. 5.3 end of drillhole GTD-08-56 and Fig. 5.15). The zone is dominated by M1, M2, A and B-type stockwork veins. Quartz veins commonly exhibit pits along their centreline or adjacent to vein margins that may have been occupied by sulfides and fine-grained recrystallized textures of M1 and M2 veins (Fig. 5.15C). This core of barren veins appears to grade outward into a zone of sparse weakly mineralized (~ 0.3 g/t Au and 0.3 ppm Cu) quartz - sulfide - magnetite veins.

5.6.11 Actinolite - magnetite, chlorite - epidote and chlorite - calcite alteration assemblage

A concentric halo of propylitic mineral assemblages extends up to 2.5 km around the zone of porphyry mineralization, and also the Tumpangpitu lithocap (Fig. 5.2). This green rock alteration zone contacts directly with early, high temperature quartz - magnetite - biotite - K-feldspar alteration below 550 m bsl (Fig. 5.3). Minor actinolite has formed within and around ore grade porphyry Cu-Au-Mo mineralization associated with quartz - magnetite - biotite - K-feldspar alteration. This passes outwards to epidote - chlorite and distal calcite - chlorite. At surface, on the margins of the Tumpangpitu lithocap, propylitic alteration has developed distal to the illite - smectite alteration assemblage, defining a zonation pattern of inner epidote - chlorite and outer calcite - chlorite (Fig. 5.2). Unaltered rocks have rarely been observed beyond the propylitic halo surrounding Tumpangpitu, most likely due to the large alteration footprint and level of erosion. Epidote, chlorite and calcite alteration mineral assemblages are also associated with the Tumpangpitu and Tanjung Jahe diatremes. The propylitic alteration zone has been split

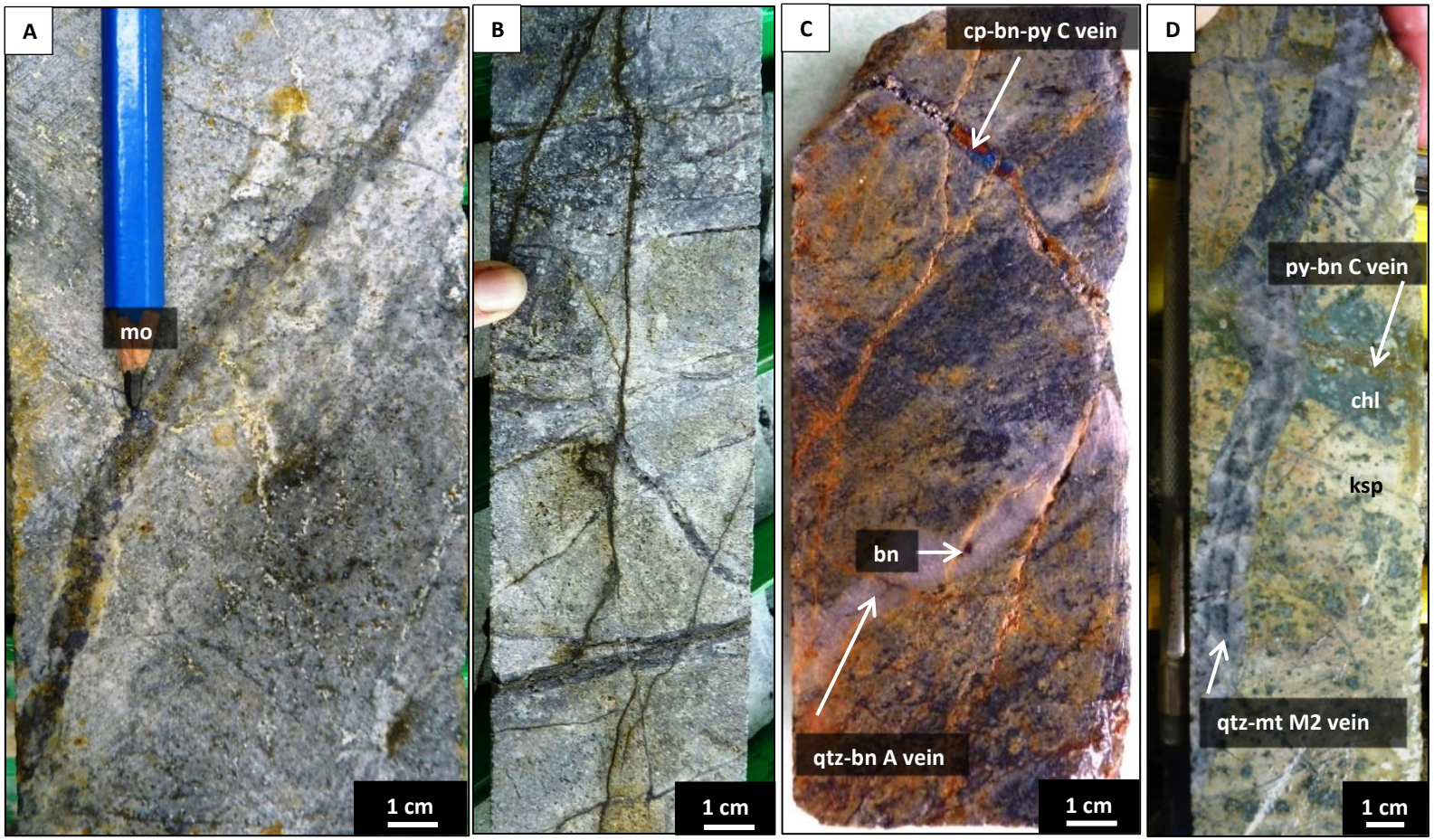

Figure 5.12. Examples of porphyry B and C veins in drillcore from Tumpangpitu. Abbreviations: bn = bornite, bt = biotite, cc = chalcocite, chl = chlorite, cp = chalcopyrite, ksp = K-feldspar, mt = magnetite, py = pyrite, qtz = quartz.

A) *Drillhole GTD-10-172; 368 m, 174240 mE, 9046440 mN.* Quartz - pyrite - molybdenite - bornite - chalcopyrite B vein in phase 5 fine-grained tonalite overprinted by quartz - pyrophyllite - dickite - K-alunite alteration.

B) *Drillhole GTD-10-172; 391.5 m, 174240 mE, 9046440 mN.* Porphyry quartz - molybdenite - bornite B veining crosscut by pyrite D vein in quartz - muscovite - kaolinite altered phase 5 fine-grained tonalite.

C) *Drillhole GTD-10-146; 886.75 m, 173595 mE, 9046376 mN.* Early sugary quartz A type vein and later pyrite - bornite - chalcopyrite C vein overprinting sandstone.

D) *Drillhole GTD-10-146: 699.5 m 173595 mE, 9046376 mN.* Shreddy chlorite after biotite replacing primary mafic minerals. Fine-grained pale pink K-feldspar in matrix of phase 5 tonalite. Early quartz - magnetite M1 vein with no alteration halo crosscut by late pyrite - bornite C vein with chlorite halo.

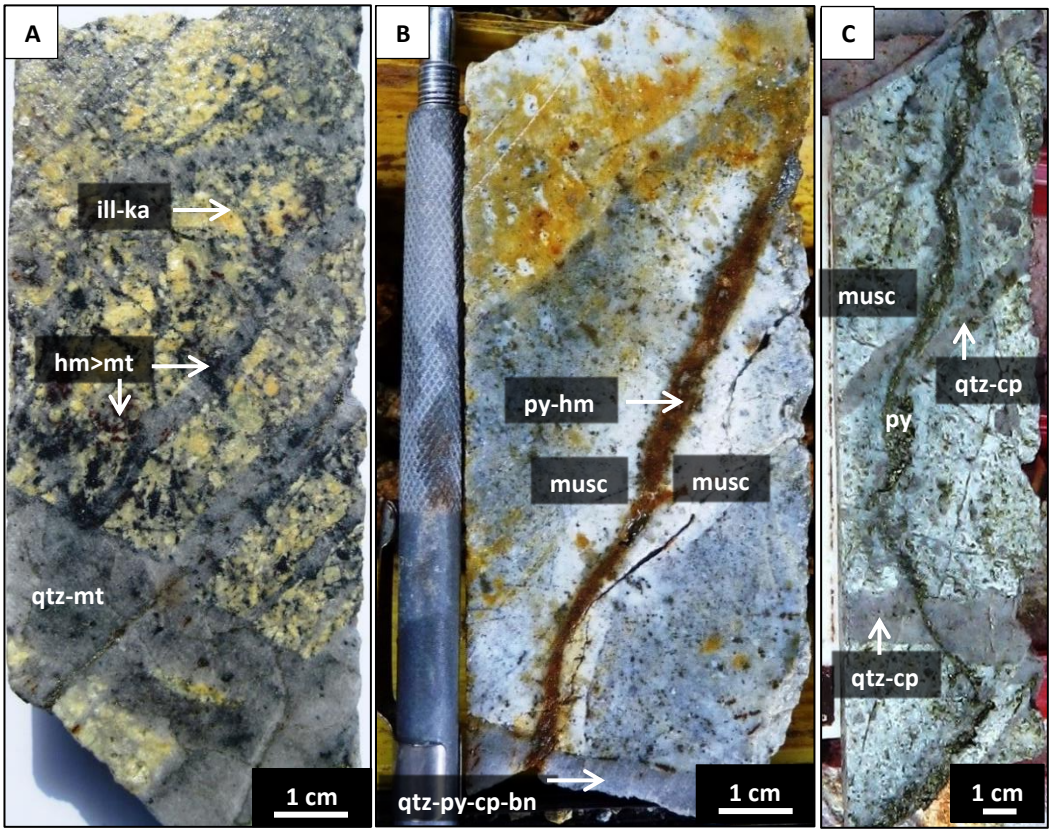

Figure 5.13 Examples of quartz - muscovite ± illite alteration and D veins in drillcore from Tumpangpitu. Abbreviations: cp = chalcopyrite, hm = hematite, ill = illite, ka = kaolinite, musc = muscovite, mt = magnetite, py = pyrite, qtz = quartz.

A) *Drillhole GTD-10-166: 1023 m, 174156 mE, 9046095 mN.* Quartz - magnetite - biotite - K-feldspar altered phase 6 tonalite porphyry overprinted by quartz - illite - kaolinite alteration causing partial oxidation of magnetite to hematite. Muscovite and kaolinite have replaced original plagioclase feldspar phenocrysts.
B) *Drillhole GTD-10-138; 916.4 m, 174149 mE, 9046090 mN.* Pyrite - quartz D vein with muscovite alteration selvedge crosscuts through quartz - pyrite - chalcopyrite - bornite B vein.
C) *Drillhole GTD-08-35; 820 m, 174080 mE, 9046551 mN.* Pyrite - quartz - muscovite vein crosscuts and offsets quartz - chalcopyrite B veins in coarse-grained phase 6 tonalite.

into three main mineral assemblages from proximal to distal; 1) actinolite - magnetite; 2) chlorite - epidote and 3) chlorite - calcite.

5.6.11.1 Actinolite - magnetite alteration assemblage and veins

An inner zone of poorly developed actinolite associated with magnetite has developed locally around Tumpangpitu. It overlaps with the central high grade quartz - magnetite - biotite - K-feldspar - altered Cu-Au-Mo ore zone. The actinolite alteration zone has only rarely been documented from deep drillholes (e.g., 5.7C), where it has affected sedimentary wallrocks (e.g., Fig. 5.9D). Actinolite has developed within both phase 5 and 6 tonalite porphyry intrusions and has overprinted 100 m of country rock laterally outwards from the ore zone. Actinolite is present as veinlets and veins (< 0.1 - 1 cm) and

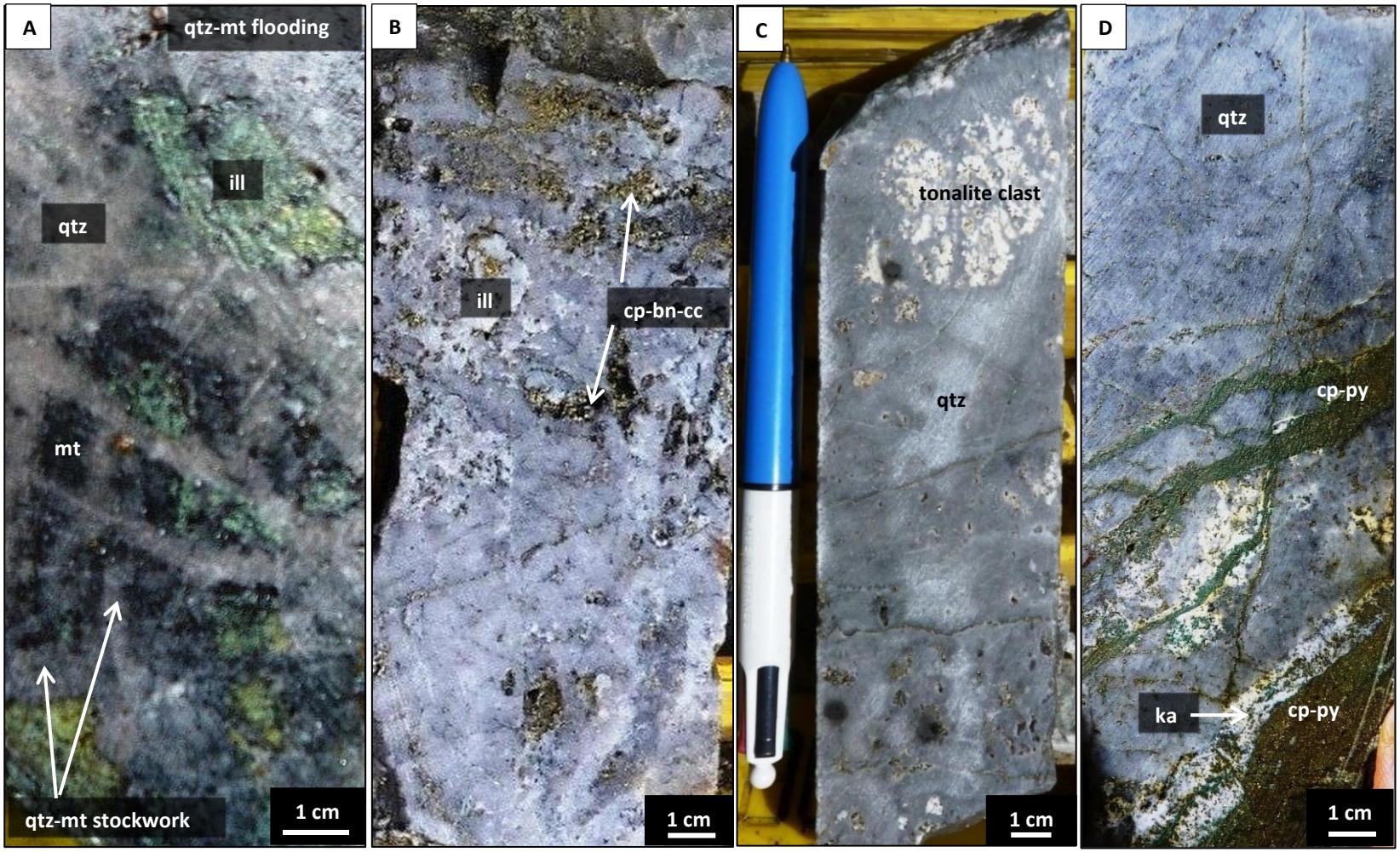

Figure 5.14 Quartz flooding in drillcore from Tumpangpitu. Abbreviations: bn = bornite, cc = chalcocite, cp = chalcopyrite, mt = magnetite, qtz = quartz.

A) *Drillhole GTD-10-146: 794 m, 173595 mE, 9046376 mN.* Zone of intense quartz - magnetite M2 stockwork veining grading into quartz flooding. Green illite in phase 5 fine-grained tonalite.
B) *Drillhole GTD-10-160 507.8 m, 174152 mE, 9046092 mN.* Quartz stockwork veining and massive silicification. Disseminated chalcopyrite - bornite - chalcocite in quartz - illite altered phase 5 tonalite.
C) *Drillhole GTD-10-160: 480.8 m, 174152 mE, 9046092 mN.* Quartz flooding around stockwork veined tonalite clast, kaolinite - K-alunite alteration.
D) *Drillhole GTD-10-160; 481.85 m, 174152 mE, 9046092 mN.* Chalcopyrite - pyrite - bornite C veins overprinting quartz altered tonalite.

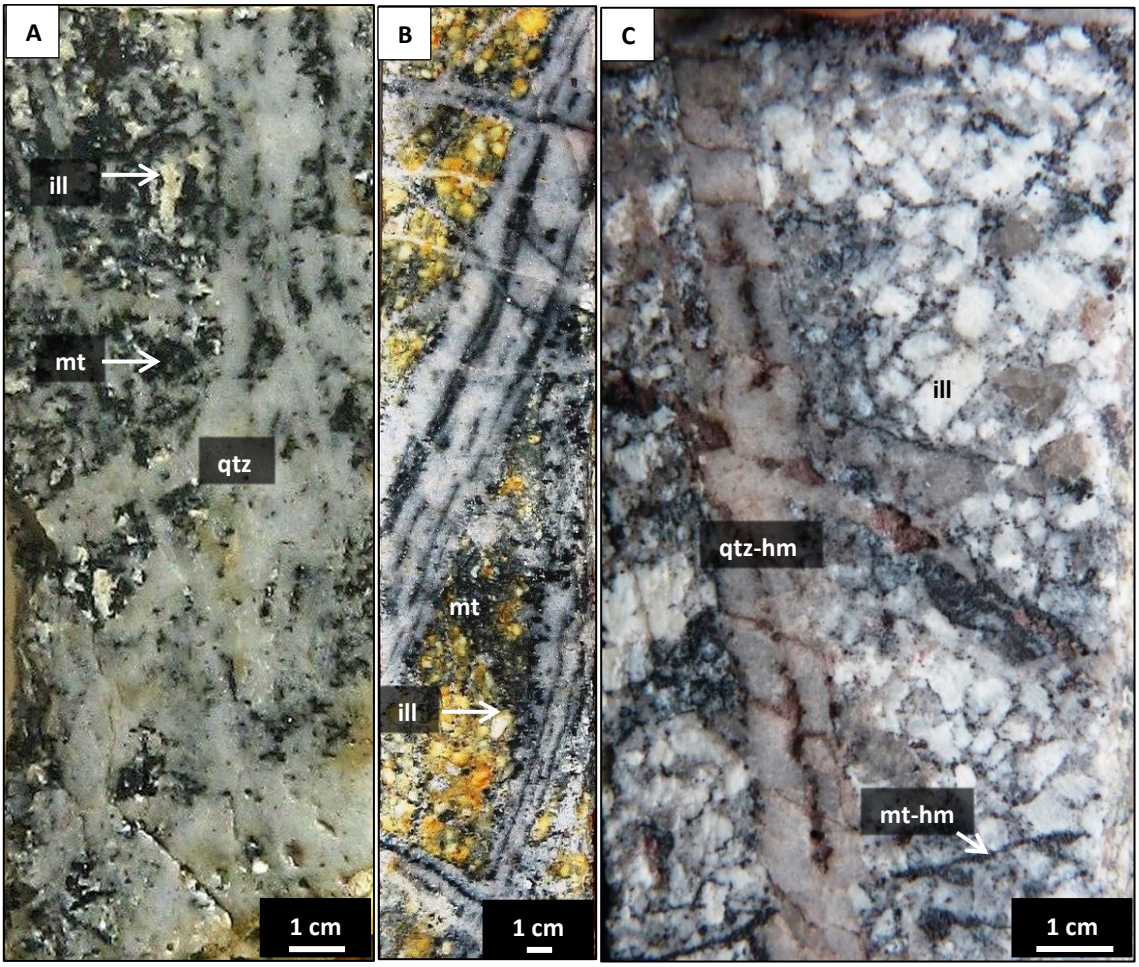

Figure 5.15. Drillcore from unmineralized stockwork zone at Tumpangpitu. Abbreviations: hm = hematite, ill = illite, mt = magnetite, qtz = quartz.
A) Drillhole GTD-08-35 690.5 m, 174080 mE, 9046551 mN. Unmineralized quartz - magnetite porphyry stockwork overprinted by illite; magnetite is partially oxidised to hematite in coarse-grained phase 6 tonalite.
B) Drillhole GTD-08-56 780m, 173878 mE, 9046141 mN. Unmineralized quartz - magnetite stockwork in coarse-grained quartz - magnetite - biotite altered phase 6 tonalite overprinted by quartz - illite - kaolinite.
Drillhole GTD-08-35; 710m, 174080 mE, 9046551 mN. B type porphyry stockwork vein with centreline devoid of sulfide in quartz - illite altered phase 6 tonalite.

disseminations of coarse-grained forest green needles or laths intergrown with magnetite or fine-grained disseminations with magnetite surrounding early M1 and M2 veins. Actinolite also occurs within the M1 and M2 stage porphyry veins. Actinolite veins and veinlets are irregular, and have diffuse contacts with their wallrocks. Accessory minerals within the actinolite - magnetite alteration zone include secondary biotite and retrograde chlorite.

5.6.11.2 Epidote - chlorite alteration assemblage and veins

Epidote and chlorite define an alteration zone between the actinolite and chlorite - calcite alteration zones at depths greater than 550 m bsl at Tumpangpitu. They occur at surface for a distance of 1.5 km of wallrock surrounding Tumpangpitu, Zone B porphyries and the Tujuh Bukit lithocap (Fig. 5.2). Chlorite -

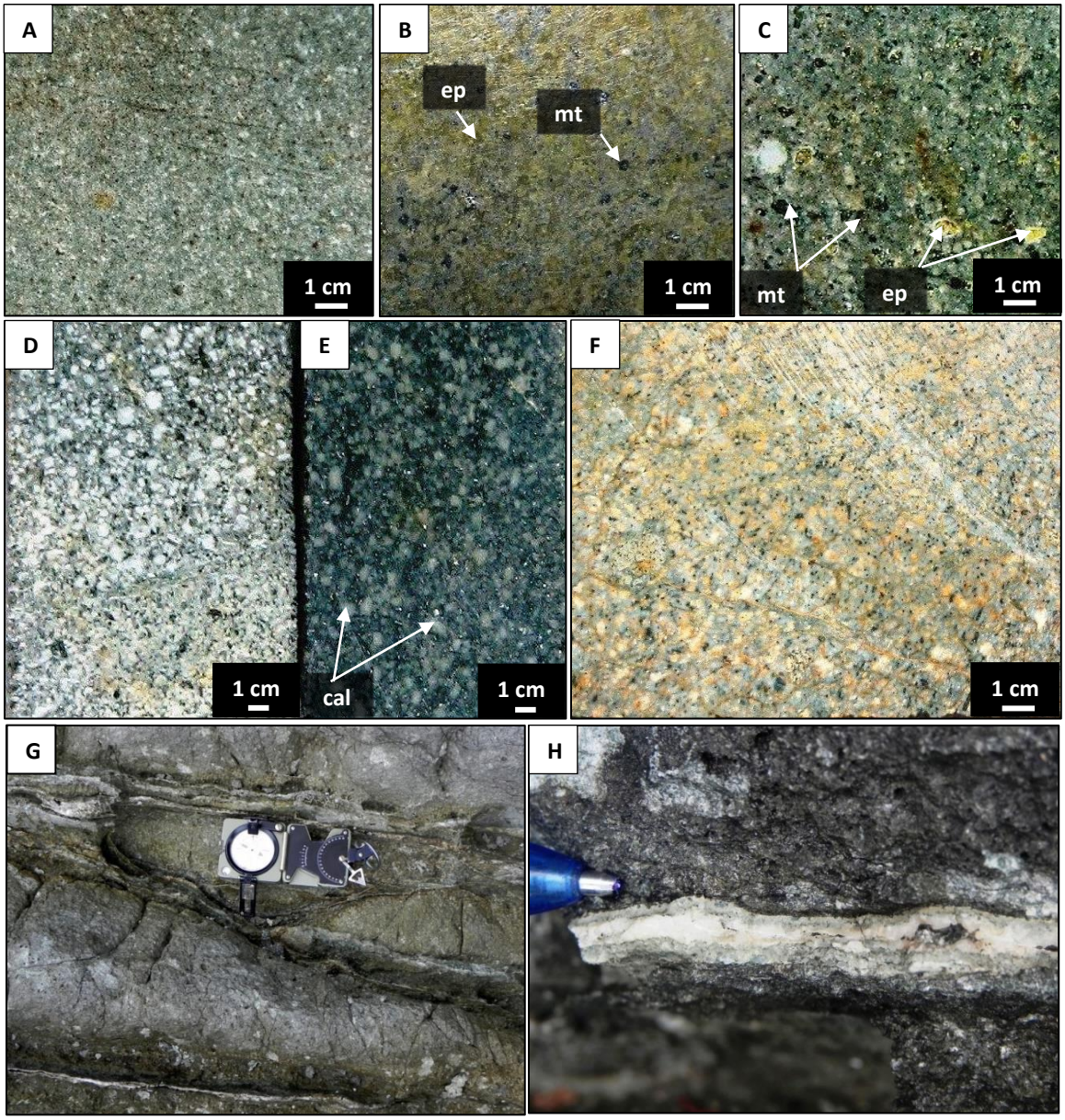

Figure 5.16. Illite - smectite ± chlorite ± kaolinite, chlorite - calcite ± epidote alteration assemblages and associated veining in phase 2 diorite from drillcore and coastal exposures at Tumpangpitu. Abbreviations: cal = calcite, ep = epidote, mt = magnetite.

A) Drillhole GTD-08-26; 17 m, 173578 mE, 9045841 mN. Chlorite - illite alteration.

B) Drillhole GTD-08-29; 394 m, 173574 mE, 9045837 mN. Chlorite - epidote - magnetite alteration. Epidote has replaced feldspar (plagioclase), magnetite is euhedral.

C) Drillhole GTD-08-58; 230.5 m, 174669 mE, 9045454 mN. Chlorite - epidote - calcite - montmorillonite - alteration. Epidote and illite have replaced the cores of plagioclase phenocrysts.

D) Drillhole GTD-09-129; 46.6 m. 173503 mE, 9046136 mN. Chlorite - illite - montmorillonite - kaolinite alteration.

E) Drillhole GTD-08-26; 256 m, 173578 mE, 9045841 mN. Chlorite - calcite alteration.

F) Drillhole GTD-08-26; 256 m, 173578 mE, 9045841 mN. Chlorite - illite - montmorillonite - kaolinite alteration.

G) 173711 mE, 9044413 mN, RL; 3 m. Laminated quartz - calcite - chlorite - epidote veins in outcrop.

H) 173711 mE, 9044413 mN, RL; 3 m. Syntaxial cavity fill crystal growth of quartz - calcite - chlorite - epidote vein in coastal exposure.

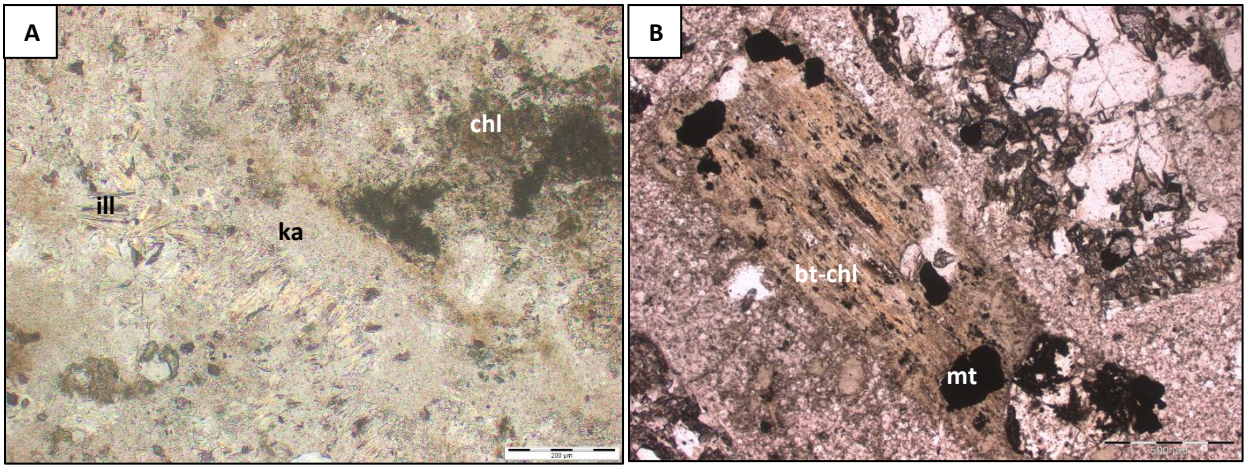

Figure 5.17. Petrographic images from illite - smectite and chlorite - calcite alteration zones.
A) *Drillhole GTD-10-166: 651 m, 174156 mE, 9046095 mN.* 10 x magnification kaolinite - illite - chlorite altered phase 7 quartz diorite.
B) *Drillhole GTD-10-167: 91.7 m, 173890 mE, 9046413 mN.* Biotite phenocryst partially replaced by chlorite with euhedral primary magnetite grains in chlorite - calcite altered phase 7 quartz diorite.

epidote altered rocks contain minor accessory magnetite and illite. There is an increasing abundance of calcite with distance from Tumpangpitu (Fig. 5.2). Epidote has replaced the cores of plagioclase phenocrysts and is intergrown with chlorite (Fig. 5.16C). Epidote also occurs in narrow monomineralic veinlets 1 - 3 mm wide.

5.6.11.3 Chlorite - calcite alteration assemblage and veins

Calcite along with chlorite dominate the propylitic alteration mineral assemblage at surface (Fig. 5.2) and on sections (Fig. 5.3), forming halos of up to 2.5 km distant from the Tumpangpitu lithocap to unaltered rocks. Accessory minerals include illite after feldspars together with epidote. Chlorite - calcite - veins and veinlets are common around the periphery of Tumpangpitu and the Tujuh Bukit lithocap. The veins are generally laminated with quartz and chlorite margins and commonly exhibit syntaxial cavity-fill crystal growth of calcite into open cavities in the center of veins (Fig.16H). Vein and veinlet thickness ranges from 1 mm to 2 cm. Detailed measurements during coastal mapping have shown a consistent concentric dip of chlorite - calcite veins towards the center of the Tumpangpitu porphyry system (Harrison, 2009; Gray, 2010).

5.7 High- and intermediate-sulfidation epithermal veins and related alteration assemblages

5.7.1 Introduction

Late stage fault-hosted enargite and tennantite - tetrahedrite-bearing veins have crosscut M, A, B and C veins and related alteration assemblages at Tumpangpitu (Figs. 5.18 - 5.20; Table 5.2). They are classified as high-sulfidation epithermal (HSE) where they contain enargite and other high-sulfidation state minerals such as covellite and bornite (e.g., Einaudi et al., 2003), typically accompanied by alunite. Intermediate-sulfidation veins are classified as those containing tetrahedrite - tennantite - chalcopyrite with the absence of enargite (e.g., Hedenquist et al., 2000). Base metal-rich intermediate-sulfidation veins with sphalerite and galena were the last to form at Tumpangpitu. High- and intermediate-sulfidation state veins are intimately related to fault zones, in particular the Cliff fault beneath Zone A (Fig. 5.3). The widest veins (up to 50 cm) are associated with major inter-mineralization normal faults (Fig. 5.2). Smaller veins (2 mm to 2 cm), are concentrated near faults, and decrease in abundance away from fault zones. The sulfide content of HSE-1, HSE-2 and ISE veins decreases and gangue minerals increase with distance away from inter-mineralization fault zones. All epithermal veins have crosscut or re-opened most of the other vein stages at Tumpangpitu, although some appear to have formed contemporaneous with D veins. Using assays when logging sulfides in these veins was essential to determine the presence of fine-grained Ag-sulfosalts that can be hard to distinguish from enargite and other fine-grained black sulfides. Veins are characterized by four main phases, in order from early to late;

1) HSE-1; enargite/luzonite - pyrite ± covellite ± bornite ± chalcocite veins associated with altered zones of vuggy and massive quartz - alunite, quartz - pyrophyllite (below 220 m) ± barite, dickite, kaolinite, locally diaspore, topaz, zunyite, native sulfur, andalusite and APS minerals
2) HSE-2; enargite/luzonite - tennantite/tetrahedrite - pyrite ± minor chalcopyrite intergrown with or overprinted by Ag-sulfosalts including stannite and colusite veins associated with massive quartz - alunite, quartz - pyrophyllite ± alunite ± diaspore ± topaz ± zunyite ± andalusite ± APS minerals, quartz - dickite ± kaolinite, locally barite and distal quartz - kaolinite - illite
3) ISE-1; tetrahedrite-tennantite-bearing veins (without enargite) ± chalcopyrite and Ag-sulfosalts including stannite and colusite, associated with quartz - kaolinite ± dickite and quartz - illite alteration and which locally contain barite
4) ISE-2; base metal sphalerite - galena veins associated with illite ± kaolinite ± montmorillonite alteration

The epithermal veins have alteration halos that vary from proximal quartz and highly crystalline muscovite to illite - smectite to illite - chlorite - montmorillonite to distal chlorite - calcite ± epidote alteration assemblages.

5.7.2 Late stage veins

5.7.2.1 Enargite veins (HSE-1; high-sulfidation epithermal)

Weathered fault-hosted enargite veins host most of the high-sulfidation-derived oxide ore at Tumpangpitu. At depth, the veins contain enargite/luzonite - pyrite ± covellite ± bornite ± chalcocite. Enargite commonly has the form of black or metallic grey, tabular or prismatic needles up to 2 cm in length (Fig. 5.18A). Enargite and luzonite have mutual grain boundaries with each other, and in some portions luzonite commonly occurs as lamellar intergrowths in enargite (Fig. A-). Bornite locally forms large (up to 2 cm), radiating crystals intergrown with alunite within veins (Fig. 5.18C). Spectacular specimens of coarse-grained, indigo-blue covellite occur as euhedral hexagonal plates up to 1 cm in veins and as cements or open-space fillings in the hydrothermal breccias intergrown with euhedral, platy alunite (Fig. 5.18F). Gangue minerals constitute up to 25 % of the vein and include alunite, pyrophyllite, dickite, quartz and locally barite, diaspore, topaz, zunyite, andalusite and APS (aluminium phosphate sulfate) minerals. Vein alunite commonly occurs as euhedral blades (Fig. 5.18D, 5.23A and B) and contains anhedral inclusions of APS minerals identified by EPMA analysis (Fig. 5.27F). Hypogene alunite is granular-textured and fine-grained (< 1 mm). HSE-1 veins are associated with several alteration assemblages, including; vuggy and massive quartz - alunite, and quartz - pyrophyllite, the latter present below 220 m bsl. Pyrite is typically the earliest-formed sulfide mineral in HSE-1 veins.

Adjacent to major fault zones, HSE-1 veins have the form of clast-supported vein breccias with angular, monomict clasts of wallrock and sulfides, cemented by enargite/luzonite - pyrite ± covellite ± bornite ± chalcocite. HSE-1 veins have cut or re-opened most of the other vein stages at Tumpangpitu, but appear to have formed contemporaneous with deeper-seated D veins.

5.7.2.2 Enargite-tennantite-tetrahedrite veins (HSE-2; high-sulfidation epithermal)

Enargite/luzonite - tennantite-tetrahedrite veins are fault-hosted. They contain pyrite ± minor chalcopyrite intergrown with, or overprinted by, sulfosalts including tennantite and tetrahedrite. Tennantite and tetrahedrite in HSE-2 veins have generally replaced enargite, pyrite, chalcopyrite, bornite, chalcocite and covellite. Tennantite-tetrahedrite occurs as replacements after enargite, luzonite and pyrite grains, partially or completely. Tennantite-tetrahedrite preferably replaces enargite more than pyrite. Electron microprobe (EMPA) analyses have identified Sn-sulfides; stannite Cu_2FeSnS_4, colusite $Cu_3(As, Sn,V,Fe)S_4$ nekrasovite $Cu_{26}V_2(Sn,As,Sb)_6S_{32,}$ mawsonite $Cu_6Fe_2SnS_{8,}$ vinciennite $Cu_{10}Fe_4SnAsS_{16}$ and other Cu, Ag, As, Sn, Sb, V-bearing sulfides and sulfosalts associated with HSE-2 veins (Fig. 5.30C). Sn-sulfides

crosscut bornite, chalcocite and covellite (Fig. 5.27H and I) and appear to have formed contemporaneously with tennantite. Pyrite is recognized as the earliest sulfide mineral in HSE-2 veins. HSE-2 veins have cut or re-opened most of the other vein stages at Tumpangpitu. The majority of tennantite-tetrahedrite occurrences are as massive black, steel grey sulfosalts intergrown with pyrite, locally defining syntaxial crystal growth textures along vein margins (Fig. 5.20A). Tetrahedrite-tennantite crystals, where coarse-grained in open spaces within veins, have formed euhedral individual hexatetrahedral crystals, locally with barite (Fig. 5.20B). Gangue minerals constitute up to 25 % of the HSE-2 veins, and include alunite, pyrophyllite, quartz, dickite, kaolinite, illite and locally barite, diaspore, topaz, zunyite, andalusite and APS minerals. Barite locally forms large (up to 2 cm) euhedral crystals or fine-grained, sugary-textured aggregates (Fig. 5.20B). HSE-2 veins have alteration halos that include massive quartz - alunite, quartz - pyrophyllite ± alunite, quartz - dickite ± kaolinite and distal quartz - kaolinite - illite. Bornite has partly to entirely replaced chalcopyrite and has rims of chalcocite and covellite (Fig. 5.30). Bornite, chalcocite and covellite have embayed and infilled fractures in pyrite (Fig. 5.30) and commonly enclose residual pyrite grains. Solid solution lamellar chalcocite replacement of bornite and covellite replacement of chalcocite has resulted in ragged and irregular grain boundaries (Fig. 5.28).

5.7.2.3 Tennantite-tetrahedrite ± chalcopyrite veins (ISE-1; intermediate-sulfidation epithermal)

Tennantite-tetrahedrite-pyrite ± chalcopyrite veins crosscut and overprinted enargite-bearing vein phases HSE-1 and HSE-2. Pyrite is the earliest-formed sulfide mineral in ISE veins. Vein gangue minerals include illite, kaolinite and locally, barite and dickite. ISE-1 veins are associated with alteration mineral assemblages of quartz - kaolinite ± dickite, quartz - kaolinite - muscovite, quartz - muscovite with halos of illite - smectite and distal chlorite. Inter-banded and laminated colloform vein textures are common displayed by tennantite - tetrahedrite, chalcopyrite, sphalerite and pyrite and are indicative of open space infilling (Fig. 5.20F).

Tennantite-tetrahedrite has been identified in drillcore as massive, earthy steel-grey-coloured sulfosalt along fractures (e.g., Fig. 5.20A), as euhedral hextetrahedrons with barite (Fig. 5.20B) or banded laminated veins with massive pyrite (Fig. 5.20F). Tetrahedrite-tennantite commonly occurs as fine-grained disseminations in veins and country rock and therefore is difficult to identify from other dark coloured sulfides such as enargite and chalcocite. Drillcore logging with assays of Cu, As, Sb and Ag, petrographic, SEM and electron probe analysis was essential for helping to identify tetrahedrite-tennantite and other Ag-bearing sulfosalts. ISE-1 veins have cut or re-opened most of the other vein stages at Tumpangpitu, but appear to be contemporaneous with D veins.

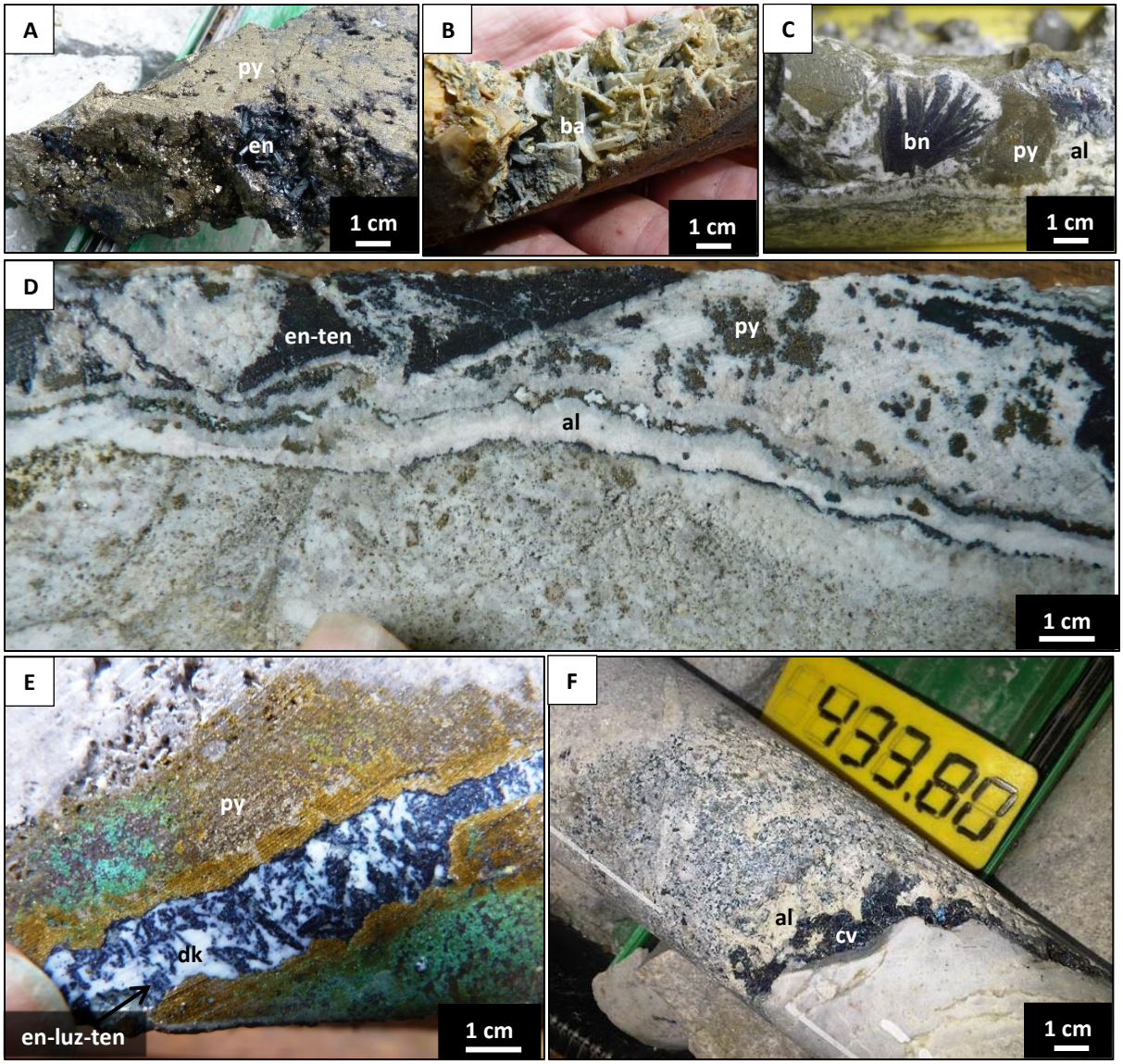

Figure 5.18. High-sulfidation epithermal HSE-1 and HSE-2 veins from drillcore at Tumpangpitu. Abbreviations: al = alunite, ba = barite, cv = covellite, dk = dickite, en = enargite, luz = luzonite, py = pyrite, ten = tennantite.

A) *Drillhole GTD-10-167; 299.8 m, 173890 mE, 9046413 mN.* Massive pyrite - enargite - covellite HSE-1 vein proximal to central fault zone.

B) *Drillhole GTD-08-56:* m, *173878 mE, 9046141 mN.* HSE-1 enargite vein with large > 1 cm barite crystals.

C) *Drillhole GTD-10-163; 528.2 m.* HSE-1 vein with euhedral radiating bornite crystals with pyrite and alunite.

D) *Drillhole GTD-09-112; 219 m, 173877 mE, 9046141 mN.* HSE-2 vein with crystalline alunite, pyrite - enargite and tennantite. Grade 0.05 g/t Au, 0.13% Cu, 5g/t Ag, 249 ppm As in quartz - dickite - kaolinite altered phase 2 diorite.

E) *Drillhole GTD-09-112; 227.6 m. 173877 mE, 9046141 mN.* HSE-1 vein with bladed enargite - luzonite - tennantite - dickite with massive pyrite - chalcocite halo. Grade 0.3 g/t Au, 4580 ppm Cu, 1170 ppm As, 15 g/t Ag, 133 ppm Sb (assay interval 226 - 228 m) in quartz - dickite - kaolinite altered phase 2 diorite.

F) *Drillhole GTD-12-335; 433.8 m, 174208 mE, 9045951 mN.* High-sulfidation bladed covellite with crystalline alunite in quartz - dickite altered upper facies Tumpangpitu diatreme breccia.

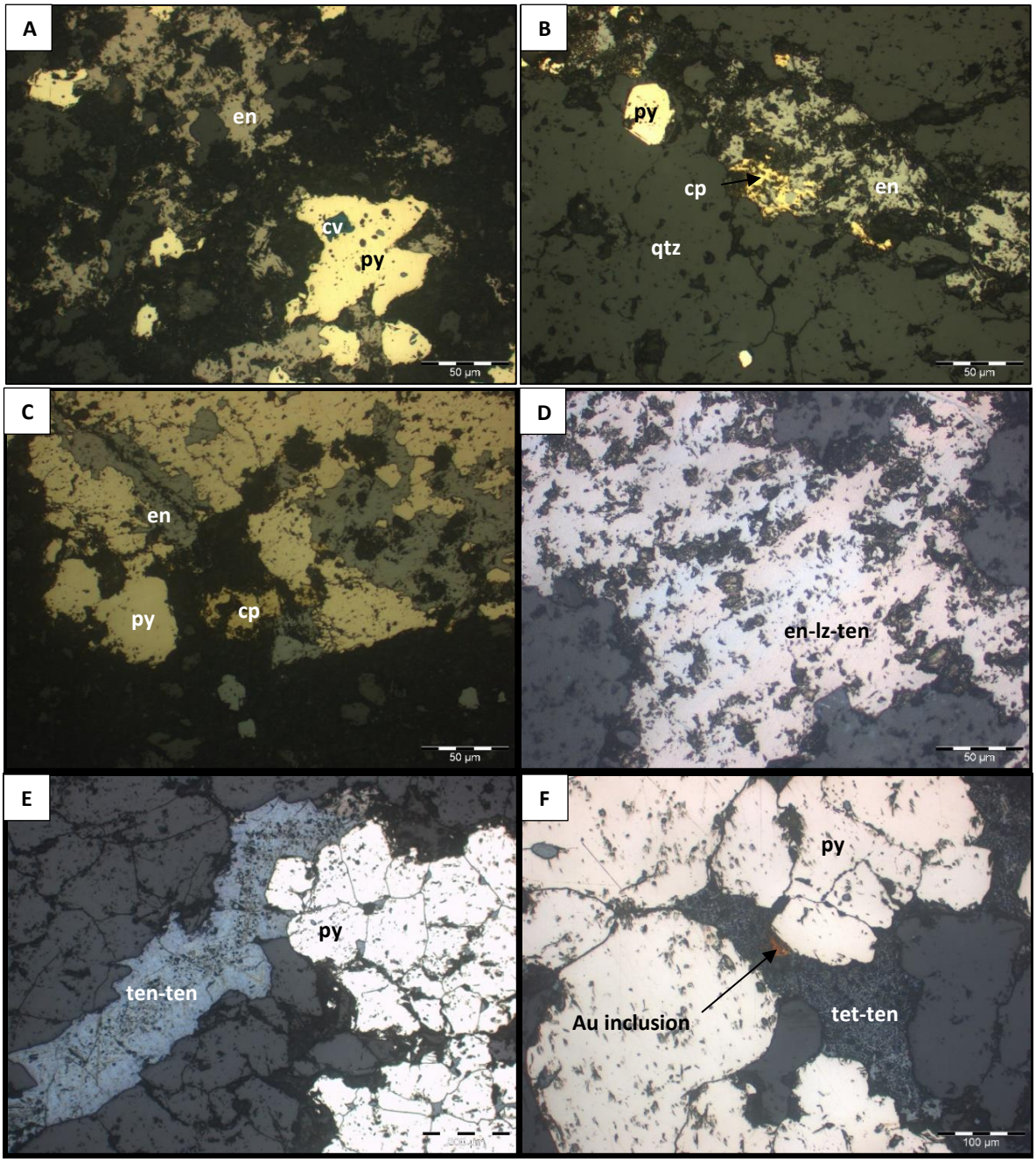

Figure 5.19. Petrographic images from high-sulfidation epithermal HSE-1 and HSE-2 veins from drillcore at Tumpangpitu. Abbreviations: and = andalusite, al = alunite, ba = barite, cv = covellite, dk = dickite, en = enargite, luz = luzonite, py = pyrite, ten = tennantite. All microprobe data in Appendix A2.

A) Drillhole GTD-09-112; 818.6 m, 173877 mE, 9046141 mN. HSE-1 vein enargite has overprinted pyrite grains with covellite inclusions. Grade 0.87 ppm Au, 4150 ppm Cu, 1190 ppm As, 2 ppm Ag, 1 ppm Sb.

B) Drillhole GTD-09-112; 818.6 m, 173877 mE, 9046141 mN. HSE-1 vein enargite has replaced chalcopyrite.

C) Drillhole GTD-09-112; 818.6 m, 173877 mE, 9046141 mN. HSE-1 vein enargite after chalcopyrite and as inclusions in pyrite vein.

D) Drillhole GTD-09-78; 53 m, 174984 mE, 9045284 mN. Massive enargite - luzonite - tennantite HSE-2 vein; grade 2.73 ppm Au, 6290 ppm Cu, 9760 ppm As, 8 ppm Ag, 0.5 ppm Sb (assay interval 52 - 54 m).

E) Drillhole GTD-10-137; 829.7m, 175020 mE, 9045397 mN. Tennantite-tetrahedrite around contact of pyrite and infilled fractures in HSE-2 vein (microprobe data Fig. A2-2).

F) Drillhole GTD-10-137; 812m, 175020 mE, 9045397 mN. Gold grain in HSE-2 tennantite-tetrahedrite vein.

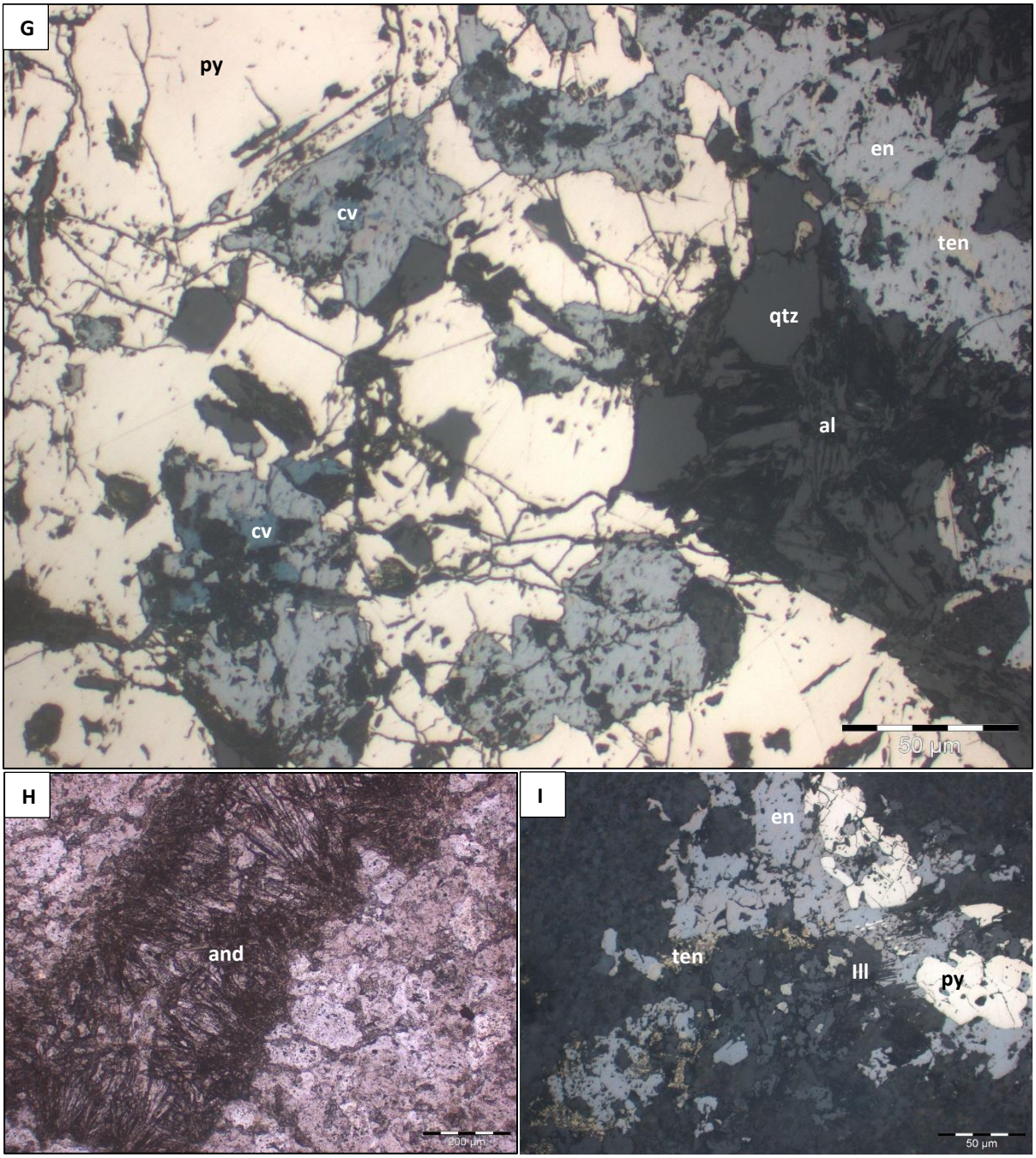

Figure 5.19. *(Contd.).*

G) Drillhole GTD-09-112; 185.75 m, 173877 mE, 9046141 mN. Enargite and tennantite have overprinted covellite in HSE-2 vein in phase 2 diorite (microprobe data and photomicrographs A2-1).

H) Drillhole GTD-09-112; 800 m, 173877 mE, 9046141 mN. Andalusite vein in phase 5 tonalite.

I) Drillhole GTD-09-112; 808 m, 173877 mE, 9046141 mN. Illite intergrown with tetrahedrite-tennantite in HSE-2 vein. 0.64 ppm Au, 5440 ppm Cu, 1620 ppm As, 2 ppm Ag, 0.5 ppm Sb (assay interval 52 - 54 m).

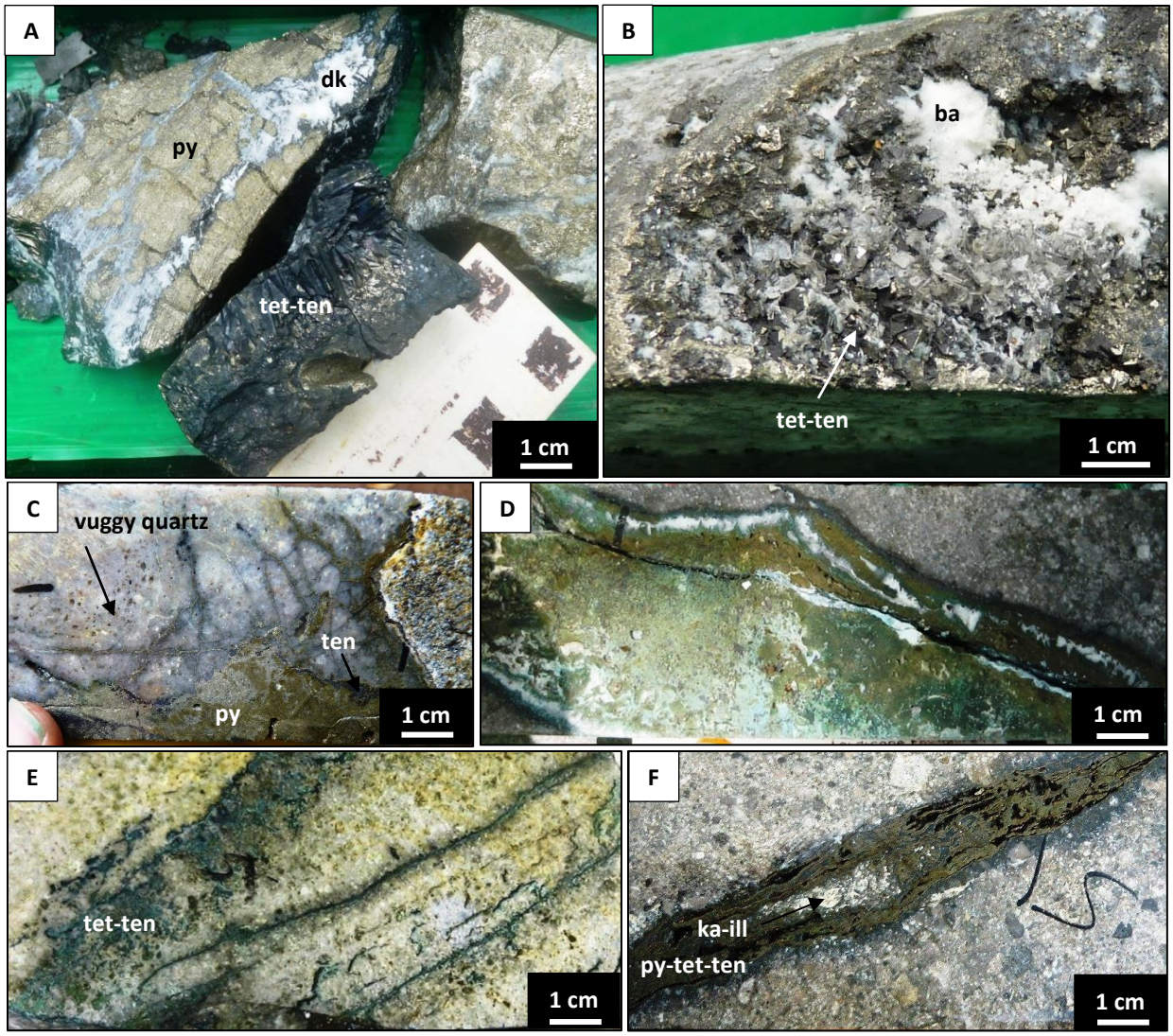

Figure 5.20. Tennantite-tetrahedrite bearing HSE-2 and ISE-1 veins in drillcore from Tumpangpitu. Abbreviations: al = alunite, ba = barite, dk = dickite, en = enargite, ka = kaolinite, ill = illite, luz = luzonite, py = pyrite, ten = tennantite, tet = tetrahedrite.

A) *Drillhole GTD-10-167; 222.6 m, 173890 mE, 9046413 mN.* Massive, ISE-1 steel grey tetrahedrite - tennantite - pyrite with dickite in phase 7 quartz diorite.
B) *Drillhole GTD-10-167; 255 m, 173890 mE, 9046413 mN.* Tetrahedrite - tennantite - barite fracture infill crosscutting kaolinite, pyrophyllite and K-alunite (SWIR analysis) altered phase 7 quartz diorite.
C) *Drillhole GTD-08-56; 258.6 m, 173878 mE, 9046141 mN.* ISE-1 pyrite vein with tennantite margin crosscutting vuggy quartz - alunite altered lower facies Tumpangpitu diatreme.
D) *Drillhole GTD-08-35; 206 m, 174080 mE, 9046551 mN.* Pyrite - enargite - tennantite - tetrahedrite - barite HSE-2 vein crosscutting lower facies Tumpangpitu diatreme.
E) *Drillhole GTD-08-42: 54 m, 173495 mE, 9046564 mN.* Tennantite - tetrahedrite - chalcopyrite ISE-1 stringers and veins overprinting phase 2 diorite in quartz - dickite altered zone.
F) *Drillhole GTD-08-56; 113.9 m, 173878 mE, 9046141 mN.* Banded pyrite - tetrahedrite - tennantite - chalcopyrite - kaolinite - illite ISE-1 vein cross cutting lower facies diatreme breccia with shale clasts.

5.7.3 Final stage veins

5.7.3.1 Base metal veins (ISE-2; intermediate-sulfidation epithermal)

Base metal veins at Tumpangpitu are composed of sphalerite - galena - pyrite ± chalcocite. They form massive to semi-massive sulfide veins with minor euhedral quartz. Gangue minerals include illite, muscovite, kaolinite and minor quartz, montmorillonite and locally barite. Both honey coloured (low Fe) sphalerite and black (high Fe) sphalerite have been documented (Fig. 5.21B). Euhedral sphalerite and galena have grown into open spaces in veins or fractures (Fig. 5.21B). Both sulfides form fine-grained disseminations and have cemented breccias (Fig. 5.21D). Euhedral galena is characterized by prismatic cubic crystals, whereas sphalerite has formed hexatetrahedral crystals. The veins are distributed in a concentric fashion in and around the outer contacts of the Tumpangpitu lithocap and the porphyry complex. ISE-2 veins, disseminations and cemented breccias form a Pb-Zn enrichment halo, visible in soil geochemical datasets (Fig. 5.32). Intermediate-sulfidation state sphalerite and galena veins have crosscut all stages of porphyry and epithermal veins and commonly fill fractures in HSE and ISE-1 veins (Fig. 5.20C). Sphalerite and galena define the last stage of sulfide precipitation at Tumpangpitu.

5.7.3.2 Gypsum veins

Supergene gypsum veins represent the final stage of veining and waning of the hydrothermal system at Tumpangpitu and dominance of meteoric fluids. Gypsum veins have a thickness of 0.1 to 3 cm with no alteration halo. They comprise massive clear, waxy coarse-grained gypsum and are distributed exclusively above the paleowater table (approximately 300 m bsl). Accessory minerals in gypsum veins include calcite, chlorite and minor pyrite. Gypsum has not yet been recorded to replace anhydrite in porphyry stockwork veins as the latter are distributed 500 m bsl.

5.7.4 Late stage alteration mineral assemblages

5.7.4.1 Vuggy quartz - alunite

Alteration of wallrocks adjacent to HSE-1 veins has produced zones of vuggy quartz and alunite at Tumpangpitu. Vuggy quartz - alunite zones are characterized by intense leaching of the host rock to form voids or vugs after mafic and feldspar phenocrysts infilled with crystalline alunite (Fig. 5.22A). Vuggy quartz - alunite alteration occurs in the upper 200 m of present-day exposure of the Tumpangpitu lithocap, defining NW-trending resistant, topographically prominent quartz ridges. The ridges follow structures and are known as Zones A (70 x 20 m), C (35 x 10 m) and E which dip steeply towards the porphyry tonalite complex (Figs. 5.2 and 5.3). Another series of narrow north-trending vuggy quartz - alunite ridges (15 x 1-2 m) occur at Zone B, and Zone B East 1.5 km south of Tumpangpitu (Fig. 5.2). Accessory minerals include native sulfur and rutile. The vuggy quartz bodies are the centres of high-sulfidation epithermal Au-Ag ± Cu mineralization and host the majority of gold and silver in subsequent supergene oxide ore at Tumpangpitu (Fig. 5.3).

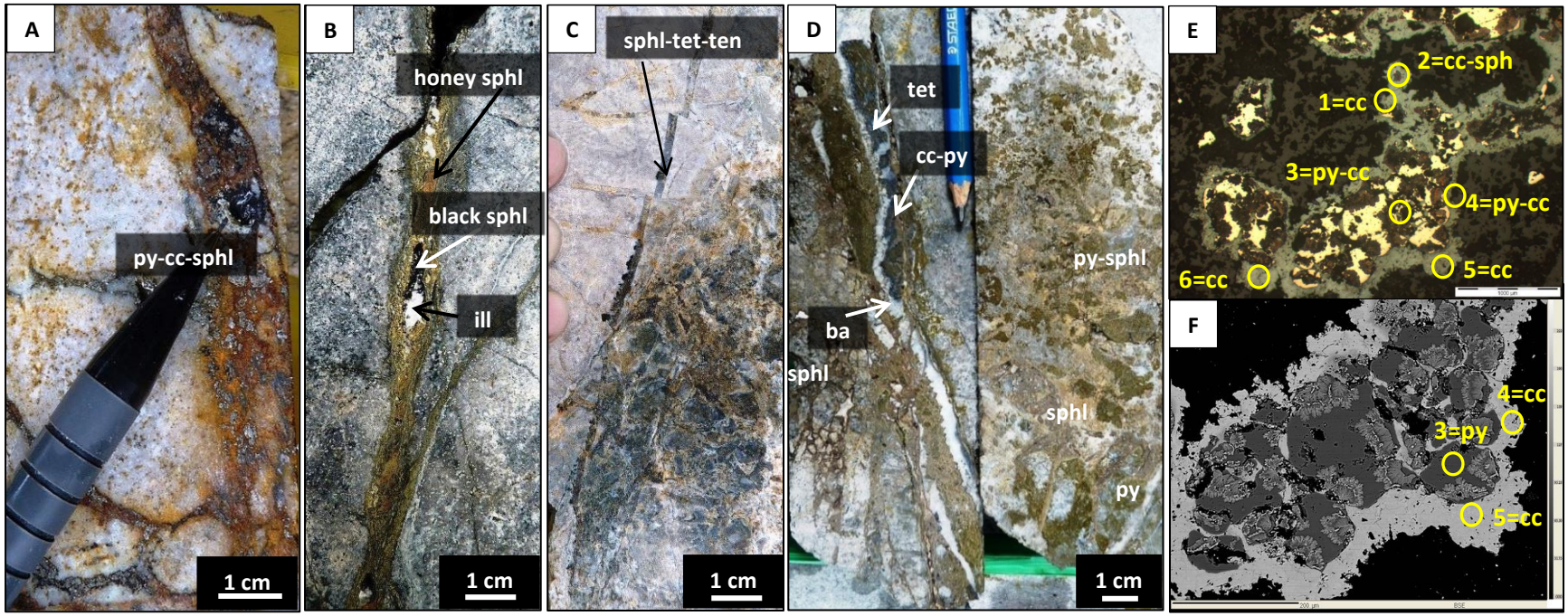

Figure 5.21. Sphalerite - galena veins (ISE-2) from drillcore at Tumpangpitu. Abbreviations: ba = barite, cc = chalcocite, py = pyrite, sph = sphalerite, ten = tennantite, tet = tetrahedrite.

A) *Drillhole GTD-08-26; 206 m, 173578 mE, 9045841 mN.* Pyrite - sphalerite - chalcocite ISE-2 veins in Tumpangpitu upper facies diatreme breccia. Chalcocite has coated pyrite grains.

B) *Drillhole GTD-10-172; 373 m, 174240 mE, 9046440 mN.* Pyrite - sphalerite ISE-2 vein with centreline illite and euhedral hexatetrahedral black-honey coloured Fe-sphalerite in quartz - dickite - pyrophyllite - alunite altered phase 5 tonalite and andesitic rock.

C) *Drillhole GTD-10-183; 822 m, 174575 mE, 9045597 mN.* Sphalerite - tetrahedrite - tennantite ISE-2 veins have crosscut porphyry quartz stockwork veins in phase 5 tonalite.

D) *Drillhole GTD-10-172; 365 m, 174240 mE, 9046440 mN.* Pyrite - sphalerite - tetrahedrite - chalcocite - barite ISE-2 veins and massive disseminated sphalerite - pyrite cemented breccia overprinting quartz - pyrophyllite - alunite - dickite altered phase 5 tonalite.

E) Sample 43001.20 P1: drillhole GT011, 201 m, 173837mE, 9046060mN, chalcocite coating pyrite - sphalerite vein (yellow circles = probe positions).

F) Sample 43001.20 P2: drillhole GT011: 201 m, 173837mE, 9046060mN, chalcocite coating pyrite - sphalerite vein (yellow circles = probe positions).

5.7.4.2 Massive quartz - alunite

Alteration of wallrocks adjacent to both HSE-1 and HSE-2 veins has produced massive quartz - alunite alteration halos up to 10 m wide (Fig. 5.2). This alteration assemblage occurs adjacent to the vuggy quartz zones and is characterized by massive pervasive microcrystalline quartz rather than vuggy textured quartz (Fig. 5.23B). Alunite can be sparry, granular, or microcrystalline. It is fine-grained, subhedral and pervasive to coarse-grained, euhedral, bladed and intergrown with quartz. Alunite has replaced the groundmass and phenocrysts in the porphyry intrusions. Pervasive replacement of feldspar by white and pink-coloured, crystalline to amorphous alunite is especially well developed. Crystalline alunite veins cut the millimetre- to centimetre-wide alunite crystals that have replaced phenocrysts (Fig. 5.23C). Accessory alteration minerals include dickite, kaolinite and at deeper levels, pyrophyllite, diaspore, topaz, zunyite and andalusite. Euhedral pyrite and alunite have mutual grain boundaries suggesting that they coprecipitated. Alunite is both white (Fig. 5.23A) and pink coloured (Fig. 5.23B). Hypogene alunite is commonly fine-grained (< 1 mm) and disseminated throughout the matrix of the host lithology. Alunite also commonly forms 1 - 5 mm rosette crystals coating fractures (Fig. 5.23A). No clear correlation of colour (white or pink) exists with composition (Na or K) determined by SWIR analysis. However, based on textural observations and SWIR analysis, hypogene alunite is commonly Na-rich (Fig. 5.23D) and supergene alunite is K-rich. Petrographic, SEM and EPMA studies have documented alunite intergrown with quartz, diaspore and pyrophyllite and kaolinite replacing alunite (Fig. A2-5).

APS minerals commonly form cores to euhedral alunite grains (Fig. 5.27F). APS inclusions exhibit oscillatory zoning with compositions that vary between svanbergite (Sr-end member) and woodhouseite (Ca-end member) based on microprobe results (Appendix A2-1).

5.7.4.3 Quartz - pyrophyllite

Quartz - pyrophyllite alteration has two distinct modes at Tumpangpitu. It occurs as a major mineral in association with alunite, dickite, kaolinite and diaspore (Fig. 5.22C) as a large 1 x 1 km (> 220 m bsl) central zone to the lithocap, overprinting upper levels of porphyry mineralization and extending deep along structures (> 1,200 m bsl), in particular the Cliff fault (Figs. 5.3 and 5.4). At depths greater than 400 m bsl, fault-controlled quartz - pyrophyllite alteration is associated with diaspore, topaz, zunyite and andalusite, and is related spatially to both HSE-1 and HSE-2 veins. Quartz - pyrophyllite - alunite zones are interpreted to have been feeders to the vuggy quartz structures (e.g., Fig. 5.3). The quartz - pyrophyllite alteration assemblage is recognisable in drillcore as bleached white alteration zones associated with intense quartz alteration (Fig. 5.22B). Pyrophyllite has formed fine-grained masses that typically replaced muscovite. It is difficult to identify without the aid of spectral analysis. Petrographic and SEM analysis has documented pyrophyllite both intergrown with and replacing alunite (Fig. 5.27C and G.). Gold and

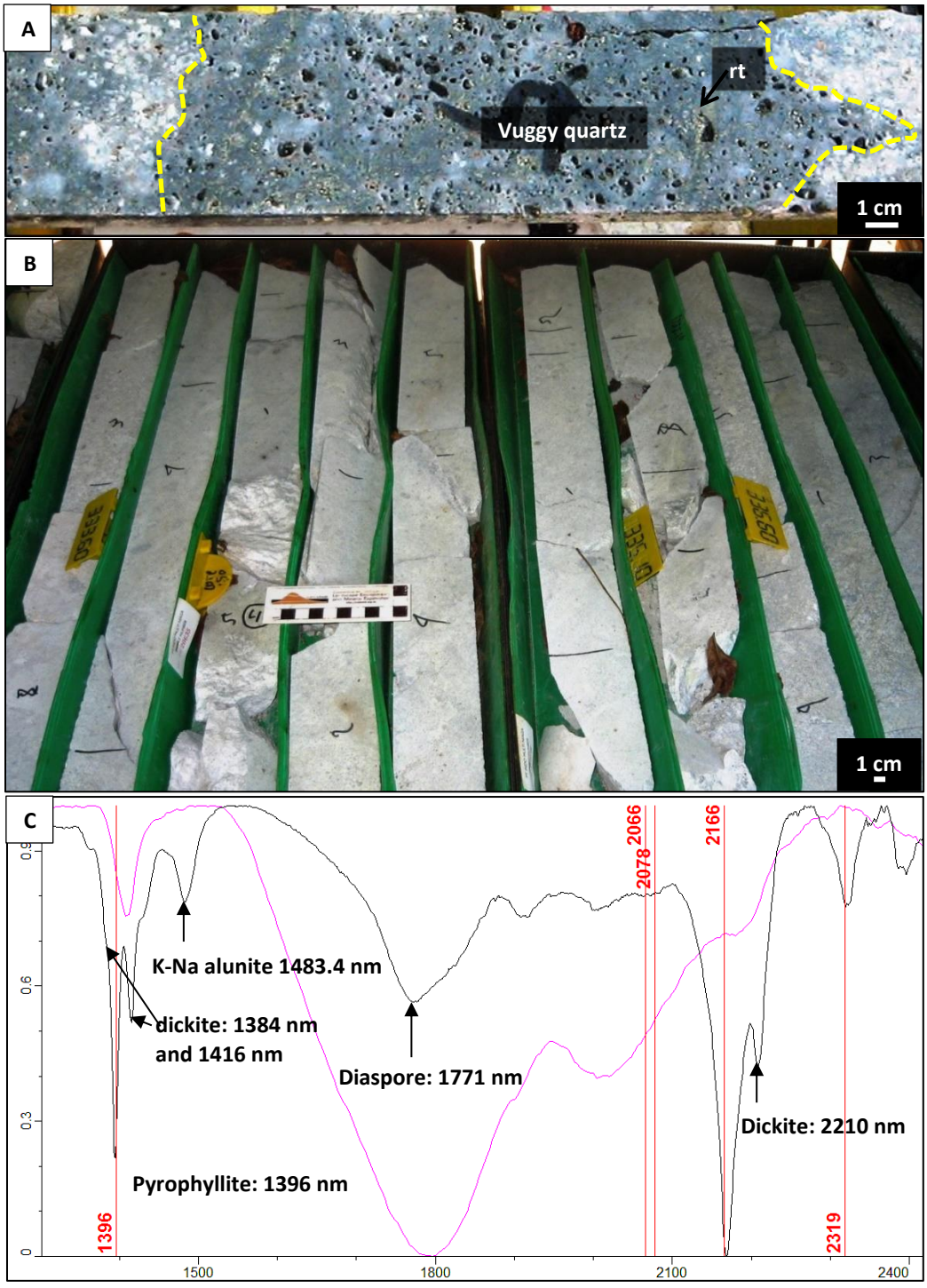

Figure 5.22. Examples of drillcore and SWIR spectrum from quartz - pyrophyllite and vuggy quartz alteration at Tumpangpitu. Abbreviations: rt = rutile.

A) *Drillhole GTD-08-35; 417.5 m, 174080 mE, 9046551 mN*. Vuggy quartz - alunite alteration of phase 7 quartz diorite. Rutile has replaced primary amphibole and biotite.

B) *Drillhole GTD-08-56; 330 - 337 m, 173878 mE, 9046141 mN*. White, bleached quartz - pyrophyllite alteration overprinting lower facies Tumpangpitu diatreme breccia.

C) *Spectrum GTD0825.077 308 m.* SWIR spectrum pyrophyllite - K-Na alunite (1483.4 nm) - diaspore - dickite (1384 nm inflexion), pyrophyllite vertical reference lines (red) and diaspore reference spectrum (pink).

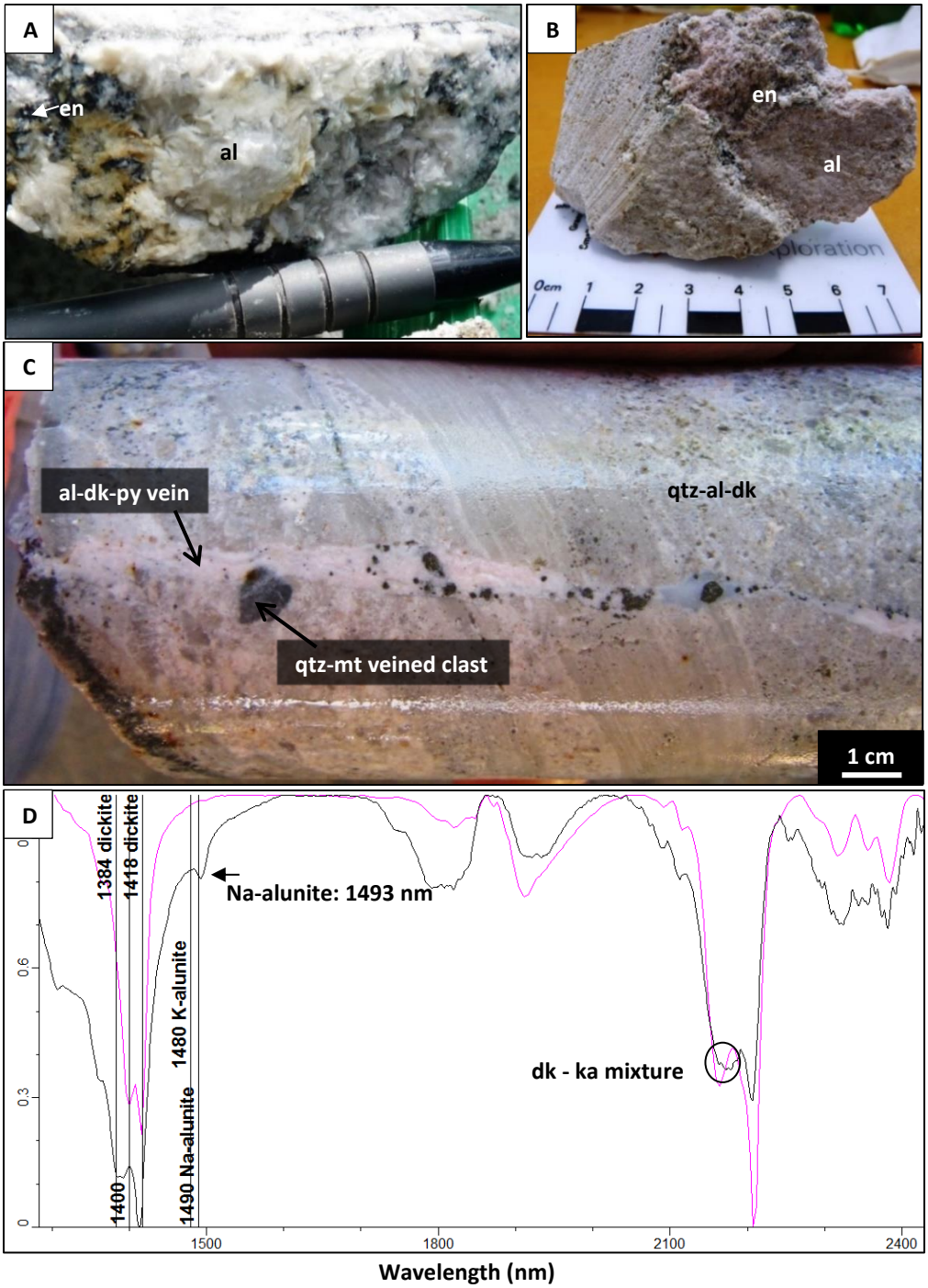

Figure 5.23. Massive quartz - alunite altered drillcore and SWIR spectrum from Tumpangpitu. Abbreviations: al = alunite, dk = dickite, en = enargite, ka = kaolinite, py = pyrite.

A) *Drillhole GTD-10-167; 242.2 m, 173890 mE, 9046413 mN.* Coarse-grained white and pink crystalline alunite with enargite needles filling fractures in phase 7 quartz diorite.

B) *Drillhole GTD-10-166: 285 m, 174156 mE, 9046095 mN.* Coarse pink crystalline alunite with enargite filling fracture in upper facies Tumpangpitu diatreme breccia.

C) *Drillhole GTD-09-112; 85.75 m, 173877 mE, 9046141 mN*. Na-alunite - dickite - pyrite vein crosscutting bedded upper facies Tumpangpitu diatreme.

D) *SWIR spectrum of vein in photo C.* Dickite - kaolinite and Na-alunite (1493 nm) with kaolinite reference spectrum (pink), alunite and dickite vertical lines (black).

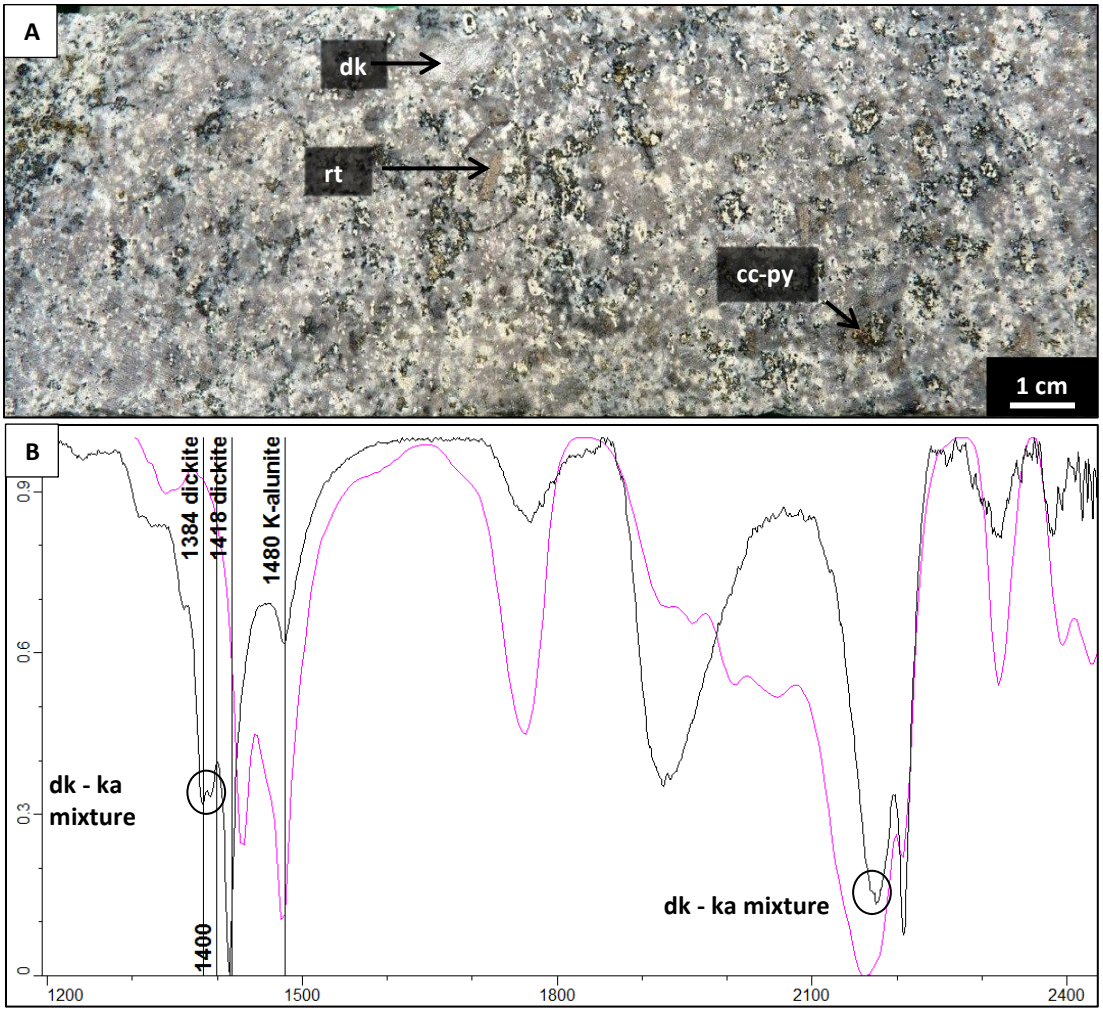

Figure 5.24. Massive quartz - dickite - kaolinite ± alunite altered drillcore and SWIR spectrum from Tumpangpitu. Abbreviations: cc = chalcocite, dk = dickite, py = pyrite, rt = rutile.

A) Drillhole GTD-10-167: 378 m, 173890 mE, 9046413 mN. Quartz - dickite - kaolinite ± K-alunite alteration of phase 7 quartz diorite. Rutile has replaced primary hornblende and biotite phenocrysts. Hypogene chalcopyrite has been replaced by bornite rimmed by chalcocite.

B) SWIR spectrum of photo A. Dickite - kaolinite and K-alunite (1479 nm) with K-alunite reference spectrum (pink), alunite and dickite vertical lines (black).

copper grades are generally low (0.1 - 0.2 ppm Au and 0.1 - 0.2 % Cu) in quartz - pyrophyllite altered rocks.

The second minor mode of quartz - pyrophyllite alteration is associated with highly crystalline white mica (pyrophyllite intergrown with both muscovite and paragonite). This alteration domain defines a bell shaped upper carapace to the quartz - muscovite - illite alteration zone that is associated with lower grade (0.2 g/t Au, 0.2 % Cu) porphyry-style mineralization at Tumpangpitu (Fig. 5.3).

5.7.4.4 Topaz

Topaz at Tumpangpitu occurs predominantly along the West fault zone 400 m below the Zone C gold oxide deposit (Fig. 5.3). Topaz has only been identified by spectral analysis and is associated spatially

with pyrophyllite, alunite, diaspore and locally andalusite. Topaz zones with high fluorine contents have metallurgical implications and have therefore been isolated on all SWIR alteration models (e.g., Fig. 5.3).

5.7.4.5 Quartz - dickite ± kaolinite

Above 220 m asl, quartz - dickite ± kaolinite forms alteration halos up to 90 m around the massive quartz - alunite alteration domain in gold oxide zones A, B and C (Fig. 5.3). Quartz - dickite ± kaolinite also defines 1 - 30 m wide halos around the quartz - pyrophyllite alteration domain below 220 m bsl (Fig. 5.3). Accessory minerals include alunite and paragonitic white micas (AlOH wavelength 2180 - 2190 nm; based on SWIR data). Quartz - dickite ± kaolinite alteration zones are characterized by white, grey or light blue/green greasy, soap-like dickite along with pervasive massive quartz (Fig. 5.24A). Dickite and kaolinite have preferentially replaced feldspars, white micas and illite. Petrographic and SEM analyses have imaged kaolinite as hexagonal booklets that commonly replaced muscovite (Fig. 5.30E). Dickite has generally replaced pyrophyllite.

5.7.4.6 Illite - smectite ± chlorite ± kaolinite

Illite - smectite ± chlorite ± kaolinite alteration is distributed in the upper 450 m bsl at Tumpangpitu, between the quartz - dickite ± kaolinite and chlorite - calcite alteration zones. Illite - smectite alteration is extensive at surface, forming a 4 km wide, 5 km long NW-trending zone (Fig. 5.2). Kaolinite has commonly replaced illite and smectite that had originally replaced plagioclase phenocrysts. Chlorite has replaced primary and hydrothermal mafic minerals. In feldspar-rich wallrocks, feldspars have been completely replaced by kaolinite but the porphyritic texture has been preserved (Fig. 5.16F). Spectral analyses has identified the smectite species as montmorillonite (dominant) and minor nontronite (Fe-bearing smectite). The nontronite is inferred to have formed after chlorite, biotite and primary magmatic hornblende and biotite in country rocks. The central parts of both the Tumpangpitu and Tanjung Jahe diatremes have been altered predominantly to illite - smectite ± chlorite ± kaolinite.

5.8 Evidence for epithermal overprinting of porphyry mineralization

At Tumpangpitu, vuggy and massive quartz - alunite, pyrophyllite, dickite, diaspore, topaz, zunyite, andalusite and kaolinite associated with high-sulfidation epithermal mineralization have overprinted quartz - magnetite - biotite - K-feldspar alteration that hosts porphyry mineralization from depths of 250 m below present day surface to depths greater than the limit of current drilling (Figs. 5.3 and 5.4; 1, 200 m). Complex sulfide and alteration mineral assemblages are present at the interface. A number of key observations helped to identify these zones of overprinting alteration. These include; magnetite destruction (Fig. 5.25), hypogene upgrading of copper sulfides (chalcopyrite sequentially replaced by bornite, chalcocite and covellite; Figs. 5.26 - 5.28), and molybdenite associated with pyrophyllite, alunite and dickite (Fig. 5.29).

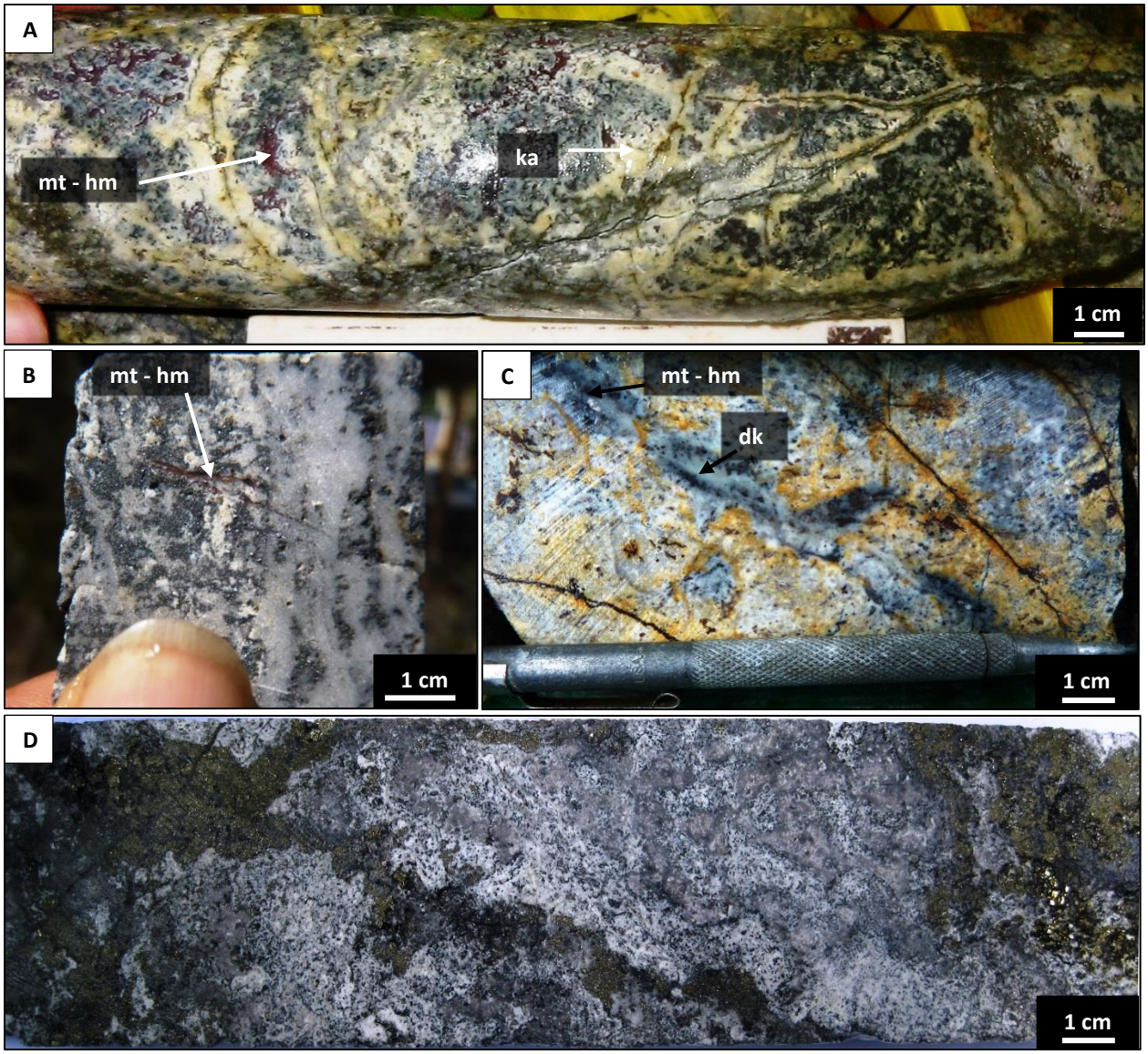

Figure 5.25. Drillcore from quartz - alunite, quartz - pyrophyllite, quartz - dickite and quartz - illite alteration overprinting onto porphyry mineralization associated with quartz - magnetite - biotite - K-feldspar alteration. Abbreviations: dk = dickite, hm = hematite, mt = magnetite.

A) *Drillhole GTD-10-139; 580 m, 173503 mE, 9046136 mN.* Quartz - alunite - dickite - pyrophyllite ± diaspore overprinting quartz - magnetite altered phase 6 tonalite. Magnetite has been replaced by hematite. Kaolinite alteration selvedges around pyrite veins.
B) *Drillhole GTD-08-35; 726 m, 174080 mE, 9046551 mN.* Partial oxidation of magnetite to hematite, close association of disseminated chalcopyrite with magnetite in phase 6 tonalite.
C) *Drillhole GTD-11-248; 303.5 m, 174385 mE, 9046285 mN.* Disseminated, feather-like magnetite oxidized to hematite and overprinted by a soap-like dickite vein in andesitic host rock adjacent to phase 6 porphyry tonalite. The rock is demagnetised and blue-grey stains or original magnetite remain enclosed by quartz - dickite alteration.
D) *Drillhole GTD-10-162; 369.3 m, 173760 mE, 9046508 mN.* Complex sulfide assemblage of fine-grained disseminated tennantite, chalcocite, bornite, chalcopyrite and molybdenite associated with an alteration mineral assemblage of quartz - kaolinite - paragonite - pyrophyllite - dickite (SWIR analyses).

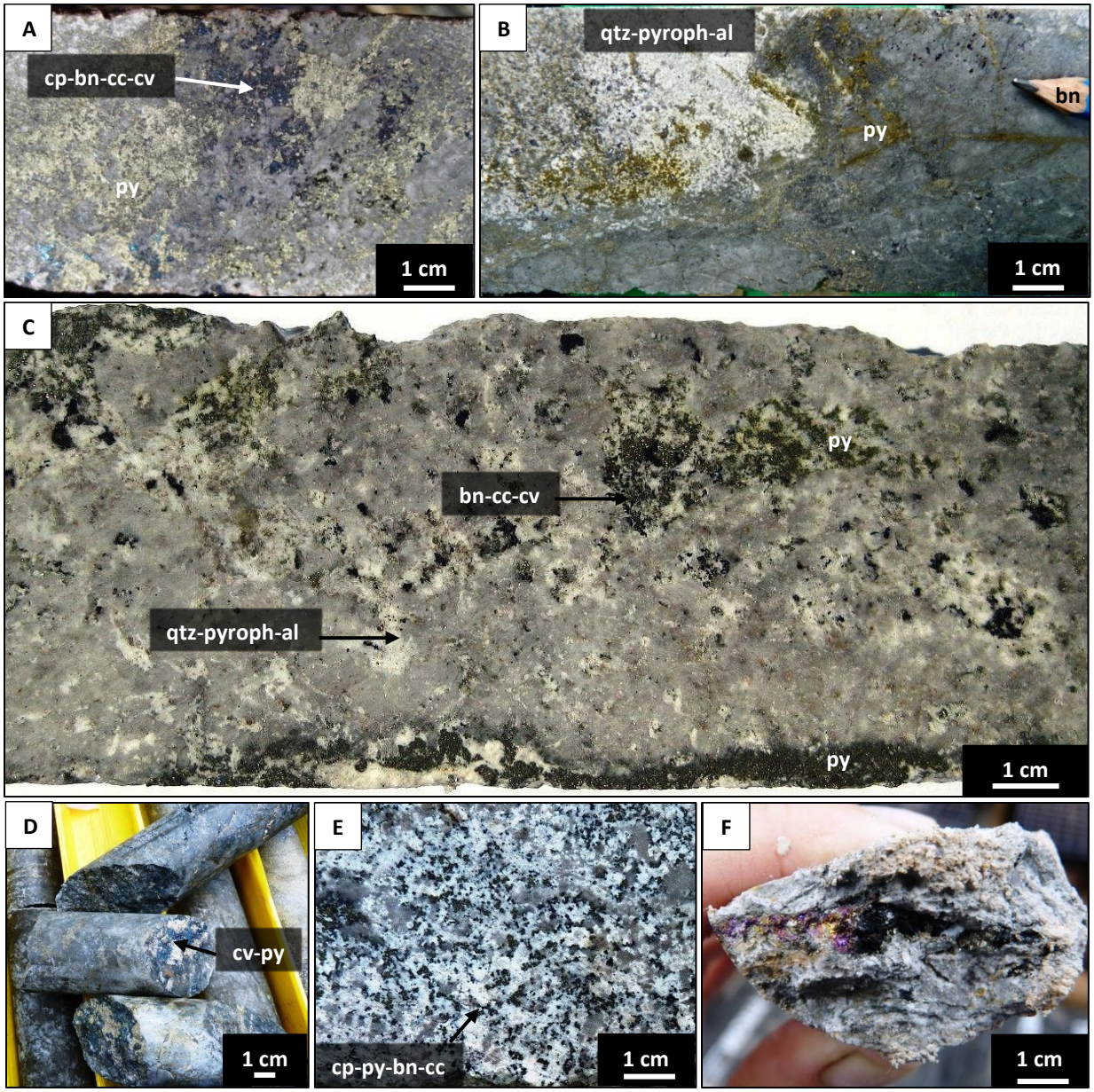

Figure 5.26. Sulfide and alteration assemblages (aided by SWIR analysis) from the telescoped zone at Tumpangpitu. Abbreviations: al = alunite, bn = bornite, cp = chalcopyrite, cv = covellite, pyroph = pyrophyllite, qtz = quartz.

A) *Drillhole GTD-10-162; 380 m, 173760 mE, 9046508 mN.* Disseminated chalcopyrite - bornite overprinted by chalcocite and covellite in quartz - dickite - pyrophyllite ± diaspore altered phase 5 tonalite.
B) *Drillhole GTD-10-172; 349 m, 174240 mE, 9046440 mN.* 0.4% disseminated bornite with quartz-pyrophyllite - Na-alunite in phase 5 tonalite.
C) *Drillhole GTD-10-163; 550 m, 174080 mE, 9046549 mN.* Disseminated bornite and pyrite with quartz - pyrophyllite - alunite in phase 5 fine-grained tonalite.
D) *Drillhole GTD-10-165; 902 m, 174159 mE, 9046084 mN.* Zone of hypogene upgrading, massive covellite and pyrite in veins and fractures in quartz - dickite altered phase 6 tonalite.
E) *Drillhole GTD-10-167; 341 m, 173890 mE, 9046413 mN.* Chalcopyrite with rims of pyrite and bornite rimmed by chalcocite in quartz - pyrophyllite - K-alunite - dickite altered phase 7 quartz diorite.
F) *Drillhole GTD-10-183; 821 m, 174575 mE, 9045597 mN.* Tetrahedrite - tennantite - covellite - bornite - chalcopyrite along fracture in quartz - dickite ± white mica altered phase 5 fine-grained tonalite.

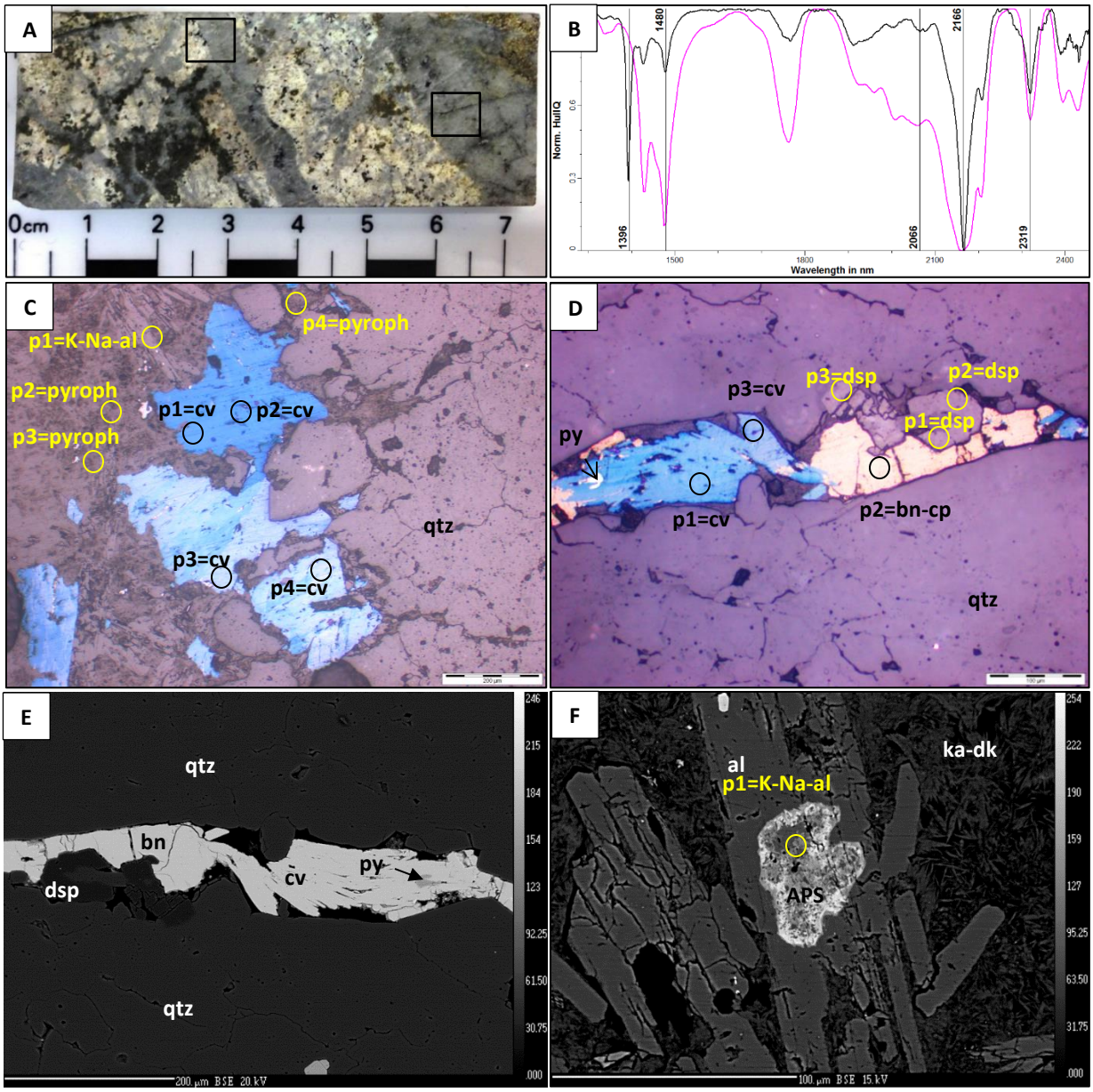

Figure 5.27. Petrographic, spectral and back scattered electron (BSE) images from drillhole GTD-11-201; 537.5 m, 174155 mE, 9046097 mN; phase 5 tonalite with pyrite - chalcopyrite - bornite - digenite - covellite and quartz - pyrophyllite - K-alunite - dickite/kaolinite. Black circles p1 to p4 represent sulfide, yellow circles are specified for alteration mineral SEM analyses. All data recorded in Appendix A2. Abbreviations: APS = aluminium phosphate sulfate, bn = bornite, cp = chalcopyrite, cv = covellite, dg = digenite, dk = dickite, ka = kaolinite, qtz = quartz.

A) Drillcore sample. Quartz A and B-type stockwork veins and tonalite matrix host disseminations of chalcopyrite converted sequentially to bornite, digenite and covellite.
B) SWIR spectrum with K-alunite reference spectrum (pink); pyrophyllite - K-alunite (absorption 1479.3 nm).
C) Photomicrograph of disseminated digenite with incipient covellite adjacent to feather-like alunite, pyrophyllite, bornite with incipient digenite and covellite along the margin of a B-type porphyry quartz vein (sample location photo A upper left).
D) Photomicrograph of chalcopyrite - bornite - covellite veinlet or fracture infill in B vein (sample location photo A centre right). Alteration mineral sites p1-p3 are diaspore.
E) BSE image of photomicrograph D.
F) BSE image of station p1 from photomicrograph D alunite crystal with APS core.

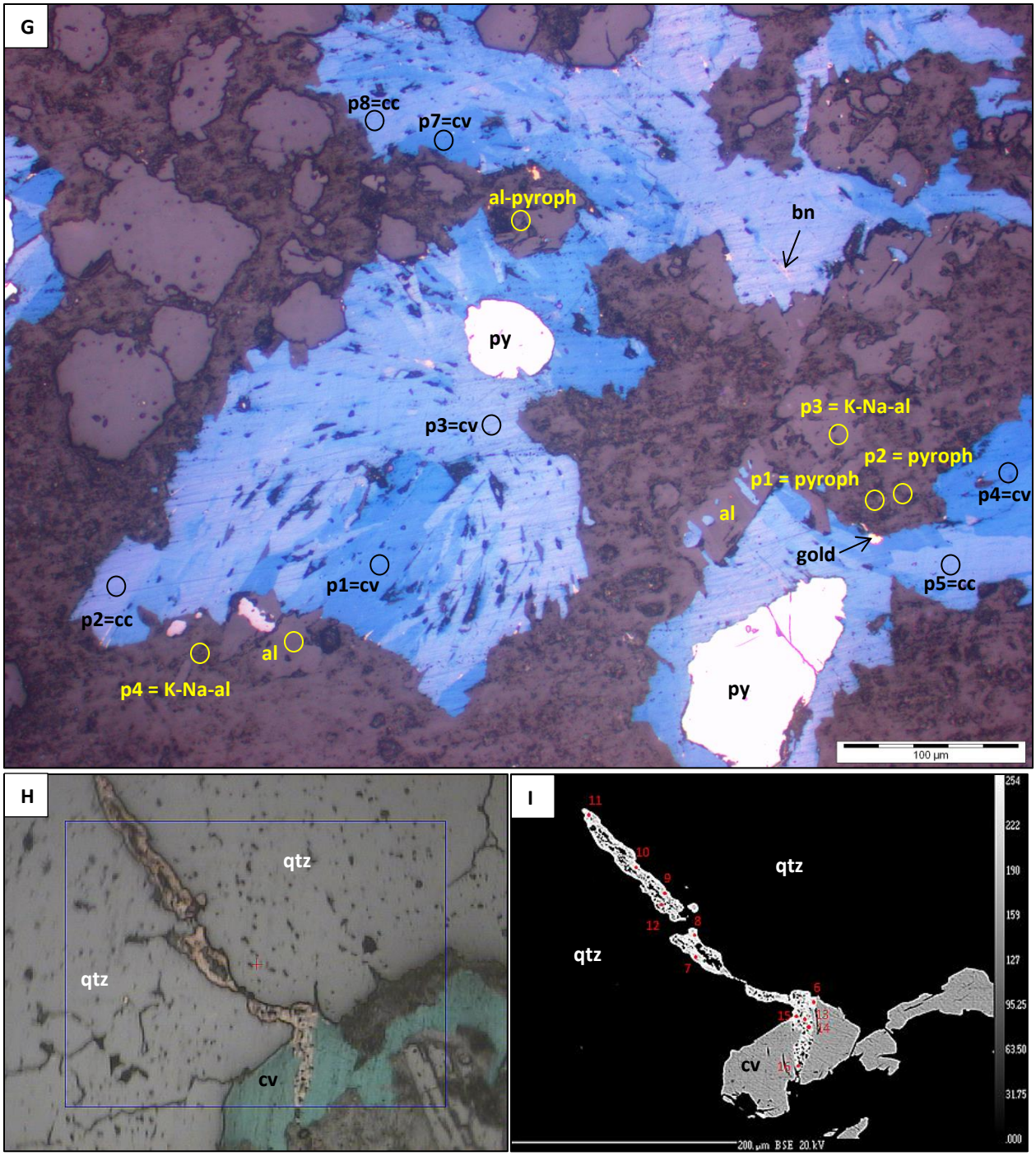

Figure 5.27. (*Contd.)*

G) Photomicrograph of chalcocite replaced by booklets of covellite with inclusion of native gold surrounding pyrite grains with quartz - K-Na-alunite - pyrophyllite and kaolinite. Bornite has been overprinted by chalcocite and covellite. Alunite has inclusions of covellite.

H) Reflected light photomicrograph of a late Sn-As-Cu-Fe bearing veinlet (nekrasovite) crosscutting quartz and a grain of covellite.

I) SEM BSE image of H.

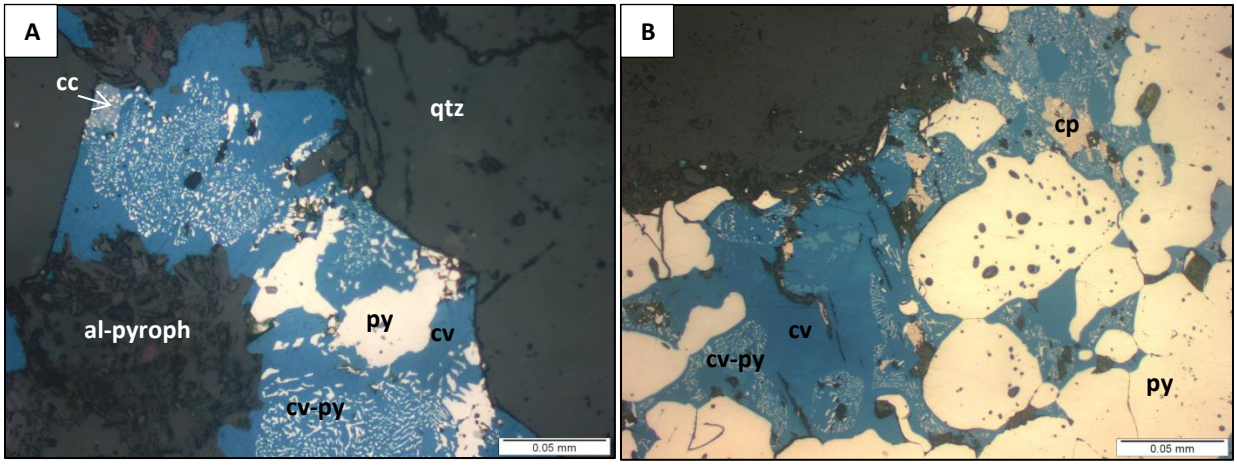

Figure 5.28. Photomicrographs from drillhole GTD-11-201; 600 m, 174155 mE, 9046097 mN. Disseminated and vein hosted porphyry-style copper sulfide mineralization showing evidence of hypogene upgrading in phase 5 tonalite overprinted by quartz - pyrophyllite - alunite alteration. Abbreviations: al = alunite, cp = chalcopyrite, cv = covellite, py = pyrite, pyroph = pyrophyllite, qtz = quartz.

A) Eutectoid intergrowths of covellite and pyrite. Chalcocite preserved in top left hand corner.
B) Covellite and pyrite directly replacing chalcopyrite.

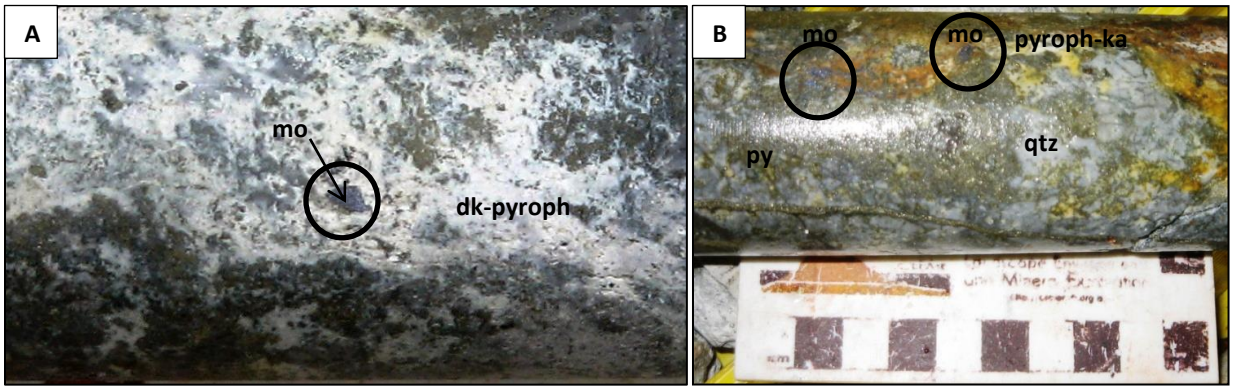

Figure 5.29. *Drillhole GTD-10-129;* 173503 mE, 9046136 mN. Drillcore from zone of disseminated molybdenite (black circles) associated with quartz - dickite/kaolinite - pyrophyllite alteration adjacent to a high-sulfidation epithermal mineralized structure in phase 5 tonalite 50 m above the porphyry stockwork mineralized shell at Tumpangpitu. Abbreviations: al = alunite, dk = dickite, ka = kaolinite, mo = molybdenite, py = pyrite, pyroph = pyrophyllite, qtz = quartz.

A) *532.9 m.* Molybdenite grain with covellite, quartz - dickite and pyrophyllite.
B) *548.2 m.* Disseminated molybdenite overprinting massive disseminated pyrite in quartz - pyrophyllite - kaolinite alteration zone.

5.8.1 Magnetite destruction

Tumpangpitu contains an extensive zone of magnetite destruction in rocks that contain relict quartz - magnetite - biotite - K-feldspar alteration. Magnetite has commonly been totally or partially replaced by hematite where overprinted by quartz - illite alteration. Magnetite has been completely altered to pyrite where potassic alteration has been overprinted by vuggy quartz, quartz - alunite, quartz - pyrophyllite and

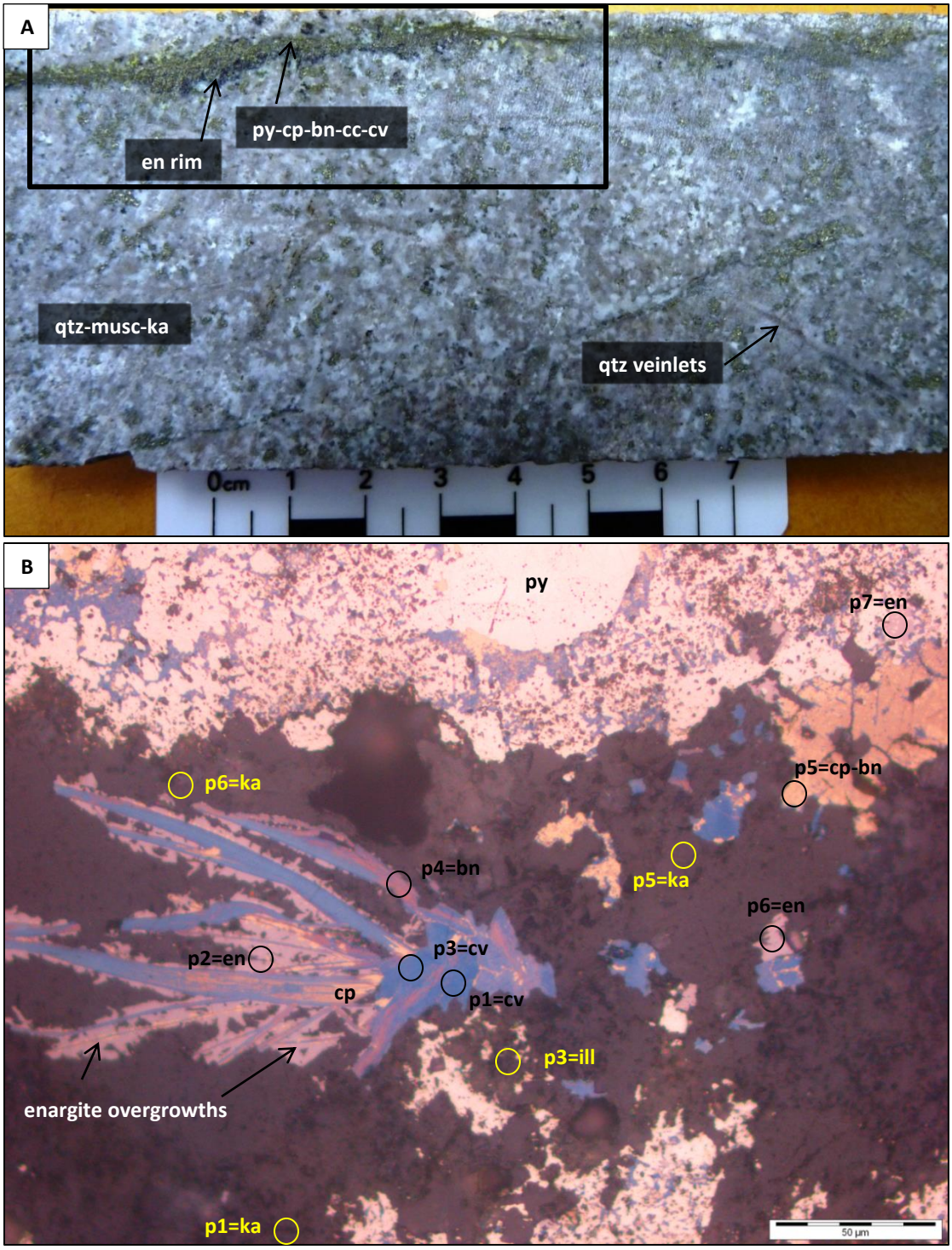

Figure 5.30. Drillhole GTD-12-292; 513 m, 174082 mE, 9046550 mN. Quartz stockwork B veins crosscut by pyrite vein with chalcopyrite - bornite - chalcocite - covellite overprinted by enargite in quartz - white mica - kaolinite altered andesitic rock crosscut by fine-grained phase 5 tonalite porphyry. Black circles represent sulfide, yellow circles alteration mineral SEM analyses. Abbreviations: al = alunite, bn = bornite, cp = chalcopyrite, cv = covellite, dg = digenite, en = enargite, py = pyrite, qtz = quartz.

A) Photograph of hand specimen.

B) Photomicrograph 40x magnification. Fibrous quench texture of chalcopyrite replaced sequentially by bornite, chalcocite then covellite and overprinted by late, feathery enargite.

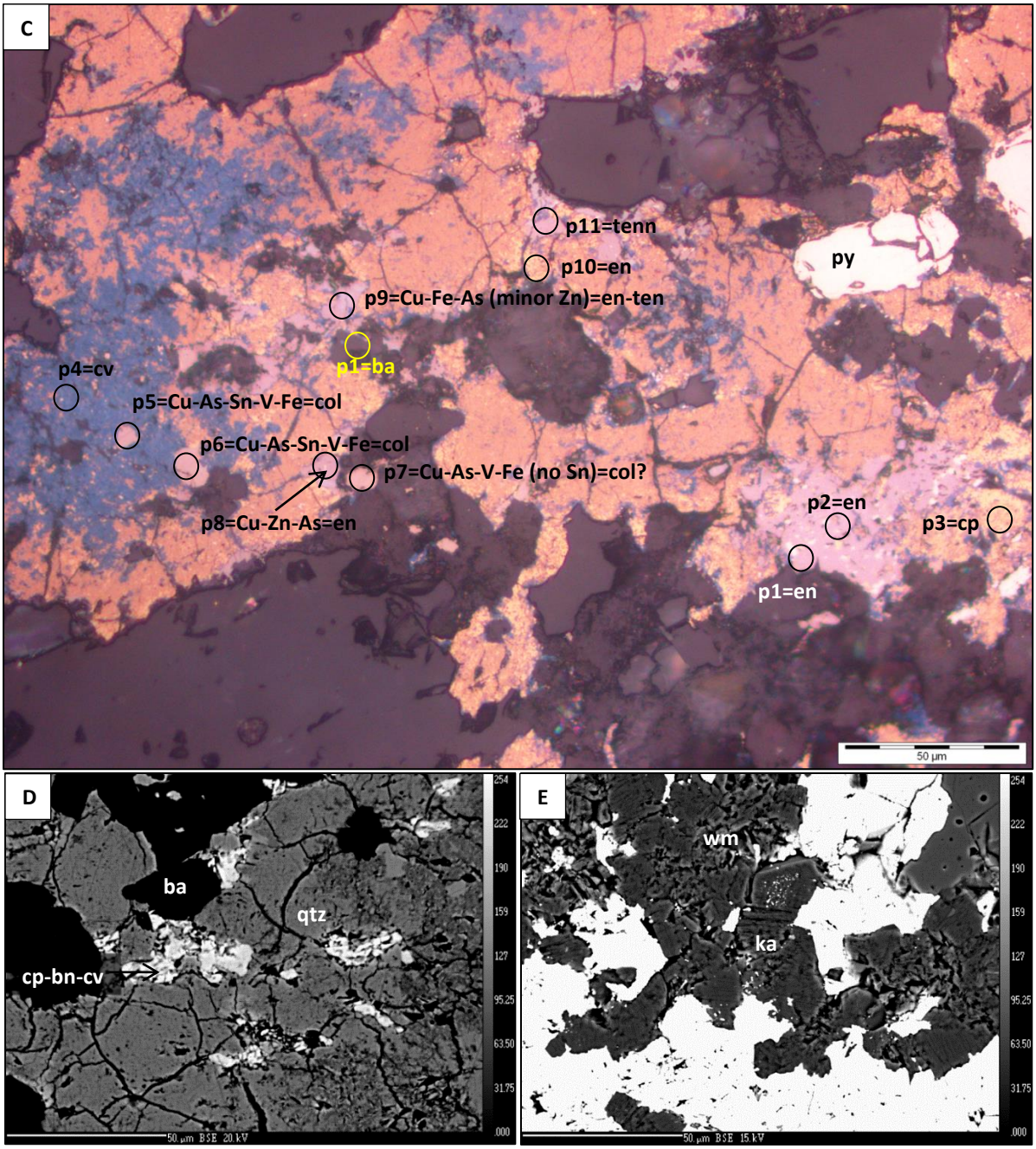

Figure 5.30 (*Contd.).* Abbreviations: ba = barite, col = colusite, cp = chalcopyrite, cv = covellite, en = enargite, ka = kaolinite, py = pyrite, qtz = quartz, tenn = tennantite, wm = white micas. All probe data listed in Appendix A2.

C) Photomicrograph 40x magnification. Chalcopyrite replaced sequentially by bornite, chalcocite then covellite and overprinted by late enargite, pale pink Sn-bearing phases; colusite ($Cu_{26}V_2(As,Sn,Sb)_6S_{32}$ and nekrasovite ($Cu_{26}V_2[Sn,As,Sb]_6S_{32}$), mauve Zn-bearing phases Cu-As-Sn-V-Fe, Cu-As-V-Fe and Cu-Fe-As-Zn sulfosalts and tennantite ($Cu[Cu_4(Fe,Zn)_2]As_4S_{13}$. Barite gangue alteration surrounds the late-stage As-bearing phases.

D) SEM BSE image of chalcopyrite - bornite - chalcocite - covellite - barite.

E) SEM BSE image chalcopyrite - bornite - chalcocite - covellite with alteration minerals kaolinite replacing K-bearing white micas.

quartz - dickite - kaolinite. Relict magnetite has been completely de-magnetized and commonly exhibits a remnant of dark grey-blue coloured staining (Fig. 5.25C). Partial replacement of magnetite with hematite is extensively developed in the quartz - illite alteration zone. (Fig. 5.3). Magnetite, in this zone, stains red streak where scratched, indicating partial de-magnetization and oxidation to hematite. Petrographic analysis has shown reaction rims of hematite on disseminated and vein-hosted magnetite grains (Fig. 5.25A and B). Along with magnetite, all other early high-temperature alteration minerals (K-feldspar, shreddy biotite and chlorite, albite, actinolite and rare anhydrite) have been completely overprinted by combinations of quartz - alunite, pyrophyllite, dickite, diaspore, zunyite, andalusite and kaolinite.

5.8.2 Sulfide replacement and hypogene upgrading

A series of complex sulfide assemblages are present in the zone where epithermal alteration has overprinted porphyry mineralization at Tumpangpitu. It is common to find over six different sulfide species in one hand specimen in this zone (Fig. 5.26F). Chalcopyrite is the most affected early-formed sulfide, and has been commonly transformed to bornite and/or chalcocite, which are in turn replaced by covellite (Fig. 5.27D and 5.28). Early formed bornite is commonly transformed to chalcocite then covellite (Fig. 5.27A)

5.8.3 Molybdenite with advanced argillic alteration

The majority of molybdenite at Tumpangpitu is associated with B type veins (Fig. 5.12A). However, there are minor occurrences where molybdenite is intergrown with quartz - alunite - pyrophyllite - dickite and kaolinite up to 150 m away from the porphyry stockwork shell (Fig. 5.3). Molybdenite also coats fracture surfaces adjacent to zones of high-sulfidation epithermal mineralized faults near the base of the Tumpangpitu lithocap, at depths greater than 500 m asl (Fig. 5.3).

5.9 Supergene chalcocite

Supergene sulfide oxidation throughout the deposit is relatively shallow, and chalcocite enrichment minor and poorly developed at Tumpangpitu. Where present, it occurs as a sooty coating of pyrite (Fig. 5.21E-F) and coats a metal scratcher in native copper when mixed with HCl. Minor supergene chalcocite has formed at the base of Zone A, below 220 m asl in phase 5 fine-grained tonalite adjacent to the Cliff fault (Fig. 5.2). Zones of chalcocite are generally less than 4 m wide either side of the Cliff fault and grade up to 1.5 % Cu. Petrographic and SEM analyses have revealed chalcocite as coatings to multiple phases of pyrite grains and all vein types recognized at Tumpangpitu, including sphalerite-galena veins (Fig. 5.21E-F). Anhedral inclusions of native copper have been identified adjacent to chalcocite and K-alunite in zones of massive disseminated pyrite, coated by chalcocite cut by K-alunite - dickite - pyrite vein in quartz - alunite - dickite - pyrophyllite alteration in fine-grained phase 5 tonalite (Fig. 5.31C). In zones where

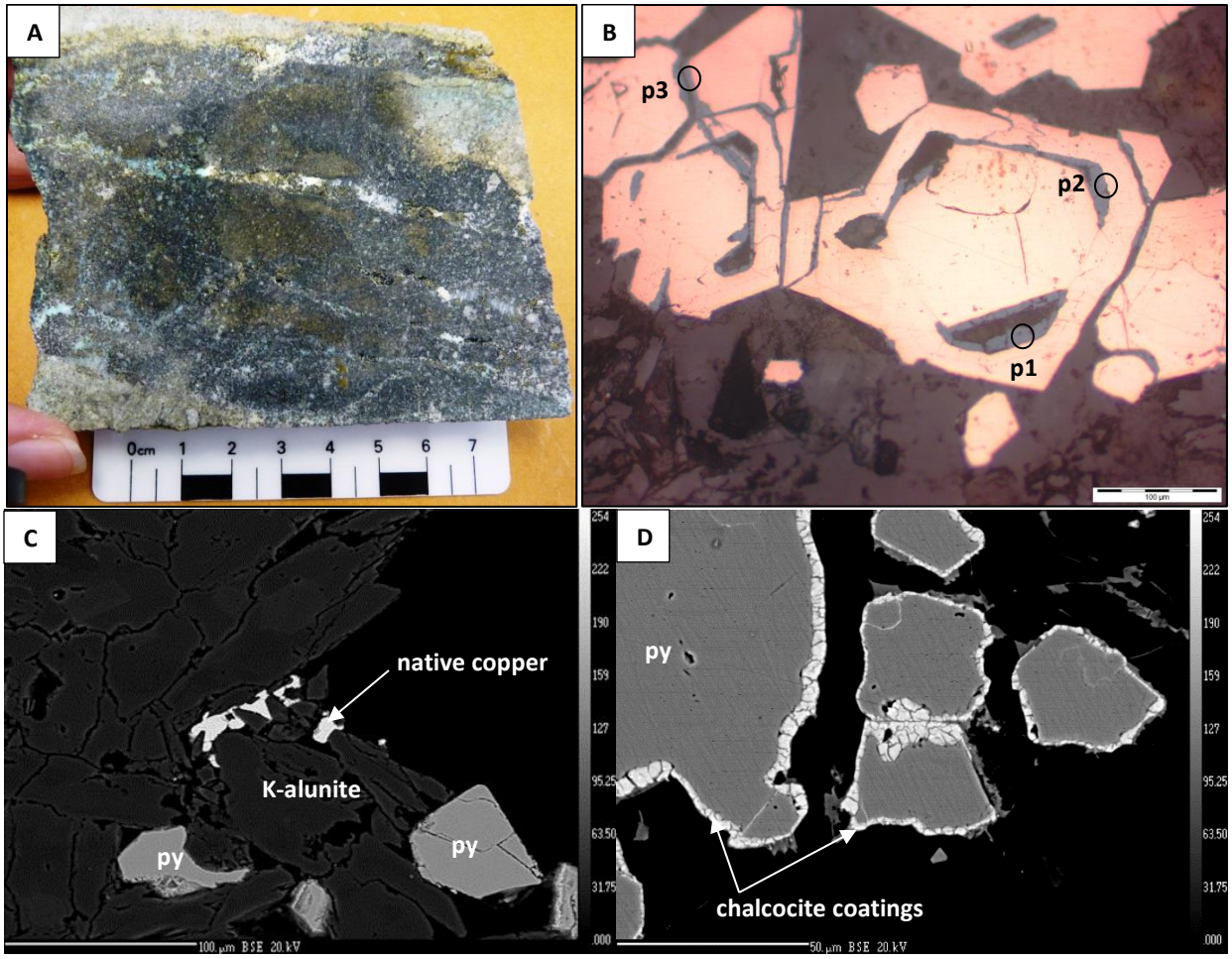

Figure 5.31 Photograph and photomicrograph of supergene chalcocite and native copper from drillhole GTD-11-201: 177.4 m, *174155 mE, 9046097 mN.* Massive disseminated pyrite - chalcocite - covellite - chalcopyrite chalcocite - native copper in phase 5 fine-grained tonalite. EMPA data in Appendix 2.

A) Massive disseminated pyrite, coated by chalcocite cut by K-alunite - dickite - pyrite vein in quartz - alunite - dickite - pyrophyllite altered fine-grained phase 5 tonalite.
B) Photomicrograph at 20x magnification of multiple phases of pyrite with blue chalcocite (yarrowite: 69 % Cu) coatings.
C) BSE image of native copper with K-alunite.
D) BSE image of pyrite grains with chalcocite (yarrowite) coatings.

supergene chalcocite has overprinted porphyry mineralization, Au:Cu ratios are modified from ~ 1:1 to ~ 1:2. Due to the minor occurrences of supergene copper, a supergene copper resource has not been calculated.

5.10 Gold-silver supergene oxidized zones

The zones of supergene oxidation at Tumpangpitu are enriched in gold and silver and depleted in copper. The degree of oxidation has been recorded as complete (100 % sulfides oxidized), strong (80 - 99

% sulfides oxidized), moderate (20 - 80 % sulfides oxidized), weak (0 - 20 % sulfides oxidized) and fresh (0 % sulfides oxidized). Oxide Au-Ag mineralization is present at the highest topographic elevations of Zones A, B and C and E (Fig. 5.2). Jarosite, goethite and hematite have all been recorded by visual and vis-NIR analysis (Fig.). Supergene jarosite is present as a weathering product at Tumpangpitu, where it has overprinted massive and vuggy quartz - alunite altered rocks in shallow-level oxidized zones, together with poorly crystalline kaolinite and smectites. Jarosite has most commonly replaced alunite and sulfides in the high grade high-sulfidation epithermal gold veins (Fig. 5.33A and C). The distribution of jarosite is strongly fault and fracture controlled at depths below the base of semi-oxidation (Fig. 5.33A) and pervasive in zones of alunite alteration in the completely oxidized zones (Fig. 5.33C). Jarosite has commonly replaced alunite around crystal and vein margins (Fig. 5.33A). Jarosite and alunite have not been observed as intergrowths. Accessory hematite is also present, mainly replacing Cu-Fe±As sulfide veins (Fig. 5.33B) and as black botroydial masses coating fractures (Fig. 5.33D). Goethite is ubiquitous, mainly replacing disseminated and vein hosted pyrite. Goethite and hematite have replaced disseminated pyrite as alternating bands overprinting mudstone matrix and around clasts in mud matrix breccias (Fig. 5.33E).

5.11 Sulfide and metal distribution

5.11.1 Metal distribution in the Tujuh Bukit district

The metal distribution in geochemical soil datasets form the Tujuh Bukit district reflects central Au and Cu and Mo associated with porphyry mineralization at Tumpangpitu, Candrian, Salakan, Katak and central Au, Cu, Ag, As, Sb and Zn associated with HSE mineralization (enargite) and ISE mineralization (tennantite - tetrahedrite) and distal concentric halos of Pb and Zn associated with base metal veins. Au-Cu-Ag-As-Zn is associated with low-sulfidation epithermal veins at Gunung Manis 4 km to the east of Tumpangpitu (Fig. 5.32). The levels of molybdenum in soils are strongly affected by erosion level. At Salakan, porphyry mineralization, including quartz - molybdenite vein stockworks are exposed at surface, whereas at Tumpangpitu the quartz - molybdenite vein stockwork is buried at between 220 m and 500 m below the lithocap producing a subdued molybdenum response (Fig. 5.32).

5.11.2 Metal distribution at Tumpangpitu

In plan view (Fig. 5.32), the general patterns of metal zoning at Tumpangpitu reflects central Au and Cu and Mo associated with porphyry mineralization, and central Au, Cu, Ag, As, Sb and Zn associated with HSE mineralization (enargite) and ISE mineralization (tennantite - tetrahedrite). There are distal concentric halos of Pb and Zn associated with base metal veins. Late stage distal galena - sphalerite veins with muscovitic alteration halos form a Pb-Zn enrichment halo around the domain of advanced argillic alteration. The Pb-Zn zone is evident in soil geochemical data and is confirmed from drillhole assays (Figs.

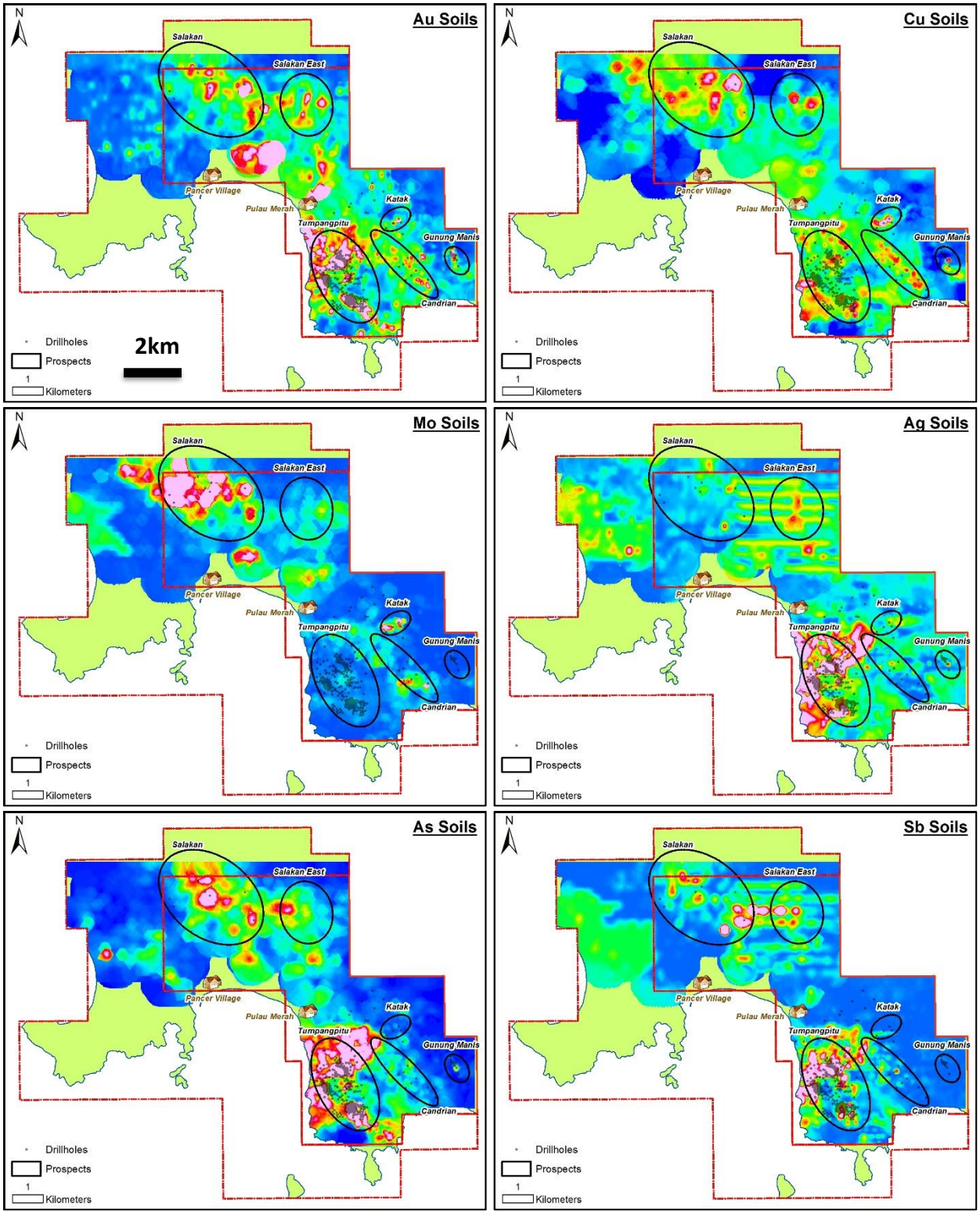

Figure 5.32. Soil geochemistry at Tujuh Bukit.

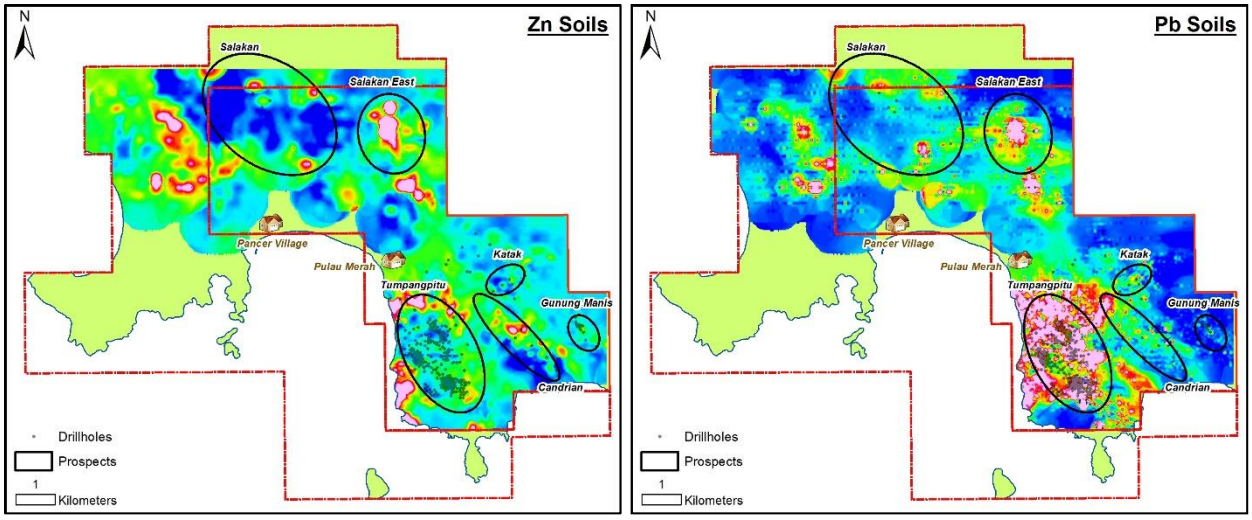

Figure 5.32 (*Contd.*). Soil geochemistry at Tujuh Bukit.

5.32 and 5.33). Tetrahedrite-tennantite occurs around the inner zone of the Pb-Zn halo. The general pattern of metal zoning with respect to the porphyry centres at Tujuh Bukit indicate central Au and Cu associated with deep porphyry mineralization, central and proximal Mo associated with porphyry and occurrence of Mo in the base of the lithocap. Enargite defines the core of the shallow level high-sulfidation mineralization and associated at deeper levels in feeder structures. Enargite mineralization has produced a strong As anomaly, grading outwards to Au, Cu, Ag, As, Sb, Zn associated with tennantite - tetrahedrite and distal Pb and Zn associated with galena - sphalerite.

5.11.3 Porphyry grade distribution

At Tumpangpitu, porphyry copper sulfide zoning is similar to that recorded at a number of porphyry deposits worldwide, e.g., Batu Hijau and Elang (Maryono et al., 2017), Northparkes porphyry deposits, NSW, Australia (Lickfold et al., 2003) comprising a bornite core encircled upwards and outwards by chalcopyrite then pyrite and distal sphalerite and galena. Bornite and pyrite have replaced chalcopyrite adjacent to HSE mineralized fault zones. Due to the limited depth penetration of drilling (< 1,200 m), the dimensions and grade of the bornite core at Tumpangpitu remains undefined. Most of the drillholes have intersected chalcopyrite associated with magnetite to depths of 1,200 m. The bornite core and chalcocite fringe are focused on phase 5 and 6 tonalites. The pyrite shell flanks the margins of the tonalites and overprints up to 500 m vertically of the hostrock sequence. This sulfide zonation sequence is consistent with the development of the sequence of porphyry veining from central M veins to A, B, C, D and distal base metal veins which overprint onto D veins. The ratio of Cu:Au related to porphyry mineralization is generally 1:1 (0.45 % Cu, 0.45 g/t Au) in quartz -magnetite - biotite - K-feldspar altered zones and changes to 2:1 in zones of supergene chalcocite (0.5 % Cu, 0.25 g/t Au) towards the base of oxidation (Fig. 5.3.)

The shape of the porphyry ore body defines an inverted teacup which is closer to the surface to the northeast beneath Zone A (220 m bsl) and deeper to the northwest beneath Zone C, partly due to truncation by the Tumpangpitu diatreme (Figs. 5.3 and 5.4). Molybdenum is associated with the B vein carapace at Tumpangpitu. It is also distributed at least 100 m above the B vein stockwork into the base of the lithocap (Fig. 5.29). The highest values (> 150 ppm Mo) occur proximal to lower zones of the Cliff fault (Fig. 5.3).

5.11.4 Epithermal grade distribution

HSE-1, HSE-2 and ISE veins are most abundant from present day surface to elevations of 80 m asl and are focused around the main vuggy quartz ledges. Below depths of 80 m asl epithermal veins are concentrated in proximity to inter-mineralization faults. Upper levels of the epithermal system are dominated by pyrite with enargite, tennantite and tetrahedrite. Below 80 m asl, pyrite with covellite, chalcocite and bornite dominate with minor chalcopyrite at deepest levels and occurrences of enargite, tennantite and tetrahedrite decrease. Enargite extends to greater depths than tennantite, tetrahedrite and Ag sulfosalts. Enargite is associated with quartz - pyrophyllite - alunite alteration along structures (:> 1200 m depth), in particular Cliff fault as reflected in the As distribution plot (Fig. 5.34E). High grade Ag (> 2. 5 ppm) hosted in tetrahedrite, tennantite and other Ag- bearing sulfosalts is restricted to the upper 250 m of the oxide zones at Tumpangpitu (Fig. 5.34D). Lower concentrations of Ag are associated with tetrahedrite-tennantite at greater depths along the Cliff fault. HSE-1, HSE-2 and ISE veins have crosscut all stages of porphyry veins in proximity to structures. The distribution of gold and copper highlights the structural controls on high grade Au-Cu±Ag (> 1 % Cu, 1 ppm Au), in particular in zones of hypogene upgrading in proximity to Cliff fault (Figs. 5.3, 5.4 and 5.34).

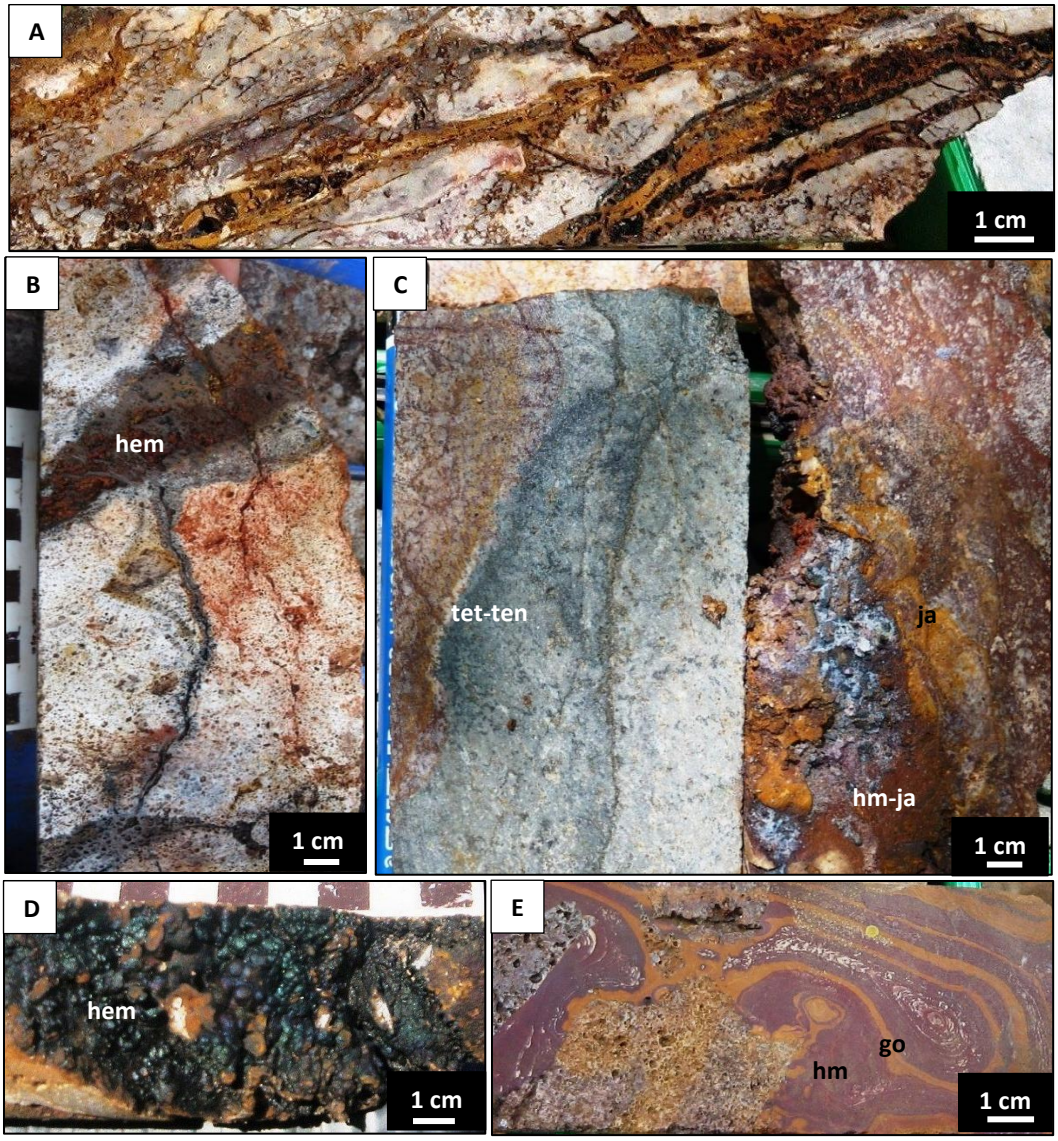

Figure 5.33. Examples of completely, strong, moderate and weak oxidation of sulfides in drillcore from Au-Ag oxide Zones A and C at Tumpangpitu. Abbreviations: al = alunite, hm = hematite, ja = jarosite, tet-tenn = tetrahedrite - tennantite.

A) *Drillhole GTD-08-40: 220 m, 174081 mE, 9046550 mN*. Strong oxidation, network of jarosite - hematite - goethite - alunite veins in phase 2 diorite. Grade: 2 m @ 0.56 ppm Au, 0.123 % Cu, 21 ppm Ag, 1840 ppm As.

B) *Drillhole GTD-09-61: 18 m, 174545 mE, 9045455 mN*. Complete oxidation. Gossanous hematite - dominant vein in pyrophyllite - alunite altered upper facies diatreme breccia. Grade: 2 m @ 0.16 ppm Au, 0.058 % Cu, 7 ppm Ag, 3030 ppm As.

C) *Drillhole GTD-10-172; 229.6 m, 174240 mE, 9046440 mN.* Moderate oxidation. Disseminated and vein hosted tetrahedrite-tennantite and pyrite in phase 5 tonalite (semi-oxidized; left of photo; Grade: 2 m @ 0.44 ppm Au, 0.16 % Cu, 138 ppm Ag, 1080 ppm As) 225.9 m (strongly oxidized; right photo; Grade: 2 m @ 0.08 ppm Au, 0.033 % Cu, 36 ppm Ag, 422 ppm As.)

D) *Drillhole GTD-09-61: 43.32 m, 174545 mE, 9045455 mN*. Complete oxidation. Glassy, botroydial hematite filling fracture in diatreme breccia. Grade: 2 m @ 0.52 ppm Au, 0.056 % Cu, 10 ppm Ag, 1370 ppm As.

E) *Drillhole GT007: 110.8 m. 174316 mE, 9045682 mN*. Complete oxidation. Alternating bands of hematite and goethite overprinting mudstone matrix around clasts in mud matrix breccia. Grade: 2 m @ 0.15 ppm Au, 0.026 % Cu, 23 ppm Ag, 1480 ppm As.

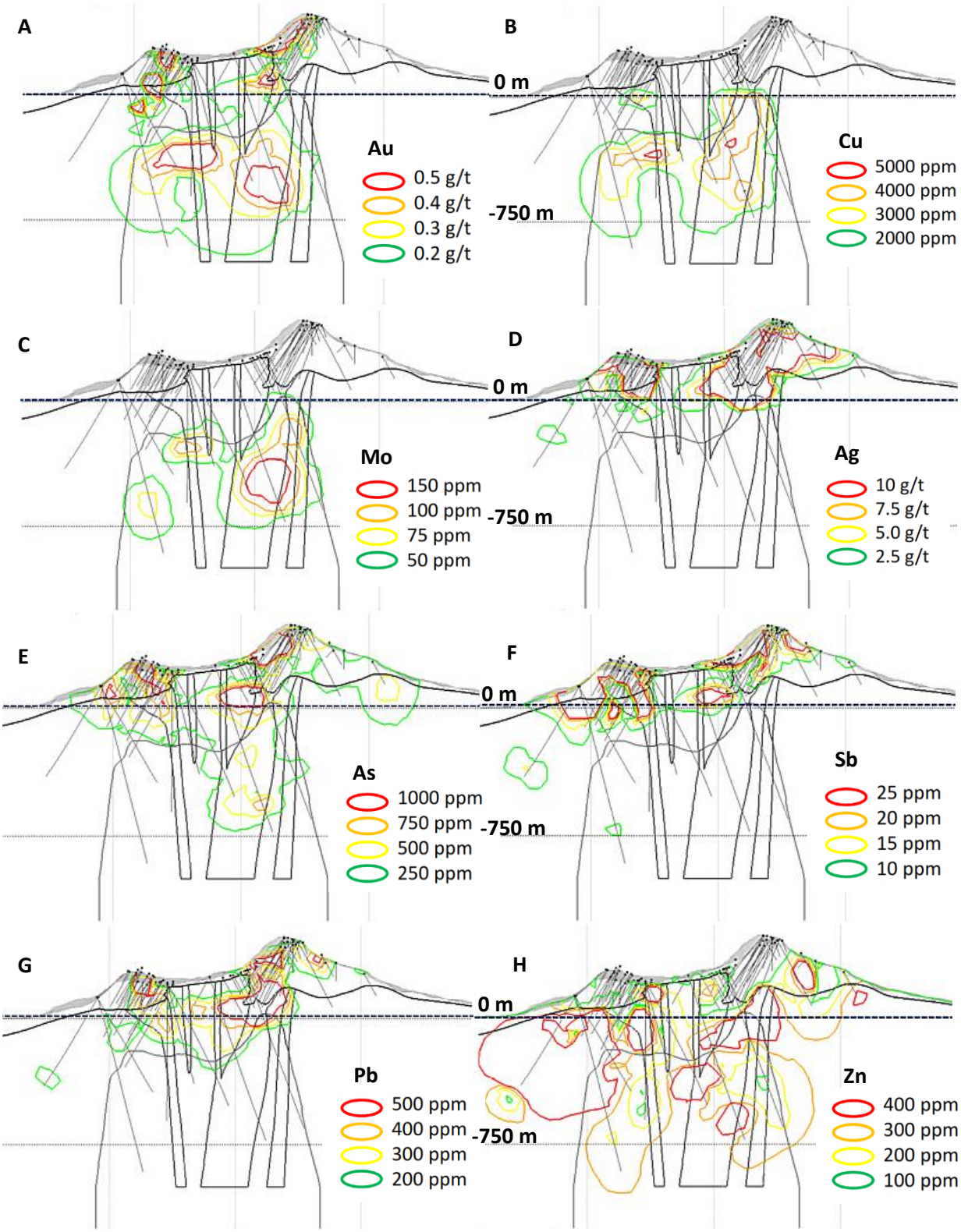

Figure 5.34. Distribution of metals on type section 11060 mN from Tumpangpitu. A) Au, B) Cu, C) Mo, D) Ag, E) As, F) Sb, G) Pb and H) Zn (Sections generated using Leapfrog courtesy of Steve Hayes).

5.12 $^{40}Ar/^{39}Ar$ and Re/Os geochronology

5.12.1 Introduction

Hydrothermal activity associated with mineralization at Tumpangpitu has been constrained by zircon dating of syn- and post-mineralization intrusions, constraining it between 4.89 ± 0.40 Ma and 3.94 ± 0.69 Ma, respectively (Table 4.1). Hydrothermal minerals have also been dated to more accurately determine the age and duration of hydrothermal activity at Tumpangpitu. These geochronologic data are used to evaluate whether a genetic link is viable between the late stage alunite - enargite veins and early porphyry-style quartz-molybdenite B veins at Tumpangpitu. This has involved laser probe $^{40}Ar/^{39}Ar$ analyses of hypogene alunite from late stage alunite-enargite veins at Tumpangpitu. The $^{40}Ar/^{39}Ar$ dating was conducted in the Geochronology laboratory at the University of Queensland, Australia. Rhenium and osmium concentrations in molybdenite from a B-stage porphyry vein were analyzed at the University of Alberta, Canada. No previous geochronologic work has been conducted at Tumpangpitu.

5.12.2 Timing of HSE veining: $^{40}Ar/^{39}Ar$ analysis - alunite separation and preparation

One drillcore sample from a downhole depth of 285 m containing coarse euhedral, saccharine pink alunite rosettes (0.5 - 3 mm diameter) was selected from a late-stage high-sulfidation state epithermal vein crosscutting the upper facies of the Tumpangpitu diatreme (Fig. 5.35A). The alunite crystals are intimately intergrown with enargite, pyrite, quartz and fine-grained pyrophyllite (Fig. 5.35A). Short wave infrared analysis of the alunite indicates that the composition is K-rich (wavelength absorption at 1481.5 nm; Fig. 5.35B).

Alunite crystals were manually separated by tweezers and submitted as mineral separates, along with the original hand specimen drillcore sample for $^{40}Ar/^{39}Ar$ dating at the Geochronology Laboratory at the University of Queensland, Australia. Four alunite grains in total were selected for incremental heating $^{40}Ar/^{39}Ar$ analysis by hand-picking under a binocular microscope (two grains from the mineral separate and two grains from the original drillcore sample).

5.12.3 $^{40}Ar/^{39}Ar$ analytical method

The alunite separates were loaded into a 21-pit aluminium disk along with the neutron fluence monitor Fish Canyon Sanidine (age 28.201 ± 0.046 Ma; Kuiper et al., 2008), following the procedure of Vasconcelos et al. (2002). The irradiation disks were closed with aluminium covers, wrapped in aluminium foil, vacuum heat sealed into quartz vials and irradiated for 14 hours in the Cadmium-lined B-1 CLICIT facility, a TRIGA-type reactor. All ages are reported using the decay constants of Steiger and Jäger (1977). After a decay period after irradiation, samples were analyzed by laser $^{40}Ar/^{39}Ar$ heating. Before analysis,

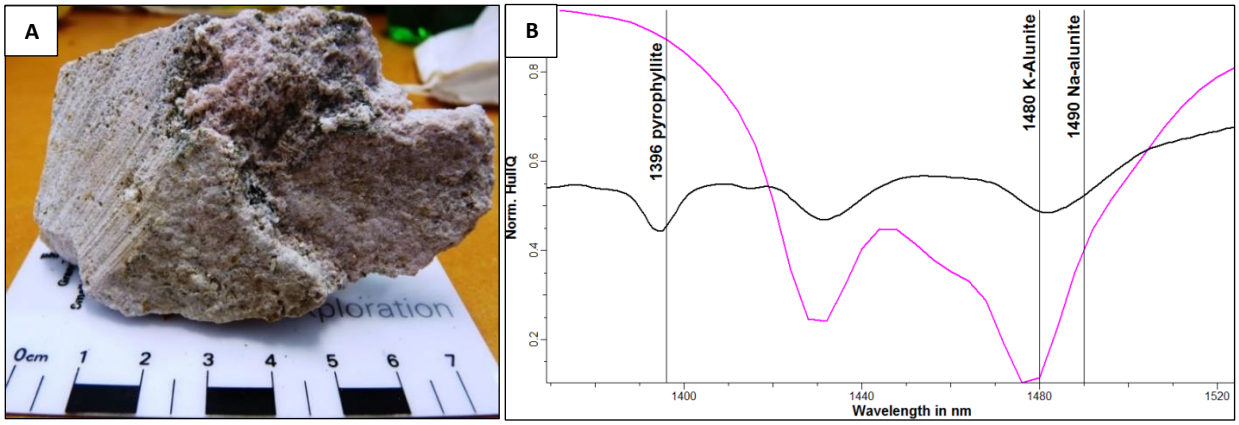

Figure 5.35. Alunite hand specimen and SWIR spectrum from drillhole GTD-10-166: 285 m, 174156 mE, 9046095 mN. Coarse pink crystalline alunite with enargite filling fracture in upper facies Tumpangpitu diatreme breccia.

A) Coarse, euhedral saccharine pink alunite intergrown with enargite, pyrite, quartz, and pyrophyllite.
B) SWIR spectrum (black line) of K-rich alunite (1481.51 nm) mixed with pyrophyllite with K-alunite reference line (pink).

the rock grains and fluence monitors were baked-out under vacuum at ~200 °C for 12 hours. Each sample was heated incrementally with a continuous-wave Ar-ion laser with a 2 mm wide defocused beam. The fraction of gas released was cleaned through a cryocooled cold-trap (T = -125 °C) and two C-50 SAES Zr-V-Fe getters and analyzed for Ar isotopes in a MAP215-50 mass spectrometer equipped with a third C-50 SAES Zr-V-Fe getter. Full system blanks and air pipettes were determined before and after each sample. The automation and analytical procedures are described in Deino and Potts (1990). The data were corrected for mass discrimination, nucleogenic interferences and atmospheric contamination following the procedures in Vasconcelos et al. (2002), using the software "MassSpec Version 7.527" developed by Alan Deino of the Berkeley Geochronology Centre, USA. A $^{40}Ar/^{36}Ar$ value of 298.56 ± 0.31 for atmospheric argon was used for the calculation of the mass spectrometer discrimination (Renne et al., 2009).

J-factors for each Al-disk were determined by the laser total fusion analyses of 15 individual aliquots of neutron fluence monitor, each aliquot consisting of one to three crystals of Fish Canyon sanidine. The mass spectrometer sensitivity was calculated based on the analysis of an air pipette (1.634 x 10^{-13} moles ^{40}Ar) on the Faraday detector (4.257 mV) equipped with a 1 x 10^{11} Ohms resistor, yielding a Faraday sensitivity of 3.84 x 10^{-9} moles/nA. The current multiplier sensitivity measured on a Balzers 217 Electron Multiplier, operated with a gain of ~145,000 is ~ 4.5 x 10^{-14} moles/nA.

5.12.4 $^{40}Ar/^{39}Ar$ age data

$^{40}Ar/^{39}Ar$ age data, argon release patterns and incremental heating plateau ages are shown for all dated samples in Table 5.3 and Figure 5.36 respectively. Plateaus based on two or more consecutive steps are on at least 50 % of the total cumulative ^{39}Ar released, the age values of which are within 2σ from

Table 5.3. Summary of new $^{40}Ar/^{39}Ar$ age determinations from alunite at Tumpangpitu.

Sample	Plateau age	± 2σ	Statistical density plot age	± 2σ	Inverse isochron age	± 2σ	$^{40}Ar/^{36}Ar$ ratio of intercept	± 2σ
7934-01	4.4	0.07	4.41	0.05	4.37	0.06	303	6
7934-02	4.42	0.07	4.41	0.05	4.37	0.06	303	6
7935-01	4.36	0.06	4.37	0.06	4.38	0.08	297	6
7935-01	4.4	0.13	4.37	0.06	4.38	0.08	297	6

the mean value calculated by weighting with inverse variance are considered statistically reliable (Fleck, 1997). Plateau age errors are reported at the 95 % confidence level (2σ), and include the errors in the irradiation correction factors and the error in J, but do not include the uncertainty in the potassium decay constants. All the data from the two mineral separates have been combined to increase the precision over the plateaus for the four individual aliquots.

Magmatic-hydrothermal alunite from Tumpangpitu exhibit well-defined plateaus (Fig. 5.36B), implying that they host radiogenic and nucleogenic gas fractions in a tight crystallographic reservoir, and that the reservoir has been closed during the history of the sample. Therefore contaminating phases are unlikely to be present.

An integrated age has been calculated by combining the results from all steps analyzed during the incremental heating analysis. If the sample did not experience ^{40}Ar loss due to weathering or ^{39}Ar loss by recoil, the integrated age in the $^{40}Ar/^{39}Ar$ method should correspond to a K-Ar age for that sample (Vasconcelos et al., 2002). The two grains of alunite analyzed from Tumpangpitu yield a reproducible plateau age of 4.391 ± 0.037 (Fig. 3.35A) that includes 100 % of the gases extracted for each grain. The statistical density plot (Fig. 5.36B) for the alunite grains yields a most probable age of 4.390 ± 0.037 Ma, indistinguishable from the plateau age. An isochron age for all the results (Fig. 5.36C; 4.385 ± 0.049 Ma, with $^{40}Ar/^{36}Ar$ intercept of 299.5 ± 3.9), is also statistically indistinguishable from the plateau and most probable ages, and is the preferred value for the age of these grains, because the isochron treatment accounts for any possible excess Ar in the sample.

5.12.5 Timing of porphyry veining: Re/Os dating of molybdenite from Tumpangpitu

Age determinations of hydrothermal molybdenite are based on the Re-Os method, whereby ^{187}Re decays to ^{187}Os with a half-life of 41.6 Ga (Smoliar et al., 1996). Molybdenite is the most robust mineral for Re/Os geochronometry, because Re concentrations are generally >50 ppm (Stein et al., 1998a).

5.12.6 Re/Os analysis - molybdenite separation and preparation

Fine-grained molybdenite (< 1 mm) was sampled from a quartz stockwork B type vein with syntaxial crystal growth and molybdenite along vein margins (Fig. 5.37) from drillcore at a downhole depth

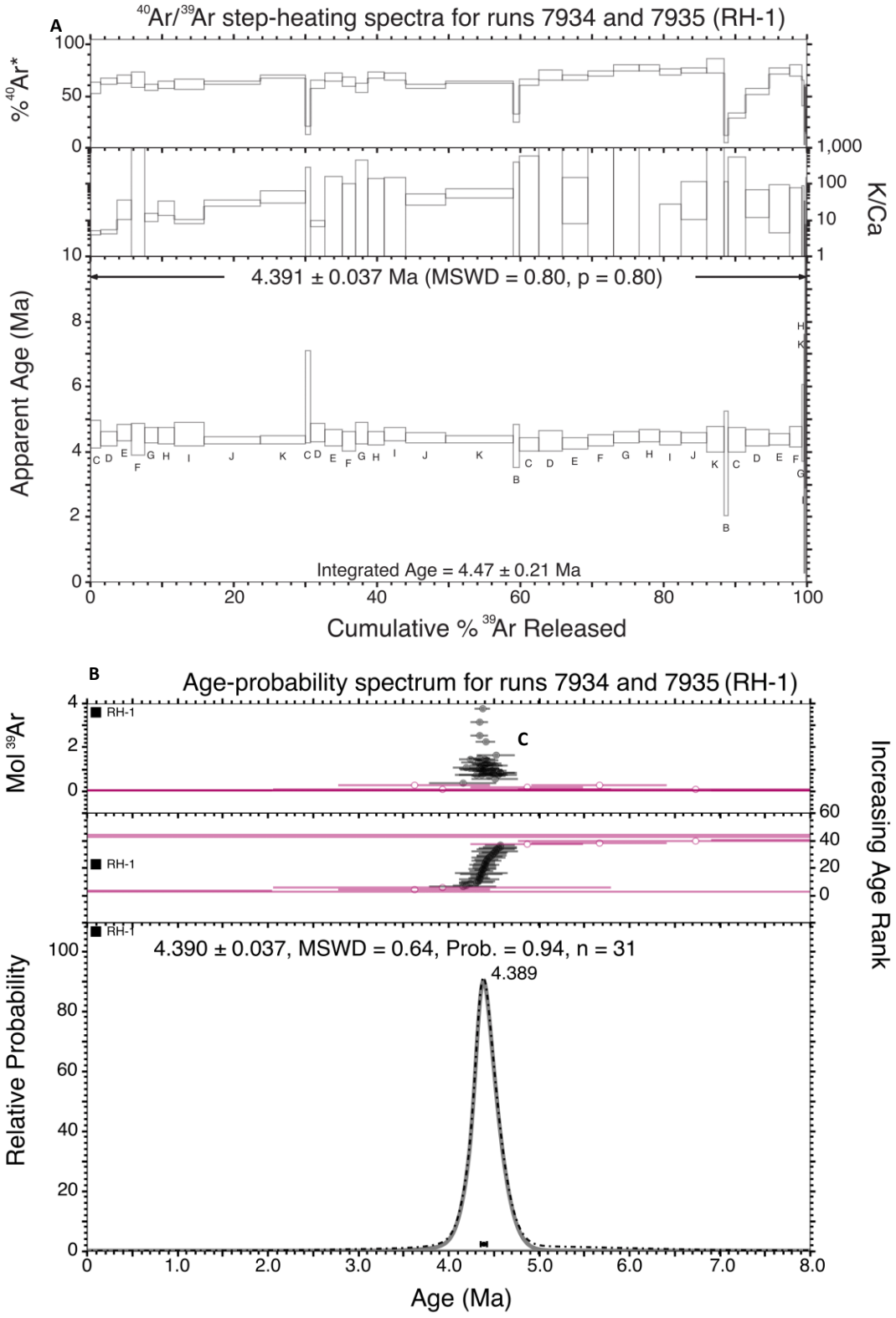

Figure 5.36. Argon step-heating release patterns and plateau ages for combined alunite samples 7934 and 7935 from Tumpangpitu.

A) $^{40}Ar/^{39}Ar$ combined step heating spectrum for samples 7934 and 7935.

B) Age probability spectrum for samples 7934 and 7935.

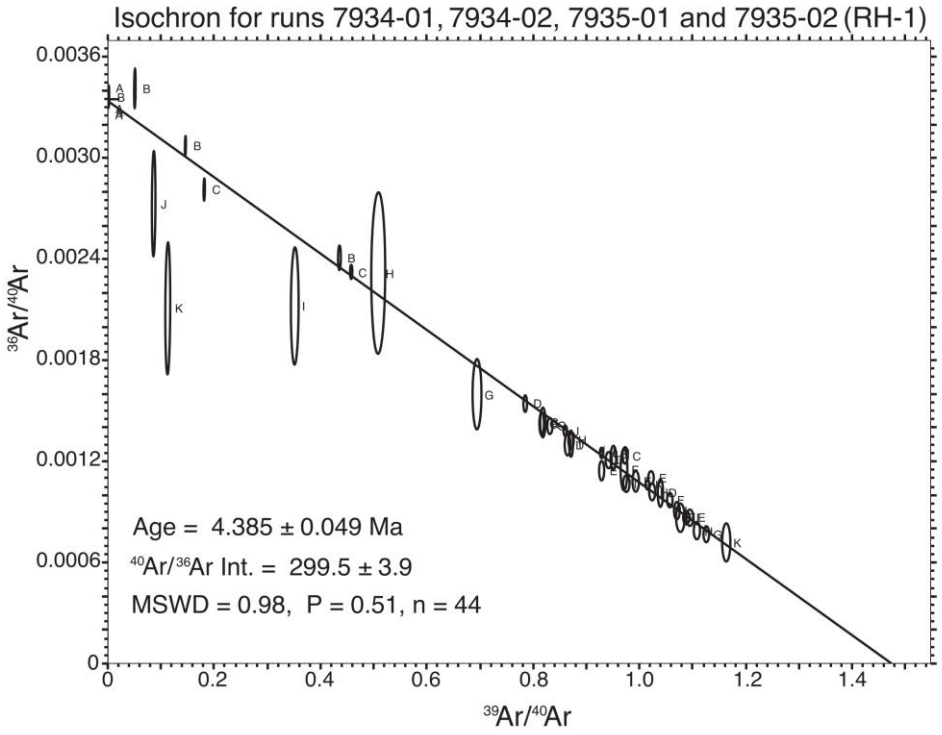

Figure 5.36. *Contd.*
C) Isochron for combined samples 7934-01, 7934-02, 7935-01 and 7935-02.

of 886 m. The vein is associated with the inter-mineralization phase 6 coarse-grained tonalite porphyry with quartz - muscovite alteration overprinted by quartz - kaolinite - pyrophyllite with minor enargite. Fine-grained molybdenite was specifically targeted to avoid potential decoupling of Re and Os across coarse-grained crystal faces (e.g., Stein et al., 2003; Selby and Creaser, 2004). For the molybdenite separates, metal-free crushing followed by gravity and magnetic concentration methods was used to obtain a molybdenite mineral separate. Two mineral separates were extracted from the one quartz - molybdenite - pyrite - chalcopyrite vein (Fig. 5.37) to determine if age determinations are affected by other minerals such as enargite, which may have been present in trace amounts in the mineral separates.

5.12.7 Re/Os analysis - analytical methods

Methods used for molybdenite analysis are described in detail by Selby and Creaser (2004) and Markey et al. (2007). The ^{187}Re and ^{187}Os concentrations in molybdenite were determined by isotope dilution mass spectrometry using Carius-tube, solvent extraction, anion chromatography and negative thermal ionization mass spectrometry techniques. A mixed double spike containing known amounts of isotopically enriched ^{185}Re, ^{190}Os, and ^{188}Os analysis was used. Isotopic analysis was made using a ThermoScientific Triton mass spectrometer by Faraday collector. Total procedural blanks for Re and Os

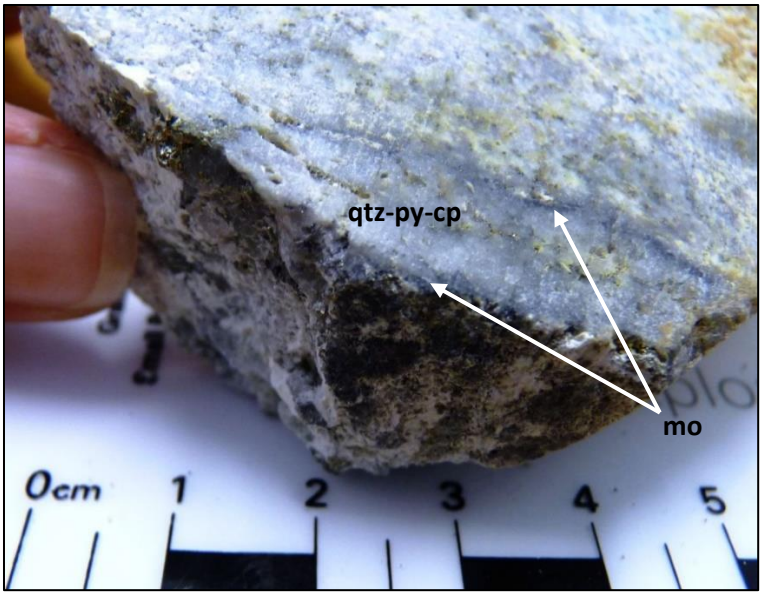

Figure 5.37. Sample GTD-10-166: 886 m, 174156 mE, 9046095 mN. Fine-grained molybdenite along the margins of a B type porphyry quartz stockwork vein from Tumpangpitu with pyrite - chalcopyrite centerline. Quartz - kaolinite - pyrophyllite with enargite overprint onto a quartz - muscovite alteration assemblage in phase 6 coarse-grained tonalite. Abbreviations: cp = chalcopyrite, mo = molybdenite, py = pyrite, qtz = quartz.

were less than 3 picograms and 2 picograms, respectively, which are insignificant for the Re and Os concentrations in molybdenite. Chinese molybdenite powder HLP-5 (Markey et al., 1998) was analyzed as a standard. For this control sample over a period of two years, an average Re-Os age determination of 221.56 ± 0.40 Ma (1 standard deviation uncertainty, n = 10) is obtained. This Re-Os age determination is identical within error to that reported by Markey et al. (1998) of 221.0 ± 1.0 Ma. The age uncertainty is quoted at 2 σ level, and includes all known analytical uncertainty, including uncertainty in the decay constant of ^{187}Re. Re and Os concentrations were determined by isotope dilution, and measured on the Negative Thermal Ionization Mass Spectrometer (NTIMS) at the University of Alberta.

5.12.8 Re/Os age data

Table 5.4 presents the analytical results for ^{187}Re and ^{187}Os concentrations and age determinations for both mineral separates (A and B) from drillcore sample GTD-10-166: 886 m. Re/Os age determinations of 4.303 ± 0.018 Ma and 4.309 ± 0.018 Ma were calculated for the molybdenite, assuming no initial ^{187}Os. The two molybdenite-rich separates yielded identical Re-Os ages, therefore the ages are unlikely to be affected by other minerals such as enargite (R. Creaser, pers. comm. 2017). The Re/Os age determinations lie within the U/Pb age determinations of the host rock (phase 6 coarse-grained tonalite; 4.34 ± 0.48 Ma to 4.03 ± 0.65 Ma; Table 4.1).

Table 5.4. Summary of new Re-Os age determinations from molybdenite at Tumpangpitu.

Sample	Re ppm	± 2σ	^{187}Re ppm^{2}	± 2	^{187}Os ppb^{1}	± 2σ	Model age (Ma)	± 2σ with l (Ma)
GTD 10-166 : 886m "A"	191.7	0.5	120.5	0.3	8.640	0.011	4.303	0.018
GTD 10-166 : 886m "B"	163.7	0.4	102.9	0.3	7.389	0.008	4.309	0.018

[1]All measured Os is radiogenic ^{187}Os (assuming no initial Os), ^{2187}Re = 62.602 % of total Re concentration, ^{187}Re decay constant = 1.666 x 10-11 y^{-1}

5.13 Discussion

5.13.1 SWIR-aided alteration zonation in the lithocap at Tumpangpitu

SWIR spectral data was an essential aid in the generation of the alteration surface maps (Fig. 5.2) and cross sections (Figs. 5.3 - 5.4) at Tumpangpitu. The alteration halo to structural feeders of the Tumpangpitu lithocap and high-sulfidation ore deposit are strongly zoned (Figs. 5.2 - 5.3), similar to zonation patterns elsewhere e.g., at the structurally controlled Summitville HSE deposit: USA (Steven and Ratte, 1960), Lepanto: Philippines (Arribas et al., 1995; Hedenquist et al., 1998) and at Quimsacocha: Ecuador (IAMGOLD, 2007). At Tumpangpitu, the alteration zonation in the lithocap, from structure to margin, shows a vertical zonation, with vuggy quartz as central bodies, roots of quartz - pyrophyllite ± disapore forming halos of massive quartz - alunite grading to quartz - dickite ± kaolinite to illite - smectite to epidote - chlorite - calcite at a scale of 10 s of meters (Fig. 5.3). Silicic zones at Tumpangpitu, vuggy or massive in texture, largely occur in proximal locations close to the feeder structure(s). There is typically a transition from high temperature pyrophyllite at depth, to lower temperature dickite and kaolinite at shallower levels (Reyes, 1990; Sillitoe, 1999; Cooke and Simmons, 2000; Hedenquist et al., 2000). These alteration minerals were accurately identified by SWIR spectroscopy (Figs. 5.2 - 5.4). In particular, the persistence of the pyrophyllite AlOH absorption features, even in samples that contain only a few percent pyrophyllite, allowed the distribution of this alteration type to be mapped effectively (Pontual et al., 1997).

5.13.1.1 SWIR-aided surface alteration maps - Tujuh Bukit

SWIR spectroscopy on soil samples at Tumpangpitu has proven effective at delineating the surface alteration footprint of the hydrothermal alteration system, particularly the low pH, high temperature- stable hydrothermal minerals of the advanced argillic alteration assemblage. By using the extendable motorized auger technique, perfected at the Tujuh Bukit project, (Lulofs, 2011; Harrison, 2014), soil can be sampled from greater depths (up to 2 m) from the base of the C horizon adjacent to altered bedrock. This study has shown that this is a very effective and low cost technique to create alteration maps over large forested areas with limited outcrop.

The surface expression of advanced argillic (Na, Na-K and K-alunite, pyrophyllite, diaspore, topaz, dickite and hypogene kaolinite) hydrothermal alteration assemblages at Tumpangpitu have been defined over an area of 4.6 km (northwest-southeast) by 2 km (northeast-southwest) using SWIR spectral analysis of alteration minerals in soil samples (Fig. 5.2). Advanced argillic alteration zones are surrounded by illite - montmorillonite ± nontronite and distal chlorite ± epidote - calcite alteration assemblages (Fig. 5.2).

A clear spatial distribution between dickite and alunite has been determined by SWIR alteration mapping (Fig. 5.2). Alunite occurs in-situ at shallow levels occupying topographic highs of oxide Au-Ag zones A, B and C, whereas dickite is more abundant down-slope (Fig. 5.2). Pyrophyllite is absent from surface samples over Au-Ag oxide zones A, B and C but is present 2.5 km to the east at the Candrian porphyry prospect where porphyry mineralization is exposed at surface and only the roots of an eroded lithocap preserved (Harrison, 2014). Pyrophyllite also occurs at sea level at the foot of Pulau Merah island (Fig. 5.2). The spatial distribution of pyrophyllite provides an indicator of erosion level of the porphyry deposits and lithocaps in the district. Pyrophyllite indicates fluid temperatures in the range of 280 - 360 °C, whereas dickite most likely formed at lower temperatures (Fig. 3.38; 200 - 280 °C; Hedenquist et al., 2000). This spatial distribution of shallow alunite followed by dickite-dominant alteration and deeper level pyrophyllite-dominant alteration is a characteristic feature at Tumpangpitu (Fig. 5.2). Candrian and Pulau Merah are therefore interpreted to have been subjected to deeper erosion levels than Tumpangpitu. The advanced argillic alteration at Tumpangpitu is spatially associated with northwest-trending ridges associated with resistant quartz-rich bodies (Fig. 5.2). The advanced argillic alteration remains open to the northwest of Pulau Merah and likely continues under the sea (Fig. 5.2). The Candrian lithocap most likely amalgamates with the Tumpangpitu lithocap, which is preserved at higher elevations (Fig. 5.2).

5.13.1.2 Tumpangpitu SWIR-aided alteration model

The Tumpangpitu SWIR-aided alteration model (Fig. 5.3) delineated a clear zonation of alteration zones from proximal quartz - pyrophyllite dominant alteration that forms the core of the lithocap at Tumpangpitu, extending upwards and outwards to vuggy quartz - alunite ledges that formed the resistant, prominent hills of Zones A and C. Massive quartz - alunite alteration surrounds the vuggy quartz ridges and grades outwards to quartz - dickite - kaolinite. An alteration assemblage of illite - smectite - chlorite defines a halo of clay-rich intermediate argillic alteration surrounding the deposit. Propylitic alteration defined by chlorite, epidote and calcite occurs distally with actinolite and epidote, forming an inner propylitic zone.

In the porphyry zone at Tumpangpitu, visual observations were more crucial for identifying anhydrous and opaque minerals that could not be detected by SWIR analysis, such as quartz, magnetite, K-feldspar and anhydrite. However spectral data was used to identify the compositions and crystallinity of

white micas associated with the quartz - muscovite overprint (Fig. 5.3). A progression in porphyry-related alteration has been observed from central quartz - magnetite - K-feldspar - biotite ± anhydrite, through rare actinolite - chlorite, to distal epidote - chlorite and chlorite - calcite alteration of country rocks. The areal extent of the late alteration zones are significantly greater than that of the early potassic-related alteration assemblage, which remains buried at a depth (Fig. 5.3). SWIR spectral data has allowed the accurate recognition of extreme telescoping of advanced argillic alteration directly on top of K-silicate altered rocks to depths of 1200 m at Tumpangpitu (Figs. 5.3 - 5.4). Due to this overprinting, the potassic ore zone was not discovered until drilling penetrated to depths of greater than 500 m below surface.

5.13.1.3 Alunite absorption feature variations

SWIR data was used to plot the wavelength of alunite at Tumpangpitu from drillcore on sections 11060 mN (Fig. 5.5) 10820 mN (Fig. 5.6). The results do not show a clear correlation of hypogene Na-alunite (wavelengths > 1490 nm) occurring closer to the porphyry source based on the results of Chang et al., (2011) in the Lepanto lithocap. Domains of Na-alunite (long wavelength) occur along central zones inferred to be major feeder paleochannels for the Zones A and C Au-Ag oxide deposit (Figs. 5.5 and 5.6).

5.13.2 Vein and alteration paragenesis - Interpretation

The eleven main vein types and associated alteration assemblages at Tumpangpitu are classified here as Early, Transitional, Late and Final (Table 5.2).

The quartz - magnetite - biotite - K-feldspar alteration assemblage is characteristic of the earliest equilibrium assemblage, which formed before final solidification of the Tumpangpitu porphyry (Table 5.1; Figs. 5.3, 5.7 - 5.10). This alteration assemblage is spatially and temporally associated with emplacement and crystallisation of the tonalite porphyry complex (Fig. 5.3). Actinolite (Fig.5.7C) and epidote (Fig. 5.16B and C) are interpreted to have formed contemporaneously in surrounding wallrocks in contact with the tonalite porphyry intrusions during this early stage. High-sulfidation epithermal veins (HSE-1 and HSE-2; Figs. 5.18 - 5.19) and associated alteration; quartz (vuggy and massive) - alunite with roots of quartz - pyrophyllite ± diaspore and quartz - dickite - kaolinite halos of the advanced argillic alteration assemblages is restricted to faults, and is interpreted to have formed contemporaneously with the early potassic style alteration (e.g., Hedenquist and Taran, 2013). Late stage quartz - muscovite alteration, zoned from muscovite-rich ± pyrophyllite above the stockwork carapace to chlorite - muscovite in the surrounding country rock, has overprinted the quartz - magnetite - biotite - K-feldspar alteration assemblage, transforming magnetite to hematite (Fig. 5.13A). These wallrock alteration halos of quartz and highly crystalline muscovite ± pyrophyllite to illite - smectite (near to present day surface) to illite - smectite - chlorite to chlorite - calcite (Fig. 5.3) alteration assemblages with increasing distance from the veins are

interpreted to have formed contemporaneously with high-sulfidation epithermal mineralization associated with alunite and pyrophyllite.

Final stage alteration is associated with intermediate sulfidation ISE-2 base metal sphalerite - galena veins (Fig. 5.21) with associated quartz - muscovite alteration and chlorite alteration halos. These veins and alteration assemblages are interpreted as the final stage of hydrothermal activity at Tumpangpitu.

5.13.2.1 Early

Early phase alteration at Tumpangpitu resulted from high temperature (>500 °C) magmatic coupled brine and vapour that formed the quartz - magnetite - biotite - K-feldspar alteration assemblage coupled with the formation of an early advanced argillic altered lithocap (e.g., Hedenquist and Taran, 2013). Porphyry quartz stockwork veins (M1, M2 and A) exhibit wavy, discontinuous, ptygmatic textures in ductile plastic rock (high temperature hypersaline liquid and vapour) under lithostatic pressure. Cu sulfides (bornite and chalcopyrite), are present at depth, whereas ascent of the vapour would have most likely formed a barren lithocap as documented at other linked porphyry-epithermal deposits e.g., Lepanto, Philippines (Arribas et al., 1995; Hedenquist and Taran, 2013). Propylitic alteration at Tumpangpitu shows a subtle zoning reflective of volatile addition from high temperature (actinolite and epidote) to lower temperature chlorite - calcite alteration assemblages. The inner actinolite zone adjacent to the outer margins of the quartz - magnetite - biotite - K-feldspar alteration zone is not well developed, possibly due to the low boron content of the melt (e.g., Sillitoe, 2010).

The absence of a wallrock alteration halo around M1, M2 and A veins suggests that they were in chemical equilibrium with local wallrocks during precipitation (e.g., Seedorff et al., 2005). During Early phase alteration, Fe is scavenged from the wallrock and magnetite has replaced primary mafic sites along with shreddy biotite (Fig. 5.10). M1, M2 and A veins are interpreted to have formed by replacement of wallrock or primary mafics in the tonalite porphyries, or as a skarn-like replacement in thin limestone units of the sedimentary wallrocks at Tumpangpitu. M veinlets are interpreted to have formed, in part by replacement of wallrock, because there is no evidence of open-space filling. The lack of anhydrite observed at Tumpangpitu is likely to be due to 1) poor preservation as a result of overprinting of advanced argillic alteration > 1000 m on top of potassic alteration and 2) restricted depths of drilling (deepest drillhole 1,200 m); it is likely more abundant at greater depths, not yet intersected.

5.13.2.2 Transitional

Transitional phase alteration at Tumpangpitu is inferred to have resulted from lower temperature magmatic-hydrothermal fluids, that were white mica stable (up to pyrophyllite ≤ 350°C), forming straight, continuous quartz veins (B) with muscovitic halos, molybdenite and Cu sulfides (chalcopyrite, bornite,

chalcocite; Hedenquist and Taran, 2013). Shallow HSE ore and ISE-1 veins with chalcopyrite and tennantite are associated with this phase. Cooling of fluids led to a change in mineral stability, resulting in complex overprinting relationships. This stage is associated with the addition of fluorine as topaz and zunyite (Fig. 5.3).

C veins are poorly developed at Tumpangpitu, perhaps as a result of the collapse of the magmatic-hydrothermal system and intense telescoping of high-sulfidation mineralization over porphyry mineralization after the transitional stage of porphyry mineralization. Alternatively, Cu sulfides in C veins may have been sulfidized to pyrite during the advanced argillic overprint (e.g., Fig. 5.14D).

5.13.2.3 Late

Late stage alteration at Tumpangpitu occurred under hydrostatic pressure, with brittle rock behaviour at temperatures of 350°C or less based on the clay alteration assemblages (e.g., Gustafson and Hunt, 1975; Arif and Baker, 2003; Hedenquist and Taran, 2013). These conditions resulted from lower temperature magmatic fluids, mixed on the margins with meteoric water coupled with the formation of continuous, planar D veins with pyrite centrelines associated with quartz - muscovite alteration (Fig. 5.13B and C). Associated sulfides include pyrite with chalcopyrite, bornite, covellite and enargite. D veins are typical of porphyry systems in a retrograde state, during cooling of the magmatic-hydrothermal system (Seedorff et al., 2005).

Hypogene advanced argillic alteration, vuggy and massive quartz - alunite with halos of quartz - kaolinite - dickite and roots of pyrophyllite ± diaspore, formed in the epithermal environment from condensates of magmatic vapour that contain SO_2 and HCl, which exsolved from the underlying tonalite intrusive source (Hedenquist and Taran, 2013). Leaching of the host rock by acidic condensates (pH ~1; White, 1991), formed the vuggy quartz - alunite cores that subsequently hosted high grade Au-Ag mineralization as HSE-1 veins; enargite/luzonite - pyrite ± covellite ± bornite ± chalcocite and HSE-2; enargite/luzonite - tennantite/tetrahedrite - pyrite ± minor chalcopyrite intergrown with or overprinted by Ag-sulfosalts stannite and colusite. Intermediate sulfidation (ISE-1; tetrahedrite-tennantite-bearing veins (without enargite) ± chalcopyrite and Ag-sulfosalts stannite and colusite) epithermal veins, along with HSE-1 and HSE-2 veins have crosscut or reopened most of the porphyry stockwork vein stages at Tumpangpitu, although their relationship to D veins is ambiguous. Pyrite, recognized as the earliest sulfide mineral in HSE-1, HSE-2 and ISE-1 veins, is inferred to be the same generation as pyrite in D veins. However, HSE-1, HSE-2 and ISE-1 veins are locally cut by D veins and vice versa, suggesting contemporaneous, multiple cycles of epithermal mineralization and D vein formation (e.g., Masterman, 2003). The presence of minor tennantite with pyrite in D veins (Table 5.2) suggests that D veins formed contemporaneously with HSE

and ISE veins and are associated with the introduction of copper and gold by magmatic fluids (e.g., Perello et al., 2012).

Late stage alteration is associated with the precipitation of Cu-Au sulfides at Tumpangpitu. The locations of HSE and ISE veins were controlled by the Cliff fault, and to a lesser extent by the East fault beneath Zone A and West fault at Zone C (Figs. 5.2 - 5.4). The vuggy quartz zones associated with the cores of the HSE deposits at Zones A and C at Tumpangpitu are the upper manifestations of the structurally controlled high temperature quartz - pyrophyllite ± diaspore alteration at depth (Fig. 5.3). The presence of diaspore together with pyrophyllite and quartz along these fault zones at 10 m bsl (Fig. 5.3) constrains the temperatures of alteration to at least 275 °C (Hedenquist and Taran, 2013). The late tennantite - enargite HSE-2 and ISE-1 veins associated with feldspar destructive alteration are strongly structurally controlled and banded, representative of multiple influxes of magmatic-hydrothermal fluid under pressure. Sn-minerals including stannite (Cu_2FeSnS_4), colusite ($Cu_3(As, Sn,V,Fe)S_4$), nekrasovite ($Cu_{26}V_2(Sn,As,Sb)_6S_{32,}$), mawsonite ($Cu_6Fe_2SnS_8$) and vinciennite ($Cu_{10}Fe_4Sn(As,Sb)S_{16}$) are associated with both HSE-2 and ISE-1 veins.

5.13.2.4 Final

Final stage alteration at Tumpangpitu occurred under hydrostatic pressure conditions at fluid temperatures of < 300° C, resulting in the formation of ISE-2 veins (pyrite - sphalerite - galena) associated with illite ± kaolinite ± montmorillonite alteration (e.g., Hedenquist and Taran, 2013). Base metal sulfides galena and sphalerite were the last species to precipitate from the ore forming fluids due to their higher solubilities relative to copper and gold (Cooke et al., 2005). ISE-2 veins have formed a Pb-Zn halo encircling the Tumpangpitu lithocap, evident in soil geochemical datasets (Fig. 5.32).

5.13.3 Unmineralized porphyry stockwork zone

Densely sheeted and banded stockwork veins (M1, M2, A and B-type veins) have pits along vein centrelines and margins that may have been occupied by sulfides, and fine-grained recrystallized textures (Fig. 5.15C). The veins occur in the central unmineralized vein stockwork zone at Tumpangpitu (Fig. 5.3; in phase 6 tonalite at the end of drillhole GTD-08-56 and Fig. 5.15) and are similar to veins documented from the Maricunga porphyry gold systems of northern Chile (Muntean and Einaudi, 2000), Sari Gunay, Iran (Richards et al., 2006), Boyongan, Philippines (Braxton, 2007) and Batu Hijau, Sumbawa (Maryono et al., 2012). At Boyongan, a barren quartz stockwork is associated with an inter-mineralization stock that has undergone quartz, biotite, magnetite and K-feldspar alteration (Braxton, 2007).

5.13.4 Quartz flooding

The zones of intense quartz veining/flooding observed at Tumpangpitu (Fig. 5.14) are likely to have originated as sub-vertical or steeply-inclined zones of sheeted porphyry veins, localized along structures that penetrate down onto the tonalite stock. These were probably fault zones that focused fluid flow. Repeated fractures could have produced sheeted veins. Porphyry C and D veins, as well as high-sulfidation state mineralization overprinted the silicic zones, consistent with the hypothesis that quartz flooding was a product of the development of an intense A and B quartz vein stockwork and associated silicic alteration overprinted by later quartz - muscovite alteration overprinting the porphyry stockwork carapace. CL imaging of quartz from these zones is recommended in order to determine the number of generations of quartz precipitation and possible sources and mechanisms of quartz flooding.

5.13.5 Sulfide distribution and paragenesis at Tumpangpitu - Interpretation

Bornite and chalcopyrite are the dominant sulfides associated with magnetite in M type veins and veinlets (Figs. 5.8 - 5.11). The veins and veinlets contain hypogene bornite and chalcopyrite, overprinted by late hypogene chalcocite and covellite with quartz. Native gold occurs as refractory inclusions in the copper sulfides in A veins. Chalcopyrite, bornite and molybdenite are the dominant sulfides in B veins. In A, B and C veins, a late overprint of bornite, chalcocite and covellite have embayed and infilled fractures in pyrite and commonly enclose residual pyrite grains (Fig. 5.11). These textural relationships suggests that bornite and pyrite are not an equilibrium assemblage (Lee, 1994). D veins are dominated by pyrite with minor chalcopyrite and rare tennantite. At Tumpangpitu, enargite is the principal Cu-As sulfide in high-sulfidation state epithermal veins (HSE-1) and has partially replaced early pyrite, molybdenite, chalcopyrite, bornite and chalcocite. Tennantite with minor enargite and tetrahedrite in HSE-2 veins also overprinted early-formed porphyry-related sulfides including chalcopyrite, bornite and molybdenite. Colusite, stannite and nekraskovite co-precipitated with tennantite and enargite (Fig. 5.27, 5.30, A2-1B, A2-1H and A2-3A). Sphalerite and galena were the last hypogene sulfides to precipitate. Sphalerite veins have been coated by secondary chalcocite associated with weak supergene chalcocite development along fault zones beneath the Zone A oxide Au-Ag deposit. (Fig. 5.3; 5.21E). Sulfide zonation patterns define a bornite-rich core, surrounded upwards and outwards by chalcopyrite and then pyrite zones. These have been crosscut by fault-controlled enargite and tennantite-tetrahedrite, which have in turn been overprinted by Sn-bearing sulfides and sulfosalts. Sphalerite and galena occur in distal veins (Fig. 5.32).

5.13.6 Fluid geochemistry

The principal epithermal ore minerals at Tumpangpitu are enargite ± luzonite, with tennantite-tetrahedrite, chalcopyrite, Sn-bearing sulfosalts, sphalerite, galena, native gold/electrum and gold-silver tellurides. Early deposition of enargite - luzonite was followed by gold-silver mineralization, and by

tennantite, chalcopyrite and tellurides (Table 5.2; A2-1; Fig. A2-2D). The formation of the tennantite - chalcopyrite - pyrite assemblage after the enargite stage indicates an evolution through time from high-sulfidation state (HSE-1 and HSE-2 veins) to intermediate-sulfidation mineralization (ISE-1 veins). Cooling resulted in the formation of the covellite - chalcocite ± telluride assemblage, in a return to high-sulfidation state conditions, when native gold/electrum and gold-silver tellurides as inclusions occluded by chalcocite (Fig. A2-2D) and covellite (Fig. 5.27G) similar to relationships at Rosario (Masterman et al, 2012) and El Indio, Chile (Holley et al., 2016). Replacement of enargite - luzonite by chalcopyrite - tennantite (Figs. 5.19, 5.30, A2-1, A2-4 and A2-6) may have been caused by fluid evolution over time, due to interaction with the rock buffer (Einaudi et al., 2003). Eutectoid intergrowths of covellite and pyrite (Fig. 5.28A) and covellite and pyrite directly replacing chalcopyrite (5.28B) suggests solid solution between these sulfides.

5.13.7 Alteration mineral paragenesis at Tumpangpitu - Interpretation

Temperature stability ranges of hydrothermal minerals common in epithermal systems have been deduced from empirical studies of active geothermal systems (e.g., Reyes, 1990; Watanabe and Hedenquist 2001) and by experimental results (e.g., Hemley et al., 1980; Fig. 5.38). Temperature variations of hydrothermal fluids can therefore be estimated using mineral assemblages and can provide indicators of paleoisotherms in hydrothermal systems.

5.13.7.1 Temperature gradients

Alunite, diaspore and APS minerals can coexist at temperatures between 250° and 320°C (Fig. 5.38). The presence of andalusite implies higher temperatures, up to 400°C (Hemley et al., 1980; Watanabe and Hedenquist, 2001). Dickite and pyrophyllite occur over a wide temperature range, depending on silica saturation (Hemley et al., 1980). At quartz saturation, the temperature that these phases coexist is 250° to 300°C (Hemley et al., 1980; Watanabe and Hedenquist, 2001). The maximum temperature for the illite - smectite assemblage is ~200°C (Fig. 5.38). The thermal stability range for euhedral epidote that has replaced plagioclase is generally > 240° (Fig. 5.16C; Henley and Ellis, 1983). The propylitic assemblage of epidote - chlorite that fringes Tumpangpitu is therefore inferred to have formed at temperatures exceeding ~ 240°C.

The quartz - muscovite and illite - smectite alteration assemblages formed as outer alteration halos to pyrophyllite - dickite alteration halos (Figs. 5.2 - 5.3). The temperature of formation of the pyrophyllite - dickite assemblage would have been around 250º to 300ºC, whereas the distal illite - smectite assemblage formed at temperatures ≤ 200ºC (Fig. 5.38). Therefore, the muscovite - illite - quartz alteration assemblage that separates the advanced argillic and argillic assemblages probably formed between 200º and 250ºC,

consistent with the temperature stability of muscovite shown in Figure 5.38. The actinolite - chlorite and epidote - chlorite alteration assemblages that surround the Tumpangpitu porphyry complex are inferred to have formed at higher temperatures than the illite - smectite alteration assemblage (> 280º for actinolite; > 250 ºC for epidote; Fig. 5.38).

5.13.7.2 pH gradients

The fluids responsible for the quartz - alunite and quartz - pyrophyllite - dickite alteration assemblages had a pH value of about 2 - 4 (Stoffregen, 1987). If the pH was lower, then aluminium would dissolve and so pyrophyllite, diaspore and andalusite would be leached to form residual quartz (Arribas, 1995). Pyrophyllite is not present above 80 m bsl in the Tumpangpitu lithocap, where vuggy quartz dominates. In these areas, the pH was likely < 2, because most of the rock components have been leached (Fig. 5.3; Arribas, 1995). Aluminium-rich minerals (pyrophyllite, diaspore and locally andalusite) were stable in the higher temperature environments along feeder structures, whereas at lower temperature, distal to the structures and shallower depth, alunite becomes stable. At low temperatures (< 200 °C) and a pH of < 2, alunite can dissolve, leaving residual vuggy quartz at high condensate/rock ratios (>10:1), when SO_2>>H_2S in the original volcanic vapour (Hedenquist and Taran, 2013).

Lateral zonation in alteration assemblages at Tumpangpitu vary from central vuggy quartz - alunite to massive quartz - alunite to quartz - pyrophyllite to quartz - kaolinite - dickite to illite - smectite to distal chlorite - calcite alteration assemblages, as the result of wall-rock reaction that neutralized acidic fluids. Similar alteration zonation has been documented in a number of high-sulfidation deposits including Summitville (Stoffregen, 1987), Lepanto, Philippines (Chang et al, 2011) and Quimsacocha, Ecuador (IAMGOLD, 2009). At Tumpangpitu, high temperature alteration assemblages are zoned laterally from a pyrophyllite core through muscovite and illite - smectite to outer chlorite - epidote alteration assemblages. This alteration pattern is interpreted as neutralisation of acidic fluids as they were dispersed laterally from the axis of flow.

5.13.7.3 Hydrology

The styles of advanced argillic alteration at Tumpangpitu appear to relate to paleopermeability. Vuggy and residual quartz formed by replacement of the host rocks by strongly acidic fluids in zones of high permeability (e.g. major fracture zones or porous volcanic rocks). These reactions enhanced permeability and encouraged the influx of more fluid (White, 1991). In the Zone C supergene oxide gold deposit, the advanced argillic assemblages occur as narrow alteration envelopes around faults that host massive sulfides. This implies that, at the current level of exposure, the principal direction of paleofluid

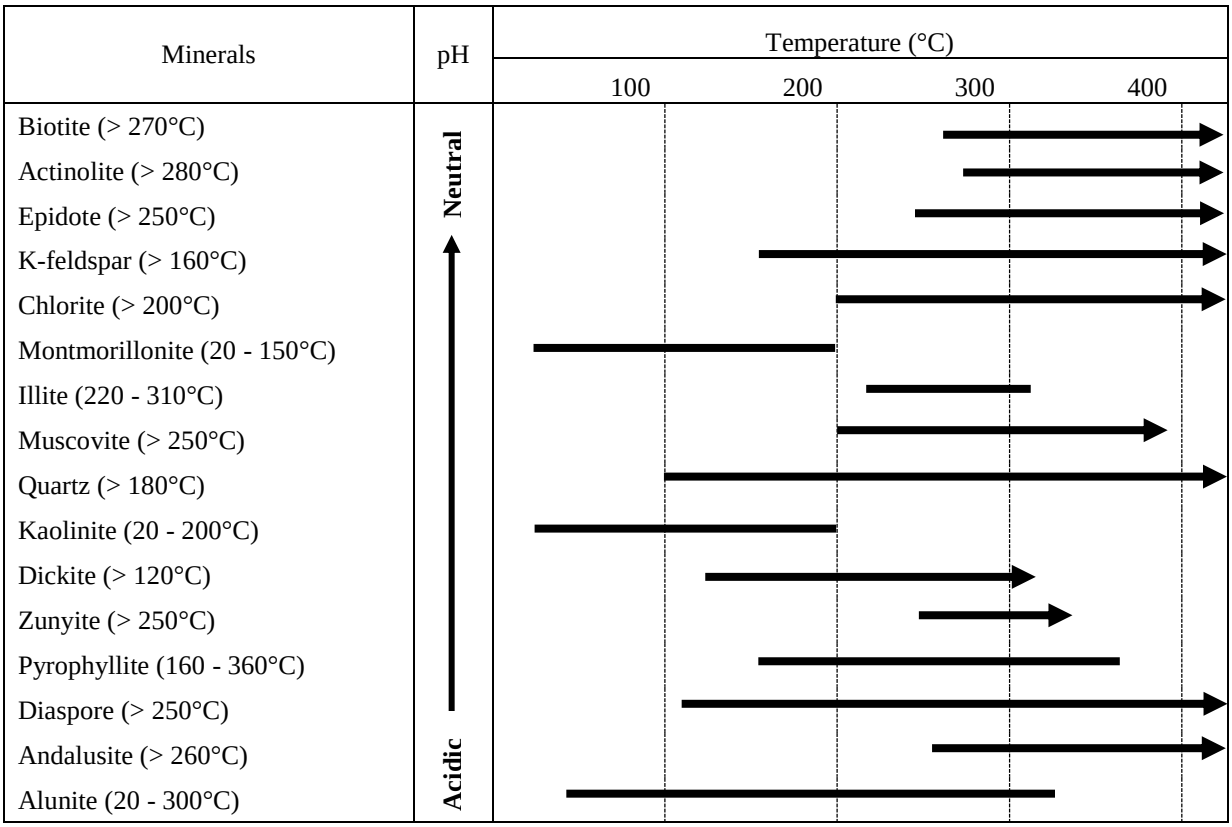

Fig. 5.38. Temperature stability of hydrothermal minerals that occur at Tumpangpitu, arranged by their stability with respect to pH (modified after Hemley et al., 1980; Reyes, 1990).

flow was along the faults (upwards and/or laterally). The narrow alteration halos to the veins thus reflects minimal lateral seepage of acid fluids from the faults, rather than flow into a permeable zone.

5.13.8 Temporal relationship between epithermal and porphyry mineralization

Tumpangpitu is a good example of a large, mineralized lithocap that overprints > 1 km of porphyry Cu-Au-Mo mineralization. Overprinting was facilitated, in part by the evolution of a normal fault system (Chapter 3; Figs. 5.2 and 5.40; Gray, 2011). All lithocaps have structural roots that can facilitate the overprinting of advanced argillic alteration onto underlying porphyry ore bodies (e.g., Sillitoe, 2010). The distance between the base of a lithocap and the top of an underlying porphyry deposit varies globally. In some cases, the high-sulfidation environment is juxtaposed or telescoped directly onto the porphyry environment (e.g., Tampakan; Philippines - Rohrlach, 2005; Sillitoe, 2010; Lepanto-Far Southeast; Philippines - Arribas et al., 1995; Hedenquist et al., 1998; Chang et al., 2011; Butte, Montana - Hedenquist and Taran, 2013; Rosario, Chile - Masterman, 2013; Chuquicamata, Chile - Sillitoe, 2000; Caspiche, Chile - Sillitoe, 2013). Advanced argillic alteration, telescoped into a high grade porphyry deposit is well developed at Chuquicamata, northern Chile. Late stage high-sulfidation state mineralization and associated

alteration directly overprinted early porphyry mineralization related to a broad zone of potassic alteration (Sillitoe, 2000; Ossendon et al., 2001; Barra et al., 2013). The overprinting veins have grey quartz - muscovite alteration halos, and alunite at upper levels. Hypogene upgrading is evident with bornite - covellite overprinting chalcopyrite. Enargite veins are partially preserved at upper levels (Ossandon et al., 2001).

Rapid syn-hydrothermal uplift and/or mass wasting can cause a lithocap to overprint underlying porphyry deposit(s). This process is related to 'telescoping', (Sillitoe, 1994). The exposure of porphyry stockwork veining on Pulau Merah island at sea level, implies that the 3.98 ± 0.22 Ma Pulau Merah deposit is deeply eroded. Early to Middle Miocene basement limestone and sedimentary rocks are also exposed at sea level. Mud-matrix breccias and charcoal fragments in the Tumpangpitu diatreme occur just 300 m above the sedimentary basement (Chapter 3), indicating a near-surface environment during diatreme formation at 2.7 ± 1.0 Ma. Collectively, these features indicate erosion as a result of the subsequent epithermal overprint onto the porphyry system. Observations that support this interpretation include multiple, overlapping generations of pyrophyllite (Figs. 5.27C and G), extensive replacement of magnetite by hematite (Figs. 5.25A-C), occurrence of molybdenite in veins with advanced argillic alteration halos (Fig. 5.29), hypogene upgrading of porphyry copper sulfides by copper sulfosalts (Figs. 5.26F, 5.27D, 5.28 and 5.30) and overprinting of enargite by tennantite-tetrahedrite (Figs. 5.19I and 5.30C) within the Tumpangpitu lithocap, also provide evidence of telescoping in the Tujuh Bukit district.

The transition from the top of a porphyry deposit to overlying lithocap has been documented at El Salvador, Chile (Wantanabe and Hedenquist, 2011); Rosario, Chile (Masterman, 2012) and Caspiche, Chile (Sillitoe et al., 2013). Fluids evolve from early high temperature brine-vapour mixtures (> 500 °C, 5-20 wt % NaCl) associated with potassic alteration to lower temperature vapour condensates and liquids (< 350 °C 10 wt % NaCl) that form lithocaps (Rye et al., 1999; Wantanabe and Hedenquist, 2011; Hedenquist and Taran, 2013). At the El Salvador Cu-Au porphyry deposit in Chile, pyrophyllite is a retrograde replacement of muscovite and andalusite alteration, the latter overlying the copper ore shell (Wantanabe and Hedenquist, 2011).

5.13.8.1 Spatial distribution of pyrophyllite at Tumpangpitu

Pyrophyllite at Tumpangpitu has two distinct distributions. Pyrophyllite is intimately intergrown with and locally replaces muscovite at deep levels (> 230 m bsl; Fig. 5.3) associated with the porphyry stockwork carapace. At the same level, illite has also replaced pyrophyllite (Fig.). Pyrophyllite is also associated with dickite, kaolinite and alunite at both at shallow levels in the epithermal alteration zone (200 m asl) and at depth along major structures (up to 900 m bsl) and is a dominant component of the Tumpangpitu lithocap (Figs. 5.2, 5.3, 5.26 and 5.29). Pyrophyllite alteration has overprinted the porphyry

stockwork zone, particularly along major fault zones (Figs. 5.3 -5.4). A 480 x 450 m zone of quartz - pyrophyllite alteration forms the core of the lithocap on type section 11060 mN and distinct feeder zones to the vuggy quartz - alunite HSE ore deposits of Zones A and C (Fig. 5.3). Pyrophyllite is absent at the present day surface in the supergene oxide gold deposits A (470 m asl) and C (275 m asl), but occurs below 250 m asl in Zone A, at 200 m asl in Zone C and at sea level adjacent to the deeply eroded tonalite porphyry stock of Pulau Merah island (Fig. 5.2). The formation of hypogene pyrophyllite at the expense of muscovite may occur by the following reaction:

$$2\ KAl_3Si_3O_{10}(OH)_2 + 2\ H^+ + 6\ SiO_2 = 3\ Al_2Si_4O_{10}(OH)_2 + 2\ K^+$$

Two reaction paths can produce this reaction. The first is a simple cooling path that can assist a transition from muscovite to pyrophyllite (1A; Fig. 5.39; White, 1991). Cooling of a fluid in equilibrium with muscovite at initial constant K/H molar ratio can result in pyrophyllite formation. This process may be associated with replacement of muscovite associated with quartz - alunite, pyrophyllite, diaspore then to dickite. Pyrophyllite can also be replaced by illite if K/H values increase due to interaction of fluids with country rock (path 1B; Fig. 5.39; Hemley, 1959; Sverjensky et al., 1991; Hedenquist et al., 1998). Mineral precipitation and/or dissolution, acidic species dissociation, and other changes in fluid chemistry, need to retain a near constant [K+]/[H+] ratio in the fluid for the chemical reaction to progress in this fashion with decreasing temperature.

A second path involves vapour condensation. Condensation of magmatic vapour into groundwater forms acidic solutions (pH < 2), decreasing the (K/H) ratio by liberating K^+ and consuming H^+ resulting in vuggy and massive quartz - alunite alteration and formation of a lithocap (path 2; Fig. 5.39). In this case, pyrophyllite formed at higher temperature conditions (near 300 °C), spatially above muscovite (up to 375 °C), dickite (120 °C), kaolinite (< 200; Hemley et al., 1969; Hedenquist et al., 1994a; 1994b; Watanabe and Hedenquist, 2011 and Hedenquist, 2015).

The two possible reaction paths for producing pyrophyllite alteration are illustrated in Figure 5.39. The observed zonation from muscovite-altered rocks in deep levels associated with the porphyry stockwork carapace at Tumpangpitu to pyrophyllite - dickite altered rocks at shallow levels in the lithocap is inferred to have occurred by cooling of a fluid, at relatively constant K/H values, as it ascended from the quartz - muscovite zone to the pyrophyllite - dickite zone (path 1A; Fig. 5.39; Wantanabe and Hedenquist, 2001). At high water to rock ratios, the fluid cooled from muscovite-stable to pyrophyllite-stable, similar to the reaction paths inferred by Garay et al., (2012) at the Calaorco HSE deposit and lithocap and La Arena Cu-Au porphyry deposit, Peru. They documented patchy pyrophyllite - dickite - diaspore after residual quartz, which they argued was caused by cooling from muscovite to pyrophyllite-stable quartz-saturated conditions.

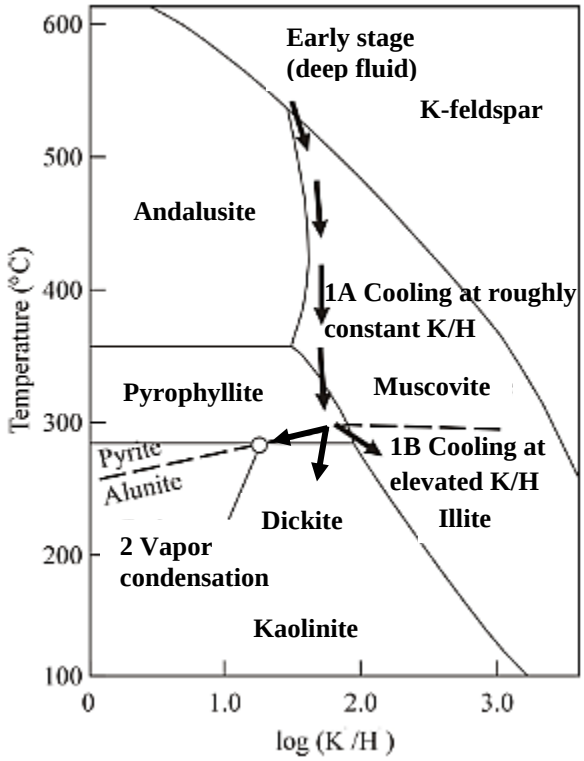

Figure 5.39. Temperature-log (K/H) diagram showing the stabilities of Al silicate minerals at quartz saturation (from Jones and Hemley, 1964; Hemley et al., 1969; adapted from Wantanabe and Hedenquist, 2001; Masterman, 2003; Hedenquist 2015). At high water to rock ratios, the fluid cools from muscovite-stable to pyrophyllite-stable (path 1A). Muscovite is replaced by pyrophyllite on cooling (the transition upward) where log (K/H) ratios increase during fluid evolution (path 1B). Pyrophyllite occurs with alunite, dickite and kaolinite at shallow levels where log (K/H) ratios are low due to condensation of magmatic vapours into ground water to produce an acidic solution at temperatures < 250 - 300°C (path 2).

Pyrophyllite that occurs with alunite, dickite and kaolinite at shallow levels in Tumpangpitu (Figs. 5.2, 5.3, 5.26 and 5.29) is inferred to have formed where magmatic vapours condensed into ground water to produce an acidic solution at temperatures around 300º to 250 ºC (path 2; Fig. 5.39). Hypogene muscovite occurs in the deep, high temperature parts of the porphyry system, whereas pyrophyllite is stable in both the porphyry and epithermal alteration zones (Fig. 5.3). Path 2 is a distinctly different fluid from path 1, the former created by vapor (separated from the brine at depth) condensing into groundwater (Hedenquist, pers. comm. 2017). Both paths 1 and 2 (Fig. 5.39) are inferred to have occurred at Tumpangpitu, probably with considerable overlap of the two pathways in the zone of juxtaposition, where epithermal mineralization has overprinted porphyry mineralization associated with extensive quartz - pyrophyllite alteration (Fig. 5.3).

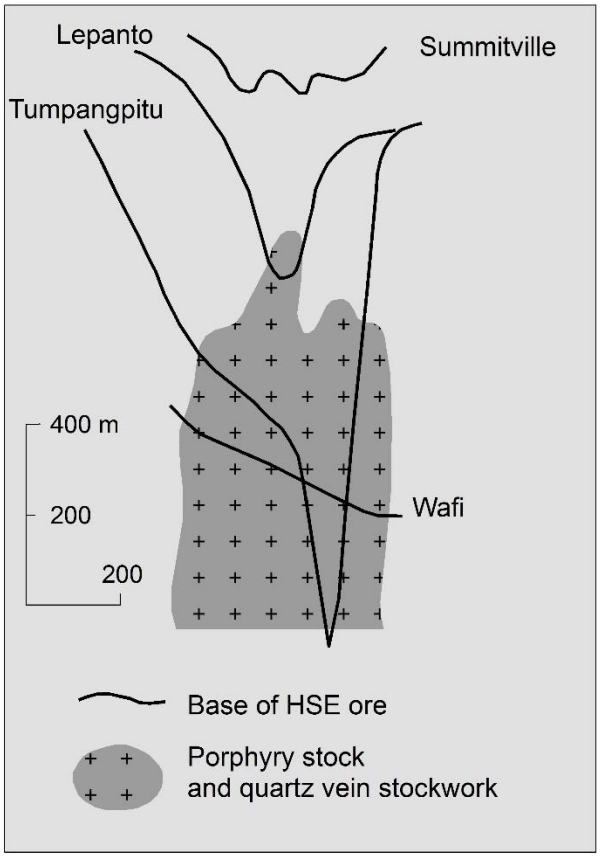

Figure 5.40. Schematic model comparing the base of high-sulfidation (HS) ore with respect to the underlying porphyry stock and the associated quartz vein stockwork at a selection of hybrid porphyry-epithermal deposits (modified from Sillitoe, 1999).

5.13.8.2 Sulfide transitions in the telescoped zone

Advanced argillic alteration at Tumpangpitu has overprinted quartz - magnetite alteration and associated porphyry stockwork veining, converting magnetite to hematite and pyrite over a vertical interval of more than 1 km (Figs. 5.3, 5.25 and 5.40). Chalcopyrite has been replaced by pyrite during quartz - muscovite alteration (Fig.5.14D). Bornite, digenite, chalcocite and covellite with pyrite replaced chalcopyrite during advanced argillic alteration (Figs. 5.11, 5.26 - 5.28 and 5.30). Similar sulfide transitions have been documented from other hybrid high-sulfidation epithermal-porphyry deposits, including El Salvador (Gustafson and Hunt, 1975), Wafi-Golpu, PNG where advanced argillic alteration has overprinted 200 m onto the top of the porphyry stockwork (Fig. 5.40; Sillitoe, 1999), Caspiche, Chile (Sillitoe et al., 2013) and at the Calaorco Au-HSE deposit and La Arena Cu-Au porphyry deposit, Peru (Garay et al., 2012). Covellite occurs at Tumpangpitu as exsolution lamellae with pyrite, interpreted to be eutectoid intergrowths (Fig. 5.28). Covellite has partially replaced pyrite growth bands, and grain boundaries between luzonite, tennantite-tetrahedrite, pyrite and chalcopyrite (Figs. 5.19, 5.27, 5.28, 5.30, A2-2E, A2-4 and A2-7B). The modes of occurrence of covellite as veinlets cutting chalcopyrite and as

replacements along grain boundaries suggests that it is paragenetically the latest-formed copper sulfide. Evidence for hypogene upgrading of the original porphyry ore zones during the advanced argillic overprint is provided by the Cu ore grade contours on Figure 5.34. Complex sulfide transitions are present in the zone where Cu and Sn-sulfosalts overprinted the porphyry-related sulfides. Chalcopyrite was converted sequentially through bornite and chalcocite to covellite (Figs. 5.26, 5.28 and 5.30). Petrographic, SEM and EPMA analysis have documented chalcopyrite as lamellar intergrowths with covellite (Fig. 5.28A) and covellite and pyrite directly replacing chalcopyrite (5.28B).

5.13.8.3 Molybdenite coexisting with advanced argillic alteration

The occurrence of molybdenite in rocks altered to pyrophyllite, alunite, dickite and hypogene kaolinite (Fig. 5.29) is unlikely to have occurred by the re-mobilization of molybdenite from the porphyry (B-stage quartz veins) into the lower levels of the epithermal system. Another interpretation could be that molybdenite precipitated from a vapour phase with alunite and pyrophyllite (e.g., So et al., 2010). Alternatively, the molybdenite could be relict from the potassic stage.

5.13.8.4 Spatial distribution of intermediate-sulfidation epithermal mineralization

Intermediate-sulfidation veins containing tetrahedrite - tennantite and chalcopyrite associated with low temperature alteration assemblages of illite and carbonate typically form outside of a lithocap (e.g., Sillitoe, 2013). At Tumpangpitu, tennantite-tetrahedrite is commonly disseminated throughout the host rock of the Tumpangpitu lithocap, forming halos to high-sulfidation feeder structures, as well high-grade (up to 2 g/t Au, 20 g/t Ag) banded sulfide veins along the same structures that host HSE mineralization (Figs. 5.3 - 5.4). Petrographic evidence for tennantite-tetrahedrite directly overprinting enargite (Figs. 5.30 and A2-4). Most of the ISE mineralization at Tumpangpitu formed within the lithocap and is associated with pyrophyllite, dickite, kaolinite and illite, and have commonly overprinted HSE veins.

Many porphyry deposits along the Sunda Banda arc with intact overlying high-sulfidation mineralized lithocaps exhibit the temporal evolution from porphyry-style mineralization, overprinted by HSE mineralization, in turn overprinted by ISE mineralization (e.g., Elang, Sumbawa, Maryono et al., 2017; Selodong, SW Lombok, Rompo et al., 2012). At Batu Hijau and Elang on Sumbawa, and at Wonogiri in central Java, late epithermal mineralization has a strong structural control and tetrahedrite-tennantite mineralization has crosscut porphyry mineralization at depth. In these examples, high-sulfidation mineralization is preserved at upper levels in lithocaps that have not completely been eroded (e.g., at Elang; Garwin, 2000; Maryono et al., 2012; Maryono et al., 2017).

5.13.9 Duration of hydrothermal activity at Tumpangpitu

Geochronologic data from ^{40}Ar-^{39}Ar dating of alunite (4.385 ± 0.0049 Ma; 2σ error) and Re-Os dating of molybdenite (4.303 ± 0.018 Ma; 2σ error) has defined a short time period between the high-sulfidation epithermal and porphyry mineralization events. Field relationships have recorded high-sulfidation epithermal veins crosscutting porphyry stockwork veins that contain molybdenite. The short duration of hydrothermal activity requires rapid telescoping of near-surface high-sulfidation epithermal mineralization onto deep-seated porphyry mineralization at Tumpangpitu. Assuming that the phase 5 tonalite (5.40 ± 0.46 Ma to 4.27 ± 0.54; Table 4.5) was emplaced at a depth of ~ 2 km and uplifted to ~700 m below present day surface by the time of diatreme formation (2.7 ± 1.0 Ma; Table 4.5; Figs. 5.3 - 5.4), a conservative uplift rate of 0.3 km/yr is estimated if 4 m.y separates the two events. Faster rates would apply if the time period was less (Table 4.5). The large errors on the U-Pb age determinations for both the phase 5 tonalite and Tumpangpitu diatreme precludes refinement of the uplift rate. It is not possible to better constrain the uplift rates and depth of porphyry mineralization without fluid inclusion studies and more precise age determinations (e.g., ID TIMS).

5.13.10 Age and duration of hydrothermal events at Tumpangpitu

There are paragenetic reversals of some vein types at Tumpangpitu. For example, quartz - magnetite (M2) veins mostly crosscut magnetite-only (M1) veins, but some M1 veins crosscut M2 veins locally (Fig. 5.9B). Similar reversals in vein crosscutting relationships have been documented at Batu Hijau and Elang (Garwin, 2000; Maryono et al., 2012). A likely explanation is multiple pulses or injections of mineralization over relatively short ore-forming periods, characteristic of the Late Miocene nested tonalite porphyries of the Sunda Banda arc. Three different phases of tonalite porphyries (Old, Intermediate and Young Tonalite) have been defined by crosscutting relationships at Batu Hijau (Clode et al., 1999) and Charlie, Delta and Echo tonalite at Elang in Sumbawa (Maryono et al., 2005), each with different metal budgets. Multiple tonalite phases have also been defined at Brambang, Lombok and Hu'u in Sumbawa (Rompo et al, 2012; Maryono et al., 2015). Garwin (2000) and Maryono et al. (2017) dated individual tonalite phases at Batu Hijau and Elang respectively, however the resolution of the U-Pb technique is not sufficient to produce absolute ages that conform to the crosscutting relationships observed in the field.

Porphyry Au-Cu systems are characterized by multiple magmatic events and hydrothermal pulses that may persist for several million years and consist of numerous short-lived hydrothermal pulses that generally last on the order of 50,000 to 100,000 yr (Arribas et al., 1995; Henry et al., 1997; Garwin, 2000; Muntean and Einaudi, 2001; Ossandón et al., 2001; Padilla Garza et al., 2001; Seedorff et al., 2005). When compared to the duration of mineralization at other porphyry deposits e.g., long-lived mineralization at Los Pelambres, Chile (at least 1.85 m.y as determined by vein crosscutting relationships and Re/Os age

determinations; Stein, 2014) and short-lived hydrothermal systems ranging from 100,000 to 300,000 yrs (e.g., El Teniente pulses of < 100,000 years, separated by gaps of up to 300,000 years; Re/Os determinations; Spencer et al., 2015); Lihir, Papua New Guinea, (Carman et al., 2003) and FSE-Lepanto, Philippines (Hedenquist et al., 1998), Tumpangpitu fits into the short lived category. Hydrothermal activity associated with mineralization at Tumpangpitu has been constrained by U-Pb age determinations from syn- to late mineralization porphyries that were emplaced between 5.40 ± 0.46 and 3.94 ± 0.69 Ma. Re/Os and Ar/Ar geochronological age determinations from Tumpangpitu suggest that pulses of magmatism were short lived, and U/Pb age determinations from mineralized tonalites suggest porphyry mineralization persisted over at least 1.91 m.y. Volcanic-hydrothermal activity associated with the Tumpangpitu diatreme occurred during epithermal mineralization (diatreme matrix zircon age of 2.7 ± 1.0 Ma). Clasts of high-sulfidation state mineralized rocks are a minor, but significant, component of the diatreme, and late-stage epithermal veins cutting the diatreme, demonstrate an inter-mineralization timing with respect to epithermal activity in the district, implying that epithermal mineralization continued intermittently for 1 to 1.5 m.y. after porphyry mineralization ceased at Tumpangpitu.

Tumpangpitu (U/Pb ages: 5.4 ± 0.46 Ma to 4.03 ± 0.65 Ma) and Pulau Merah (U/Pb age: 3.98 ± 0.21 Ma), cannot be distinguished on the basis of radiometric age determinations. They are interpreted to be cogenetic, with telescoping of the two environments caused by rapid uplift and exhumation, with ridge subduction being a major geodynamic factor in uplift during this period (e.g., Cooke et al., 2005; Cooke et al., 2011; Hollings et al., 2011). Crosscutting relationships between porphyry and epithermal veins observed at both Tumpangpitu and Pulau Merah imply that the evolution of porphyry-style to multiple events of both high-sulfidation and intermediate-sulfidation style mineralization contributed to their rich metal endowment.

5.13.11 Potential metal sources

Features that distinguish Tumpangpitu from other porphyry deposits along the Sunda Banda arc, such as Selodong, Lombok (Rompo et al., 2012) Batu Hijau and Elang, Sumbawa (Garwin, 2000; Maryono et al., 2012, 2017), include a lack of actinolite in the inner propylitic alteration zone, abundant molybdenite and Sn-bearing sulfosalts in the high-sulfidation ores. The presence of Sn sulfosalts, and the abundance of molybdenite at Tumpangpitu, could indicate a significant crustal contribution to the melts. These features indicate an increased contribution from continental source rocks over oceanic crustal sources. Additional radiogenic isotope data would provide useful data and additional insights into the degree of fluid contribution from oceanic or continental source rocks. (U-Th)/He thermochronometry on apatite would provide insights into the rate of exhumation of the deposit.

5.14 Conclusions

Au-Cu-Mo porphyry-style mineralization at Tumpangpitu is associated with quartz vein stockworks and disseminations of chalcopyrite and bornite overprinted by hypogene chalcocite and covellite. These formed in the upper portions of a nested tonalite porphyry intrusive complex. A progression in alteration has been observed from a central domain of quartz - magnetite - biotite - K-feldspar associated with high grade porphyry mineralization, laterally outwards through minor actinolite - chlorite, to epidote - chlorite and then calcite - chlorite. Structurally controlled quartz - muscovite alteration overprinted quartz - magnetite alteration.

High-sulfidation mineralization at Zones A, B and C occurs in vuggy quartz - alunite ridges surrounded by halos of quartz - dickite - kaolinite, illite - montmorillonite/nontronite ± kaolinite ± chlorite and chlorite - calcite ± epidote alteration, with decreasing quartz content away from the central vuggy quartz - alunite zones. Quartz - alunite - dickite assemblages are dominant at shallower levels in the epithermal system and quartz - pyrophyllite ± diaspore ± topaz at deeper levels.

Fault-controlled high-sulfidation state enargite ± covellite ± bornite HSE-1 and HSE-2 veins were overprinted by intermediate-sulfidation state tetrahedrite - tennantite - chalcopyrite ISE-1. Sn-bearing sulfosalts overprinted all epithermal and porphyry vein stages. These epithermal features overprinted porphyry mineralization at deeper levels of the system (below 280 m bsl to more than 1,200 m bsl), with complex sulfide overprinting relationships and hypogene upgrading at the interface between the porphyry and epithermal domains. Sphalerite and galena in ISE-2 veins comprise the final hypogene event of mineralization and form a concentric halo within and around epithermal and porphyry mineralization at Tumpangpitu.

Geochronological data from ^{40}Ar-^{39}Ar dating of alunite (4.385 ± 0.049 Ma) and Re-Os dating of molybdenite (4.303 ± 0.018 Ma) has defined a short time period between the high-sulfidation epithermal and porphyry mineralization events respectively. The ages of mineralization are in accordance with U-Pb age determinations from the Tumpangpitu mineralized intrusive complex, from 4.89 ± 0.40 Ma (phase 4 tonalite) to 4.03 ± 0.65 Ma (phase 6 tonalite). Absolute age determinations confirm cross-cutting relationships observed in the field (Fig 5.3), consistent with a genetic association between the Tumpangpitu porphyry complex and overlying high and intermediate-sulfidation epithermal deposits.

Chapter 6: Sulfur Isotope Geochemistry

6.1 Introduction

This chapter presents sulfur isotopic data on sulfides and sulfates from epithermal and porphyry mineralization at Tumpangpitu. This dataset is used to investigate temporal and spatial variations in isotopic compositions in order to evaluate potential ore depositional mechanisms. In combination with geochronological data (Chapters 4 and 5), and spectral parameters from alunite, the sulfur isotope data are used to evaluate the link between high-sulfidation epithermal and porphyry mineralization. These datasets are also used to assess whether they can be used as vectors towards porphyry and/or epithermal mineralization, which could potentially provide additional exploration tools to aid in the discovery of new porphyry and epithermal deposits in the Tujuh Bukit region.

6.2 Background

Reactions involving oxidation-reduction of sulfur compounds are known to produce isotopic fractionation (> 0.2 % of the S^{32}/S^{34} ratio) if equilibrium or partial equilibrium is achieved (Ault and Kulp, 1960). The principal applications of sulfur isotope analyses have been to determine the sources of sulfur, temperature of deposition among coexisting (contemporaneously deposited) minerals of sulfide ores from magmatic-hydrothermal fluids, and processes of ore formation (e.g., Rye, 2005). Sulfur may be present in fluids as any one of several species. Since isotope fractionation depends on bond strength, the predicted order of S enrichment is: $SO_4^{2-} > SO_3^{2-} > SO_2 >$ SCO $> S_x \sim H_2S \sim HS^{1-} > S^{2-}$ (Ohmoto and Rye, 1979). The spatial and temporal variations of $\partial\,^{34}S$ values have been used to trace fluid sources that precipitated sulfides, sulfates and metals in hydrothermal ore deposits. These data can help constrain likely ore-forming processes and the geometry of the magmatic-hydrothermal system (e.g., Ohmoto, 1972; Ohmoto and Rye, 1979, Ohmoto and Goldhaber, 1997).

Porphyry copper systems typically have sulfide $\partial\,^{34}S$ values near zero (± 5‰; e.g., Sasaki et al., 1984; Ohmoto and Rye, 1979; Ohmoto and Goldhaber, 1997). High-sulfidation epithermal systems can have sulfate $\partial\,^{34}S$ values from ~ 0 to > 30 ‰ (e.g., Hedenquist and Garcia, 1990; Rye et al. 1992; Cooke et al. 2011). SO_2 and H_2S are the predominant sulfur species in high temperature (> 350° to 400°C) magmatic-hydrothermal fluids. At temperatures below 350° to 400°C, SO_4^{2-} becomes the predominant oxidized sulfur species. Under oxidizing condition ($SO_4/H_2S > 1$), the ^{34}S isotope will preferentially fractionate into the oxidized sulfur species (Ohmoto and Goldhaber, 1997) resulting in a strong shift towards higher ^{34}S values for precipitation of sulfate minerals at lower temperatures, such as alunite, jarosite and barite. Sulfide species precipitating from the oxidized fluid will be enriched in ^{32}S and have low $\partial\,^{34}S$ values (Rye et al.,

1993). Variations in the redox state of the fluid have been interpreted to explain variations of $\partial^{34}S_{sulfide}$ values reported from porphyry copper deposits at El Salvador, Chile, (Field and Gustafson, 1976); Cadia, central New South Wales, Australia (Harper, 2000; Wilson, 2003; Wilson et al. 2007), El Teniente, Chile (Cannell, 2004) and Dinkidi, Philippines (Wolfe and Cooke, 2011). Variations in $\partial^{34}S_{sulfate}$ values from high-sulfidation epithermal gold and related porphyry deposits have been documented at Lepanto, Philippines (Hedenquist and Garcia, 1990); Pascua-Lama, Argentina (Deyell et al., 2005) and in the Baguio district of the Philippines (Cooke et al., 2011).

6.3 Methodology

In this study a total of 45 sulfur isotope analyses were conducted on 2.5 x 5 cm petrographic offcuts, mainly from type section 11060 mN (Fig. 6.6). Samples were chosen from mineralized and non-mineralized rocks from both the high-sulfidation epithermal and porphyry mineralized zones at Tumpangpitu (Figs. 6.1, 6.2 and 6.6). Pyrite, alunite and jarosite were the principal minerals analyzed from several of the major high-sulfidation epithermal veins, and from hydrothermal breccias from oxide zones A, B and C at Tumpangpitu (Fig. 6.6). These three minerals are the most abundant sulfur-bearing phases in the epithermal zone and can provide insights into the physiochemical conditions and mechanisms of sulfide and sulfate deposition (e.g. Ohmoto and Rye, 1979). Paragenetic stages of alunite were documented based on relative timing (crosscutting relationships) with respect to the Tumpangpitu diatreme (HSE-1; pre-diatreme; HSE-2: syn-diatreme; HSE-3; post-diatreme). Additional samples of ore-stage massive disseminated enargite with vuggy quartz (Fig. 6.1A, B), coarse (0.5 - 1 cm) euhedral crystalline laths of barite ± anhydrite (Fig. 6.1C) and native sulfur were also analyzed from the high-sulfidation epithermal zone.

In the porphyry zone, pyrite and chalcopyrite were sampled for sulfur isotopic analysis from both vein and disseminations from proximal potassic altered rock (quartz - magnetite - biotite ± K-feldspar) and distal propylitic (chlorite - calcite ± epidote) altered host rock. In the supergene zone, jarosite was sampled for sulfur isotopic analysis.

Analyses were conducted on 24 sulfate samples (alunite, jarosite, and barite ± anhydrite), 20 sulfide samples (chalcopyrite, pyrite, enargite) and one sample of native sulfur from a total of 37 samples from 17 diamond drillholes at Tumpangpitu. Samples were chosen predominantly from section 11060 mN (Fig. 6.6), in order to investigate the spatial variations of the sulfide and sulfate $\partial^{34}S$ values with respect to the buried tonalite porphyry complex at Tumpangpitu. One co-existing sulfide - sulfate pair of pyrite-alunite was analyzed from the high-sulfidation zone, where textural evidence from microscopic analysis (Chapter 5) indicated that both sulfate and sulfide coexist in textural equilibrium.

6.3.1 Analytical methods

Pure sulfide and sulfate phases were identified, documented and imaged using optical ± SEM and microprobe analysis at CODES (Centre of Excellence in Ore Deposits) and the CSL (Central Science Laboratory), University of Tasmania, Australia (Figs. 6.1, 6.2; Chapter 5). Sulfur isotope compositions were analyzed on mineral separates drilled from samples of pure (> 90 %) coarse-grained sulfide and sulfate minerals amenable to hand drilling (Fig. 6.1A). These were analyzed using the conventional techniques of Robinson and Kusakabe (1975) and described by Ohmoto and Goldhaber (1997). The alunite and jarosite were sampled from massive monomineralic occurrences of the minerals as disseminations or veins (Fig. 6.1D), and barite was hand-picked from monomineralic veins where it was present as coarse crystals (Fig. 6.1C). Analyses of six samples of jarosite (10-43001-05a, 10-43001-05b, 11-43001-06, 12-43001-09a, 12-43001-09b and 13-43001-16) were repeated because the amount of sulfur was too low to be measured reliably. They were repeated in a second batch of analyses using approximately ten times the weight of the first batch (Table 6.1).

Between 0.10 to 4.91 mg of powdered mineral separates were weighed in tin capsules and analyzed for isotopic compositions using flash combustion isotope ratio mass spectrometry (varioPYRO cube coupled to Isoprime100 mass spectrometer) at the CSL, University of Tasmania. The SO_2 produced during combustion was collected in a trap, then fed into the mass spectrometer and measured against an SO_2 reference gas. Stable isotope abundances are reported in delta (∂) values as the deviations from conventional standards in parts per mil (‰) from the following equation:

A) $\partial\,^{34}S\ (‰) = [(R_{sample}/R_{standard} - 1) \times 1000]$

where R = the ratio $^{34}S/^{32}S$. The results are expressed in standard $\delta^{34}S$ per mil (‰) notation, relative to the Canyon Diablo Troilite (CDT). International reference standards including sphalerite (NBS-123; $\delta^{34}S$ = +17.44 ‰), Ag_2S (IAEA-S-1; $\delta^{34}S$ = -0.3 ‰, IAEA-S-2; $\delta^{34}S$ = +22.66 ‰ and IAEA-S-3; $\delta^{34}S$ = -32.3 ‰), sulfur (Soufre de Lacq; $\delta^{34}S$ = +16.9 ‰), barite, $BaSO_4$ (IAEA-SO-5; $\delta^{34}S$ = +0.48 ‰, IAEA-SO-6; $\delta^{34}S$ = -34.1 ‰ and NBS-127; $\delta^{34}S$ = +20.32 ‰) with known isotopic compositions, together with SO_2 reference gas ($\delta^{34}S$ ~ CDT), were measured for instrument calibration after every sixth sample. The analytical performance of the instrumentation, drift correction and linearity performance were calculated from the repetitive analysis of these standards. Analytical uncertainties for all analyses are estimated at 0.2 ‰. All results are listed in Tables 6.1, 6.2 and summarized in Figures 6.4 to 6.7.

6.3.2 SWIR and vis-NIR analysis

All forty-five samples selected for sulfur isotope analysis were also analyzed by vis-NIR and SWIR spectral analysis using a TerraSpec analytical spectral device at CODES, University of Tasmania. Each spectrum was interpreted manually by the author using TSG Pro (The Spectral Geologist professional) software

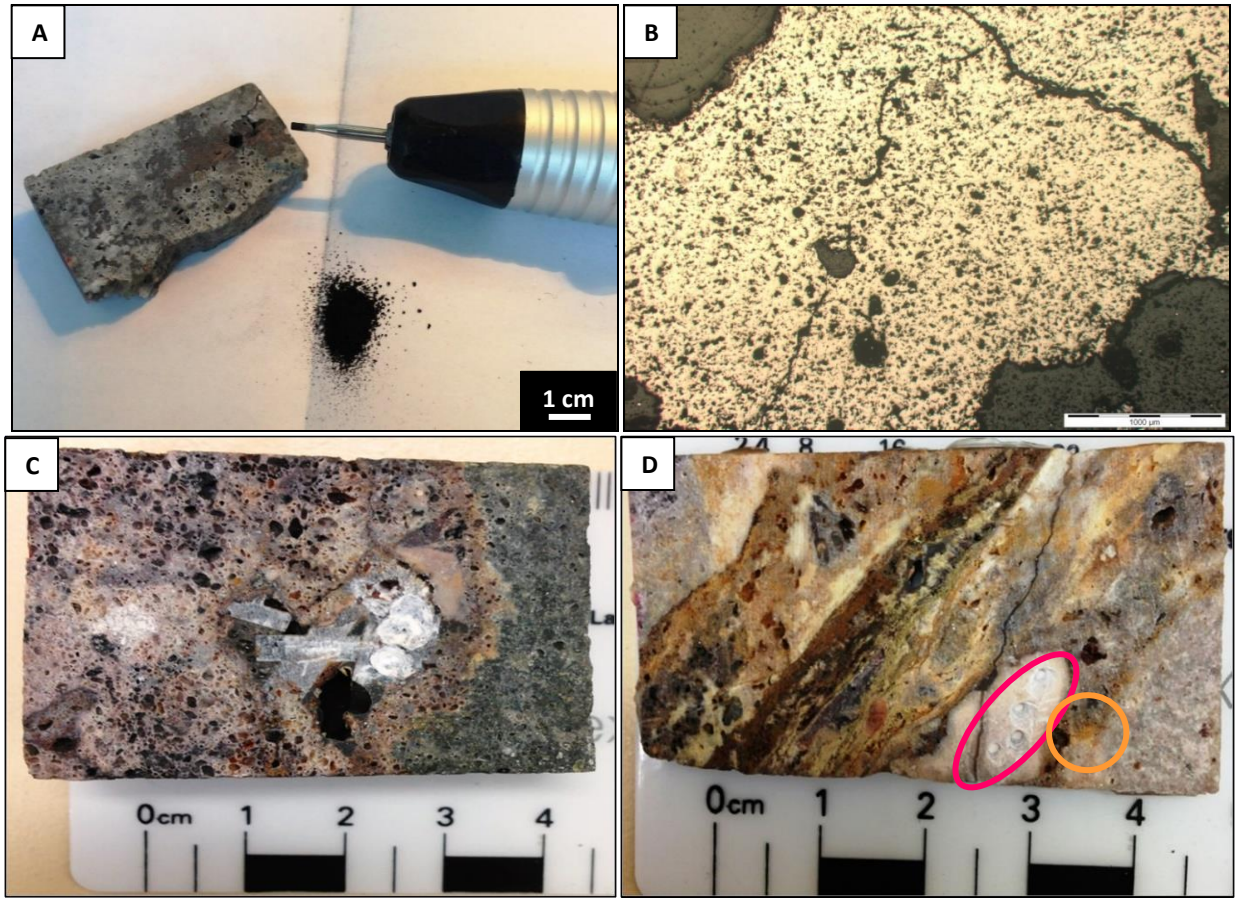

Figure 6.1. Examples of samples of sulfides and sulfates analyzed for sulfur isotopic compositions from the sulfide and oxide high-sulfidation epithermal zones at Tumpangpitu. All sample data listed in Table 6.1.

A) *Sample 1-43005.04, drillhole GTD-09-78/53 m, 174984 mE, 9045284 mN, elevation 344 m*. Sample of vuggy quartz and massive enargite showing sampled area of enargite and hand drill.
B) Reflected light photomicrograph of sample A; 2.5x magnification of single phase massive enargite.
C) *Sample 21-43002.23, drillhole GTD-012/110.2 m, 174494 mE, N9046597 mN, elevation 442 m.* Hand specimen of cavity infilled with coarse barite and partially preserved anhydrite.
D) *Sample 24-43002.27, drillhole GTD-012/298 m, 174494 mE, N9046597 mN, elevation 442 m.*. Hand specimen showing sampled areas of alunite (pink ovoid) and jarosite (orange circle) from oxidized high-sulfidation vein crosscutting phase 2 diorite.

and a library of reference spectra from TSG and +1000 reference spectra from the United States Geological Survey spectral database (USGS, 2013). Vis-NIR analysis was conducted on reflectance spectra and SWIR analysis on normalized hull quotient spectra. The aims of the spectral analysis were threefold:

1) Determine the alteration mineral species from SWIR spectra
2) Determine the iron oxide species from vis-NIR and SWIR spectra (jarosite, hematite and goethite)
3) Determine the wavelength of alunite (K-alunite < 1480 nm; K-Na-alunite = 1480 to 1485 nm; Na-K alunite = 1485 to 1490 nm; Na-alunite = > 1490 nm; Pontual et al., 2011)

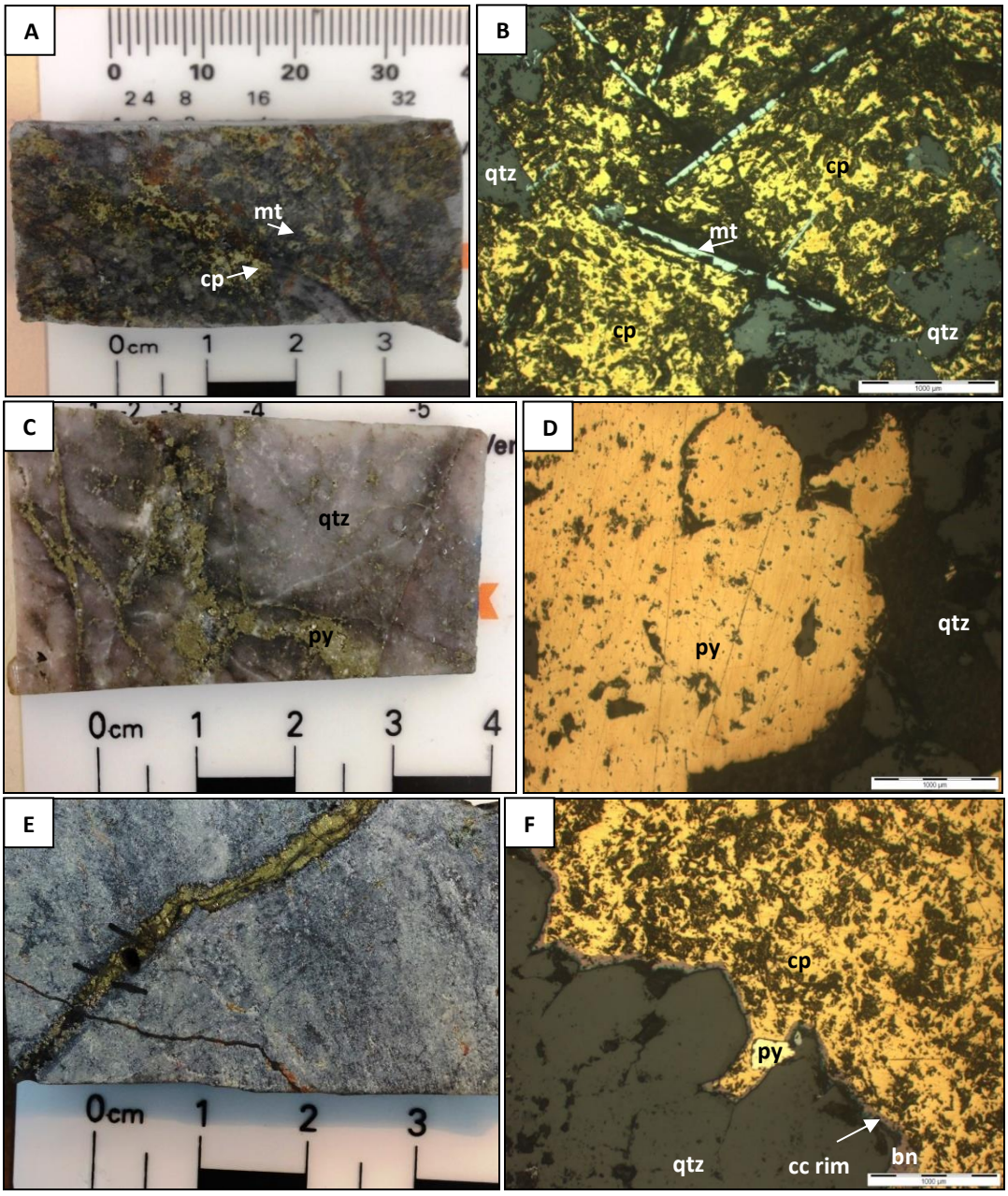

Figure 6.2. Samples of sulfide phases from porphyry mineralization at Tumpangpitu. All sample data listed in Table 6.2. Abbreviations: bn = bornite, cc = chalcocite, cp = chalcopyrite, mt = magnetite, py = pyrite, qtz = quartz.

A) *Sample 30-43003.05, drillhole GTD-08-29/600.20 m, 173574 mE, 9045837 mN, elevation 128 m*. Hand specimen of chalcopyrite associated with magnetite in phase 6 tonalite porphyry.
B) Reflected light photomicrograph of photo A; 20 x magnification; pure chalcopyrite grain with laths of magnetite
C) *Sample 32-43003.25, drillhole GTD-08-35/726.42 m, 174080 mE, 9046551 mN, elevation 257 m.* Hand specimen of pyrite veins from zone of quartz flooding.
D) Reflected light photomicrograph of photo C; 20 x magnification, pyrite as single sulfide phase.
E) *Sample 5-43006.55, drillhole GTD-10-138/886.75 m, 174149 mE, N904609 mN, elevation 266 m.* Early pyrite veined re-opened by chalcopyrite C vein with bornite - chalcocite margins in bedded sandstone with quartz - magnetite - biotite - chlorite alteration.
F) Reflected light photomicrograph of photo E; 10 x magnification (pure phase chalcopyrite interior sampled).

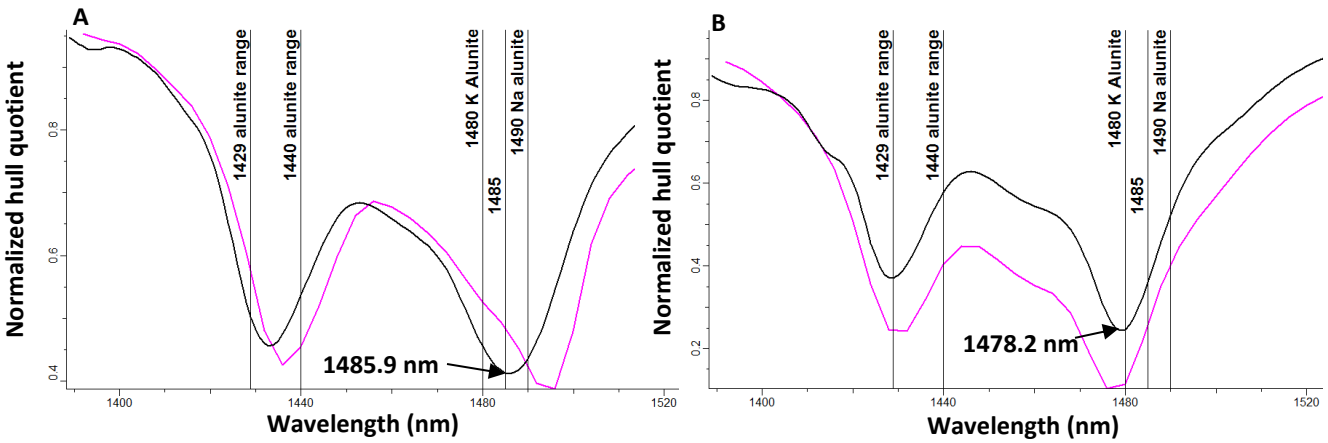

Figure 6.3. SWIR spectra from alunite samples from Tumpangpitu submitted for sulfur isotope analysis.

A) *Sample 23-43002.26*. SWIR spectrum (black line) of Na-K alunite with absorption feature positioned at 1485.9 nm with Na-alunite reference spectrum (pink line).
B) *Sample 29-43002.33*. SWIR spectrum (black line) of K-alunite with absorption feature positioned at 1478.2 nm with K-alunite reference spectrum (pink line).

All spectral data are documented in Table 6.1 and examples of wavelength values from alunite illustrated in Figure 6.3.

6.4 Results

6.4.1 Sulfur isotopic compositions

Sulfur isotopic results are documented in Tables 6.1 to 6.2 and illustrated in Figures 6.4 to 6.7. Of the 45 analyses, 24 were conducted on sulfates, including 13 on alunite, 9 on jarosite and 2 on barite ± anhydrite. A total of 21 analyses were conducted on sulfides, including 6 on pyrite and 5 on chalcopyrite both from the porphyry mineralized zone. Sulfides from the high-sulfidation epithermal veins, disseminations and fracture fills included eight analyses of pyrite and one of enargite. One analysis of medium-grained (> 2 mm) crystals of native sulfur from cavities in vuggy quartz - alunite altered rock was also acquired.

The $\delta^{34}S_{CDT}$ values of the sulfates range from -1.8 to 26.2 ‰. The $\delta^{34}S_{CDT}$ values for alunite range from 17.7 to 26.2 ‰ with a median value of 23.4 ‰. A large and overlapping range of -1.8 to 22.2 ‰ was found for jarosite. This range has been split into two; a low $\delta^{34}S$ range (Jarosite - 1) of -1.8 to 7.3 ‰ with a median value of 2.9 ‰ and a high $\delta^{34}S$ range (Jarosite - 2) of 16.9 to 22.2 ‰ with a median value of 19.7 ‰. Two samples of barite ± anhydrite have values of 22.5 to 22.7 ‰, with a median value of 22.1 ‰. The native sulfur sample returned a value of -2.8 ‰. The $\delta^{34}S$ values of the sulfides range from - 8.4 to 2.2 ‰; -8.4 to 1.3 ‰ for epithermal-related pyrite with a median value of -1.7 ‰; - 5.3 ‰ for one sample of enargite; 0.7 to 2.2 ‰ for porphyry-related pyrite; with a median value of 1.5 ‰ and -2.2 to 2.0 ‰ for chalcopyrite from porphyry stockwork veins with a median value of 0.4 ‰ (Tables 6.1 and 6.2, Fig. 6.4).

Table 6.1. Sulfur isotope data as per mil values relative to CDT for samples of epithermal vein and breccia-hosted mineralization from Tumpangpitu.

Sample ID	Coordinates /elevation (m)	Lithology	Alteration minerals	Alunite λ (nm)	Oxidation/ Fe oxide	Description/paragenetic stage	Weight (mg)	$\delta^{34}S_{raw}$	$\delta^{34}S_{CDT}$
Alunite									
17-43002.12	174670E/ 9045452N/379	Diatreme breccia	Vuggy quartz + K-Na-alunite	1482	COX/ hematite - goethite	Coarse rosettes of white and pink alunite (HSE-2)	1.3	20.7	26.2
16-43002.11	174670E/ 9045452N/379	Diatreme breccia	Vuggy quartz + K-Na-alunite	1482	COX/ hematite	Fine-grained white alunite in matrix (HSE-2)	1.2	19.8	25.3
26-43002.29	174496E/ 9046108N/47	Phase 7 quartz diorite	Quartz + K-alunite	1479	COX/ goethite - hematite	Massive fine-grained white crystalline alunite vein (HSE-2)	1.1	21.0	24.5
2-43005.13b	173877E/ 9046141N/214	Tumpangpitu diatreme	Quartz + K-Na-alunite + dickite + kaolinite WX	1482	UNOX	Alunite - dickite vein crosscutting diatreme (HSE-3)	1.3	18.4	23.8
24-43002.27a	174494E/ 9046597N/442	Hydrothermal breccia	Quartz + K-alunite + pyrophyllite + Kaolinite-WX	1480	COX/ jarosite - hematite - goethite	Massive fine-grained patch of pink alunite (HSE-1)	1.2	20.3	23.8
28-43002.31a	174496E/ 9046108N/68.5	Hydrothermal breccia	Quartz + K-Na-alunite	1483	COX/hematite - goethite	Massive fine-grained white alunite in matrix (HSE-2)	1.1	20.2	23.6
29-43002.33	174496E/ 9046108N/116	Phase 7 quartz diorite	Quartz + K-alunite + Kaolinite-PX	1478	COX/ hematite - goethite	Pink crystalline alunite in matrix (HSE-2)	1.3	19.9	23.4
27-43002.30	174496E/ 9046108N/67	Hydrothermal breccia	Quartz + K-Na alunite	1484	COX/ hematite	Massive fine-grained white crystalline alunite in breccia matrix (HSE-2)	1.2	19.7	23.2
20-43002.22	174494E/ 9046597N/442	Volcanic breccia	Vuggy quartz + K-Na alunite + Kaolinite-PX	1483	COX/ hematite	Disseminated alunite in breccia matrix (HSE-1)	1.2	17.7	23.1
23-43002.26	174494E/ 9046597N/442	Diatreme breccia	Quartz + Na-K alunite	1486	COX/ hematite	Coarse crystalline alunite (HSE-2)	1.3	17.4	20.7
18-43002.14a	174315E/ 9046735N	Volcanic breccia	Quartz + K-Na-alunite		COX/ hematite	Pervasive alunite from matrix (HSE-1)	1.4	15.0	20.3
25-43002.28	174494E/ 9046597N/442	Hydrothermal breccia	Quartz + K-Na alunite	1481	COX/hematite - goethite	Massive fine-grained white crystalline alunite in vein halo (HSE-1)	1.3	15.5	18.7
22-43002.25b	174494E/ 9046597N/442	Diatreme breccia	Vuggy quartz + alunite		COX/ goethite - hematite	Alunite in matrix (HSE-2)	1.3	14.5	17.7

Table 6.1. *(Contd.)*

Sample ID	Coordinates / elevation (m)	Lithology	Alteration minerals	Alunite λ (nm)	Oxidation/ Fe oxide	Description/paragenetic stage	Weight (mg)	$\delta^{34}S_{raw}$	$\delta^{34}S_{CDT}$
Barite									
21-43002.23	174494E/ 9046597N/442	Diatreme breccia	Quartz + barite		SOX/ hematite - goethite	Cavity with barite and partially preserved anhydrite (HSE-1)	1.3	19.0	22.5
22-43002.25a	174494E/ 9046597N/442	Diatreme breccia	Vuggy quartz + alunite		COX/ goethite -hematite	Barite crystals along vein margin (HSE-2)	1.2	18.3	21.7
Jarosite									
28-43002.31b	174496E/ 9046108N/69	Hydrothermal breccia	Quartz + K-alunite	1481	COX/ jarosite -goethite -hematite	Jarosite veinlet with hematite	0.5	18.8	22.2
18-43002.14b	174315E/ 9046735N/25	Volcanic breccia	Quartz + K-Na-alunite	1485	COX/goethite - hematite - jarosite	Zone of jarosite adjacent to fracture	0.4	14.4	19.7
24-43002.27b	174494E/ 9046597N/442	Hydrothermal breccia	Quartz + K alunite-pyrophyllite + Kaolinite-WX	1486	COX/ jarosite -hematite -goethite	Massive patch of jarosite adjacent to alunite in oxidized vein	0.4	13.7	16.9
10-43001-05a	173823E/ 9045956N/277	Hydrothermal breccia	Vuggy quartz		COX/ goethite - jarosite	Massive jarosite after alunite surrounding vuggy quartz zone	4.9	4.4	7.3
10-43001-05b	173823E/ 9045956N/277	Hydrothermal breccia	Vuggy quartz		COX/ Goethite -jarosite	Massive jarosite after alunite surrounding vuggy quartz zone	4.8	2.8	5.6
12-43001-09a	173823E/ 9045956N/277	Phase 2 diorite	Vuggy quartz		COX/ Jarosite - hematite - goethite	Massive gossan HSE vein	4.6	1.0	3.8
12-43001-09b	173823E/ 9045956N/277	Phase 2 diorite	Vuggy quartz		COX/ Jarosite - hematite - goethite	Massive gossan HSE vein	4.7	-0.6	2.1
11-43001-06	173823E/ 9045956N/277	Phase 2 diorite	Vuggy quartz		COX/ Goethite - jarosite	Jarosite vein	4.6	-1.7	1.0
13-43001-16	173837E/ 9046060N/250	Hydrothermal breccia	Vuggy quartz + alunite		COX/ Jarosite - hematite - goethite	Massive gossan HSE vein	4.8	-4.4	-1.8
Sulfur									
9-43001.04	173823E/ 9045956N/277	Phase 7 quartz diorite	Vuggy quartz + alunite + kaolinite WX		COX/ goethite	Native sulfur in vuggy quartz cavities (HSE-1)	0.1	-2.2	2.8

Table 6.1. *(Contd.)*

Sample ID	Coordinates / elevation (m)	Lithology	Alteration minerals	Alunite λ (nm)	Oxidation	Description/paragenetic stage	Weight (mg)	$\delta^{34}S$ raw	$\delta^{34}S_{CDT}$
Pyrite									
19-43002.19	174315E/ 9046735N/482	Phase 2 diorite	Quartz + dickite		UNOX	Disseminated 1-2 mm grains of pyrite from matrix with dickite (HSE)	0.2	-3.6	1.3
7-43006.67	173503E/ 9046136N/203	Phase 7 quartz diorite	Quartz + pyrophyllite + diaspore		UNOX	Pyrite replacing hornblende (HSE)	0.2	-4.3	0.6
2-43005.13a	173877E/ 9046141N/214	Tumpangpitu diatreme	Quartz + K-Na-alunite + dickite + kaolinite WX	1482	UNOX	Alunite - dickite vein crosscutting diatreme breccia (HSE-3)	0.2	-4.7	0.2
6-43006.62	173503E/ 9046136N/203	Phase 7 quartz diorite	1) Quart + biotite + K-feldspar; 2) chlorite + illite;		UNOX	Pyrite replacing hornblende	0.3	-6.4	-1.6
3-43006.29	173877E/ 9046141N/214	Tumpangpitu diatreme	Quartz + kaolinite WX		UNOX	Late, euhedral cubes and hexagons of pyrite along fracture surface	0.2	-6.6	-1.8
15-43002.09	174537E/ 9046858N/337	Phase 2 diorite	Quartz + pyrophyllite + dickite + diaspore		UNOX	Disseminated pyrite (HSE)	0.2	-6.6	-1.8
8-43006.71	173595E/ 9046376N/107	Phase 7 quartz diorite	Quartz + dickite + kaolinite WX		UNOX	Pyrite replacing hornblende (HSE)	0.	-7.2	-2.4
14-43002.04	174537E/ 9046858N/337	Phase 2 diorite	1) Quartz + K-feldspar; 2) kaolinite-WX + illite		UNOX	Pyrite vein (D vein)	0.2	-13.1	-8.4
Enargite									
1-43005-04	174984E/ 9045284N/344	Dacite crystal lithic tuff	Vuggy quartz		UNOX	Massive enargite and vuggy quartz (HSE-1)	0.5	-10.0	-5.3

Abbreviations: CDT = Canyon Diablo Troilite, Kaolinite WX = hypogene kaolinite, Kaolinite PX = poorly crystalline kaolinite, HSE = high-sulfidation epithermal veins, HSE-1 = high-sulfidation epithermal stage 1 (pre-Tumpangpitu diatreme), HSE-2 = high-sulfidation epithermal stage 2 (syn-Tumpangpitu diatreme), HSE-3 = high-sulfidation epithermal stage 3 (post-Tumpangpitu diatreme), UNOX = unoxidized, SOX = strongly oxidized, COX = completely oxidized, WOX = weakly oxidized, he = hematite, go = goethite, ja = jarosite; all easting and northing coordinates are recorded for drillhole collar locations and elevation for downhole depths, λ = wavelength. Errors are ± 0.2 ‰.

Table 6.2 Sulfur isotope data as per mil values relative to CDT for samples of porphyry-style mineralization from Tumpangpitu.

Sample ID	Coordinates /RL (m)	Lithology	Alteration minerals	Oxidation	Description/paragenetic stage	Weight (mg)	$\delta^{34}S_{raw}$	$\delta^{34}S_{CDT}$
Pyrite								
34-43003.36	174512E/ 9046872N/338	Phase 5 tonalitic breccia	Quartz + pyrophyllite	UNOX	Quartz flooding with abundant pyrite along fractures	0.3	-0.	2.2
35-43004.09	173878E/ 9046141N/214	Phase 5 tonalitic breccia	1) Quartz + magnetite + biotite; 2) chlorite + illite	UNOX	Late coarse-grained pyrite along fracture surface	0.3	-0.9	1.8
36-43004.15	173878E/ 9046141N/214	Phase 6 tonalite	1) Quartz + magnetite + biotite; 2) chlorite + illite	UNOX	Late pyrite after magnetite along fracture surface	0.3	-1.2	1.5
37-43004.20	173878E/ 9046141N/214	Phase 6 tonalite	1) Quartz + magnetite + biotite; 2) hematite + chlorite + illite	UNOX	Disseminated pyrite after magnetite replaced by hematite	0.3	-1.3	1.3
32-43003.25	174080E/ 9046551N/257	Phase 5 tonalite	1) Quartz + biotite; 2) chlorite + illite	UNOX	Quartz flooding; abundant pyrite along fractures	0.3	-1.4	1.3
33-43003.35	174512E/ 9046872N/338	Andesite	1) Actinolite; 2) epidote; 3) calcite	UNOX	Pyrite replacing hornblende phenocrysts in propylitic halo	0.3	-1.9	0.7
Chalcopyrite								
5-43006.55	174149E/ 9046090N/266	Sandstone	1) Quartz + K-feldspar + biotite + magnetite; 2) chlorite + illite	UNOX	Chalcopyrite - bornite - chalcocite - covellite vein with pyrite margin; chalcopyrite interior of vein sampled	0.4	-2.9	2.0
4-43006.51	174149E/ 9046090N/266	Phase 5 tonalite	1) Quartz + magnetite + biotite; 2) chlorite + illite + hematite	UNOX	Quartz - magnetite - chalcopyrite porphyry vein stockwork, no pyrite; Chalcopyrite - anhydrite association	0.5	-4.0	0.9
31-43003.06a	173574E/ 9045837N/128	Phase 5 tonalite	1) Quartz + biotite; 2) chlorite + illite	UNOX	Chalcopyrite from magnetite - chalcopyrite vein crosscutting and offsetting quartz vein	0.6	-2.2	0.4
31-43003.06b	173574E/ 9045837N/128	Phase 5 tonalite	1) Quart + biotite; 2) chlorite + illite	UNOX	Duplicate of 31-43003.6a	0.5	-2.6	0.0
30-43003.05	173574E/ 9045837N/128	Phase 5 tonalite	Quartz + biotite + chlorite	UNOX	Quartz - magnetite - chalcopyrite vein with disseminated chalcopyrite halo	0.5	-4.7	-2.2

Abbreviations: CDT = Canyon Diablo Troilite, Kaolinite WX = hypogene kaolinite, UNOX = unoxidized, all easting and northing coordinates are recorded for drillhole collar locations and downhole depths. Errors are ± 0.2 ‰.

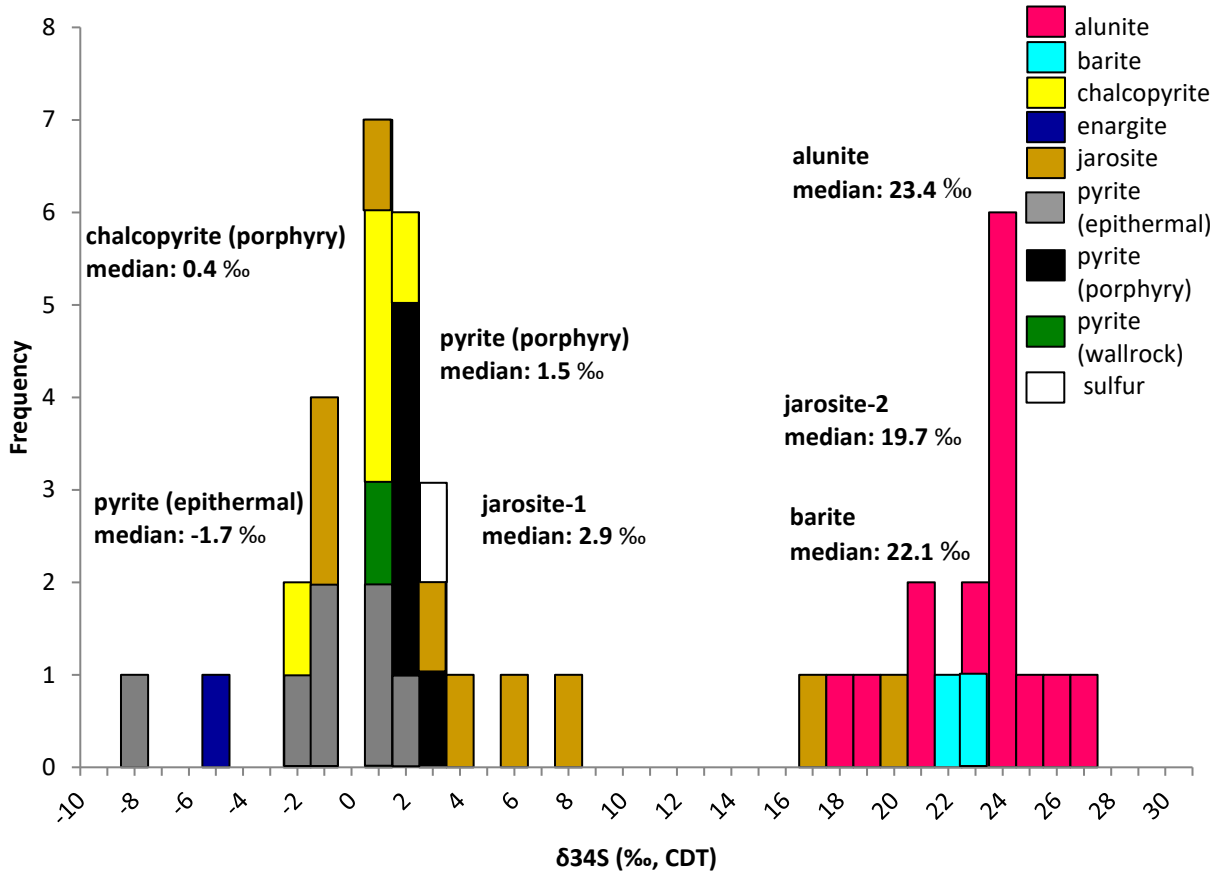

Figure 6.4. Histogram of $\delta^{34}S$ values for epithermal and porphyry-related minerals from Tumpangpitu. Note that one pyrite sample from propylitic altered wallrocks with very low $\delta^{34}S$ was not included in the median calculations, in order to highlight the correlation between $\delta^{34}S$ values of sulfides from the porphyry mineralized zone. All data presented in Tables 6.1 and 6.2.

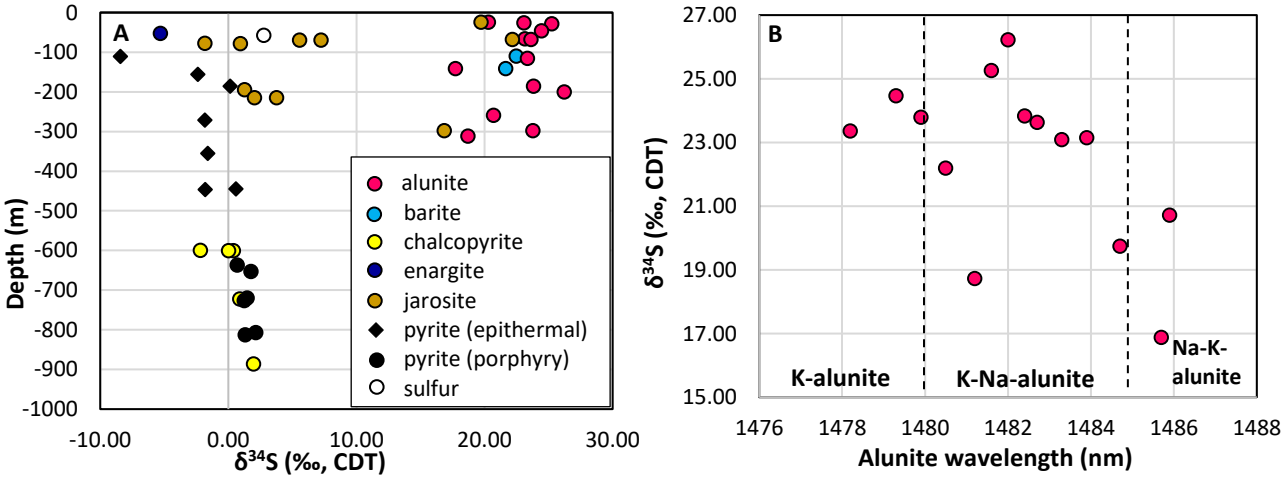

Figure 6.5. Relationships between $\delta^{34}S$ values (‰, CDT) of epithermal and porphyry vein samples, elevation and alunite wavelength at Tumpangpitu. All data listed in Tables 6.1 and 6.2.
A) $\delta^{34}S$ values plotted against drillhole downhole depth.
B) $\delta^{34}S$ values from alunites plotted against the alunite absorption feature position determined from SWIR analysis.

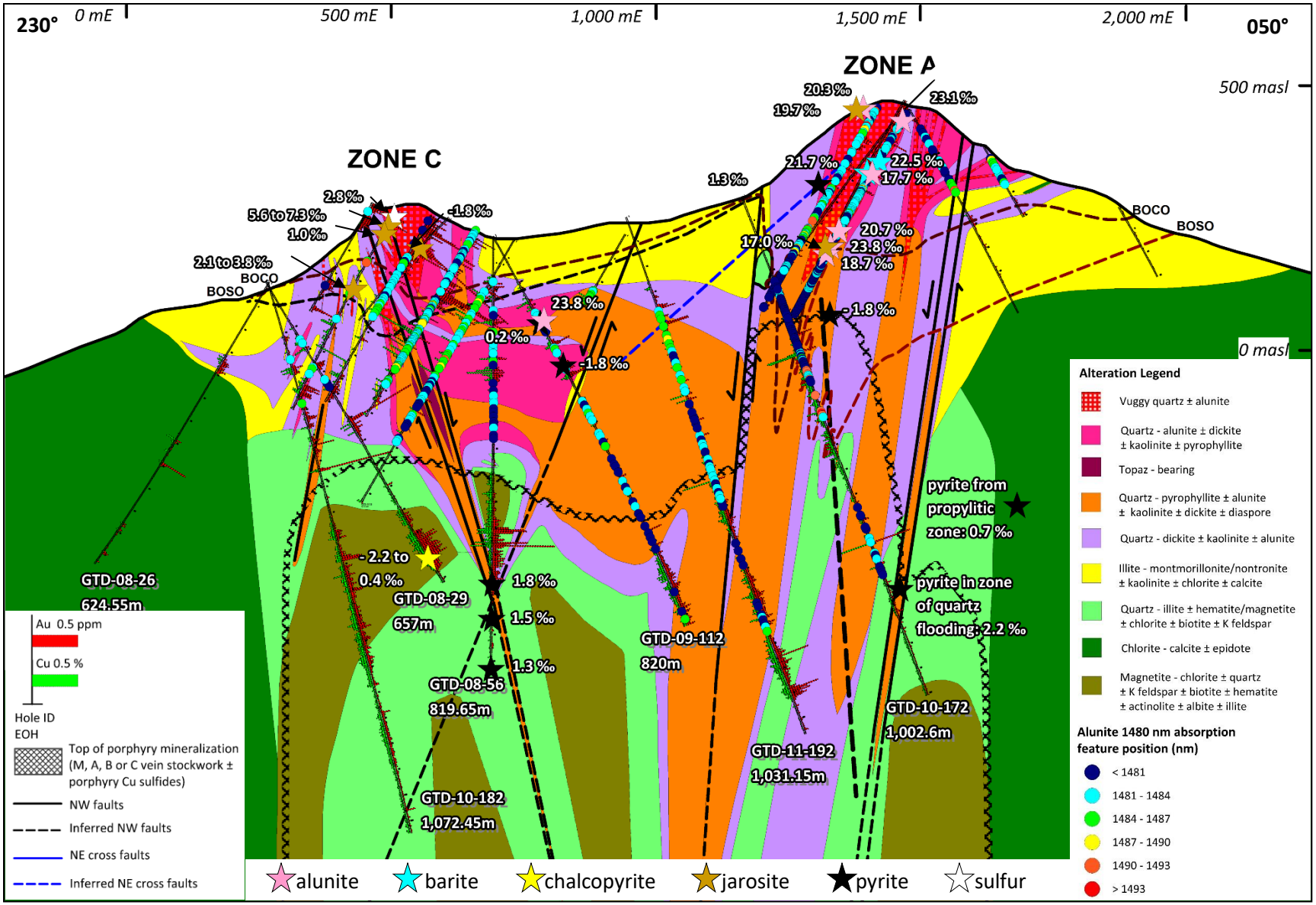

Figure 6.6. Sulfur isotope data and alunite absorption feature position plotted on alteration type section 11060 mN at Tumpangpitu. Abbreviations: BOCO = base of complete oxidation, BOSO = base of semi-oxidation. All sulfur isotope data listed in Tables 6.1 and 6.2.

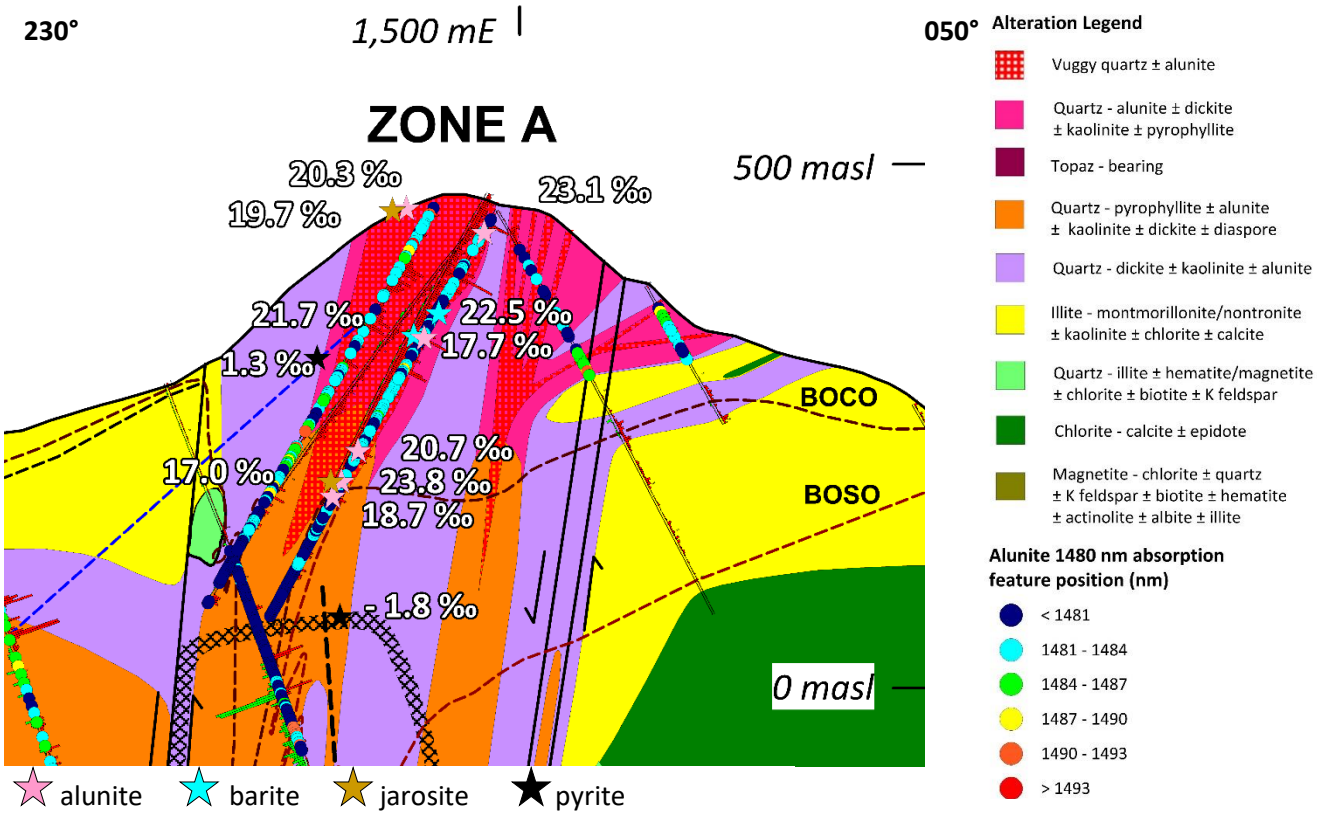

Figure 6.7. Sulfur isotope data and alunite SWIR data for Zone A high-sulfidation gold oxide deposit plotted on alteration type section 11060 mN at Tumpangpitu. Abbreviations: BOCO = base of complete oxidation, BOSO = base of semi-oxidation, masl = meters above average sea level. All sulfur isotope data listed in Tables 6.1 and 6.2.

The $\delta^{34}S$ values for pyrite from the porphyry Cu-Au-Mo zone associated with quartz - magnetite - biotite - K-feldspar potassic alteration have higher values than the $\delta^{34}S_{sulfide}$ value of pyrite (0.7 ‰) sampled from chlorite - calcite ± epidote propylitic altered andesitic wall rock (Fig. 6.6). Chalcopyrite from well-mineralized porphyry stockwork zones yielded a higher median value (0.4 ‰) than both the pyrite value from the propylitic halo and the median value of pyrite from epithermal zones ($\delta^{34}S_{sulfide}$: - 1.7 ‰; Fig. 6.6). The $\delta^{34}S_{sulfide}$ values of pyrite and chalcopyrite from porphyry stockwork veins generally decrease with increasing elevation towards the Tumpangpitu lithocap (Figs. 6.5A and 6.6).

Differences in $\delta^{34}S$ values from sulfides or sulfates from the same vein sample e.g., duplicate samples of jarosite (10-43001-05a, 10-43001-05b, 12-43001-09a and 12-43001-09b; Table 6.1) are probably due to fine scale $\delta^{34}S$ variations in the sulfide and sulfate crystals.

6.4.2 Alunite wavelength

The position of the alunite absorption feature around 1485 nm generally increases with decreasing values of $\delta^{34}S$ (Fig. 6.5B). The zonation towards Na-compositions and lighter $\delta^{34}S$ values on the type alteration section at Tumpangpitu (Fig. 6.6) define a lateral zonation pattern of K-alunite (< 1480 nm) to Na-K alunite (> 1485 nm), towards the main gold-hosting vuggy quartz ledge beneath Zone A.

6.5 Discussion

Based on mapping, logging and geochronological data presented in Chapters 4 and 5, high-sulfidation epithermal mineralization was overprinted onto the tonalite porphyry complex (Fig. 6.6). The new sulfur isotope data provides an opportunity to assess genetic relationships between the porphyry and epithermal deposits at Tumpangpitu, fluid sources, supergene processes and the application of new potential exploration vector techniques.

6.5.1 Source of sulfur and hydrothermal-magmatic fluids at Tumpangpitu

Measured $\delta^{34}S_{sulfide}$ (-8.4 to +2.2 ‰) from pyrite and chalcopyrite, $\delta^{34}S_{sulfate}$ (+17.7 to +26.2 ‰) values from alunite and barite and $\delta^{34}S_{sulfur}$ (2.8 ‰) are consistent with predominantly magmatic sources (i.e., values near 0‰; Ohmoto and Rye, 1979; Field and Fifarek, 1985) for the porphyry and high-sulfidation epithermal veins from Tumpangpitu (Tables 6.1 to 6.2; Figs. 6.4 to 6.7).

The sulfur isotope data compiled in Figures 6.4 to 6.7 and Tables 6.1 to 6.2 show that there are two distinct modes of $\delta^{34}S_{sulfide}$ values for pyrites from Tumpangpitu. The pyrites from the porphyry zone span a range of $\delta^{34}S_{sulfide}$ values between 1.3 and 2.2 ‰ (excluding the wallrock pyrite value of 0.7 ‰), with a mean value of 1.5 ‰ consistent with a predominance of H_2S in the mineralizing fluids (i.e., reducing conditions; Cooke et al. 2011). By contrast, predominantly negative $\delta^{34}S_{sulfide}$ values (-8.4 to +1.3 ‰) with a median value of -1.7 ‰ were obtained from pyrite from epithermal mineralization located inside and adjacent to the Tumpangpitu lithocap (Figs. 6.4 to 6.7; Tables 6.1 and 6.2). The sulfide sulfur isotope compositions appear to be influenced spatially with regards to proximity to the Tumpangpitu lithocap and generally have a negative correlation with increasing elevation (Figs. 6.5A, 6.6 and 6.7).

6.5.2 Sulfur isotope data from porphyry Cu-Au-Mo mineralization at Tumpangpitu

A number of porphyry deposits, including Butte, Montana, USA (Lang and Cheney, 1971); El Salvador, Chile, (Field and Gustafson, 1976); Endeavour 26 North (Heithersay and Walshe, 1995), Cadia, New South Wales, Australia (Harper, 2000; Wilson, 2003; Wilson et al., 2007); Dinkidi, Philippines (Wolfe, 2001; Wolfe and Cooke, 2011); Rosario, Chile (Masterman, 2003); El Teniente, Chile (Cannell, 2004) and deposits of the Baguio district of the Philippines (Cooke et al., 2011) have distinctive sulfur isotopic zonation patterns where $\delta^{34}S_{sulfide}$ values are characterized by low values. This corresponds to bornite- and chalcopyrite-rich sulfide precipitation from an oxidized (sulfate-predominant) magmatic fluids, with sulfate minerals also depositing and resulting in the negative shift of sulfide mineral compositions. Pyrite grains that occur in the propylitic alteration halos typically have $\delta^{34}S_{sulfide}$ values near 0 ‰. A gradual increase in $\delta^{34}S_{sulfide}$ values has been recognized outwards from the deposit cores through the propylitic halos (Wilson et al. 2007). These spatial and temporal variations of $\delta^{34}S_{sulfide}$ values have the potential use as exploration vectors. The applicability of this technique to Tumpangpitu is provided in the following sections.

6.5.2.1 Pyrite

Pyrite was sampled from several paragenetic stages (porphyry to epithermal) including fine-grained disseminated pyrite replacing magnetite in quartz - magnetite ± biotite ± K-feldspar altered zones, coarse-grained euhedral pyrite along fracture surfaces and two samples of pyrite from quartz flooded zones in phase 5 and 6 tonalite porphyries (Table 6.2; Fig. 6.2). The $\delta^{34}S_{sulfide}$ pyrite values generally become more negative with depth in the Tumpangpitu tonalite complex away from the lithocap (Figs. 6.4 and 6.6). One sample of disseminated pyrite replacing hornblende phenocrysts was taken from andesitic wallrock in the actinolite-chlorite-epidote altered inner propylitic zone. It returned a $\delta^{34}S_{sulfide}$ value of 0.7 ‰ (Table 6.2), isotopically lighter than all the $\delta^{34}S_{sulfide}$ values returned from pyrite from the mineralized porphyry zone. $\delta^{34}S_{sulfide}$ values near 0 ‰ are present in pyrite from propylitic altered wallrocks surrounding porphyry deposits in a number of deposits worldwide (e.g. Cadia, New South Wales, Australia; Wilson et al., 2007) and are thought to be the result of water-rock interaction during propylitic alteration which caused magmatic sulfate reduction and concomitant oxidation of ferrous iron-bearing minerals, resulting in enrichment of $\delta^{34}S_{sulfide}$ in pyrite.

6.5.2.2 Chalcopyrite

Sulfur isotope compositions of chalcopyrite as disseminations and in A type veins (terminology after Gustafson and Hunt, 1975) porphyry-style quartz - magnetite - biotite ± K-feldspar - chalcopyrite ± anhydrite stockwork veins from Phase 5 tonalite at Tumpangpitu have low $\delta^{34}S_{sulfide}$ values, mostly between 0 and + 2 ‰ (with the exception of one chalcopyrite value from a paragenetically earlier vein of -2.2 ‰; Table 6.2). One sample of chalcopyrite collected from the interior of a chalcopyrite - bornite - chalcocite - covellite C type porphyry vein crosscutting sandstone hostrock > 50 m away from the contact of Phase 5 tonalite porphyry (Fig. 6.2E and F) returned the highest $\delta^{34}S_{sulfide}$ value for chalcopyrite (2.0 ‰; Table 6.2). The range of $\delta^{34}S_{sulfide}$ values from Tumpangpitu suggest that the sulfides precipitated from fluids with compositions close to the H_2S/SO_4 buffer, similar to $\delta^{34}S_{sulfide}$ values reported from other porphyry deposits worldwide (e.g., Heithersay and Walshe, 1995). A porphyry fluid evolution pathway from early high-temperature oxidizing fluids allowing gold complexes to be soluble in solution and resulting in precipitation of abundant magnetite and inclusions of hematite within early porphyry stockwork veins (Chapter 5) before transitioning down a redox gradient due to water/rock interaction to more reduced conditions with increasing distance from the Tumpangpitu tonalite stock would likely cause a progression towards the predominance of H_2S in the mineralizing fluids. The sample coverage of chalcopyrite from Tumpangpitu is too sparse to determine whether progressively higher $\delta^{34}S_{sulfide}$ values characterize a transition upwards, similar to trends documented elsewhere (e.g., Wilson et al., 2007). The limited data available suggests that $\delta^{34}S_{sulfide}$ chalcopyrite values (> - 2 ‰) occur close to and within the Tumpangpitu porphyry, and then increase with increasing elevation (Fig. 6.6).

6.5.3 Sulfur isotope data from high-sulfidation epithermal mineralization at Tumpangpitu

In high-sulfidation systems, ore fluids are considered to be of mixed magmatic-meteoric origin, resulting from the adsorption of magmatic vapours or brines by shallow meteoric water (e.g., Rye, 1993, Arribas, 1995; Hedenquist et al., 1998, Cooke and Simmons, 2000, Muntean and Einaudi, 2001). Mineralogical observations (e.g., vuggy or massive residual quartz; Fig. 6.1C) and sulfur isotope data presented here indicate that high-sulfidation Au-Ag-Cu ore at Tumpangpitu precipitated from fluids that were H_2S and SO_4^{2-} dominant, and had a wide temperature range from 200° to 350°C (Chapter 5, Fig. 6.10). Gold was likely transported as a bisulfide complex, suggesting that boiling was the ore-forming process along with gas condensation, fluid mixing and water-rock interaction (Hedenquist et al., 1998; Cooke and Simmons, 2000). Fluid mixing either with cool, near-surface ground waters and/or seawater (due to the proximity of the coastline to Tumpangpitu) also has the potential to cause gold precipitation in the epithermal environment (e.g., Spycher and Reed, 1989; Cooke and McPhail, 2001). Seawater would affect the sulfur isotopic signatures by shifting $\sum\delta^{34}S$ values closer to seawater $\sum\delta^{34}S$ values.

6.5.3.1 Pyrite and enargite

Acidic hydrothermal solutions formed the advanced argillic alteration, followed by mineralization associated with oxidized magmatic-hydrothermal fluids in the high-sulfidation epithermal zones at Tumpangpitu, which precipitated sulfides with mainly negative $\delta^{34}S$ values (-8.4 to 1.3 ‰) that are distinct from the $\delta^{34}S$ sulfide values associated with the Tumpangpitu porphyry (generally 0 to 2 ‰; Tables 6.1 - 6.2; Fig. 6.4).

The lowest $\delta^{34}{}_{sulfide}$ values were recorded from enargite (-5.3 ‰) and pyrite (-8.4 ‰) from high-sulfidation epithermal zones located towards the southern margin of the Tumpangpitu lithocap. These epithermal samples extend to more negative values than in the porphyry stockwork veins, possibly due to a change in oxidised sulfur speciation, because 4 moles of SO_2 disproportionate 3 moles of SO_4^{2-} and 1 mole of H_2S at ~400ºC; (Ohmoto and Rye, 1979; Rye et al., 1992; Fig. 6.8). The $\delta^{34}S_{sulfide}$ value from enargite is lower than most of the pyrite associated with alunite in the high-sulfidation epithermal zone (Figs. 6.4 and 6.5). This trend could reflect decreasing redox potential to more reduced conditions with increasing proximity to the tonalite porphyry stock, suggesting a progression toward H_2S predominance in the mineralizing fluids (e.g., Cooke et al. 2011).

6.5.3.2 Alunite

The heavy $\delta^{34}{}_{sulfate}$ values for alunites from Tumpangpitu (17.7 to 26.2 ‰; Table 6.1; Figs. 6.5 - 6.7) indicates that hypogene alunite formed at high temperature (>200 ºC; Ohmoto and Rye 1979). The wide range of $\delta^{34}S_{sulfate}$ values, variations of SWIR values caused by K-Na substitutions in alunite (Chang et al., 2011; Figs. 6.3, 6.6 and 6.7), and abundance of jarosite and other iron oxides in the weathered oxide Au-Ag zones, suggests that alunite sulfur isotope compositions may have been partially modified by supergene processes involving meteoric water and/or seawater (Rye, 2005). The lowest $\delta^{34}S_{sulfate}$ values of alunites

either indicate higher temperatures of formation, assuming they precipitated in equilibrium with pyrite e.g., at Rosario, Chile, Masterman (2003), or supergene weathering associated with iron oxides, particularly jarosite around the margins of alunite grains and veins (Fig. 6.1D). Alunite $\delta^{34}S_{sulfate}$ data are higher than the sulfides, native sulfur and the majority of jarosite $\delta^{34}S$ values in the deposit (Fig. 6.4). The 25 ‰ difference between the median $\delta^{34}S^{CDT}$ of alunite and pyrite from the high-sulfidation epithermal zone (Fig. 6.4) is consistent with sulfate derived from the disproportionation of SO_2 producing SO_4^{2-} and H_2S in a magmatic vapour plume that typically is initially H_2S dominant as it separates from brine at the brittle-ductile transition (Rye et al., 1992; Rye, 1993, 2005; Arribas, 1995; Rye, 2005; Fig. 6.8) and is interpreted to reflect a magmatic-hydrothermal origin. These vapours were most likely focused into structures and open spaces in veins and hydrothermal breccias. Water-rock reaction is recorded as restricted (5 - 10 mm wide) alteration halos around veins and breccias. Continued influx of heat, volatiles, and fluids into previously condensed magmatic vapours were most likely responsible for alteration and metal deposition during high-sulfidation epithermal mineralization at Tumpangpitu (e.g., Rye, 2005). A strong increase in the precipitation of sulfate can be observed at low temperatures along with the formation of large volumes of H_2SO_4 and the ensuing rock alteration may overwhelm the rock buffer such that H_2S/SO_4^{2-} will locally decrease and the fluids may become SO_4^{2-}dominant (Giggenbach, 1997; Cooke et al., 2011). H_2S that is derived directly from the devolatilizing magma, or via the disproportionation of SO_2 after magma degassing, typically will react with Fe-bearing minerals in the wallrocks to produce pyrite, or will be oxidized in a steam-heated environment, or will vent to the surface (Rye, 2005). Condensed magmatic vapour may also be the source of high-sulfidation gold mineralization characterized by enargite and covellite (e.g., Hedenquist et al., 1998).

Alunite $\delta^{34}{}_{sulfate}$ values from the Tumpangpitu lithocap do not show a clear correlation with elevation (Fig. 6.5A), instead they show a lateral zonation towards more negative values in the cores of high-sulfidation epithermal veins and hydrothermal breccias in oxides Zone A and C (Figs. 6.6 and 6.7). Sulfur isotope zonation patterns defined by alunite can potentially identify upflow zones so that the data can be an exploration vector towards conduits for mineralizing magmatic-hydrothermal fluids (Cooke et al., 2011). This spatial variation can be seen in the Zone A gold oxide deposit (Fig. 6.7), where the $\delta^{34}S_{sulfate}$ values decrease and there is a compositional change in the Na-content of alunite towards central feeder zones of vuggy quartz based on SWIR analysis (Figs. 6.5 and 6.7).

6.5.3.3 Barite

Barite generally forms in more neutral pH environments in the upper and distal levels of porphyry and epithermal deposits, but can still provide useful information on late-stage and post-ore processes in the magmatic-hydrothermal environment (Rye, 2005). Barite is interpreted to form from the mixing of reduced Ba-bearing fluids with oxidized, sulfate-bearing fluids (Cooke et al., 2000). Mixing of reduced and oxidized waters is a depositional mechanism for barite (Holland and Malinin, 1979; Cooke et al., 2000). The barite samples from a vuggy quartz altered zone of high-sulfidation epithermal mineralization at Tumpangpitu

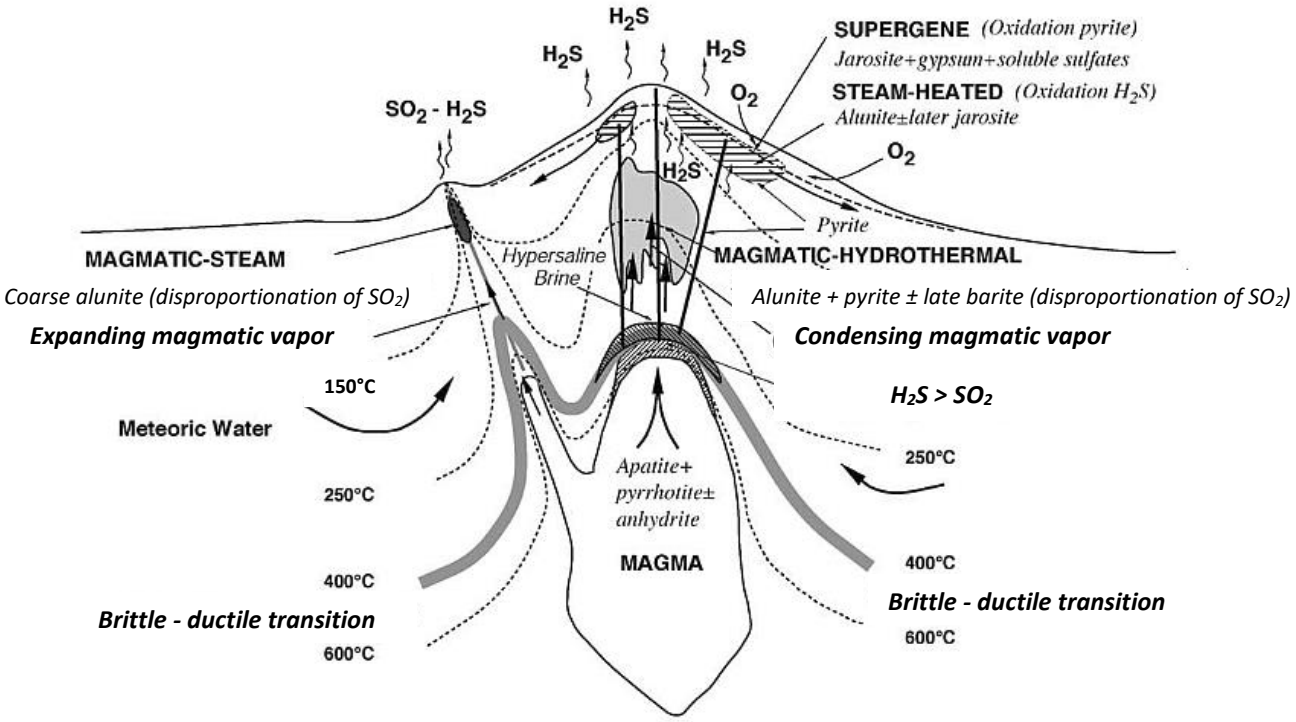

Figure. 6.8. Model showing inferred relationships between the porphyry and acid sulfate environments to magma, water-rich carapace, the brittle-ductile transition, and the location of sulfur-bearing minerals (Rye, 2005).

(Fig. 6.1C) are interpreted to be predominantly of hypogene origin, possibly due to reduced, Ba-bearing brine mixing with oxidized condensed magmatic vapour (e.g. Rye, 2005). Based on the large (> 1cm) bladed euhedral crystal form and the median $\delta^{34}S_{sulfate}$ value of barite (22.1 ‰) correlating with that of hypogene alunite (22.4 ‰; Table 6.1, Fig. 6.4).

6.5.3.4 Jarosite

$\delta^{34}S_{sulfate}$ values from jarosite span a wide range (-1.8 to 22.2 ‰) overlapping with both the high $\delta^{34}S$ sulfate and low $\delta^{34}S$ sulfide values from the high-sulfidation epithermal ore zones (Fig. 6.4). $\delta^{34}S_{sulfate}$ values from jarosite fall into two populations; a group from 16.9 to 22.2 ‰ overlapping the alunite and barite $\delta^{34}S_{sulfate}$ values (Table 6.1) and a lower range from -1.8 to 7.3 ‰ similar to the range of $\delta^{34}S$ values from sulfides and native sulfur (Fig. 6.4). $\delta^{34}S_{sulfate}$ values from jarosite appear to trend to lower values in and around high-sulfidation epithermal veins that now contain gossanous Au-Ag-rich veins within the Zone A and C oxide deposits (Figs. 6.6 and 6.7). One sample of jarosite, taken from a completely oxidized gossanous high-sulfidation Au vein adjacent to a major fault (Fig. 6.9B), has the lowest $\delta^{34}S_{sulfate}$ value (-1.8 ‰) out of all the sulfates analyzed from Tumpangpitu. This value correlates with the median $\delta^{34}S_{sulfide}$ value for pyrite (-1.7 ‰) from high-sulfidation epithermal mineralized zones (Fig. 6.4) and is therefore interpreted to be consistent with sulfate derived from the oxidation of precursor sulfides. The three samples of jarosite with $\delta^{34}S_{sulfate}$ values of 16.9 to 22.2 ‰ (Table 6.1, Fig. 6.9A) are all associated with veinlets of alunite and replacement halos around alunite grains.

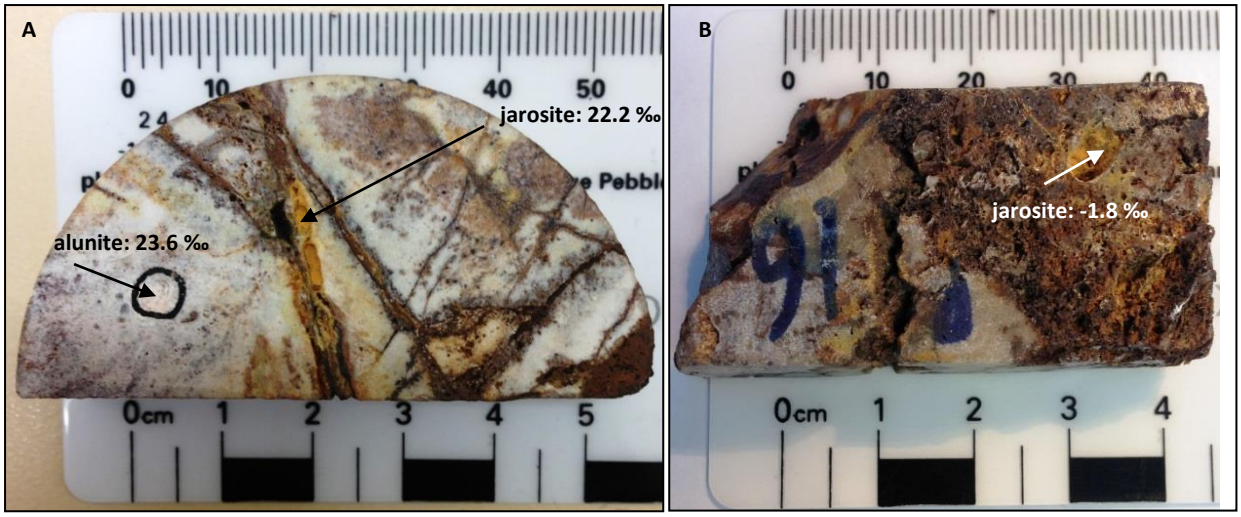

Figure 6.9. Examples of hand specimens of both light and heavy $\delta^{34}S$ values from samples of vein-hosted jarosite in oxidized high-sulfidation epithermal zones at Tumpangpitu. All sulfur isotope data and sample locations listed in Table 6.1.

A) *Sample 28-43002.31, drillhole GT014/68.5m, 174496 mE, 9046108 mN, elevation 377m.* Jarosite-hematite-alunite veinlet with heavy $\delta^{34}S$ value of 22.2 ‰ crosscutting matrix of hydrothermal breccia with disseminated alunite with $\delta^{34}S$ value of 23.6 ‰.
B) *Sample 13-43001-16, drillhole GT011/78.1m, 173837mE, 904606mN, elevation 250m.* $\delta^{34}S$ value of -1.8 ‰ from jarosite associated with hematite from gossanous Au-rich vein.

6.5.3.5 Supergene processes affecting jarosite deposition

Jarosite only occurs above the base of oxidation (BOCO and BOSO on Figs. 6.6, 6.7 and 6.9) in oxide zones A, B and C. Its distribution is fundamentally controlled by weathering, oxidation and supergene processes. Supergene processes relating to precipitation of jarosite could have involved SO_2-dominant low-density magmatic vapour enters the steam-heated environment and deposits alunite ± jarosite ± kaolinite ± smectite assemblages (Rye, 2005). However, the jarosite samples from Tumpangpitu are all associated with alunite, and in most cases jarosite has partly replaced alunite (Fig. 6.1D). This association is interpreted to be related to leaching processes associated with sulfuric acid formed above the paleowater table by the oxidation of H_2S distilled off the underlying magmatic-hydrothermal system (e.g. Rye, 2005). Jarosite precipitates at lower pH, higher fO_2 and higher Fe^{3+} activities than alunite over the entire temperature range of its stability (Stoffregen, 1993). These extreme values limit hydrothermal jarosite formation to the vadose zone or to shallow environments such as the massive and vuggy quartz-altered rocks that have little acid-neutralizing capacity in the weathered oxide zones of Tumpangpitu, environments where fluids with high fO_2 and low pH values can occur.

6.5.3.6 SWIR and vis-NIR spectral analysis

K-rich alunites with SWIR absorption features < 1480 nm are generally thought to correlate with supergene alunite (e.g., Chang et al., 2011; Zhang et al., 2016). Na-rich alunites with wavelengths > 1490 nm are representative of hypogene alunites formed closer to intrusive sources including Au-Cu ± Mo

porphyry stocks at higher temperature than K-alunite (Chang et al., 2011; Harrison, 2014; Zhang et al., 2016). A spectral zonation of more Na-rich compositions (i.e. higher SWIR values) and lower $\delta^{34}S$ values is present in and around the main gold-hosting vuggy quartz ledge beneath Zone A at Tumpangpitu (Figs. 6.6 and 6.7). This technique may be a potential vector towards weathered high-sulfidation epithermal and porphyry mineralization elsewhere.

6.5.4 Sulfur contamination

Mixing of isotopically distinct sulfur sources can generate variable $\delta^{34}S_{sulfide}$ values as well as $\delta^{34}S_{sulfate}$ values (e.g., Ohmoto and Goldhaber, 1997). The presumption that the bulk $\delta^{34}S$ value of the hydrothermal fluids remained constant throughout formation of different sulfide generations implies that there was no mixing with exotic sulfur, such as isotopically light sedimentary sulfide, leaching of existing sulfides, sulfate, or seawater contamination. It is possible that external sulfur reservoirs may have influenced mineralization at Tumpangpitu. Seawater $\delta^{34}S$ contamination is a major possibility when considering the present day proximity of Tumpangpitu and Pulau Merah to the coastline (Fig. 3.35). Seawater may have potentially affected the $\delta^{34}S$ values during the deposition of jarosite, based on the wide range of $\delta^{34}S$ values defined for jarosite in the vadose gold oxide zones at Tumpangpitu (Figs. 6.4, 6.6 and 6.7). Contamination of magmatic sulfur by seawater or sedimentary sulfide, possibly due to assimilation or sulfide dissolution during alteration could also have potentially affected $\delta^{34}S$ of sulfides precipitating from magmatic-hydrothermal mineralizing fluids at Tumpangpitu (Ohmoto and Rye, 1979, Cooke et al. 2011). Seawater may have been contained within pore waters in the volcanosedimentary rocks when mineralization started, contributing a second source of sulfur. Seawater could also have potentially contributed sulfur in the weathering profile if entrained into the system. If sulfur sources were mixed, the composition will change, possibly shifting curves to nearer to seawater $\sum\delta^{34}S$ values. Barite could also have mixed magmatic and seawater sources. Additional stable isotope analyses, including strontium analyses on barites and copper oxides at Tumpangpitu and Pulau Merah island are required to confirm and calculate relative contributions of the potential sources of sulfur contamination. Other potential sources of contamination include sulfur scavenged from the leaching of sulfides in gold oxide zones.

6.5.5 Pyrite - alunite equilibrium temperature

Sulfur isotope data on alunite - pyrite pairs of minerals produce one of the best isotope geothermometers for epithermal systems in the temperature range 200 - 350 ˚C (Rye, 2005). The variation in $\delta^{34}S_{sulfate}$ values for alunite from Tumpangpitu (17.7 to 26.2 ‰; Fig. 6.4) is attributed to deposition over a range of temperatures. The range is larger than that defined by the sulfides, suggesting that the sulfate was derived from either the oxidation of sulfides or H_2S degassed during the collapse of the hydrothermal system or deposition at lower temperature from H_2S predominant fluids (Fig. 6.10). In either case, limited sulfur isotope exchange between sulfate and sulfide species is inferred based on the positive $\delta^{34}S_{sulfate}$ values for

this stage of alteration (Fig. 6.4). The temperature of formation has been estimated using the isotopic fractionation equation of Ohmoto and Rye (1979) for coexisting alunite and pyrite.

Sulfur isotope thermometry was attempted for one alunite-pyrite pair from a late-stage (post-ore) vein crosscutting the upper facies Tumpangpitu diatreme. Both alunite and pyrite are interpreted to have formed contemporaneously in the same vein based on textural observations (Chapter 5). The $\delta^{34}S_{sulfate}$ value of the alunite (sample 2-43005.13b; Table 6.1) is 23.8 ‰ and that of coexisting pyrite is 0.2 ‰ (sample 2-43005.13a; Table 6.1; Fig. 6.10). The calculated isotopic equilibrium $\Delta^{34}S_{alun-py}$ temperature is 250 ºC using the equation of Ohmoto and Rye 1979; Fig. 6.10). This result could be explained by equilibrium precipitation of alunite and pyrite from a fluid with a $\sum\delta^{34}S$ value of ~3 ‰ and a H_2S/SO_4^{2-}(aq) ratio of about 5 (i.e., reduced conditions).

Pyrite - alunite fractionation at Summitville (Stoffregen, 1987; Rye et al., 1990) and Rosario, Chile (Masterman, 2003) are similar to that at Tumpangpitu and other deposits (Arribas et al., 1995), suggesting that the results of the current study are feasible. However, additional detailed analyses and microsampling of coexisting sulfate and sulfide grains from all paragenetic stages of alteration and mineralization at Tumpangpitu, along with fluid inclusion, oxygen, deuterium and strontium isotopes are required to better constrain the bulk sulfur isotope compositions and temperatures of formation.

6.5.6 Sulfur isotope fractionation model

A model for temperature controlled sulfur isotope fractionation in pyrite, chalcopyrite, bornite, $SO_{2(g)}$, and $SO_{4(aq)}$, is illustrated in Figure 6.10 (modified after Wilson et al., 2007). The model was generated by assuming a 3 ‰ value of $\Sigma^{34}S$ (bulk sulfur composition of the hydrothermal fluid) and $H_2S/SO_4 = 5$ i.e., reducing (H_2S predominant) conditions. The 3 ‰ $\Sigma^{34}S$ is the closest fit to the $\delta^{34}S$ value obtained from native sulfur in vugs from the high-sulfidation ore zone at Tumpangpitu (2.76 ‰; Table 6.1). This value falls within the average range reported for porphyry copper deposits (Ohmoto and Rye, 1979; Sasaki et al., 1984; Taylor, 1987). It is compatible with derivation of sulfur from an igneous source, either as magmatic-hydrothermal fluids or by dissolution of igneous sulfides (Ohmoto and Rye, 1979). The range of sulfur isotope compositions for all of the sulfide minerals analyzed at Tumpangpitu is -8.4 to 2.2 ‰, with a median value of 0.5 ‰ (Tables 6.2, 6.2 and Fig. 6.4). These $\delta^{34}S_{sulfide}$ values are consistent with the inferred bulk composition of sulfur in the hydrothermal fluid (3‰), whereas those of alunite are much higher (median value 23.4 ‰; Fig. 6.4). The data are consistent with sulfuric acid being derived by disproportionation of SO_2 during the condensation of magmatic vapour at temperatures below 400 ºC (Fig. 6.8). It appears likely that reduced (H_2S-predominant) magmatic-hydrothermal fluids prevailed in the porphyry and epithermal deposits of the Tujuh Bukit district. Fluids have been close to the H_2S-SO_4^{2-} redox buffer, however, in order to stabilize alunite (e.g., Deyell et al. 2005).

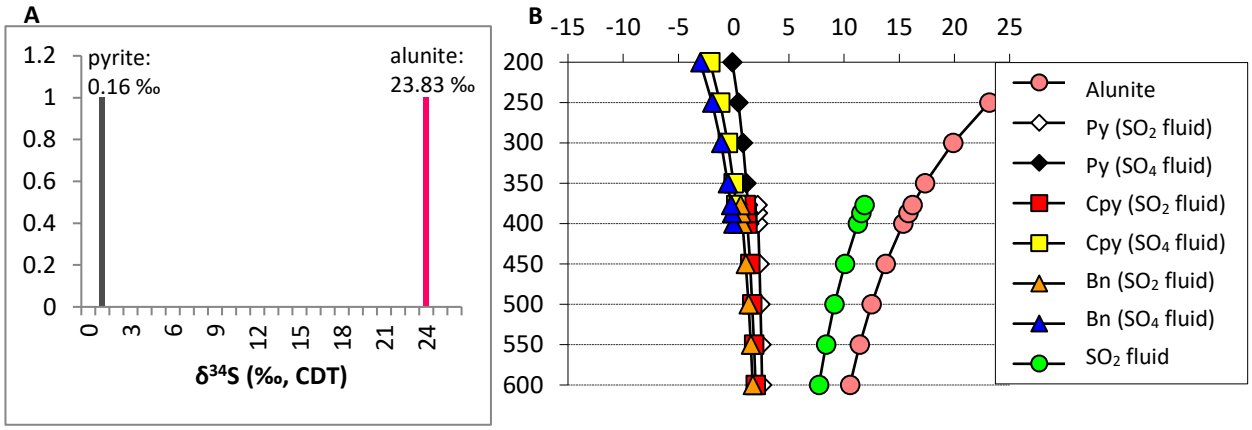

Figure 6.10. Sulfur isotope ranges and sulfide - sulfate fractionation models from an alunite - pyrite pair at Tumpangpitu. Sulfide-sulfate fractionation curves were calculated using the relations of Ohmoto and Rye (1979) using $\Sigma^{34}S$ = 3 ‰ H_2S/SO_4 = 5. Calculations were made using an unpublished spreadsheet (D. Cooke, unpublished data). Diagram modified after Wilson et al. (2007).

A) *Sample 2-43005.13a and 2-43005.13b.* δ^{34}SCDT values from a pyrite - alunite vein.
B) Modelling results from alunite and pyrite.

6.5.7 Constraints on alteration and ore deposition

Alunite in most high-sulfidation epithermal systems generally precedes mineralization (e.g., Stoffregen, 1987; White, 1991; Rye, 1993; Cooke and Simmons, 2000). However, evidence provided in Chapter 5 documents alunite occurring throughout the paragenesis of Tumpangpitu with pre- syn- and post-mineralization timings with respect to the multiple-stages of Au-Ag-Cu high-sulfidation epithermal mineralization. These results are similar to observations made by Deyell et al. (2005) at Pascua-Lama, Argentina. Constraints on the evolution of the Tumpangpitu magmatic-hydrothermal system from pre-ore alteration through main-stage ore deposition to post-ore processes cannot be easily deduced from sulfur isotope systematics for alunite from this study, as the sulfur isotope signature all fall in the range of heavy $\delta^{34}S_{CDTsulfate}$ values, consistent with a strong magmatic-hydrothermal origin and deposition between 200 to 325°C (Fig. 6.10). Additional sampling of alunite from all paragenetic stages of alteration at Tumpangpitu, oxygen and hydrogen isotope analyses, are required to identify steam-heated alunite that formed from aqueous sulfate created by the oxidation of H_2S at or above the water table (Schoen et al., 1974), which would have meteoric isotopic signatures (e.g., Rye et al., 1992; Ebert and Rye, 1997) with magmatic-hydrothermal alunite.

6.5.8 Genetic links between deposit styles

Tumpangpitu is a large, complex system that formed from episodic magmatic-hydrothermal activity over a comparatively short period of time. Absolute age determinations imply that the Tumpangpitu epithermal veins ($^{40}Ar/^{39}Ar$ alunite age: 4.391 ± 0.037 Ma; Chapter 5) are close in age to the porphyry deposit (Re/Os molybdenite age; 4.306 ± 0.018 Ma; Chapter 5), although mapping and crosscutting relationships (Chapters 4 and 5) show that the porphyry vein stockwork formed before high-sulfidation epithermal veining. The sulfur isotope compositions of sulfides from both porphyry and epithermal deposits

overlap (Tables 6.1- 6.2; Figs. 6.4 to 6.7). These features are consistent with a genetic link between the porphyry and overlying epithermal deposits at Tumpangpitu.

6.6 Conclusions

High-sulfidation epithermal mineralization at Tumpangpitu is interpreted to have been a late-stage manifestation of magmatic-hydrothermal activity associated with the Tumpangpitu porphyry tonalite complex. Rapid uplift and exhumation promoted telescoping of the epithermal veins into the early-formed porphyry stockwork (Fig. 6.6).

The sulfur isotope results from the Tumpangpitu porphyry and epithermal deposits are consistent with a common, homogenized sulfur source that was predominantly magmatic, with a $\delta^{34}S$ value of around 3 ‰, and mineralizing fluids that were most likely reduced (H_2S-predominant with H_2S/SO_4^{2-} around 5 ‰; Fig. 6.10; Rye, 1993; Wilson et al., 2007).

The most negative $\delta^{34}S_{sulfide}$ values from pyrite and enargite veins occurred within and adjacent to the Tumpangpitu lithocap (Fig. 6.6). $\delta^{34}S_{sulfide}$ values from pyrite are around zero in the propylitic-altered wallrock on the periphery of the Tumpangpitu porphyry (Fig. 6.6). Chalcopyrite in mineralized zones of porphyry reach negative $\delta^{34}SC_{sulfide}$ values around -2 ‰. This zonation can be explained by an oxidized fluid (SO_2/H_2S = 5) being progressive reduced by wallrock interaction as it migrated outwards from the tonalite stock.

Significant meteoric input is recognized in the precipitation of supergene jarosite in the final stages of the hydrothermal system. The aqueous sulfate required to precipitate jarosite during late stage alteration and oxidation events was likely derived from the oxidation of precursor sulfides, given their abundance within the Tumpangpitu system and the correlation of low $\delta^{34}S_{sulfide}$ pyrite and $\delta^{34}S_{sulfate}$ jarosite-1 values from the high-sulfidation zones (Fig. 6.4). Gold and silver enrichment combined with leaching of copper most likely accompanied this stage. The occurrence of jarosite with both supergene (jarosite-1) and hypogene (jarosite-2) isotopic signatures suggests that most magmatic activity in the region had ceased by ~ 4 Ma (Fig. 6.4 and Chapter 5). Alternatively, jarosite-1 and jarosite-2 could have both formed by supergene processes, one may have formed by alteration of sulfide, the other from alteration of alunite (Cooke, pers. comm, 2016).

These results show that sulfur isotope analyses combined with SWIR spectral analysis have potential applications in the exploration of porphyry deposits in the Sunda-Banda arc, by mapping fluid upflow zones whereby zones of depleted $\delta^{34}S_{sulfide}$ values correlate with SWIR variations indicating Na-compositions of alunite. Such correlations are most prospective for high-grade high-sulfidation epithermal mineralization.

Additional sulfur isotope data, coupled with hydrogen, deuterium and strontium stable isotope data would provide a more detailed review of the fluid geochemistry from all mineralization styles in the Tujuh Bukit district.

Chapter 7: Conclusions and Genetic Model

7.1 Introduction

Tumpangpitu is a significant new discovery of porphyry Au-Cu-Mo and epithermal Au-Ag ± Cu epithermal mineralization in the Tujuh Bukit district of SE Java, a region that was previously explored by a number of companies over 17 years. This chapter summarizes the main conclusions of the current study and presents a genetic model of the evolution of Tumpangpitu. Models for the juxtaposition of epithermal and porphyry mineralization and the application of SWIR data towards geometallurgical models are included. Finally, implications for exploration and recommendations for further work are discussed.

7.2 Geodynamic setting

The Tujuh Bukit district formed within an evolving oceanic island arc setting. During the Pliocene, dilatant movements on north-easterly trending crustal scale strike-slip fault networks in eastern Java were most likely related to the collision of the northern edge of the Roo Rise and the subsequent collision of the Australian craton (Figs. 2.3 and 3.32). Important changes in plate motions and configuration of tectonic elements from 5 Ma (Audley-Charles, 2004) most likely favoured the development of the world class porphyry and epithermal deposits that characterize the eastern Sunda arc (Figs. 2.1 and 2.2). Cretaceous zircons in the Tanjung Jahe diatreme implies that the Tujuh Bukit district may be close to or on the eastern margin of the Cretaceous ± Archean fragment of ancient Gondwana, which is interpreted to underlie East Java (Figs. 4.14 - 4.16; Smyth et al. 2007). The igneous rocks of the Southern mountains in East Java were originally defined as middle Eocene to Late Miocene (Smyth et al. 2007; Hall and Sevastjanova, 2012). Dating of the igneous rocks of the Tujuh Bukit district allows their age bracket to be redefined as middle Eocene to Early Pliocene. The presence of Sn sulfosalts, and the abundance of molybdenite at Tumpangpitu, could indicate a significant crustal contribution to intrusions of the Tujuh Bukit district.

7.3 Evolution of the Tumpangpitu magmatic-hydrothermal system

Figure 7.1 summarizes the temporal evolution of the Tumpangpitu Au-Cu-Mo porphyry and high- to intermediate- sulfidation epithermal Au-Ag-Cu deposits. A timeline based on crosscutting relationships and radiometric age determinations for the Tujuh Bukit district is summarized below:

7.3.1 Sedimentation and andesitic volcanism (21.14 - 8.40 Ma)

Sedimentary and andesitic volcanic hostrocks were deposited in a shallow marine subaqueous to emergent setting (40 - 60 m bmsl) during the Late Miocene, between 20.67 ± 0.47 and 8.69 ± 0.29 Ma (Table 4.1). Limestone intervals are inferred to mark preserved shallow-marine carbonate horizons

formed during periods of volcanic quiescence. The local Miocene andesitic sequence is inferred to have erupted as effusive lava flows, rather than explosive volcanism, due to the lack of pyroclastic material.

7.3.2 Tanjung Jahe diatreme breccia and phase 1 hornblende quartz diorite (9.00 - 8.31 Ma)

A relatively dry, pre-mineralization andesitic volcanic breccia pipe was emplaced at Tanjung Jahe, 2.5 km south of Tumpangpitu Zone A (Fig. 3.1) between 8.78 ± 0.22 Ma and 8.52 ± 0.21 Ma (U/Pb age determinations). Juvenile clasts in lower facies breccia (Fig. 3.11B) provide evidence of a direct magmatic contribution to breccia formation and help to infer fragmentation processes (Davies, 2002, 2008a). Accretionary lapilli and low- angle cross stratification, in combination with features such as slumping along faults, channelling of beds and lack of sag structures beneath large fragments in upper facies breccia (Fig. 3.12B), indicate low temperature, wet pyroclastic base surge deposits that overlie fall out and co-surge fallout ash fall deposits. Early (phase 1) hornblende quartz diorite dikes emplaced during this period occur as clasts within the Tanjung Jahe diatreme (clast U/Pb age; 8.46 ± 0.36 Ma; Fig. 3.11E). The presence of minor mineralized clasts of chalcocite - pyrite and copper oxides (Fig. 3.11C) in the lower facies breccia suggests that minor, localized mineralization also occurred prior to 8.78 ± 0.22 Ma in the Tujuh Bukit district.

7.3.3 Andesitic to dacitic volcanism (~ 5.74 Ma)

Volcanic breccias, including welded crystal tuffs, are preserved in the upper levels of Zone A Au-Ag deposit (Figs. 3.1, 3.4, 7.1 A-C; U/Pb age: 5.74 ± 0.48 Ma). The pre-mineralization volcanosedimentary stratigraphy is interpreted to be the product of volcanic ash fall, debris flow deposits and explosive volcanic activity as pyroclastic deposits. The polymictic nature of clasts in the lithic tuffs is consistent with a near-vent source (Rohrlach, 2010) and may have formed from a few eruptive cycles, since bedding is typically not observed.

7.3.4 Phase 2 diorite (6.01 - 4.91 Ma)

A large pre-mineralization (2.5 x 4.6 km) calc-alkaline dioritic pluton was emplaced during the Late Miocene (U/Pb ages: 5.81 ± 0.20 Ma to 5.18 ± 0.27 Ma). Depth of emplacement is interpreted to have been relatively shallow, at a hypabyssal level, since columnar jointing is a common feature where this unit is exposed along the coastline. The juxtaposition of the large phase 2 pluton and the overlying volcanic breccias, implies significant unroofing prior to porphyry mineralization (Fig. 7.1A)

7.3.5 Katak tonalite porphyry (~ 5.26 Ma)

Emplacement of a NW-trending chain of inferred sub-economic porphyry and epithermal prospects (Katak tonalite porphyry; U/Pb age: 5.26 ± 0.47 Ma, Candrian tonalite porphyry, Salakan tonalite porphyry and Gunung Manis low-sulfidation epithermal prospect) 2.7 km to the east of the strongly mineralized Pulau Merah - Tumpangpitu - Zone B corridor (Fig. 4.12) occurred during intrusion of the Katak porphyry. These poorly endowed porphyry and epithermal prospects formed

approximately 1 m.y prior to the well-mineralized deposits of Tumpangpitu and Pulau Merah, similar to temporal relationships between sub-economic prospects and ore deposits in the Batu Hijau and Elang districts of Sumbawa (Fig. 4.13; Garwin, 2000; Maryono et al., 2017). The intrusions in the Tujuh Bukit, Batu Hijau and Elang districts are progressively younger and more fertile from north to south, suggesting local reversals in the overall belt's south to north younging direction of magmatism. This may be due to complexity in the architecture of the downgoing slab and overriding plate.

7.3.6 Magmatism and Au-Cu-Mo porphyry mineralization (5.29 - 3.38 Ma)

A period (up to 1.91 m.y) of Late Miocene to Early Pliocene calc-alkaline magmatism resulted in the formation of the Tumpangpitu mineralized intrusive complex, from 4.89 ± 0.40 Ma (phase 4 tonalite) to 4.03 ± 0.65 Ma (phase 6 tonalite). The Re-Os age determination of molybdenite (4.303 ± 0.018 Ma; Table 5.3) is consistent with the timeline defined by U-Pb age determinations (Fig. 4.10).

After emplacement of the tonalite porphyry complex (Fig. 7.1A), magmatic fluids were most likely exsolved from the uppermost part of the crystallising stock at temperatures exceeding 500 ºC (Arribas, 1995). The magmatic-hydrothermal system that resulted in high temperature (> 400 ºC) porphyry-style Au-Cu ore and early alteration assemblages of quartz - magnetite - biotite - K-feldspar ± actinolite ± anhydrite established itself as the intrusions crystallised. At temperatures above 400 ºC the porphyry and country rock would have behaved plastically under a dominantly lithostatic pressure regime, (e.g., Fournier, 1999) resulting in the formation of early stage discontinuous, ptygmatic M1, M2 (Fig. 5.9A, B and D), and early biotite (EB) veinlets (Fig. 5.7E) associated with chalcopyrite, bornite, chalcocite and covellite (Table 5.2). The fluid most likely was a co-existing high density brine and low density vapour (Henley and McNabb, 1978; White, 1991; Arribas, 1995).

Quartz - magnetite - biotite - K-feldspar alteration assemblages, associated with continuous A veins (Figs. 5.8B, E and F, 5.9C), were superimposed up to 150 m laterally on the host rocks when the magmatic-hydrothermal brines reacted with the wall rocks. Actinolite (Fig.5.7C) and epidote (Fig. 5.16B, C G and H) are interpreted to have formed contemporaneously in surrounding wallrocks in contact with the tonalite porphyry intrusions during this early stage, with epidote preferentially replacing plagioclase feldspars in the tonalite porphyries (Fig. 5.16C). Au-Cu-Mo porphyry and epithermal mineralization at Pulau Merah (U/Pb age: 3.98 ± 0.21 Ma) is inferred to be contemporaneous with the emplacement of the Tumpangpitu porphyry complex. Vapour separated from the brine and ascended buoyantly to shallow levels where it condensed into groundwater and caused advanced argillic alteration near outflow zones, initiating the formation of the Tujuh Bukit lithocap during this period (e.g., White, 1991; Fig. 5.3 and 7.1C).

7.3.7 Collapse of the Tumpangpitu magmatic-hydrothermal system

As cooling of the tonalite stock progressed, convection in the magma stops and the fluid and heat flux from the conductively cooling parent magma chamber decreased abruptly (Hedenquist et al.,

1998). Transitional stage B veins (Fig. 5.12A; Table 5.2) comprising molybdenite intergrown with quartz; constitute the main molybdenite mineralizing event at Tumpangpitu. B veins are inferred to have resulted from lower temperature magmatic-hydrothermal fluids that were white mica-stable (up to pyrophyllite ≤ 350°C; Hedenquist and Taran, 2013). B veins post-dated the M, EB and A veins, but pre-dated both the C (Figs. 5.11B-C, 5.12C) and D veins (Fig. 5.13) that are associated with quartz - muscovite - illite and have outer alteration selvedges of chlorite (Fig. 5.12D). The molybdenite-bearing B veins are inferred to have formed as the stock cooled and crystallized contemporaneous with muscovite and illite alteration that overprinted the quartz - magnetite - biotite - K-feldspar alteration assemblage (Fig. 5.3).

Late stage D veins (Fig. 5.13; Table 5.2) and associated quartz - muscovite ± pyrophyllite ± illite alteration at Tumpangpitu are strongly associated with major fault zones and occurred under hydrostatic pressure and brittle rock conditions, probably at temperatures of < 350°C (e.g., Gustafson and Hunt, 1975; Arif and Baker, 2003). D veins are typical of porphyry systems in a retrograde state, potentially involving the ingress of cooler, oxidized meteoric fluids after the collapse and cooling of the magmatic-hydrothermal system (Seedorff et al., 2005). However, muscovite and pyrophyllite are inferred to be dominantly of magmatic origin (e.g., Hedenquist et al., 1998; Watanabe and Hedenquist, 2001). Stable isotope analyses could confirm this.

7.3.8 Phase 7 quartz diorite (4.83 - 3.25 Ma)

An unmineralized quartz diorite stock with inter- to post-mineralization timing was emplaced through the centre of the Tumpangpitu tonalite complex between 4.26 ± 0.57 Ma and 3.94 ± 0.69 Ma (U/Pb zircon ages; Fig. 7.1B; Table 4.1). Phase 7 is weakly altered to chlorite ± epidote ± calcite and chlorite - illite alteration assemblages and has been overprinted by quartz - muscovite and advanced argillic alteration assemblages adjacent to major fault zones (Fig. 5.3).

7.3.9 Lithocap formation and high-sulfidation Au-Cu-Ag epithermal mineralization

Formation of high-sulfidation epithermal mineralization and the associated lithocap at Tumpangpitu has been constrained by ^{40}Ar-^{39}Ar dating of alunite to the same time period (4.385 ± 0.049 Ma). At least three stages of high-sulfidation epithermal mineralization occurred during the formation of the Tumpangpitu lithocap. These can be divided into pre-, syn- and post-diatreme emplacement. High-sulfidation epithermal ore zones at Tumpangpitu are mainly associated with HSE-1 enargite/luzonite - pyrite ± covellite ± bornite ± chalcocite veins with vuggy quartz - alunite alteration and HSE-2 enargite - luzonite - tennantite - tetrahedrite - pyrite ± chalcopyrite ± bornite ± chalcocite veins associated with massive quartz - alunite, pyrophyllite - dickite ± kaolinite ± barite ± sulfur ± diaspore ± topaz ± zunyite ± APS minerals ± Sn-sulfosalts controlled by major faults (Figs. 5.18, 5.19; Table 5.2). Alteration zones at the highest levels of exposure at Tumpangpitu are characterized by vuggy quartz - alunite transitioning down to pyrophyllite and dickite then downward and outward to

quartz - muscovite alteration (Fig. 5.3). Pyrophyllite-rich alteration is interpreted to have resulted from upward cooling of a fluid initially in equilibrium with muscovite (Fig. 5.39). Muscovite occurs beneath the pyrophyllite zone, and occurs at deep levels overprinting the stockwork vein carapace at Tumpangpitu (Fig. 5.3).

White (1991) proposed a two-stage genetic model for high-sulfidation epithermal deposits. The first stage is characterized by magmatic gases that contain SO_2 and HCl which cause intense leaching of wallrock and development of advanced argillic alteration assemblages. Central zones of barren quartz - pyrophyllite in the Tumpangpitu lithocap (Fig. 5.3) potentially provide evidence for early advanced argillic alteration being caused by a fluid devoid of metals. In White's (1991) model, mineral deposition occurs in stage two when fertile brines exploit the permeable acid leached zone, mix with ground waters and precipitate high-sulfidation ore (White, 1991, Arribas, 1995). The magmatic vapours responsible for alteration and mineralization most likely exsolved from the underlying tonalite intrusive sources (e.g., Hedenquist and Taran, 2013).

7.3.10 Formation of intermediate-sulfidation veins

Late stage tennantite - tetrahedrite - chalcopyrite-bearing ISE veins with quartz - dickite - kaolinite, kaolinite - muscovite - illite alteration halos that are surrounded by montmorillonite - chlorite alteration halos (Fig. 5.20) overprinted HSE-1 and HSE-2 veins. The hydrothermal system must have cooled down to temperatures at which the illite - chlorite assemblage was stable (~250 ºC). The coexistence of minor tennantite with pyrite in D veins (Table 5.2) suggests that D veins formed in multiple cycles contemporaneously with HSE and ISE veins and are associated with a late phase introduction of copper and gold (e.g., Perello et al., 2012).

ISE-2 veins (Fig. 5.21; Table 5.2) contain sphalerite - galena and pyrite and are associated with kaolinite - muscovite ± illite alteration halos that surround and overprint outer portions of the Tumpangpitu porphyry and lithocap. ISE-2 veins were the final ore-forming magmatic-hydrothermal event in the district, overprinting the intrusive complex along late NW- and NE-trending faults.

7.3.11 Tumpangpitu diatreme (~ 2.7 Ma)

Cu-Au-Mo mineralization associated with the intrusive complex was terminated by the formation of a huge (2.2 x 3.1 km) diatreme, probably one of the five largest porphyry-related diatremes recorded in the world in terms of surface dimensions (Table 3.2). It has preserved an entire vertical sequence comprising root zones (Fig. 3.8), lower facies massive polymict breccia (Fig. 3.27), upper facies bedded breccia (Figs. 3.25 - 3.26), tuffisite dikes (Fig. 3.29) apron breccias (3.24) and a partially preserved maar (Fig. 3.28). Parts of the porphyry stockwork were destroyed by the emplacement of the diatreme, as demonstrated by the entrainment of numerous porphyry and epithermal mineralized clasts (Figs. 3.22, 3.23 and 7.1D). Additional features including fluidization, mixing, rounding and comminution of clasts, clasts of Late Miocene sedimentary rocks, phases 2-7 intrusives,

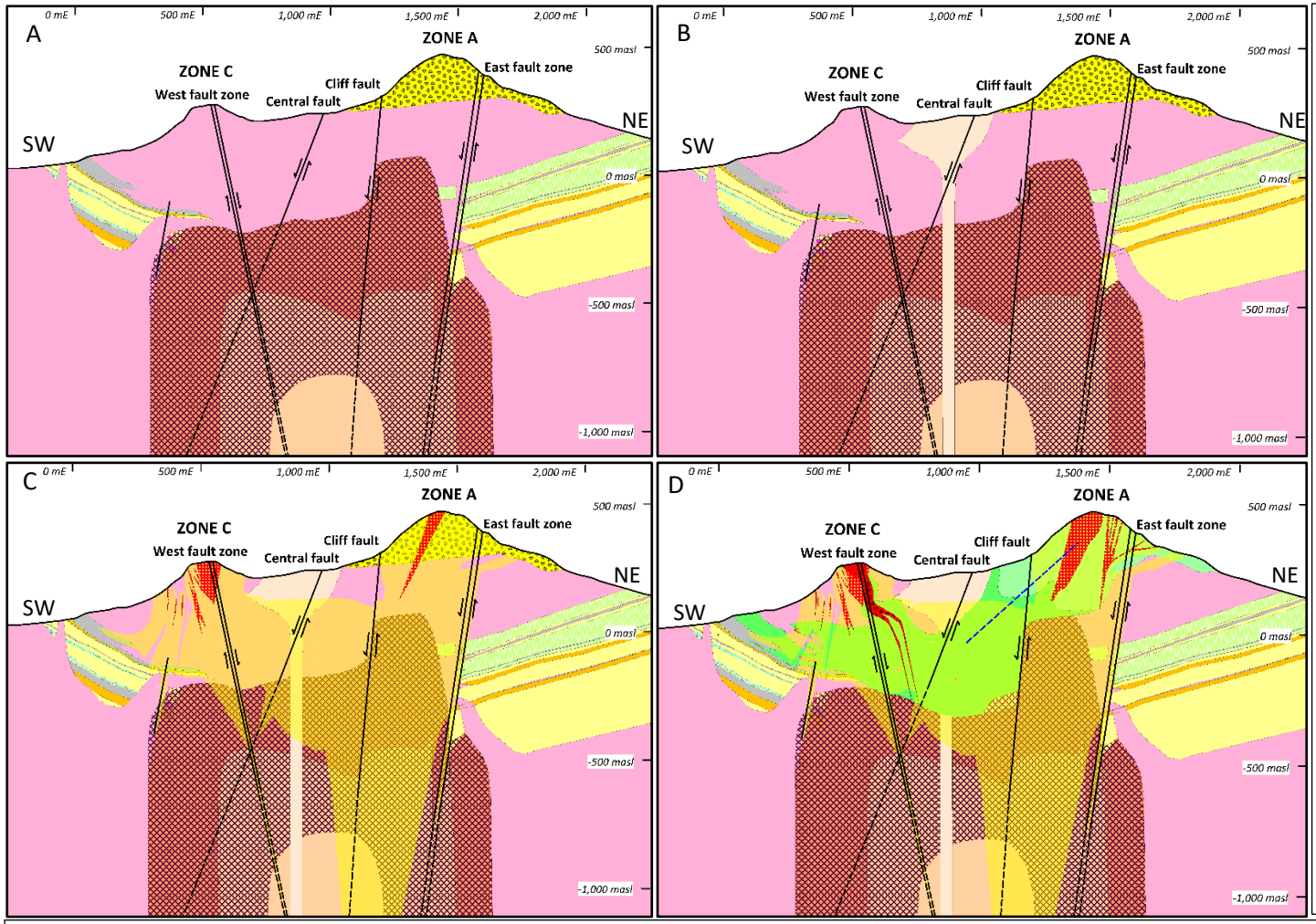

Figure 7.1. Schematic models from type section 11060 mN through Tumpangpitu, showing evolution of the magmatic-hydrothermal system.

A) 6.01 - 4.91 Ma: sedimentary host sequence intruded by phase 2 diorite batholith (6.01 - 4.91 Ma); volcanic breccia deposited around 5.74 ± 0.48 Ma (U/Pb age); **5.29 - 3.38 Ma:** emplacement of phase 4, phase 5 and 6 inter-mineralization tonalite porphyries associated with Au-Cu-Mo mineralization (Re/Os age: 4.303 ± 0.018 Ma)

B) 4.83 - 3.38 Ma: Phase 7 late-mineralization quartz diorite intruded the centre of the deposit

C) 5.29 - 2.7 Ma: Formation of lithocap associated with HSE-1 and HSE-2 veins; early formation of vuggy quartz-alunite ledges of Zones A and C (^{40}Ar-^{39}Ar alunite age: 4.385 ± 0.049 Ma) and late stage ISE-1 and ISE-2 veins

D) ~ 2.7 Ma: emplacement of Tumpangpitu diatreme, destruction of phase 7 quartz diorite feeder dike, upper levels of porphyry stockwork carapace, vuggy quartz and HSE mineralization at Zone A; late events of HSE and ISE mineralization along both NW and NE-striking faults continue post-diatreme emplacement overprinting the Tumpangpitu diatreme (Zone A)

polyphase brecciation, accretionary lapilli and charcoal fragments at depths greater than 100 m below present-day surface, are consistent with a large diatreme breccia complex that formed by multiple eruptions from vents during catastrophic phreatomagmatic explosions and subsequent sedimentary infill. Groundwater ingress to late-mineralization porphyry stocks (e.g., phase 7 quartz diorite) could have been the trigger for late stages of phreatomagmatic activity at Tumpangpitu (e.g., Sheridan and Wohletz, 1983; Davies et al., 2008; Sillitoe et al., 2013).

7.3.12 Post-diatreme epithermal mineralization (< 2.7 Ma)

Sulfur isotope data from an HSE-2 alunite - pyrite vein that crosscut the Tumpangpitu diatreme indicate that temperatures cooled to about 250 ºC (Fig. 6.10) after diatreme emplacement. Magmatic vapour most likely ascended along faults and condensed at elevations associated with vuggy quartz - alunite alteration that hosts gold-silver mineralization at Zones A, B and C, possibly facilitated by increased permeability created by the diatreme. Massive quartz - pyrophyllite - dickite ± diaspore ± zunyite associated with HSE-1 and HSE-2 veins, hydrothermal breccias, ISE-1 and ISE-2 veins formed below 50 m asl, now mainly occupying the Cliff fault of Zone A (Figs. 5.3 and 7.1D). Early zones of HSE and ISE mineralization that were hosted by volcanic breccias were disrupted at Zone A during the formation of the Tumpangpitu diatreme (Fig. 7.1D). This is apparent from the clasts of vuggy quartz + enargite, and tetrahedrite-tennantite within the diatreme (Fig. 3.23).

The minimum age of magmatic-hydrothermal activity as defined by late-stage phreatomagmatic activity is 1.7 Ma, implying a duration of up to 3.59 m.y for epithermal mineralization events. The absolute duration could be refined with more precise U-Pb zircon dating using ID-TIMS. The emplacement of post-mineralization dikes (phase 8), and the formation of the Tumpangpitu diatreme signalled the end of magmatism, and ultimately the termination of magmatic-hydrothermal activity.

7.3.13 Uplift, exhumation, oxidation and erosion

Following phase 5 and 6 intrusive emplacement and associated porphyry Au-Cu-Mo mineralization and alteration, the Tumpangpitu porphyry complex was partially exhumed, deeply oxidized and overprinted by epithermal mineralization and the Tumpangpitu lithocap. Exhumation resulted in telescoping of the epithermal environment onto the core of the Tumpangpitu porphyry complex, and superimposed two distinct mineralization styles (high-sulfidation epithermal and porphyry) within the same ore deposit. Weathering and erosion resulted in the leaching of copper from the high- and intermediate sulfidation veins and enrichment of Au and Ag. Complex Cu-Fe sulfides were dominantly oxidized to hematite (Fig. 5.33B, C and D), pyrite formed goethite (Fig. 5.33E) and alunite was replaced by jarosite (Fig. 5.33A).

^{40}Ar-^{39}Ar geochronology from one of the latest HSE veins that crosscut the Tumpangpitu diatreme (4.385 ± 0.049 Ma; Figs. 5.35 and 5.36) and the Re/Os age determination from porphyry

stockwork B veins from phase 6 tonalite (4.303 ± 0.018 Ma; Fig. 5.37) indicates a short time period between the high-sulfidation epithermal and porphyry mineralization events. This suggests that the porphyry ore forming hydrothermal system at Tumpangpitu was partially exhumed prior to the formation of high-sulfidation ore and alteration assemblages and rapid rates of uplift and erosion in the vicinity of the Sunda-Banda magmatic arc (e.g., Seedorff et al. 2005). Large errors on the U-Pb geochronology prevent the precise calculation of uplift rates.

7.4 Models for the juxtaposition of epithermal and porphyry mineralization

The complex sulfide distribution, epithermal veins and advanced argillic alteration superimposed deep into the early-formed porphyry orebody was most likely a result of climatic and geodynamic factors.

7.4.1 Uplift, exhumation and erosion

Rapid uplift and erosion is the most likely mechanism whereby the epithermal environment is juxtaposed on top of the porphyry environment (Cooke et al., 2011). Tjia et al. (1972) calculated uplift rates of 4.5 - 9 mm/year in tectonically active areas of east Indonesia and 1.4 - 2.5 mm/year for the southern arm of Sulawesi.

The formation of large volumes of weak, unstable alteration clays such as dickite, kaolinite, illite and smectite during epithermal mineralization at Tumpangpitu, could have resulted in weak, unstable slope surfaces, facilitating mass wasting of surficial material downslope and potentially accelerating exhumation. Landscape degradation would incrementally decrease confining pressures, allowing superposition of advanced argillic alteration onto the porphyry complex, albeit at the district to local scale. Superposition of the shallow epithermal system onto the deeper seated porphyry complex requires active unroofing at the time of hydrothermal vein formation (e.g., Richards et al., 2006).

The degree of superposition at Tumpangpitu was extreme. A vertical interval greater than 1 km of porphyry mineralization has been overprinted by epithermal mineralization at Tumpangpitu (Figs. 5.3, 5.4 and 5.40). Although no direct geological evidence is available to quantify the volume of rock removed during inter-mineralization exhumation, it is speculated that around 1 - 2 km could have been eroded during the lifespan of the Tumpangpitu system (e.g., Sillitoe, 1999). Inter-mineralization removal of the thickness of 1.5 to 2 km of lithocap from above porphyry copper systems has been proposed for deposits from Cenozoic magmatic arcs (Sillitoe, 1989; Perello, 1994; Sillitoe, 1995; Perello et al 1996, 1998). Heat to sustain hydrothermal fluid circulation at Tumpangpitu during subsequent overprinting was most likely provided by intrusion of inter and late-mineralization stocks.

7.4.2 Geodynamics - ridge subduction

Magmatic-hydrothermal systems in eastern Java formed after the onset of arc-parallel extension and tensional reactivation of north-easterly trending crustal scale strike slip fault networks in (Hall and

Sevastjanova, 2012). Arc transverse faults (Fig. 2.3) localized the rapid ascent of magma and controlled the emplacement of the Miocene intrusive complex at Tumpangpitu and facilitated the efficient release of volatiles and metals at high crustal levels. The subduction of the buoyant Roo Rise oceanic plateau, beneath Java is inferred to have caused a kink, or tear in the down-going slab (Garwin, 2002; Garwin et al., 2005), which would have enhanced the delivery of mantle-derived melts enriched in copper and gold to the overlying arc (Garwin, 2002, Fiorentini and Garwin, 2010).

Normal faulting that was active during the epithermal overprint facilitated the advanced argillic alteration overprint onto the porphyry deposit at Tumpangpitu. Intersections where NE-trending strike slip structures offset NW-trending regional structures may have provided structural conduits for late mineralizing porphyry intrusions to ascend to surface (Figs. 5.2 - 5.4). Normal faulting at Tumpangpitu, possibly induced by gravitational collapse, accelerated exhumation of the Miocene sedimentary basement and helped to promote overprinting of the high-sulfidation environment onto the Tumpangpitu porphyry.

7.4.3 Sector collapse model

Significant mass wasting involves the collapse of a large volume of overlying rock from a volcanic edifice (e.g., Sillitoe, 1999; Blackwell et al., 2014). Collapse can be facilitated by listric faulting and slope instability from the formation of clays such as kaolinite, dickite and smectites. Examples of sector collapse can be seen by the cleaved surfaces in the young topography at the active White Island epithermal system in New Zealand (Moon et al., 2009) and at Lihir, PNG (Carman et al., 2003) and many other volcanoes (Blackwell et al., 2014). Listric slump surface in the topography and a short-lived time span between porphyry and epithermal mineralization provides key evidence for sector collapse (~0.5 Ma for Lihir; Carman et al., 2003). If a large collapse event occurs during the formation of a porphyry deposit, it does not have enough time to develop, as it will transcend into the epithermal environment. At White Island, the breached volcanic amphitheatre and related debris avalanche deposits collapsed sector features are readily observed, as it is an active system and the island is not vegetated. Tumpangpitu formed during the Late Miocene to Early Pliocene and is now densely vegetated with teak forests, therefore surface morphology features are not clearly visible. Erosion may also have masked any listric slip feature. Half donut-shaped features noted in topographic features from RTP magnetic datasets (Fig. 1.5) could be remnant sector collapse surfaces. Sector collapse would help to explain the dramatic juxtaposition of epithermal onto the porphyry environments in such a short period of time, if a large, positive volcanic landform previously existed at this site.

7.5 Application of SWIR data to geometallurgical models at Tumpangpitu

SWIR spectral analyses at Tumpangpitu produced robust alteration models that can be applied to geometallurgy in terms of optimizing mine planning, comminution, and mineral process design. The alteration assemblages defined by SWIR analysis at Tumpangpitu (Figs. 5.3 - 5.4) have formed

volumetrically large zones that relate directly to the style of mineralization, metal ratios, and physical rock properties with implications for genetic, resource, metallurgical and geotechnical modelling. Specifically, the high abundance of swelling clays, including smectites such as beidellite (Na-smectite) montmorillonite (Al-smectite), nontronite (Fe-smectite), interlayered illite-smectite and hydrated halloysite identified in the weathered Au-Ag oxide ore deposits and extensive zones of illite - smectite ± kaolinite alteration overlying and surrounding the deposit (Fig. 5.3), can cause reduced permeability during heap leaching (Allen et al., 2007). Their presence could have important implications during mine development.

Allen et al. (2007) modelled the effect on the permeability of reagent to ore by adding a 5 mm layer of montmorillonite and kaolinite in vials with a small amount of water on top. The montmorillonite swelled enough to pop the top off the vial and, after five years, the water still did not reach the material (ore) in the bottom of the vial. Only a minor amount of water percolated to the bottom of the kaolinite vial over the same period (Allen et al., 2007; Fig. 7.2). Even in small quantities, (e.g., 5 % smectite, 15 % halloysite/kaolinite; Fig. 7.2; Allen et al., 2007; Bradshaw, 2013) these clays can affect viscosity, scavenge reagents and coat valuable particles (slime coating), increasing cyanide reagent consumption, increase kWh/ton and decrease gold recovery from oxide ore during the heap leach process (Allen et al., 2007). All these factors can result in delays in gold production, pools on the surface of heap leach piles and reduced metal recovery. Swelling clays, when mixed in a heap leach stockpile can virtually shut down the permeability of the sodium cyanide solution accessing the gold ore in the heap leach pads (Allen et al., 2007). Swelling clays can come loose from the agglomerated ore, migrate within the heap, concentrate in pore spaces and often plug up flow channels in the heap (Allen et al., 2007; Harrison, 2015). Cement is commonly added as a binder during the agglomeration process and lime is added for pH control (Allen et al., 2007). Their presence, combined with the sodium cyanide commonly used to leach, can raise the pH of the leach solution to 10 or even 12. Highly alkaline solutions can cause dissolution of minerals, such as kaolinite. Kaolinite can be dissolved and then precipitated as other clay species (including swelling smectites) if sufficient silica and the appropriate cations are available in solution. Silica gels and amorphous materials can also be created from the dissolved kaolinite and other minerals and act as retardants to the flow of leach solutions in the heap. Clays and micas also affect gold and copper extraction from sulfide during flotation, consequently affecting metal recovery (Bradshaw, 2013). Features of minerals such as the fluorine content of topaz, or high-arsenic contents in sulfosalts such as enargite, luzonite and tennantite have metallurgical significance. Their early recognition is important for mine planning, as well as exploration decisions.

Arsenic-rich ores can be associated with alunite, pyrophyllite, dickite, kaolinite, disapore, topaz and alteration minerals, all easily identifiable using SWIR analysis. SWIR data can identify the high to low-temperature sequence of alteration minerals that define the alteration halo around HSE ore zones, aiding in the identification of As-rich ores. The discrimination of high-arsenic ore zones from low arsenic- zones is crucial to avoid penalties and mill processing issues. Identification of zones of topaz

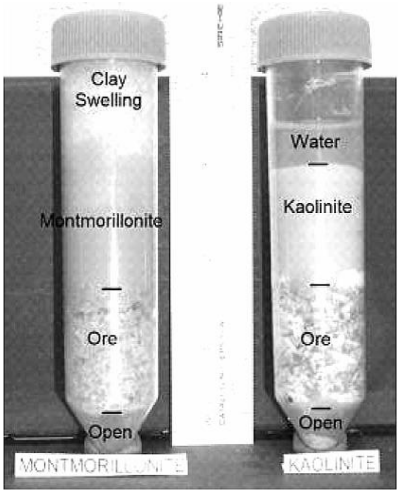

Figure 7.2. Experimental studies showing the effect of permeability when a 5 mm layer of montmorillonite or kaolinite is added to ore (Allen et al., 2007).

Provides a proxy to defining zones of fluorine-rich ore. SWIR spectral analysis led to the initial recognition of topaz at Tumpangpitu, which has a diagnostic absorption features at 2,083 nm (Pontual et al., 2008). The presence of more than 1000 ppm fluorine affects the sulfuric acid units integrated to copper smelters (e.g., Viana et al., 1998). Price penalties are also applied to copper concentrates with high fluorine contents.

7.5.1 Mitigation

SWIR-aided spectral mapping can prove to efficiently differentiate swelling clays from non-swelling clays (Fig. 5.43). Before a heap leach operation is built, the operator should evaluate the clays in the ore and test the agglomeration procedure. The mineralogy and the chemistry of the leach environment must be known, how the minerals and solutions interact, and the products of this interaction must be known. There are at least three significant distributions of swelling clays at Tumpangpitu:

1) Smectites, illite-smectites and halloysite within the Au-Ag oxide ore zones (weathering related clays; Fig. 5.3)
2) Illite - smectite ± kaolinite alteration zone surrounding high-sulfidation epithermal mineralization at all Au-Ag oxide deposits (Figs. 5.2 and 5.3)
3) Smectites that may be generated within the heap leach pile at elevated pH (> 10)

An approach to mitigation would be to conduct SWIR analysis on all drillcore and rockchip samples from the open pit, plot these data on sections and 3D models to define zones of smectite, including beidellite (domain 1), other smectites (domain 2), smectite-illite (domain 3), halloysite (domain 4), hypogene kaolinite-dickite (domain 5), illite/white micas (domain 6), and pyrophyllite(domain 7) to allow planning for blending of primary high swelling clay zones (domains 1 - 4), sticky clay zones (domain 5) and pre-cursors to swelling smectite zones at alkaline pH in leach pad

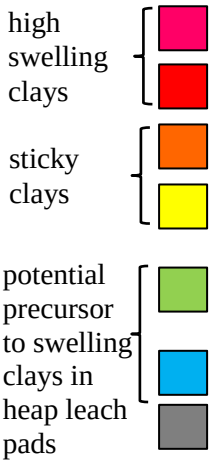

1. **Beidellite (no. 1 swelling clay)**
2. **Smectites (all other swelling clays; montmorillonite, nontronite and saponite)**
3. **Halloysite (kaolinite PX; can be hydrated)**
4. **Kaolinite WX - dickite (hypogene; small clay particle size blocks pores/channels in HL restricting access to ore and pre-cursor to smectite in alkaline HL cyanide solution)**
5. **Illite/white micas (muscovite and paragonite; pre-cursors to illite-smectite in alkaline HL cyanide solution)**
6. **Pyrophyllite (possible processing issues)**
7. **Alunite**

Figure 7.3. Mineral domain geometallurgy model for oxide Au-Ag deposits (Harrison, 2015).

(domains 5-7) with low swelling clay zones e.g., quartz-rich vuggy quartz and massive quartz - alunite ore zones (Fig. 5.43; Harrison, 2015). This type of clay domain model can be used to develop a processing strategy for current and future mining. These models provide key information regarding the volume, geometry, and spatial relationships of clay alteration zones. For advanced exploration and development projects, the information provided by SWIR analyses can be vital for helping to anticipate geometallurgical relationships and recoveries (i.e., flotation and process design) and rock hardness (geotechnical and mine planning; Harraden et al, 2013).

Mitigation strategies include investigating whether particle size (degree of crushing) has an effect on permeability within the heap leach pile, reduction of the irrigation flowrate to increase leaching time, increase particle size to improve permeability, but without decreasing the recovery of gold. Additional mitigation strategies include blending of ores to stay below a certain % of clay (e.g., 20 % clay-rich ore and 80 % quartz-rich ore), addition of a binding agent which would increase permeability, ploughing, mixing, reduction of heap heights in leach pads to increase the surface area and elimination of fines after crushing (leaching of fines by the acid pugging/curing process or by a resin in pulp process; Allen et al., 2007).

Some limitations of spectral analysis include its inability to quantify the volume of clay present. Further XRD or QEMSCAN analysis is required to provide volumetric analyses. Spectral analysis does not independently produce the data sets required for advanced deposit models. Careful geologic logging of drillcore together with data acquired from microprobe analysis, XRD, and geochemical analysis are required to provide a comprehensive framework for data interpretation, in order to produce a successful geologic model for feasibility purposes (Harraden et al., 2013; Harrison and Maryono, 2012; Harrison, 2015). The application of SWIR spectral analysis to determine the extent and variability in hydrothermal alteration in porphyry and epithermal deposits should be one essential component of the deposit-scale geological model and, in turn, the geometallurgical and process models.

7.6 Exploration implications and applications

The discovery of Tumpangpitu has provided a great success story after decades of exploration. At Tumpangpitu, it took 17 years of exploration by various companies before the deep porphyry deposit was intersected in 2008 (Norris, 2011). Good geological observations, the correlation of molybdenum soil anomalies with hydrothermal magnetite identified from RTP magnetic surveys, the integration of spectral data with varied datasets, alongside a fundamental understanding of the lithocap environment and vectoring from near surface alteration-mineralization intersected by shallow oxide drillholes were crucial to understanding the exploration targets that resulted in these discoveries. The porphyry gold and copper resource more than tripled from 8 Moz of Au in 2010 to 28 Moz of Au by 2012 (Intrepid Mines Ltd, 2010, 2012).

7.6.1 District exploration

Delineation of remnant Miocene volcanic centers that host Late Miocene-Pleistocene volcanic complexes with nested multiphase intrusion centers is a key selection criterion for discovering fertile districts along the Sunda-Banda magmatic arc (Fig. 1.3). Maryono et al. (2017) used radiometric dating to define a cut off age of 5 Ma between well-endowed porphyries (< 5 Ma) and poorly endowed porphyries (> 5Ma) of the Sunda-Banda arc. On a district scale, these well-endowed porphyries appear to have formed ~ 1 km southwest of the poorly endowed porphyries e.g., at Batu Hijau (Garwin, 2000, Maryono et al., 2017), Elang (Maryono et al., 2017) and Tumpangpitu. The productive porphyry districts are associated with large lithocaps (>20 km^2; Fig. 2.7) and post-mineralization diatreme breccia bodies.

The combination of soil geochemistry (low level Mo anomalies) and ground-airborne magnetic data (small discrete subtle magnetic anomalies) have provided direct tools to delineate mineralized porphyry zones under large lithocap bodies at Tumpangpitu. The latest 3D modelling of airborne magnetic data indicates biotite - magnetite alteration zones at depth at Elang, Tumpangpitu, Brambang and Hu'u (Maryono et al., 2017)

7.6.2 Mapping mineralized clasts in diatremes

Mapping the spatial locations and density of mineralized porphyry clasts in diatreme breccia bodies (mainly upper facies mill breccias at Tumpangpitu) intersected in near surface drillholes, provided an excellent exploration tool for targeting mineralized porphyry at depth at Tumpangpitu and can be applied to exploration for porphyry deposits worldwide. The presence of chalcopyrite and bornite-mineralized and veined clasts, as well as quartz - magnetite ± K-feldspar clasts (Fig. 3.22), provided strong evidence for the presence of a mineralized potassic zone in the underlying porphyry system. Such clasts have now been recognized at a number of localities in drillholes from Tumpangpitu and led to the discovery of deep mineralized porphyry overprinted by HSE mineralization in Zone B,

1.5 km south of Tumpangpitu (Fig. 5.2). The first drillhole intersection at Zone B from 790 m depth returned assays of 86 m @ 1.11g/t Au and 0.56% Cu (drillhole GTD-10-137; Intrepid Mines Ltd, 2010).

7.6.3 SWIR spectroscopy

The application of SWIR analysis at Tumpangpitu is an essential aid to characterize alteration types and their distribution, as well as its application towards geometallurgy. Spectral analysis at Tumpangpitu proved effective at defining zones containing pyrophyllite, which is megascopically and microscopically difficult to distinguish from white mica, but has a distinctive absorption feature at 2,167 nm in SWIR spectra (Pontual et al., 2008). SWIR spectral analysis also led to the initial recognition of topaz and zunyite, which have diagnostic absorption features at 2,083 nm and 2,137 nm, respectively (Pontual et al., 2008). Mineral parameter vectors found to be effective at Tumpangpitu include the alunite peak position between 1480 nm and 1490 nm on the SWIR spectrum shifting towards Na-alunite at higher wavelengths (>1490 nm) in samples along major faults that are closer to the inferred intrusive source of acidic condensates (Figs. 5.3, 5.5 and 5.6).

Results of spectral analysis should prove applicable elsewhere, such as where an extensive lithocap exists with zones of weak to barren mineralization in remote, inaccessible regions. In such an environment where geochemical rock chip sampling techniques may fail to provide direct indicators of the hidden targets, spectral analysis has the potential to provide an alternative target. Identification of concealed porphyry targets at Tumpangpitu under the lithocap, confirmed by the results of scout drill testing, was facilitated by the integration of spectral data, subtle soil geochemical data and geophysical magnetic anomalies which constitute compelling data for scout drill testing. Erosion and weathering must also be considered, the latter masking ore in places but potentially improving the ore quality through oxidation, as is the case at Tumpangpitu. After all of these datasets are considered, and the SWIR data plotted as alteration, reconstruction of the topography and hydraulic gradient during hydrothermal activity, combined with identification of the zones of paleofluid flow through alteration mineralogy can assist with the generation of drill targets. The directional indicators and mineralization signatures found in this study have the potential to indicate the likely direction to the intrusive center during exploration of similar porphyry - epithermal districts.

7.6.4 Lithocap dimensions

Delineation of the lateral surface extent of lithocaps and understanding their internal alteration zoning is crucial, as they may be used as a proxy for the size of the underlying mineralized porphyry intrusions (Fig. 2.7; Cooke, 2013; Harrison, 2014; Maryono et al., 2017). In addition, there is potential for deeper porphyry and peripheral epithermal intermediate-sulfidation vein mineralization (Chang et al., 2011). Some world-class porphyry deposits have been discovered under large lithocaps, including Tumpangpitu and Far Southeast, Philippines (Chang et al., 2011). Understanding alteration vectoring in the lithocap environment is therefore key to targeting high-sulfidation epithermal deposits and

underlying porphyry mineralization at depth. The presence of a lithocap indicates the level of erosion is consistent with epithermal depths, and so there is potential for epithermal and/or porphyry mineralization nearby (Chang et al., 2011). This is clearly demonstrated in the Tujuh Bukit district and at many other locations worldwide.

7.7 Future work

Some recommendations for future work and research are:

- Geological, alteration and structural mapping in the open pits at Tumpangpitu gold oxide deposits and new road cut exposures would help to refine all deposit-scale models.
- Additional sampling for sulfur isotope analysis to include a wider selection of porphyry-related sulfides (molybdenite, bornite, chalcocite and covellite), intermediate-sulfidation tetrahedrite-tennentite bearing veins within and adjacent to the lithocap, distal base metal galena-sphalerite veins that surround Tumpangpitu, as well as sulfides and sulfosalts from the low-sulfidation epithermal prospect at Gunung Manis 4 km east of Tumpangpitu (Fig. 3.18).
- Apatite (U-Th)/He thermochronometry would provide added insights into the fluid contributed from oceanic or continental source rocks, and the rate of exhumation of the deposit and source magma composition respectively.
- CL imaging of quartz flooding zones to determine processes of formation.
- Fluid inclusion studies would aid in providing information on depths of formation for individual vein types.
- $^{40}Ar/^{39}Ar$ dating of other K-bearing minerals including biotite, muscovite and all phases of alunite veining (pre- syn- and post Tumpangpitu diatreme) are needed for constraining the duration of epithermal mineralization.
- Further Re/Os age determination on molybdenite from B veins from all phase 4, 5 and 6 inter-mineralization porphyry tonalites at Tumpangpitu to refine the ages of mineralization.
- SWIR, XRD and XRF-aided clay domain geometallurgical models to aid in Au-Ag extraction by heap leach process.
- $\delta^{18}O$ and δD analyses on alteration minerals (e.g., biotite, illite, muscovite, pyrophyllite, dickite, alunite, etc.) would provide constraints on the various types of hydrothermal fluids involved in alteration of the rocks and ore formation, and on the amount of mixing that occurred between the different fluids.

REFERENCES

Allan, M.M., Morrison, G.W., and Yardley, B.W.D., 2011, Physiochemical evolution of a porphyry-breccia system: a laser ablation ICP-MS study of fluid inclusions in the Mount Leyshon Au deposit, Queensland, Australia: Economic Geology, v. 106, p. 413-436.

Angeles, C.A., Prihatmoko, S., and Walker, J.S., 2002, Geology and alteration-mineralization characteristics of the Cibaliung epithermal gold deposit, Banten, Indonesia: Resource Geology, v. 52, p. 329-339.

Arc Exploration Ltd., 2013, Trenggalek geochronology, company presentation, 4p.

Arancibia, O.N., and Clark, A.H., 1996, Early magnetite - amphibole - plagioclase alteration-mineralization in the Island copper porphyry copper-gold-molybdenum deposit, British Columbia: Economic Geology, v. 91, p. 402-438.

Arribas, A., Jr., 1995, Characteristics of high-sulfidation epithermal deposits, and their relation to magmatic fluid, in Thompson, J. F. H., ed., Magmas, Fluids, and Ore Deposits: Mineralogical Association of Canada Short Course Series, v. 23, p. 419-454.

Arribas, A., Jr., Cunningham, C. G., Rytuba, J. J., Rye, R. O., Kelly, W. C., Podwysocki, M. H., McKee, E. H., and Tosdal, R. M., 1995a, Geology, geochronology, fluid inclusions and isotope geochemistry of the Rodalquilar gold alunite deposit, Spain: Economic Geology, v. 90, p. 795-822.

Arribas, A., Jr., Hedenquist, J.W., Itaya, T., Okada, T., Concepción, R.A., and Garcia, J.S., Jr., 1995b, Contemporaneous formation of adjacent porphyry and epithermal Cu-Au deposits over 300 ka in northern Luzon, Philippines: Economic Geology, v. 23, p. 337-340.

Arif, J., Baker, T., 2004, Gold paragenesis and chemistry at Batu Hijau, Indonesia: implications for gold-rich porphyry copper deposits: Mineralium Deposita, v. 39, p. 523-535.

Auger Resources Ltd., 2012, Progressing a major gold-copper project, Wonogiri, Indonesia: corporate presentation, 22p. http://www.augur.com.au/index.cfm/reports- announcements/2012-presentations/progressing-a-major-gold-copper-project-wonogiri-indonesia/

Audley-Charles, M.G., 2004, Ocean trench blocked and obliterated by Banda forearc collision with Australian proximal continental slope: Tectonophysics, v. 389, p. 65-79.

Baker, J., Peate, D., Waight, T. and Meyzen, C., 2004, Pb isotopic analysis of standards and samples using a Pb-207-Pb-204 double spike and thallium to correct for mass bias with a double-focusing MC-ICP-MS: Chemical Geology, v. 211, p. 275-303.

Baumgartner, R., Fontbonté, L., Spikings, R., Ovtcharova, M., Schaltegger, U., Schneider, G., Page, L., and Gutjahr., 2009, Bracketing the age of hydrothermal-magmatic activity at the Cerro de Pasco epithermal polymetallic deposit, Central Peru: A U-Pb and $^{40}Ar/^{39}Ar$ study: Economic Geology, v. 104, p. 479-504.

Bawasu, M.L., and Espi, J.O., 2015, Timing of ore mineralization at the Golpu and Nambonga North porphyry copper-gold deposits, Papua New Guinea: Insights from Re-Os Ages: Abstract to poster presentation, SEG conference, Hobart, Australia, 1p.

Basuki, A., Sumanagara, D.A., and Sinambela, D., 1994, The Gunung Pongkor gold-silver deposit,

West Java, Indonesia: Van Leeuwen, T.M., Hedenquist, J.W., James, L.P., and Dow, J.A.S. (eds.), Indonesian mineral deposits: Discoveries of the past 25 years: Journal of Geochemical Exploration, v. 50, p. 371-391.

Bendezú, R., and Fontboté, L., 2009, Cordilleran epithermal Cu-Zn-Pb-(Au-Ag) mineralization in the Colquijirca district, Central Peru: deposit-scale mineralogical patterns: Economic Geology, v. 104, p. 905-944.

Black, L. P., and Gulson, B. L., 1978, The age of the Mud Tank Carbonatite, Strangways Range, Northern Territory: BMR Journal of Australian Geology and Geophysics, v.3, p. 227-232.

Black, L. P., Kamos, L., Allen, C.M., Aleinikoff, J.N., Davis, D.W., Korsch, R.J., and Foudoulis, C., 2003, TEMORA 1: a new zircon standard for Phanerozoic U-Pb geochronology: Chemical Geology, v. 200, p. 155-170.

Black, L.P., Kamo, S.L., Allen, C.M., Davis, D.W., Aleninikoff, J.N., Valley, J.W., Mundil, R., Campbell, I.H., Korsch, R.J., Williams, I.S., and Foudoulis, C., 2004, Improved $^{206}Pb/^{238}U$ microprobe geochronology by the monitoring of a trace-element related matrix effect; SHRIMP, ID-TIMS, ELA-ICP-MS, and oxygen isotope documentation for a series of zircon standards: Chemical Geology, v. 205, p. 115-140.

Blackwell, J.L., Cooke, D.R., McPhie, J., and Simpson, K.A., 2014, Lithofacies association and Evolution of the volcanic host succession to the Minifie ore zone: Ladolam gold deposit, Lihir island, Papua New Guinea: Economic Geology, v. 109, p. 1137-1160.

Bradshaw, D., 2013, Influential minerals and their effect on processing: Masters of Economic Geology program, Geometallurgy short course presentation, CODES, University of Tasmania, 15 p.

Braxton, D.P., 2007, Boyongan and Bayugo porphyry copper-gold deposits NE Mindanao, Philippines: Geology, geochemistry and tectonic evolution: Unpublished PhD thesis, University of Tasmania, 307 p.

Braxton, D.P., Cooke, D.R., Ignacio, A.M., Rye, R.O., and Waters, P.J., 2009, Ultra-deep oxidation and exotic copper formation at the Late Pliocene Boyongan and Bayugo porphyry copper-gold deposits, Surigao, Philippines: Geology, mineralogy, paleoaltimetry, and their implications for geologic, physiographic, and tectonic controls: Economic Geology, v. 104, p. 333-349.

Brimhall, G.H., 1977, Early fracture-controlled disseminated mineralization at Butte, Montana: Economic Geology, v. 72, p. 37-59.

Cannell, J.B., 2004, El Teniente porphyry copper-molybdenum deposit, central Chile: Unpublished Ph.D. thesis, University of Tasmania, 317 p.

Cannell, J., Cooke, D.R., Walshe, J.L., and Stein, H., 2005, Geology, mineralization, alteration, and structural evolution of the El Teniente porphyry Cu-Mo deposit: Economic Geology, v. 100, p. 979-1003.

Carlile, J. C., and Mitchell, A. H. G., 1994, Magmatic arcs and associated gold and copper mineralization in Indonesia: Journal of Geochemical Exploration, v. 50, p. 91-142.

Carman, G.D., 2003, Geology, mineralization, and hydrothermal evolution of the Ladolam gold deposit, Lihir Island, Papua New Guinea: Society of Economic Geologists Special Publication, no. 10, p. 247-284.

Chang, Z., Vervoort, J. D., McClelland, W. C., and Knaack, C., 2006, U-Pb dating of zircon by LA-

ICP-MS: Geochemistry, Geophysics, Geosystems, v. 7, no. 5, p. 1-14.

Chang, Z., Hedenquist, J.W., White, N.C., Cooke, D.R., Roach, M., Deyell, C.L., Garcia, J., Gemmell, B.J., McKnight, S., and Cuison, L., 2011, Exploration tools for linked porphyry and epithermal deposits: example from the Mankayan intrusion-centered Cu-Au district, Luzon, Philippines: Economic Geology, v. 106, p. 1365-1398.

Chávez, W.X., 2000, Supergene oxidation of copper deposits: Zoning and distribution of copper oxide minerals: Society of Economic Geologists Newsletter, v. 41, p. 1-21.

Chiaradia, M., Fontboté , L., and Paladines, A., 2004, Metal sources in mineral deposits and crustal rocks of Ecuador (1° N-4° S): A lead isotope synthesis: Economic Geology, v. 99, p. 1085-1106.

Chiaradia, M., Schaltegger, U., Spikings, R., Wotzlaw, J-R., and Ovtcharova, M., 2013, How accurately can we date the duration of magmatic-hydrothermal events in porphyry systems? - An invited paper: Economic Geology, v. 108, p. 565-584.

Clark, A.H., 1993, Are outsize porphyry copper deposits either anatomically or environmentally distinctive?: Society of Economic Geologists Special Publication 2, p. 213-282.

——1995, Giant ore deposit. II. Controls on the scale of orogenic magmatic-hydrothermal mineralization: Department of Geological Sciences, Queens University, Kingston, Ontario, 753p.

Clark, A.H., and Arancibia, O.N., 1996, The occurrence, paragenesis and implications of magnetite-rich alteration-mineralization in calc-alkaline porphyry copper deposits, in Clark, A.H., ed., Giant ore deposits-II: Proceedings of the Second Giant Ore Deposits Workshop, Kingston, Ontario, Canada, p. 583–640.

Clode, C., Proffett, J., Mitchell, P., and Munajat, I., 1999, Relationships of intrusion, wall-rock Alteration and mineralization in the Batu Hijau copper-gold porphyry deposit: Pacrim ’99 Congress, Bali, Indonesia, 1999, Proceedings: Melbourne, Australian Institute of Mining and Metallurgy, p. 485-498.

Cloos, H., 1941, Bau und Tatigkeit von Tuffschloten. Untersuchungen an dem Schwäbischen Vulkan: Geol. Rundsch, v. 32, p. 705-800.

Compston, W., 1999, Geological age by instrumental analysis: the 29th Hallimond Lecture: Mineralogical Magazine, v. 63, p. 297-311.

Cooke, D.R., McPhail, D.C., and Bloom, M.S., 1996, Epithermal gold mineralization, Baguio district, Philippines, geology, mineralization, alteration and the thermochemical environment of ore deposition: Economic Geology, v. 91, p. 243-272.

Cooke, D.R., and Simmons, S.F., 2000, Characteristics and genesis of epithermal gold deposits: Reviews in Economic Geology, v. 13, p. 221-244.

Cooke, D.R., Hollings, P.H., and Walshe, J.L., 2005, Giant porphyry deposits: Characteristics, distribution and tectonic controls: Economic Geology, v. 100, p. 801-818.

Cooke, D. R., Deyell, C. L., Waters, P. J., Gonzales, R. I., and Zaw, K., 2011, Evidence for magmatic-hydrothermal fluids and ore-forming processes in epithermal and porphyry deposits of the Baguio district, Philippines: Economic Geology, v. 106, p. 1399-1424.

Cooke, D.R., and Wilson, A.J., 2013, Leached caps and supergene enrichment processes in porphyry

copper deposits: Course presentation, Ore deposits of South America fieldtrip, Masters of Economic Geology program, CODES, University of Tasmania,16p.

Cooke, D.R., 2013, The porphyry-epithermal interface: workshop presentation, MGEI Annual Convention, Bali, Indonesia, 9p.

Coote, A., 2009, Petrological studies of diamond core from GTD29, GTD35, GTD46, GTD49, GTD55, GTD42, GTD53 and GTD45 of the Tumpangpitu porphyry copper-gold project, East Java: Consultants report to Intrepid Mines Ltd: 66p.

Coote, A., 2010, Petrological studies of surface rockchip samples and diamond core from the Tujuh Bukit copper-gold project area, Java, Indonesia: Consultant report to Intrepid Mines Ltd: 59p.

Daly, M.C., Cooper, M.A., Wilson, I., Smith, D.G., and Hooper, B.D.G, 1991, Cenozoic plate tectonics and basin evolution in Indonesia: Marine and Petroleum Geology, v. 8, p. 2-21.

Davies, A.G.S, 2002, Geology and genesis of the Kelian gold deposit, East Kalimantan, Indonesia: PhD thesis, University of Tasmania, 405 p.

Davies, A.G.S., Cooke, D.R., Gemmell, J.B., and Simpson, K, 2008a, Diatreme breccias at the Kelian gold mine, Kalimantan, Indonesia: Precursors to epithermal gold mineralization: Economic Geology, v.103, p. 689-716.

Davies, A.G.S., Cooke, D.R., Gemmell, J.B., Leeuwen T.V., Cesare, P., and Hartshorn, G, 2008b, Hydrothermal breccias and veins at the Kelian gold mine, Kalimantan, Indonesia: genesis of a large epithermal gold deposit: Economic Geology, v.103, p. 717-757.

Deino, A. and Potts, R., 1990, Single-crystal $^{40}Ar/^{39}Ar$ dating of the Olorgesailie Formation, southern Kenya rift: Journal of Geophysical Research, v. 95, p. 8453-8470.

Deyell, C.L., Leonardson, R, Rye, R.O, Thompson, J.F.H, Bissig, T, and Cooke D.R, 2005, Alunite in the Pascua-Lama high-sulfidation deposit: constraints on alteration and ore deposition using stable isotope geochemistry: Economic Geology, v.100, p. 131-148.

Dilles, J. H. and Einaudi, M. T., 1992, Wall rock alteration and hydrothermal flow paths about the Ann-Mason porphyry copper deposit, Nevada-a 6 km vertical reconstruction: Economic Geology, v. 87, p. 1963-2001.

Einaudi, M.T., Hedenquist, J.W., and Inan, E., 2003, Sulfidation state of hydrothermal fluids: The porphyry-epithermal transition and beyond: Society of Economic Geologists Special Publication, v. 10, p. 285-313.

Einaudi, M. T., 1997, Mapping altered and mineralized rocks: An introduction to the Anaconda method: Unpublished short-course notes, Stanford University, 16 p.

Fryer, B.J., Jackson, S.E., Longerich, H.P., 1993, The application of laser ablation microprobe-inductively coupled plasma-mass spectrometry (LAM-ICP-MS) to in situ (U)-Pb Geochronology: Chemical Geology, v. 109, p. 1-8.

Fiorentini, M.L., and Garwin, S.L, 2010, Evidence of a mantle contribution in the genesis of magmatic rocks from the Neogene Batu Hijau district in the Sunda Arc, South Western Sumbawa, Indonesia: Contributions to Mineralogy and Petrology, v. 159, p. 819-837.

Fleck, R.J., Sutter J.F., and Elliot D.H., 1977, Interpretation of discordant $^{40}Ar/^{39}Ar$ age-spectra of Mesozoic tholeiites from Antarctica: Geochimica et Cosmochimica Acta, v. 41, p. 15-32.

Foden, J.D. and Varne, R., 1980, The petrology and tectonic setting of Quaternary-Recent volcanic centers of Lombok and Sumbawa, Sunda arc: Chemical Geology, v. 30, p. 201-226

Gaibor, A., Dunkley, P., Wehrle, A., Lesage, G., Boer, D. Den and Froilan, C., (2013) The discovery and understanding of the Far Southeast copper-gold porphyry, Luzon, Philippines. Proceedings, New Gen Gold conference, Pay Dirt Media, Perth, p. 233-247.

Garwin, S.L., 2000, The setting, geometry and timing of intrusion-related hydrothermal systems in the vicinity of the Batu Hijau porphyry copper-gold deposit, Sumbawa, Indonesia: Unpublished Ph.D. thesis, University of Western Australia, Nedlands, Western Australia, Australia, 320 p.

Garwin, S., 2002, The geologic setting of intrusion-related hydrothermal systems near the Batu Hijau porphyry copper-gold deposit, Sumbawa, Indonesia: Society of Economic Geologists Special Publication 9, p. 333-366.

Garwin, S., Hall, R., and Watanabe, Y., 2005, Tectonic setting, geology and gold and copper mineralization in Cenozoic magmatic arcs of Southeast Asia and the west Pacific, in Hedenquist, J., Goldfarb, R. and Thompson, J. (eds.), Economic Geology 100thAnniversary Volume, p. 891-930.

Gemmell, J, B., 2012, Low and intermediate sulfidation epithermal deposits: Red Metals Presentation Masters of Economic Geology program, CODES, University of Tasmania, 11 p.

Gray, D., 2011, Structural geology review, Tujuh Bukit project, East Java, Indonesia: Unpublished Internal consultant report by Geostructures Pty Ltd. for Intrepid Mines Ltd, 64 p.

Gray, D., 2012, Faulting and 3D structural model development for Tumpangpitu, Tujuh Bukit project, East Java, Indonesia: Unpublished Internal consultant report by Geostructures Pty Ltd. for Intrepid Mines Ltd, 36 p.

Gustafson, L., B., and Hunt, J., P., 1975, The porphyry copper deposit at El Salvador, Chile: Economic Geology, v. 70, p. 857-912.

Gustafson, L.B. and Quiroga G., Jorge, 1995, Patterns of mineralization and alteration below the porphyry copper orebody at El Salvador, Chile: Economic Geology, v. 90, p. 2-16.

Hall, R., 2002, Cenozoic geological and plate tectonic evolution of SE Asia and the SW Pacific: computer-based reconstructions, model and animations: Journal of Asian Earth Sciences, v. 20, p. 353-431.

Hall, R., 2008, Continental growth at the Indonesian margins of southeast Asia: Arizona Geological Society Digest, v. 22, p. 245-258.

Hall, R., 2009, The Eurasian SE Asian Margin as a modern example of an accretionary orogeny: Cawood P. A. and Kroner A. eds, Accretionary Orogen in space and time: Geological Society of London Special Publication, v. 318, p. 351-372.

Hall, R., 2012, Late Jurassic–Cenozoic reconstructions of the Indonesian region and the Indian Ocean: Tectonophysics, v. 570-571, p. 1-41

Hall, R., and Sevastjanova, I., 2012, Australian crust in Indonesia: Australian Journal of Earth Sciences, v. 59, p. 827-844.

Halpin, J.A., Torsten, J., McGoldrick, P., Meffre, S., Berry, R. F., Everard, J.L., Calver, C. R.,

Thompson, J., Goemann, K., and Whittaker, J.M., 2014, Authigenic monazite and detrital zircon dating from the Proterozoic Rocky Cape Group, Tasmania: Links to the Belt-Purcell Supergroup, North America: Precambrian Research, v. 250, p. 50-67.

Hamilton, W. B., 1979, Tectonics of the Indonesian region: United States Geological Survey Professional Paper 1078, Washington DC, 345 p.

Harley, S.L. and Kelly, N.M., 2007. Zircon: Tiny but timely: Elements, v. 3, p. 13-18.

Harraden, C.L., Mcnulty, B.A., Gregory, M.J., and Lang, J.R., 2013, Shortwave infrared spectral analysis of hydrothermal alteration associated with the Pebble porphyry copper-gold-molybdenum deposit, Iliamna, Alaska: Economic Geology, v. 108, p. 483-494.

Harbury, N.A., and Kallagher, H.J., 1991, The Sunda outer-arc ridge, north Sumatra, Indonesia: Journal of southeast Asian Earth Sciences, v.6, no. 3-4, p. 463-476.

Harijoko, A., Sanematsu, K., Duncan, R. A., Prihatmoko, S., and Watanabe, K., 2004, Timing of the mineralization and volcanism at Cibaliung gold deposit, western Java, Indonesia: Resource Geology, v. 54, p. 187-196.

Harris, A.C., and Golding, S., 2002, New evidence of magmatic-fluid-related phyllic alteration: Implications for the genesis of porphyry Cu deposits: Geology, v. 30, p. 335-338.

Harrison, R.L., 2009, Coastal mapping report, Tujuh Bukit Project: Unpublished internal technical report for Intrepid Mines Ltd, 18 p.

Harrison, R.L., 2011, The practical application of spectral analysis in geological modeling and regional exploration at the Tujuh Bukit project, East Java, Indonesia: Conference presentation IAGI Makassar, Sulawesi, Indonesia, 32 p.

Harrison, R.L., 2012, Salakan prospect 2012 drill program, summary report SND-12-001: Unpublished internal technical report for Intrepid Mines Ltd, 38p.

Harrison, R.L., and Maryono, A., 2012, Tumpangpitu porphyry-high sulfidation epithermal deposit, Tujuh Bukit Project, Indonesia - geology, alteration and mineralization: Red Metals Symposium Presentation, CODES, University of Tasmania, 51 p.

Harrison, R.L., and Rohrlach, B.D., 2013, Application of TerraSpec spectral data in exploration at Cascabel, Northern Ecuador: Investor report for SolGold Plc, 9 p.

Harrison, R.L., 2014, The application of short wave infrared (SWIR) spectral analysis in exploration for the Candrian porphyry copper-gold-molybdenum and high-sulfidation epithermal prospect, Tujuh Bukit district, southeast Java, Indonesia: Master of Economic Geology thesis, University of Tasmania, 126 p.

Harrison, R.L., 2015, Practical application of spectral data towards deposit modelling and Geometallurgy: consultant workshop presentation for J Resources Nusantara, 61 p.

Harrison, R.L., Maryono, A., Norris, M.S., Rohrlach, B.D., Cooke, D.R., Thompson, J.M., Creaser, R.A., and Thiede, D.S., 2017, Geochronology of the Tumpangpitu porphyry gold-copper-molybdenum and high-sulfidation epithermal gold-silver-copper deposit - Evidence for pre- and post-mineralization diatremes in the Tujuh Bukit district, Southeast Java, Indonesia: Economic Geology (in press).

Hedenquist, J.W., and Lowenstern, J.B., 1994, The role of magmas in the formation of hydrothermal

ore deposits: Nature, v. 370, p. 519-527.

Hedenquist, J.W., Arribas, A., Jr., and Reynolds, T.J., 1998, Evolution of an intrusion-centered hydrothermal system; Far Southeast-Lepanto porphyry and epithermal Cu-Au deposits, Philippines: Economic Geology, v. 93, p.373-404.

Hedenquist, J.W., and Garcia, J.S., Jr, 1990 Sulfur isotope systematics in the Lepanto mining district, northern Luzon, Philippines: Mining Geology, v. 40, 219, p. 67.

Hedenquist, J.W., Arribas, A.R, and Gonzalez-Urien, E., 2000, Exploration for epithermal gold deposits: Reviews in Economic Geology, v.13, p. 245-277.

Hedenquist, J.W., and Taran, Y.A., 2013, Modeling the formation of advanced argillic lithocaps: volcanic vapor condensation above porphyry intrusions: Economic Geology, v. 108, p.1523-1540.

Hehnke, C., Ballantyne, G., Martin, H., Hart, W., Schwarz, A., and Stein, H., 2012, Geology and exploration progress at the Resolution porphyry Cu-Mo deposit, Arizona: Economic Geology Special Publication, v. 16, p. 147-166.

Henley, R.W., and McNabb, A., 1978, Magmatic vapor plumes and groundwater interaction in porphyry copper emplacement: Economic Geology, v. 73, p. 1-20.

Henley, R.W., and Ellis, A.J., 1983, Geothermal systems ancient and modern:A geochemical review: Earth-Science Reviews, v. 19, p. 1-50.

Herrmann, W., Blake, M., Doyle, M., Huston, D., Kamprad, J., Merry, N., and Pontual, S., 2001, Short wavelength infrared (SWIR) spectral analysis of hydrothermal alteration zones associated with base metal sulfide deposits at Rosebery and Western Tharsis, Tasmania, and Highway-Reward, Queensland: Economic Geology, v. 96, p. 939-955.

Holley, E.A., Bissig, T., and Monecke, T., 2016, The Veladero high-sulfidation epithermal gold deposit, El Indio-Pascua belt, Argentina: Geochronology of alunite and jarosite: Economic Geology, v.111, p.311-330.

Hoschke, T., 2010, Geophysical signatures of copper-gold porphyry and epithermal gold deposits, and implications for exploration: ARC Centre of Excellence in Ore Deposits, University of Tasmania, 47 p.

Hoschke, T., 2012, Geophysical signatures of SW Pacific porphyry deposits: Presentation, Red Metals Symposium, CODES, University of Tasmania, 8 p.

Hoskin, P.W.O., and Schaltegger, U., 2003, The composition of zircon and igneous and metamorphic petrogenesis: Reviews in Mineralogy and Geochemistry, v. 53, p. 27-62.

Huspeni, J., 2012, Newmont Mining Corporation presentation, Profitable growth with disciplined returns:
http://newmont.q4web.com/files/doc_presentations/Diggers%20%20Dealers%20v5.pdf

IAMGOLD., 2007, The epithermal deposit for Au, Cu, Ag Quimsacocha Project, Azuay Province, Ecuador: Presentation, 48 p.

IAMGOLD., 2009, Quimsacocha Gold Project, Azuay Province, Ecuador: NI-43-101 Technical Report, 187 p. https://secure.kaiserresearch.com/i/jk/tr16/TRIMG20090201.pdf

Idrus, A., Kolb, J. and Meyer F.M., 2007, Chemical composition of rock forming minerals in copper-gold-bearing tonalite porphyry intrusions at the Batu Hijau deposit, Sumbawa Island, Indonesia: Implications for crystallisation conditions and fluorine-chlorine fugacity, Resource Geology, v.57, p. 102-113.

Imai, A., Shinomiya, J., Soe, T.M., Setijadi, D.L., Watanabe, K., and Warmada, W., 2007, Porphyry-type mineralization at Selogiri area, Wonogiri Regency, Central Java, Indonesia: Resource Geology, v. 57, p. 220-240.

Intrepid Mines Ltd., 2008, Tujuh Bukit Technical Report, 120 p.

Intrepid Mines Ltd., 2009, Tujuh Bukit Technical Report, 114 p. (http://www.asx.com.au/asxpdf/20090204/pdf/31fwm1q2029rkr.pdf)

Intrepid Mines Ltd., 2010, Tujuh Bukit Technical Report, 193 p. (http://intrepidmines.com.au/wp-content/uploads/reports-and-presentations-archive/NI43-101_Nov_2010_FINAL_ASX.pdf)

Intrepid Mines Ltd., 2011, Tujuh Bukit Technical Report, 169 p. (http://intrepidmines.com.au/wp-content/uploads/2012/06/NI43-101-Technical-Report-Tujuh-Bukit-Mineral-Resource-PDF.pdf)

Intrepid Mines Ltd., 2012, Tujuh Bukit Technical Report, 152 p. (http://intrepidmines.com.au/reports-and-presentations/tujuh-bukit-technical-report-november-2012/)

Irianto, B., and Clark, G.H., 1995, The Batu Hijau porphyry copper-gold deposit, Sumbawa Island, Indonesia, in Mauk, J.L., and St. George, J.D., eds., 1995, Parcim Congress, Auckland, New Zealand, Glenside, South Australia, Australian Mineral Foundation, Proceedings, p. 299-304.

Jackson, S.E., Pearson, N.J., Griffin, W.L., Belousova, E.A., 2004, The application of laser ablation-inductively coupled plasma-mass spectrometry to in situ U-Pb zircon geochronology: Chemical Geology, v. 211, p. 47-69.

Jones, S., Herrmann, W., and Gemmell, JB., 2005, Short wavelength infrared spectral characteristics of the HW Horizon: Implications for exploration in the Myra Falls volcanic-hosted massive sulfide camp, Vancouver Island, British Columbia, Canada: Economic Geology, v.100, p. 273-294.

Katili, J. A., 1975, Volcanism and plate tectonics in the Indonesian island arcs: Tectonophysics, v. 26, p. 165-188.

Kavalieris, I., and Bat-Erdene, K., 2011 Notes on the geology and alteration of Tujuh Bukit porphyry Cu-Au project, East Java, Indonesia: Unpublished internal consultant report for Intrepid Mines Ltd, 15 p.

Kirkham, R.V., and Dunne, K.P.E., 2000, World distribution of porphyry, porphyry-associated skarn, and bulk-tonnage epithermal deposits and occurrences: Geological Survey of Canada Open File 3792a, 26 p.

Kerrich, R., Goldfarb, R.J., Groves, D.I., and Garwin, S., 2000, The geodynamics of world-class gold deposits: Characteristics, space-time distribution, and origins: Reviews in Economic Geology, v. 13, p. 501-551.

Kohno, Y., Setijadji, L., D., Utami, P., Harijoko, A., Pecskay, Z., Imai, A., and Watanabe, K., 2005, Geochronology and petrogenesis of Merapi-Merbabu-Telomoyo-Ungaran volcanoes, Central Java, Indonesia: Proceedings Joint Covention HAGI-IAGI-PERHAPI, Surabaya, p. 267-232.

Kosler, J., 2001, Laser-ablation ICPMS study of metamorphic minerals and processes in Sylvester, P. J., ed., Laser-ablation-ICPMS in the Earth Sciences; principles and applications Mineralogical Association of Canada Short Course Handbook, v. 29, p. 185-202.

Kosler, J., and Sylvester P.J., 2003, Present trends and the future of zircon in geochronology; laser ablation ICPMS: Reviews in Mineralogy and Geochemistry v. 53, p. 243-275.

Kuiper, K.F., Deino, A., Hilgen, F.J., Krijgsman, W., Renne, P.R., and Wijbrans, J.B., 2008, Synchronizing rock clocks of Earth history: Science, v. 320, p. 500-504.

Kyne, R., Hollings, P., Jansen, N.H., and Cooke, D.R., 2013, Supergene and hypogene halloysite in a porphyry-epithermal environment at Cerro la Mina, Chiapas, Mexico: Economic Geology, v. 108, p. 1147-1161.

Landtwing, M.R., Dillenbeck, E.D., Leake, M.H., and Heinrich, C.A., 2002, Evolution of the breccia-hosted porphyry Cu-Mo-Au deposit at Agua Rica, Argentina: progressive unroofing of a magmatic hydrothermal system: Economic Geology, v. 97, p. 1273-1292.

Lang, J.R., and Titley, S.R., 1998, Isotopic and geochemical characteristics of Laramide magmatic systems in Arizona and implication for the genesis of porphyry copper deposits: Economic Geology, v. 93, p. 138-170.

Lawlis, E., Cooke, D.R., and Harris, A. C., 2015, Volcanic-hydrothermal breccias at the Lihir alkalic gold deposit, Papua New Guinea: SGA Conference abstract, 4 p.

Leys, C., Cloos, M., New, B.T.E., and MacDonald, D.G., 2012, Gold, copper ± molybdenum deposits of the Ertsberg-Grasberg district, Papua, Indonesia: Economic Geology, v. 16, p. 215-235.

Li, X., Long, W.G., Li, Q.L., Liu, Y., Zheng, Y.F., Yang, Y.H., Chamberlain, K.R., Wan, D.F., Guo, C.H., Wang, X.C., and Tao, H., 2010, Penglai zircon megacrysts: A potential new working reference material for microbeam determination of Hf-O isotopes and U-Pb Age: Geostatistics and Bioanalytical Reviews, v. 34, p. 117-134.

Lickfold, V., Cooke, D.R., Smith, S.G., 2003, Endeavour copper-gold porphyry deposits, Northparkes, New South Wales: Intrusive history and fluid evolution: Economic Geology, v. 98, p.1607-1636.

Longo, A.A., Dilles, J.H., Grunder, A.L., and Duncan, R., 2010, Evolution of calc-alkaline volcanism and associated hydrothermal gold deposits at Yanacocha, Peru: Economic Geology, v. 105, p. 1191-1240.

Lorenz, V., McBirney, A. R., and Williams, H., 1970, An investigation of volcanic depressions: Part III.Maars, tuff-rings, and diatremes: NASA Research Report NGR-38-003-012, 198 p.

Lorenz, V., 1973, On the formation of maars: Bulletin of Volcanology v. 37, p. 183-204.

Lorenz, V., 1986, On the growth of maars and diatremes and its relevance to the formation of tuff rings: Bulletin of Volcanology, v. 48, p. 265-274.

Lorenz, V., 2003, Maar-diatreme volcanoes, their formation and their setting in hard-rock or soft-rock environments: Geolines, v. 15, p, 72-83.

Lorenz, V., and Kurszlaukis, K., 2007, Root zone processes in the phreatomagmatic pipe emplacement model and consequences for the evolution of maar-diatreme volcanoes: Journal of Volcanology

and Geothermal Research, v. 159, p. 4-32.

Lowell, J.D., and Guilbert, J.M., 1970, Lateral and vertical alteration mineralization zoning in porphyry ore deposits: Economic Geology, v. 65, p. 373-408.

Lubis, H., Maryono, A., Perdanakusumah, A., and Hermawan, W., 2005, The Elang porphyry copper and gold mineralization style, Sumbawa, Indonesia: Indonesian Mineral and Coal Discoveries: IAGI Special Issues, p. 1-17.

Lubis, H., Prihatmoko S., and Heryunanto, Y., 2012, Geology and exploration for low sulfidation epithermal gold-silver mineralization in Kerta, Banten: MGEI annual convention, Malang Indonesia: proceedings, p. 39-71.

Ludwig, K. R., 2001, Isoplot/Ex, a geochronological toolkit for Microsoft Excel: Special Publication, Berkeley Geochronological. Centre, Berkeley, California, v.1a-43.

Lulofs, D., 2011 Soil Sampling Procedure, Tujuh Bukit Project: Unpublished report for Intrepid Mines Ltd, 13p.

MacDonald, P.J., Bissig, T., Hart, C.J.R., Barreno, J., and Viera, F., 2011, The hydrothermal evolution of the Quimsacocha high sulfidation Au-Ag-Cu deposit, Azuay Province, ecuador [ext. abs.]: SGA Biennial Conference, Antofagasta, Chile, September 2011, Abstracts 3p.

MacDonald, G.D., and Arnold, L.C., 1994, Geological and geochemical zoning of the Grasberg igneous complex, Irian Jaya, Indonesia: Journal of Geochemical Exploration, v. 50, p. 143-178.

Manske, S.L., and Paul, A.H., 2002, Geology of a major new porphyry copper center in the Superior (Pioneer) district, Arizona: Economic Geology, v. 97, p. 197-220.

Marcoux, E., Milesi, J.P., Soeharto, S., and Rinawan, R., 1993, Noteworthy mineralogy of the Au-Ag-Sn-W (Bi) epithermal ore deposit of Cirotan, West Java, Indonesia: Canadian Mineralogist, v. 31, p.727-744.

Marcoux, E. and Milesi, J.P., 1994, Epithermal gold deposits in West Java, Indonesia: geology, age and crustal source. Journal of Geochemical Exploration, v. 50, p. 393-408.

Markey, R.J., Stein, H.J., and Morgan, J.W., 1998, Highly precise Re-Os dating for molybdenite using alkaline fusion and NTIMS: Talanta, v. 45, p. 935-946.

Markey, R.J., Stein, H.J., Hannah, J.L., Selby, D and Creaser, R.A., 2007, Standardizing Re-Os geochronology: A new molybdenite Reference Material (Henderson, USA) and the stoichiometry of Os salts: Chemical Geology, v. 244, p. 74-87.

Masterman, G.J., 2003, Structural and geochemical evolution of the Rosario copper-molybdenum porphyry deposit and related copper-silver veins, Collahuasi district, northern Chile: Unpublished PhD thesis, University of Tasmania, 310 p.

Masterman, G. J., Cooke D. R., and Moore R. L., 2005, Geology and discovery of porphyry Cu-Mo-Ag deposits in the Collahuasi district, Northern Chile: Porter T. M, (Ed), Super Porphyry Copper and Gold Deposits: A Global Perspective, v.1 p. 175-188.

Maryono, A., Priowasono, E., 2000, Final report on the Gold-Ridge-Santong program: Unpublished internal technical report for PT. Newmont Nusa Tenggara, 6 p.

Maryono, A. and Setyandhaka, D., 2001, Rinti Project Report 2001, Sumbawa Indonesia: Newmont internal company report, 45 p.

Maryono, A., Lubis, H., Perdankusumah, A. and Hermawan, W., 2005, The Elang porphyry copper and gold mineralization style Sumbawa, Indonesia: Indonesian Minerals and Coal Discoveries: IAGI conference, p. 34-51.

Maryono, A., Rompo, I., and Maula, S., 2013, 2012 Annual report, PT Bintang Bulaeng Perkasa, West Lombok NTB: Unpublished internal technical report for PT Buena Perseda Mining Services, 44p.

Maryono, A., Setijadji, L.D., Arif, J., Harrison, R.L., and Soeriaatmadja, E., 2012, Gold, silver and Copper metallogeny of the Eastern Sunda Magmatic Arc, Indonesia: Masyarakat Geologi Ekonomi Indonesia Eastern Sunda Banda Arc resources seminar Malang, East Java, Indonesia, 18p.

Maryono, A., Rompo, I., and Maula S., 2013, Brambang Project Report 2010 to 2012, SW Lombok: Buena Persada internal company report, 89 p.

Maryono, A., Harrison, R.L., Rompo, I., Priowasono, E., and Norris, M., 2016, Successful techniques in exploring the lithocap environment of the Sunda magmatic arc, Indonesia: Conference paper MGEI 8th Annual convention, Bandung, Indonesia, 9 p.

Maryono, A., Harrison, R.L., Cooke, D.R., Rompo, I., and Hoschke, T.G., 2017, Tectonics and geology of porphyry copper-gold deposits along the eastern-Sunda magmatic arc, Indonesia: Economic Geology (in press).

Maula, S., and Levet, B.K., 1996, Porphyry copper-gold signatures and the discovery of the Batu Hijau deposit, Sumbawa, Indonesia: Australian Mineral Foundation, Conference Proceedings, p. 101-103.

Maynard, S.R., 1995, Gold mineralization associated with mid-Tertiary magmatism and tectonism, Ortiz Mountains, Santa Fe County, New Mexico: Geology of the Santa Fe Region: New Mexico Geological Society 46th Annual Fall Field Conference Guidebook, p. 161-166.

Meffre, S., Large, R. R., Scott, R., Woodhead, J., Chang, Z., Gilbert, S. E., Danyushevsky, L. V., Maslennikov, V., and Hergt, J. M., 2008, Age and pyrite Pb-isotopic composition of the giant Sukhoi Log sediment-hosted gold deposit, Russia: Geochimica et Cosmochimica Acta, v. 72, p. 2377-2391.

Meldrum, SJ., Aquino, R.S., Gonzales, R.I., Burke, RJ., Suyadi, A., Irianto, B., and Clarke, D.S., 1994, The Batu Hijau porphyry copper-gold deposit, Sumbawa Island, lndonesia: Journal of Geochemical Exploration, v. 50, p. 203-220.

Menzies, D., 2013, Geochemical/alteration zonation and structural controls on the Wafi-Golpu Porphyry Cu-Au resource, a world class deposit in PNG: Conference presentation, Geology and mineral exploration East Asia: from Russia to PNG, 38 p.

Menzies, D., Shakesby, S., Wass, J., Finn, D., Fitzpatrick, N., Morehari, G., Tekeve, B., Alupian, B., Kur, J., Kulinasi, N., Miam, G., Larsen, J., Peter, D., and Golias, P, 2013, The Wafi-Golpu porphyry Cu-Au deposit: Mineralization and alteration zonation, surface geochemical expression and paragenesis: Conference paper and presentation, AIG, Bali, Indonesia, 44 p.

Metcalfe, I., 1996, Pre-Cretaceous evolution of SE Asian terranes. In Hall, R. and Blundell, D.J.(Eds.), Tectonic evolution of Southeast Asia: Geological Society Special Publication, v. 106, p. 97-122.

Meyer, C., 1965, An early potassic type of wall-rock alteration at Butte, Montana: The American Mineralogist, v. 50. p. 1717-1722.

Milési, J.P., Marcoux, E., Nehlig, P., Sunarya, Y., Sukandar, A., and Felenc, J., 1993, Cirotan, West Java, Indonesia: A 1.7 Ma hybrid epithermal Au-Ag-Sn-W deposit: Economic Geology, 89, p. 227-245.

Milési, J.P., Marcoux, E., Sitorus, T., Simandjuntak, M., Leroy, J., and Baily, L., 1999, Pongkor (West Java, Indonesia): A Pliocene supergene-enriched epithermal Au-Ag-(Mn) deposit: Mineralium Deposita, v.34, p. 131-149.

Miller, J.S., Matzel, J.E.P., Miller, C.F., Burgess, S.D., and Miller, R.B., 2007, Zircon growth and recycling during the assembly of large, composite arc plutons: Journal of Volcanology and Geothermal Research, v. 167, p. 282-299.

Min K., Mundil R., Renne P.R., and Ludwig K.R., 2000, A test for systematic errors in $^{40}Ar/^{39}Ar$ geochronology through comparison with U/Pb analysis of a 1.1-Ga rhyolite: Geochimica et Cosmochimica Acta, v. 64, p. 73-89.

Moon, V.J., Bradshaw, J., and De Lange, W., 2009, Geomorphic development of White Island Volcano based on slope stability modelling: Engineering Geology v. 104, 15p.

Moore, G.F., and Karig, D.E., 1980, Structural geology of Nias island, Indonesia: implications for subduction and tectonics: Amercian Journal of Science, v. 280, p.193-223.

Moyle, A.L., Doyle, B.J., Hoogvliet, H., and Ware, A.R., 1990, Ladolam gold deposit, Lihir Island: Monograph Series - Australasian Institute of Mining and Metallurgy, v. 14, p. 1793-1805.

Mutschler, F.E., Ludington, S., and Bookstrom, A.A., 1999, Giant porphyry related metal camps of the World-a database: USGS Open File Report 99-556, 6 p. (http://geopubs.wr.usgs.gov/open-file/of99–556/).

Newcrest Mining Ltd., 2017, Annual mineral resources and ore reserves statement, 10p. http://www.newcrest.com.au/media/our_business/Newcrest_Fast_Facts_-_March_2017.pdf

Newhall, C.H., and Dzurizin, D., 1988, Historical unrest at large calderas of the world: U.S. Geological Survey Bulletin 1855, v. 1, 598p.

Norris, M., 2011, The discovery history of the Tujuh Bukit copper-gold project, East Java, Indonesia: Conference presentation, New Generation Gold Mines (NewGenGold), Perth, Australia, 70 p.

Northern Dynasty Minerals Ltd, 2014, Pebble resource estimate, 1p. https://www.sec.gov/Archives/edgar/data/1164771/000106299315000646/exhibit99-1.htm

Ohmoto, H., 1972, Systematics of sulfur and carbon isotopes in hydrothermal ore deposits: Economic Geology, v. 67, p. 551-578.

Ohmoto, H., and Rye, R.O., 1997, Isotopes of sulfur and carbon, *in* Barnes, H.L., ed., Geochemistry of hydrothermal ore deposits, third edition: New York, Wiley, p. 517-611.

Ossandon, G., Freraut, R., Gustafson, L.B., Lindsay, D.D., and Zentilli, M., 2001, Geology of the Chuquicamata Mine: A progress report: Economic Geology, v. 96, p. 249-270.

Perelló, J., Cox, D., Garamjav, D., Sandorj, S, Diakov, S., Schissel, D., Munkhbat, T., and Oyun, G.,

2001, Oyu Tolgoi, Mongolia: Siluro-Devonian porphyry Cu-Au-(Mo) and high-sulfidation Cu mineralization with a Cretaceous chalcocite blanket: Economic Geology, v. 96, p. 1407-1428.

Perelló, J., Sillitoe, R., Mpodozis, C., Brockway, H., and Posso, H., 2012, Geologic setting and evolution of the porphyry copper-molybdenum and copper-gold deposits at Los Pelambres, Central Chile: Economic Geology Special Publication no. 16, p. 79-104.

Piquer, J., Skarmeta, J., and Cooke, D.R., 2015, Structural evolution of the Rio Blanco-Los Bronces district, Andes of central Chile: controls on stratigraphy, magmatism and mineralization: Economic Geology, v. 110, p. 995-2023.

Post, J.L., and Noble, P.L., 1993, The near-infrared combination band frequencies of dioctahedral smectites, micas and illites: Clays and Clay Minerals, v. 41, p. 639-644.

Pontual, S., Merry, N., and Gamson, P., 2008a, GMEX Spectral analysis guides for mineral exploration Volume 1: Spectral interpretation field manual, Kew, Victoria 3101, Australia, Ausspec International Pty. Ltd., 189 p.

Pontual, S., Merry, N., and Gamson, P., 2008b, GMEX Volume 2: Practical applications handbook: Kew, Victoria 3101, Australia, AusSpec International Pty. Ltd., p. 51-60.

Pontual, S., Merry, N., and Gamson, P., 2008c, GMEX Volume 3: Porphyry alteration systems: Kew, Victoria 3101, Australia, AusSpec International Pty. Ltd., 75 p.

Pontual, S., Merry, N., and Gamson, P., 2008d, GMEX Volume 4: Epithermal alteration systems: Kew, Victoria 3101, Australia, AusSpec International Pty. Ltd., 62 p.

Quadt, A.V., Erni, M., Martinek, K., Moll, M., Peytcheva, I, and Heinrich, C.A., 2011, Zircon crystallization and the lifetimes of ore-forming magmatic hydrothermal systems: Geology, v. 39, no. 8, p. 731-734.

Renne, P.R., Cassata, W.S., and Morgan, L.E., 2009, The isotope composition of atmospheric argon $^{40}Ar/^{39}Ar$ geochronology: Time for a change?: Quaternary Geology, v. 4, p. 288-298.

Reyes, A.G., 1990, Petrology of Philippine geothermal systems and the application of alteration mineralogy to their assessment: Journal of Volcanology and Geothermal Research, v. 43, p. 279-309.

Rohrlach, B.D., and Loucks, R. R., 2005, Multi-million-year cyclic ramp up of volatiles in a lower crustal magma reservoir trapped below the Tampakan copper-gold deposit by Mio-Pliocene crustal compression in the southern Philippines: Porter, T.M. (Ed), 2005 Super Porphyry Copper & Gold Deposits - A Global Perspective, PGC Publishing, Adelaide, v. 2, p. 369 - 407.

Rohrlach, B.D., and Norris, M., 2006, Banyuwangi Project, East Java, Technical Overview: Unpublished technical report for Indophil Resources NL, 20 p.

Rohrlach, B.D., 2010, Recognition of sediments in the Tumpangpitu stratigraphy: unpublished technical note for Intrepid Mines Ltd, 12 p.

Rohrlach, B.D., 2011, The discovery history and geology of the Tujuh Bukit copper-gold project, East Java, Indonesia: Conference presentation, Round Up, Vancouver, Canada, 35 p.

Rompo, I., Maryono, A., and Rowe, A., 2012, Porphyry Cu-Au and epithermal Au-Ag mineralization

systems in southwest Lombok: Conference paper MGEI BESA (Indonesian Society of Economic Geologists, Eastern Sunda Banda Arc) Resources Seminar Malang, E. Java, Indonesia, 13 p.

Rosana, M. F. and Matsueda, H., 2002, Cikidang hydrothermal gold deposit in western Java, Indonesia: Resource Geology, v. 52, p. 341-352.

Rowland, J.V., and Simmons, S.F., 2012, Hydrologic, magmatic, and tectonic controls on hydrothermal flow, Taupo Volcanic Zone, New Zealand: Implications for the formation of epithermal vein deposits: Economic Geology, v. 107, p. 427-457.

Russell, N., Kesler, S.E., 1991 Geology of the maar-diatreme complex hosting precious metal mineralization at Pueblo Viejo, Dominican Republic: Geological Society of America, v. 262, p. 203.

Rye, R.O., 2005, A review of the stable-isotope geochemistry of sulfate minerals in selected igneous environments and related hydrothermal systems: Chemical geology, v. 215, p. 5-36.

Sack, P.J., Berry, R.F., Meffre, S., Falloon, T.J., Gemmell, J.B., Friedman, R.M., 2011. In situ location and U-Pb dating of small zircon grains in igneous rocks using laser ablation-inductively coupled plasma-quadrupole mass spectrometry: Geochemistry, Geophysics, Geosystems v. 12.

Sasaki, A., Ulriksen, C. E., Sato, K., and Ishihara, S., 1984, Sulfur isotope reconnaissance of porphyry copper and manto-type deposits in Chile and the Philippines: Bulletin of the Geological Survey of Japan, v. 35.

Schmidt, R.G., Hearn, B.C., 1971, Development of a diatreme: Atlas of volcanic phenomena, U.S Geological Survey, p. 14.

Seedorff, E., Dilles, J.H., Proffett, J.M., Jr., Einaudi, M.T., Zurcher, L., Stavast, W.J.A., Johnson, D.A., and Barton, M.D., 2005, Porphyry deposits: characteristics and origin of hypogene features: Economic Geology, 100th Anniversary Volume, p. 251-298.

Selby, D., and Creaser, R.A., 2004, Macroscale NTIMS and microscale LA-MC-ICP-MS Re-Os isotopic analysis of molybdenite: Testing spatial restrictions for reliable Re-Os age determinations, and implications for the decoupling of Re and Os within molybdenite: Geochimica et Cosmochimica Acta, v. 68, p. 3897-3908.

Seran, H., and Farmer, C., 2013, Scratching at the surface: Hidden mineralization at Wetar?: Majalah Geologi Indonesia, v. 28, p. 51-63.

Setijadji, L.D., Kajino, S., Imai, A., and Watanabe, K., 2006, Cenozoic island arc magmatism in Java island (Sunda Arc, Indonesia): Clues on relationships between geodynamics of volcanic centers and ore mineralization: Resource Geology, v. 56, p. 267-291.

Setijadji, L.D., and Maryono, A., 2012, Geology and arc magmatism of the Eastern Sunda Arc, Indonesia: Conference paper MGEI BESA (Indonesian Society of Economic Geologists, Eastern Sunda Banda Arc) Resources Seminar Malang, E. Java, Indonesia, 31 p.

Shannon, J.R., Walker, B.M., Carten, R.B., Geraghty, E.P., 1982, Unidirectional solidification textures and their significance in determining relative ages of intrusions at the Henderson Mine, Colorado: Geology v. 10, p. 293-297

Sheridan, M.F., and Wohletz, K.H., 1981, Hydrovolcanic explosions: The systematics of water-pyroclast equilibration: Science, v. 212, p. 1387-1389.

Sillitoe, R.H., and Gappe, I.M., Jr., 1984, Philippine porphyry copper deposits: Geologic setting and characteristics: UNDP Technical support for regional offshore prospecting in East Asia, United Nations Economic and Social Commission for Asia and the Pacific, 89 p.

Sillitoe, R.H., 1985, Ore-related breccias in volcanoplutonic arcs: Economic Geology, v. 80, p. 1467-1514.

Sillitoe, R.H., 1993, Epithermal models: Genetic types, geometrical controls and shallow features: Geological Association of Canada Special Paper, v. 40, p. 403-417.

Sillitoe, R.H., 1995a, Exploration of porphyry copper lithocaps: Australasian Institute of Mining and Metallurgy, Publication Series, v. 9, p. 527-532.

Sillitoe, R.H., 1999, Styles of high-sulphidation gold, silver and copper mineralization in the porphyry and epithermal environments: Australian Institute of Mining and Metallurgy, PacRim '99, Bali, Indonesia, 10-13 October, Proceedings, p. 29-44.

Sillitoe, R.H., 2010, Porphyry copper systems: Economic Geology, v. 105, p. 3-41.

Sillitoe, R.H., 2010b, Exploration and discovery of base- and precious-metal deposits in the circum-Pacific Region- a 2010 perspective: Resource Geology Special Issue No. 22, 139 p.

Sillitoe, R.H., 2013, Geology of the Caspiche porphyry gold-copper deposit, Maricunga belt, Northern Chile: Economic Geology, v. 108, p. 585-604.

Sillitoe, R.H., and Bonham, H.F.J., 1984, Volcanic landforms and ore deposits: Economic Geology, v. 79, p. 1286-1298.

Sillitoe, R.H., Baker, E.M., and Brook, W.A., 1984, Gold deposits and hydrothermal eruption breccias associated with a maar volcano at Wau, Papua New Guinea: Economic Geology, v. 79, p. 638-655.

Sillitoe, R.H., Grauberger, G.L., and Elliott, J.E., 1985, A diatreme-hosted gold deposit at Montana Tunnels, Montana: Economic Geology, v. 80, p.1707-1721.

Sillitoe, R.H., and Hedenquist, J.W., 2003, Link ages between volcano-tectonic setting, ore-fluid compositions and epithermal precious metal deposits: Economic Geology, Special Publication, v. 10, p. 315-343.

Sillitoe, R.H., Tolman, J., and Van Kerkvoort, G., 2013, Geology of the Caspiche porphyry gold-copper Deposit, Maricunga Belt, Northern Chile: Economic Geology, v. 108, p. 585-604.

Simmons, S.F., White, N.C., and John, D., 2005, Geological characteristics of epithermal and base metal deposits: Economic Geology 100th Anniversary Volume, p. 485-522.

Sjoekri, A., 1998, Application of geographic information systems for mineral exploration in southwest Sumbawa, Indonesia: unpublished master thesis, Colorado School of Mines, 226 p.

Skewes, M.A., and W. Atkinson Jr., 1985, Petrology of the early formed hydrothermal veins within the central potassic alteration zone of the Los Pelambres porphyry copper deposit, Chile: Revista Geologica de Chile, v. 25-26, p. 39-56.

Slama, J., Kosler, J., Condon, D.J., Crowley, J.L., Gerdes, A., Hanchar, J.M., Horstwood, M.S.A.,

Morris, G.A., Nasdala, L., Norberg, N., Schaltegger, U., Schoene, B., Tubrett, M.N., Whitehouse, M.J., 2008. Plesovice zircon - A new natural reference material for U-Pb and Hf isotopic microanalysis: Chemical Geology, v. 249, p. 1-35.

Smyth, H., Hall, R., Hamilton, P.J., and Kinny, P, 2003, Volcanic origin of quartz-rich sediments in East Java: Proceedings Indonesian petroleum association 29th annual convention and exhibition, p. 542-559.

Smyth, H., Hall, R., Hamilton, J., and Kinny, P, 2005, East Java, Cenozoic basins, volcanoes and ancient basement: Proceedings Indonesian petroleum association 13th annual convention and exhibition, p. 251-266.

Smyth, H., Hamilton, P.J., Hall, R., and Kinny, P, 2007, The deep crust beneath island arcs: Inherited zircons reveal a Gondwana continental fragment beneath East Java, Indonesia Earth and Planetary Science Letters, v. 258, p. 269-282.

Smyth, H.R., Hall R., and Nichols, G.J., 2008, Cenozoic volcanic arc history of East Java, Indonesia: The stratigraphic record of eruptions on an active continental margin, in Draut, A.E., Clift, P.D., and Scholl, D.W., eds., Formation and Applications of the Sedimentary Record in Arc Collision Zones: Geological Society of America Special Paper, v. 436, p. 199-222,

Smyth, H., Crowley, Q.G., Hall, R., Kinny, P.D., Hamilton, P.J., and Schmidt, D.N., 2011, A Toba-scale eruption in the Early Miocene: The Semilir eruption, East Java, Indonesia: Lithos, v. 126, p. 198-211.

Soeria-Atmadja, R., Maury, R. C., Bellon, H., Pringgoprawiro, H., Polves, M., and Priadi, B., 1994, Tertiary magmatic belts in Java. Journal of Southeast Asian Earth Science, v. 9, p. 13-27.

Steiger, R. H., Jäger, E., 1977, Subcommission on geochronology: Convention on the use of decay constants in geo- and cosmochemistry: Earth and Planetary Science Letters, v. 36, p. 359-362.

Stein, H., Scherstén, A., Hannah, J. and Markey, R., 2003, Subgrain scale decoupling of Re and ^{187}Os and assessment of laser ablation ICP-MS spot dating in molybdenite: Geochimica et Cosmochimica Acta, v. 67, p. 3673-3686.

Stein, H.J., 2014, Dating and tracing the history of ore formation: Holland, H.D. and Turekian, K.K. (editors) Treatise on Geochemistry, second edition, Oxford: Elsevier, v. 13, p. 87-118.

Stoffregen, R.E., 1987. Genesis of acid-sulfate alteration and Cu–Au–Ag mineralization at Summitville, Colorado: Economic Geology, v. 82, p. 1575-1591.

Sutopo, B., 2013, The Martabe Au-Ag high-sulfidation epithermal deposits, Sumatra, Indonesia: Implications for ore genesis and exploration: Unpublished PhD thesis, University of Tasmania, 352 p.

Teal, L., and Benevides, A., 2010, History and geologic overview of the Yanacocha mining district, Cajamarca, Peru: Economic Geology, v. 105, p. 1173-1190.

Thompson, A.J.B., Hauff, P.L., and Robitaille, A.J., 1999, Alteration mapping in exploration: Application of short-wave infrared (SWIR) spectroscopy: Society of Economic Geologists Newsletter, v. 39, p. 16-27.

Takahashi, R., Shingo, Y., Imai, A., Watanabe, K., Harijoko, A., Warmada, I.W., and Idrus, A., 2011, Mineralogical description and ore-forming condition at the Trenggalek gold prospect, east Java,

Indonesia. Proceedings of the 1st Asia Africa Mineral Resources Conference 2011, Fukuoka, p. 121-125.

Takahashi, R., Imai, A., Shingo, Y., Watanabe, K., Harijoko, A., Warmada, I.W., and Idrus, A., Setijadji, L.D., Phoumephone, P., Schersten, A., and Page, L., 2014, Characteristics of epithermal gold mineralization in the Trenggalek district, East Java, Indonesia: Resource Geology, v. 64, Issue 2, p. 149-166.

Tappert, M., Rivard, B., Giles, D., Tappert, R., and Mauger, A., 2011, Automated drill core logging using visible and near-infrared reflectance spectroscopy: A case study from the Olympic Dam IOCG deposit, South Australia: Economic Geology, v. 106, p. 289-296.

Tjia, H.D., S. Fujii, K. Kigoshi, A. Sugimura & T. Zakaria (1972)- Radiocarbon dates of elevated shorelines, Indonesia and Malaysia. Part 1: Quaternary Research v. 2, p. 487-495.

Tosdal, R.M., and Richards, J.P., 2001, Magmatic and structural controls on the development of porphyry Cu ± Mo ± Au deposits: Reviews in Economic Geology, v. 14, p. 157-181.

Tsuji, Y., Imamura, F., Matsutomi, H., Synolakis, C.E., Nanang, P.T., Jumadi, Harada, S., Han, S.S., Arai, K., and Cook, B, 1995, Field survey of the East Java earthquake and tsunami of June 3, 1994: Journal of Pure and Applied Geophysics Volume 144, Issue 3-4, p. 839-854.

Turner, S.J., 1997, The Yanacocha epithermal gold deposits, northern Peru: High-sulfidation mineralization in a flow dome setting: Unpublished Ph.D. thesis, Colorado, Colorado School of Mines, 341 p.

Turquoise Hill Resources, Ltd, 2016, Oyu Tolgoi Technical Report, 596 p. http://www.turquoisehill.com/i/pdf/2016-10-tr-trq-r77gvc.pdf

University of Southern California, 1994. http://www.usc.edu/dept/tsunamis/indonesia/java/: 1p.

Valentine, G.A., and Fisher, R.V., 2000, Pyroclastic surges and blasts: Encyclopedia of Volcanoes, p. 571-580.

Van Bemmelen, R.S., 1949, The geology of Indonesia, v. II. Economic Geology: The Hague, Netherlands, Government Printing Office, 265 p.

Vasconcelos, P.M., Onoe A.T., Kawashita K., Soares A.J., and Teixeira W., 2002, $^{40}Ar/^{39}Ar$ geochronology at the Instituto de Geociências, USP: instrumentation, analytical procedures, and calibration: Annals of the Brazilian Academy of Sciences, v. 74, p. 297-342.

Viana, A., Jr., Andrade, P. M., Neto, J. Duarte., Pereira, G. S. P, and Torres, V. M, 1998, New process to remove fluorine from copper concentrates: SME Transactions, v. 304, Sec. 1, 4 p.

Vidal, C., and Ligarda, R., 2004, Enargite-gold deposits at Marcapunta, Colquijirca mining district, central Perú: Mineralogic and geochemical zoning in subvolcanic, limestone-replacement deposits of high-sulfidation epithermal type: Society of Economic Geology Special Publication, v. 11, p. 231-242.

Wakita, K., 2000, Cretaceous accretionary - Collision complexes in central Indonesia: Journal of Asian Earth Sciences, v. 18, p. 739-749.

Wakita, K., and Munasri, B., W., 1994, Cretaceous Radiolarians from the Luk-Ulo Melange Complex in the Karangsambung area, Central Java, Indonesia: Journal of Southeast Asian Earth Sciences, v. 9, p. 29-43.

Walker, G.P.L., 1984, Characteristics of dune-bedded pyroclastic surge bedsets: Journal of Volcanology and Geothermal Research, v. 20, p. 281-296.

Wallier, S., Rey, R., Kouzmanov, K., Pettke, T., Heinrich, C.H., Leary, S., O'Connor, G., Tˇamas¸, C.G., Vennemann, T., and Ullrich, T., 2006, Magmatic fluids in the breccia-hosted epithermal Au-Ag deposit of Rosia Montana˛, Romania: Economic Geology, v. 101, p. 923-954.

Warmada, I.W., Soe, M.T., Sinomiya, J., Setijadji, L.D., Imai, A., and Watanabe, K., 2007, Petrology and geochemistry of Intrusive rocks from Selogiri Area, Central Java, Indonesia: Resource Geology, v. 57, p. 124-135.

Warnaars, F.W., Holmgren, C., and Barassi, S., 1985, Porphyry copper and tourmaline breccias at Los Bronces-Rio Blanco, Chile: Economic Geology, v. 80, p. 1544-1565.

Wheller, G.E., Varne, R., Foden, J.D. and Abbott, M.J., 1987, Geochemistry of Quaternary volcanism in the Sunda-Banda arc, Indonesia, and three-component genesis of island-arc basaltic magmas, Journal of Volcanology and Geothermal Research, v. 32, p. 137-160.

White, N.C. and Hedenquist, J.W., 1990, Epithermal environments and styles of mineralization: variations and their causes, and guidelines for exploration: Journal of Geochemical Exploration, v. 36, p. 445-474.

White, N.C., 1991, High sulfidation epithermal gold deposits: Characteristics and a model for their origin: Geological Survey of Japan Report, v. 277, p. 9-20.

White, N.C., 2012, High-sulfidation epithermal deposits - Characteristics, origins and issues: Red Metals Presentation, CODES, University of Tasmania, 32 p.

Whitford, D. J., 1975, Strontium isotopic studies of the volcanic rocks of the Sunda arc, Indonesia, and their petrogenetic implications: Geochimica et Cosmochimica Acta, v. 39, p. 1287-1302.

Wiedenbeck, M., Alle, P., Corfu, F., Griffin W.L., Meier, M., Oberli, F., Vonquadt A., Roddick, J.C., and Speigel W., 1995, Three natural zircon standards for U-Th-Pb, Lu-Hf, trace-element and REE analyses: Geostandards Newsletter v. 19, p. 1-23.

Wolfe, R.C., and Cooke, D. R., 2011, Geology of the Didipio region and genesis of the Dinkidi alkalic porphyry Cu-Au deposit and related pegmatites, Northern Luzon, Philippines: Economic Geology, v. 106, p. 1279-1315.

York, D., 1969, Least squares fitting of a straight line with correlated errors: Earth and Planetary Science Letters, v. 5, p. 320-324.

Yuningsih, E.T., Matsueda, H., Setyaraharja, E.P., and Rosana, M.F., 2011, The Arinem Te-bearing gold-silver-base metal deposit, West Java, Indonesia: Resource Geology, v. 62, p. 140-158.

APPENDIX 1: U-Pb DATA

Table A1-1. $^{206}Pb/^{238}U$ determinations for zircons from intrusive and host rocks at Tumpangpitu.

Sample	^{204}Pb (ppm)	^{206}Pb (ppm)	^{207}Pb (ppm)	^{208}Pb (ppm)	^{232}Th (ppm)	^{238}U (ppm)	$^{208}Pb/^{232}Th$	± 1σ (%)	$^{207}Pb/^{206}Pb$	± 1σ (%)	$^{238}U/^{206}Pb$	± 1σ (%)	$^{206}Pb/^{238}U$	± 1σ (%)	$^{206}Pb/^{238}U$ age (Ma)
Sedimentary and andesitic volcanic rocks															
Sandstone; drillhole GTD-10-138; 964 m															
MY08A065	0.03	0.52	0.13	0.41	109	145	0.0039	5.66	0.2488	9.38	263.27	12.66	0.0038	4.81	18.2 ± 1.1
MY08A071	0.02	0.74	0.19	0.64	206	179	0.0031	4.47	0.2501	6.49	240.48	9.66	0.0042	4.01	19.9 ± 1.0
MY08A059	0.00	1.16	0.06	0.42	401	372	0.0011	3.16	0.0581	9.19	317.64	9.63	0.0031	3.03	20.0 ± 0.6
MY08A064	0.00	1.25	0.06	0.59	586	401	0.0010	3.24	0.0494	8.17	318.38	8.91	0.0031	2.80	20.1 ± 0.6
MY08A069	0.00	0.46	0.04	0.17	120	140	0.0014	6.41	0.0952	12.83	299.36	12.32	0.0033	4.12	20.2 ± 0.9
MY08A072	0.00	0.34	0.04	0.18	129	97	0.0014	12.00	0.1126	16.73	286.49	20.33	0.0035	7.09	20.6 ± 1.6
MY08A061	0.00	0.78	0.13	0.49	243	203	0.0020	3.86	0.1901	7.08	253.92	10.42	0.0039	4.10	20.7 ± 1.0
MY08A070	0.01	0.58	0.03	0.24	246	192	0.0010	5.90	0.0498	17.85	307.99	15.60	0.0032	5.07	20.8 ± 1.1
MY08A066	0.01	1.03	0.10	0.53	445	307	0.0012	5.00	0.1016	10.09	282.54	10.72	0.0035	3.79	21.2 ± 0.9
MY08A060	0.03	1.03	0.34	1.04	233	194	0.0053	3.86	0.3791	4.50	174.32	7.63	0.0057	4.38	21.4 ± 1.2
MY08A068	0.00	0.81	0.05	0.23	213	234	0.0010	5.86	0.0591	10.58	294.02	13.04	0.0034	4.44	21.5 ± 1.0
MY08A067	0.00	0.34	0.02	0.11	97	100	0.0012	6.89	0.0555	19.02	291.09	14.31	0.0034	4.92	21.9 ± 1.1
MY08A063	0.00	0.92	0.05	0.31	261	262	0.0012	3.75	0.0666	9.19	283.57	8.82	0.0035	3.11	22.1 ± 0.7
MY08A062	0.00	0.44	0.03	0.13	101	121	0.0012	6.27	0.0650	13.06	277.03	12.40	0.0036	4.48	22.7 ± 1.0
Sandstone; drillhole GTD-08-46; 825.50 m															
MY08A014	0.01	0.97	0.21	0.57	180	346	0.0033	4.84	0.2171	7.04	328.68	16.41	0.0030	4.99	15.4 ± 0.9
MY08A021	0.00	0.45	0.11	0.31	42	136	0.0073	9.29	0.2537	10.83	297.95	17.24	0.0034	5.78	15.9 ± 1.2
MY08A016	0.00	0.91	0.05	0.16	207	375	0.0008	11.06	0.0521	9.96	400.94	13.43	0.0025	3.35	15.9 ± 0.5
MY08A009	0.02	0.92	0.07	0.24	179	359	0.0013	5.15	0.0800	9.29	379.08	12.77	0.0026	3.37	16.3 ± 0.6
MY08A020	0.00	0.86	0.10	0.19	176	331	0.0011	9.28	0.1243	11.70	354.87	16.48	0.0028	4.64	16.4 ± 0.8
MY08A008	0.01	0.48	0.06	0.13	55	175	0.0023	8.00	0.1285	11.06	352.71	17.16	0.0028	4.87	16.4 ± 0.9
MY08A007	0.01	0.62	0.07	0.17	91	222	0.0019	5.63	0.1215	9.44	353.55	14.49	0.0028	4.10	16.5 ± 0.7
MY08A012	0.00	0.62	0.04	0.10	95	235	0.0010	7.15	0.0711	9.73	375.35	14.07	0.0027	3.75	16.6 ± 0.6
MY08A015	0.00	0.73	0.04	0.11	139	285	0.0008	8.28	0.0552	10.58	381.80	15.20	0.0026	3.98	16.7 ± 0.7
MY08A017	0.00	0.61	0.03	0.09	98	244	0.0009	7.47	0.0465	15.92	385.85	15.18	0.0026	3.93	16.7 ± 0.7
MY08A018	0.03	0.98	0.14	0.40	172	351	0.0024	5.22	0.1462	6.71	337.02	12.24	0.0030	3.63	16.7 ± 0.7

Table A1-1. ***(Contd.)***

Sample	^{204}Pb (ppm)	^{206}Pb (ppm)	^{207}Pb (ppm)	^{208}Pb (ppm)	^{232}Th (ppm)	^{238}U (ppm)	^{208}Pb/^{232}Th	± 1σ (%)	^{207}Pb/^{206}Pb	± 1σ (%)	^{238}U/^{206}Pb	± 1σ (%)	^{206}Pb/^{238}U	± 1σ (%)	^{206}Pb/^{238}U age (Ma)
MY08A011	0.01	0.53	0.03	0.07	71	198	0.0010	8.18	0.0594	13.68	374.19	16.71	0.0027	4.46	16.9 ± 0.8
MY08A019	0.00	0.92	0.05	0.14	162	344	0.0008	6.28	0.0601	9.26	367.28	11.21	0.0027	3.05	17.2 ± 0.5
MY08A010	0.02	1.02	0.04	0.16	209	390	0.0007	5.33	0.0413	11.21	372.23	12.89	0.0027	3.46	17.3 ± 0.6
MY08A013	0.01	0.84	0.11	0.30	149	292	0.0021	5.61	0.1272	7.91	329.17	12.64	0.0030	3.84	17.6 ± 0.7
Andesite; drillhole GTD-10-172; 363 m															
JN13A136	0.00	0.13	0.06	0.12	24	43	0.0053	10.34	0.4875	21.15	326.60	33.40	0.0031	10.23	8.7 ± 2.7
JN13A133	0.00	0.11	0.04	0.08	20	37	0.0046	16.30	0.3966	38.10	319.85	45.17	0.0031	14.12	11.2 ± 4.2
JN13A138	0.02	0.15	0.05	0.18	30	44	0.0063	20.09	0.3649	21.29	291.22	27.74	0.0034	9.53	13.2 ± 2.5
JN13A135	0.03	0.12	0.04	0.11	13	37	0.0088	10.44	0.3329	26.32	304.90	31.88	0.0033	10.45	13.5 ± 2.7
JN13A134	0.03	1.63	0.38	1.67	1429	673	0.0013	5.54	0.2324	8.06	358.39	21.53	0.0028	6.01	13.7 ± 0.9
JN13A139	0.00	0.13	0.04	0.13	23	41	0.0061	14.95	0.3288	35.26	290.75	55.28	0.0034	19.01	14.2 ± 4.2
JN13A140	0.01	0.12	0.01	0.04	38	56	0.0013	20.58	0.0481	113.35	445.94	57.15	0.0022	12.82	14.4 ± 2.1
JN13A137	0.00	0.15	0.04	0.11	29	49	0.0038	9.67	0.2670	27.80	312.76	28.91	0.0032	9.24	14.8 ± 2.4
Sandstone rockchip ARM-TB-56 E173050 N9047657															
FE03A212	0.00	0.10	0.01	0.01	42	77	0.0003	34.56	0.049	30.10	814.219	64.41	0.0012	7.91	7.9 ± 0.6
FE03A226	0.00	0.25	0.02	0.08	188	188	0.0004	8.93	0.069	14.66	757.207	38.54	0.0013	5.09	8.3 ± 0.4
FE03A213	0.00	0.10	0.01	0.02	45	74	0.0004	27.00	0.079	22.82	743.227	55.26	0.0013	7.43	8.3 ± 0.6
FE03A223	0.00	0.09	0.01	0.03	39	62	0.0007	14.72	0.119	22.83	700.979	56.13	0.0014	8.01	8.3 ± 0.7
FE03A211	0.01	0.07	0.01	0.02	23	47	0.0006	25.53	0.117	26.90	701.683	65.66	0.0014	9.36	8.4 ± 0.9
FE03A225	0.00	0.11	0.01	0.04	55	74	0.0008	11.31	0.132	17.33	669.019	46.68	0.0015	6.98	8.6 ± 0.7
FE03A217	0.00	0.08	0.01	0.01	23	59	0.0004	40.91	0.063	41.80	723.256	64.11	0.0014	8.86	8.7 ± 0.8
FE03A219	0.02	0.21	0.01	0.05	100	149	0.0004	12.27	0.066	17.11	719.984	37.92	0.0014	5.27	8.7 ± 0.5
FE03A221	0.00	0.11	0.01	0.04	48	73	0.0006	15.61	0.059	31.82	724.109	54.93	0.0014	7.59	8.8 ± 0.7
FE03A214	0.00	0.11	0.00	0.03	47	76	0.0005	18.54	0.064	34.53	715.788	51.87	0.0014	7.25	8.8 ± 0.7
FE03A220	0.02	0.22	0.04	0.12	120	133	0.0008	9.96	0.164	10.82	623.461	32.12	0.0016	5.15	8.8 ± 0.5
FE03A216	0.00	0.10	0.01	0.02	35	66	0.0005	24.23	0.038	40.01	725.545	52.46	0.0014	7.23	8.9 ± 0.7
FE03A218	0.00	0.20	0.01	0.07	127	135	0.0005	9.97	0.078	15.60	693.587	33.55	0.0014	4.84	8.9 ± 0.5
FE03A222	0.00	0.23	0.01	0.05	122	163	0.0004	10.70	0.071	15.54	696.142	33.37	0.0014	4.79	9.0 ± 0.4
FE03A215	0.00	0.07	0.01	0.02	31	44	0.0006	26.52	0.076	40.49	690.738	72.89	0.0014	10.6	9.0 ± 1.0
FE03A224	0.00	0.11	0.01	0.05	63	71	0.0007	13.02	0.113	19.32	655.11	44.3	0.0015	6.76	9.0 ± 0.7

Table A1-1. ***(Contd.)***

Sample	^{204}Pb (ppm)	^{206}Pb (ppm)	^{207}Pb (ppm)	^{208}Pb (ppm)	^{232}Th (ppm)	^{238}U (ppm)	^{208}Pb/^{232}Th	± 1σ (%)	^{207}Pb/^{206}Pb	± 1σ (%)	^{238}U/^{206}Pb	± 1σ (%)	^{206}Pb/^{238}U	± 1σ (%)	^{206}Pb/^{238}U age (Ma)
Phase 1; hornblende quartz diorite															
Rockchip ARM-TB-43 E173050 N9047657															
FE03A241	0.00	0.08	0.01	0.02	40	63	0.0004	20.67	0.06	37.24	835.353	77.54	0.0012	9.28	7.6 ± 0.7
FE03A238	0.00	0.13	0.03	0.11	83	80	0.0017	10.78	0.293	12.10	574.779	49.87	0.0017	8.68	7.7 ± 0.8
FE03A242	0.00	0.14	0.03	0.08	48	81	0.0016	8.80	0.266	12.11	587.484	37.92	0.0017	6.45	7.9 ± 0.7
FE03A234	0.00	0.07	0.02	0.04	29	45	0.0012	14.56	0.234	16.13	617.987	53.19	0.0016	8.61	7.9 ± 0.8
FE03A237	0.00	0.08	0.00	0.01	29	54	0.0002	51.25	0.139	23.19	711.13	65.72	0.0014	9.24	8.0 ± 0.8
FE03A240	0.02	0.10	0.01	0.02	44	66	0.0004	23.31	0.174	14.70	670.456	57.86	0.0015	8.63	8.1 ± 0.8
FE03A243	0.00	0.10	0.01	0.01	50	79	0.0002	32.75	0.077	29.06	756.568	58.61	0.0013	7.75	8.2 ± 0.7
FE03A239	0.00	0.09	0.02	0.05	38	55	0.0011	14.03	0.236	14.96	587.267	48.12	0.0017	8.19	8.3 ± 0.8
FE03A233	0.00	0.11	0.01	0.04	49	77	0.0008	14.87	0.089	28.77	718.808	54.02	0.0014	7.52	8.5 ± 0.7
FE03A231	0.00	0.16	0.01	0.05	85	116	0.0005	12.04	0.07	20.37	731.668	42.29	0.0014	5.78	8.5 ± 0.5
FE03A229	0.00	0.15	0.02	0.05	65	95	0.0008	12.82	0.16	16.42	639.459	48.76	0.0016	7.63	8.6 ± 0.7
FE03A232	0.01	0.16	0.02	0.05	79	109	0.0007	14.42	0.121	18.38	662.587	43.7	0.0015	6.60	8.8 ± 0.6
FE03A235	0.00	0.16	0.01	0.04	85	111	0.0005	14.71	0.069	19.39	707.047	48.01	0.0014	6.79	8.8 ± 0.6
FE03A230	0.00	0.23	0.01	0.09	147	162	0.0006	10.94	0.065	19.68	686.976	38.27	0.0015	5.57	9.2 ± 0.5
Tanjung Jahe diatreme															
Rockchip ARM-TB-44 E175347 N9043797															
DE09A141	0.00	0.08	0.01	0.02	43	67	0.0005	14.37	0.0983	17.47	762.21	52.64	0.0013	6.91	7.9 ± 0.6
DE09A127	0.01	0.09	0.01	0.02	46	75	0.0004	16.49	0.0650	19.80	781.74	47.88	0.0013	6.13	8.0 ± 0.5
DE09A125	0.01	0.02	0.00	0.00	7	14	0.0007	42.12	0.0405	81.92	785.15	116.96	0.0013	14.90	8.2 ± 1.3
DE09A130	0.00	0.14	0.07	0.15	25	54	0.0061	7.11	0.4621	9.30	365.88	22.35	0.0027	6.11	8.3 ± 1.1
DE09A137	0.00	0.18	0.11	0.29	18	42	0.0160	7.42	0.5946	6.52	234.22	17.58	0.0043	7.51	8.4 ± 1.5
DE09A135	0.00	0.11	0.00	0.02	37	85	0.0006	13.40	0.0541	22.76	746.07	42.99	0.0013	5.76	8.5 ± 0.5
DE09A132	0.00	0.04	0.00	0.01	12	30	0.0008	27.08	0.0791	33.80	719.59	63.12	0.0014	8.77	8.6 ± 0.8
DE09A140	0.01	0.05	0.00	0.02	16	38	0.0010	18.54	0.1027	23.37	689.35	62.36	0.0015	9.05	8.7 ± 0.8
DE09A139	0.00	0.13	0.02	0.05	63	87	0.0010	12.12	0.1689	12.73	627.08	43.81	0.0016	6.99	8.7 ± 0.7
DE09A142	0.00	0.09	0.01	0.01	29	59	0.0003	21.74	0.0998	19.40	690.23	45.63	0.0014	6.61	8.7 ± 0.6
DE09A131	0.00	0.10	0.01	0.02	45	73	0.0005	15.34	0.0573	19.80	729.81	43.65	0.0014	5.98	8.7 ± 0.5

Table A1-1. ***(Contd.)***

Sample	^{204}Pb (ppm)	^{206}Pb (ppm)	^{207}Pb (ppm)	^{208}Pb (ppm)	^{232}Th (ppm)	^{238}U (ppm)	^{208}Pb/^{232}Th	± 1σ (%)	^{207}Pb/^{206}Pb	± 1σ (%)	^{238}U/^{206}Pb	± 1σ (%)	^{206}Pb/^{238}U	± 1σ (%)	^{206}Pb/^{238}U age (Ma)
DE09A133	0.01	0.10	0.01	0.03	45	70	0.0006	14.64	0.0853	24.15	698.43	44.90	0.0014	6.43	8.8 ± 0.6
DE09A124	0.01	0.12	0.01	0.03	45	85	0.0006	12.96	0.0668	18.42	713.27	40.37	0.0014	5.66	8.8 ± 0.5
DE09A134	0.01	2.21	0.11	1.74	3955	1588	0.0004	2.10	0.0494	4.18	727.21	12.83	0.0014	1.76	8.8 ± 0.2
DE09A136	0.00	0.11	0.00	0.02	41	79	0.0005	14.60	0.0423	24.40	729.18	40.02	0.0014	5.49	8.8 ± 0.5
DE09A138	0.01	0.09	0.00	0.02	43	65	0.0006	13.43	0.0627	22.06	692.77	42.41	0.0014	6.12	9.1 ± 0.6
DE09A126	0.01	0.09	0.01	0.02	30	56	0.0006	15.11	0.0922	21.47	648.46	35.38	0.0015	5.46	9.4 ± 0.6
DE09A128	0.00	0.10	0.01	0.02	51	69	0.0005	13.74	0.0507	30.77	679.79	43.01	0.0015	6.33	9.4 ± 0.6
DE09A129	0.00	0.47	0.02	0.11	204	254	0.0006	5.54	0.0548	9.37	535.76	15.37	0.0019	2.87	11.9 ± 0.3
Rockchip ARM-TB-40 E175408 N9043609															
DE09A114	0.00	0.10	0.02	0.04	36	70	0.0013	12.13	0.2678	17.09	625.27	45.01	0.0016	7.20	7.4 ± 0.8
DE09A118	0.00	0.14	0.04	0.12	44	74	0.0028	6.01	0.3582	7.95	513.81	27.80	0.0019	5.41	7.6 ± 0.6
DE09A104	0.00	0.14	0.01	0.07	111	128	0.0007	30.69	0.0711	24.95	789.69	54.00	0.0013	6.84	7.9 ± 0.6
DE09A117	0.01	0.11	0.01	0.21	64	84	0.0006	15.23	0.1419	18.50	709.42	51.82	0.0014	7.30	8.0 ± 0.7
DE09A105	0.00	0.12	0.01	0.02	50	92	0.0003	18.97	0.0713	17.37	779.42	42.27	0.0013	5.42	8.0 ± 0.5
DE09A103	0.00	0.23	0.09	0.26	86	101	0.0033	4.46	0.4138	5.14	427.51	18.70	0.0023	4.37	8.1 ± 0.5
DE09A110	0.00	0.14	0.03	0.06	50	96	0.0014	13.68	0.2023	14.81	625.85	50.54	0.0016	8.08	8.3 ± 0.8
DE09A098	0.01	0.28	0.06	0.18	123	162	0.0015	5.65	0.2430	6.52	582.24	24.81	0.0017	4.26	8.3 ± 0.4
DE09A113	0.00	0.10	0.01	0.02	39	72	0.0005	14.81	0.0824	22.56	739.53	41.57	0.0014	5.62	8.3 ± 0.5
DE09A097	0.00	0.14	0.01	0.03	67	108	0.0005	15.40	0.0705	21.33	749.28	46.54	0.0013	6.21	8.3 ± 0.5
DE09A116	0.01	0.91	0.07	0.44	877	664	0.0005	3.30	0.0809	4.95	730.85	16.30	0.0014	2.23	8.4 ± 0.2
DE09A106	0.01	0.09	0.01	0.01	33	68	0.0005	16.91	0.0674	23.14	743.60	52.89	0.0013	7.11	8.4 ± 0.6
DE09A111	0.00	0.16	0.01	0.03	82	128	0.0004	12.49	0.0467	16.82	749.64	36.88	0.0013	4.92	8.6 ± 0.4
DE09A119	0.00	0.17	0.04	0.12	36	82	0.0039	14.77	0.3293	16.83	475.64	56.24	0.0021	11.82	8.7 ± 1.4
DE09A109	0.00	0.15	0.01	0.04	63	106	0.0007	10.60	0.0916	13.28	688.69	33.18	0.0015	4.82	8.8 ± 0.4
DE09A107	0.00	0.05	0.00	0.01	13	31	0.0011	19.74	0.0874	25.65	671.19	58.78	0.0015	8.76	9.1 ± 0.8
DE09A112	0.00	0.08	0.00	0.01	23	56	0.0004	25.51	0.0602	26.45	680.67	46.17	0.0015	6.78	9.3 ± 0.7
DE09A120	0.00	0.19	0.01	0.03	87	134	0.0004	11.94	0.0490	15.67	684.14	29.29	0.0015	4.28	9.4 ± 0.4
DE09A102	0.00	0.08	0.01	0.01	28	54	0.0004	23.03	0.0663	29.43	665.48	44.47	0.0015	6.68	9.4 ± 0.7
DE09A115	0.00	0.37	0.02	0.07	59	109	0.0011	9.15	0.0528	11.46	297.05	10.92	0.0034	3.68	21.5 ± 0.8
DE09A101	0.00	6.94	0.36	0.54	100	437	0.0053	3.97	0.0512	3.14	64.71	0.68	0.0155	1.05	98.5 ± 1.0
DE09A108	0.00	###	0.55	2.62	542	767	0.0050	1.58	0.0477	1.65	64.93	0.53	0.0154	0.81	98.5 ± 0.8

Table A1-1. ***(Contd.)***

Sample	^{204}Pb (ppm)	^{206}Pb (ppm)	^{207}Pb (ppm)	^{208}Pb (ppm)	^{232}Th (ppm)	^{238}U (ppm)	^{208}Pb/^{232}Th	± 1σ (%)	^{207}Pb/^{206}Pb	± 1σ (%)	^{238}U/^{206}Pb	± 1σ (%)	^{206}Pb/^{238}U	± 1σ (%)	^{206}Pb/^{238}U age (Ma)
Volcanic breccia															
Drillhole GTD-08-49; 19.70 m															
MY22A079	0.02	0.04	0.01	0.04	23	48	0.0014	22.73	0.3759	69.42	1408.86	325.21	0.0007	23.08	2.7 ± 1.6
MY22A075	0.01	0.04	0.00	0.01	44	65	0.0002	33.69	0.0987	79.38	1763.82	276.89	0.0006	15.70	3.4 ± 0.6
MY22A078	0.00	0.02	0.00	0.02	16	31	0.0015	52.18	0.0607	291.04	1271.45	257.01	0.0008	20.21	5.0 ± 1.5
MY22A073	0.00	0.03	0.00	0.00	15	28	0.0002	95.48	0.1520	96.48	1050.35	194.12	0.0010	18.48	5.3 ± 1.5
MY22A082	0.02	0.09	0.01	0.04	121	104	0.0003	13.62	0.0611	119.73	1148.18	105.68	0.0009	9.20	5.5 ± 0.7
MY22A084	0.01	0.09	0.00	0.04	125	102	0.0003	13.25	0.0364	57.67	1127.85	109.76	0.0009	9.73	5.7 ± 0.6
MY22A081	0.00	0.11	0.01	0.05	148	116	0.0003	10.13	0.0665	32.58	1081.40	92.10	0.0009	8.52	5.8 ± 0.5
MY22A074	0.01	0.10	0.01	0.07	236	114	0.0003	8.76	0.0597	74.12	1073.27	82.53	0.0009	7.69	5.9 ± 0.6
MY22A077	0.00	0.12	0.00	0.06	199	130	0.0003	9.39	0.0237	137.05	1077.89	102.01	0.0009	9.46	6.0 ± 0.6
MY22A083	0.00	0.37	0.23	0.61	100	84	0.0058	5.84	0.6215	7.92	234.61	23.03	0.0043	9.82	7.5 ± 1.9
MY22A076	0.00	0.04	0.00	0.04	28	30	0.0015	67.18	0.0565	372.00	734.15	182.81	0.0014	24.90	8.7 ± 3.2
MY22A080	0.22	2.96	2.49	5.94	48	58	0.1304	4.73	0.8381	2.52	18.21	0.86	0.0549	4.71	8.9 ± 10.1
Phase 2; Old diorite															
Drillhole GT010; 319.60 m															
MY22A110	0.05	0.34	0.20	0.52	375	161	0.0013	4.07	0.5814	7.98	492.91	31.67	0.0020	6.42	4.2 ± 0.8
MY22A112	0.14	3.07	2.42	6.24	976	285	0.0063	4.80	0.7881	1.90	92.62	4.43	0.0108	4.79	4.6 ± 1.6
MY22A117	0.02	0.20	0.03	0.21	748	244	0.0003	11.02	0.1576	24.65	1133.67	128.17	0.0009	11.31	4.9 ± 0.6
MY22A105	0.00	0.12	0.01	0.04	202	143	0.0002	12.61	0.0820	24.16	1193.66	102.21	0.0008	8.56	5.2 ± 0.5
MY22A109	0.00	0.22	0.02	0.24	858	239	0.0003	5.60	0.0725	59.34	1144.09	97.04	0.0009	8.48	5.4 ± 0.6
MY22A103	0.03	0.42	0.07	0.56	1503	399	0.0003	5.57	0.1600	19.40	986.47	105.96	0.0010	10.74	5.6 ± 0.7
MY22A108	0.04	0.27	0.03	0.28	904	280	0.0003	4.29	0.1170	17.16	1047.09	55.47	0.0010	5.30	5.6 ± 0.3
MY22A111	0.00	0.04	0.00	0.01	43	47	0.0003	26.06	0.0289	289.52	1129.92	165.15	0.0009	14.62	5.7 ± 1.0
MY22A115	0.01	0.60	0.10	0.85	2131	575	0.0004	8.02	0.1630	10.44	947.13	47.40	0.0011	5.00	5.8 ± 0.3
MY22A113	0.26	7.28	4.31	14.97	16616	2550	0.0009	1.77	0.5905	1.38	345.72	9.47	0.0029	2.74	5.8 ± 0.3
MY22A114	0.00	0.48	0.02	0.67	2303	537	0.0003	5.56	0.0475	20.73	1098.16	46.90	0.0009	4.27	5.9 ± 0.3

Table A1-1. ***(Contd.)***

Sample	^{204}Pb (ppm)	^{206}Pb (ppm)	^{207}Pb (ppm)	^{208}Pb (ppm)	^{232}Th (ppm)	^{238}U (ppm)	^{208}Pb/^{232}Th	± 1σ (%)	^{207}Pb/^{206}Pb	± 1σ (%)	^{238}U/^{206}Pb	± 1σ (%)	^{206}Pb/^{238}U	± 1σ (%)	^{206}Pb/^{238}U age (Ma)
MY22A116	0.00	1.16	0.07	1.97	6833	1265	0.0003	2.09	0.0569	7.50	1067.73	32.68	0.0009	3.06	6.0 ± 0.2
MY22A104	0.00	0.58	0.23	0.86	1607	391	0.0006	7.75	0.3971	9.45	593.73	83.55	0.0017	14.07	6.0 ± 1.0
MY22A106	0.00	0.79	0.25	1.12	2817	621	0.0004	3.17	0.3177	9.20	689.89	85.09	0.0014	12.33	6.1 ± 0.8
MY22A107	0.00	1.9	1.0	3.5	3826	807	0.0009	4.23	0.5141	3.64	411.80	14.83	0.0024	3.60	6.4 ± 0.5
Drillhole GTD-09-129; 102 m															
JN06B105	0.02	0.24	0.15	0.36	279	124	0.0014	8.76	0.6268	12.03	478.13	49.64	0.0021	10.38	3.6 ± 1.3
JN06B100	0.01	0.06	0.01	0.04	94	68	0.0004	11.30	0.2004	76.77	1051.21	126.10	0.0010	12.00	4.9 ± 1.3
JN06B106	0.02	0.07	0.03	0.08	51	39	0.0016	13.14	0.4916	41.41	567.94	99.35	0.0018	17.49	5.0 ± 3.0
JN06B101	0.00	0.13	0.03	0.10	213	113	0.0005	9.62	0.2677	47.00	906.79	99.12	0.0011	10.93	5.1 ± 1.3
JN06B107	0.04	0.21	0.10	0.28	216	87	0.0012	9.38	0.4969	14.77	444.17	48.80	0.0023	10.99	6.2 ± 1.5
JN06B099	0.00	0.04	0.00	0.03	79	40	0.0003	15.74	0.0303	615.77	960.62	164.54	0.0010	17.13	6.8 ± 2.0
JN06B098	0.02	0.18	0.08	0.25	112	81	0.0023	8.29	0.4448	9.21	436.14	40.94	0.0023	9.39	7.3 ± 1.0
Drillhole GTD-08-46; 300 m															
JN06B057	0.00	0.03	0.00	0.02	40	38	0.0005	19.79	0.1271	117.66	1241.34	238.1	0.0008	19.18	4.7 ± 1.3
JN06B048	0.04	0.51	0.26	0.95	1134	287	0.0009	4.14	0.5163	6.12	556.89	33.6	0.0018	6.04	4.7 ± 0.5
JN06B050	0.01	0.04	0.01	0.04	40	38	0.0011	32.96	0.1977	79.08	983.30	141.8	0.0010	14.42	5.3 ± 1.5
JN06B058	0.00	0.17	0.02	0.11	305	189	0.0004	7.31	0.1018	29.84	1097.61	89.5	0.0009	8.15	5.5 ± 0.5
JN06B055	0.00	1.99	0.75	3.81	7447	1475	0.0006	3.58	0.3774	8.43	666.19	46.8	0.0015	7.02	5.6 ± 0.6
JN06B051	0.00	0.06	0.01	0.03	55	60	0.0006	11.92	0.1364	23.75	1010.80	135.4	0.0010	13.40	5.6 ± 0.8
JN06B056	0.00	0.35	0.03	0.47	1683	384	0.0003	3.27	0.0716	18.58	1087.69	50.3	0.0009	4.62	5.7 ± 0.3
JN06B054	0.01	0.13	0.01	0.08	258	134	0.0003	9.53	0.1005	169.05	1026.12	100.2	0.0010	9.76	5.8 ± 1.5
JN06B053	0.00	0.09	0.01	0.05	143	97	0.0004	12.97	0.0635	176.62	1062.44	103.0	0.0009	9.69	5.8 ± 1.0
JN06B049	0.00	0.17	0.02	0.22	586	144	0.0004	9.74	0.1491	26.20	906.87	126.5	0.0011	13.95	6.2 ± 0.9
Drillhole GTD-08-42; 54.40 m															
MY08A077	0.02	0.03	0.00	0.02	52	47	0.0004	16.06	0.1212	33.26	1342.78	199.93	0.0007	14.89	4.3 ± 0.7
MY08A087	0.01	0.07	0.02	0.06	118	79	0.0005	10.83	0.2243	123.88	1082.70	127.82	0.0009	11.81	4.6 ± 2.2
MY08A078	0.01	0.06	0.00	0.03	90	85	0.0003	17.71	0.0670	39.08	1309.25	136.47	0.0008	10.42	4.8 ± 0.5
MY08A082	0.00	0.05	0.01	0.04	82	53	0.0005	26.56	0.2421	51.60	964.66	113.30	0.0010	11.74	5.0 ± 1.2
MY08A080	0.00	0.07	0.01	0.06	178	84	0.0003	9.43	0.1019	27.03	1162.40	120.80	0.0009	10.39	5.2 ± 0.6
MY08A090	0.00	0.08	0.00	0.05	166	94	0.0003	10.87	0.0564	64.77	1200.35	138.15	0.0008	11.51	5.3 ± 0.7

Table A1-1. ***(Contd.)***

Sample	^{204}Pb (ppm)	^{206}Pb (ppm)	^{207}Pb (ppm)	^{208}Pb (ppm)	^{232}Th (ppm)	^{238}U (ppm)	^{208}Pb/^{232}Th	± 1σ (%)	^{207}Pb/^{206}Pb	± 1σ (%)	^{238}U/^{206}Pb	± 1σ (%)	^{206}Pb/^{238}U	± 1σ (%)	^{206}Pb/^{238}U age (Ma)
MY08A081	0.02	0.12	0.01	0.07	242	138	0.0003	8.08	0.0709	23.15	1175.61	109.11	0.0009	9.28	5.3 ± 0.5
MY08A079	0.00	0.09	0.01	0.04	164	93	0.0003	12.11	0.1349	19.19	1063.31	116.64	0.0009	10.97	5.4 ± 0.6
MY08A086	0.00	0.08	0.01	0.05	133	90	0.0004	11.38	0.0783	51.92	1138.92	126.33	0.0009	11.09	5.4 ± 0.7
MY08A076	0.00	0.06	0.02	0.08	36	39	0.0022	9.87	0.3833	59.20	626.94	88.41	0.0016	14.10	5.9 ± 3.1
MY08A085	0.00	0.10	0.01	0.04	129	107	0.0003	13.06	0.0589	45.95	1075.13	122.79	0.0009	11.42	5.9 ± 0.7
MY08A089	0.01	0.13	0.01	0.06	153	124	0.0004	10.51	0.0621	44.18	1010.83	96.37	0.0010	9.53	6.2 ± 0.6
MY08A088	0.00	0.06	0.01	0.03	91	63	0.0003	16.33	0.0820	33.44	972.50	114.15	0.0010	11.74	6.3 ± 0.8
MY08A083	0.01	0.03	0.00	0.01	22	24	0.0003	39.99	0.1122	245.37	912.78	170.47	0.0011	18.68	6.5 ± 2.7
MY08A084	0.00	0.06	0.01	0.04	46	54	0.0009	12.48	0.1418	134.52	861.78	100.83	0.0012	11.70	6.6 ± 2.0
Drillhole GTD-09-112; 446 m															
Ap24B018	0.06	0.70	0.48	1.38	1746	333	0.0008	7.44	0.6899	11.36	423.58	49.79	0.0024	11.75	2.8 ± 1.6
Ap24B009	0.02	0.68	0.47	1.29	786	248	0.0017	5.00	0.6935	9.62	354.63	29.08	0.0028	8.20	3.3 ± 1.6
Ap24B020	0.43	9.04	6.41	17.39	6292	1711	0.0027	1.80	0.7228	2.03	197.61	4.27	0.0051	2.16	4.7 ± 0.7
Ap24B014	0.06	2.13	1.07	3.44	4521	1280	0.0008	3.88	0.4999	6.76	552.08	43.36	0.0018	7.85	5.0 ± 0.6
Ap24B019	0.06	2.25	1.38	4.90	6182	831	0.0008	3.35	0.6122	4.44	361.89	15.55	0.0028	4.30	5.1 ± 0.7
Ap24B015	0.10	2.47	1.16	4.77	8226	1496	0.0006	2.44	0.4698	4.23	577.70	22.15	0.0017	3.83	5.2 ± 0.4
Ap24B017	0.05	1.39	0.37	2.36	5742	1215	0.0004	2.68	0.2685	6.27	852.44	35.46	0.0012	4.16	5.4 ± 0.3
Ap24B011	0.03	0.97	0.17	1.72	5295	963	0.0003	3.01	0.1964	7.84	951.48	50.16	0.0011	5.27	5.5 ± 0.3
Ap24B013	0.00	0.49	0.11	0.75	1725	426	0.0005	6.65	0.2738	16.40	796.29	68.83	0.0013	8.64	5.8 ± 0.7
Ap24B008	0.03	1.16	0.56	2.15	2345	512	0.0009	3.94	0.5079	5.59	423.27	25.61	0.0024	6.05	6.3 ± 0.7
Ap24B010	0.00	0.08	0.02	0.07	69	55	0.0011	13.11	0.3030	75.32	679.57	114.29	0.0015	16.82	6.4 ± 2.9
Ap24B012	0.04	0.39	0.24	0.66	292	172	0.0020	6.54	0.4479	44.45	474.73	53.21	0.0021	11.21	6.7 ± 3.5
Ap24B016	0.14	2.62	1.86	5.18	1355	353	0.0037	2.69	0.7267	2.95	136.31	5.55	0.0073	4.07	6.7 ± 1.4
Drillhole GTD-10-104; 357.20 m															
Ap24B026	0.03	0.43	0.06	0.49	1714	459	0.0003	5.42	0.1424	17.86	1109.74	72.93	0.0009	6.57	5.1 ± 0.4
Ap24B025	0.01	0.57	0.17	0.88	1966	463	0.0004	5.05	0.2977	9.46	812.51	55.46	0.0012	6.83	5.4 ± 0.5
Ap24B023	0.02	0.35	0.10	0.44	848	280	0.0005	5.24	0.2987	49.02	786.09	77.82	0.0013	9.90	5.6 ± 1.6
Ap24B027	0.02	0.23	0.04	0.23	559	220	0.0004	6.61	0.1814	51.70	948.72	81.04	0.0011	8.54	5.6 ± 0.9

Table A1-1. ***(Contd.)***

Sample	^{204}Pb (ppm)	^{206}Pb (ppm)	^{207}Pb (ppm)	^{208}Pb (ppm)	^{232}Th (ppm)	^{238}U (ppm)	^{208}Pb/^{232}Th	± 1σ (%)	^{207}Pb/^{206}Pb	± 1σ (%)	^{238}U/^{206}Pb	± 1σ (%)	^{206}Pb/^{238}U	± 1σ (%)	^{206}Pb/^{238}U age (Ma)
Rockchip ARMTB-48 E175652 N9044061															
DE09A153	0.00	0.03	0.00	0.00	14.47	26.74	0.0002	64.72	0.2830	15.96	1156.05	158.37	0.0009	13.70	3.9 ± 0.6
DE09A146	0.01	0.02	0.00	0.01	22.27	30.94	0.0004	36.80	0.1889	108.25	1325.27	169.50	0.0008	12.79	4.0 ± 1.4
DE09A150	0.00	0.03	0.00	0.01	45.04	43.14	0.0003	20.60	0.0986	28.87	1316.31	166.69	0.0008	12.66	4.6 ± 0.6
DE09A149	0.00	0.03	0.00	0.01	36.10	37.08	0.0002	34.78	0.0806	40.11	1254.70	148.27	0.0008	11.82	4.9 ± 0.6
DE09A156	0.00	0.04	0.00	0.01	39.17	43.84	0.0003	19.41	0.1894	26.11	1065.80	91.93	0.0009	8.63	4.9 ± 0.6
DE09A148	0.01	0.03	0.00	0.01	32.10	36.43	0.0003	31.29	0.0664	51.44	1248.32	132.87	0.0008	10.64	5.0 ± 0.6
DE09A151	0.00	0.02	0.00	0.00	10.50	22.70	0.0004	75.37	0.1632	40.56	1089.54	251.39	0.0009	23.07	5.0 ± 1.3
DE09A158	0.00	0.12	0.01	0.04	141.08	143.84	0.0003	9.10	0.0756	21.69	1217.85	70.53	0.0008	5.79	5.1 ± 0.3
DE09A159	0.00	0.07	0.00	0.01	46.94	91.24	0.0003	20.94	0.0635	23.79	1225.43	85.85	0.0008	7.01	5.1 ± 0.4
DE09A155	0.00	0.03	0.00	0.01	32.07	37.50	0.0004	22.27	0.1178	29.09	1137.46	131.43	0.0009	11.55	5.2 ± 0.6
DE09A147	0.00	0.04	0.00	0.01	30.92	41.93	0.0003	25.30	0.0944	66.45	1166.31	130.67	0.0009	11.20	5.2 ± 0.7
DE09A154	0.00	0.14	0.01	0.08	282.26	162.68	0.0003	6.76	0.0613	22.02	1147.65	58.20	0.0009	5.07	5.5 ± 0.3
DE09A157	0.00	0.04	0.00	0.01	37.42	42.73	0.0002	21.96	0.0877	25.59	1103.92	112.75	0.0009	10.21	5.5 ± 0.6
DE09A152	0.00	0.02	0.00	0.00	8.16	18.69	0.0004	58.62	0.0894	52.55	1060.58	172.05	0.0009	16.22	5.7 ± 1.0
Phase 4; Very coarse-grained tonalite															
Drillhole GTD-12-334; 911.12 m															
MY08A115	0.00	0.04	0.03	0.09	25	31	0.0038	16.31	0.6951	142.10	695.78	185.47	0.0014	26.66	1.7 ± 11.6
MY08A122	0.00	0.05	0.01	0.02	47	58	0.0004	20.01	0.1963	50.98	1161.40	160.20	0.0009	13.79	4.5 ± 0.9
MY08A120	0.01	0.09	0.00	0.04	133	122	0.0003	12.49	0.0464	54.46	1390.50	132.68	0.0007	9.54	4.6 ± 0.5
MY08A110	0.00	0.10	0.02	0.08	115	110	0.0007	8.10	0.2156	68.73	1075.27	102.84	0.0009	9.56	4.7 ± 1.2
MY08A109	0.01	0.15	0.01	0.10	341	206	0.0003	10.88	0.0581	27.17	1337.81	99.63	0.0007	7.45	4.7 ± 0.4
MY08A118	0.00	0.06	0.01	0.02	64	70	0.0003	15.81	0.1626	9.68	1157.34	133.67	0.0009	11.55	4.7 ± 0.6
MY08A111	0.00	0.26	0.14	0.41	188	142	0.0022	6.47	0.5290	21.98	523.58	41.39	0.0019	7.91	4.8 ± 1.9
MY08A113	0.02	0.04	0.00	0.01	29	48	0.0002	47.46	0.0200	98.04	1322.03	204.71	0.0008	15.48	4.9 ± 0.8
MY08A116	0.00	0.03	0.00	0.01	21	36	0.0005	30.44	0.0200	143.70	1270.98	241.12	0.0008	18.97	5.1 ± 1.0
MY08A114	0.00	0.05	0.00	0.01	45	65	0.0003	30.04	0.0607	42.47	1185.76	163.03	0.0008	13.75	5.3 ± 0.8
MY08A117	0.00	0.05	0.00	0.02	59	64	0.0003	20.84	0.0128	167.83	1179.26	157.23	0.0008	13.33	5.5 ± 0.8
MY08A112	0.03	0.03	0.00	0.01	20	30	0.0003	56.38	0.0902	736.70	1090.57	196.01	0.0009	17.97	5.6 ± 5.1

Table A1-1. ***(Contd.)***

Sample	^{204}Pb (ppm)	^{206}Pb (ppm)	^{207}Pb (ppm)	^{208}Pb (ppm)	^{232}Th (ppm)	^{238}U (ppm)	^{208}Pb/^{232}Th	± 1σ (%)	^{207}Pb/^{206}Pb	± 1σ (%)	^{238}U/^{206}Pb	± 1σ (%)	^{206}Pb/^{238}U	± 1σ (%)	^{206}Pb/^{238}U age (Ma)
Phase 5; Fine-grained tonalite															
Drillhole GTD-08-35; 554.95 m															
MY08A036	0.02	0.06	0.04	0.10	14	32	0.0069	7.55	0.7682	60.42	556.26	71.99	0.0018	12.94	1.0 ± 6.8
MY08A026	0.00	0.06	0.01	0.02	50	86	0.0003	24.30	0.0926	30.33	1481.01	190.35	0.0007	12.85	4.1 ± 0.5
MY08A033	0.00	0.08	0.01	0.04	95	119	0.0004	12.80	0.0957	30.04	1468.16	172.19	0.0007	11.73	4.1 ± 0.5
MY08A034	0.01	0.05	0.02	0.05	48	37	0.0010	12.55	0.4764	139.62	708.33	98.47	0.0014	13.90	4.1 ± 7.7
MY08A028	0.00	0.06	0.02	0.05	32	52	0.0017	11.15	0.3686	118.85	916.70	134.98	0.0011	14.72	4.2 ± 3.9
MY08A024	0.00	0.02	0.00	0.01	10	24	0.0008	58.98	0.0877	49.07	1463.03	328.72	0.0007	22.47	4.2 ± 1.0
MY08A027	0.00	0.07	0.01	0.02	62	98	0.0004	18.23	0.0996	31.36	1430.62	179.07	0.0007	12.52	4.2 ± 0.6
MY08A031	0.01	0.05	0.00	0.01	19	75	0.0004	45.87	0.0200	145.46	1485.05	236.62	0.0007	15.93	4.3 ± 0.7
MY08A032	0.00	0.03	0.00	0.00	23	36	0.0001	114.69	0.1214	18.75	1336.16	269.63	0.0007	20.18	4.4 ± 0.9
MY08A025	0.01	0.09	0.01	0.01	76	101	0.0002	28.24	0.0877	393.41	1090.69	121.63	0.0009	11.15	5.6 ± 2.7
MY08A029	0.02	0.11	0.01	0.05	131	120	0.0003	10.28	0.0711	31.65	1062.13	93.18	0.0009	8.77	5.9 ± 0.5
MY08A030	0.00	0.04	0.00	0.01	34	43	0.0003	29.56	0.0294	75.46	1035.80	168.15	0.0010	16.23	6.2 ± 1.0
MY08A037	0.00	0.13	0.01	0.03	144	131	0.0002	14.01	0.0497	42.68	1005.98	81.44	0.0010	8.10	6.4 ± 0.5
MY08A035	0.00	0.06	0.01	0.05	51	38	0.0010	10.23	0.2395	99.91	600.75	77.12	0.0017	12.84	8.1 ± 3.4
Drillhole GTD-08-56; 463 m															
JN06B075	0.01	0.03	0.01	0.02	14	26	0.0017	17.99	0.4963	40.97	999.45	176.24	0.0010	17.63	2.8 ± 1.7
JN06B074	0.01	0.03	0.01	0.01	21	44	0.0007	25.24	0.2056	124.44	1428.30	249.30	0.0007	17.45	3.6 ± 1.6
JN06B066	0.00	0.03	0.00	0.00	22	48	0.0002	78.82	0.0960	29.55	1477.46	242.15	0.0007	16.39	4.1 ± 0.7
JN06B069	0.01	0.03	0.00	0.01	31	49	0.0005	26.84	0.1004	123.16	1444.97	210.12	0.0007	14.54	4.2 ± 0.9
JN06B078	0.00	0.02	0.00	0.01	20	35	0.0005	30.01	0.1206	187.27	1402.90	288.45	0.0007	20.56	4.2 ± 1.6
JN06B072	0.02	0.14	0.08	0.19	50	75	0.0038	5.44	0.5529	26.30	542.23	42.49	0.0018	7.84	4.3 ± 2.2
JN06B070	0.01	0.03	0.00	0.02	29	47	0.0006	20.08	0.1124	112.10	1377.31	219.59	0.0007	15.94	4.3 ± 1.0
JN06B080	0.02	0.10	0.06	0.16	22	43	0.0077	5.51	0.6145	58.74	408.58	41.62	0.0024	10.19	4.4 ± 7.2
JN06B077	0.01	0.05	0.01	0.03	25	55	0.0014	13.62	0.2291	180.52	1094.66	138.22	0.0009	20.63	4.5 ± 3.1
JN06B067	0.01	0.06	0.00	0.03	47	78	0.0006	14.48	0.0822	141.76	1343.91	167.98	0.0007	12.50	4.6 ± 0.9
JN06B068	0.00	0.02	0.00	0.01	19	34	0.0005	35.00	0.0762	44.73	1353.58	299.25	0.0007	22.11	4.6 ± 1.0
JN06B073	0.02	0.07	0.02	0.06	43	69	0.0015	10.01	0.3166	44.47	918.07	99.80	0.0011	10.87	4.6 ± 1.3
JN06B079	0.00	0.06	0.01	0.04	24	54	0.0015	15.54	0.2619	120.29	1001.58	159.25	0.0010	15.90	4.7 ± 2.7

Table A1-1. ***(Contd.)***

Sample	^{204}Pb (ppm)	^{206}Pb (ppm)	^{207}Pb (ppm)	^{208}Pb (ppm)	^{232}Th (ppm)	^{238}U (ppm)	^{208}Pb/^{232}Th	± 1σ (%)	^{207}Pb/^{206}Pb	± 1σ (%)	^{238}U/^{206}Pb	± 1σ (%)	^{206}Pb/^{238}U	± 1σ (%)	^{206}Pb/^{238}U age (Ma)
JN06B065	0.01	0.07	0.00	0.01	64	93	0.0002	28.50	0.0309	235.54	1274.78	195.59	0.0008	15.34	5.2 ± 0.9
JN06B076	0.03	0.04	0.00	0.01	18	40	0.0004	42.90	0.0610	55.74	1074.26	181.98	0.0009	16.94	5.9 ± 1.0
JN06B064	0.00	0.02	0.01	0.02	6	14	0.0038	15.51	0.2633	89.63	618.94	192.34	0.0016	31.08	7.5 ± 3.9
Drillhole GTD-11-201; 600 m															
NO14A049	0.00	0.04	0.01	0.02	46	67	0.0003	24.79	0.1324	36.45	1659.07	295.28	0.0006	17.80	3.5 ± 0.7
NO14A044	0.02	0.02	0.01	0.01	18	30	0.0003	66.30	0.2877	44.20	1248.86	280.71	0.0008	22.48	3.6 ± 1.2
NO14A057	0.01	0.07	0.03	0.07	33	68	0.0020	9.92	0.4238	37.29	903.02	110.85	0.0011	12.27	3.7 ± 1.5
NO14A050	0.00	0.06	0.01	0.01	90	103	0.0001	47.35	0.0813	43.20	1594.84	192.87	0.0006	12.09	3.9 ± 0.5
NO14A058	0.00	0.09	0.03	0.07	52	91	0.0014	9.64	0.3695	37.13	975.74	98.49	0.0010	10.09	3.9 ± 1.2
NO14A051	0.02	0.03	0.00	0.01	23	51	0.0002	65.05	0.0166	251.80	1603.80	287.10	0.0006	17.90	4.2 ± 0.8
NO14A056	0.00	0.07	0.00	0.02	55	97	0.0003	25.52	0.0694	104.56	1460.08	161.79	0.0007	11.08	4.3 ± 0.6
NO14A052	0.01	0.03	0.00	0.01	45	44	0.0003	26.86	0.0200	229.31	1332.53	234.74	0.0008	17.62	5.0 ± 0.9
NO14A053	0.00	0.09	0.07	0.18	12	19	0.0153	20.19	0.7087	18.08	204.08	29.19	0.0049	14.30	5.1 ± 5.2
NO14A054	0.00	0.02	0.00	0.00	11	28	0.0002	194.00	0.0403	349.65	1205.92	234.18	0.0008	19.42	5.4 ± 1.4
NO14A055	0.00	0.03	0.00	0.01	22	36	0.0003	48.51	0.0200	667.67	1138.40	198.55	0.0009	17.44	5.8 ± 1.4
Phase 6; Coarse-grained tonalite															
Drillhole GTD-11-201; 988 m															
MY08A142	0.00	0.03	0.01	0.02	42	62	0.0005	20.39	0.2242	167.26	1995.96	342.89	0.0005	17.18	2.5 ± 1.6
MY08A148	0.01	0.14	0.09	0.24	65	72	0.0038	6.71	0.6790	51.49	512.64	48.71	0.0020	9.50	2.5 ± 5.6
MY08A147	0.00	0.06	0.02	0.05	30	52	0.0018	11.72	0.4442	31.54	922.66	119.59	0.0011	12.96	3.5 ± 1.3
MY08A155	0.00	0.15	0.11	0.24	23	39	0.0112	6.15	0.7316	106.38	234.03	28.80	0.0043	12.30	3.7 ± 27.1
MY08A151	0.00	0.03	0.00	0.01	27	49	0.0003	34.57	0.0261	123.92	1728.44	296.53	0.0006	17.16	3.7 ± 0.7
MY08A144	0.00	0.19	0.11	0.26	102	111	0.0026	6.87	0.5720	13.81	567.34	52.50	0.0018	9.25	3.8 ± 1.2
MY08A146	0.01	0.02	0.00	0.00	15	29	0.0003	51.83	0.0200	#####	1608.50	390.11	0.0006	24.25	4.0 ± 2.8
MY08A149	0.02	0.05	0.00	0.02	55	76	0.0003	23.85	0.0874	32.10	1505.70	182.85	0.0007	12.14	4.1 ± 0.5
MY08A154	0.00	0.04	0.01	0.03	27	46	0.0010	19.90	0.2899	115.53	1095.20	189.07	0.0009	17.26	4.1 ± 2.6
MY08A143	0.00	0.16	0.05	0.16	114	147	0.0013	11.68	0.3221	29.84	962.56	171.31	0.0010	17.80	4.4 ± 1.1
MY08A153	0.02	0.11	0.00	0.03	134	163	0.0003	13.72	0.0378	80.36	1424.05	135.49	0.0007	9.51	4.5 ± 0.5
MY08A152	0.00	0.05	0.01	0.03	44	57	0.0008	58.88	0.1263	49.91	1238.57	178.51	0.0008	14.41	4.7 ± 0.8

Table A1-1. ***(Contd.)***

Sample	^{204}Pb (ppm)	^{206}Pb (ppm)	^{207}Pb (ppm)	^{208}Pb (ppm)	^{232}Th (ppm)	^{238}U (ppm)	^{208}Pb/^{232}Th	± 1σ (%)	^{207}Pb/^{206}Pb	± 1σ (%)	^{238}U/^{206}Pb	± 1σ (%)	^{206}Pb/^{238}U	± 1σ (%)	^{206}Pb/^{238}U age (Ma)
MY08A145	0.02	0.18	0.08	0.22	107	114	0.0021	5.55	0.4604	11.27	633.05	47.75	0.0016	7.54	4.8 ± 0.8
MY08A150	0.02	0.08	0.03	0.10	24	64	0.0041	8.21	0.3616	53.95	777.39	95.38	0.0013	12.27	5.0 ± 2.1
MY08A156	0.00	0.15	0.09	0.24	20	52	0.0114	5.78	0.5841	14.50	349.38	39.28	0.0029	11.24	5.9 ± 2.1
Drillhole GTD-11-201; 1097 m															
MY08A133	0.00	0.04	0.01	0.04	34	48	0.0013	12.22	0.3067	134.99	1320.25	222.34	0.0008	16.84	3.3 ± 2.6
MY08A129	0.00	0.02	0.01	0.01	13	28	0.0004	51.04	0.2541	8.38	1383.49	309.87	0.0007	22.40	3.4 ± 0.8
MY08A126	0.00	0.06	0.00	0.01	46	94	0.0001	41.93	0.0644	39.17	1656.51	228.93	0.0006	13.82	3.8 ± 0.5
MY08A132	0.01	0.07	0.02	0.04	84	91	0.0005	14.14	0.2292	22.28	1275.05	188.71	0.0008	14.80	3.9 ± 0.7
MY08A134	0.01	0.07	0.01	0.02	100	105	0.0002	21.82	0.0846	43.82	1568.08	214.91	0.0006	13.71	3.9 ± 0.6
MY08A127	0.00	0.08	0.01	0.02	94	135	0.0002	20.70	0.0788	143.37	1576.14	159.51	0.0006	10.12	3.9 ± 0.7
MY08A130	0.00	0.06	0.00	0.02	73	93	0.0002	21.13	0.0761	241.66	1489.31	179.08	0.0007	12.02	4.2 ± 1.1
MY08A135	0.00	0.04	0.00	0.02	42	57	0.0004	20.53	0.0468	296.07	1488.26	256.15	0.0007	17.21	4.3 ± 1.1
MY08A136	0.00	0.11	0.04	0.12	148	92	0.0009	13.12	0.4168	83.76	775.46	135.21	0.0013	17.44	4.4 ± 3.8
MY08A131	0.01	0.28	0.12	0.30	146	196	0.0020	8.97	0.4326	53.85	742.77	105.04	0.0013	14.14	4.4 ± 2.6
MY08A138	0.00	0.04	0.00	0.01	19	58	0.0003	49.72	0.0458	29.29	1387.27	214.56	0.0007	15.47	4.6 ± 0.7
MY08A139	0.00	0.07	0.00	0.01	71	100	0.0002	29.96	0.0375	103.44	1343.14	148.32	0.0007	11.04	4.8 ± 0.6
MY08A128	0.03	0.55	0.34	0.94	247	191	0.0038	3.58	0.6106	8.09	354.55	19.74	0.0028	5.57	5.2 ± 1.2
MY08A137	0.01	0.26	0.18	0.50	200	60	0.0027	6.80	0.6838	11.93	214.87	25.52	0.0047	11.88	5.8 ± 3.2
Drillhole GTD-11-192; 891 m															
JN13A157	0.00	0.02	0.01	0.02	11	25	0.0018	34.02	0.3720	40.89	1450.66	593.44	0.0007	40.91	2.6 ± 1.4
JN13A164	0.00	0.03	0.01	0.01	18	46	0.0004	118.07	0.2973	25.66	1565.94	376.06	0.0006	24.01	2.8 ± 0.8
JN13A155	0.00	0.04	0.01	0.02	29	53	0.0006	45.42	0.2721	46.93	1410.70	307.41	0.0007	21.79	3.3 ± 1.0
JN13A160	0.00	0.05	0.01	0.02	57	81	0.0003	51.72	0.1477	69.24	1718.72	294.92	0.0006	17.16	3.3 ± 0.7
JN13A156	0.00	0.04	0.01	0.01	30	54	0.0002	94.50	0.2056	40.33	1388.41	249.11	0.0007	17.94	3.7 ± 0.8
JN13A150	0.00	0.03	0.00	0.01	23	43	0.0003	99.12	0.0550	189.95	1549.12	397.51	0.0006	25.66	4.1 ± 1.2
JN13A152	0.00	0.03	0.00	0.03	21	42	0.0014	27.07	0.0609	214.00	1358.59	351.86	0.0007	25.90	4.7 ± 1.4
JN13A149	0.00	0.06	0.00	0.01	47	82	0.0003	53.82	0.0468	176.85	1362.37	185.72	0.0007	13.63	4.7 ± 0.8
JN13A159	0.00	0.04	0.00	0.01	26	59	0.0004	70.85	0.0200	454.07	1397.89	280.91	0.0007	20.09	4.8 ± 1.1
JN13A163	0.00	0.04	0.01	0.02	36	51	0.0006	43.66	0.0200	638.24	1319.35	392.41	0.0008	29.74	5.0 ± 1.7
JN13A154	0.01	0.02	0.00	0.04	20	26	0.0020	21.98	0.1625	65.95	1081.80	345.00	0.0009	31.89	5.1 ± 1.8

Table A1-1. ***(Contd.)***

Sample	^{204}Pb (ppm)	^{206}Pb (ppm)	^{207}Pb (ppm)	^{208}Pb (ppm)	^{232}Th (ppm)	^{238}U (ppm)	^{208}Pb/^{232}Th	± 1σ (%)	^{207}Pb/^{206}Pb	± 1σ (%)	^{238}U/^{206}Pb	± 1σ (%)	^{206}Pb/^{238}U	± 1σ (%)	^{206}Pb/^{238}U age (Ma)
JN13A162	0.01	0.04	0.00	0.02	39	57	0.0005	42.17	0.0344	194.79	1256.49	251.01	0.0008	19.98	5.2 ± 1.1
JN13A158	0.02	0.22	0.15	0.60	53	54	0.0118	36.41	0.6836	11.90	238.35	30.45	0.0042	12.77	5.3 ± 2.9
JN13A153	0.01	0.07	0.02	0.06	41	61	0.0014	15.34	0.2682	36.60	869.57	142.35	0.0011	16.37	5.3 ± 1.3
JN13A161	0.00	0.04	0.01	0.02	15	33	0.0012	44.14	0.2104	43.61	829.16	176.43	0.0012	21.28	6.2 ± 1.6
JN13A151	0.02	0.04	0.00	0.02	24	44	0.0008	36.66	0.0931	97.43	960.07	183.17	0.0010	19.08	6.3 ± 1.4
Drillhole GTD-08-56; 807 m															
JN06B097	0.03	0.11	0.06	0.11	44	95	0.0025	9.24	0.5690	71.45	859.71	120.37	0.0012	14.00	2.5 ± 3.9
JN06B092	0.00	0.05	0.01	0.02	43	76	0.0004	21.24	0.1736	135.98	1507.27	188.36	0.0007	12.50	3.6 ± 1.4
JN06B089	0.01	0.04	0.02	0.04	38	36	0.0010	17.05	0.4409	78.02	884.77	139.54	0.0011	15.77	3.6 ± 3.2
JN06B094	0.01	0.07	0.01	0.03	87	106	0.0004	13.44	0.1416	27.07	1484.73	157.35	0.0007	10.60	3.8 ± 0.5
JN06B091	0.00	0.10	0.01	0.02	133	155	0.0002	16.92	0.0696	48.44	1620.27	153.82	0.0006	9.49	3.9 ± 0.4
JN06B096	0.02	0.32	0.18	0.55	499	171	0.0011	5.72	0.5607	10.76	519.78	33.58	0.0019	6.46	4.3 ± 1.0
JN06B088	0.01	0.07	0.01	0.05	90	85	0.0005	12.37	0.1776	97.89	1234.00	142.38	0.0008	11.54	4.4 ± 1.3
JN06B090	0.01	0.22	0.07	0.21	230	213	0.0009	8.05	0.3150	10.75	972.23	71.08	0.0010	7.31	4.4 ± 0.4
JN06B087	0.00	0.08	0.02	0.06	45	85	0.0014	10.24	0.2705	61.62	1035.87	123.09	0.0010	11.88	4.5 ± 1.4
JN06B095	0.01	0.05	0.01	0.05	25	58	0.0019	13.00	0.2211	57.42	1065.85	167.41	0.0009	15.71	4.7 ± 1.2
JN06B093	0.11	2.60	1.99	5.39	2750	306	0.0020	10.84	0.7644	3.82	115.60	16.99	0.0087	14.70	5.3 ± 2.3
Drillhole GTD-12-292; 1012 m															
MY01A185	0.00	0.07	0.03	0.05	33	69	0.0015	25.57	0.4433	48.33	1033.41	255.28	0.0010	24.70	3.1 ± 1.9
MY01A183	0.00	0.05	0.01	0.02	39	96	0.0005	29.84	0.1448	23.86	1771.86	315.89	0.0006	17.83	3.2 ± 0.6
MY01A177	0.00	0.08	0.05	0.09	21	41	0.0044	14.05	0.6284	80.14	518.40	88.62	0.0019	17.10	3.3 ± 7.9
MY01A178	0.03	0.03	0.00	0.01	24	54	0.0002	94.45	0.0768	178.63	1748.82	480.57	0.0006	27.48	3.5 ± 1.2
MY01A174	0.00	0.05	0.02	0.05	17	44	0.0026	19.97	0.4108	10.84	942.16	207.66	0.0011	22.04	3.7 ± 0.9
MY01A173	0.00	0.02	0.01	0.00	11	32	0.0003	161.66	0.2284	16.40	1333.09	405.87	0.0008	30.45	3.7 ± 1.2
MY01A181	0.03	0.04	0.00	0.01	27	59	0.0004	56.74	0.0873	214.77	1531.61	419.12	0.0007	27.36	4.0 ± 1.5
MY01A180	0.00	0.03	0.00	0.01	21	45	0.0003	76.92	0.0217	854.50	1521.07	435.35	0.0007	27.36	4.2 ± 1.6
MY01A184	0.00	0.12	0.00	0.04	130	178	0.0003	17.08	0.0340	80.40	1492.44	192.91	0.0007	12.93	4.3 ± 0.6
MY01A179	0.02	0.04	0.00	0.02	27	60	0.0006	34.25	0.0688	261.97	1398.20	365.42	0.0007	26.13	4.5 ± 1.6
MY01A182	0.02	0.07	0.01	0.02	39	84	0.0004	34.17	0.1086	129.02	1257.90	204.19	0.0008	16.23	4.7 ± 1.2

Table A1-1. ***(Contd.)***

Sample	^{204}Pb (ppm)	^{206}Pb (ppm)	^{207}Pb (ppm)	^{208}Pb (ppm)	^{232}Th (ppm)	^{238}U (ppm)	^{208}Pb/^{232}Th	± 1σ (%)	^{207}Pb/^{206}Pb	± 1σ (%)	^{238}U/^{206}Pb	± 1σ (%)	^{206}Pb/^{238}U	± 1σ (%)	^{206}Pb/^{238}U age (Ma)
MY01A176	0.01	0.06	0.00	0.01	29	68	0.0003	65.52	0.0673	63.41	1149.53	183.68	0.0009	15.98	5.5 ± 0.9
MY01A175	0.00	0.07	0.01	0.04	40	61	0.0010	22.05	0.2016	283.01	937.42	169.65	0.0011	18.10	5.5 ± 5.1
Drillhole GTD-11-248; 409 m															
JN13A173	0.02	0.05	0.05	0.10	22	33	0.0049	13.52	0.8240	26.19	567.50	115.28	0.0018	20.31	0.2 ± 3.1
JN13A181	0.00	0.09	0.04	0.11	70	81	0.0015	13.13	0.4904	36.70	904.94	119.29	0.0011	13.18	3.1 ± 1.7
JN13A176	0.02	0.35	0.27	0.64	46	66	0.0157	5.87	0.7748	12.02	162.09	18.23	0.0062	11.25	3.2 ± 4.7
JN13A179	0.00	0.02	0.00	0.03	27	43	0.0011	22.30	0.1615	118.78	1644.69	525.20	0.0006	31.93	3.3 ± 1.4
JN13A180	0.02	0.14	0.03	0.10	284	205	0.0004	9.85	0.2111	30.59	1384.68	123.67	0.0007	8.93	3.7 ± 0.5
JN13A185	0.02	0.08	0.03	0.07	61	90	0.0012	11.92	0.3488	32.28	1060.49	135.56	0.0009	12.78	3.7 ± 1.0
JN13A186	0.02	0.14	0.08	0.19	70	78	0.0028	8.38	0.5684	22.36	549.34	61.13	0.0018	11.13	4.0 ± 1.9
JN13A182	0.02	0.14	0.08	0.19	49	73	0.0040	7.43	0.5749	18.04	519.09	46.10	0.0019	8.88	4.1 ± 1.7
JN13A174	0.00	0.02	0.00	0.00	15	34	0.0001	403.46	0.0200	710.14	1583.61	535.57	0.0006	33.82	4.2 ± 1.6
JN13A184	0.02	0.03	0.01	0.01	21	37	0.0006	56.64	0.1952	47.87	1217.53	317.20	0.0008	26.05	4.3 ± 1.3
JN13A175	0.00	0.14	0.03	0.10	190	159	0.0005	11.30	0.1826	50.91	1144.22	117.17	0.0009	10.24	4.7 ± 0.8
JN13A183	0.02	0.68	0.52	1.36	60	85	0.0237	5.11	0.7601	4.51	118.66	9.13	0.0084	7.69	5.4 ± 2.5
JN13A177	0.00	0.08	0.05	0.11	12	30	0.0092	9.36	0.5805	21.37	365.69	49.96	0.0027	13.66	5.7 ± 2.9
JN13A178	0.01	0.26	0.18	0.47	58	63	0.0084	4.84	0.6600	7.23	229.57	13.75	0.0044	5.99	6.3 ± 1.8
Phase 7; Quartz diorite															
Drillhole GTD-10-167; 91.7 m															
JN13A117	0.00	0.03	0.01	0.00	22	45	0.0001	157.65	0.4266	21.84	1592.70	425.27	0.0006	26.70	2.1 ± 0.7
JN13A115	0.01	0.03	0.01	0.01	31	58	0.0003	91.25	0.2730	37.38	1989.58	540.31	0.0005	27.16	2.3 ± 0.8
JN13A110	0.02	0.07	0.04	0.06	48	78	0.0014	12.98	0.4918	28.22	1025.86	169.93	0.0010	16.56	2.7 ± 1.2
JN13A118	0.00	0.04	0.01	0.03	61	82	0.0006	23.55	0.2030	58.17	1808.74	330.87	0.0006	18.29	2.9 ± 0.7
JN13A109	0.01	0.04	0.01	0.02	46	79	0.0004	42.83	0.1922	97.96	1788.03	304.59	0.0006	17.03	2.9 ± 1.0
JN13A111	0.00	0.03	0.01	0.00	19	39	0.0002	206.71	0.3306	35.99	1231.31	281.41	0.0008	22.85	3.3 ± 1.1
JN13A107	0.01	0.12	0.01	0.06	267	176	0.0002	15.03	0.1187	69.04	1467.75	306.92	0.0007	20.91	4.0 ± 0.9
JN13A114	0.00	0.69	0.05	0.55	2729	1096	0.0002	6.83	0.0751	13.93	1535.73	63.12	0.0007	4.11	4.0 ± 0.2
JN13A113	0.00	0.52	0.03	0.34	1651	794	0.0002	4.31	0.0537	19.60	1487.65	72.02	0.0007	4.84	4.3 ± 0.2
JN13A106	0.02	0.06	0.00	0.01	57	88	0.0001	95.77	0.0315	327.17	1480.61	223.82	0.0007	15.12	4.4 ± 0.9

Table A1-1. ***(Contd.)***

Sample	^{204}Pb (ppm)	^{206}Pb (ppm)	^{207}Pb (ppm)	^{208}Pb (ppm)	^{232}Th (ppm)	^{238}U (ppm)	^{208}Pb/^{232}Th	± 1σ (%)	^{207}Pb/^{206}Pb	± 1σ (%)	^{238}U/^{206}Pb	± 1σ (%)	^{206}Pb/^{238}U	± 1σ (%)	^{206}Pb/^{238}U age (Ma)
JN13A120	0.02	0.09	0.02	0.05	63	86	0.0008	20.53	0.2907	38.94	976.04	138.01	0.0010	14.14	4.6 ± 1.1
JN13A116	0.01	0.10	0.00	0.03	106	143	0.0003	20.83	0.0385	145.97	1391.04	149.18	0.0007	10.72	4.7 ± 0.6
JN13A119	0.01	0.08	0.00	0.01	65	110	0.0002	62.90	0.0200	502.74	1368.04	182.81	0.0007	13.36	4.9 ± 0.9
JN13A108	0.01	0.03	0.00	0.01	21	43	0.0005	70.01	0.0246	407.47	1225.08	264.56	0.0008	21.60	5.4 ± 1.3
JN13A112	0.00	0.05	0.00	0.01	40	60	0.0003	78.69	0.0244	431.49	1108.16	251.23	0.0009	22.67	6.0 ± 1.6
Drillhole GTD-10-139; 355 m															
JN13A085	0.00	0.02	0.01	0.00	16	30	0.0001	243.00	0.3198	72.86	1771.54	749.26	0.0006	42.29	2.4 ± 1.5
JN13A089	0.00	0.03	0.01	0.01	20	44	0.0003	119.93	0.3321	39.37	1631.58	385.16	0.0006	23.61	2.5 ± 0.9
JN13A090	0.00	0.05	0.01	0.02	65	78	0.0003	49.01	0.2691	44.85	1528.28	290.56	0.0007	19.01	3.0 ± 0.9
JN13A087	0.00	0.03	0.00	0.01	28	46	0.0002	111.53	0.0909	191.24	1770.31	567.90	0.0006	32.08	3.4 ± 1.4
JN13A093	0.00	0.05	0.01	0.01	35	61	0.0003	67.73	0.2529	96.49	1282.67	226.47	0.0008	17.66	3.7 ± 1.7
JN13A098	0.00	0.06	0.01	0.03	54	92	0.0006	25.36	0.1132	109.97	1506.15	264.37	0.0007	17.55	3.9 ± 1.0
JN13A086	0.00	0.05	0.00	0.01	45	74	0.0003	75.22	0.0524	235.11	1536.31	291.28	0.0007	18.96	4.2 ± 1.0
JN13A088	0.01	0.04	0.00	0.01	25	62	0.0005	64.64	0.0406	320.39	1514.82	303.99	0.0007	20.07	4.3 ± 1.1
JN13A092	0.00	0.05	-0.01	0.02	50	84	0.0004	42.37	0.0200	316.33	1531.99	244.52	0.0007	15.96	4.3 ± 0.8
JN13A091	0.00	0.03	0.00	0.02	22	48	0.0008	47.13	0.0200	694.70	1515.41	395.31	0.0007	26.09	4.4 ± 1.4
JN13A094	0.01	0.07	0.01	0.01	55	91	0.0001	134.86	0.0976	96.44	1350.63	217.91	0.0007	16.13	4.5 ± 0.9
JN13A100	0.01	0.08	0.02	0.05	67	85	0.0008	16.68	0.2585	36.37	1020.89	136.42	0.0010	13.36	4.6 ± 1.0
JN13A096	0.01	0.15	0.03	0.13	129	172	0.0011	12.16	0.2167	43.46	1039.19	131.45	0.0010	12.65	4.9 ± 1.0
JN13A099	0.00	0.06	0.01	0.02	31	62	0.0007	38.97	0.1389	72.03	1022.07	168.55	0.0010	16.49	5.6 ± 1.2
Drillhole GTD-10-146; 156 m															
MY01A143	0.00	0.02	0.01	0.01	8	21	0.0012	56.34	0.5151	131.26	1225.36	416.63	0.0008	34.00	2.1 ± 4.6
MY01A146	0.01	0.04	0.00	0.02	34	64	0.0006	35.50	0.0757	198.33	1820.75	503.63	0.0005	27.66	3.4 ± 1.2
MY01A144	0.00	0.05	0.00	0.01	16	49	0.0006	60.50	0.3612	44.33	1119.65	211.67	0.0009	18.91	3.5 ± 1.3
MY01A136	0.01	0.05	0.00	0.02	52	83	0.0003	40.75	0.0913	284.41	1678.90	311.62	0.0006	18.56	3.6 ± 1.4
MY01A142	0.00	0.06	0.01	0.01	38	93	0.0002	73.29	0.1073	33.61	1640.62	306.06	0.0006	18.66	3.6 ± 0.7
MY01A139	0.02	0.06	0.00	0.00	56	104	0.0001	123.83	0.0200	187.20	1763.40	355.58	0.0006	20.16	3.7 ± 0.8
MY01A145	0.00	0.04	0.00	0.01	38	71	0.0002	111.16	0.0200	207.44	1724.62	358.81	0.0006	20.81	3.7 ± 0.8
MY01A138	0.00	0.55	0.01	0.51	2530	860	0.0002	5.92	0.0215	57.58	1658.78	145.72	0.0006	8.78	3.9 ± 0.4
MY01A141	0.03	0.04	0.01	-0.01	23	51	0.0001	81.14	0.1977	91.03	1296.08	277.85	0.0008	21.44	4.0 ± 1.4

Table A1-1. ***(Contd.)***

Sample	^{204}Pb (ppm)	^{206}Pb (ppm)	^{207}Pb (ppm)	^{208}Pb (ppm)	^{232}Th (ppm)	^{238}U (ppm)	^{208}Pb/^{232}Th	± 1σ (%)	^{207}Pb/^{206}Pb	± 1σ (%)	^{238}U/^{206}Pb	± 1σ (%)	^{206}Pb/^{238}U	± 1σ (%)	^{206}Pb/^{238}U age (Ma)
MY01A147	0.00	0.03	0.00	0.02	23	47	0.0010	45.42	0.0200	206.98	1553.59	442.95	0.0006	28.51	4.1 ± 1.2
MY01A149	0.00	0.14	0.00	0.05	184	207	0.0003	16.93	0.0215	153.96	1466.37	167.95	0.0007	11.45	4.4 ± 0.6
MY01A135	0.00	0.03	-0.01	0.01	17	35	0.0006	54.74	0.0200	193.15	1397.83	437.78	0.0007	31.32	4.6 ± 1.5
MY01A140	0.00	0.06	0.00	0.01	47	81	0.0002	63.70	0.0375	624.93	1373.48	246.12	0.0007	17.92	4.7 ± 1.6
MY01A137	0.00	0.05	0.00	0.02	32	59	0.0005	46.71	0.0200	183.52	1185.08	289.24	0.0008	24.41	5.4 ± 1.4
MY01A148	0.00	0.04	0.00	0.01	14	40	0.0005	64.94	0.0210	238.41	1150.39	305.56	0.0009	26.56	5.6 ± 1.6
Drillhole GTD-10-166; 651 m															
MY01A160	0.01	0.05	0.01	0.00	62	88	0.0001	159.08	0.2528	54.89	1898.57	420.94	0.0005	22.17	2.5 ± 0.8
MY01A161	0.05	0.09	0.04	0.08	73	109	0.0011	14.26	0.4037	48.40	1203.75	190.51	0.0008	15.83	2.9 ± 1.4
MY01A164	0.00	0.02	0.00	0.01	20	39	0.0003	117.79	0.0200	345.20	2022.10	763.86	0.0005	37.78	3.2 ± 2.1
MY01A170	0.02	0.04	0.01	0.01	18	50	0.0005	57.58	0.2208	7.98	1394.27	310.42	0.0007	22.26	3.6 ± 0.8
MY01A159	0.00	0.15	0.02	0.07	249	240	0.0003	15.04	0.1234	23.69	1576.12	180.13	0.0006	11.43	3.7 ± 0.4
MY01A166	0.02	0.02	-0.01	0.01	20	38	0.0007	49.98	0.0200	262.14	1736.19	608.04	0.0006	35.02	3.7 ± 1.4
MY01A169	0.00	0.19	0.01	0.06	318	302	0.0002	17.80	0.0415	75.55	1561.03	146.44	0.0006	9.38	4.1 ± 0.4
MY01A167	0.00	0.11	0.01	0.03	94	179	0.0003	24.92	0.0457	197.55	1552.38	247.22	0.0006	15.93	4.2 ± 0.8
MY01A158	0.00	0.11	0.01	0.04	159	156	0.0003	22.22	0.1160	237.95	1406.19	170.12	0.0007	12.10	4.2 ± 1.7
MY01A162	0.03	0.06	0.01	0.00	25	76	0.0002	141.21	0.1427	25.29	1326.68	337.98	0.0008	25.48	4.3 ± 1.1
MY01A157	0.00	0.09	0.00	0.02	110	142	0.0002	30.43	0.0330	86.08	1509.25	204.25	0.0007	13.53	4.3 ± 0.6
MY01A168	0.00	0.11	0.02	0.10	101	137	0.0009	11.79	0.1841	70.37	1210.37	152.73	0.0008	12.62	4.4 ± 1.0
MY01A165	0.00	0.08	0.00	0.04	114	114	0.0003	21.68	0.0200	189.54	1365.21	225.20	0.0007	16.50	4.7 ± 0.8
MY01A163	0.00	0.06	0.00	0.01	40	75	0.0003	44.57	0.0200	234.76	1352.61	267.61	0.0007	19.78	4.8 ± 1.9
Drillhole GTD-08-35; 472.1 m															
Ap24B041	0.00	0.41	0.32	0.77	27	59	0.0269	5.22	0.7790	8.36	152.17	13.21	0.0066	8.68	3.2 ± 3.5
Ap24B040	0.02	0.19	0.11	0.23	78	117	0.0031	11.00	0.6064	22.60	581.95	99.60	0.0017	17.12	3.2 ± 2.0
Ap24B029	0.00	0.04	0.01	0.02	29	47	0.0007	31.58	0.3301	48.03	1214.21	269.73	0.0008	22.21	3.4 ± 1.3
Ap24B031	0.01	0.04	0.01	0.03	23	55	0.0013	22.10	0.1486	81.37	1524.04	347.58	0.0007	22.81	3.7 ± 1.1
Ap24B034	0.00	0.09	0.05	0.11	29	64	0.0039	12.85	0.5070	68.47	704.86	101.45	0.0014	14.39	3.8 ± 4.1
Ap24B037	0.01	0.08	0.03	0.10	29	72	0.0033	19.63	0.3852	43.80	963.09	150.53	0.0010	15.63	3.8 ± 1.5
Ap24B035	0.00	0.15	0.02	0.10	202	224	0.0005	13.12	0.1425	39.82	1477.35	214.86	0.0007	14.54	3.8 ± 0.6
Ap24B039	0.00	0.06	0.01	0.01	29	86	0.0005	39.18	0.0952	170.69	1471.32	247.66	0.0007	16.83	4.1 ± 1.1

Table A1-1. ***(Contd.)***

Sample	^{204}Pb (ppm)	^{206}Pb (ppm)	^{207}Pb (ppm)	^{208}Pb (ppm)	^{232}Th (ppm)	^{238}U (ppm)	^{208}Pb/^{232}Th	± 1σ (%)	^{207}Pb/^{206}Pb	± 1σ (%)	^{238}U/^{206}Pb	± 1σ (%)	^{206}Pb/^{238}U	± 1σ (%)	^{206}Pb/^{238}U age (Ma)
Ap24B030	0.01	0.07	0.01	0.01	37	92	0.0004	48.45	0.1384	114.62	1343.30	223.86	0.0007	16.67	4.2 ± 1.2
Ap24B032	0.00	0.06	0.01	0.02	38	70	0.0006	29.99	0.1722	103.34	1205.95	228.30	0.0008	18.93	4.5 ± 1.5
Ap24B036	0.04	0.05	0.01	0.03	27	61	0.0011	23.00	0.1732	138.06	1154.84	200.50	0.0009	17.36	4.7 ± 1.9
Ap24B033	0.01	0.10	0.05	0.16	20	46	0.0078	9.33	0.5223	33.11	449.49	64.34	0.0022	14.31	5.7 ± 3.2
Ap24B038	0.00	0.08	0.03	0.06	23	42	0.0027	17.11	0.3493	98.16	516.64	132.84	0.0019	25.71	7.7 ± 5.8
Tumpangpitu diatreme															
Drillhole GTD-10-172; 12 m															
MA10D703	0.02	0.01	0.00	0.00	12.59	23.98	0.0004	35.47	0.2130	8.08	1913.29	349.23	0.0005	18.25	2.7 ± 0.5
MA10D693	0.01	0.03	0.01	0.01	24.39	45.35	0.0005	21.85	0.2140	67.33	1546.06	205.15	0.0006	13.27	3.3 ± 0.9
MA10D689	0.00	0.02	0.00	0.01	14.11	39.24	0.0005	28.13	0.0998	17.88	1671.31	221.18	0.0006	13.23	3.6 ± 0.5
MA10D709	0.00	0.03	0.00	0.00	15.00	41.16	0.0001	71.61	0.1677	18.47	1470.53	181.85	0.0007	12.37	3.7 ± 0.5
MA10D711	0.00	0.03	0.00	0.00	23.93	50.70	0.0001	77.13	0.1138	20.70	1531.89	194.89	0.0007	12.72	3.8 ± 0.5
MA10D710	0.00	0.02	0.00	0.00	19.50	38.74	0.0002	56.60	0.0836	15.68	1563.28	206.47	0.0006	13.21	3.9 ± 0.5
MA10D696	0.00	0.02	0.00	0.00	12.18	33.93	0.0002	83.92	0.1057	35.30	1517.01	206.54	0.0007	13.62	3.9 ± 0.6
MA10D712	0.00	0.03	0.00	0.01	23.42	48.27	0.0005	28.86	0.0613	151.60	1587.99	194.44	0.0006	12.24	4.0 ± 0.7
MA10D691	0.00	0.04	0.00	0.01	23.68	60.89	0.0004	26.47	0.1302	22.39	1443.95	151.85	0.0007	10.52	4.0 ± 0.5
MA10D705	0.00	0.02	0.00	0.00	15.66	36.66	0.0003	52.93	0.0887	30.79	1519.94	214.47	0.0007	14.11	4.0 ± 0.6
MA10D704	0.00	0.03	0.00	0.00	29.25	49.64	0.0002	50.35	0.0480	33.99	1595.73	199.61	0.0006	12.51	4.0 ± 0.5
MA10D690	0.00	0.11	0.02	0.04	147.08	151.13	0.0003	10.50	0.1554	14.19	1377.86	91.44	0.0007	6.64	4.0 ± 0.3
MA10D702	0.00	0.02	0.00	0.00	11.20	30.93	0.0000	2249.77	0.0462	76.47	1551.15	229.60	0.0006	14.80	4.2 ± 0.6
MA10D694	0.00	0.06	0.00	0.02	53.15	91.95	0.0004	16.78	0.0720	33.92	1479.32	113.24	0.0007	7.66	4.2 ± 0.3
MA10D688	0.00	0.04	0.01	0.03	83.16	59.87	0.0004	13.63	0.1240	22.95	1350.41	128.64	0.0007	9.53	4.3 ± 0.4
MA10D697	0.01	0.03	0.00	0.00	16.76	40.97	0.0002	40.16	0.0854	32.19	1401.12	160.80	0.0007	11.48	4.4 ± 0.5
MA10D695	0.01	0.06	0.00	0.01	52.33	94.35	0.0002	17.40	0.0411	99.95	1457.13	124.63	0.0007	8.55	4.4 ± 0.4
MA10D707	0.01	0.12	0.03	0.09	84.31	131.29	0.0012	8.20	0.2345	12.09	1103.81	78.04	0.0009	7.07	4.4 ± 0.4
MA10D708	0.01	0.04	0.01	0.03	23.29	44.46	0.0015	12.33	0.2859	67.12	989.36	91.63	0.0010	9.26	4.5 ± 1.6
MA10D701	0.00	0.02	0.00	0.00	13.30	32.93	0.0001	116.10	0.0487	84.57	1365.24	170.37	0.0007	12.48	4.7 ± 0.6
MA10D692	0.00	0.04	0.00	0.01	20.78	52.50	0.0003	30.85	0.0459	44.46	1360.98	140.15	0.0007	10.30	4.7 ± 0.5
MA10D706	0.00	0.04	0.00	0.01	21.06	50.18	0.0004	26.86	0.0619	277.39	1287.91	130.51	0.0008	10.13	4.9 ± 1.2

213 nm laser @ 5 Hz, 60 % power, 2J/cm^2, 32 µm spot size. Absolute element concentration assumed stoichiometric zirconium in the zircons. The standard NIST 610 was used to calculate mass bias and drift. Analyses excluded from the age calculation are shown in grey.

APPENDIX 2: ELECTRON MICROPROBE DATA

Compositional mineral analyses were acquired on an electron microprobe (Cameca SX100 (TCP/IP Socket) equipped with 5 tunable wavelength dispersive spectrometers at the Central Science Laboratory, University of Tasmania

Table A2-1: Sulfides

Sample ID	Hole ID	Depth (m)	Figure	Point	S (wt %)	Ag (wt %)	Cu (wt %)	Zn (wt %)	Sb (wt %)	As (wt %)	Fe (wt %)	Se (wt %)	Te (wt %)	Pb (wt %)	Sn (wt %)	V (wt %)	Mn (wt %)	Total (wt %)	Mineral
43005.13 GTD-09-112/185.75m 1	GTD-09-112	186	A2-1A	1	33.22	0.04	48.60	0.00	0.22	18.17	0.51	0.00	0.00	0.06	0.05	0.00	0.00	100.86	Enargite
43005.13 GTD-09-112/185.75m 2	GTD-09-112	186	A2-1A	2	28.69	0.09	45.66	0.00	0.28	19.69	5.93	0.00	0.04	0.14	0.07	0.00	0.02	100.59	Tennantite
43005.13 GTD-09-112/185.75m 3	GTD-09-112	186	A2-1B	3	32.85	0.04	48.53	0.01	0.25	18.33	0.23	0.00	0.01	0.08	0.10	0.04	0.02	100.50	Enargite
43005.13 GTD-09-112/185.75m 4 Sn,V	GTD-09-112	186	A2-1B	4	31.82	0.03	49.54	0.10	1.03	8.76	0.33	0.07	0.13	0.00	5.70	3.22	0.00	100.73	Colusite
43005.13 GTD-09-112/185.75m 5 Sn,V	GTD-09-112	186	A2-1B	5	31.53	0.05	49.88	0.13	0.72	8.79	0.55	0.05	0.41	0.03	6.12	3.14	0.00	101.39	Colusite
43005.13 GTD-09-112/185.75m 6	GTD-09-112	186	A2-1A	6	28.81	0.11	45.71	0.00	0.25	19.49	5.81	0.00	0.04	0.10	0.09	0.00	0.00	100.42	Tennantite
43005.13 GTD-09-112/185.75m 7	GTD-09-112	186	A2-1C	7	32.81	0.09	48.70	0.00	0.32	17.79	0.42	0.00	0.05	0.03	0.08	0.01	0.02	100.33	Enargite
43005.13 GTD-09-112/185.75m 8	GTD-09-112	186	A2-1D	8	25.45	0.42	73.28	0.00	0.04	0.09	0.53	0.03	0.11	0.04	0.08	0.01	0.00	100.08	Chalcocite (Spionkopite)
43005.13 GTD-09-112/185.75m 9	GTD-09-112	186	A2-1E	9	28.88	0.50	69.30	0.00	0.07	0.12	0.59	0.08	0.00	0.05	0.12	0.01	0.01	99.73	Chalcocite (Yarrowite)
43005.13 GTD-09-112/185.75m 10	GTD-09-112	186	A2-1E	10	28.88	0.06	45.84	0.04	0.29	19.79	5.67	0.04	0.05	0.08	0.08	0.01	0.00	100.82	Tennantite
43005.13 GTD-09-112/185.75m 11	GTD-09-112	186	A2-1E	11	33.09	0.07	48.63	0.21	0.45	17.93	0.34	0.00	0.22	0.03	0.38	0.01	0.00	101.37	Enargite
43005.13 GTD-09-112/185.75m 12	GTD-09-112	186	A2-1F	12	24.99	0.25	75.42	0.00	0.05	0.07	0.23	0.01	0.05	0.02	0.02	0.00	0.00	101.10	Chalcocite (Geerite)
43005.13 GTD-09-112/185.75m 13	GTD-09-112	186	A2-1G	13	28.64	0.77	68.68	0.00	0.03	0.10	2.27	0.06	0.01	0.00	0.01	0.00	0.00	100.58	Chalcocite (Spionkopite)
43005.13 GTD-09-112/185.75m 14	GTD-09-112	186	A2-1H	14	31.65	0.02	48.94	0.04	0.41	10.38	0.54	0.02	0.07	0.00	4.57	3.03	0.00	99.66	Colusite
43005.13 GTD-09-112/185.75m 15	GTD-09-112	186	A2-1H	15	32.75	0.09	48.48	0.13	0.45	10.90	0.42	0.06	0.33	0.00	3.06	3.14	0.01	99.81	Colusite

Table A2-1: Sulfides *(Contd.)*

Sample ID	Hole ID	Depth (m)	Figure	Point	S (wt %)	Ag (wt %)	Cu (wt %)	Zn (wt %)	Sb (wt %)	As (wt %)	Fe (wt %)	Se (wt %)	Te (wt %)	Pb (wt %)	Sn (wt %)	V (wt %)	Mn (wt %)	Total (wt %)	Mineral
43005.13 GTD-09-112/185.75m 16	GTD-09-112	186	A2-1H	16	32.03	0.06	49.05	0.00	0.59	11.59	1.33	0.05	0.62	0.04	2.01	3.12	0.00	100.49	Colusite
43005.13 GTD-09-112/185.75m 17	GTD-09-112	186	A2-1H	17	28.62	0.12	44.78	0.05	0.13	19.93	6.38	0.08	0.02	0.00	0.11	0.01	0.01	100.24	Tennantite
43005.42d GTD-10-137/829.7m 1	GTD-10-137	830	A2-2A	1	22.18	0.06	72.67	0.00	0.03	0.00	3.09	0.05	0.04	0.06	0.04	0.00	0.00	98.21	Chalcocite
43005.42d GTD-10-137/829.7m 2	GTD-10-137	830	A2-2A	2	23.06	0.07	68.96	0.00	0.04	0.64	4.11	0.07	0.00	0.02	0.28	0.16	0.01	97.41	Chalcocite
43005.42d GTD-10-137/829.7m 3	GTD-10-137	830	A2-2B	3	23.97	0.03	69.23	0.00	0.00	0.01	6.07	0.07	0.06	0.00	0.03	0.00	0.00	99.45	Chalcocite
43005.42d GTD-10-137/829.7m 4	GTD-10-137	830	A2-2B	4	25.66	0.01	62.71	0.00	0.01	0.00	10.11	0.03	0.05	0.00	0.03	0.00	0.01	98.63	Bornite
43005.42d GTD-10-137/829.7m 5	GTD-10-137	830	A2-2C	5	24.67	0.08	65.79	0.00	0.03	0.00	8.87	0.09	0.03	0.04	0.05	0.00	0.00	99.64	Chalcocite
43005.42d GTD-10-137/829.7m 6	GTD-10-137	830	A2-2C	6	23.70	0.07	70.55	0.00	0.01	0.02	6.01	0.04	0.04	0.03	0.04	0.01	0.01	100.52	Chalcocite
43005.42d GTD-10-137/829.7m 7	GTD-10-137	830	A2-2C	7	23.63	0.03	70.40	0.00	0.00	0.00	6.15	0.07	0.04	0.02	0.01	0.00	0.00	100.35	Chalcocite
43005.42d GTD-10-137/829.7m 8	GTD-10-137	830	A2-2D	8	22.47	0.05	75.00	0.00	0.02	0.00	2.03	0.06	0.04	0.02	0.03	0.00	0.00	99.72	Chalcocite
43005.42d GTD-10-137/829.7m 9	GTD-10-137	830	A2-2D	9	21.46	0.03	76.79	0.00	0.01	0.00	0.84	0.08	0.04	0.00	0.03	0.00	0.01	99.30	Chalcocite (Anilite)
43005.42d GTD-10-137/829.7m 10 w/Te,Sb	GTD-10-137	830	A2-2D	10	26.14	0.03	47.34	0.00	6.59	4.26	0.59	0.03	14.39	0.00	0.05	0.00	0.00	99.42	Telluride
43005.42d GTD-10-137/829.7m 11	GTD-10-137	830	A2-2E	11	24.27	0.06	66.95	0.00	0.02	0.03	7.69	0.04	0.03	0.05	0.03	0.00	0.00	99.18	Covellite
43005.42d GTD-10-137/829.7m 12 w/As	GTD-10-137	830	A2-2E	12	32.52	0.04	46.47	0.00	0.01	18.23	1.06	0.05	0.01	0.06	0.02	0.00	0.00	98.47	Enargite
7_GTD-12-292_513m P1 1	GTD-12-292	513	A2-4A	1	31.03	0.04	66.08	0.06	0.06	0.02	3.27	0.10	0.02	0.03	0.03	0.01	0.00	100.61	Covellite
7_GTD-12-292_513m P1 2	GTD-12-292	513	A2-4A	2	34.42	0.07	36.13	0.02	0.01	0.00	28.19	0.04	0.03	0.03	0.02	0.01	0.01	98.94	Chalcopyrite
7_GTD-12-292_513m P1 3	GTD-12-292	513	A2-4A	3	31.63	0.10	54.34	0.04	0.01	0.01	13.32	0.05	0.01	0.13	0.02	0.01	0.01	99.55	Bornite-chalcopyrite
7_GTD-12-292_513m P1 4	GTD-12-292	513	A2-4A	4	31.48	0.07	53.38	0.00	0.05	0.01	14.07	0.07	0.04	0.03	0.04	0.02	0.00	99.21	Bornite-chalcopyrite

Table A2-1: Sulfides *(Contd.)*

Sample ID	Hole ID	Depth (m)	Figure	Point	S (wt %)	Ag (wt %)	Cu (wt %)	Zn (wt %)	Sb (wt %)	As (wt %)	Fe (wt %)	Se (wt %)	Te (wt %)	Pb (wt %)	Sn (wt %)	V (wt %)	Mn (wt %)	Total (wt %)	Mineral
7_GTD-12-292_513m P2 1	GTD-12-292	513	5.30B;A2-4B	1	32.84	0.04	66.34	0.08	0.01	0.01	0.71	0.11	0.04	0.01	0.01	0.01	0.01	100.01	Covellite
7_GTD-12-292_513m P2 2	GTD-12-292	513	5.30B;A2-4B	2	32.73	0.09	48.23	0.02	0.02	17.32	1.18	0.06	0.02	0.03	0.00	0.00	0.03	99.62	Enargite
7_GTD-12-292_513m P2 3	GTD-12-292	513	5.30B;A2-4B	3	32.82	0.07	65.84	0.02	0.02	0.03	1.40	0.00	0.01	0.01	0.03	0.00	0.02	100.19	Covellite
7_GTD-12-292_513m P2 4	GTD-12-292	513	5.30B;A2-4B	4	33.51	0.01	58.57	0.05	0.00	0.00	7.11	0.07	0.04	0.03	0.04	0.01	0.01	99.25	Bornite
7_GTD-12-292_513m P2 5	GTD-12-292	513	5.30B;A2-4B	5	32.40	0.04	44.41	-0.01	0.02	0.03	20.81	0.00	0.03	0.03	0.05	0.01	0.02	97.73	Chalcopyrite-bornite
7_GTD-12-292_513m P2 6	GTD-12-292	513	5.30B;A2-4B	6	32.04	0.03	46.38	0.05	0.05	17.36	0.60	0.05	0.02	0.03	0.07	0.01	0.00	96.60	Enargite
7_GTD-12-292_513m P2 7	GTD-12-292	513	5.30B;A2-4B	7	34.67	0.01	45.31	0.06	0.03	16.60	4.57	0.03	0.03	0.02	0.05	0.02	0.01	101.24	Enargite
7_GTD-12-292_513m P3 1	GTD-12-292	513	A2-4D	1	30.30	0.01	60.57	0.02	0.01	0.18	4.93	0.10	0.06	0.03	0.11	0.07	0.00	96.37	Bornite
7_GTD-12-292_513m P3 2	GTD-12-292	513	A2-4D	2	30.43	0.10	45.50	3.47	0.03	18.63	1.76	0.00	0.03	0.04	0.07	0.06	0.00	100.05	Tennantite
7_GTD-12-292_513m P3 3	GTD-12-292	513	A2-4D	3	34.98	-0.04	35.10	0.03	0.02	0.00	28.00	0.05	0.01	0.08	0.04	0.00	0.01	98.26	Chalcopyrite
7_GTD-12-292_513m P3 4	GTD-12-292	513	A2-4D	4	33.55	0.02	43.62	0.05	0.02	0.03	21.18	0.07	0.05	0.05	0.02	0.01	0.00	98.47	Chalcopyrite
7_GTD-12-292_513m P3 5	GTD-12-292	513	A2-4D	5	31.52	0.04	48.65	9.13	0.03	0.04	11.42	0.08	0.01	0.16	0.07	0.00	0.01	101.14	Chalcopyrite-tenantite
7_GTD-12-292_513m P3 6	GTD-12-292	513	A2-4D	6	32.02	0.01	47.09	0.02	0.01	18.20	0.57	0.02	0.02	0.00	0.04	0.02	0.01	97.93	Enargite
7_GTD-12-292_513m P3 7	GTD-12-292	513	A2-4D	7	33.34	0.05	46.91	0.04	0.02	16.06	3.16	0.06	0.05	0.12	0.41	0.65	0.00	100.75	Enargite
7_GTD-12-292_513m P3 8	GTD-12-292	513	A2-4E	8	32.95	0.07	47.94	0.03	0.01	17.84	1.10	0.06	0.05	0.02	0.04	0.00	0.00	100.05	Enargite
7_GTD-12-292_513m P3 9	GTD-12-292	513	A2-4E	9	33.02	0.15	47.79	0.04	0.07	17.76	0.75	0.03	0.00	0.01	0.07	0.01	0.01	99.58	Enargite
7_GTD-12-292_513m P4 1	GTD-12-292	513	5.30C	1	32.05	0.07	47.11	0.03	0.01	17.06	1.35	0.04	0.05	0.01	0.14	0.12	0.00	97.88	Enargite
7_GTD-12-292_513m P4 2	GTD-12-292	513	5.30C	2	32.07	0.03	47.06	0.01	0.01	17.82	1.34	0.07	0.05	0.01	0.01	0.02	0.00	98.36	Enargite

Table A2-1: Sulfides *(Contd.)*

Sample ID	Hole ID	Depth (m)	Figure	Point	S (wt %)	Ag (wt %)	Cu (wt %)	Zn (wt %)	Sb (wt %)	As (wt %)	Fe (wt %)	Se (wt %)	Te (wt %)	Pb (wt %)	Sn (wt %)	V (wt %)	Mn (wt %)	Total (wt %)	Mineral
7_GTD-12-292_513m P4 3	GTD-12-292	513	5.30C	3	32.99	0.08	42.93	-0.02	0.04	0.04	21.35	0.08	0.01	0.02	0.01	0.01	0.00	97.51	Chalcopyrite-bornite
7_GTD-12-292_513m P4 4	GTD-12-292	513	5.30C	4	30.95	0.02	61.13	0.02	0.00	0.10	2.45	0.03	0.03	0.01	0.09	0.02	0.02	94.80	Covellite
7_GTD-12-292_513m P4 5	GTD-12-292	513	5.30C	5	31.89	0.04	50.00	0.03	0.04	10.42	0.89	0.06	0.02	0.03	4.58	2.73	0.00	100.66	Colusite
7_GTD-12-292_513m P4 6	GTD-12-292	513	5.30C	6	31.98	0.05	49.93	-0.01	0.10	10.07	0.95	0.01	0.00	0.04	5.04	2.94	0.00	101.05	Colusite
7_GTD-12-292_513m P4 7	GTD-12-292	513	5.30C	7	32.28	0.02	48.25	-0.02	0.10	12.50	0.50	0.01	0.10	0.03	0.28	3.13	0.00	97.16	Colusite?
7_GTD-12-292_513m P4 8	GTD-12-292	513	5.30C	8	32.32	0.07	44.62	0.06	0.04	17.05	3.08	0.03	0.03	0.01	0.05	0.04	0.01	97.26	Enargite
7_GTD-12-292_513m P4 9	GTD-12-292	513	5.30C	9	32.31	0.06	46.84	0.20	0.01	16.69	2.44	0.00	0.02	0.07	0.04	0.03	0.01	98.70	Enargite-tenantite
7_GTD-12-292_513m P4 10	GTD-12-292	513	5.30C	10	33.37	0.09	46.11	0.03	0.02	16.26	2.93	0.00	0.07	0.09	0.03	0.01	0.00	98.99	Enargite
7_GTD-12-292_513m P4 11	GTD-12-292	513	5.30C	11	28.87	0.06	42.75	7.12	0.05	19.05	1.00	0.01	0.02	0.12	0.02	0.00	0.00	99.07	Tennantite
7_GTD-12-292_513m P5	GTD-12-292	513	A2-4G	1	31.66	0.03	54.83	0.00	0.02	0.03	12.45	0.08	0.02	0.09	0.08	0.00	0.01	99.24	Bornite
7_GTD-12-292_513m P5	GTD-12-292	513	A2-4G	2	30.74	0.08	60.83	0.03	0.01	0.04	2.15	0.07	0.01	0.03	0.04	0.02	0.01	93.96	Covellite
7_GTD-12-292_513m P5	GTD-12-292	513	A2-4G	3	32.32	0.02	40.76	0.18	0.00	0.02	20.85	0.13	0.01	0.13	0.06	0.03	0.03	94.50	Chalcopyrite
7_GTD-12-292_513m P6 1	GTD-12-292	513	A2-4H	1	34.26	0.00	35.95	0.01	0.02	-0.02	28.01	0.05	0.08	0.05	0.04	0.00	0.00	98.43	Chalcopyrite
7_GTD-12-292_513m P6 2	GTD-12-292	513	A2-4H	2	34.65	0.04	34.80	0.02	0.02	0.03	29.40	0.06	0.07	0.02	0.03	0.01	0.02	99.09	Chalcopyrite
7_GTD-12-292_513m P6 3	GTD-12-292	513	A2-4H	3	34.81	0.02	33.73	0.03	0.01	0.00	30.12	0.06	0.05	0.05	0.03	0.00	0.01	98.84	Chalcopyrite
11_GTD-12-334_177.4m P2 1	GTD-11-201	177	5.31B	1	28.87	0.08	69.32	0.05	0.01	0.03	1.35	0.05	0.05	0.02	0.07	0.01	0.00	99.74	Chalcocite (Yarrowite)
11_GTD-12-334_177.4m P2 2	GTD-11-201	177	5.31B	2	28.69	0.08	69.71	0.04	0.05	0.02	1.62	0.11	0.06	0.04	0.11	0.02	0.01	100.41	Chalcocite (Yarrowite)
11_GTD-12-334_177.4m P2 3	GTD-11-201	177	5.31B	3	29.59	0.03	68.08	0.07	0.01	0.03	2.24	0.05	0.07	0.01	0.09	0.01	0.01	100.07	Chalcocite-bornite

Table A2-1: Sulfides *(Contd.)*

Sample ID	Hole ID	Depth (m)	Figure	Point	S (wt %)	Ag (wt %)	Cu (wt %)	Zn (wt %)	Sb (wt %)	As (wt %)	Fe (wt %)	Se (wt %)	Te (wt %)	Pb (wt %)	Sn (wt %)	V (wt %)	Mn (wt %)	Total (wt %)	Mineral
11_GTD-12-334_177.4m P4 1	GTD-11-201	177	5.31D	1	28.99	0.06	69.14	0.03	0.04	0.01	2.84	0.07	0.02	0.06	0.03	0.00	0.01	101.22	Chalcocite (Yarrowite)
11_GTD-12-334_177.4m P4 2	GTD-11-201	177	5.31D	2	28.91	0.02	67.47	0.05	0.04	0.01	3.77	0.05	0.05	0.00	0.01	0.00	0.01	100.28	Chalcocite (Yarrowite)
11_GTD-12-334_177.4m	GTD-11-201	177	5.31C	1	0.06	0.08	99.85	0.04	0.03	0.03	0.21	0.04	0.00	0.10	0.08	0.00	0.00	100.44	native copper
11_GTD-12-334_177.4m	GTD-11-201	177	5.31C	2	0.08	0.16	99.33	0.07	0.01	0.00	0.18	0.09	0.05	0.05	0.07	0.02	0.00	99.84	native copper
3_GTD-11-201_537.5m P1 1	GTD-11-201	538	5.27 D-E;A2-3B	1	33.24	0.01	66.14	0.04	0.01	0.01	0.05	0.08	0.04	0.00	0.09	0.00	0.01	99.61	Covellite
3_GTD-11-201_537.5m P1 2	GTD-11-201	538	5.27 D-E;A2-3B	2	31.52	0.03	55.06	0.03	0.00	0.00	12.61	0.05	0.02	0.02	0.03	0.01	0.00	99.26	Bornite-chalcopyrite
3_GTD-11-201_537.5m P1 3	GTD-11-201	538	5.27 D-E;A2-3B	3	33.19	0.04	66.29	0.09	0.03	0.01	0.05	0.14	0.04	0.00	0.03	0.01	0.00	99.66	Covellite
3_GTD-11-201_537.5m P1 4	GTD-11-201	538	5.27 D-E;A2-3B	4	34.07	0.01	66.11	0.07	0.00	0.01	0.10	0.07	0.05	0.08	0.05	0.00	0.01	100.33	Covellite
3_GTD-11-201_537.5m P3 2	GTD-11-201	538	5.27G	2	33.52	0.06	66.23	0.03	0.06	0.04	0.03	0.06	0.07	0.07	0.05	0.00	0.00	99.96	Covellite
3_GTD-11-201_537.5m P3 3	GTD-11-201	538	5.27G	3	33.23	0.07	66.57	0.08	0.04	0.01	0.08	0.09	0.06	0.04	0.00	0.01	0.01	100.03	Covellite
3_GTD-11-201_537.5m P3 5	GTD-11-201	538	5.27G	5	33.47	0.02	66.21	0.07	0.01	0.01	0.04	0.09	0.03	0.03	0.07	0.01	0.01	99.88	Covellite
3_GTD-11-201_537.5m P3 7	GTD-11-201	538	5.27G	7	33.36	0.06	65.93	0.03	0.02	0.01	0.02	0.07	0.01	0.04	0.05	0.01	0.00	99.42	Covellite
3_GTD-11-201_537.5m P2 3	GTD-11-201	538	5.27G	3	33.47	0.02	66.19	0.02	0.01	0.02	0.01	0.04	0.00	0.02	0.00	0.01	0.00	99.68	Covellite
3_GTD-11-201_537.5m P2 4	GTD-11-201	538	5.27G	4	33.30	0.02	66.28	0.05	0.02	0.00	0.00	0.02	0.04	0.03	0.03	0.01	0.01	99.59	Covellite
3_GTD-11-201_537.5m P3 1	GTD-11-201	538	5.27G	1	33.16	0.07	66.30	0.07	0.04	0.03	0.03	0.09	0.02	0.03	0.04	0.01	0.00	99.74	Covellite
3_GTD-11-201_537.5m P3 4	GTD-11-201	538	5.27G	4	33.22	0.06	65.85	0.07	0.03	0.01	0.02	0.07	0.02	0.00	0.05	0.00	0.00	99.26	Covellite
3_GTD-11-201_537.5m P3 6	GTD-11-201	538	5.27G	6	32.97	0.00	66.19	0.03	0.00	0.02	0.03	0.13	0.05	-0.04	0.02	0.00	0.00	99.34	Covellite
3_GTD-11-201_537.5m P2 1	GTD-11-201	538	5.27C	1	33.48	0.03	65.88	0.09	0.05	-0.02	0.01	0.08	0.01	-0.04	0.06	0.00	0.00	99.45	Covellite

Table A2-1: Sulfides *(Contd.)*

Sample ID	Hole ID	Depth (m)	Figure	Point	S (wt %)	Ag (wt %)	Cu (wt %)	Zn (wt %)	Sb (wt %)	As (wt %)	Fe (wt %)	Se (wt %)	Te (wt %)	Pb (wt %)	Sn (wt %)	V (wt %)	Mn (wt %)	Total (wt %)	Mineral
3_GTD-11-201_537.5m P2 2	GTD-11-201	538	5.27C	2	33.68	0.04	65.68	0.07	0.03	0.01	0.00	0.07	0.04	0.05	0.04	0.01	0.01	99.45	Covellite
3_GTD-11-201_537.5m P4 16	GTD-11-201	538	5.27H-I;A2-3A	16	31.28	0.07	49.67	0.08	0.02	7.11	0.44	0.01	0.02	0.01	9.62	2.70	0.01	100.98	Nekrasovite
3_GTD-11-201_537.5m P4 15	GTD-11-201	538	5.27H-I;A2-3A	15	31.88	-0.03	48.49	0.09	0.03	6.06	0.54	0.02	0.04	0.06	10.53	2.82	0.01	100.53	Nekrasovite
3_GTD-11-201_537.5m P4 14	GTD-11-201	538	5.27H-I;A2-3A	14	31.52	0.01	48.95	0.05	0.00	6.83	0.90	0.09	0.00	0.04	10.79	2.56	0.01	101.55	Nekrasovite
3_GTD-11-201_537.5m P4 13	GTD-11-201	538	5.27H-I;A2-3A	13	31.33	0.04	49.06	0.03	0.04	5.99	1.05	0.03	0.04	0.04	10.34	2.40	0.01	100.32	Nekrasovite
3_GTD-11-201_537.5m P4 6	GTD-11-201	538	5.27H-I;A2-3A	6	30.33	0.01	45.83	0.34	0.07	1.60	1.34	0.03	0.06	0.05	18.63	2.80	0.01	100.85	Nekrasovite
3_GTD-11-201_537.5m P4 7	GTD-11-201	538	5.27H-I;A2-3A	7	30.45	0.03	46.88	0.18	0.02	4.44	0.83	0.01	0.02	0.02	13.50	2.88	0.00	99.25	Nekrasovite
3_GTD-11-201_537.5m P4 8	GTD-11-201	538	5.27H-I;A2-3A	8	31.39	0.01	48.57	-0.02	0.01	8.52	0.21	0.01	0.02	0.11	8.22	2.99	0.00	100.01	Nekrasovite
3_GTD-11-201_537.5m P4 12	GTD-11-201	538	5.27H-I;A2-3A	12	30.83	0.05	48.97	0.48	0.05	2.54	1.46	0.05	0.03	0.02	12.16	2.12	0.00	98.64	Nekrasovite
3_GTD-11-201_537.5m P4 9	GTD-11-201	538	5.27H-I;A2-3A	9	30.36	0.03	47.97	0.03	0.03	7.39	0.33	0.00	0.04	0.02	9.80	3.05	0.01	99.00	Nekrasovite
3_GTD-11-201_537.5m P4 10	GTD-11-201	538	5.27H-I;A2-3A	10	30.98	0.06	48.27	0.07	0.03	7.53	0.41	0.01	0.00	0.03	10.50	2.91	0.01	100.78	Nekrasovite
3_GTD-11-201_537.5m P4 11	GTD-11-201	538	5.27H-I;A2-3A	11	31.18	0.05	47.50	0.07	0.02	7.57	0.58	0.00	0.02	0.06	10.25	2.83	0.00	100.00	Nekrasovite
3_GTD-11-201_537.5m P4 5	GTD-11-201	538	5.27H-I;A2-3A	5	29.73	0.05	45.27	0.90	0.05	2.47	1.41	0.08	0.01	0.02	16.61	2.74	0.01	99.25	Nekrasovite
3_GTD-11-201_537.5m P4 4	GTD-11-201	538	A2-5B	4	33.58	0.06	52.68	0.08	0.01	0.01	12.80	0.09	0.01	0.10	0.05	0.01	0.01	99.27	Bornite
3_GTD-11-201_537.5m P4 3	GTD-11-201	538	A2-5B	3	32.80	0.03	52.37	0.07	0.02	0.01	13.15	0.04	0.01	0.08	0.00	0.01	0.00	98.43	Bornite
3_GTD-11-201_537.5m P4 2	GTD-11-201	538	A2-5B	2	33.58	0.01	50.93	0.03	0.00	0.01	14.01	0.03	0.04	-0.02	0.01	0.00	0.00	98.54	Bornite
3_GTD-11-201_537.5m P4 1	GTD-11-201	538	A2-5B	1	33.76	0.07	51.56	0.00	0.02	0.01	13.87	0.05	0.02	-0.03	0.03	0.00	0.00	99.36	Bornite
43003.20 1	GTD-08-35	634	A2-6A	1	32.82	0.02	49.01	-0.03	0.22	18.15	0.22	-0.01	0.14	0.07	0.09	0.01	0.00	100.69	Enargite

Table A2-1: Sulfides *(Contd.)*

Sample ID	Hole ID	Depth (m)	Figure	Point	S (wt %)	Ag (wt %)	Cu (wt %)	Zn (wt %)	Sb (wt %)	As (wt %)	Fe (wt %)	Se (wt %)	Te (wt %)	Pb (wt %)	Sn (wt %)	V (wt %)	Mn (wt %)	Total (wt %)	Mineral
43003.20 2	GTD-08-35	634	A2-6A	2	33.42	0.02	49.11	0.02	0.18	18.02	0.02	0.01	0.04	0.00	0.12	0.02	0.01	100.89	Enargite
43003.20 3	GTD-08-35	634	A2-6A	3	32.92	0.01	49.08	0.03	0.33	17.72	0.04	0.01	0.06	0.02	0.20	0.01	0.00	100.41	Enargite
43003.20 4	GTD-08-35	634	A2-6A	4	32.85	0.03	49.35	0.02	0.16	17.97	0.03	0.02	0.22	0.01	0.10	0.02	0.03	100.64	Enargite
43005.4	GTD-09-78	53	A2-6B	1	32.80	0.07	49.08	0.03	0.78	17.40	0.01	0.14	0.04	0.06	0.53	0.02	0.01	100.72	Enargite
43005.4	GTD-09-78	53	A2-6B	2	32.54	0.02	49.09	0.04	0.65	17.58	0.00	0.19	0.02	0.10	0.41	0.00	0.01	100.38	Enargite
43005.4	GTD-09-78	53	A2-6B	3	32.96	-0.02	49.06	0.05	0.60	17.44	0.01	0.02	0.06	0.02	0.53	0.02	0.00	100.60	Enargite
43001.20 p2 1	GT011	201	A2-6E	1	32.68	0.01	0.66	66.30	-0.02	0.00	0.03	0.01	0.01	0.01	0.04	0.01	0.00	99.68	Sphalerite
43001.20 p2 2	GT011	201	A2-6E	2	32.94	0.00	1.32	65.70	0.01	0.03	0.12	0.05	0.03	-0.07	0.01	0.01	0.01	100.18	Sphalerite
43001.20 p2 3	GT011	201	A2-6E	3	23.21	0.10	77.06	0.19	0.01	0.02	0.01	0.05	0.01	0.06	0.02	0.00	0.02	100.73	Chalcocite (Anilite)
43001.20 p2 4	GT011	201	A2-6E	4	23.69	0.08	77.58	0.23	0.02	0.03	0.00	0.03	0.01	0.01	0.00	0.01	0.01	101.62	Chalcocite (Anilite)
43001.20 p2 5	GT011	201	A2-6E	5	23.00	0.09	76.89	0.02	0.00	-0.02	0.18	0.01	0.02	0.03	0.04	0.01	0.01	100.22	Chalcocite (Anilite)
43001.20 p2 6	GT011	201	A2-6E	6	31.96	0.02	6.13	60.55	0.01	0.00	0.29	0.09	0.03	0.06	0.02	0.01	0.01	99.16	Sphalerite
43001.20 p2 7	GT011	201	A2-6E	7	32.90	0.04	0.10	66.69	0.04	0.00	0.05	0.03	0.06	0.04	0.00	0.00	0.03	99.90	Sphalerite
43001.20 p1 1	GT011	201	A2-6C-D	1	22.62	0.02	78.04	0.07	0.01	-0.01	0.01	0.07	0.04	0.03	0.04	0.00	0.00	100.76	Chalcocite (digenite)
43001.20 p1 2	GT011	201	A2-6C-D	2	27.41	0.10	39.46	31.56	0.00	0.00	0.35	0.07	0.00	0.00	0.03	0.01	0.00	98.99	Chalcocite-sphalerite
43001.20 p1 3	GT011	201	A2-6C-D	3	41.65	0.16	24.28	0.01	0.01	0.01	31.50	0.07	0.02	0.01	0.02	0.01	0.00	97.71	Pyrite-chalcocite
43001.20 p1 4	GT011	201	A2-6C-D	4	40.04	0.13	25.74	0.02	0.02	0.00	29.88	0.01	0.04	0.04	0.04	0.00	0.00	95.84	Pyrite-chalcocite
43001.20 p1 5	GT011	201	A2-6C-D	5	21.41	0.09	75.79	0.21	0.02	-0.02	0.30	0.09	0.02	0.07	0.05	0.01	-0.02	97.88	Chalcocite (Geerite)
43001.20 p1 6	GT011	201	A2-6C-D	6	21.87	0.03	76.60	0.05	-0.01	-0.03	0.80	0.09	0.07	0.07	0.00	-0.01	0.01	99.54	Chalcocite (Geerite)

Table A2-1: Sulfides *(Contd.)*

Sample ID	Hole ID	Depth (m)	Figure	Point	S (wt %)	Ag (wt %)	Cu (wt %)	Zn (wt %)	Sb (wt %)	As (wt %)	Fe (wt %)	Se (wt %)	Te (wt %)	Pb (wt %)	Sn (wt %)	V (wt %)	Mn (wt %)	Total (wt %)	Mineral
43001.20 p2 4	GT011	201	A2-6E	4	34.64	0.03	35.46	-0.05	-0.01	0.02	28.16	0.03	-0.01	-0.01	0.03	0.00	0.00	98.28	Pyrite-chalcocite
43001.20 p2 5	GT011	201	A2-6E	5	52.10	0.03	1.14	0.02	0.02	0.01	45.36	0.05	0.03	0.04	0.05	0.01	0.01	98.83	Pyrite
43003.19 p2 1	GTD-08-35	622	A2-6F	1	33.07	0.05	65.14	0.05	0.02	0.00	0.06	0.06	0.02	0.01	0.02	0.01	0.01	98.38	Covellite
43003.19 p2 2	GTD-08-35	622	A2-6F	2	32.73	0.06	64.74	0.05	0.04	0.00	0.00	0.03	0.02	0.03	0.04	0.01	0.01	97.66	Covellite
43003.19 p2 3	GTD-08-35	622	A2-6F	3	33.29	0.01	64.53	0.03	0.02	0.01	0.03	0.09	0.05	-0.02	0.03	0.00	0.00	97.96	Covellite
43002.06 1	GT001B	158	A2-7B	1	31.72	0.10	33.94	0.29	0.09	1.97	26.42	0.05	0.04	0.06	0.04	0.01	0.00	94.73	Chalcopyrite
43002.06 3	GT001B	158	A2-7B	3	34.66	0.06	32.86	0.04	0.01	0.03	30.55	0.09	0.02	-0.05	0.04	0.00	0.02	98.28	Chalcopyrite
43002.06 6	GT001B	158	A2-7B	6	32.85	0.59	64.51	0.02	0.03	0.12	0.66	0.06	0.02	-0.03	0.02	0.02	-0.01	98.80	Covellite
43002.06 7	GT001B	158	A2-7B	7	26.24	0.73	54.88	0.05	0.11	0.15	0.26	0.06	0.07	-0.03	0.02	0.01	0.00	82.55	Covellite
43002.06 2	GT001B	158	A2-7B	2	28.90	0.06	42.40	7.98	0.13	18.84	0.78	0.04	0.10	0.71	0.03	0.01	-0.01	99.99	Tennantite
43002.06 4	GT001B	158	A2-7B	4	52.94	0.06	0.12	0.02	0.01	0.01	46.35	0.03	0.00	-0.07	0.01	-0.01	0.00	99.49	Pyrite
43002.06 5	GT001B	158	A2-7B	5	29.06	0.00	43.76	0.71	0.50	18.95	6.84	0.00	0.03	0.09	0.03	0.00	-0.02	99.96	Tennantite

Table A2-1: Alunite *(Contd.)*

Sample ID	Hole ID	Depth	Figure	Point	F (wt %)	Si (wt %)	Sr (wt %)	K (wt %)	Ca (wt %)	S (wt %)	P (wt %)	Na (wt %)	Al (wt %)	Fe (wt %)	Ba (wt %)	H (wt %)	O (wt %)	Total	Mineral
11 P1 1	GTD-11-201	177.4	A2-5B	1	0.01	0.02	0.16	6.95	0.00	14.98	0.06	1.28	19.45	0.14	0.02	1.47	53.40	97.86	K-Na-alunite
11 P1 2	GTD-11-201	177.4	A2-5B	2	0.15	0.00	0.07	2.86	0.48	15.31	0.02	3.38	20.69	0.24	0.05	1.49	55.23	99.98	Na-K-alunite
11 P4 1	GTD-11-201	177.4	A2-5D	1	0.02	0.01	0.18	5.23	0.07	15.16	0.07	1.88	20.09	0.22	0.08	1.48	54.29	98.77	K-Na-alunite
11 P4 3	GTD-11-201	177.4	A2-5D	3	0.32	0.01	0.17	6.39	0.02	14.65	0.01	1.48	19.75	0.19	0.05	1.47	53.06	97.51	K-Na-alunite
11 P4 5	GTD-11-201	177.4	A2-5A	5	0.01	0.00	0.14	6.69	0.04	14.94	0.00	1.35	19.55	0.06	0.10	1.47	53.36	97.70	K-Na-alunite
3 P2 1	GTD-11-201	537.5	5.27C;F	1	0.20	0.53	0.12	8.38	0.03	14.54	0.05	0.41	19.73	0.19	0.02	1.46	53.51	99.16	K-Na-alunite
3 P3 3	GTD-11-201	537.5	5.27G	3	0.05	0.08	0.28	6.59	0.13	14.70	0.27	1.19	20.03	0.01	0.44	1.47	53.82	99.07	K-Na-alunite
3 P3 4	GTD-11-201	537.5	5.27G	4	0.08	0.05	0.11	4.03	0.04	14.64	0.13	2.91	20.24	0.03	0.22	1.49	53.86	97.83	K-Na-alunite
43002	GT012	298	A2-7A	1		0.02	0.09	4.38	0.16	15.46	0.02	3.03	20.93	0.01	0.22	1.48	55.62	101.42	K-Na-alunite
43002	GT012	298	A2-7A	2		0.00	0.78	3.04	0.31	13.82	0.58	0.54	23.58	0.01	3.46	1.45	55.42	102.99	K-Na-alunite
43002	GT012	298	A2-7A	3		0.01	0.24	3.77	0.12	14.66	0.05	3.26	21.01	0.04	0.24	1.48	54.50	99.39	K-Na-alunite
43002	GT012	298	A2-7A	4		0.02	0.18	4.36	0.11	15.41	0.04	2.60	20.77	0.10	0.15	1.49	55.33	100.57	K-Na-alunite
43002	GT012	298	A2-7A	5		0.03	0.43	5.64	0.12	14.97	0.08	1.50	20.22	0.01	0.07	1.48	54.09	98.64	K-Na-alunite
43002	GT012	298	A2-7A	6		-0.01	0.55	4.74	0.26	14.53	0.13	1.61	20.38	-0.01	1.92	1.46	53.57	99.14	K-Na-alunite
43002	GT012	298	A2-7A	8		-0.01	0.42	5.95	0.17	14.71	0.34	1.36	20.52	0.07	0.82	1.46	54.27	100.08	K-Na-alunite
43003.19 P2 1	GTD-08-35	622.1	A2-7D	1		0.01	0.00	3.91	0.42	15.54	0.02	2.75	20.59	-0.03	0.12	1.49	55.40	100.23	K-Na-alunite
43003.19 P2 3	GTD-08-35	622.1	A2-7D	3		0.01	0.07	3.45	0.54	15.03	0.07	3.08	21.03	0.00	0.08	1.49	55.15	100.01	K-Na-alunite
43003.19 P2 4	GTD-08-35	622.1	A2-7D	4		0.06	0.04	4.15	0.37	15.14	0.02	2.62	22.53	-0.01	-0.14	1.48	56.48	102.76	K-Na-alunite
43003.19 P2 5	GTD-08-35	622.1	A2-7D	5		0.02	0.14	8.76	0.00	14.00	0.17	0.29	20.77	0.01	0.16	1.45	53.13	98.91	K-Na-alunite

Table A2-1: Alunite *(Contd.)*

Sample ID	Hole ID	Depth	Figure	Point	Si (wt %)	Sr (wt %)	K (wt %)	Ca (wt %)	S (wt %)	P (wt %)	Na (wt %)	Al (wt %)	Fe (wt %)	Ba (wt %)	H (wt %)	O (wt %)	Total	Mineral
43003.19 P3 1	GTD-08-35	622.1	A2-7E	1	0.02	0.04	2.95	0.32	14.78	0.05	3.59	20.83	0.01	0.08	1.50	54.59	98.58	Na-K-alunite
43003.19 P3 2	GTD-08-35	622.1	A2-7E	2	0.05	0.06	6.64	0.02	14.27	0.04	1.55	21.15	0.00	0.08	1.47	53.84	99.01	K-Na-alunite
43003.19 P3 3	GTD-08-35	622.1	A2-7E	3	0.04	0.01	2.37	0.50	15.19	0.01	3.92	21.43	0.03	0.10	1.50	55.75	100.57	Na-K-alunite
43003.19 P3 4	GTD-08-35	622.1	A2-7E	4	0.14	0.11	5.97	0.02	14.72	0.09	2.33	21.26	0.01	0.07	1.47	54.94	100.99	K-Na-alunite
43003.19 P3 5	GTD-08-35	622.1	A2-7E	5	0.07	0.06	6.88	0.01	14.94	0.08	0.95	21.19	0.02	0.08	1.47	54.83	100.54	K-Na-alunite
43003.19 P1 1	GTD-08-35	622.1	A2-7C	1	0.01	0.06	2.66	0.68	15.34	0.01	2.78	20.05	0.03	0.06	1.51	54.57	97.74	Na-K-alunite
43003.19 P1 2	GTD-08-35	622.1	A2-7C	2	0.03	0.12	2.90	0.60	15.55	0.02	2.87	20.13	0.00	0.04	1.50	55.03	98.78	K-Na-alunite
43003.19 P1 3	GTD-08-35	622.1	A2-7C	3	0.01	0.08	6.33	0.01	14.32	0.09	1.83	19.67	0.05	0.05	1.48	52.68	96.37	K-Na-alunite
43003.19 P1 4	GTD-08-35	622.1	A2-7C	4	0.13	0.05	5.17	0.20	15.09	0.04	2.07	19.88	0.02	0.04	1.49	54.12	98.07	K-Na-alunite
43003.19 P1 5	GTD-08-35	622.1	A2-7C	5	0.12	0.06	4.18	0.10	15.08	0.02	2.66	20.11	0.03	0.01	1.49	54.32	98.19	K-Na-alunite

Table A2-1: APS Minerals *(Contd.)*

Sample ID	Hole ID	Depth	Figure	Point	F (wt %)	Si (wt %)	Sr (wt %)	K (wt %)	Ca (wt %)	S (wt %)	P (wt %)	Na (wt %)	Al (wt %)	Fe (wt %)	Ba (wt %)	H (wt %)	O (wt %)	Total	Mineral
11 P1 7	GTD-11-201	177.4	A2-5B	7	0.11	0.04	0.85	0.13	7.89	8.20	6.51	0.50	19.39	0.06	0.31	1.45	53.08	98.52	APS-Woodhouseite
7 P6 4	GTD-12-292	513	A2-4H	4	0.07	0.49	5.17	0.43	3.12	10.25	4.37	0.26	14.17	5.09	1.11	1.40	49.20	95.14	APS-Svanbergite
43002	GT012	298	A2-7A	7	NA	0.07	6.97	0.60	3.61	8.11	6.03	0.45	18.82	0.07	0.66	1.41	50.84	97.49	APS-Svanbergite
43003.19 P2 2	GTD-08-35	622.1	A2-7D	2	NA	0.19	1.49	0.07	7.64	7.54	6.88	0.38	19.33	0.12	0.68	1.44	52.62	98.38	APS-Woodhouseite

Table A2-1: Kaolinite *(Contd.)*

Sample ID	Hole ID	Depth	Figure	Point	F (wt %)	Si (wt %)	Sr (wt %)	K (wt %)	Ca (wt %)	S (wt %)	P (wt %)	Na (wt %)	Al (wt %)	Fe (wt %)	Ba (wt %)	H (wt %)	O (wt %)	Total	Mineral
11 P1 3	GTD-11-201	177.4	A2-5B	3	0.26	20.46	0.00	0.01	0.00	0.04	0.02	0.01	20.63	0.07	0.07	1.56	54.14	97.27	Kaolinite
11 P1 4	GTD-11-201	177.4	A2-5B	4	0.25	20.42	0.00	0.05	0.01	0.08	0.03	0.02	20.75	0.01	0.04	1.56	54.26	97.44	Kaolinite
11 P1 5	GTD-11-201	177.4	A2-5B	5	0.22	19.48	0.06	0.23	0.01	0.81	0.02	0.11	20.89	0.12	0.01	1.56	54.48	97.95	Kaolinite
11 P1 6	GTD-11-201	177.4	A2-5B	6	-0.03	20.07	0.04	0.00	0.01	0.06	0.00	0.00	20.09	0.23	0.05	1.57	53.30	95.19	Kaolinite
11 P4 2	GTD-11-201	177.4	A2-5D	2	0.26	20.70	0.03	0.01	0.01	0.02	0.07	0.05	20.82	0.26	0.01	1.55	54.47	98.04	Kaolinite
11 P4 4	GTD-11-201	177.4	A2-5A	4	0.10	20.87	0.06	0.01	0.01	0.00	0.02	0.02	20.75	0.07	0.05	1.56	54.65	97.89	Kaolinite
7 P1 1	GTD-12-292	513	A2-4A	1	0.47	20.29	0.02	0.01	0.04	0.08	0.00	0.00	20.47	0.45	0.02	1.55	53.89	97.20	Kaolinite
7 P1 2	GTD-12-292	513	A2-4A	2	0.37	20.48	0.04	0.08	0.02	0.11	0.02	-0.01	20.51	0.35	0.02	1.55	54.17	97.56	Kaolinite
7 P1 4	GTD-12-292	513	A2-4A-A4	4	0.16	20.90	0.04	0.71	0.06	0.03	0.01	0.06	20.55	0.12	0.08	1.55	54.65	98.67	Kaolinite
7 P2 1	GTD-12-292	513	5.30B; A2-4B	1	0.17	19.22	0.04	0.04	0.03	0.01	0.04	0.05	21.30	0.75	0.01	1.55	53.44	96.55	Kaolinite
7 P2 2	GTD-12-292	513	5.30B; A2-4B	2	0.35	20.48	0.04	0.02	0.03	0.09	0.02	0.08	21.29	0.49	0.07	1.55	54.88	99.25	Kaolinite
7 P2 4	GTD-12-292	513	5.30B; A2-4I	4	0.62	20.35	0.03	0.02	0.01	0.27	0.04	0.01	20.72	0.49	0.06	1.55	54.48	98.57	Kaolinite
7 P2 5	GTD-12-292	513	5.30B; A2-4B	5	0.36	20.39	0.04	0.04	0.04	0.24	0.07	-0.01	21.22	0.13	0.02	1.55	54.93	99.03	Kaolinite
7 P2 6	GTD-12-292	513	5.30B; A2-4B	6	0.20	20.42	0.08	0.03	0.02	0.08	0.03	0.03	20.44	0.47	0.02	1.56	54.01	97.13	Kaolinite
7 P3 1	GTD-12-292	513	A2-4D	1	0.39	20.73	0.04	0.00	0.03	0.06	0.06	0.01	20.51	0.33	0.01	1.55	54.31	97.84	Kaolinite
7 P3 2	GTD-12-292	513	A2-4D	2	0.19	20.14	0.04	0.00	0.02	0.35	0.00	0.02	20.31	1.25	0.02	1.55	54.17	97.93	Kaolinite
7 P3 3	GTD-12-292	513	A2-4D	3	0.42	20.40	0.06	0.02	0.01	0.08	0.00	0.02	20.40	0.32	0.06	1.55	53.93	97.02	Kaolinite
7 P4 2	GTD-12-292	513	A2-4I	2	0.44	20.50	0.02	0.01	0.03	0.09	0.02	0.02	20.63	0.24	0.10	1.55	54.21	97.74	Kaolinite
7 P4 3	GTD-12-292	513	A2-4L	3	0.44	20.47	0.05	0.02	0.02	0.37	0.02	0.01	20.67	0.25	0.04	1.55	54.71	98.60	Kaolinite
7 P6 1	GTD-12-292	513	A2-4H	1	0.46	19.83	0.02	0.01	0.03	0.03	0.01	0.10	21.16	0.36	0.03	1.55	53.90	97.38	Kaolinite
7 P6 2	GTD-12-292	513	A2-4H	2	0.30	19.95	0.05	0.03	0.03	0.03	0.01	0.06	21.33	0.28	0.00	1.55	54.18	97.69	Kaolinite
7 P6 3	GTD-12-292	513	A2-4H	3	0.73	21.64	0.04	0.02	0.05	0.21	0.02	0.06	21.02	0.49	0.04	1.54	56.07	101.69	Kaolinite

Table A2-1: Alteration minerals *(Contd.)*

Sample ID	Hole ID	Depth	Figure	Point	F (wt %)	Si (wt %)	Sr (wt %)	K (wt %)	Ca (wt %)	S (wt %)	P (wt %)	Na (wt %)	Al (wt %)	Fe (wt %)	Ba (wt %)	H (wt %)	O (wt %)	Total	Mineral
3 P1 1 Al	GTD-11-201	537.5	5.27 D-E;A2-3B	1	0.08	0.01	0.06	0.03	0.02	0.02	0.01	0.02	44.19	0.11	0.04	1.68	52.67	98.50	Diaspore
3 P1 2 Al	GTD-11-201	537.5	5.27 D-E;A2-3B	2	0.03	0.08	0.03	0.01	0.04	0.02	0.08	0.00	44.77	0.00	0.05	1.68	53.37	99.84	Diaspore
3 P1 3 Al	GTD-11-201	537.5	5.27 D-E;A2-3B	3	0.03	0.04	0.01	0.00	0.02	0.01	0.01	0.00	44.84	0.04	0.01	1.68	53.29	99.87	Diaspore
3 P2 2	GTD-11-201	537.5	5.27C	2	0.02	27.76	0.07	0.12	0.01	0.05	0.02	0.22	14.26	0.10	0.02	1.16	53.72	97.39	Pyrophyllite
3 P2 3	GTD-11-201	537.5	5.27C	3	0.06	28.24	0.04	0.24	0.01	0.05	0.02	0.30	15.25	0.07	0.00	1.15	55.16	100.57	Pyrophyllite
3 P2 4	GTD-11-201	537.5	5.27C	4	0.07	26.96	0.03	0.07	0.03	0.10	0.02	0.15	14.36	0.15	0.06	1.16	52.98	95.96	Pyrophyllite
3 P2 5	GTD-11-201	537.5	5.27C	5	0.11	28.15	0.01	0.23	0.01	0.02	0.04	0.32	15.16	0.02	0.04	1.15	54.83	99.90	Pyrophyllite
3 P3 1	GTD-11-201	537.5	5.27G	1	0.07	28.13	0.00	0.15	0.03	0.16	0.03	0.25	14.82	0.07	0.02	1.15	54.75	99.57	Pyrophyllite
3 P3 2	GTD-11-201	537.5	5.27G	2	0.04	25.79	0.05	0.15	0.14	0.04	0.02	0.12	13.04	0.02	0.03	1.17	50.29	90.41	Pyrophyllite
7 P1 3	GTD-12-292	513	A2-4C	3	0.35	20.65	0.01	1.29	0.01	0.02	0.04	0.15	20.58	0.14	0.07	1.53	54.46	99.30	Illite
7 P2 3	GTD-12-292	513	5.30B; A2-4B	3	0.65	19.68	0.00	3.82	0.05	0.11	0.38	0.24	20.96	0.85	0.30	1.48	54.64	103.15	Illite
7 P5 1	GTD-12-292	513	A2-4G;4N	1	0.73	20.75	0.00	7.07	0.02	0.01	0.20	0.47	19.72	0.17	0.01	0.51	47.17	96.81	Muscovite
7 P5 2	GTD-12-292	513	A2-4G;4N	2	1.05	20.70	0.00	6.25	0.02	0.03	0.14	0.63	20.00	0.23	0.09	0.51	47.24	96.89	Muscovite
7 P5 3	GTD-12-292	513	A2-4G;4N	3	1.22	20.23	0.04	7.06	0.02	0.05	0.18	0.77	20.38	0.73	0.03	0.51	47.42	98.50	Muscovite
7 P5 4	GTD-12-292	513	A2-4G;4N	4	0.46	20.77	0.05	2.21	0.04	0.04	0.15	0.19	20.32	0.23	0.03	1.52	54.66	100.56	Muscovite-kaolinite
7 P4 1	GTD-12-292	513	5.30C	1	0.00	0.02	0.35	0.01	0.11	13.93	0.01	0.09	0.26	0.34	61.21	0.00	28.49	104.83	Barite

Table A2-2 Analytical conditions for EPMA sulfide analyses

Element/Line	Crystal	On peak time (s)	Off peak time (s)	Standard	Analytical error (rel %)	Detection limit (99 %)
S ka	PET	20	10	Marcasite (Astimex block)	0.59	0.034
Ag la	PET	20	13.5	Acanthite Ag_2S (A4)	56.21	0.069
Cu ka	LLIF	50	40	Cuprite (Astimex block)	0.13	0.032
Zn ka	LLIF	50	25	Sphalerite (Astimex block)	-27.22	0.038
Sb la	LPET	20	8	Stibnite (Astimex block)	60.51	0.042
As la	TAP	40	40	Gallium Arsenide (Astimex block)	-82.57	0.035
Fe ka	LLIF	50	40	Marcasite (Astimex block)	0.51	0.011
Se la	TAP	30	13.5	Zinc selenide ZnSe (A12)	39.97	0.046
Te la	LPET	20	9	Bismuth telluride Bi_2Te_3 (A2)	37.71	0.037
Pb ma	PET	20	20	Pb metal (Pb-Co block)	80.07	0.094
Sn la	LPET	20	10	Cassiterite (Astimex block)	48.14	0.041
V ka	LLIF	20	9	V metal (Cameca block)	-233.85	0.026
Mn ka	LLIF	30	20	Bustamite (Astimex block)	-333.51	0.017

Table A2-3 Analytical conditions for EPMA alteration mineral analyses

Element/Line	Crystal	On peak time (s)	Off peak time (s)	Standard	Analytical error (rel %)	Detection limit (99 %)
F ka	PC0	20	25	Topaz (UTAS4 block)	-285.68	0.080
Si ka	TAP	8	6	Clinopyroxene, Delegate (UTAS1 block)	-77.44	0.041
Sr la	TAP	15	14	$SrTiO_3$-Nb (UTAS4 block)	21.73	0.058
K ka	PET	10	10	Microcline (UTAS3 block)	2.16	0.048
Ca ka	PET	10	10	Clinopyroxene, Delegate (UTAS1 block)	-789.02	0.045
S ka	LPET	10	10	Celestite (Astimex block)	1.19	0.037
P ka	LPET	10	10	Apatite Durango (Apatites block)	29.29	0.021
Na ka	TAP	8	4	(K-)Anorthoclase, Kakanui, USNM133868 (UTAS3 block)	6.20	0.075
Al ka	TAP	8	6	Plagioclase, Labradorite, USNM115900 (UTAS1 block)	0.93	0.046
Fe ka	LLIF	10	10	Hematite (Astimex block)	25.21	0.059
Ba la	LLIF	30	30	Baryte (Astimex block)	321.13	0.105

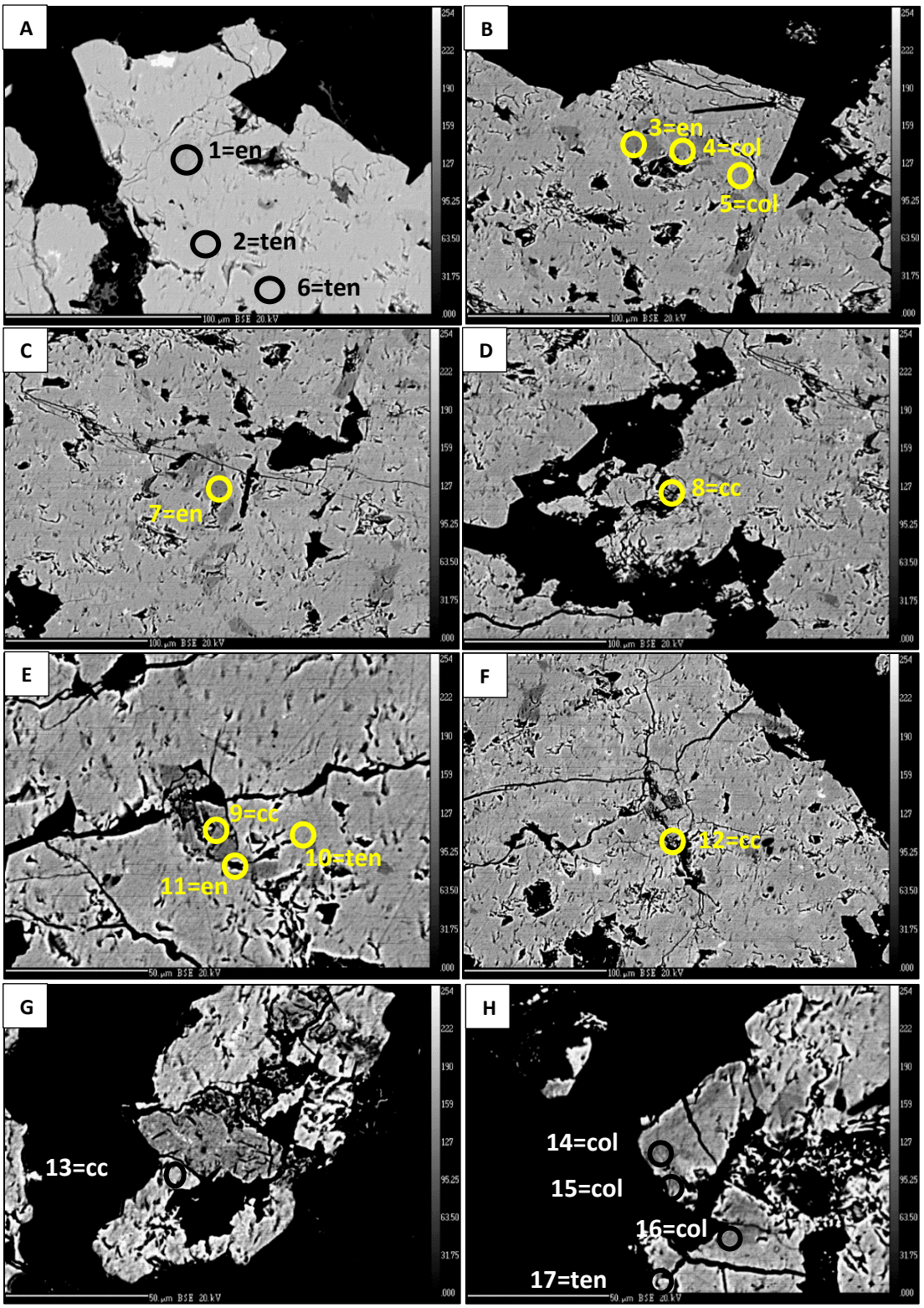

Figure A2-1. Photomicrographs and probe positions (black and yellow circles) of sulfides from drillhole GTD-09-112: 185.75 m, 173877 mE, 9046141 mN. Enargite, tennantite and colusite have overprinted chalcocite and covellite in HSE-2 veins in phase 2 diorite. A-H Probe sample IDs 43005_13_GTD-09-112_185_75m_1 to 43005_13_GTD-09-112_185_75m_17. All EPMA data listed in Table A-2. Abbreviations: cc = chalcocite, col= colusite, en = enargite, ten = tennantite.

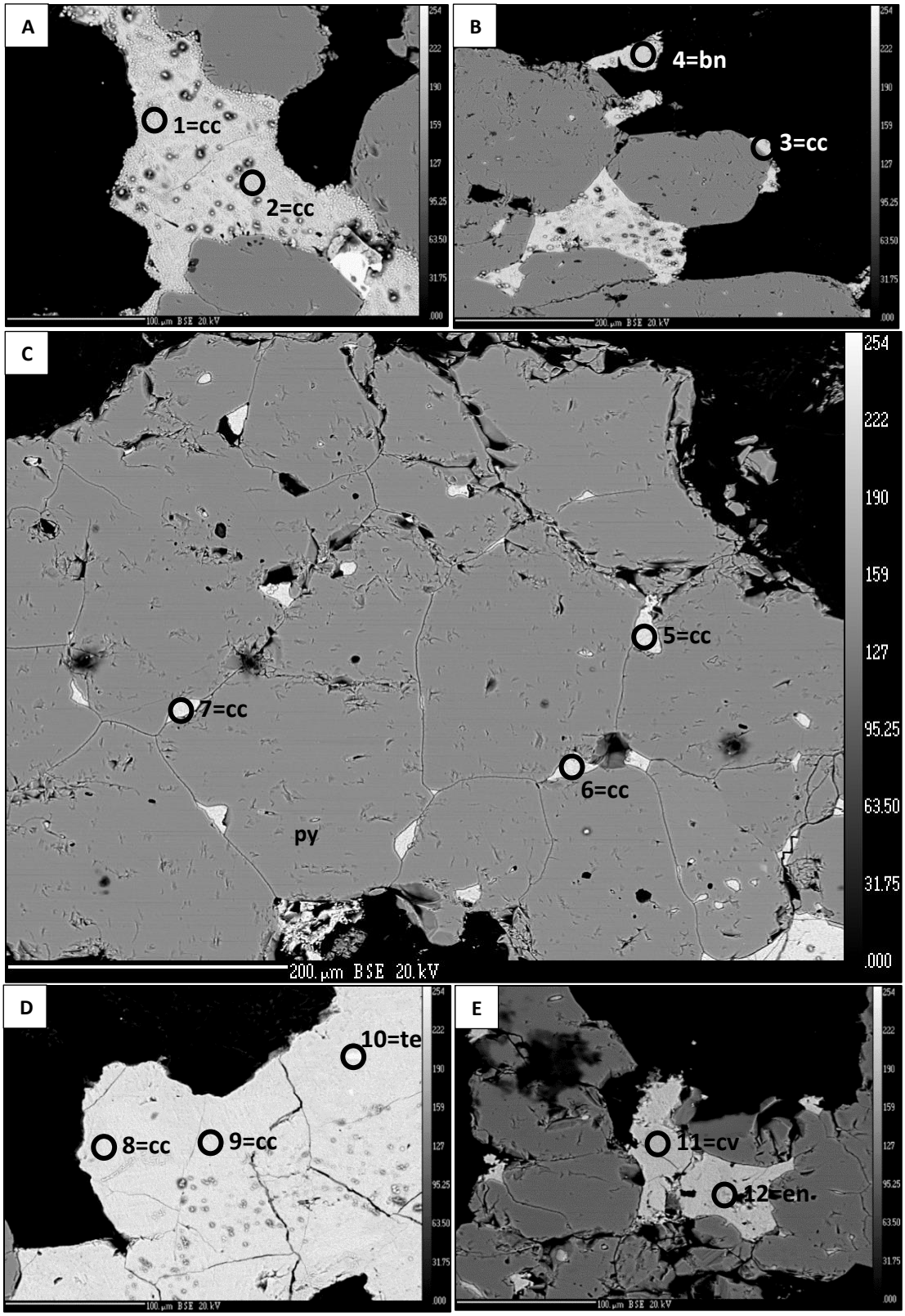

Figure A2-2. Photomicrographs and probe positions (black circles) of sulfides from drillhole GTD-10-137: 829.7 m, 175020 mE, 9045397 mN. Chalcocite, bornite, covellite and enargite have infilled fractures and coated pyrite in HSE-2 veins. Minor telluride inclusions detected in chalcocite. All EPMA data listed in Table A-2. Abbreviations: bn = bornite, cc = chalcocite, cv = covellite, en = enargite, te = telluride.

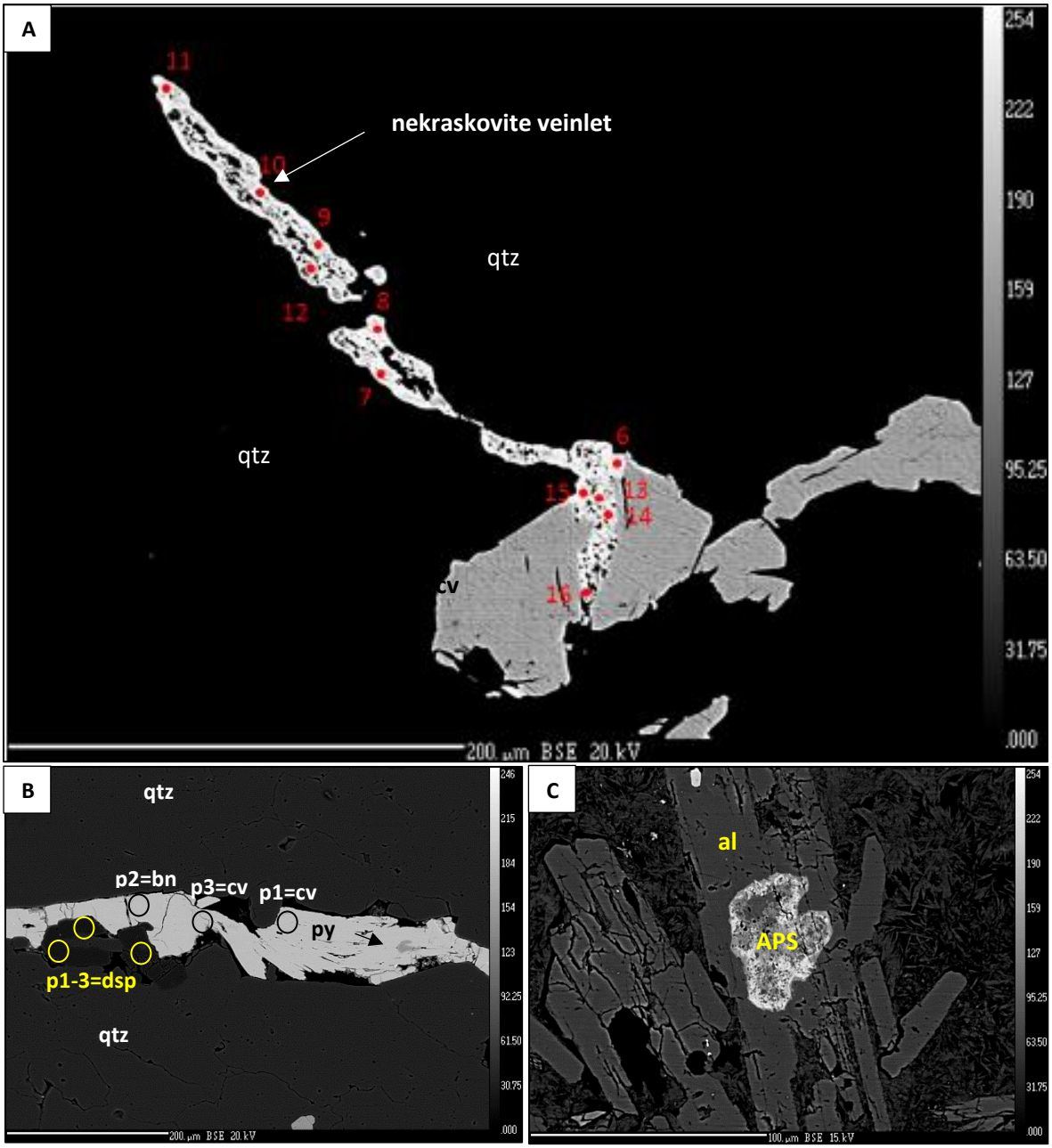

Figure A2-3. Photomicrographs and probe positions (black and red circles = sulfide analyses; yellow circles = alteration mineral analyses) A) Drillhole GTD-11-201: 537.5m: 174155 mE, 9046097 mN; phase 5 tonalite with pyrite - chalcopyrite - bornite - digenite - covellite and quartz - pyrophyllite - K-alunite - dickite/kaolinite; P4 late Sn-As-Cu-Fe bearing veinlet (nekrasovite) has crosscut quartz and a grain of covellite; B) 3_GTD-11-201_537-5m_P1 covellite - bornite - pyrite veinlet with diaspore; C) 3_P1_Sr-Ca-APS. All EPMA data listed in Table A-2. Abbreviations: al = alunite, APS = aluminium phosphate sulfate, bn = bornite, cv = covellite, dsp = diaspore, py = pyrite, qtz = quartz.

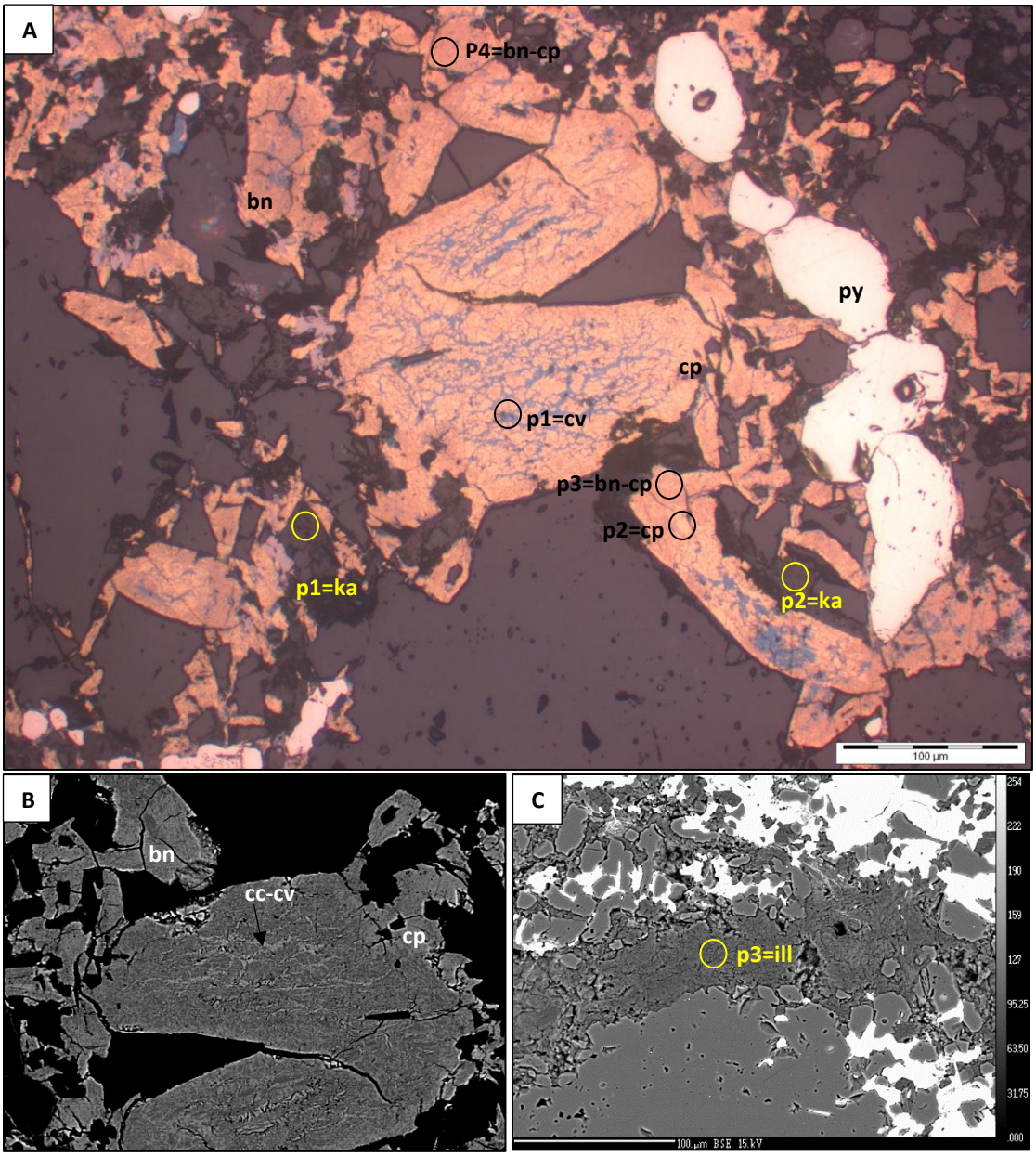

Figure A2-4. Photomicrographs and probe positions (black circles = sulfide analyses; yellow circles = alteration mineral analyses) from quartz stockwork B-type vein crosscut by pyrite vein with chalcopyrite - bornite - chalcocite - covellite overprinted by enargite in quartz - white mica - kaolinite altered andesitic rock crosscut by fine-grained phase 5 tonalite porphyry. Drillhole GTD-12-292 513m 174082 mE, 9046550 mN. A) P1 20x magnification; chalcopyrite grains with fractured cores converted to bornite then chalcocite with kaolinite; B) Photomicrograph 40x magnification chalcopyrite cores converted to bornite with chalcocite and covellite along fractures in grain; C) Illite vein. All EPMA data listed in Table A-2. Abbreviations: bn = bornite, cc = chalcocite, cp = chalcopyrite, cv = covellite, ill = illite, py = pyrite, qtz = quartz.

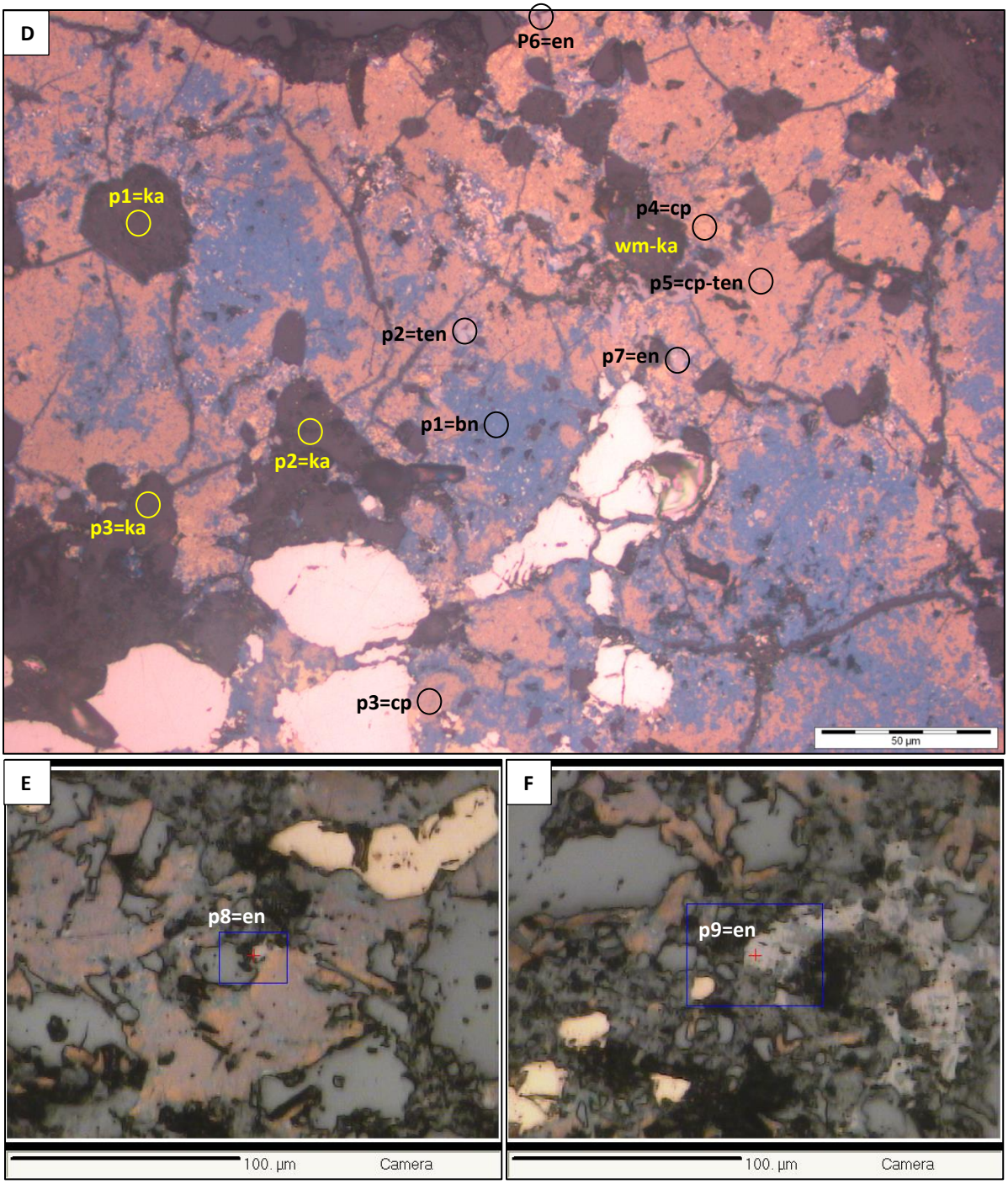

Figure A2-4 *(contd.)* D) p3 40x chalcopyrite - bornite - chalcocite - covellite overprinted by enargite and tennantite; E) P8 large enargite grain; F) P9 enargite overprinting chalcopyrite - bornite - chalcocite. Abbreviations: bn = bornite, cc = chalcocite, cp = chalcopyrite, cv = covellite, en = enargite, ill = illite, ka = kaolinite, py = pyrite, qtz = quartz, ten = tennantite, wm = white mica.

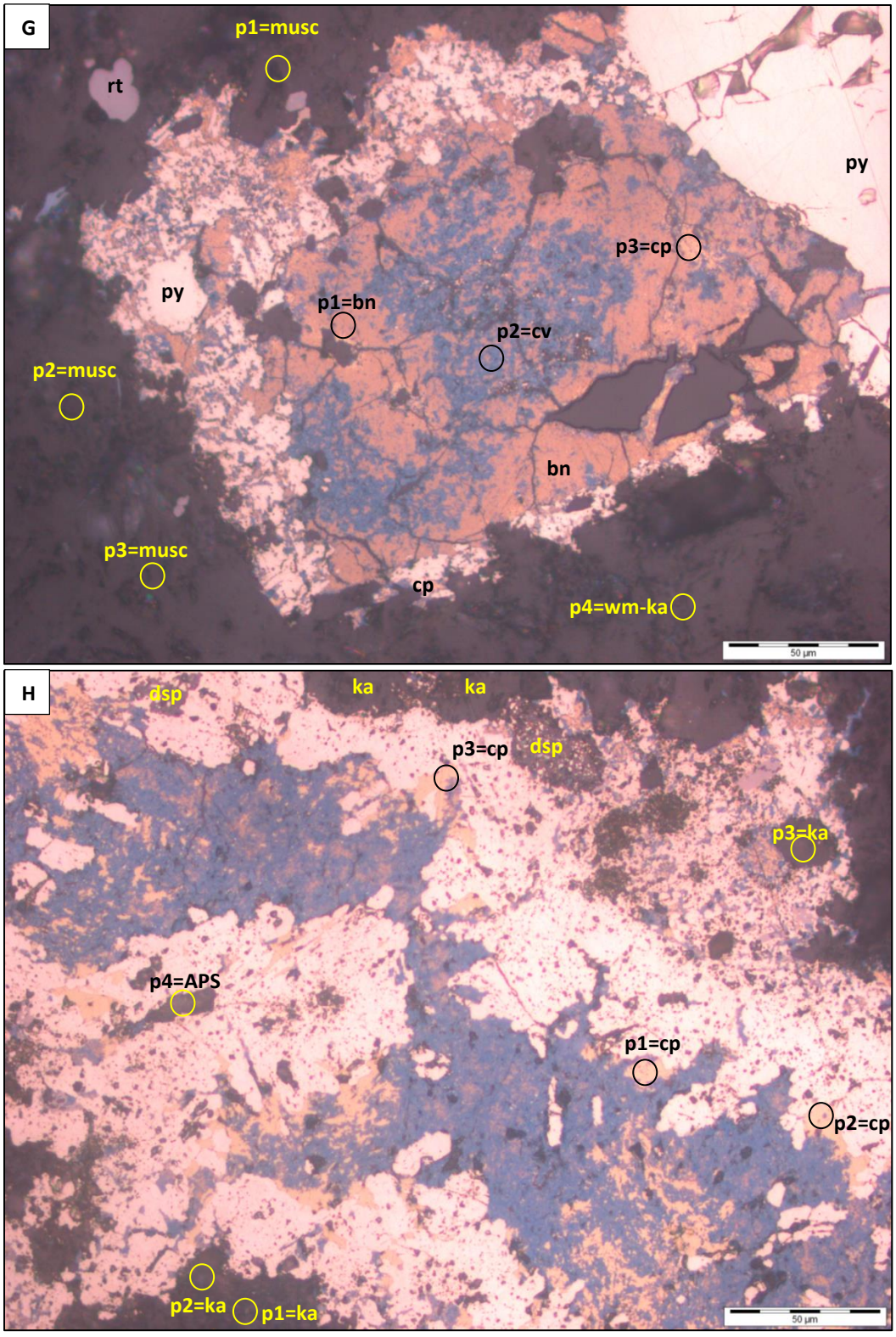

Figure A2-4 *(contd.)* G) p5 40x magnification pyrite rim. Chalcopyrite grain converted to bornite, chalcocite and covellite; muscovite - kaolinite alteration; H) p6 40x magnification; chalcopyrite preserved, partly converted to bornite and chalcocite; no As overprint. Abbreviations: bn = bornite, cc = chalcocite, cp = chalcopyrite, cv = covellite, dsp = diaspore, en = enargite, ill = illite, ka = kaolinite, musc = muscovite, py = pyrite, qtz = quartz, rt = rutile, ten = tennantite, wm = white mica.

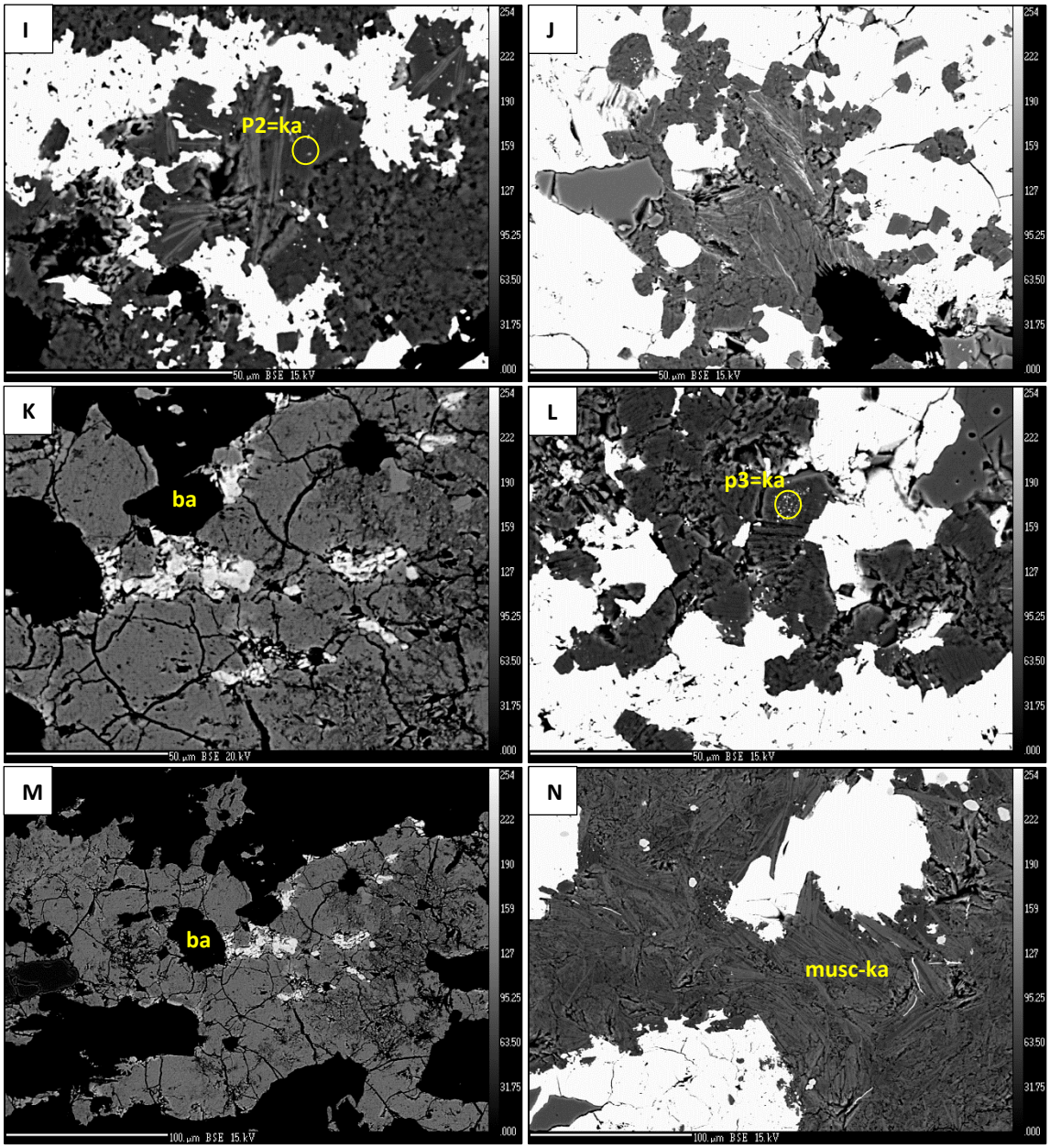

Figure A2-4. *(contd.)* I) 7_P2_alt_minerals kaolinite has replaced K-bearing white mica; J) 7_P3_alt_minerals; K) 7_GTD_12-292_513m_P4_baryte_BSE; L) 7_P4_alt_minerals; M) 7_P4_baryte; N) 7_P5_alt minerals; white mica - kaolinite intergrowths. Abbreviations: ba = barite, ka = kaolinite, musc = muscovite.

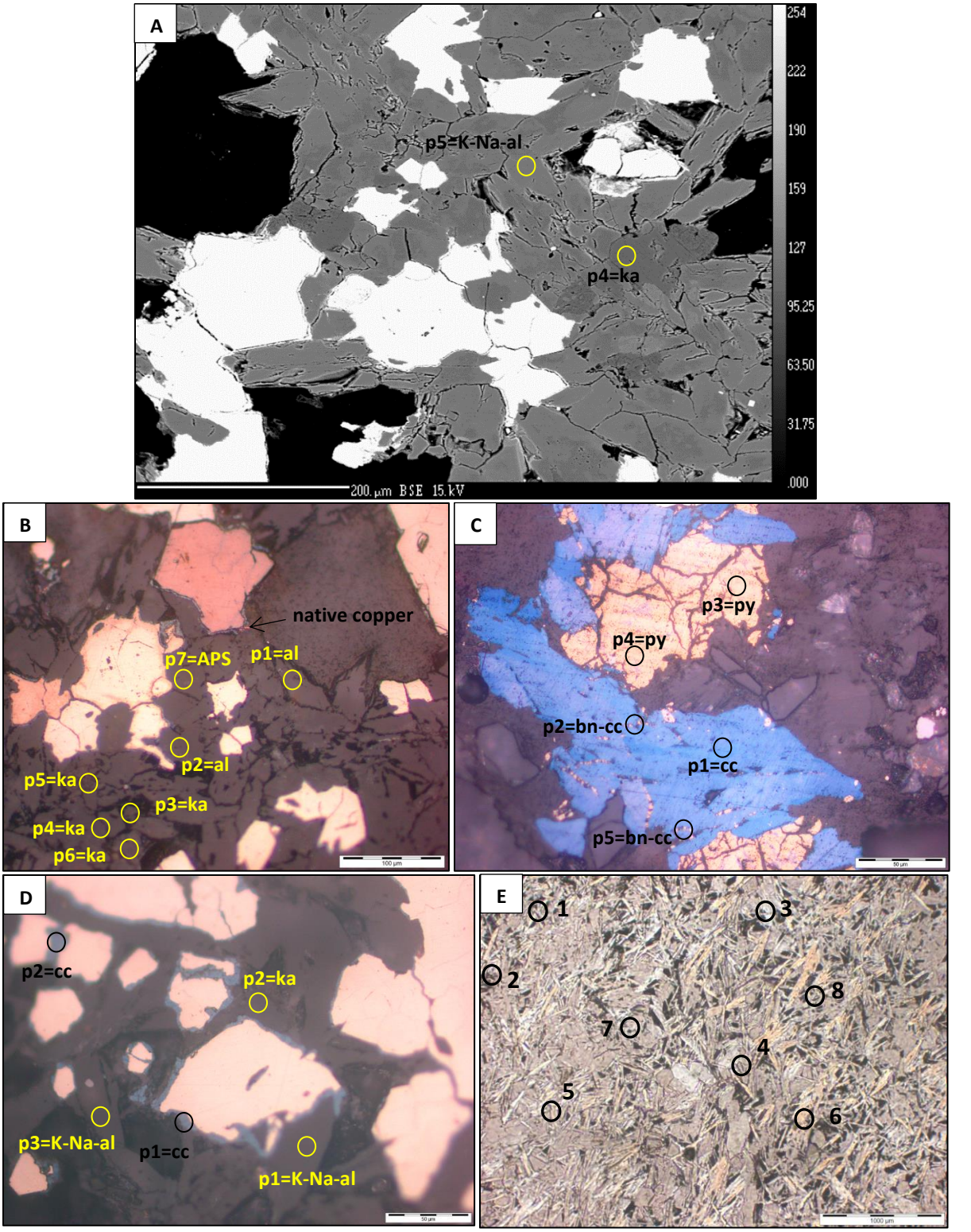

Figure A2-5. Photomicrographs and probe positions (black circles = sulfide analyses; yellow circles; alteration minerals) from Drillhole GTD-11-201: 177.4m, 174155 mE, 9046097 mN. A) 11_P1_alt_minerals; K-Na alunite and kaolinite. B) Kaolinite and alunite with APS inclusions. C) 537.5m P4 bornite with incipient chalcocite and covellite. D) Pyrite grains with chalcocite rims; Na-K alunite and kaolinite. E) Sample 43002.27: drillhole GT012 298 m, 174494mE, 9046597mN: acicular K-Na alunite crystals and APS minerals. All EPMA data listed in Table A-2. Abbreviations: al = alunite, cc = chalcocite, ka = kaolinite.

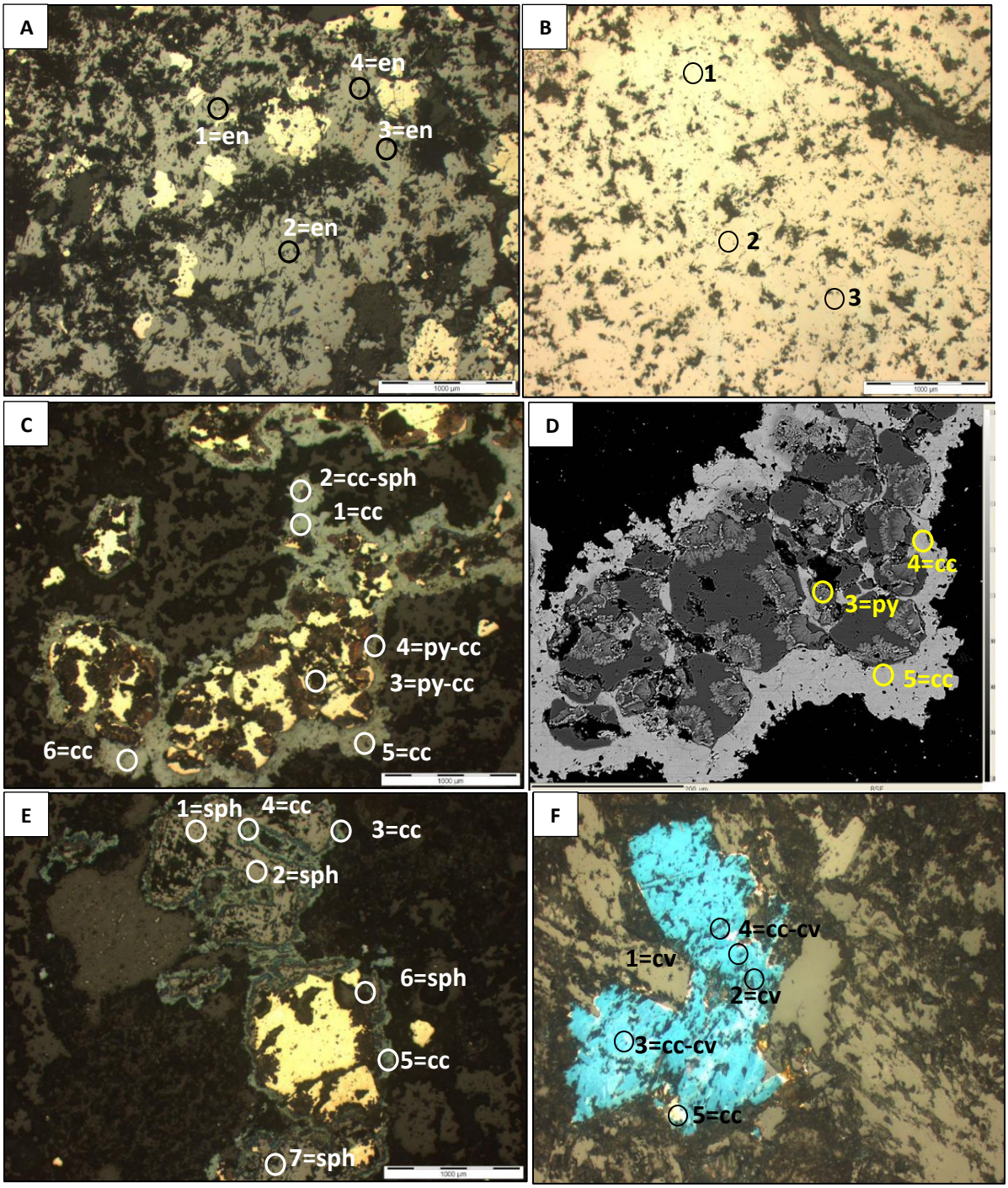

Figure A2-6. Photomicrographs and probe positions from A) Sample 43003.20: drillhole GTD-08-35: 634m: enargite, grey and pink zones with pyrite B) Sample 43005.4: drillhole GTD-09-78: 53 m, 174984mE, 9045284mN: massive enargite C) Sample 43001.20 P1: drillhole GT011, 201 m, 173837mE, 9046060mN, chalcocite coating pyrite - sphalerite vein. D) Sample 43001.20 P2: drillhole GT011: 201 m, 173837mE, 9046060mN, chalcocite coating pyrite - sphalerite vein. E) Sample 43003.20 p2: drillhole GTD-08-35: 622.1 m, 174080mE, 9046551mN: chalcocite coating pyrite and sphalerite vein. F) Sample 43003.19 p2: drillhole GTD-08-35: 622.1 m, 174080mE, 9046551mN: chalcocite - covellite grain. All EPMA data listed in Table A-2. Abbreviations: cc = chalcocite, en = enargite, py = pyrite, sph = sphalerite.

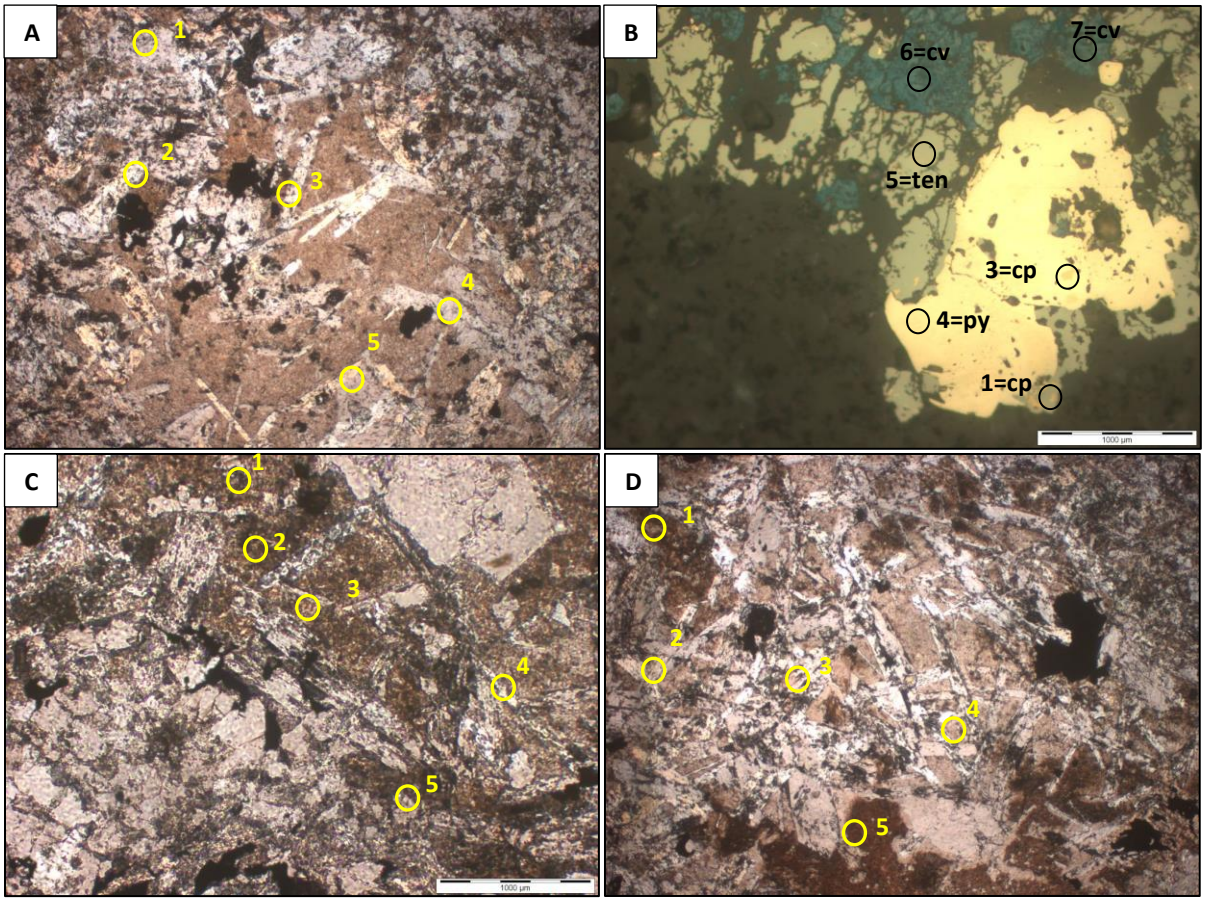

Figure A2-7. Photomicrographs and probe positions (black circles = sulfide analyses; yellow circles; alteration minerals) A) 43003.19 p3, drillhole GTD-08-35: 622.1 m, 174080mE, 9046551mN: acicular alunite crystals B) 43002.06: drillhole GT001B: 157.5 m, 174537 mE, 9046858 mN: tetrahedrite-tennantite (grey) with inclusions of chalcopyrite (yellow); grey phase is overprinted by covellite (blue). C) 43003.19 p1 drillhole GTD-08-35: 622.1 m, 174080mE, 9046551mN: alunite needles for probe_comp D) 43003.19 p2 drillhole GTD-08-35: 622.1 m, 174080mE, 9046551mN acicular alunite crystals. All EPMA data listed in Table A-2. Abbreviations: cp = chalcopyrite, cv = covellite, py = pyrite, ten = tennantite.